The Structural, Metamorphic and Thermal History of the Sonnblick Dome, southeast Tauern Window, Austria.

Steven Michael Reddy

Submitted in fulfilment of the requirements

for the degree of Doctor of Philosophy

Department of Earth Sciences

The University of Leeds, U.K.

July 1990.

Abstract

Within the southeastern Tauern Window, the Sonnblick Dome is a large, NE-verging, antiformal structure composed of orthogneisses of the Zentralgneis Complex. This unit represents part of the European crystalline basement, or Penninic domain, over which the Adriatic microplate was thrust during Alpine continental collision.

The igneous precursors to the gneisses formed as granitoids above a subduction zone during the Hercynian. During Alpine continental collision, overthrusting of the African-derived Austroalpine units toward the northwest produced a foliation that becomes more intense towards the tectonic contact of the gneiss and the overlying Peripheral Schieferhülle. This foliation was folded during the formation of the Sonnblick Dome, which is interpreted to have developed during progressive top-to-NW shearing in the hangingwall of an oblique ramp.

Shear zones also developed oblique to the northwest transport direction and led to imbrication in the basement. These shear zones are commonly marked by retrogression of the primary mineralogy and the development of mica-schists. Although this alteration is associated with syn-deformational fluid infiltration, a spatial relationship between reaction site and deformation suggests that the energy associated with deformation contributed to reactions during shear zone formation.

As a response to tectonic thickening, pressures and temperatures in the Pennine basement increased. Peak Alpine metamorphic conditions are estimated to be 540±50°C and 8±1kbar and probably represent conditions developed during uplift from initially greater depths. White mica isotopic ages suggest that the peak of metamorphism took place at 25-28Ma, with older ages being observed towards the southeastern end of the Dome. Post-metamorphic cooling rates appear to be variable throughout the Dome, with faster rates being found for the southeastern end of the Dome. After 20Ma ago, cooling rates around the Dome became more uniform (17-27°C/Ma). Rapid cooling rates in the area are associated with rapid, post-metamorphic uplift rates. These were probably accomodated by gravity-driven extension of the tectonically thickened crust. Evidence for post-metamorphic extension is represented by ductile shear bands, which are associated with thinning of the more micaceous units found at higher levels in the Dome.

This thesis is dedicated to the memory of my father,
who gave me 25 years of support, encouragement
and friendship, and is greatly missed.

Acknowledgments

First of all, thanks to Bob Cliff and Andy McCaig for supervision over the last few years and for returning earlier drafts of chapters before the ink had time to dry. Special thanks must go to Andy for taking time out in Austria to teach me the finer points of rally driving. Thanks must also go to Rob Knipe, Gareth Davies and Bruce Yardley for providing helpful comments on various aspects of this thesis. Giles Droop, Jan Behrmann and Jorn Kruhl are thanked for discussing various aspects of Eastern Alpine geology both in and out of the field.

Many, many thanks to Franz, Hilde, Franz Jr. and Monica Grüber for being invaluable friends in Austria and for introducing me to the 'joy of Schnappes'. Die Familie Öberbucher in the Weißseehaus are also thanked for their hospitality and their ability to produce excellent Kaisersmarrn. Emma Postlethwaite and Chiu Wong are thanked for being mad enough to be field-assistants and Bob East and Paul Schofield are thanked for dragging me out for a beer occasionally.

Rod Green has provided not only excellent advice on 'what to do in the lab' (or should that be 'not what to do in the lab'), but kept us smiling while we did it. Both he and Phil are thanked for letting me win at darts. Tom and Dennis are thanked for teaching me the art of mineral separation and Alan Gray taught me how to drive the XRF. Colin, Keith and Mary from the section lab are thanked for excellent 'thins' and the ability to cope with the 'rush job'. Thanks to Dave Rex and Phil Guise for my single Ar sample.

I'd like to thank all the postgrads at Leeds for making life at Leeds so enjoyable. In particular Graham, Keith, Pete Bentham, Andy Farmer, Pete Bishop, Troy, Neil and Lochy have provided innumerable excuses for popping down to the Fav.

Pete Bishop has proved to be a first class editor, organiser and general dogsbody in the last stages of the writing-up and is greatly appreciated. Thanks also to Jo, Alison, Soph, The Andys (B+F), Rowena, Lochy, Neil and Simon for help in the final stages of this thesis. Apologies to anyone that I have forgotten to mention.

Karen is thanked for putting up with me over the last few months and for helping with colouring, compiling and with life in general. I appreciate it.

This thesis would not have been possible without the unending moral and financial support of my family, and especially my parents, for the last 25 years. I am eternally grateful to them.

The project was carried out under the tenure of a NERC post-graduate studentship, financed by NERC, my parents and the DSS.

Table of Contents

Chapter 3

Rock Types Within the Sonnblick Dome.

Chapter 4

The Structural History of the Sonnblick Dome.

Chapter 5

Metamorphism in the Sonnblick Dome

Chapter 6

Metasomatic Shear Zone Development within the Sonnblick Gneisses.

Chapter 7

Geochronology of the Sonnblick Dome.

Chapter 8

Appendices

Mineral Abbreviations used within this Thesis

ab = albite
alm = almandine
amph = amphibole
an = anorthite
ann = annite
bte = biotite
cel = celadonite
chl = chlorite
clin = clinochlore
ctd = chloritoid
cz = clinozoisite
daph = daphnite
east = eastonite
ed = edenite
ep = epidote
gr = grossular
gt = garnet
ksp = K-feldspar
mu = muscovite
naph = Na-phlogopite
pa = paragonite
phl = phlogopite
py = pyrope
qtz (or q)= quartz
sp = spessartine
wm = white mica

Chapter 1

Introduction

The dynamic and kinematic development of a mountain belt will be strongly dependent upon the interaction of the structural, metamorphic and thermal histories of the belt and therefore, a multidisciplined approach is required to fully understand their development during continental collision.

The general rheological stratification within the crust will have an important significance on the localization of deformation and the structural development of the mountain belt, while changes in the lithospheric thermal structure with time will have implications for the overall mechanical and rheological evolution of the crust and the way in which stress and strain localization varies temporally during continental collision. The mechanical behaviour of the crust will also be significantly affected by the presence of a fluid phase and it is important to understand the pathways by which this fluid passes through the crust and the processes by which fluid and rock interact. The study of the mutual interaction of deformation and metamorphic processes during fluid-rock interaction are also fundamental considerations and have implications for many other fields of geology.

In these respects, the mid-crust is an important area for the study of tectonic processes since it is this area, across which a transformation from dominantly brittle to dominantly plastic deformation processes takes place. In order to understand the processes taking place within the middle crust during continental collision, it is important to be able to constrain deformation and thermal histories.

1:1 Objectives of the Study

This thesis is an integrated geological project which examines the structural, metamorphic and thermal development of the Sonnblick Dome within the Penninic Zentralgneis Complex of the southeast Tauern Window, Austria in order to assess the geological evolution of an area of that underwent orogenic processes at mid-crustal levels during Alpine continental collision. Such a study is of interest since it may aid the future understanding of the larger scale dynamics and kinematics of the Alpine mountain chain and provide a framework in which the processes associated with continental

collision, at mid-crustal levels and during continental collision, may be studied and assessed.

The major objectives of the study are:-

1) To investigate the structural evolution of an area of gneissic basement and construct a deformation history for the area.

2) To constrain the pressure-temperature (P-T) history of the Sonnblick Dome using standard metamorphic petrological and thermobarometric techniques, in combination with radiometric dating in order to constrain the metamorphic history and the retrograde cooling path and to delimit uplift and cooling rates for the area.

As part of this study, the effects of fluid infiltration and fluid-rock interaction within actively deforming and metamorphosing mid-crustal rocks has been investigated so that some of the processes associated with deformation within the mid-crust during continental collision could be established.

1.2 Fieldwork Logistics and Methodology

The Sonnblick Dome in the south east Tauern Window of Austria is a mountainous region of the Eastern Alps with an area of about 100km^2 which varies topographically from 600 metres to over 3000 metres. The domed morphology of the area enables in excess of 3km of structural level to be observed directly, and provides an excellent section through an area of crust which lies only a few kilometres below a major thrust zone between the Pennine and Austroalpine basement.

Three fieldseasons, totalling 28 weeks fieldwork, were undertaken in the Sonnblick area. The aims of this fieldwork were to differentiate primary igneous units within the Sonnblick orthogneiss complex from deformation-induced lithological variations and to map out areas of differing deformation intensity within the gneisses to constrain the distribution of strain within the gneiss complex. The structural history of the area was to be deduced and combined with detailed microstructural studies on samples collected during the fieldwork to develop a model for the structural evolution of the Sonnblick Dome. Samples for metamorphic, geochemical and geochronological studies were also to be collected.

The first season (6 weeks) comprised reconnaisance mapping of the Dome in order to identify the best area for more detailed work in the subsequent seasons. Several sections through the Dome were traversed along road sections extending up from the Mölltal. In the second (13 weeks) and third (9 weeks) seasons, mapping in the centre of the Dome was undertaken. An area of approximately 8km^2 has been mapped across the Dome from the Peripheral Schieferhülle at Baumbach Spitze in the north to the Peripheral Schieferhülle of the Rote Wand in the south. The mapped area lies close to the centre of the Dome and was chosen as the best area to map for several reasons. The area is quite high and consequently well exposed, although this exposure is often inaccessible due to the mountainous terrain. The Duisbürger Hütte and the Weißseehaus provide accomodation within the area, the latter was used as a base camp for much of the time spent in the field. The recently reconstructed road along Fraganttal to the Weißsee (the 'Panoramastraße') allows rapid, easy access to theWeißseehaus at a height of 2400m.

Fieldslips used in this work were 1:10,000 enlargements of 1:50,000 topographic maps (sheets 154, 155, 180, 181) and were supplied by the Geologische Bundesanstalt, Wien. In areas where more detailed mapping was required, fieldslips were enlarged by hand. Notebook and sample localities were recorded directly onto the fieldslips and the height above sea level was recorded using an altimeter. The altimeter was periodically corrected throughout the day to account for drift associated with changing atmospheric conditions. Grid references relate to those published on the 1:25,000 Alpenverein map (No. 42) of the Sonnblick area and are marked on plate 1.

The original 1:50,000 topographic maps and the 1:25,000 Alpenvereins and Kompass maps of the Sonnblick area fail to give any declination correction and all orientation measurements are therefore to magnetic north.

A total of 687 samples were collected and where possible, these were oriented. Orientation of samples basically follows the methodology of Prior *et al* (1987) except that dip and dip azimuth were recorded insted of dip, strike and dip direction. Structural data, throughout this thesis, are presented using this convention. Specimen numbers are sequential and consist of the specimen number and the year of collection (eg. sample number / year collected). Samples numbers referred to in the text which do not have a 'year of collection' label, refer to a thin section catalogue number.

1:3 Laboratory Methods

All laboratory work and sample preparation was undertaken at the University of Leeds and included X-ray fluorescence (XRF), Rb-Sr isotope analyses, plus electron microprobe and microscopy techniques. The details of sample preparations and analytical techniques are given in Appendices 1 and 2.

1.4 Thesis Layout

Chapter 2 provides an introduction to Alpine and Eastern Alpine geology and gives a brief review of previous work carried out in the southeast Tauern Window. This establishes the framework in which this study is set. The different rock types within the Sonnblick Dome and the rationale behind the chosen lithological divisions are discussed in Chapter 3. This chapter also briefly describes the Schieferhülle rocks observed in the vacinity of the mapped area and presents some geochemical data on the Sonnblick orthogneisses.

The structural history of the Dome in terms of the different structural levels within the Domeis discussed in Chapter 4. Evidence is provided on a variety of scales to develop the structural evolution of the Dome and to relate this temporally to the Alpine metamorphic peak. The structural history is discussed and a model is presented which accounts for the observed structural history.

Chapter 5 considers the metamorphic evolution of the Sonnblick area and presents data showing a polyphase history within some of the Sonnblick lithologies. The conditions of metamorphism are assessed from petrological considerations and from thermobarometric techniques. Applied thermobarometric techniques are discussed and the results are assessed.

The importance of the relationship between deformation and metamorphism are illustrated in Chapter 6, which describes geochemical, petrographical and microstructural data collected from a strongly altered metasomatic shear zone within the basement complex. The interaction of deformation and metamorphism associated with fluid rock interaction are discussed.

Chapter 7 presents geochronological data from the Sonnblick area. Rb-Sr mineral data are used to constrain the uplift and cooling path of the gneisses and constrain the

retrograde PTt path of the Dome. Isotopic data from the shear zone studied in Chapter 6 is presented and discussed in terms of the timing of metamorphism and deformation.

Chapter 8 discusses the major conclusions from this study and identifies some areas of further research which have resulted from this study.

Chapter 2
The Geological Framework of the Alps

2:1 Introduction

The Alpine mountain belt is a recently exposed orogenic zone which extends from the Atlantic in the west to join the Dinarides and Carpathian mountains in the east. The belt is associated with Mesozoic basin development and later continental collision due to relative movements between the European and African lithospheric plates and the minor plate known as Adria. The fact that the mountain belt is recently exposed coupled with its small size and easy logistical and political access, relative to other young orogenic belts such as the Himalayas, makes the Alps an excellent example for the study of orogenic processes associated with continental collision. Over 150 years of research in the Alpine area (reviewed by Hsü 1989) has led to the acquisition of a huge data base which has helped to establish some of the basic tenets of modern geology. However, there are still many controversies and problems in terms of Alpine geological structure, kinematics and evolution (eg. Coward and Dietrich 1989) which are still generating interest (eg. Coward *et al* 1989).

The Alpine belt comprises numerous rock types, such as crystalline continental basement material, oceanic crustal material and various sedimentary facies, which range from relatively undeformed, unmetamorphosed cover sediments to polyphase deformed and metamorphosed rocks uplifted from depths of up to 100km (Chopin 1984, 1987; Goffé and Chopin 1987). The Alps have been subdivided into four main palaeogeographical and structural domains (Frey *et al* 1974 and Figure 2.1) which are defined largely on Mesozoic sedimentary facies.

1) **The Dauphiné-Helvetic domain.** Mesozoic cover sediments in the Helvetic Domain were deposited on the northern continental margin of Tethys and consist of Lower and Middle Jurassic shales, sandstones and limestones upon which Upper Jurassic limestones were deposited. Lower Cretaceous limestone-shale facies and Upper Cretaceous pelagic limestones of the Helvetic domain were in turn covered by Eocene to Lower Oligocene flysch deposits (Trümpy 1980). Mesozoic sediments were deposited on a pre-Westphalian basement comprising paraschists, granitic gneisses, migmatites, amphibolites, marbles and rare slices of ultrabasic rocks with abundant Hercynian granites. Basement complexes belonging to this domain are the Argentera, Pelvoux, Belledonne, Mt. Blanc, Aiguilles Rouge, Gotthard and Aar massifs.

Figure 2.1 SKETCH MAP OF THE GEOLOGIC-TECTONIC UNITS IN THE ALPS

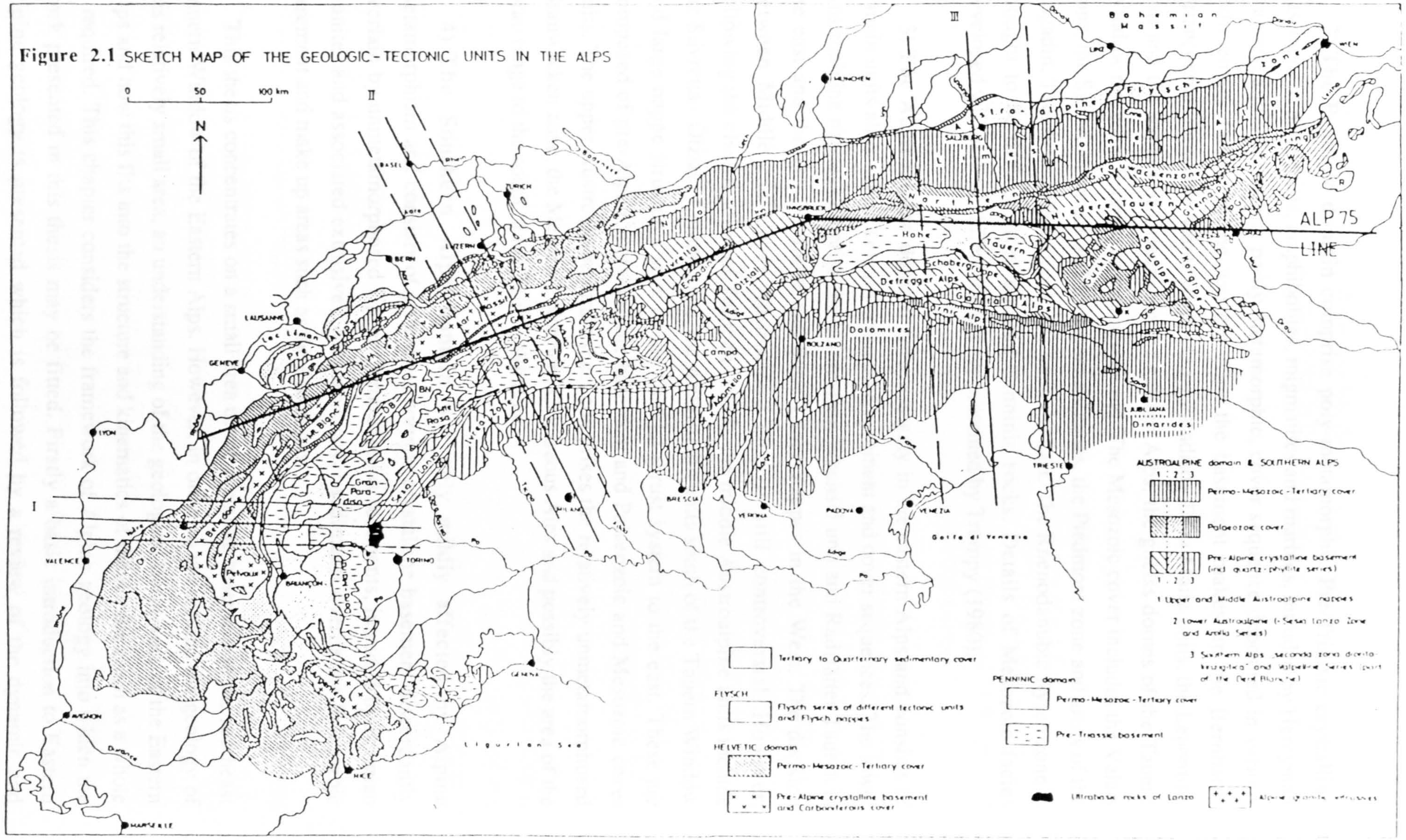

Fig. 1. Sketch map of the geologic-tectonic units in the Alps (after Frey et al., 1974).

2) **The Penninic domain** comprise poly-metamorphic Pre-Triassic crystalline basement of paraschists, amphibolites, migmatites and marbles, intruded by Hercynian granites, and a Mesozoic, partly metamorphic, cover sequence deposited in various sedimentary facies. In the western Alps the basement makes up the Bernhard-Briançonnais units, the Monte Rosa - Gran Paradiso - Dora Maira units, the Lepontine unit and the nappes of Grisons. In the eastern Alps, the gneiss domes of the Tauern Window represent Pennine basement material. The Mesozoic cover includes the Valais zone, the Subbriançonnais and Briançonnais zones, the Piédmont zone and areas of the Engadin, Tauern and Rechnitz Windows in the east. The Rhenodanubic flysch zone is thought to be derived from uplifted Penninic rocks. Details of Mesozoic facies developed within these different areas are presented by Trümpy (1980).

3) **The Austroalpine domain** occurs largely in the eastern Alps and consists of 3 main units all of which contain crystalline basement and cover sequences. The lower Austroalpine nappes comprise the Semmering-Wechsel unit and Radstätter Tauern in the east and the Dent Blanche and Sesia-Lanzo nappes in the West. The division between Middle and Upper Austroalpine units is still controversial. However, following the classification of Tollman (1977), the middle Austroalpine units include the Silvretta - Ötztal - Campo units, the Altkristallin units south of the Tauern Window and large nappe structures such as the Gurktal thrust system to the east. These are composed of pre-Alpine metamorphic basement and Palaeozoic and Mesozoic cover units. The upper Austroalpine thrust sheet comprises the relatively unmetamorphosed Grauwacken zone, the Mesozoic Northern Calcareous Alps and possibly the area of the Drau range to the south of the Tauern Window.

4) **The Southern Alps domain** was only mildly affected by Alpine metamorphism and consists of poly-metamorphic crystalline basement discordantly overlain by unmetamorphosed Upper Carboniferous sediments, intruded by Permian granites and associated extrusives. Mesozoic cover sediments overlie the Palaeozoic basement and make up areas such as the Dolomites.

This thesis concentrates on a small area of the Penninic basement in the southeast Tauern Window of the Eastern Alps. However, in order to understand the geology of this relatively small area, an understanding of the geological framework of the Eastern Alps and how this fits into the structure and kinematics of the Alpine chain as a whole is required. This chapter considers the framework of Alpine geology into which the work presented in this thesis may be fitted. Firstly a basic introduction to Eastern Alpine geology is presented which is followed by a review of the dynamic and

kinematic development of the Alpine chain. An introduction to the southeast Tauern Window and to previous work carried out in the Sonnblick area is given at the end of this chapter.

2:2 The Geology of the Eastern Alps

2:2.1 Introduction

An outline of the geology of the Eastern Alps has been given by a number of authors in the recent past (eg. Oxburgh 1968; Tollman 1977; Janoschek and Matura 1980). However, at present major controversies still exist (as illustrated by Flügel and Faupl 1989) and no unifying model for Eastern Alpine evolution exists.

The Eastern Alps form an east-west oriented mountainous range which represents the eastward continuation of the Swiss Alps towards the Vienna and Pannonian basins of eastern Austria and Hungary. Two major geological units make up the Eastern Alps, the structurally lower Pennine complex which is found as a series of tectonic windows beneath the tectonically emplaced Austroalpine units of the Adriatic Peninsula (Figure 2.2a). These two units are bounded to the north by molasse deposits situated on the southern margin of the Bohemian Massif, and a thin, discontinuous strip of material belonging to the Helvetic Domain. In the south, the Periadriatic Lineament marks the boundary with the Southern Alps.

The general characteristics of the Pennine and Austroalpine domains have been mentioned earlier. However, in order to set the framework for the study of the Sonnblick area of the Pennine domain, the geology of these units and their relationship to each other is expanded.

2:2.2 The Austroalpine Domain

The Austroalpine unit occupies the highest tectonic position in the Eastern Alps and has classically been considered to be comprised of three units, the Lower Austroalpine, the Middle Austroalpine and the Upper Austroalpine. Each subdivision of the Austroalpine has a Pre-alpine crystalline basement and a Palaeozoic-Mesozoic cover. Although the relationships between these units is still controversial (Tollmann 1977, 1987a; Frank 1983, 1987), recent work has enabled a well constrained palaeogeographical model for the deposition of the Permo-Mesozoic Austroalpine

Figure 2. Geological map showing the main tectonic units of the Eastern Alps (modified after Flügel and Faupl 1987).

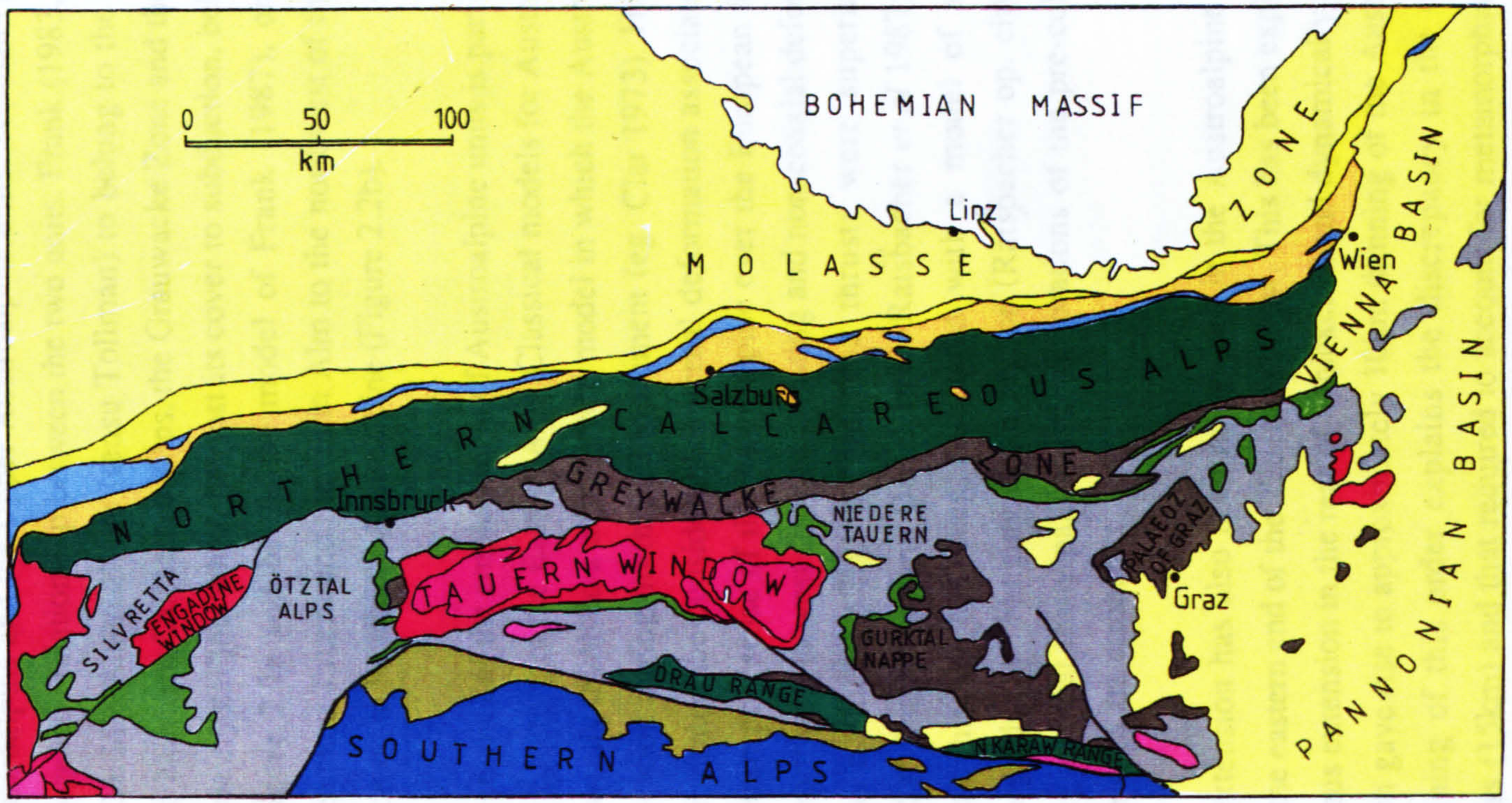

sequence to be developed (Lein 1987; Hausler 1987; Tollman 1987b; Decker *et al* 1987; Faupl *et al* 1987).

One of the major controversies of Eastern Alpine geology is the relationship between the Middle Austroalpine and the Upper Austroalpine units. Tollman (1987a) considers there to be no genetic relationship between the two units. Frank (1983, 1987) considers most of the Middle Austroalpine (sensu Tollman) to belong to the Upper Austroalpine so that the Northern Calcareous Alps, the Grauwacke Zone and the main mass of the Austroalpine crystalline, which has lost its cover to subduction, belong to the upper unit (cf. Figure 2.2a and b). In the model of Frank (1987), only the crystalline unit of the Seckau Tauern and the Glein Alm to the northwest of the Graz Paleozoikum are considered to be middle Austroalpine (Figure 2.2b).

The timing and kinematics of the emplacement of Austroalpine units is particularly important to the tectonic history of the Eastern Alps. Classical models for Austroalpine emplacement have generally involved a thin skinned model in which the Austroalpine underwent rigid imbrication during northward movement (eg. Clar 1973). However, recent studies have illustrated the considerable internal deformation associated with Alpine collision. The transport sense of the Austroalpine over the European foreland was characterized by northwest to west directed thrusting and non-coaxial deformation upon which north to northeast verging folds and thrusts were superimposed (Ratschbacher 1986, 1987; Ratschbacher and Oertel 1987; Ratschbacher *et al* 1987; Wallis 1987). This kinematic history has been associated with a model of sinistral transpression under a gradually changing strain regime (Ratschbacher op. cit). These features combined suggest that many palinspastic restorations of the pre-collisional geology of the Eastern Alps are erroneous.

Syn-convergent extension has also been recognised in the Austroalpine (Wallis 1987) to the south of the eastern end of the Tauern Window. This has been explained in terms of late Cretaceous extension in the rear of a thickened and dynamically unstable orogenic wedge which gave rise to approximately 10km thinning of the Austroalpine (Wallis 1987). Thinning of this order explains the discrepancy in the observed Austroalpine thickness (15km) and that required to account for metamorphism in the underlying Pennine units (25km). The current view for the kinematic development of the Austroalpine is therefore dependant upon the interaction of compression and extension associated with plate convergence and gravity driven body forces in the thickened Eastern Alpine crust.

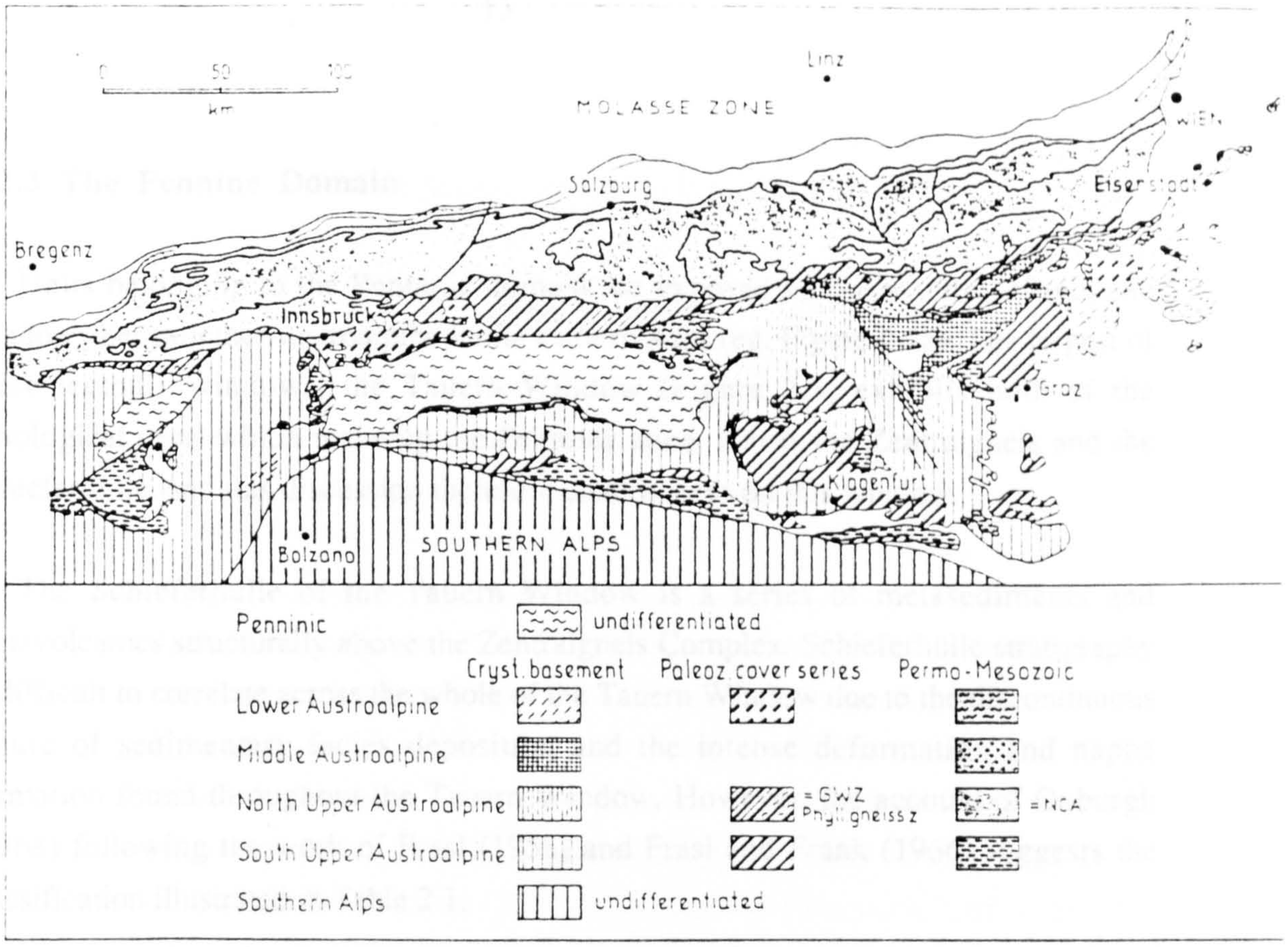

Figure 2.2b. Mapping showing the revised Austroalpine subdivisions according to Frank (1987).

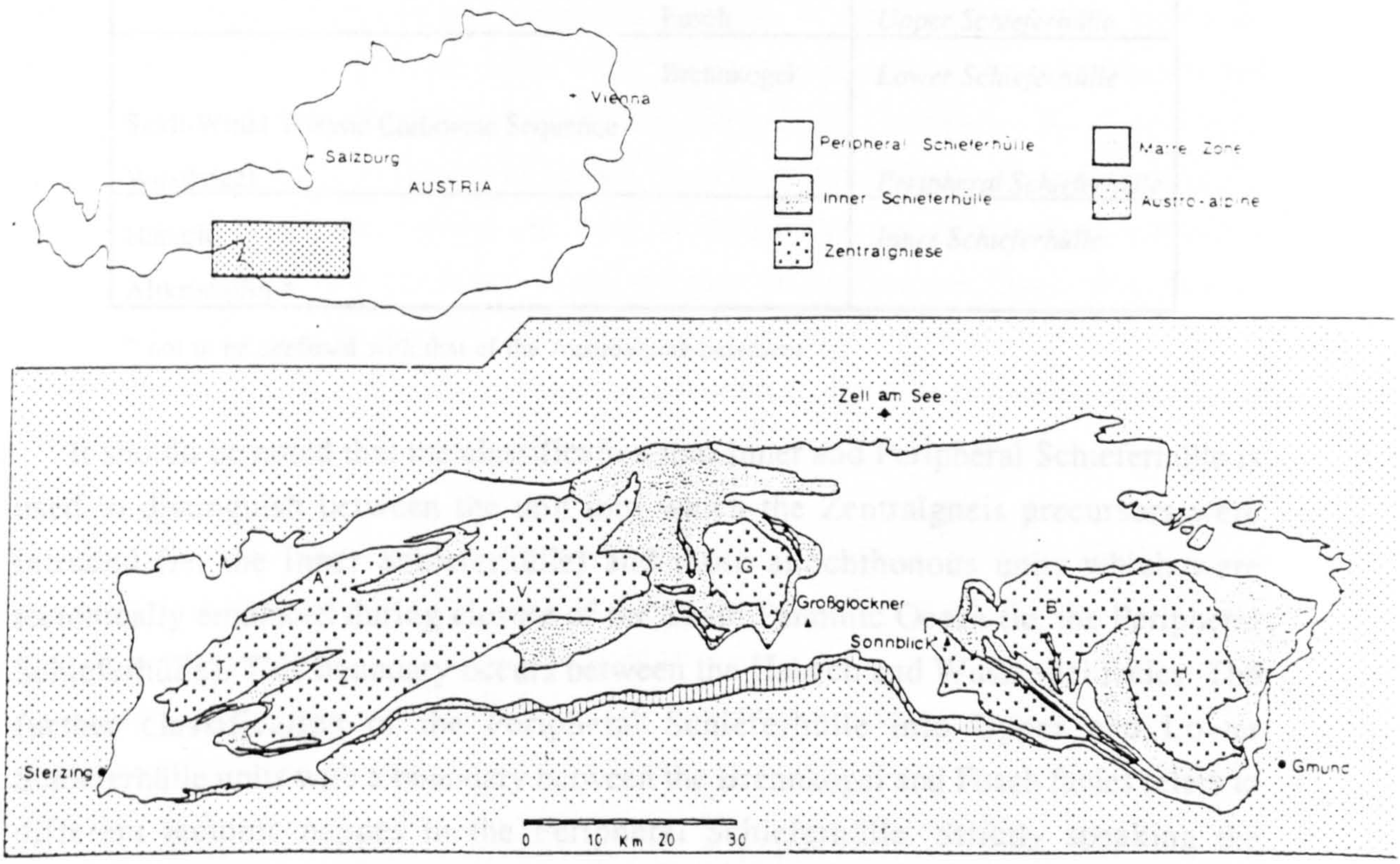

Figure 2.3. Map showing the distribution of the main Penninic units within the Tauern Window of the Austrian Alps (after Tollman 1977). The symbols T, A, Z, and V illustrate the Tuxer-Ahorn-Zillertal-Venediger massif. G is the Granatspitz Kern and B and H show the granitoids of the Badgastein-Hochalm massif respectively.

2:2.3 The Pennine Domain

Units belonging to the Penninic domain are exposed within a series of tectonic windows beneath the Austroalpine in the Eastern Alps (eg. Figure 2.2a). The largest of these tectonic windows, the Tauern Window (Figure 2.3) exhibits both of the lithological units which make up the Penninic zone, that is the Zentralgneis and the Schieferhülle, and this discussion therefore concentrates on this window.

The Schieferhülle of the Tauern Window is a series of metasediments and metavolcanics structurally above the Zentralgneis Complex. Schieferhülle stratigraphy is difficult to correlate across the whole of the Tauern Window due to the discontinuous nature of sedimentary facies deposition and the intense deformation and nappe formation found throughout the Tauern Window. However, the account of Oxburgh (1968) following the work of Frasl (1958) and Frasl and Frank (1966) suggests the classification illustrated in Table 2.1.

Table 2.1 Schieferhülle Classification

Bundnerschiefer	Hochstegen Glockner Fusch	*Upper Schieferhülle*
Seidl-Winkl Triassic Carbonate Sequence	Brennkogel	*Lower Schieferhülle*
Wustkogel		*Peripheral Schieferhülle*
Habach Altkristallin *		*Inner Schieferhülle*

* not to be confused with that of the Austroalpine basement

It should be noted that the classification into Inner and Peripheral Schieferhülle is used to distinguish between the unit into which the Zentralgneis precursors were intruded (ie. the Inner Schieferhülle) and those allochthonous units which were tectonically emplaced during closure of the South Penninic Ocean (ie. the Peripheral Schieferhülle). This boundary occurs between the Habach and Wustkogel facies. The further classification of the Peripheral Schieferhülle into Upper and Lower Schieferhülle units with a boundary between the Brennkogel and Fusch facies refers to different tectonic nappes in the Peripheral Schieferhülle. Strictly speaking the Hochstegen sequence differs from the rest of the Peripheral Schieferhülle since it was

deposited directly upon the Zentralgneis and is not therefore allochthonous (Janoschek and Matura 1980).

2:2.3 a) The Inner Schieferhülle

The Inner Schieferhülle unit of the Pre-permian basement, comprising the Altkristallin and Habach formations, forms the country rock into which the Carboniferous (Cliff 1981) precursors of the Zentralgneis were intruded. The Inner Schieferhülle has a complex polymetamorphic history including pre- or early-Hercynian eclogite formation (Droop 1983), Hercynian amphibolite facies metamorphism (Cliff *et al* 1971; Droop 1981) and contact metamorphism associated with intrusion of the Zentralgneis granitoids (Franz and Ackermand 1980; Droop 1981). Superposed on these were the effects of amphibolite facies Alpine metamorphism (Droop 1981). The Inner Schieferhülle is also structurally complex and shows at least one phase of isoclinal folding prior to granite intrusion (Cliff *et al* 1971) as well as undergoing syn-intrusive deformation and progressive Alpine deformation.

2:2.3 b) The Peripheral Schieferhülle

The Peripheral Schieferhülle forms a generally allochthonous cover to the Pre-permian basement complex and comprises a Permo-Triassic shallow water carbonate sequence, the Wustkogel and Seidl-Winkl units, and intensely metamorphosed and deformed sediments and volcanics of the Jurassic to Early Cretaceous Bündnerschiefer formation. The Bündnerschiefer formation consists of marly and pelitic oceanic facies sediments of the Glockner group and more clastic facies zones (Brennkogel and Fusch facies) which mark the north and south margins of the Penninic basin (Frisch *et al* 1987). Associated with the Glockner facies are a series of metabasites and ophiolites, with MORB to 'Within Plate' affinities, which attest to the oceanic nature of the basin (Bickle and Pearce 1975; Höck and Miller 1987).

There is evidence for three distinct Alpine metamorphic events within the Peripheral Schieferhülle. Eclogites are found in the Peripheral Schieferhülle of the central Tauern Window where they are spatially restricted to the lowest structural levels beneath the Glockner nappe. These eclogites yield P-T estimates in the order of 20kb and 550-600°C (see Frank *et al* 1987 for review) which requires burial to depths of 60-70km by subduction processes. Although the timing of eclogite formation is constrained since they formed from Mesozoic precursors and have been affected by Eoalpine metamorphism, no reliable ages data for this event are available.

Parts of the Glockner nappe preserve blueschist facies rocks which post-date eclogite facies metamorphism. These two events are considered to be unrelated (Holland 1979). Metamorphic conditions for this event, summarized by Frank *et al* (1987), have been estimated between 7-9kb and 450°C based on amphibole compositions and inferred mineral assemblages. The age of this high pressure metamorphism has been argued to take place after initial overthrusting during continental collision (Droop 1985) but prior to the second phase of recognised overthrusting (Bickle and Hawkesworth 1978). It is therefore considered to have occurred at the end of the Cretaceous (Cliff *et al* 1985).

A later greenschist to amphibolite facies Alpine metamorphism which affects all units within the Tauern Window (the Tauernkristallisation of Sander 1911) has been discussed in the recent past by several authors (eg Cliff *et al* 1971; Frey *et al* 1974; Raith *et al* 1977; Ackermand *et al* 1978; Droop 1981, 1985; Selverstone *et al* 1984; Selverstone 1985; Selverstone and Spear 1985). Metamorphism is thought to have occurred about 35-40 My ago (Hawkesworth 1976; Waters 1976). As pointed out by Cliff *et al* (1985), these dates were obtained from low grade units at high structural levels within the Tauern Window. Modelling of peak metamorphic conditions within continental crust thickened by burial beneath a tectonically emplaced crustal slab has shown that metamorphism should take place later at lower structural levels (England 1978; England and Thompson 1984). An Ar^{39}/Ar^{40} study at deeper structural levels near to the base of the Peripheral Schieferhülle in the southeast Tauern Window showing that peak metamorphism occurred 24My ago (Cliff *et al* 1985) provides evidence to support these models.

2:2.3 c) The Zentralgneis Complex

The Zentralgneis Complex forms the structurally lowest unit in the Eastern Alps and represents variably deformed and metamorphosed plutonic rocks which have intrusive ages in the order of 320 My. Three major massifs of the Zentralgneis are observed within the Tauern Window; in the east, the Hochalm-Badgastein-Sonnblick massif; in the central Tauern, the Granatspitz massif; and in the western Tauern Window in the Ahorn-Tuxer-Zillertal-Venediger massif.

The gneisses are heterogeneous due to variations in magmatic features and various groups have been distinguished based on colour index, grain size and the presence or

absence of augen (eg Cliff *et al* 1971). The primary classification is further complicated due to the effects of deformation and metamorphism of the gneissose lithology.

The original intrusives are commonly granitic through granodioritic to tonalitic following the classification of Streckeisen (1976), although subordinate quartzsyenites, quartzmonzonites, quartzmonzodiorites, quartzdiorites and diorites have been observed (Finger and Steyrer 1988). Petrographical descriptions have been made by many authors in the past (eg. Frasl 1957; Karl 1959; Cliff *et al* 1971). The petrography of the Zentralgneis observed in the Sonnblick area is given later (chapter 3).

The presence of Collision-Type granitoids in the Zentralgneis has been used to suggest a subduction environment during the Variscan changing from oceanic to continental with time (Finger and Steyrer 1988). This is discussed further in Chapter 3.

2:2.3 d) The Matrei Zone

The contact between the Austroalpine and Pennine units is locally well preserved and is marked by a discontinuous zone of intense deformation which has both Austroalpine and Pennine characteristics. The zone, known as the Matrei Zone, forms the youngest part of the Bündnerschiefer and Tauernflysch group and has been considered to reflect trench-slope sedimentation and deformation processes at the active continental margin between Pennine and Austroalpine units in the early Cretaceous (Frisch 1984; Frisch *et al* 1987). More recent work (Wallis 1987) suggests that the zone developed during Jurassic block faulting associated with rifting of Adria away from Europe and is therefore unrelated to convergence.

Post-Mid-Cretaceous imbrication of the Matrei Zone and the overlying Austroalpine unit (Behrmann and Wallis 1987) provides evidence for sinistral transpression between the colliding plates during the Cretaceous. Work in the area (Wallis 1987) has also shown that the Austroalpine-Pennine boundary at the southern margin of the Tauern Window is the expression of a 'combination of brittle tectonics representing out-of-sequence thrusting and a subsequent phase of extensional deformation'.

2:3 The Structure and Evolution of the Alps

2:3.1 Differences Between the Western and Eastern Alps

At the present day erosion level, the Western Alps differs significantly from the Eastern Alps. The Western Alps are composed of units belonging dominantly to the

Helvetic and Pennine Domains, with the former found towards the external side of the Alpine arc and the high pressure complexes of the Pennine basement being found in the internal arc of the orogen (Figure 2.1). Very little Austroalpine material is found within the Western Alps but in the Eastern Alps, the Austroalpine forms volumetrically the most important unit observed at the surface. In the east the Austroalpine overlies Penninic rocks which are only found within tectonic windows. Austroalpine units in the Eastern Alps show Barrovian-type amphibolite metamorphism and do not record the high pressure metamorphic conditions seen in the western Alps. Only a small strip of Helvetic rocks is preserved on the northern edge of the Eastern Alpine margin.

Differences between the Eastern and Western Alps are also illustrated in the present day structures of the deep Alpine crust which may be imaged by geophysical means. As an example, long range seismic probing parallel to the strike of the Alps along the 'Alp75' seismic traverse shows conspicuous lateral velocity variations in the west and Central Alps, but a more homogenous crustal profile in the Eastern Alps (Figure 2.4). This is thought to be due to a reduction in the amount of crustal shortening in the east (Mueller 1989) which may also be the reason behind the difference in erosion levels and metamorphic grades between the two areas.

The alternating low and higher velocity layers of the west are thought to represent delamination and interfingering of the crust during shortening. This theory is reinforced by the tracing of units from the northern alpine foreland beneath the Pennine block, by continuous deep sounding reflection profiling (Finckh *et al* 1987) and is supported by a similar deep-reflection pattern which has been identified along the French-Italian ECORS/CROP profile (Bayer *et al* 1987; ECORS-CROP Deep Seismic Group 1989).

2:3.2 The Plate Tectonic Framework of the Alps

The evolution of an orogenic belt due to continental collision will to some extent be a function of the pre-collisional geometrical relationships of the continents and microcontinents which make up the orogen. It is therefore important to establish the number of plates involved in the collision and their palaeogeography prior to collision.

The location of almost 7000 epicentres of <5.0 magnitude earthquakes, during the ten year period between 1970-1980, have been used to outline the present day plate boundaries between Africa and Eurasia (Waniek *et al* 1982). These data clearly indicate a 3-plate structure for Alpine orogenesis and illustrate the shape of the promontory (known as the 'Adriatic promontory', Adria or the Apulian peninsula) extending into

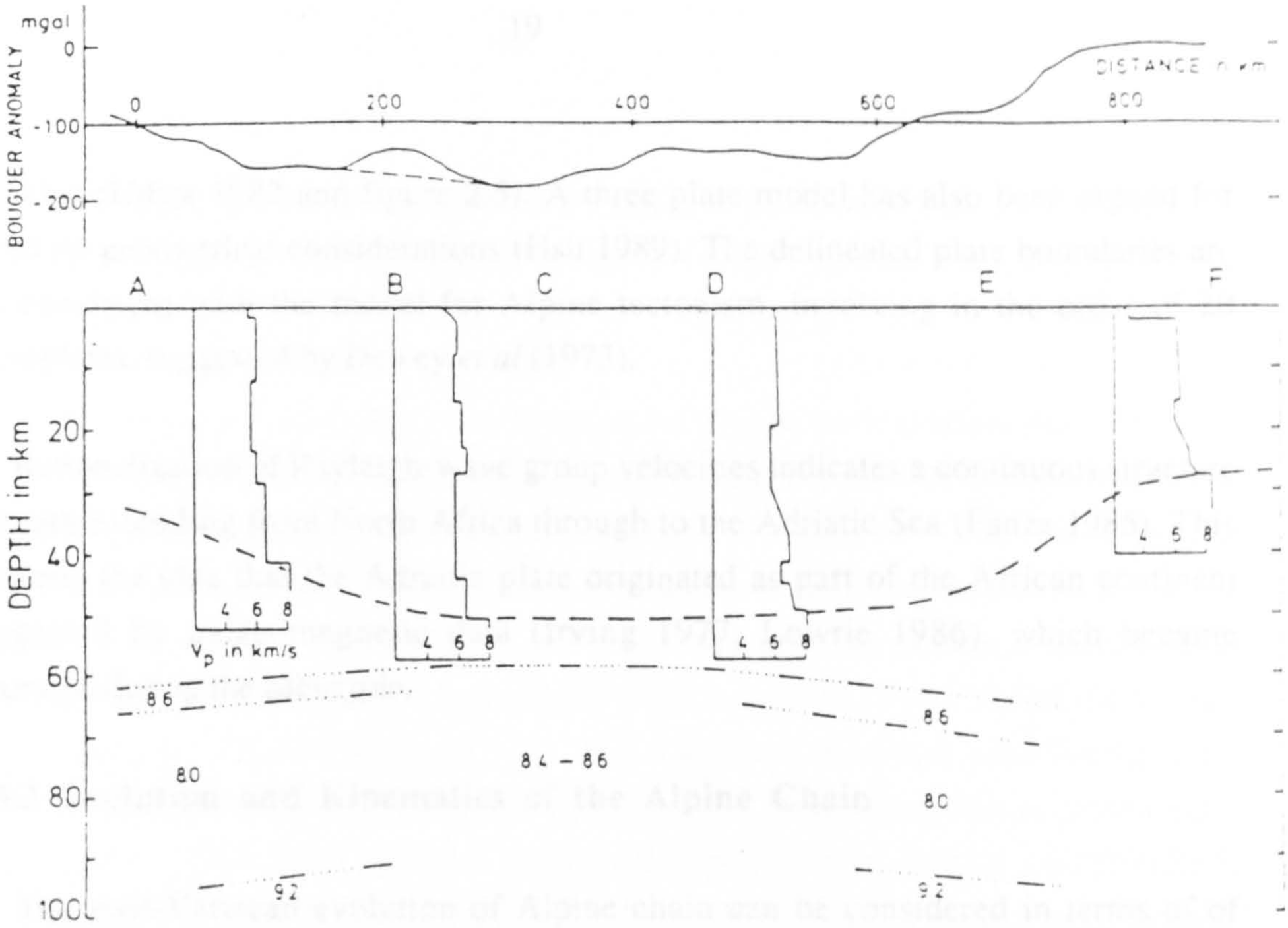

Figure 2.4. Schematic structural section along ALP75 which runs along the axial region of the Alps. Crustal structure is represented by P-wave velocities-depth distributions. The dotted line represents the crust-mantle boundary (Moho). The lower lithosphere structure is only preliminary but a high velocity 'block', extending from a depth of 60-100km, under the central Alps is observed (after Miller *et al* 1982). The difference in crustal structure between the Western, Central and Eastern Alps are reflected by the Bouguer anomaly (upper diagram) along the axial zone of the Alps (Makris 1971). The location of the section is shown on Figure 2.1. Points A and D are approximately the positions of Grenoble and Innsbruck respectively.

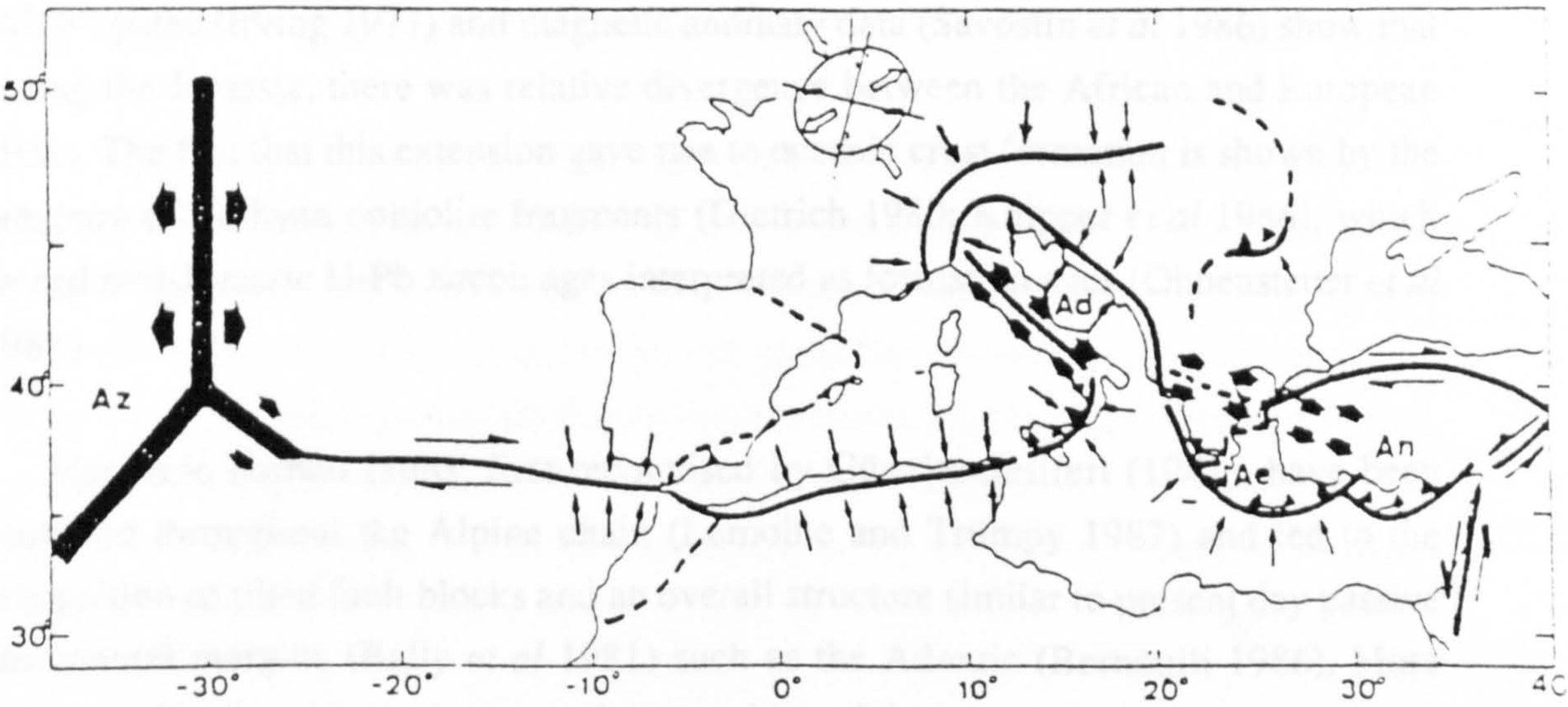

Figure 2.5 Generalized plate boundaries between N.America, Africa and Eurasia and the seismotectonic stress patterns in the eastern Atlantic, Mediterranean and Alpine region, based on recent seismic data (after Udias 1982).

the Alps (Udias 1982 and figure 2.5). A three plate model has also been argued for based on geometrical considerations (Hsü 1989). The delineated plate boundaries are not consistent with the model for Alpine tectonism, involving in the order of 20 microplates, suggested by Dewey *et al* (1973).

Rationalization of Rayleigh-wave group velocities indicates a continuous structure at depth extending from North Africa through to the Adriatic Sea (Panza 1985). This supports the idea that the Adriatic plate originated as part of the African continent suggested by palaeomagnetic data (Irving 1977, Lowrie 1986), which became separated during the Mesozoic.

2:3.3 Evolution and Kinematics of the Alpine Chain

The post-Variscan evolution of Alpine chain can be considered in terms of of several stages. Oblique extension during the opening of the Jurassic-Cretaceous Atlantic-Tethyan Ocean was followed by oblique convergence between Africa and Eurasia (Bernoulli 1986) which led to early, or Eoalpine, collision during the Cretaceous. Continued collision, resulted in the overprinting of Eoalpine features by Tertiary deformation and metamorphism, and led to uplift and the formation of the presently observed mountain belt. These are now considered.

2:3.3 a) Mesozoic Extension in the Alpine-Mediterranean Area.

There are a number of independent lines of evidence for Mesozoic extension in the Alpine area. Recent palaeogeographical reconstructions have enabled the movement of the African plate relative to that of Eurasia, to be considered. Apparent polar wander (APW) paths (Irving 1977) and magnetic anomaly data (Savostin *et al* 1986) show that during the Jurassic, there was relative divergence between the African and European plates. The fact that this extension gave rise to oceanic crust formation is shown by the presence of Tethyan ophiolite fragments (Dietrich 1980; Knipper *et al* 1986), which record mid-Jurassic U-Pb zircon ages interpreted as formation ages (Ohnenstetter *et al* 1981).

Mesozoic normal faults, first recognised by Günzler-Seiffert (1941), have been observed throughout the Alpine chain (Lemoine and Trümpy 1987) and led to the recognition of tilted fault blocks and an overall structure similar to present day passive continental margins (Bally *et al* 1981) such as the Atlantic (Bernoulli 1986). More recent studies have shown however that stretching of the upper crust was not consistent

with a simple, symmetric extension model and that two major phases of rifting, with differently oriented normal faults, occurred in the African margin (Eberli and Froitzheim 1989).

Sedimentary facies analysis has illustrated a change from shallow water, massive carbonate and evaporite platform deposition during the Middle-Upper Triassic to deposition associated with subsiding hemipelagic-pelagic basins and submarine and emergent shoals, corresponding to syn-sedimentary half graben and tilted block formation in the Jurassic (Lemoine *et al* 1986). The beginning of oceanic spreading, as opposed to continental rifting, was marked by the deposition of radiolarian cherts upon new oceanic crustal material at the ridge axis. Carbonate platforms were formed at the continental margin, which itself was undergoing slow thermal subsidence (Homewood and Latelin 1988). This time also marked the migration of detrital sedimentation, commonly associated with tectonic activity, from the continental margin to the oceanic domain (Lemoine *et al* 1986). This sedimentological and palaeotectonic evolution is also similar to that envisaged for the development of passive margins of modern oceans (eg. de Graciansky *et al* 1985).

The change from carbonate platform to deep marine environments, which correlates well with tectonic disruption of the platform during the Jurassic, has been considered to mark the initiation of the continental rifting event (Lemoine *et al* 1986; Lemoine and Trümpy 1987). These authors consider this rifting phase to be episodic and to last for about 40My prior to oceanic crust formation. This early rifting phase, associated with the break up of Pangea, development of Tethys and gradual northward opening of the Atlantic, produced structures which were reactivated during the collision event and has been considered to be of greater importance than the Alpine convergence in determining Alpine tectonics (Lemoine *et al* 1981, 1986).

The Adriatic Peninsula during this rifting event underwent considerable extension which is absent from Northern Africa (Coward and Dietrich 1989). However, Adria shows very similar APW paths to the African plate (Lowrie 1986) suggesting that the peninsula at this time was part of the African plate. By reference to palaeogeographical reconstructions, this requires that during the Jurassic and early Cretaceous, the Alpine-Mediterranean area was linked kinematically with the opening of the Atlantic and suggests that the opening of Tethys was dominated by sinistral transform movements (Bernoulli 1986).

The extensional faults developed during internal rifting have been considered responsible for the Pennine Fracture Zone (or Valais Trough) which became important in controlling later subduction of the Eurasian plate (Laubscher 1986) and is thought by some to be the site of the Tethyan Ocean and the site of the Alpine front (eg. Hunziker *et al* 1989). To the east, the Valais Trough is considered to have undergone oceanic spreading and formed the Valais Ocean during the Late Jurassic (Lemoine and Trümpy 1987) or Lower Cretaceous (Frisch 1979, 1981) based on facies analysis and palaeogeographical reconstructions. Continental arc volcanism, associated with the subduction of the eastern extension of the Valais ocean in the Pannonian region is argued to be further evidence for a widening of the ocean to the east (Kázmér and Józsa 1989).

In general, recent authors (eg. Abbaté *et al* 1981; Dercourt *et al* 1986; Coward and Dietrich 1989) consider Tethys to be a large pull apart basin in a Jurassic-Cretaceous transform domain originally controlled by Variscan structures (Authaud and Matte 1977; Coward and Dietrich 1989).

2:3.3 b) Alpine Convergence and Continental Collision.

During the Mid-Cretaceous, the extension in the Alpine region began to give way to convergence and continental collision which, during the early stages, was spatially controlled by plate geometries. Evidence for Mid-Cretaceous collision in the Eastern Alps includes unconformable Pre-Cenomanian deposition of the Northern Calcareous Alp Gosau units on top of thrust nappe structures developed in the Austroalpine of the Adriatic promontory (Janoschek and Matura 1980), the presence of syn- to post-deformational Cretaceous metamorphism in the Austroalpine basement and 90-60 Ma blueschist metamorphism which postdates an earlier high pressure metamorphic event (Frank *et al* 1987).

In the Central and Western Alps evidence for Cretaceous subduction of Pennine basement is recorded in the 110 My Ar^{39}/Ar^{40} age on metamorphic phengites from the Monte Rosa massif (Chopin and Monie 1984). Less reliable Rb-Sr ages of 114 My and 129 My on mineral and whole rock samples from the Sesia Zone (Oberhänsli *et al* 1985; Hunziker *et al* 1989) also provide evidence for Cretaceous subduction.

The kinematic framework for the Eoalpine collision can best be determined from palaeogeographical reconstructions and from palaeomagnetic data. The motion of Africa relative to Eurasia has recently been investigated by mapping of Atlantic fracture

patterns, imaged by SEASAT, in conjunction with Lamont-Doherty magnetic anomaly data (Dewey *et al* 1989). This data has refined previous data illustrating the sinistral, strike slip motion between the two plates from the Jurassic to Mid-Cretaceous (the M-O anomaly dated at 118 My), followed by the northeastwards movement of Africa relative to Europe from 118 My to about 90 My.

The movement of the Adriatic Promontory at this time is less easily understood. APW paths suggest that the promontory was coupled to the African plate until the early Tertiary (Lowrie 1986), while detailed kinematic studies in the Western Alps support decoupling since the late Cretaceous (Weston 1989). In contradiction, palaeomagnetic data (Westphal *et al* 1986), modelled in a comprehensive review by Dercourt *et al* (1986), suggests decoupling during the Cretaceous and a 30° anticlockwise rotation of the Adriatic plate between 130 and 80 My ago. Earthquake focal mechanism analyses have shown that the Adriatic Peninsula is presently still undergoing continued anticlockwise rotation (Pavoni 1980). Hsü (1989) has also argued for a 3 plate system for Alpine orogenesis based upon geometrical considerations and the fact that high pressure metamorphism occurs before Africa moves towards Europe (cf. Dewey *et al* 1989). Hsü therefore models Eoalpine orogenesis by continuing sinistral strike slip between Africa and Eurasia. In such a model, the Adriatic Promontory must decouple from the African plate during the Valanginian Stage and move in a dextrally transpressive sense relative to Europe. Unfortunately, the model of Hsü (op.cit.) neglects the northeast movement of Africa, from Aptian to Turonian times, reported by Dewey *et al* (1989). However, such a model would fit Eoalpine collisional data which needs to include west to northwest-vergent thrusting of Austroalpine units onto the southern margin of the European plate, associated with dextral transpression (Ratsbacher and Neubauer 1989), and south-vergent ophiolite nappe emplacement onto the northern margin of the Adriatic plate (Laubscher and Bernoulli 1982).

The progressive collision of the counter clockwise rotating Adriatic promontory into the Eurasian continent may have led to diachronous continent-continent collision within the Alps. However, collision is considered to have occurred prior to the Neocomian in both the Eastern Alps (Slapansky and Frank 1987) and the Central Alps (Chopin and Monie 1984; Hunziker *et al* 1989). The details of this collision are far from clear and several views on the nature of the collision have been expressed based on differences in the interpretation of Tethyan palaeogeography. The spatial and temporal differences between the Eastern and Western Alps have also complicated interpretations of Alpine tectonics and at present evidence for diachronous collision is equivocal.

Milnes (1978), Trümpy (1980) and Lemoine and Trümpy (1987) have favoured a complex Tethyan palaeogeography involving small oceans and intervening stretched continental fragments which were forced together during a long mélange-forming convergence period and then underwent post- to mid- Oligocene intra-plate compression. Such a model may be similar in style to the accretion of terranes around the Pacific (eg. Robertson and Dixon 1989).

A model involving 2-3 discrete oceanic zones, separated by micro-continents, has been expressed by Platt (1986) for the Central Alps. Frisch (1979, 1981) recognised two oceanic basins, the Northern Penninic or Valais Ocean and the Southern Penninic or Piédmont Ocean, which were separated by the Middle Penninic (Briançonnais) continental zone in the Eastern Alps and were later subducted to the south (Figure 2.6). However, only one of these oceans, the Southern Penninic Ocean, is thought to extend into the western Alps (Frisch op.cit.).

These models may be tested by recent P-wave tomographic imaging of the Alpine area (Spakman 1986a and b). Tomographic data appears to show the presence of a single subduction zone in the Western Alps which towards the Central Alps develops into a bivergent subduction system. This may be evidence for a large lithospheric root formed by the subduction of both African and European lithosphere, which is required in the restoration of Africa and Europe by material balance considerations (Laubscher 1985, 1988) and which is required by the apparent similarity in P-wave velocities of teleseismic events in the Alpine foreland and the Alps (Baer 1980). In the Eastern Alps, two southward-dipping, lithospheric slabs can be distinguished and this data therefore appears to support the plate tectonic models of Frisch (1979, 1981). However, the dip of the slabs imaged by tomographic techniques contrast the earlier models of Alpine structure which show a near vertical subduction of two lithospheric slabs (eg. Laubscher 1974, 1985; Panza and Mueller 1979).

The simplest palaeogeographic reconstruction for the Western Alps is favoured in a recent review of Alpine tectonics (Coward and Dietrich 1989) and follows the model of Laubscher (1970) and Laubscher and Bernoulli (1982). In this model, oceanic fragments observed within the Alps are not interpreted as representing the sites of sutures, where individual ocean basins have closed, but are considered as being due to the complex deformational emplacement of oceanic material derived from a single Tethyan Ocean. Such a model is consistent with the model of Frisch (1979,1981) discussed above which requires a widening of the North Penninic Ocean to the east.

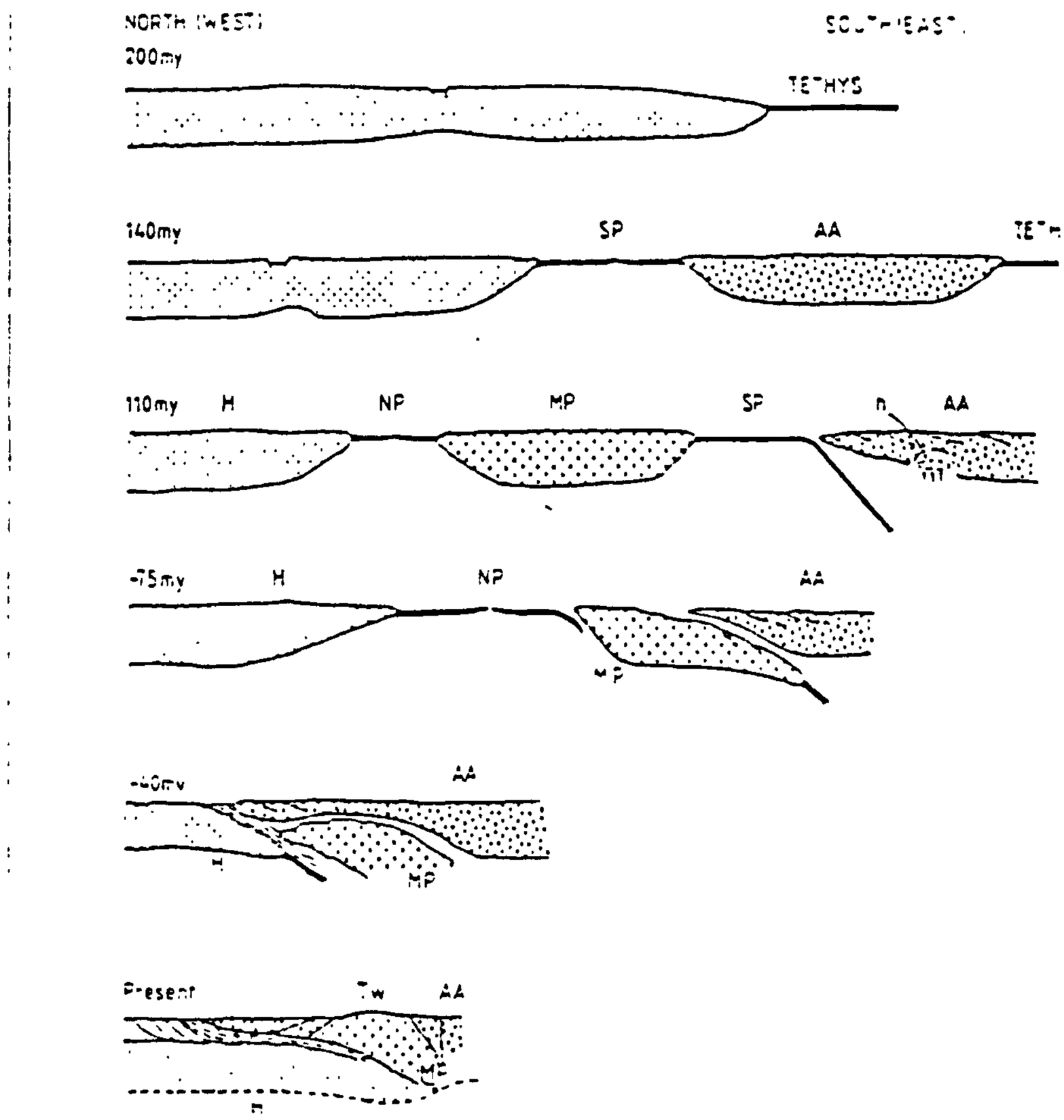

Figure 2.6. Cross-sections illustrating the tectonic development of the Eastern Alps as modelled by Frisch (1979, 1981). Initial rifting of the European crust in the Late Triassic-Early Jurassic was followed by oceanic crust development in the Lower Cretaceous. Extension within the Northern Penninic Ocean, coupled with subduction of the South Penninc Ocean beneath the Austroalpine units of the Adriatic Peninsula finally led to collision between Austroalpine and Penninc Domains. Southward subduction of the North Peninic Ocean finally led to the geological situation observed at present.

H = Helvetic Domain, MP = Midle Penninic Domain, AA = Austroalpine, SP and NP mark the Southern and Northern Penninic Oceans respectively. TW shows the location of the present day Tauern Window.

The overthrust sense observed in the Alps, as derived from kinematic indicators, range from west to northwest during Eoalpine collision in the eastern Alps to a radial pattern showing generally northwest displacements in the western Alpine arc (Platt *et al* 1989 and Figure 2.7). These displacement vectors have recently been considered to represent the resultant body force vector of a combination of the plate motion vector and the down slope gravitational flow vector associated with extension in tectonically thickened crust (Platt *et al* 1989). This model provides an important insight into the kinematics of orogenic belts although complexities within the crustal wedge, for example a pre-existing tectonic grain, may complicate the real situation (eg. Fry 1989a,b).

The model can also be combined with recent views on uplift within convergent orogens, which, in the case of the Alps, has classically been interpreted as resulting from isostatic relaxation, uplift and erosion of tectonically thickened crust (eg. Oxburgh

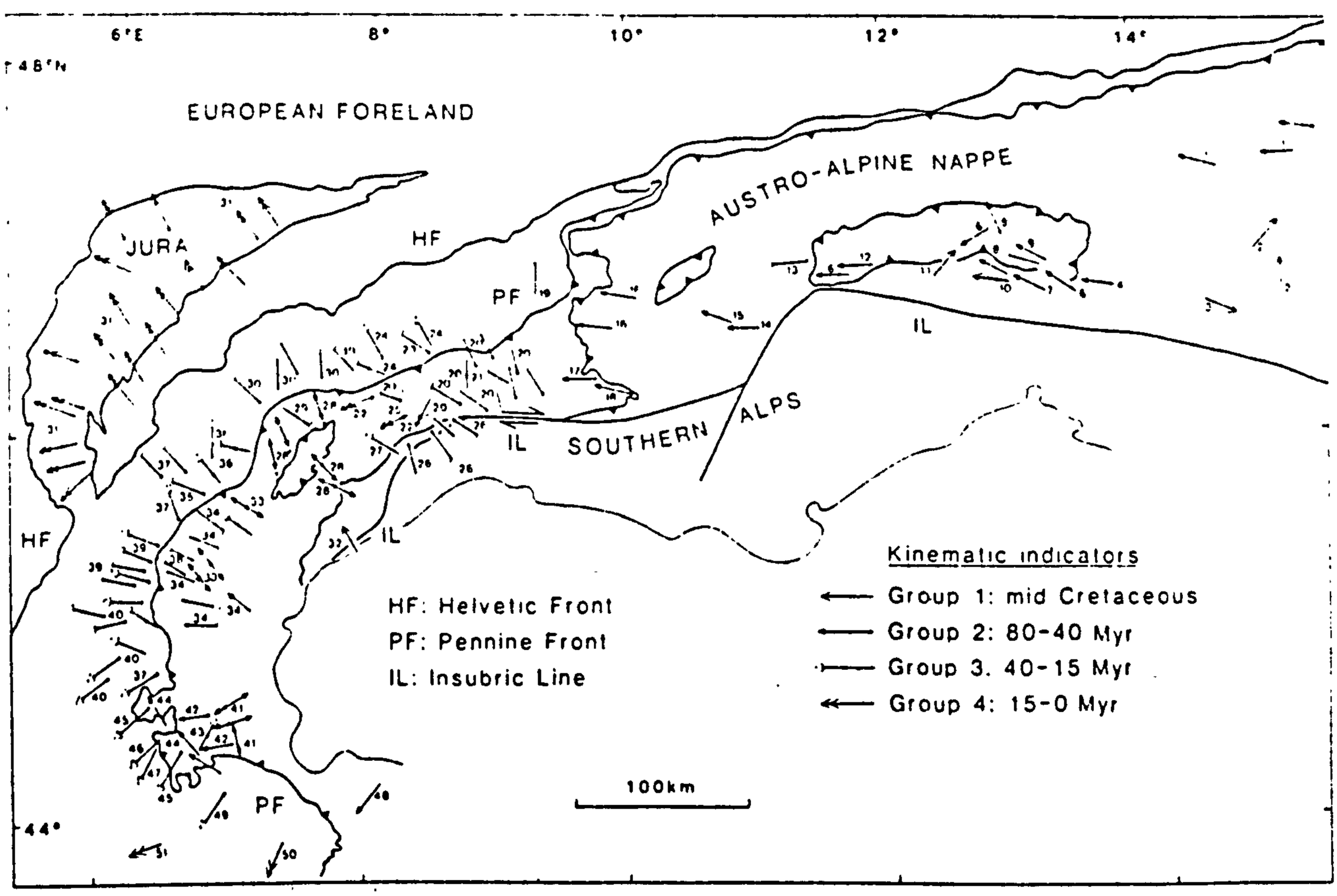

Figure 2.7. Kinematic data from the Alps plotted by age after Platt *et al* (1989). Double headed arrows show lineations were shear sense data is unavailable. Numbers refer to the list of references from which the authors took the data (see Platt *et al* 1989, Table 1).

and Turcotte 1974; Bickle *et al* 1975). Recent studies have shown that uplift within the Alps was occuring synchronously with convergence, for example the uplift of the Sesia zone during the Cretaceous (Platt 1986; Hunziker *et al* 1989). This uplift has been linked with extensional structures (Wheeler 1989) associated with tectonic thinning of a thickened orogenic wedge due to underplating of subducted material (Platt 1986; 1987). Uplift in the eastern Alps has also been linked with large extensional structures in conjunction with extrusion of crustal material along large scale strike slip zones (eg. Behrmann 1988; Selverstone 1988; Genser and Neubauer 1989). These however are discussed in the following section.

2:3.4 An evolutionary model for the Eastern Alps

A working model for the tectonic development of the Tauern Window is constrained by sedimentary facies distributions, the spatial and temporal distribution of metamorphism and evidence derived from structural studies. A model for the tectonic development of the Eastern Alps (Figure 2.6) shows the Eastern Alps as an area which has undergone continental rifting, the formation of two oceans and subsequent continental collision. The majority of Eastern Alpine models have considered simple overthrusting of a rigid Austroalpine plate over the Pennine basement with subsequent metamorphism resulting from the thermal relaxation of displaced isotherms in conjunction with isostatic uplift of the thickened crust (Cliff *et al* 1971; Cliff *et al* 1985: Droop 1985) Recent studies show that this model is an oversimplification.

Large scale thrusting in the Eastern Alps during collision is required to juxtapose the tectonic units of the Eastern Alps and to provide the thickened crust to produce the observed metamorphism. Thickened crust gave rise to blueschist facies metamorphism in the Pennine region but Barrovian facies metamorphism in the Austroalpine. This has led to the suggestion that the present geometry of the two domains represents later juxtaposition, after the Austroalpine had cooled (c.80My ago), by out-of-sequence thrusting (Wallis 1987). It was during this later thrusting that syn-convergent extension and thinning of the Austroalpine by about 10km occurred.

Recently published studies of the margins of the Tauern Window have illustrated the importance of syn-convergent extension in the evolution of the Eastern Alps, for example between the Lower and Upper Schieferhülle units (Selverstone 1985) and between the Tauern Window and Austroalpine nappes (Wallis 1987; Behrmann 1988; Selverstone 1988). Extension is observed to have occurred syn- to post- Tauern metamorphism depending upon the structural level being considered and obviously

postdated tectonic emplacement of the Austroalpine on the Pennine basement. Structural mapping has also provided evidence that syn-convergent extension played an important role in the juxtaposition of eclogite with previously unmetamorphosed units of the Bündnerschiefer in the lowest structural levels of the Peripheral Schieferhülle (Behrmann and Ratschbacher 1989a and b).

Uplift and formation of the tectonic Pennine Windows has therefore been considered to reflect extension accompanying simple shear, crustal stacking, producing net crustal thickening, followed by classical style extensional tectonics which gave rise to net crustal thinning (Ratschbacher *et al* 1989). Geometrically, this is thought to be accommodated by crustal wrenching along orogen-parallel strike slip faults (Genser and Neubauer 1989).

2:4 The Sonnblick Dome and the Southeast Tauern Window

The Sonnblick Dome is an elongate northwest striking, northeast verging, antiformal structure of the southeast Tauern Window and is found within the Zentralgneis unit of the Pennine Basement Complex (Figure 2.8). The Dome extends for about 24km along strike before rapidly thinning and passing into the Sonnblick Gneiss Lamella which extends a further 15km along the Möll valley. A maximum outcrop width of about 8km is observed perpendicular to strike.

The Dome is totally surrounded by Schieferhülle and is situated just north of the Pennine-Austroalpine boundary towards the southern margin of the Tauern Window. To the north, the Sonnblick Dome is separated from the Hochalm-Ankogel Zentralgneis massif by the Mallnitzer Mülde, a large synformal structure in the Peripheral Schieferhülle.

Mapping by Exner (1964) showed the presence of a series of discontinuous gneiss lamellae within the Peripheral Schieferhülle which could be traced around the Dome. The lamellae form relatively planar bodies, ranging from metre-scale to over 200m in thickness, which can be traced for over 40km along strike. Many of the lamellae show textures and mineralogies consistent with them having been derived from the Zentralgneis. Others however are strongly mylonitized and it is difficult to establish whether these units are orthogneisses or were derived from originally sedimentary precursors such as arkosic sandstones. Strong deformation fabrics and the commonly observed metasomatically altered shear zones at their bases suggest that these lamellae

Figure 2.8. SCHEMATIC TECTONO-STRATIGRAPHIC MAP OF THE SONNBLICKGRUPPE, EASTERN HOHEN TAUERN, AUSTRIA. (After EXNER, 1964.)

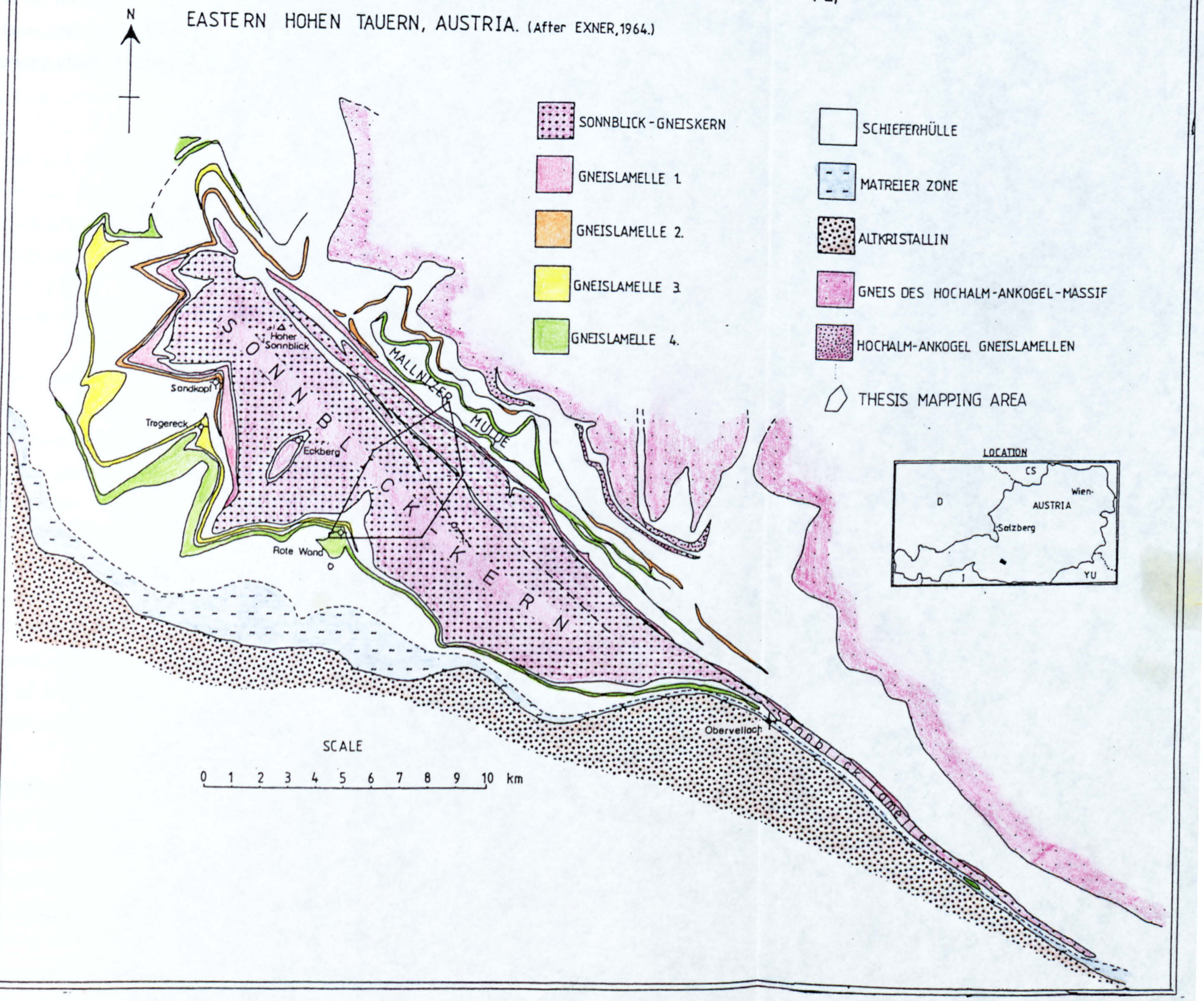

were emplaced by thrusting and imbrication of the Penninic units during continental collision.

The gross features of the Sonnblick Dome have been established by Exner (1964). However the details of lithological variation, the deformation history of the Sonnblick gneisses and the conditions of their metamorphism have so far been neglected. In the following chapters these aspects are considered.

Chapter 3

Rock Types within the Sonnblick Dome

3:1 Rationale Behind the Chosen Lithological Subdivisions

As stated in the previous chapter, the Pennine basement can be divided into three main units, one of which, the Zentralgneis Complex, is the main unit within the Sonnblick Dome and is of primary interest in this thesis. The Zentralgneis unit of the Penninic Tauern Window comprises a large variety of lithologies due to both primary textural and compositional differences in the original plutons and to subsequent deformation and alteration of the primary rock types. Following the classification and nomenclature of Streckeisen (1976), primary igneous lithologies within the whole of the Zentralgneis basement vary from granite (*sensu stricto*) through granodiorite to tonalite with subordinate quartz syenites, quartz monzonites and quartz diorites (Frasl 1957; Karl 1959; Exner 1964; Cliff *et al* 1971; Finger and Steyrer 1988).

Previous mapping of the Sonnblick gneisses (Exner 1964) did not distinguish any significant lithological variations associated with textural or compositional differences within these granite gneisses. Different textural and compositional characteristics may affect and localize deformation. Since the distribution of deformation is an important consideration in the understanding of an area's tectonic evolution, both the primary igneous variations and the ensuing modification by deformation are an important consideration in this thesis. Detailed mapping presented here shows that the Sonnblick gneisses consist of a range of primary lithologies which have been subsequently modified by varying intensities of deformation and localised syn-deformational fluid infiltration. For the purpose of this study, the Zentralgneis has been subdivided into a series of relatively homogenous, mappable units based on field criteria which reflect both primary igneous, and deformation-induced, lithological variations.

Large variations in strain within primary units has enabled a number of mappable, 'tectonic facies' to be identified. Variations associated with differing amounts of strain are often transitional over a range of several metres and the boundaries between these mapped units are commonly marked as 'inferred' contacts to indicate this. Contacts between different intrusive units are commonly more discrete.

Although deformation has given rise to lithological variations within originally homogenous rocks originally different units may have become virtually indistinguishable

under large strains. This problem of 'tectonic convergence' (Cliff *et al* 1971) makes definite conclusions regarding the nature of the original protolith difficult to prove for the rocks which record the highest strain.

In this chapter, the lithological units used to subdivide the Zentralgneis within the mapped area are described. Schieferhülle material is also exposed within the Sonnblick Dome and the different lithologies within these units are briefly described. The details of important microstructural and metamorphic relationships are related in subsequent chapters and this is particularly the case for the Schieferhülle lithologies.

3:2 Orthogneisses of the Sonnblick Dome

The Sonnblick Dome comprises a series of quartzo-feldspathic lithologies which can be regarded as variously deformed and metamorphosed plutonic rocks based on textures preserved within low strain areas of the Dome. Volumetrically the most important rock type in the Sonnblick area are coarse grained granitic augen gneisses although fine grained coarse augen gneisses, fine augen-free gneisses and leucogranites are also present.

3:2.1 Coarse Augen Gneisses

These have been subdivided into three units based on the intensity of deformation. These units are each indicated by a prefix which indicates the strain state. The boundaries between the subdivisions are defined by mesoscopic features. 'Low strain coarse augen gneisses' (LCAG) vary from essentially undeformed acid plutonic rocks to weakly foliated granite gneisses in which the foliation is defined by a weak preferred orientation of micas and quartz appears undeformed in the hand specimen (Figure 3.1a). LCAG are differentiated from Intermediate Strain coarse augen gneisses (ICAG) by elongate quartz associated with foliation development in the ICAG (Figure 3.1b). The term 'High strain coarse augen gneiss' (HCAG) is assigned to mylonitic augen gneisses in which feldspar augen have become elongated due to deformation associated with mylonitization of the protolith (Figure 3.1c). The major differences between these units are related to the amount of deformation they have undergone. Therefore, the details of the variations between these mapped units and the progressive modification of microscopic textures are presented in Chapter 4. The basic petrography of the undeformed gneiss is presented here.

Figure 3.1a. Low strain coarse augen gneiss retaining unmodified granite textures on a hand specimen scale.

Figure 3.1b. Strongly deformed intermediate coarse augen gneiss in which quartz and mica form a millimetre spaced mylonitic foliation. K-feldspar form rigid augen which occasionally show signs of recrystallization in asymmetric tails (x) or on fractures associated with brittle deformation (y).

Figure 3.1c. Strongly deformed coarse augen gneiss containing elongated feldspar augen.

Figure 3.1d. Oriented plagioclase inclusions within a perthitic K-feldspar augen in intermediate strain coarse augen gneiss. Plagioclase also contains inclusions of white mica and clinozoisite.

Figure 3.1e. Relict oscillatory zoning in plagioclase marked by the development clinozoisite inclusions in the originally more anorthite-rich zones.

Figure 3.1f. Zoned allanite rimmed by clinozoisite within a cluster of biotites in low strain coarse augen gneiss.

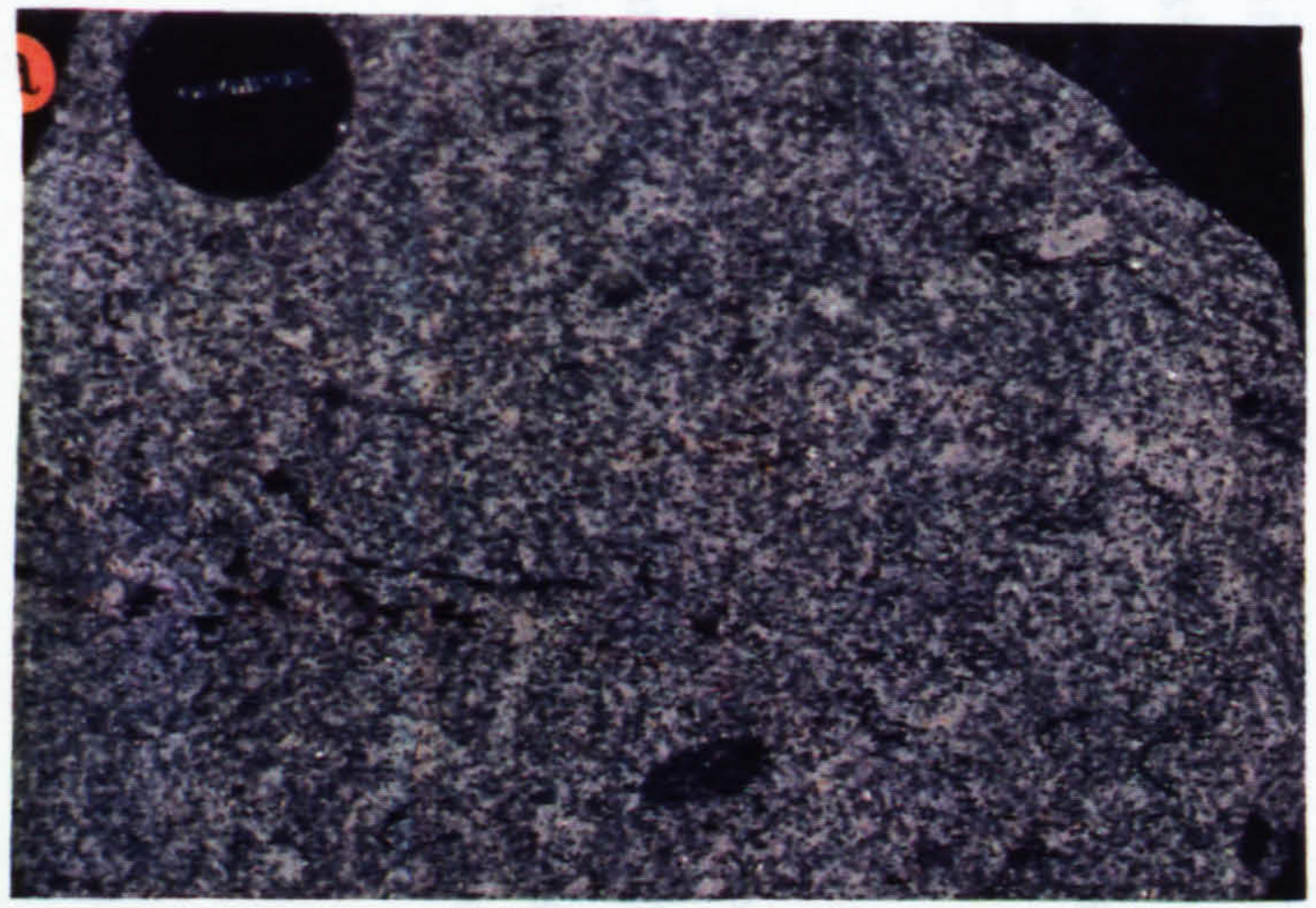

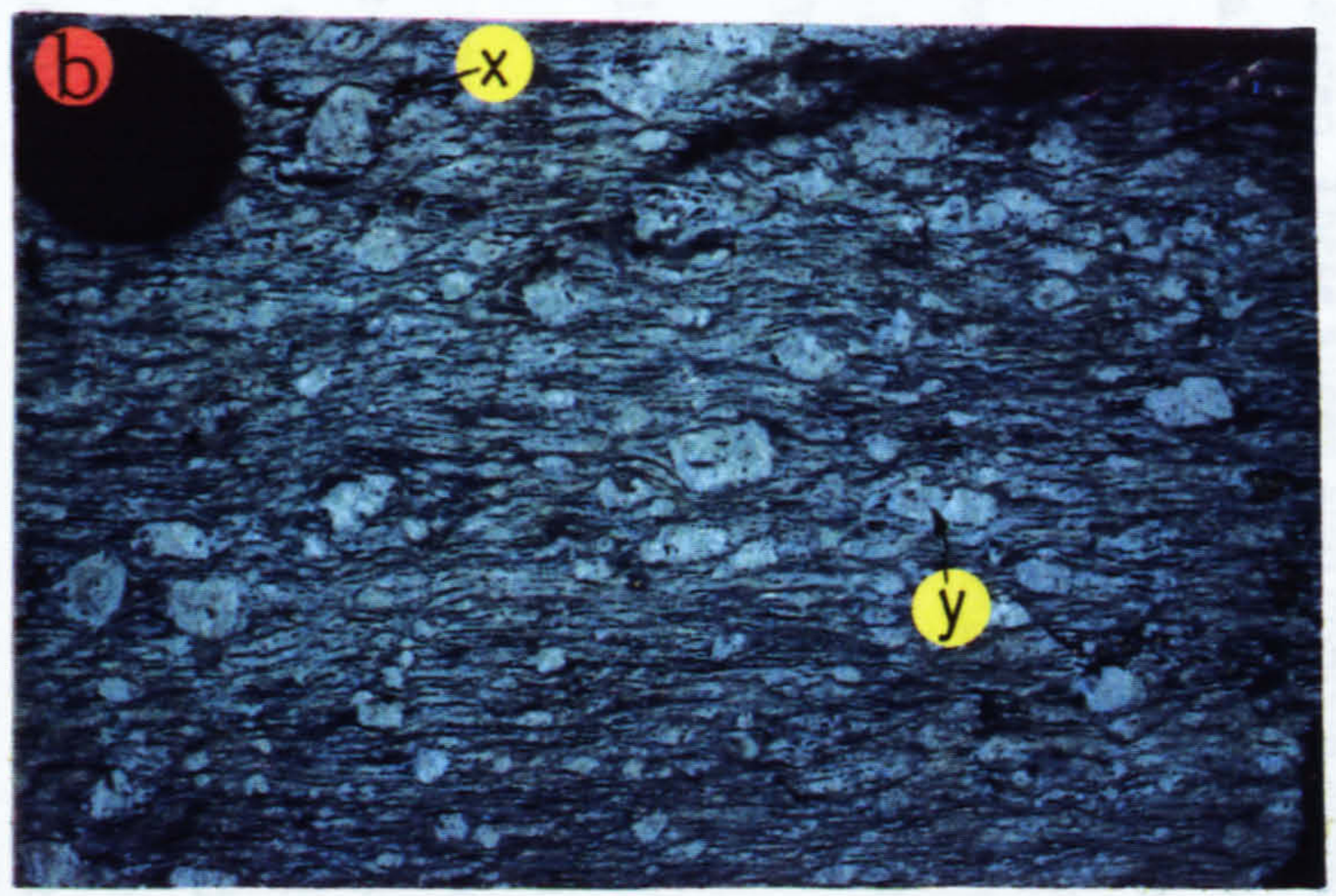
x
y

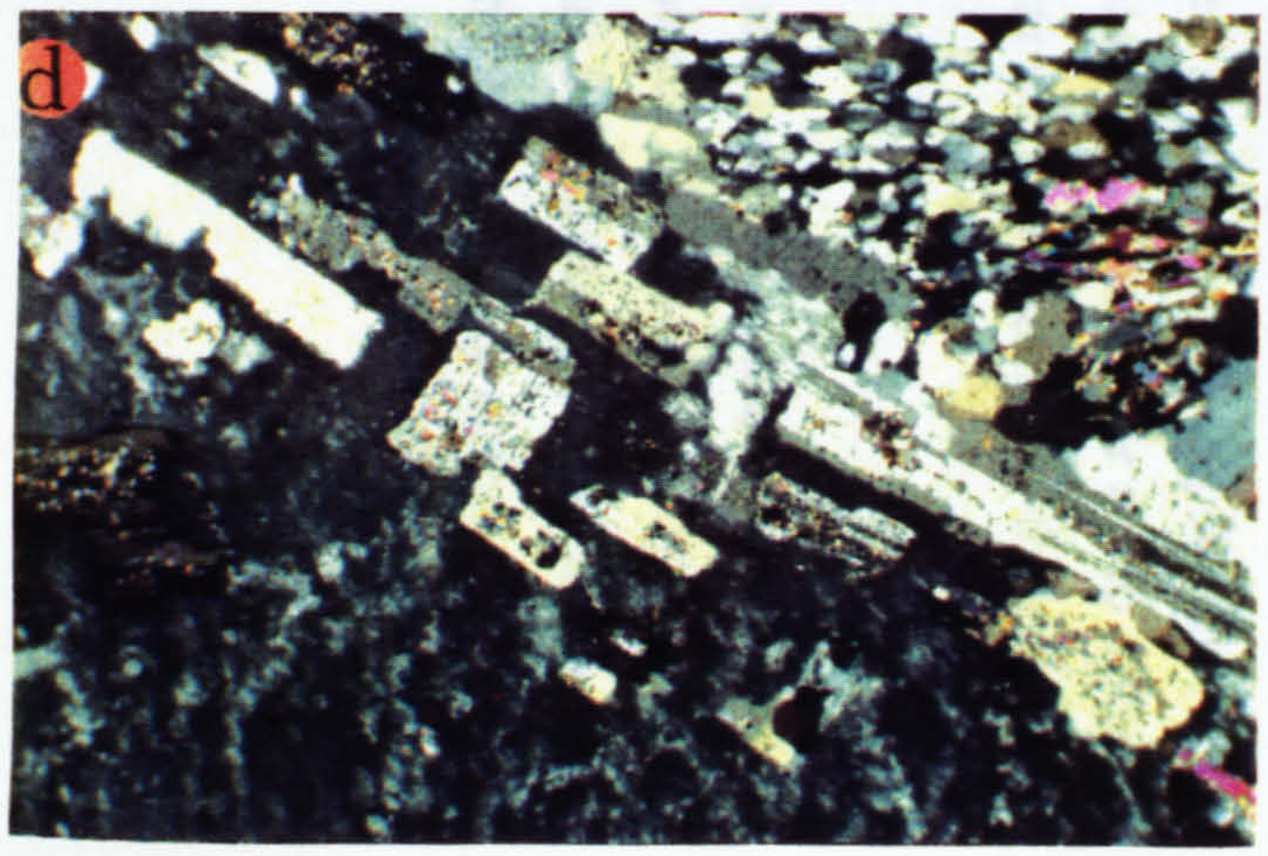

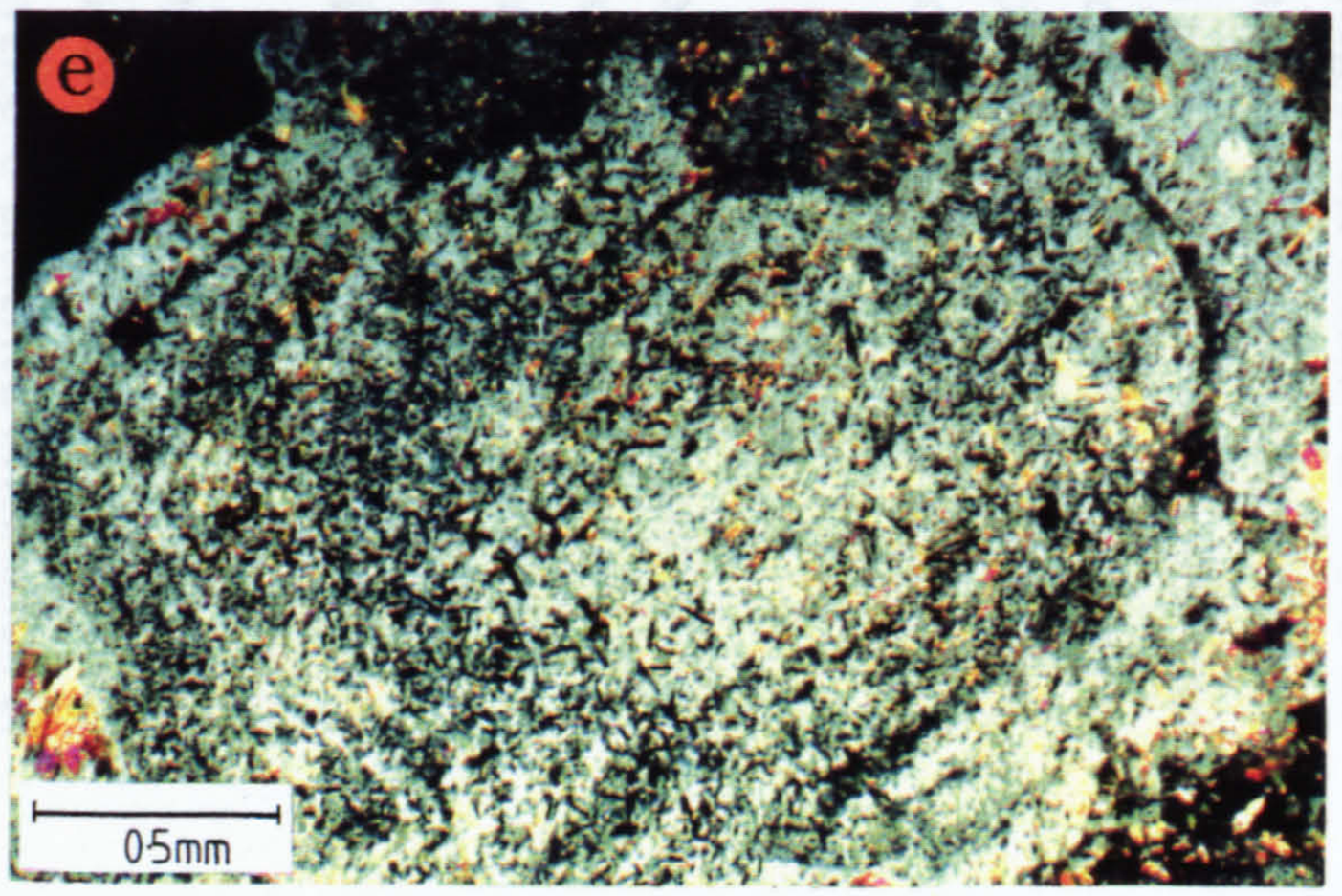
0·5mm

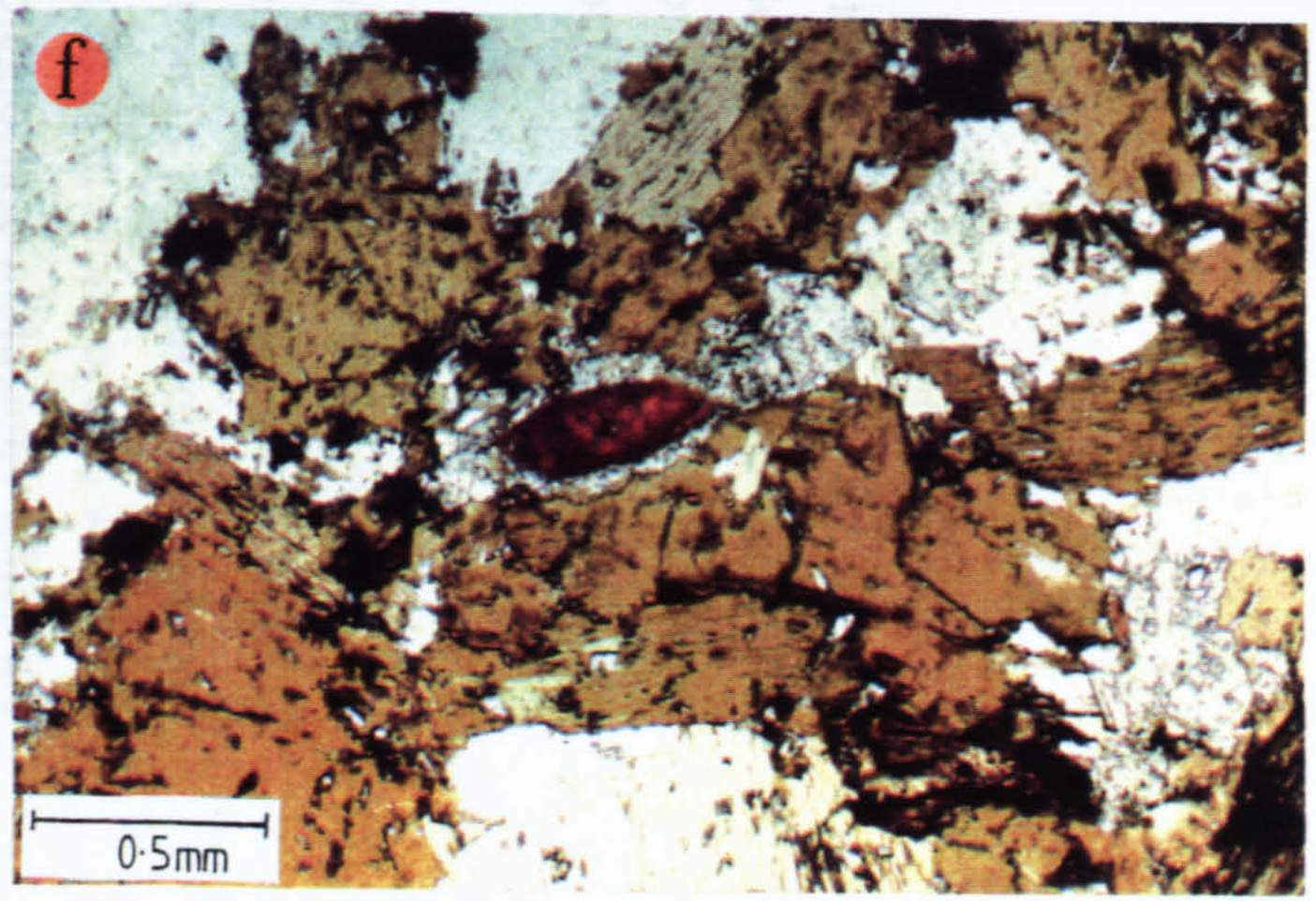
0·5mm

The coarse augen gneisses are holocrystalline and have a K-feldspar, plagioclase, quartz, biotite, white mica and epidote mineralogy with accessory sphene, apatite and zircon. The modal abundances of these phases varies due to primary differences in the original mineralogy as well as to subsequent deformation. Average modal compositions in undeformed granitic units are estimated at plagioclase ≈30%, quartz ≈30%, K-feldspar ≈25%, micas ≈10% and epidote ≈5%.

K-feldspar is euhedral, becoming more anhedral with increasing deformation, and consist of both orthoclase and locally developed microcline. Feldspar sizes vary from 1-5cm but are more commonly 2-3cm. Perthitic exsolution in the form of fairly broad sinuous lamellae, narrow braided lamellae and bleb-like areas of albite occurs within the K-feldspar augen. These augen also contain euhedral plagioclase inclusions which are commonly aligned parallel to the grain boundaries of the K-feldspar host (Figure 3.1d). These have been interpreted as primary crystallization textures (Frasl 1954, 1957 and pers.comm. 1988) and suggest that plagioclase and K-feldspar were derived from melts and are therefore igneous, and not metamorphic, in origin. Plagioclase rims surrounding the original plagioclase and replacing K-feldspar are also observed and are interpreted to be metamorphic in origin (see Chapter 6).

Plagioclase is albitic in composition and usually contains lath shaped inclusions of white mica and clinozoisite. Rarely, these inclusions are observed to be distributed in concentric zones within the plagioclase (Figure 3.1e). These clinozoisite-rich and clinozoisite-poor zones are interpreted to represent primary compositional variations developed during plagioclase crystallization, the clinozoisite bearing zones being originally the more anorthite rich, and provide evidence for primary oscillatory zoning of the igneous plagioclase. Similar observations and interpretations have been presented by (eg.Karl 1959). The inclusions of white mica and clinozoisite are usually randomly oriented within the albite although an occasionally developed preferred orientation of these inclusions, possibly along feldspar cleavage planes, suggests some dependance of recrystallization on feldspar crystallography. Plagioclase and K-feldspar up to about 5mm in size are also found in the matrix and show similar textural features to the coarser augen.

Quartz is seen as individual grains, up to several millimetres in size, which have irregular intergrown boundaries and form aggregates which in two dimensions appear about 1cm in size. In three dimensions, quartz aggregates form a continuous framework throughout the rock. Allanite and diamond-shaped sphene, which are commonly over

1mm in length, are also found within the matrix and as inclusions within K-feldspar augen. These are therefore interpreted to be igneous in origin. Allanite is zoned, occasionally twinned and commonly is rimmed by clinozoisite (Figure 3.1f). Clinozoisite in the matrix is relatively equant, subhedral to euhedral in form and individual grains are in the order of 1mm in diameter. Individual grains are commonly found in aggregates and there is a spatial relationship between clinozoisite and biotite rich domains within the gneiss.

Biotites in LCAG are up to 2mm in length and are commonly found within coarse clusters (up to 1cm) which make up approximately 10% of the rock volume (Figure 3.1f). Small inclusions of accessory phases, often associated with the development of pleochroic halos, are seen within biotite. Chlorite locally replaces biotite along cleavage planes.

As well as inclusions within plagioclase, white mica is commonly seen as envelopes surrounding K-feldspar augen. White mica also becomes modally more important with increasing deformation and the ratio of white mica to biotite generally increases with increasing foliation development.

3:2.2 Fine Augen Gneiss

This lithology is mineralogically similar to the coarser augan gneisses but differs texturally in having a finer grained matrix. Coarse K-feldspar augen are also less common than in the coarse augen gneisses (Figure 3.2a). Fine augen gneiss often contains inclusions of coarser material and occasionally observed primary lithological contacts consistently show that fine augen gneiss intrudes into the coarser rock type. Within the mapped area, this lithology is not observed in an undeformed state and therefore, the observed textures are a product of both igneous processes and of subsequent foliation development.

The matrix consists of feldspars averaging approximately 1mm in diameter which have a subhedral form and irregular grain boundaries indicative of deformation processses (Figure 3.2b). K-feldspars are dominantly orthoclase, with localized microcline development, and show little perthitic exsolution. Plagioclase is albitic in composition and commonly shows multiple twins. Inclusions of white mica and clinozoisite are not as common as within the coarser augen gneisses.

Figure 3.2a. K-feldspar augen within fine-grained matrix of 'Fine Augen Gneiss' lithology. Dolomitic carbonate material is seen in the pressure shadows around the feldspar.

Figure 3.2b. Micrographs of 'Fine Augen Gneiss' showing subhedral plagioclase with irregular grain boundaries and few inclusions. Irregular-shaped carbonate material (c) is locally seen within the matrix and is interpreted to be late-stage in origin.

Figure 3.2c. Contact between 'Coarse Augen Gneiss' (CAG) and 'Fine Gneiss' (FG). Locally observed inclusions of CAG within the FG and apophyses of FG within CAG show the finer lithology to be younger in age. A small aplitic leucogranite (A) cuts the contact between the fine and coarse gneisses and appears to be the last igneous phase intruded into the gneiss precursors.

Figure 3.2d. Micrograph illustrating the fine grained mineralogy of the 'Fine Gneiss'. Albitic plagioclase (alb), quartz (qtz) and micas dominate the mineralogy. Accessory, late-stage carbonate material (c) is also seen. Epidote forms small high relief grains which are spatially associated with the mica rich domains.

Figure 3.2.e Intergrown amphibole (a), epidote (ep), biotite (bte) with albitic plagioclase and quartz within 'Dioritic Gneiss'.

Figure 3.2.f Micrograph showing textures within amicaceous leucogranite aplite. A large mica book (wm) and anhedral plagioclase (alb) containing numerous fine white mica inclusions are surrounded by a matrix comprising quartz and white mica. Late carbonate (c) is again present.

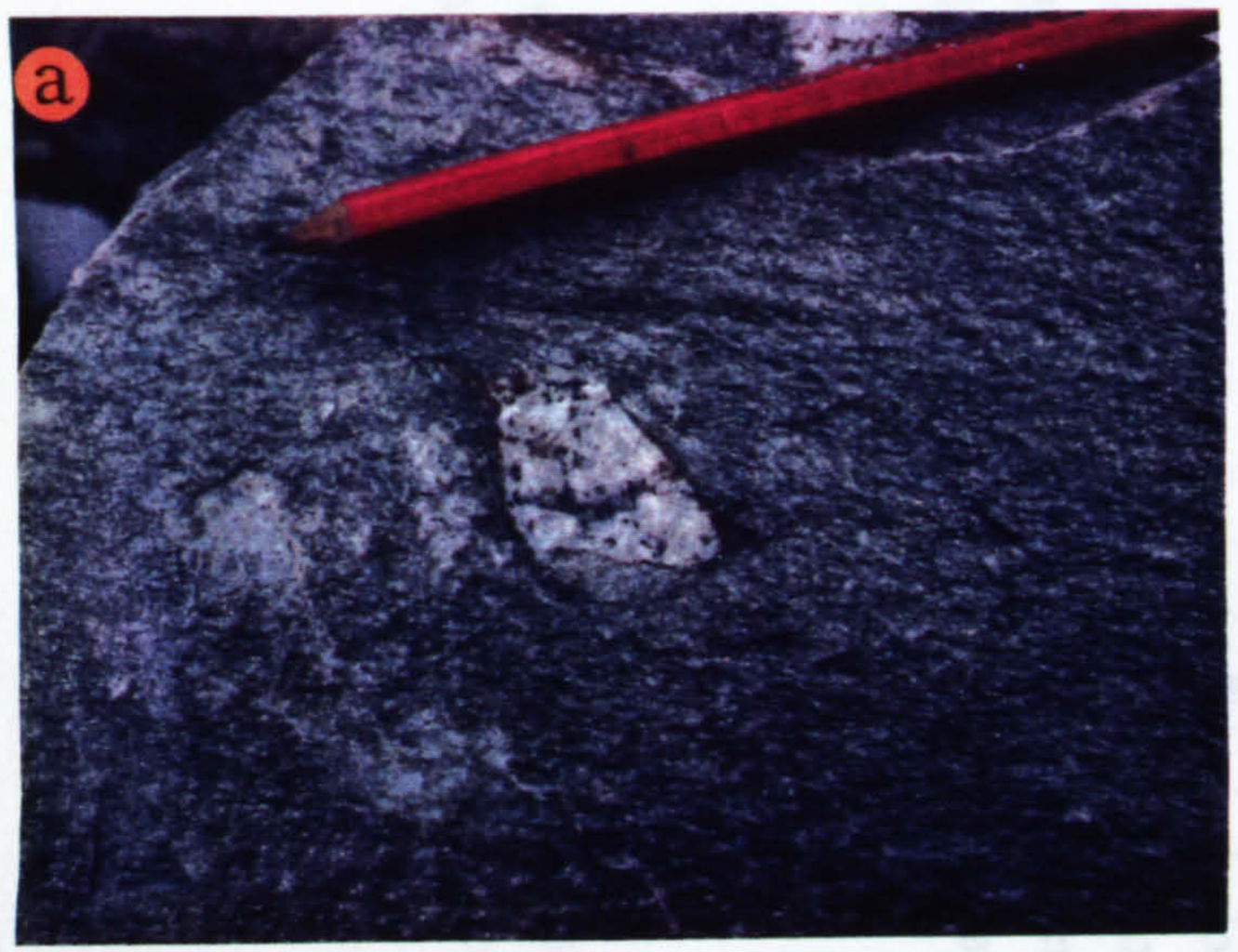
a

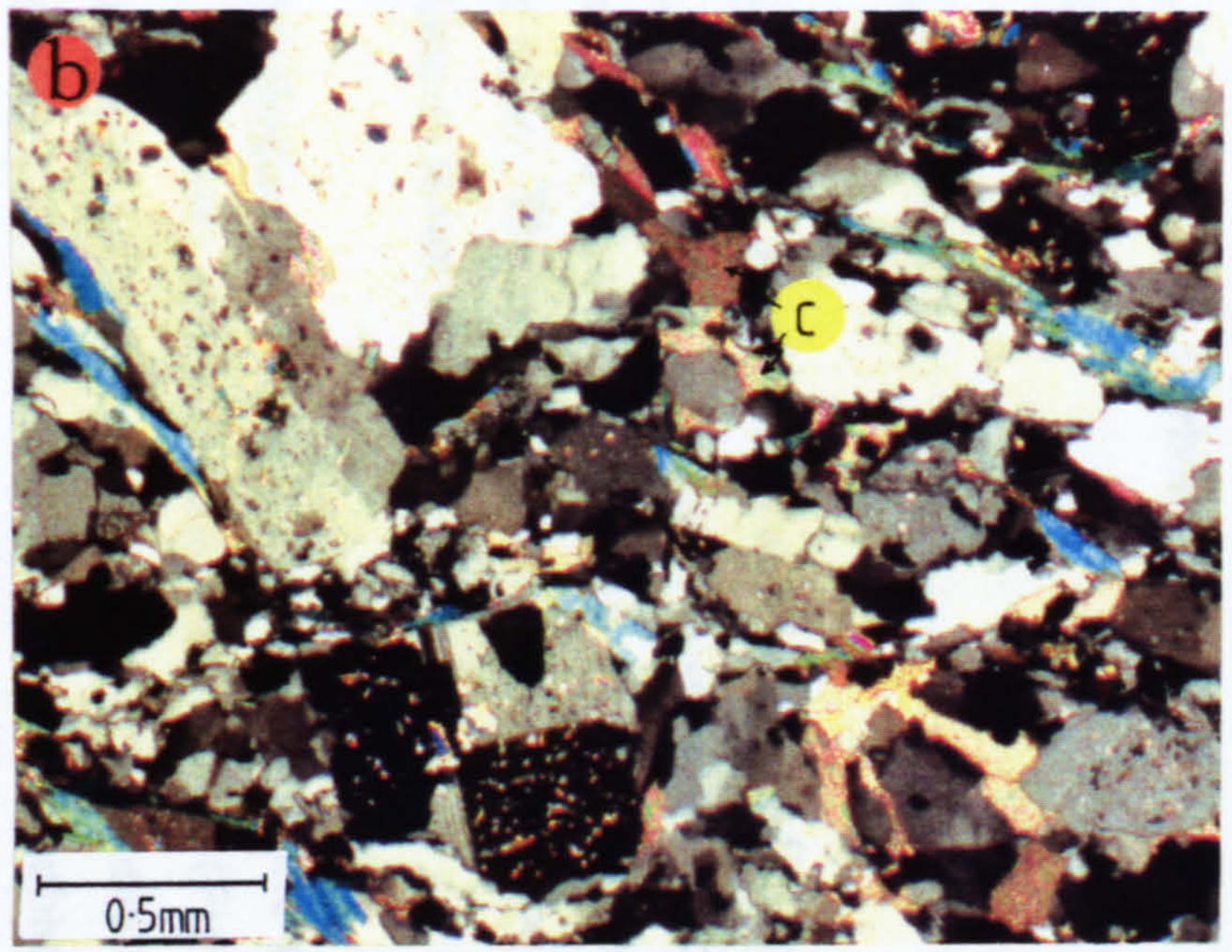
b
c
0·5mm

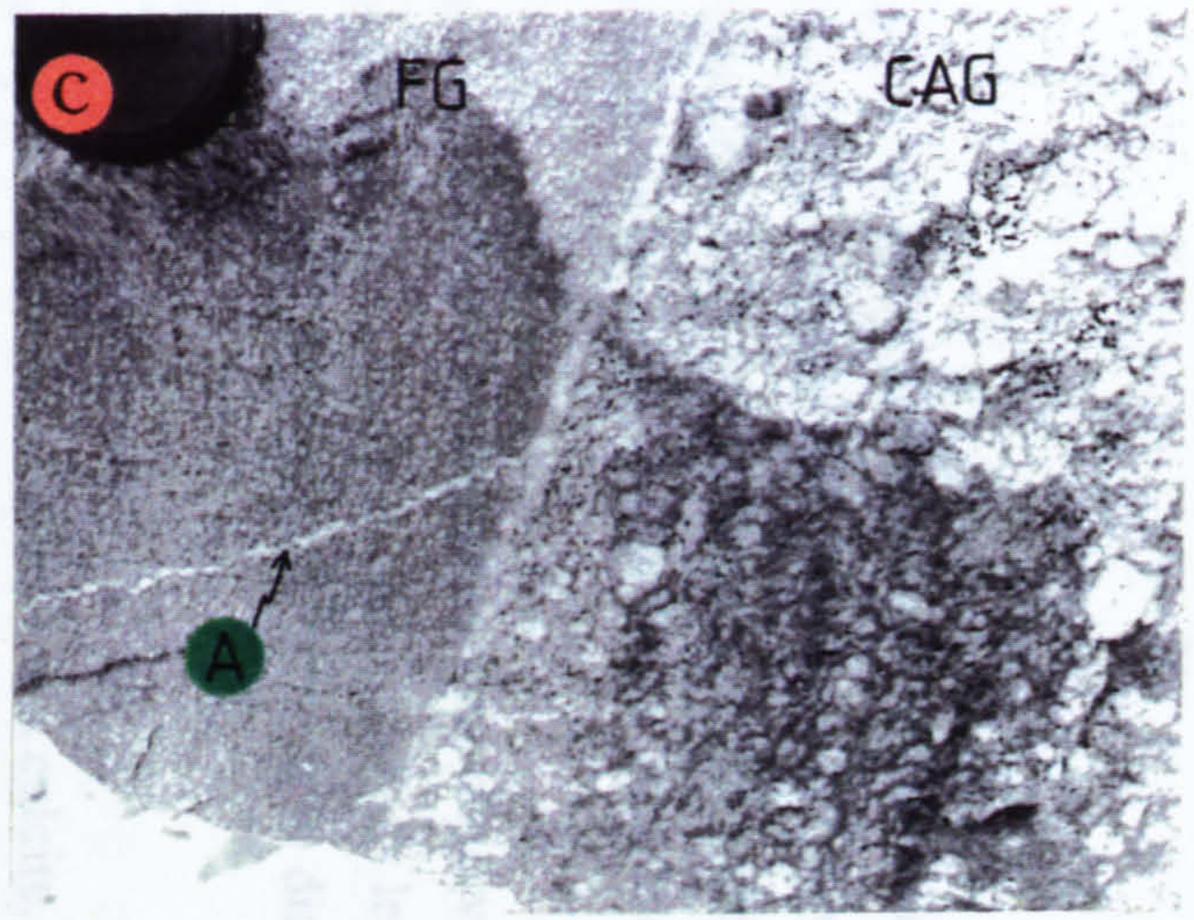
c
FG
CAG
A

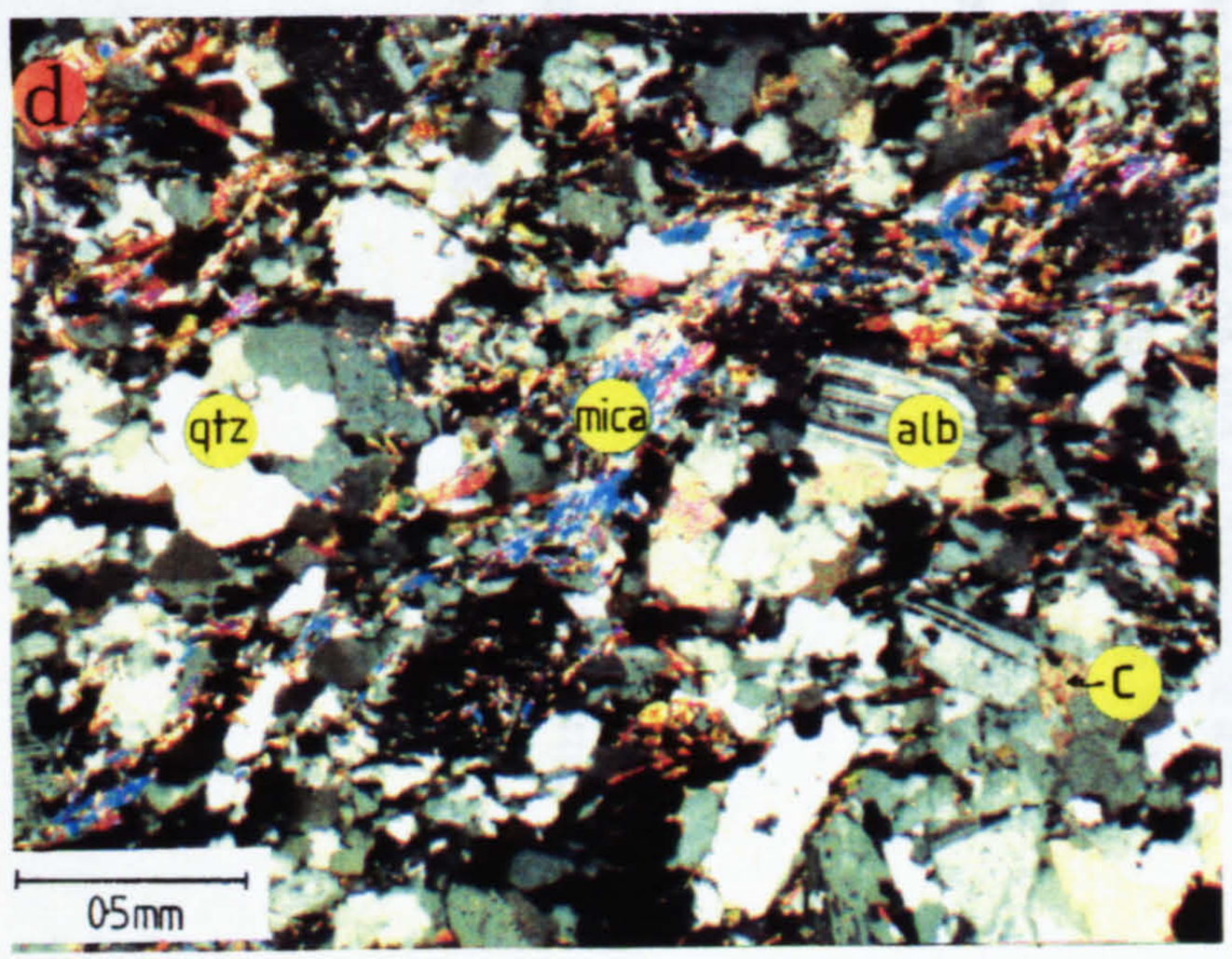
d
qtz
mica
alb
c
0·5mm

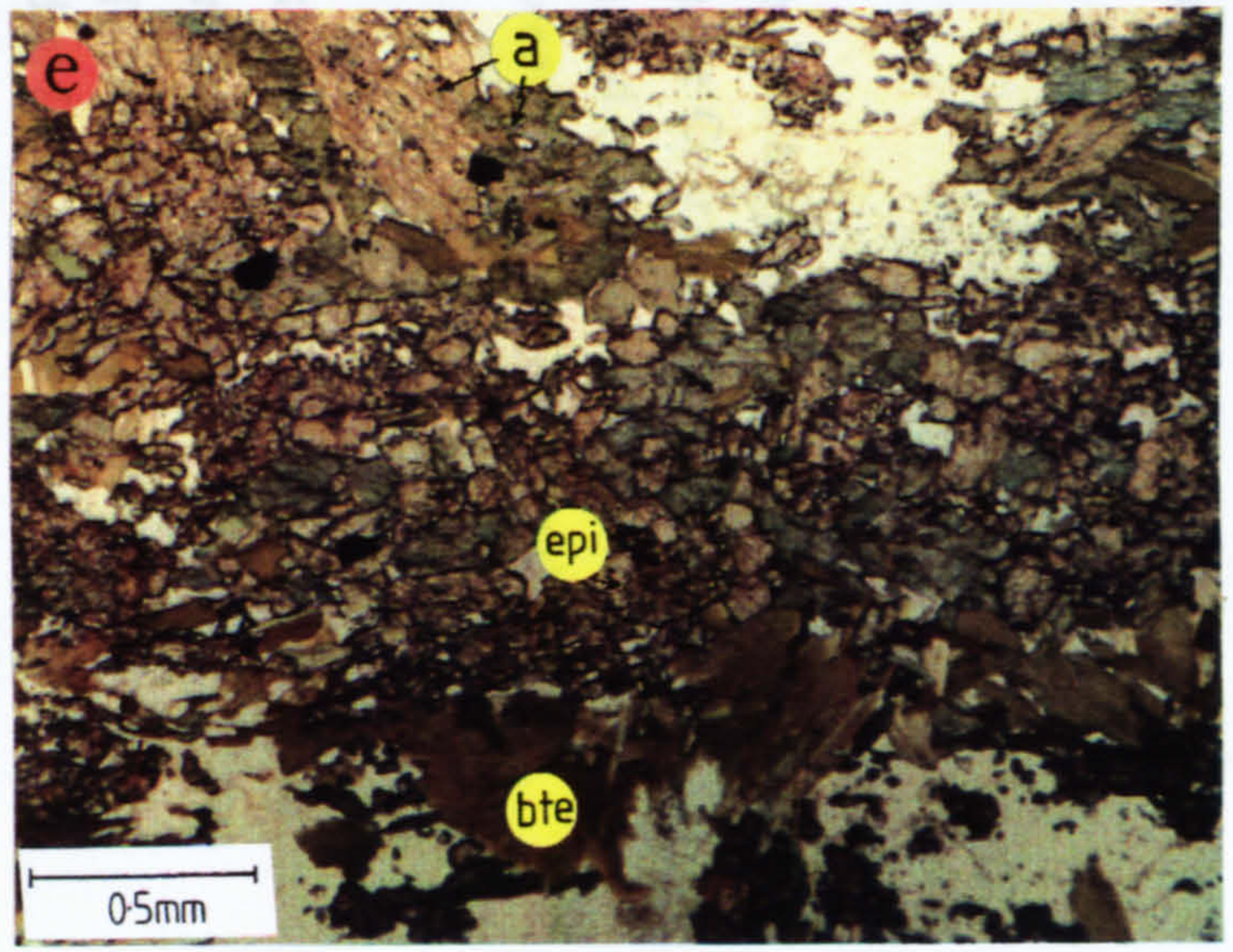
e
a
epi
bte
0·5mm

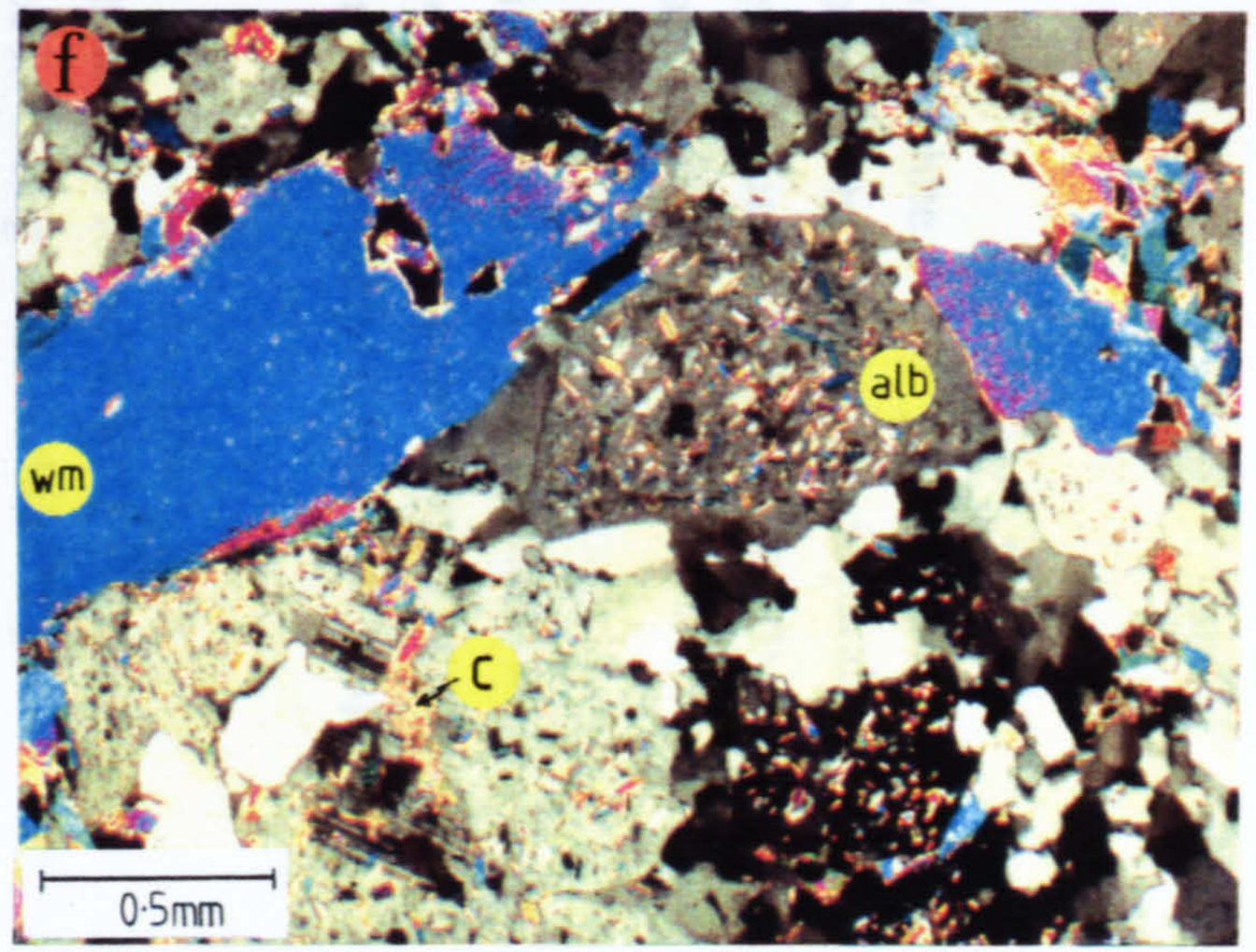
f
alb
wm
c
0·5mm

Biotite and white mica define the observed foliation and white mica is generally more abundant than biotite (ratio≈3:1). Both micas form sub-mm laths with long axis parallel to the foliation. Parallel to mica domains, there are elongate quartz domains comprising smaller grains showing typical low strain, quartz deformation microstructures (refer to Chapter 4).

Epidote mineralogy is similar to that observed in the coarse augen gneisses and varies from pistacite to clinozoisite. Epidote is less common than in the coarser augen gneiss and are smaller, being up to 0.5mm in diameter. The observed foliation wraps around these grains.

Accessory phases include apatite and calcite. The latter is found as irregular grains with decussate or concave boundaries and appear to be in-filling voids within the gneiss lithology (Figure 3.2b). Carbonate material is often seen within the pressure shadows of the larger feldspar augen.

3:2.3 Fine Gneiss

This lithology appears very similar in the field to the fine-grained matrix of the fine augen gneiss lithology and it is also seen to intrude the Coarse Augen Gneiss (Figure 3.2c). It differs however in having no large augen and having a matrix which is K-feldspar poor. The chronological relationship between the Fine Gneiss and the Fine Augen Gneiss is not clear.

Mineralogically, the rock comprises albite (45%), quartz (35%), biotite (7%), epidote (up to 5%) and white mica (up to 5%) (Figure 3.2d). Carbonate makes up 1-2 % of the lithology and other accessories, commonly apatite and zircon, make up less than 1% of the rock. Plagioclase is albitic with a subhedral form and reaches up to 1mm in length parallel to the minerals c-axis. Few inclusions of white mica and clinozoisite are observed within the plagioclase. K-feldspar was not observed although no sections were stained for K-feldspar and some small grains interspersed with quartz may be present. Micas in the matrix are generally fine-grained and approximately equal amounts of biotite and white mica are present.

3:2.4 Dioritic Gneiss

A small exposure of more mafic gneiss is exposed in the southern point of Wurten Speicher (grid ref. 160068). In hand specimen the lithology appears relatively poor in

quartz, hence the field term 'dioritic gneiss'. However, in thin section the modal mineralogy is quartz (≈25%), epidote (≈25%), plagioclase (≈20%), amphibole (≈15%) and biotite (≈15%) with accessory rutile, chlorite and apatite (Figure 3.2e).

Epidotes are subhedral to euhedral in form and have a pistacite to clinozoisite composition, the latter being most commonly observed. Individual grains are up to 0.5mm in diameter and form aggregates of epidote which are intergrown with the other mineral phases.

Green-brown pleochroic amphiboles up to 1mm in length are usually euhedral in form. No preferred orientation of the amphiboles is observed but amphibole is usually intergrown with epidote. Optical properties suggest a hornblende composition.

Biotite is commonly found in clusters and is composed of subhedral laths up to 1mm in length, parallel to 001. These laths are commonly composed of thinner biotite grains aligned sub-parallel to each other. Some grains are locally altered to chlorite.

Plagioclase and quartz both occur interstitially between the more mafic minerals and appear to make a 3-dimensional connected framework through the rock. Quartz is made up of individual grains in the order of 100μm which have irregular boundaries and microstructures indicative of low strain deformation. Plagioclase is rarely twinned but is zoned from albite in the cores to more oligoclase-rich rims.

3:2.5 Leucogranite Aplites

This lithology is a fine-grained, white lithology which occurs as dykes cutting through both the Inner Schieferhülle and the previously described Zentralgneis units (eg. Figure 3.2c). Dykes are common but are rarely persistent enough to map at 1:10000 scale. In the larger aplite units, the lithology is white mica rich and pseudo-hexagonal mica books are present. Mineralogically they differ from the augen gneisses in that they do not contain biotite and epidote is only present in some of the units sampled. Approximately 45-50% of the lithology is composed of quartz, while plagioclase and K-feldspar make up ≈25% and ≈10% respectively. White mica has a mode of 15-20%.

Quartz grains have irregular morphologies and contain deformation microstructures indicative of recovery and recrystallization processes. K-feldspar and plagioclase form 1mm subhedral to anhedral grains which have irregular grain boundaries. Plagioclase is

albitic in composition, shows multiple twinning and contains numerous inclusions of white mica which record preferred orientations within the feldspar lattice. No clinozoisite inclusions are present within albite. K-feldspar is perthitic and no evidence for reversion of orthoclase to microcline is observed. Myrmekite is also locally developed.

White mica in the matrix is composed of euhedral grains ranging from ≈100μm long laths to several millimetre wide books (Figure 3.2f). The smaller mica laths commonly define any foliation that is developed in the rock. No zoning of the mica books or laths is observed by standard optical microscopic techniques. Calcite makes up approximately 1% of the rock and the only readily observed accessory mineral is apatite.

3:2.6 White Mica Schists

These are incorporated within the 'granitic gneisses' since they are interpreted to be derived from granitic protoliths and represent the combined effects of localized deformation and metasomatic alteration within the gneisses (Chapter 6). This lithology consists largely of quartz and white mica though accessory biotite and relict, partly corroded clinozoisite are very occasionally preserved. One white mica schist unit contains syn-tectonic K-feldspar augen. Locally albite porphyroblasts replace white mica in the hinges of post-shearing folds. This lithology is more completely described and discussed in Chapter 6.

3:2.7 Mylonitic Leucogranites

High strain, fine-grained, felsic rocks are exposed within the Sonnblick Dome and can be traced for distances in excess of 1km. These differ from the fine gneisses and leucogranite aplites in having a strongly developed mylonitic foliation (Figure 3.3a). Mineralogically these units are composed of fine grained quartz, feldspar and white mica all smaller than 0.5mm in size. Locally, 1mm anhedral plagioclase augen, containing white mica inclusions, are preserved as are corroded garnets, which are pink/orange in hand specimen and are probably igneous in origin. No K-feldspar augen are observed but small anhedral perthites (up to 0.2mm) show that some K-feldspar is present in the matrix. White micas form 0.5mm laths and biotite is present but is not as abundant as white mica. This lithology is considered to be a strongly deformed mylonite unit derived from one of the fine-grained, primary igneous lithologies exposed within the Dome. The most likely candidate is the Fine Gneiss.

Figure 3.3a. Fine-grained, mylonitic leucogranite showing a strongly developed spaced foliation defined by quartz-rich and white mica-rich domains.

Figure 3.3b. Garnet-bearing amphibolite found within a 2m long sli ver within a large garnet-absent amphibolite.

Figure 3.3c. Micrograph of biotite schist lithology. Biotite is the only mica present, shows a brown-colourless pleochroic scheme and can be clearly seen to overgrow the pervasive foliation. A small epidote grain (ep) is preserved within the schist.

Figure 3.3d. Exposure of banded gneiss composed of strongly deformed augen gneiss and amphibolite. This type of banded gneiss is locally exposed within the mapped area but never on a mappable scale.

Figure 3.3e. Banded gneiss composed of partly metasomatized micaceous Coarse Augen Gneiss and mylonitized aplitic leucogranites.

Figure 3.3f. Garnet-mica schist belonging to the Inner Schieferhülle showing a strongly developed foliation defined by quartz-rich and mica-rich domains and well developed garnet porphyroblasts.


a

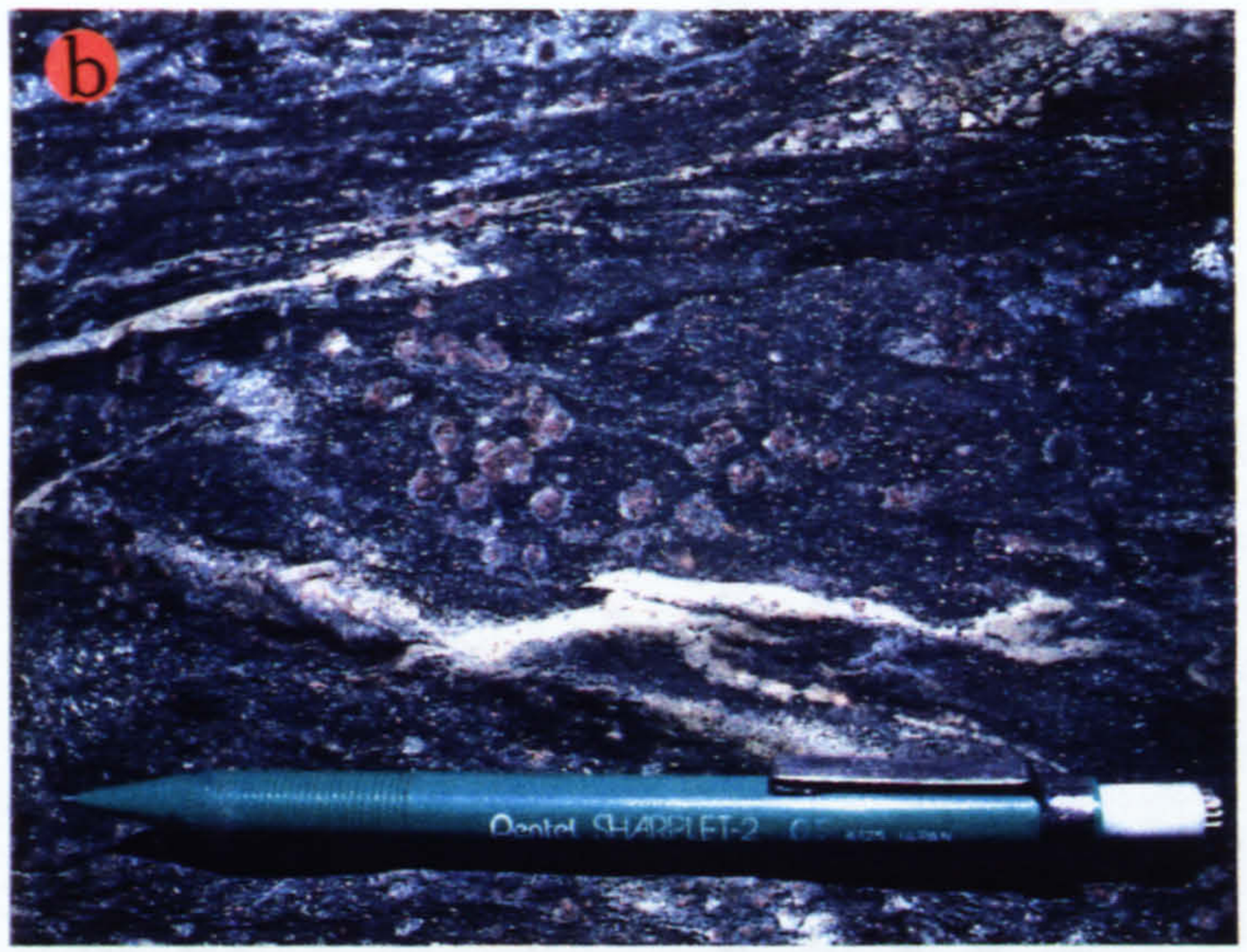
b

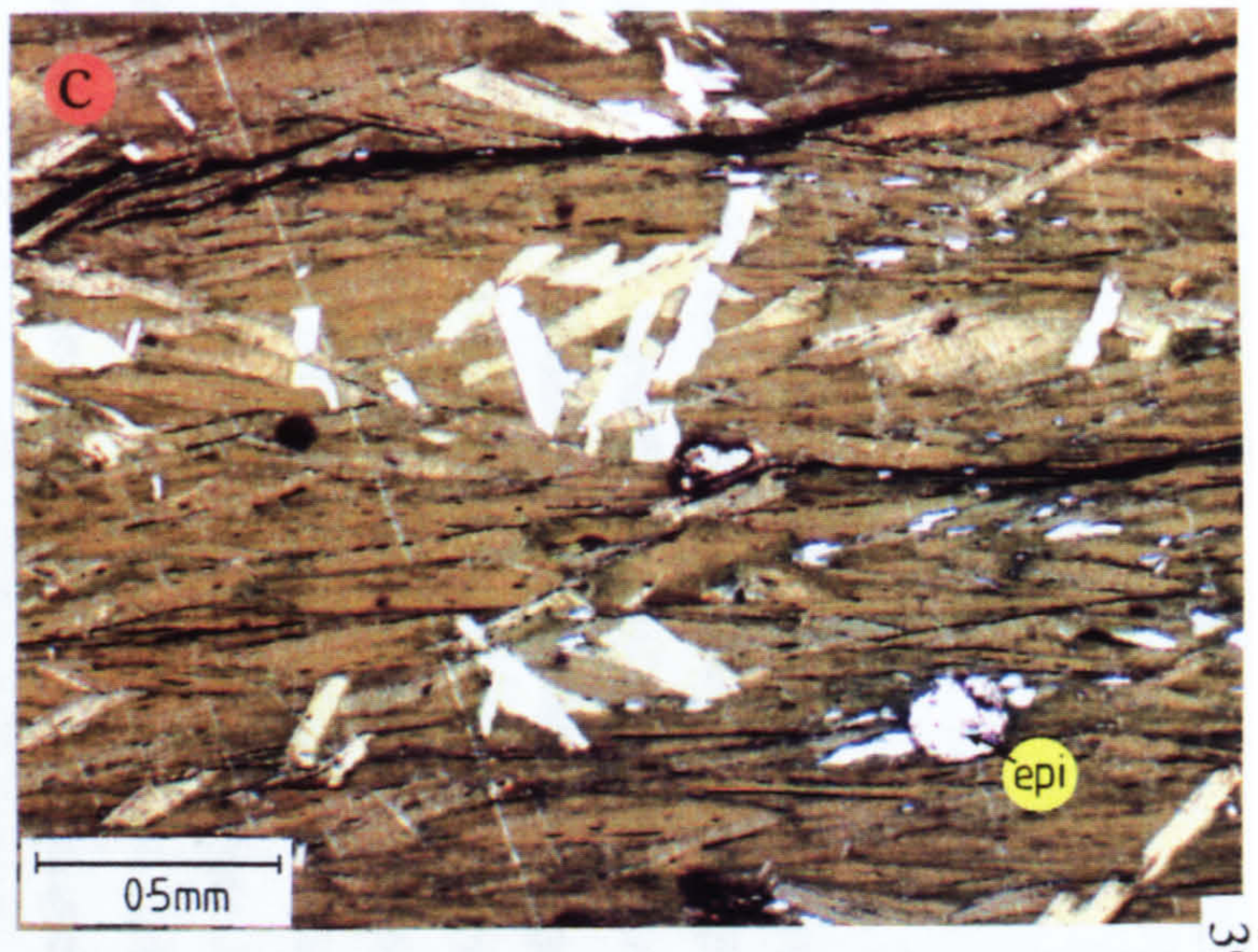
c
epi
0·5mm


d


e


f

3:3 Geochemistry of the Sonnblick Gneisses

Whole rock geochemical data for the gneisses are presented in Appendix 3:1. The dominant augen gneiss lithology in the Sonnblick region falls within the granite field of the Streckeisen (1976) classification of granitoid rocks and no variation is observed between undeformed and deformed varieties of the gneiss except when deformation is accompanied by extensive metasomatic alteration (Figure 3.4). The gneisses generally range from metaluminous to peraluminous in composition and most of the analysed samples fall within the I-Type granite fields of Chappel and White (1974) and the revised fields of White and Chappel (1983) (Figure 3.5). The data generally lie within the 'Volcanic Arc Granite' tectonic discrimination field (Pearce *et al* 1984) and the low and intermediate strain gneisses cannot be differentiated on these diagrams (Figure 3.6).

The Rb-SiO_2 discrimination diagram (Figure 3.6a) suggests a syn-collisional intrusive setting for primary granite formation and therefore differs from the volcanic arc setting indicated by the other discrimination diagrams. This may be the result of later large scale Rb mobility and enrichment during Alpine metamorphism and suggests that care must be taken when applying the genetic classification of granites to rocks which have a long history involving multiple deformation and metamorphic events.

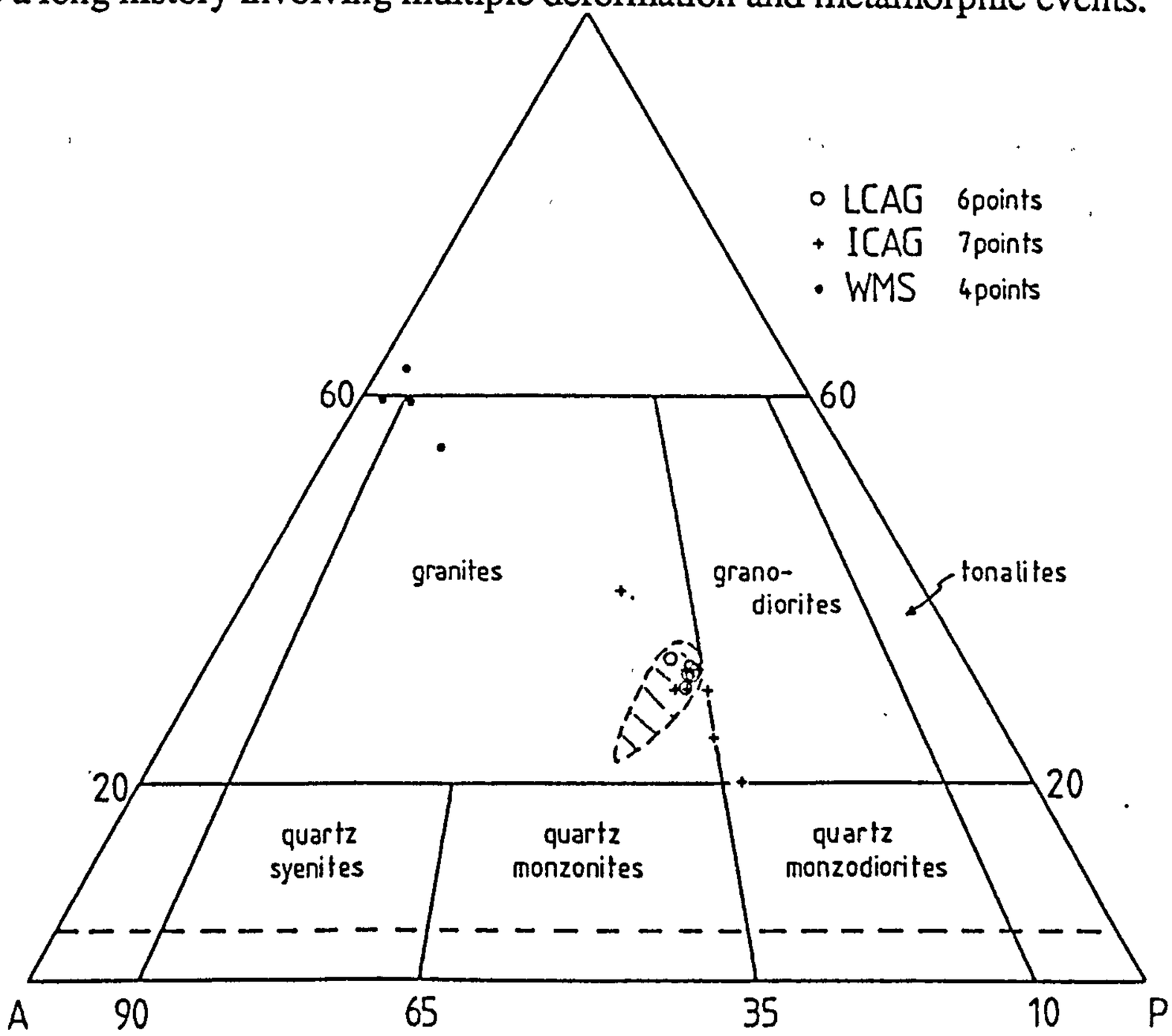

Figure 3.4. Quartz-Alkali feldspar-Plagioclase (QAP) diagram (after Streckeisen 1976) showing the coarse augen gneisses of the Sonnblick Dome to be granites (*ss*) to granodioritic in composition. Positions are calculated based on CIPW normative compositions calculated for some of the gneiss analysed by XRF (see Appendix 3). Fe^{3+} is assumed to be 10% of total Fe. The shaded area corresponds to the field of Sonnblick orthogneisses analysed by Finger and Steyrer (1988). White mica schists, interpreted to be derived from coarse augen gneisses by syn-deformational metasomatic alteration (Chapter 6) are shown for comparison.

Figure 3.5. Graphs to illustrate the geochemical character of different igneous units within the Sonnblick Dome. Abbreviations are Low Strain Augen Gneiss (LCAG); Intermediate Strain Coarse Augen Gneiss (ICAG); Fine Augen Gneiss (FAG); Fine Gneiss (FG) and Micaceous Leucogranite (ML). White Mica Schists (WMS) are shown only for comparison.

a) K_2O vs Na_2O plot which show the primary gneiss lithlogies to plot in the I-Type granite field of White and Chappel (1983).

b) Plot of mol (Al_2O_3/ Na_2O + K_2O + CaO) (=ALI) versus SiO_2. Lithologies are metaluminous to peraluminous and plot in the I-Type field below 1.1 (Chappel and White 1983) or ALI <1.05 (Pitcher 1982).

c) Plot of K_2O versus SiO_2 showing that the lithologies plot in the High-K field of the magmatic series of Peccerillo and Taylor (1986).

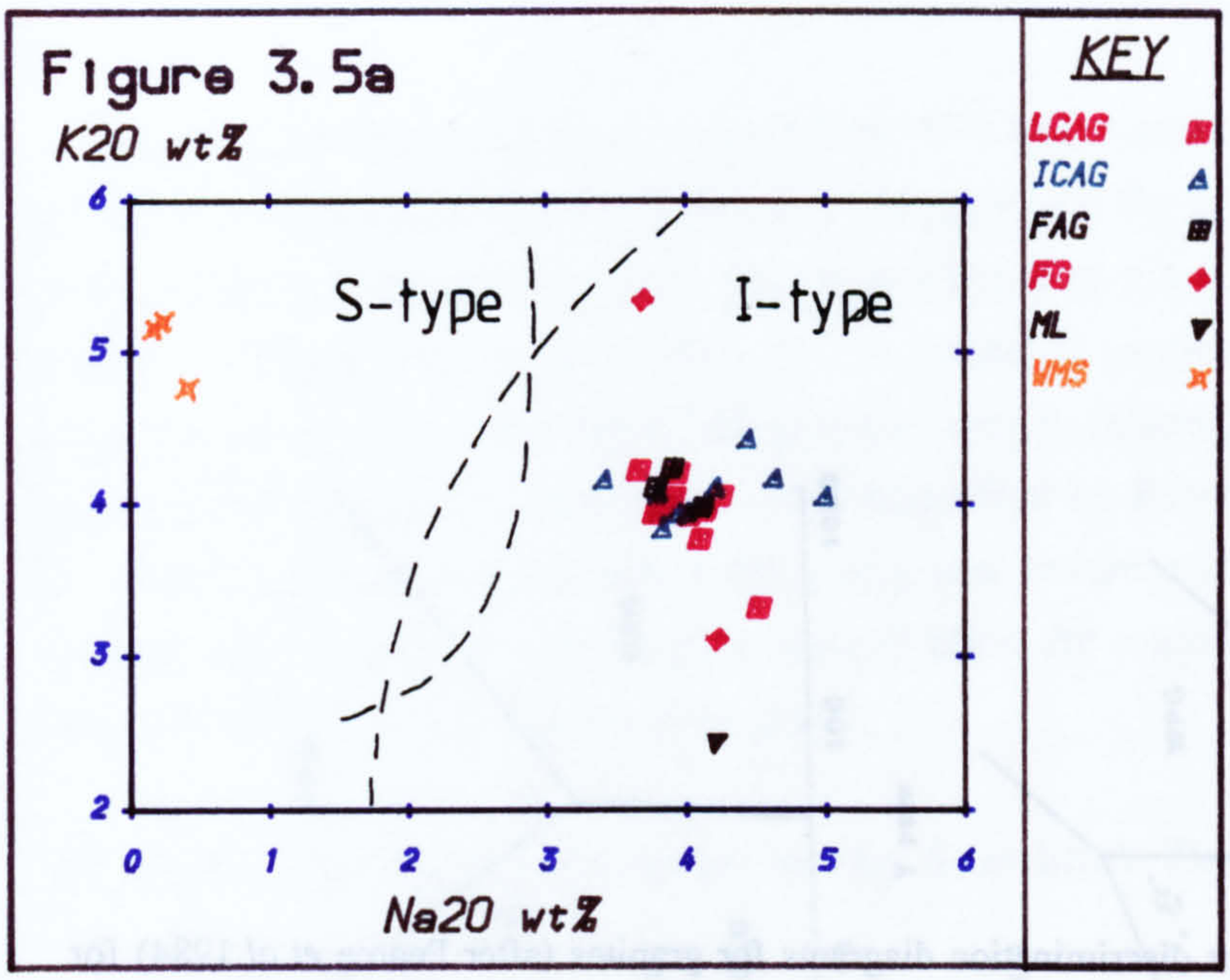
Figure 3.5a
K2O wt%
S-type
I-type
Na2O wt%
KEY
LCAG
ICAG
FAG
FG
ML
VMS

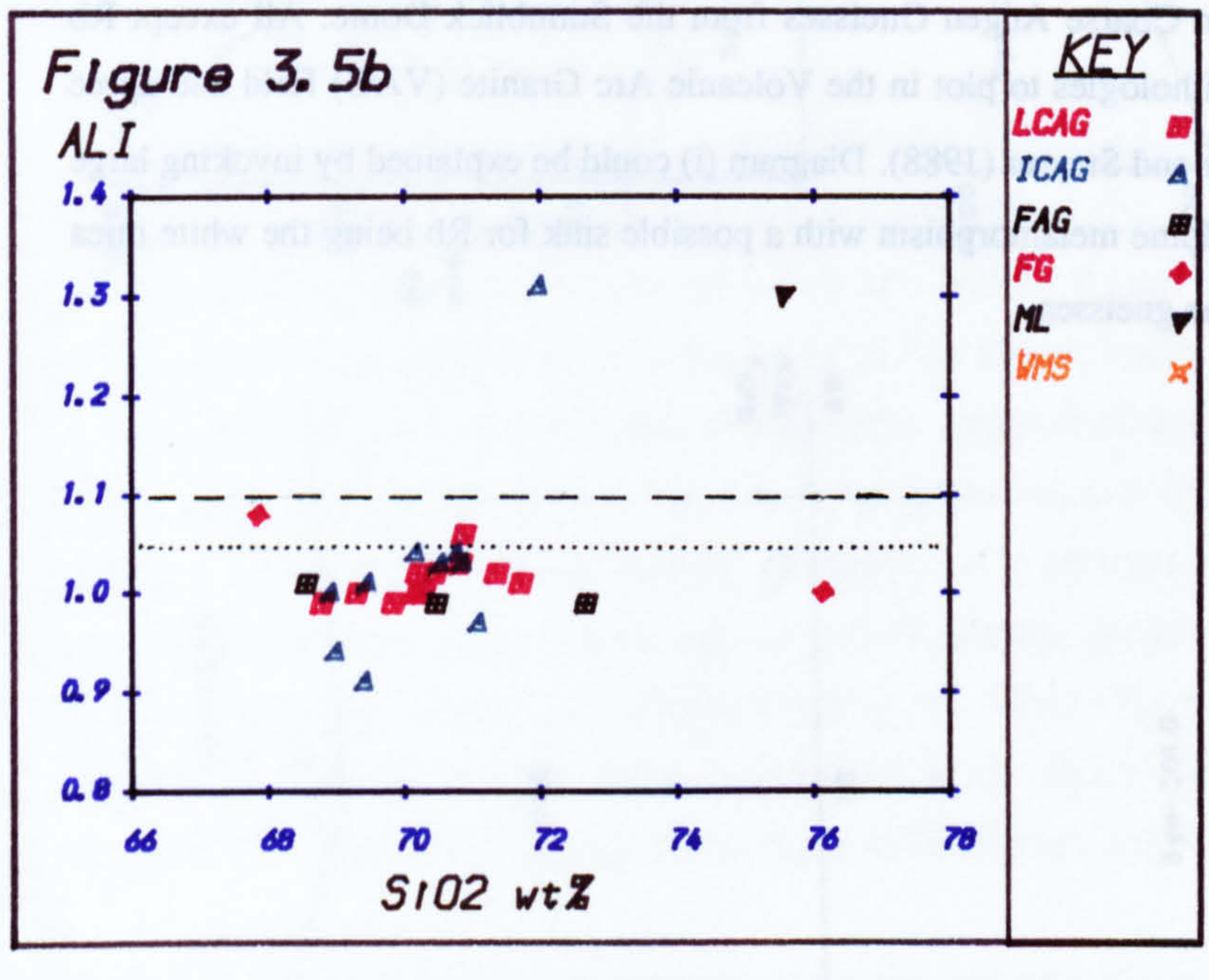
Figure 3.5b
ALI
SiO2 wt%
KEY
LCAG
ICAG
FAG
FG
ML
VMS

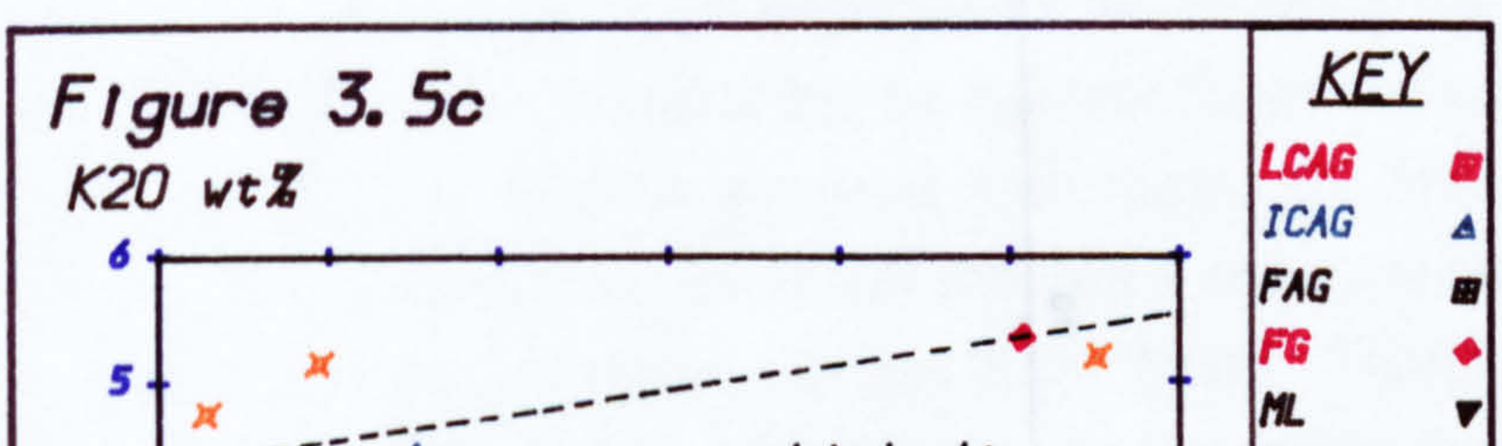
Figure 3.5c
K2O wt%
high-K
normal-K
low-K
SiO2 wt%
KEY
LCAG
ICAG
FAG
FG
ML
VMS

Figure 3.6. Trace element discrimination diagrams for granites (after Pearce *et al* 1984) for Low- and Intermediate- Strain Coarse Augen Gneisses from the Sonnblick Dome. All except Rb ppm vs SiO_2 wt% show the lithologies to plot in the Volcanic Arc Granite (VAG) field and agree with the observations of Finger and Steyrer (1988). Diagram (i) could be explained by invoking large scale Rb enrichment during Alpine metamorphism with a possible sink for Rb being the white mica commonly developed within the gneisses.

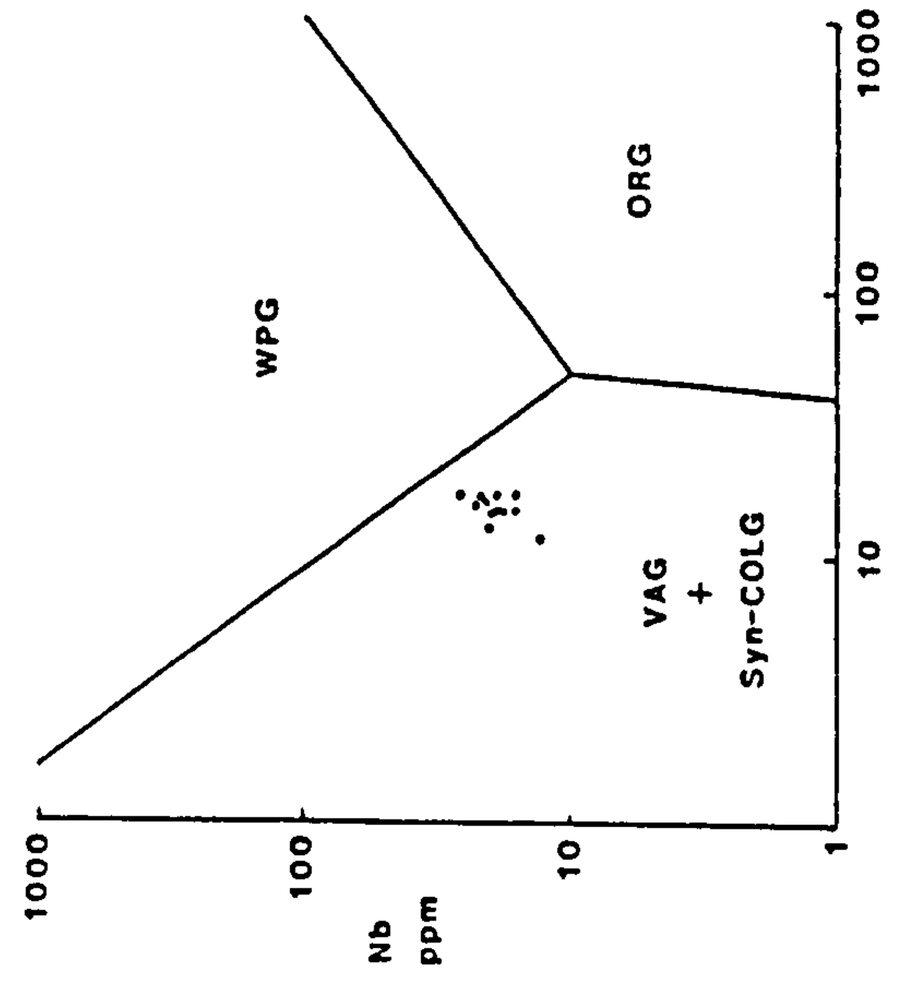
WPG
ORG
VAG
+
Syn-COLG
1000
100
10
1
Nb
ppm
1000
100
10
1
Y ppm

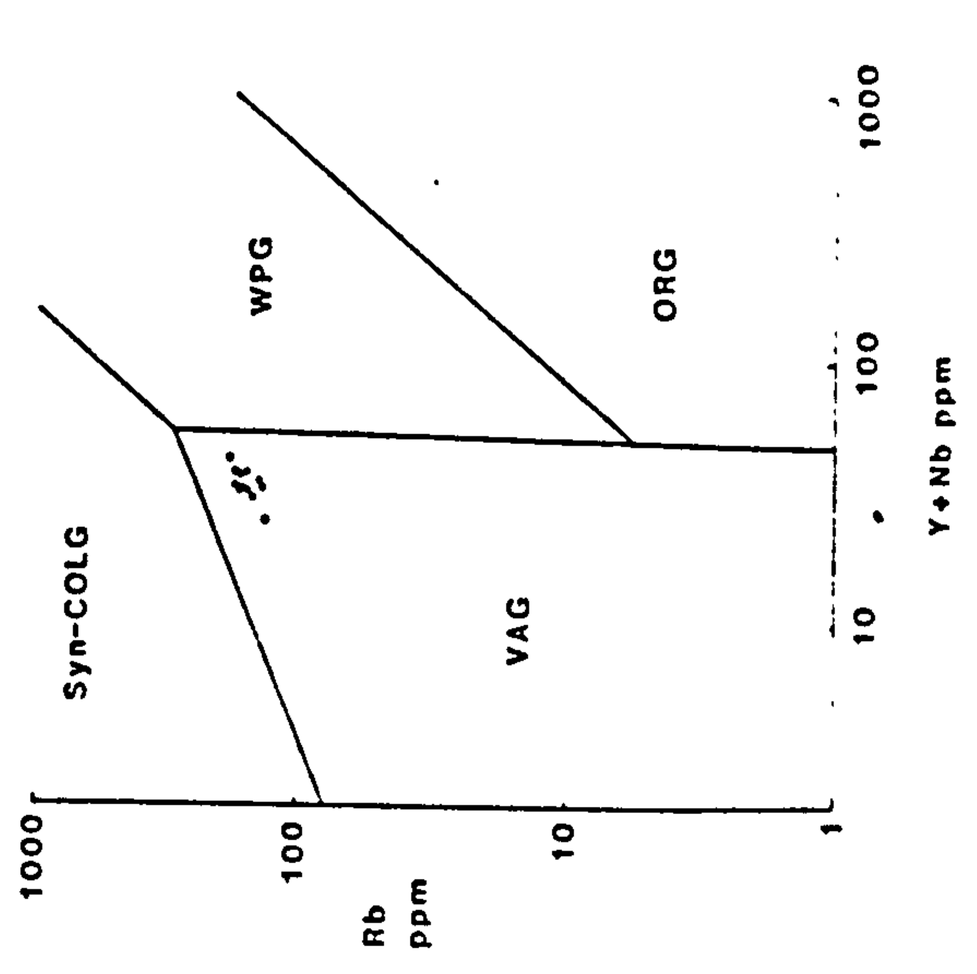
WPG
ORG
Syn-COLG
VAG
1000
100
10
1
Rb
ppm
1000
100
10
1
Y+Nb ppm

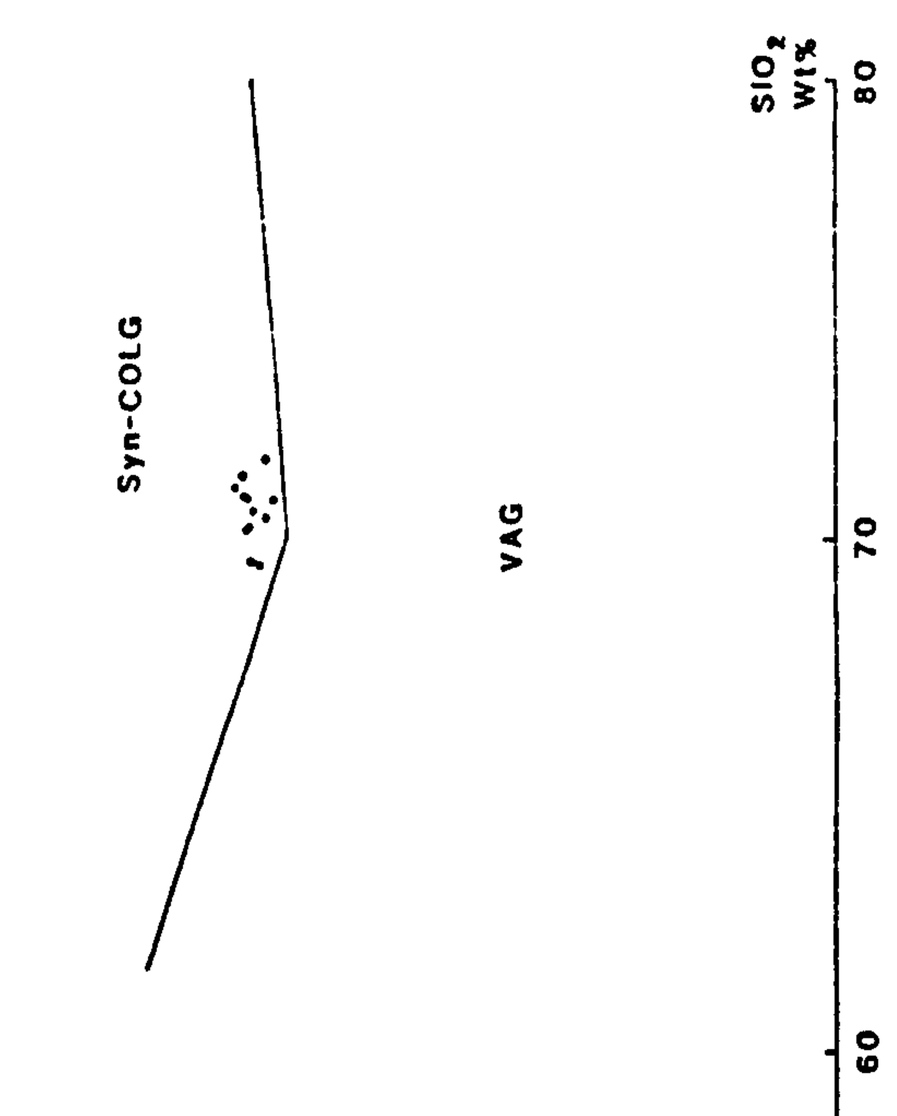
Syn-COLG
VAG
80
70
60
SiO2
Wt%

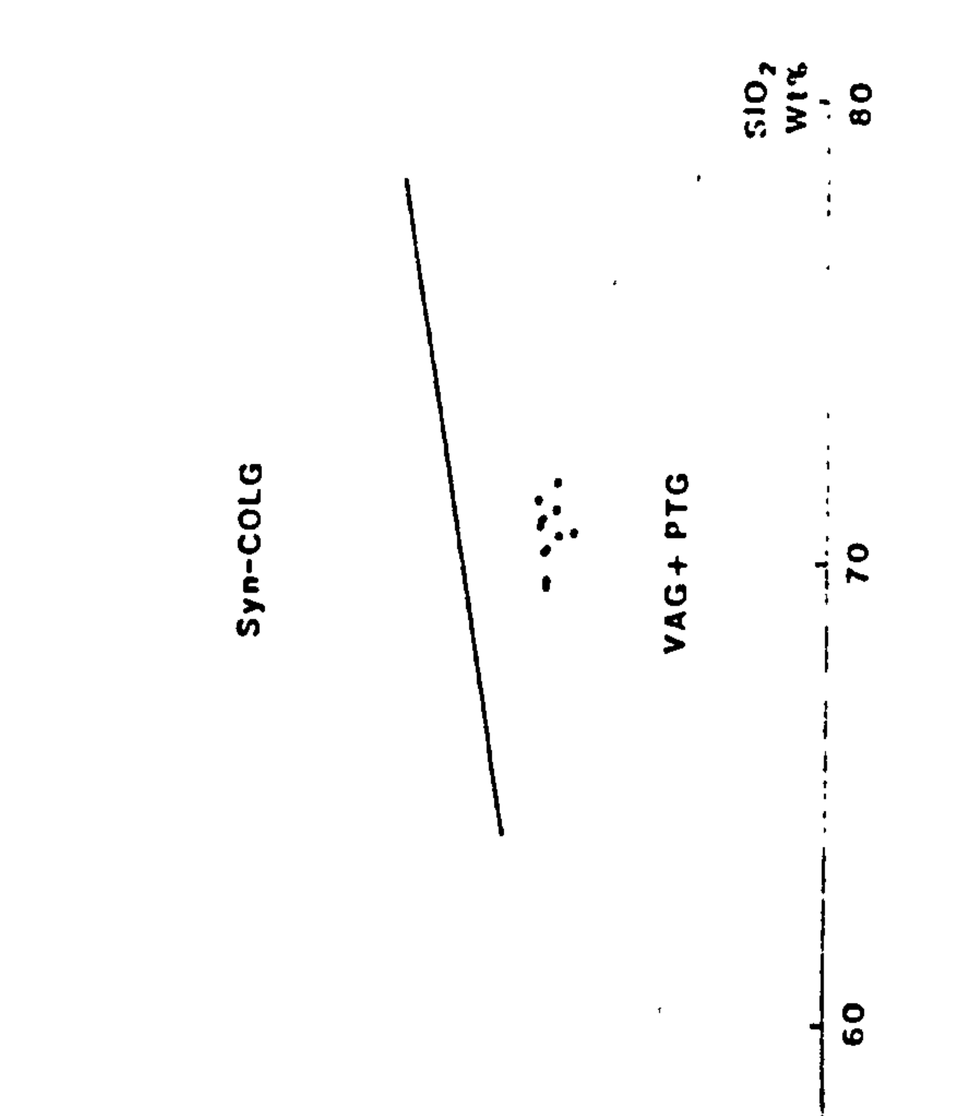
Syn-COLG
VAG+ PTG
80
70
60
SiO2
Wt%

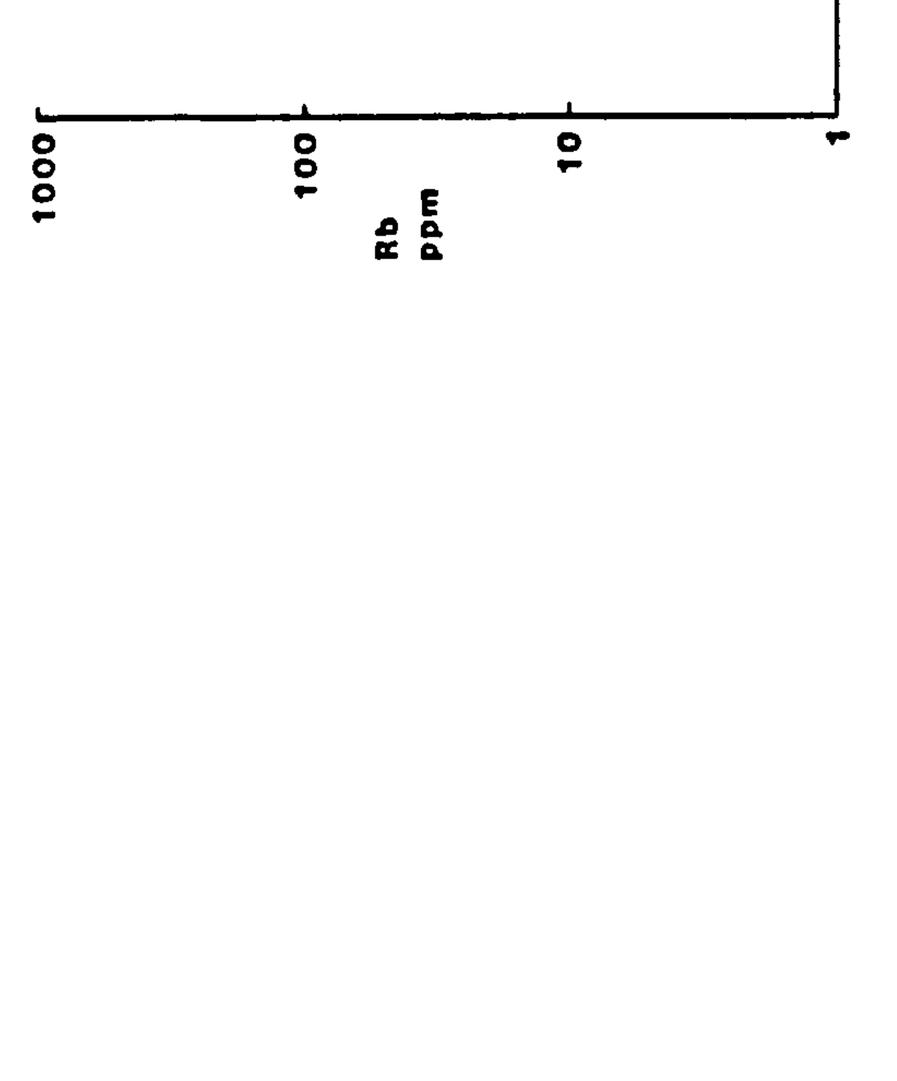
1000
100
10
1
Rb
ppm

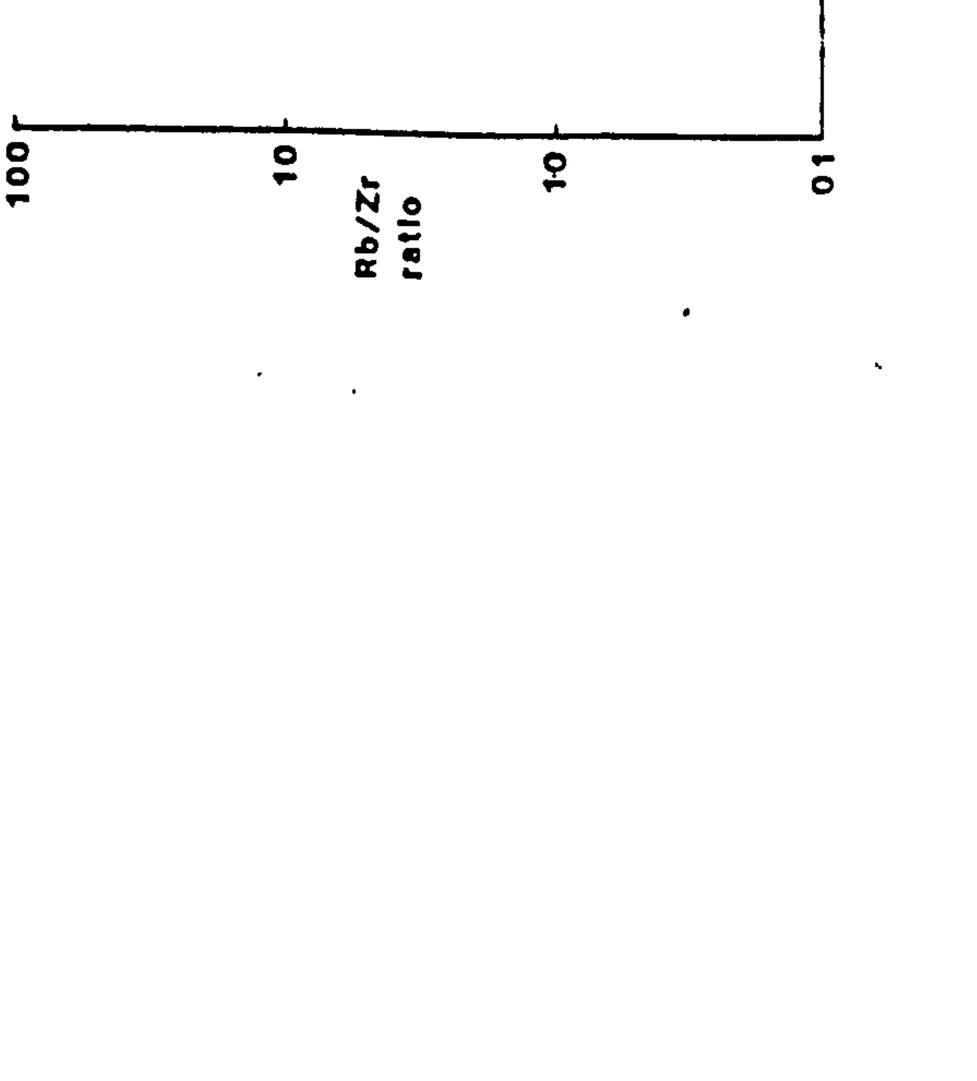
100
10
1·0
0·1
Rb/Zr
ratio

The geochemical evidence presented here does not contradict previous models for the origin of the Zentralgneis precursors which suggest that the granitic gneisses formed in a compressional continental margin due to melting above a subducting plate during the Variscan (Finger and Steyrer 1988). Such a model is supported by the morphology of separated zircons from the Sonnblick gneisses which, following the correlation between zircon morphology and granite petrology identified by Pupin (1980), suggests that the Sonnblick parental magma was a relatively low temperature and highly fractionated magma which was probably largely derived from the mantle and had calc alkaline (I-type) affinities (Dölzlmüller *et al.* In press).

3:4 Mafic Lithologies Exposed in the Sonnblick Dome

3:4.1 Amphibolites

Several amphibolite units are seen within the Sonnblick Zentralgneis Complex and in the nearby Hochalm-Ankogel massif to the north of the Sonnblick Dome. Cliff *et al* (1971) established a pre-granite intrusive age for the amphibolite units in the Hochalm area based on the presence of structures in the amphibolite that were absent from the Zentralgneis. In part of the Pennine basement amphibolites are therefore classified as a lithological unit belonging to the Inner Schieferhülle. Within the mapped area, there appears to be a spatial relationship between outcrops of amphibolite and Inner Schieferhülle. However, within the Sonnblick Dome, preserved igneous textures within undeformed amphibolites at Zirmsee (grid ref. 074147) have been used to infer that some of the amphibolites were originally basic dykes which intruded the igneous precursors to the Zentralgneis (Kieslinger 1936; Exner 1964).

Amphibolites which are found within the nappes of the Peripheral Schieferhülle in the Western Tauern Window (eg. the Kasertal formation) are interpreted to have formed as basic sills or volcanic extrusive units during the Mesozoic (Frisch 1984). If the Sonnblick amphibolites represent deformed and metamorphosed basic dykes, it is unlikely that they are of the same age as the Western Tauern Window amphibolites since leucogranite aplite units, interpreted to be Hercynian in age (Cliff *et al* 1971; Cliff 1981), cut the Sonnblick examples.

Amphibolites within the mapped area all show a well developed banding which commonly lies subparallel to a pervasive foliation along which amphiboles have a preferred orientation. For a detailed description of the undeformed dykes exposed at

Zirmsee the reader is referred to Kieslinger (1936). Mineralogically they consist of amphibole, epidote, feldspar and quartz. Opaque minerals include both 'martitic' hematite and magnetite where hematite has developed along crystallographically preferred planes in magnetite as a result of oxidation. Calcite is also present and in one example garnet is present (Figure 3.3b). This garnet bearing amphibolite is discussed further in Chapter 5.

Amphiboles are hornblendes in composition and have similar optical properties to those described for the 'dioritic gneiss'. Hornblende is elongate parallel to its c-axis and is usually about 0.5mm in length. Locally developed coarse amphiboles may reach up to several millimetres in length.

Epidotes again vary from pistacite to clinozoisite and plagioclase is albite to oligoclase in composition. Individual epidote grains usually form subhedral, rounded grains which are rarely larger than 0.5mm in diameter but which commonly form larger clusters. Feldspar and quartz occur interstitially between amphibole and epidote and have an anhedral form.

Mineralogical modes vary due to the heterogeneous development of banding within the amphibolites. Within amphibole-rich bands, hornblende may comprise over 80% of the volume, with quartz feldspar and opaque phases making up the rest. Epidote-rich bands may contain up to 50% epidote, of dominantly pistacitic composition, with quartz, feldspar and calcite. In more massive samples were banding is less discrete, modal values lie in the region of hornblende ≈50%, epidote ≈20% with quartz and feldspar totalling ≈25%.

3:4.2 Biotite Schists

Often associated with amphibolite lithologies are biotite-rich schists. These are almost entirely composed of biotite but also contain accessory epidote (Figure 3.3c). These units are relatively small and discontinuous and cannot be mapped at a scale of 1:10,000. They are generally found in areas of strong, localized deformation. This, combined with the spatial association with amphibolite units suggests that the biotite schist units represent deformed and metasomatized amphibolites.

3:5 Banded Gneisses

Two distinct banded gneiss lithologies have been seen within the Sonnblick Zentralgneis Complex. Both of these are strongly deformed and comprise a mixture of coarse augen gneiss and either amphibolite or mylonitized leucogranite. The first of these is developed on a small scale at the contacts of amphibole and coarse augen gneiss and within the mapped area cannot be shown at a scale of 1:10,000. On the shores of the Oschenigsee (grid ref. 192057), a banded gneiss similar to this lithology is spectacularly developed (Figure 3.3d) The second banded lithology is developed to the west of the Schwartzsee (grid ref. 142082) and can be traced or several hundred metres before it is no longer exposed. This unit consists of interbanded, strongly deformed, coarse augen gneiss and mylonitized aplite dykes (Figure 3.3e). The banding in both cases is a direct consequence of intense and localized deformation and a detailed discussion of these units is reserved for Chapter 4.

3:6 Paragneisses Exposed in the Sonnblick Area

Gneisses derived from sedimentary precursors exposed within the mapped area can be divided into those belonging to the Palaeozoic Inner Schieferhülle and those which form part of the Mesozoic Peripheral Schieferhülle sequence. The two different units may be distinguished by several means. The Inner Schieferhülle is carbonate free, contains aplite dykes and underwent pervasive deformation and metamorphism prior to the intrusion of the Zentralgneis precursors. Conversely, the Peripheral Schieferhülle commonly containscarbonate material, does not contain aplite dykes and only underwent Alpine tectonism. These differences enable different members of these two groups to be identified within the Sonnblick area.

3:6.1 The Inner Schieferhülle Lithologies.

Two mapped lithological units have been assigned to the Inner Schieferhülle, garnet-mica schists and micaceous phyllites.

a) Garnet-Mica Schists

There are several exposures of garnet-mica schist and the different exposures, although having many similar features at outcrop scale, show slight variations in mineralogy and preserved textures on a microscopic scale. All exposures of this lithology have a well developed foliation (Figure 3.3f).

Garnet-mica schist, exposed within a large quarry to the southeast of Wurten Speicher (grid ref. 162066), contains garnet, white mica, chlorite, quartz and chloritoid (Figure 3.7a). Small amounts of epidote and opaques are also observed. Garnet ocurs as small, subhedral, equant grains up to 0.5mm in diameter. White mica and chlorite occur together in domains which alternate with quartz domains and which define the foliation. Individual mica grains are often in excess of 1mm in length parallel to the foliation. Chlorite has a similar lath-like morphology and is less abundant than white mica. Chloritoid forms 0.5mm euhedral grains which are elongate parallel to the foliation.

In garnet-mica schists sampled from the stream section to the northwest of Wurten Speicher (grid ref. 148087), a coarse grained texture is observed. Euhedral garnets up to 3mm are observed which are distinctly zoned. Small, unzoned garnets up to 0.5mm in diameter are also present. White mica, quartz and chlorite make up the matrix. Chloritoid is absent but blue-green amphibole, which is partially replaced by chlorite, quartz and small volumes of biotite, is preserved (Figure 3.7b).

b) Dark Micaceous Phyllite

This is exposed at a height of 2120m on the Panoramastraße road section (grid ref. 165082). The rock is a fine grained, strongly deformed phyllite composed of white mica, quartz and opaque phases. The complex deformation history and lack of carbonate material suggest that this lithology is part of the Inner Schieferhülle basement.

3:6.2 Peripheral Schieferhülle Lithologies

Peripheral Schieferhülle is exposed on the two ridges (Rote Wand-Sandfeld Kopf and Strappeleben Spitze-Baumbach Spitze) which represent the highest structural levels of the mapped area. All the Peripheral Schieferhülle lithologies have a strongly developed penetrative foliation which is parallel to the contact with the underlying Zentralgneis. Only a limited amount of research has been undertaken on these lithologies during this project and only 5 lithological units have been mapped. More detailed subdivision of these lithologies has been made by Exner (1964) who also presented a brief description of the rock types and noted some of the more subtle variations in their mineralogy. Droop (1981, 1985) presents a more detailed metamorphic study of the Peripheral Schieferhülle to the northeast of the Dome. Details on the microstructure and metamorphic implications of the observed assemblages and their textures are presented in Chapters 4 and 5 respectively. The location of the the lithologies are shown in Map1.

Figure 3.7a. Chloritoid-bearing garnet-white mica schists from southeast of the Wurten Speicher. Chloritoid (ctd), garnet (gnt) and chlorite (chl) appear to be in equilibrium. The matrix is composed of white mica and quartz.

Figure 3.7b. Amphibole- and biotite- bearing garnet-white mica schist from northwest of the Wurten Speicher. Biotite (bte) and amphibole (a) appear to be in equilibrium. Retrogression to chlorite (chl) is locally observed. White mica and quartz dominate the matrix.

Figure 3.7c. Coarse marble containing interlocking dolomitic carbonate grains and euhedral white mica. Small amounts of interstitial quartz (q) are also present.

Figure 3.7d. Fine marble comprised dominantly of fine grained dolomitic carbonate. Small through-going domains of white mica are also developed.

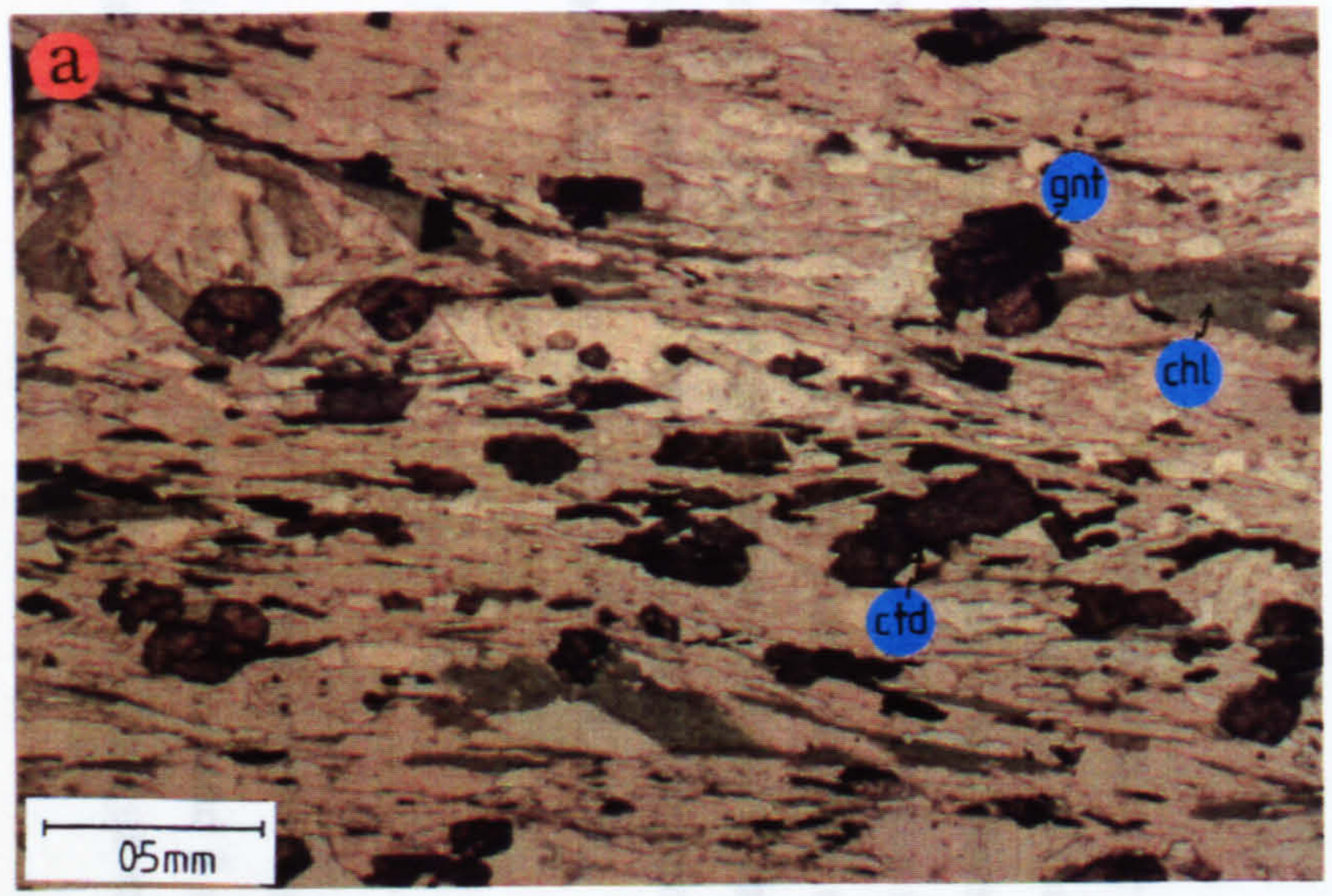

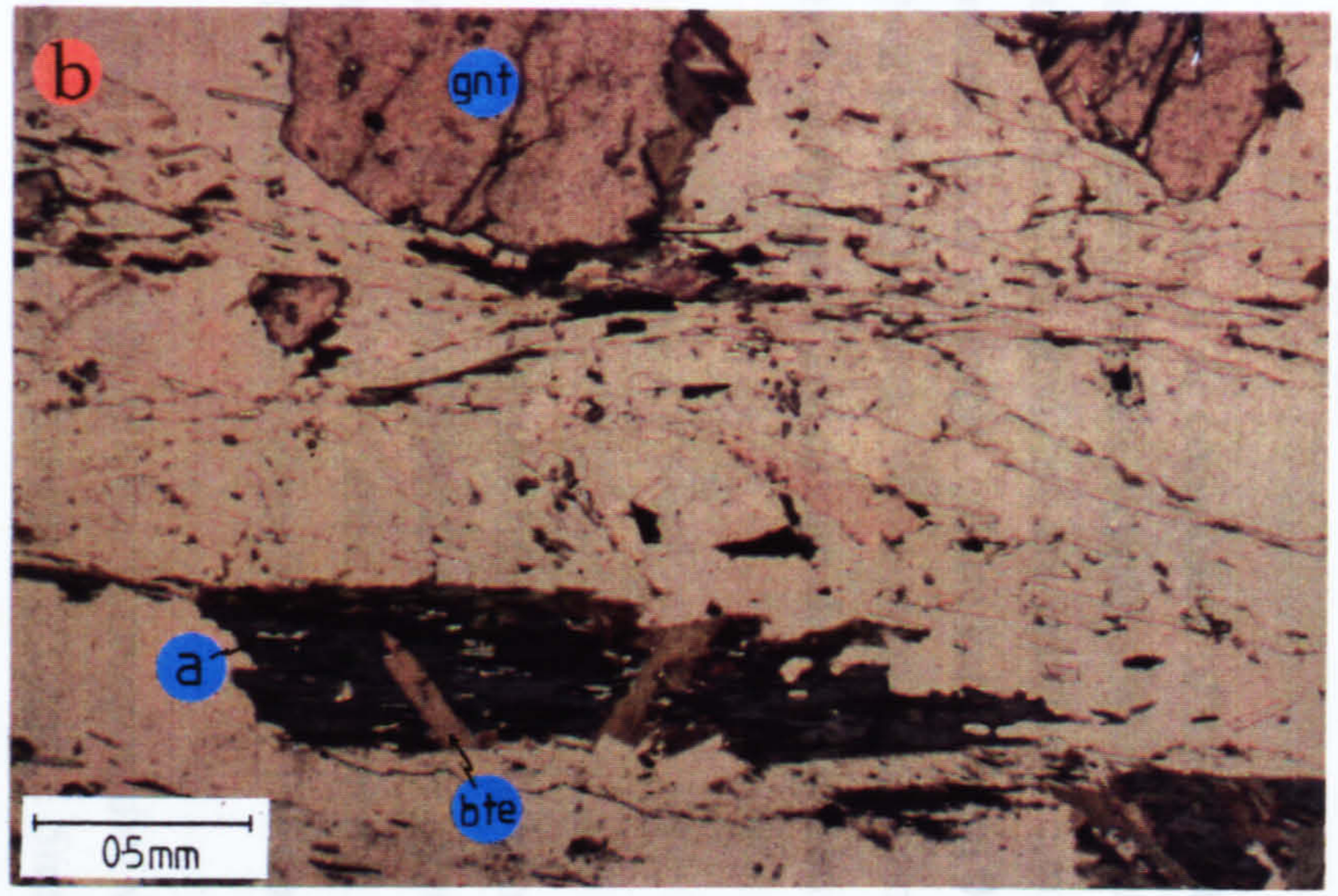

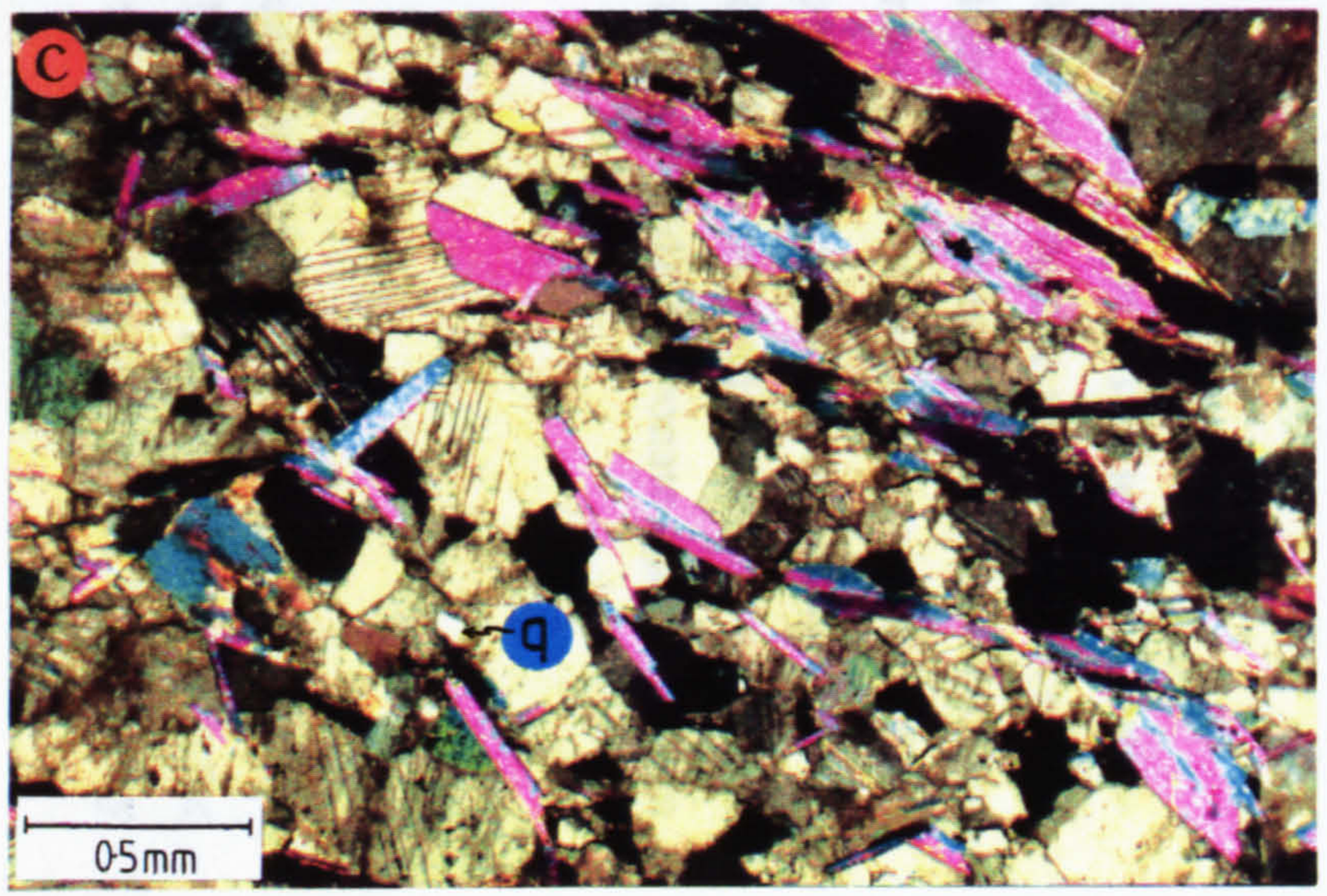

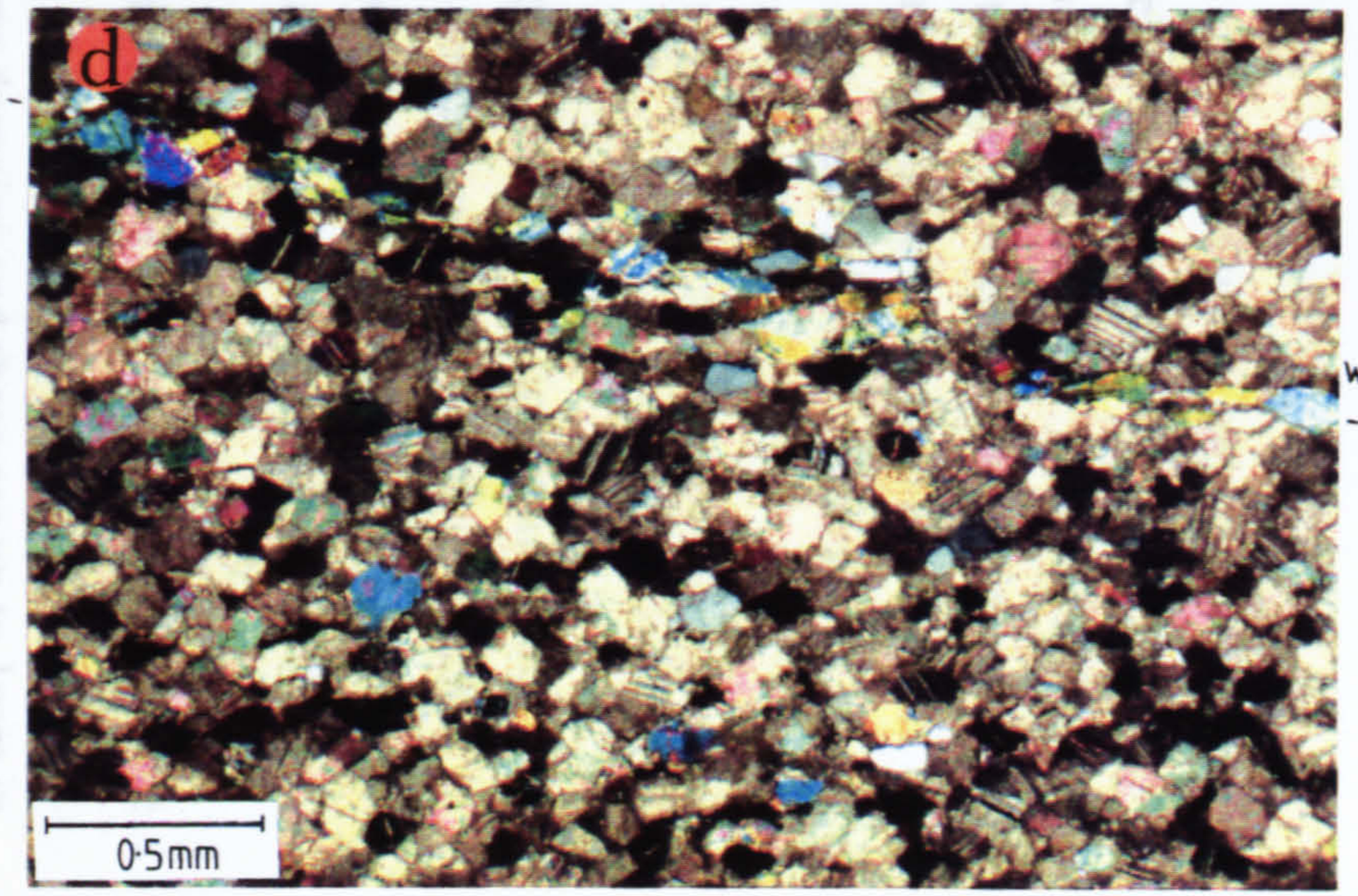

white mica domain

a) Calc-mica schists

This lithology is composed of carbonate, quartz and white mica which form relatively pure, elongate domains which parallel the deformation fabric. Grain sizes within individual domains are relatively constant while sizes vary between different domains. As an example, calcite varies from 0.1 to 1mm between domains separated by only a few millimetres. White micas are commonly elongate laths up to a millimetre in length. Both quartz and calcite show deformation features on a microscopic scale.

b) Black Phyllite

In hand specimen, this lithology is dark in colour and is very fine-grained. Some of these units contain elliptical plagioclase augen which have a long axis up to 2mm in length parallel to the foliation. In thin section these augen are composed of albite cores surrounded by distinct oligoclase rims. The core also contain fine graphite inclusions.

The matrix of the phyllite is composed of white mica and quartz domains which have variable thicknesses between 0.1 and 1.5mm. Indvidual grains are sub-mm in size. Dolomitic carbonate is observed within the quartz domains and these are up to 1mm in size. A dark opaque phase is also present.

c) Marble

Marbles in the mapped area show a variety of different grain size textures. Coarse-grained marbles comprise 1mm grains of interlocking carbonate and white mica with anhedral interstitial quartz (Figure 3.7c). Micas define a millimetre spaced, anastomosing foliation. Carbonate appears to be dolomitic in nature and makes up approximtely 60% of the rock, white mica and quartz make up about 20% each. Fine-grained marbles are richer in carbonate and consist of 90-95% calcite with quartz and mica making up the rest of the rock in approximately equal amounts (Figure 3.7d). Carbonate again forms an interlocking mosaic texture of 0.2mm grains.

d) 'Quartzite'

The term 'Quartzite' is taken from the nomenclature of Exner for unit xx along the Bogenitzen Scharte profile (Figure 1 and 2 of Exner's (1964) Tafel 7). In outcrop the lithology is seen as a series of 0.5-1m quartzo-feldspathic units which are locally very

micaceous and contain garnet porphyroblasts. In these micaceous area tourmaline is developed and lies in the plane of the well developed foliation. Thin sections of the garnet bearing sample show a garnet, white mica, quartz, chlorite, chloritoid mineralogy. Details of the features developed in this rock on a microstructural scale are discussed in Chapter 4.

e) Greenschist

A small exposure of a relatively pure, massive, pale green amphibole-rich material was exposed close to the summit of the Sandfeld Kopf. No thin sections of this have been studied.

Chapter 4
The Structural History of the Sonnblick Dome

4:1 Introduction

The aim of this chapter is to assess the deformation history of the Sonnblick Dome and develop a model for the Dome's structural evolution. This deformation history is related to recrystallization associated with peak Alpine metamorphism in order to place constraints on the timing of different stages of the deformation history which may then be used to constrain models of the development of the Eastern Alps. This chapter presents field and microstructural evidence which are interpreted in a later discussion.

4:2 Large Scale Structure of the Sonnblick Dome

The Sonnblick Dome is an elongate northwest striking, northeast verging, asymmetrical antiformal structure of the southeast Tauern Window (Figure 4.1) within the Zentralgneis unit of the Pennine Basement Complex. The Dome extends for about 24km along strike before rapidly thinning and passing into the Sonnblick Gneiss Lamella, which extends a further 15km along the Möll valley (Figure 2.8). A maximum outcrop width of about 8km is observed perpendicular to strike, while the Sonnblick Lamella has an observed outcrop width of about 10 metres at its southern limit (Exner 1964).

To the north, the Sonnblick Dome is separated from the Hochalm-Ankogel Zentralgneis massif by the Mallnitzer Mülde, a large synformal structure in the Peripheral Schieferhülle (Figure 4.1). A thin band of Schieferhülle lies to the South of the Dome and immediately to the south, is the boundary between the Pennine and Austroalpine units (refer to Figure 2.8). This contact was originally thought to be the site of subduction of the South Penninic Ocean. However, the contact has been recently interpreted to be the result of out-of-sequence thrusting in combination with a later phase of extensional deformation (Wallis 1987).

Although the major structural features of the Sonnblick Dome have been outlined by Exner (1964), a detailed structural investigation of the area has not so far been carried out. Exner (1964) recognised the overall antiformal structure of the dome and identified a series of gneiss lamellae within the overlying Peripheral Schieferhülle (Figure 2.8). These lamellae form relatively planar units which can be traced for up to 40km along

Figure 4.1. Profiles through the Sonnblick area showing the antiformal structure of the Dome (after Exner 1964). Of note are the cut offs of the Peripheral Schieferhülle against the light mica schist of the Inner Schieferhülle, to the northeast of the Dome (profile A).

Key

- Serpentine
- Greenschist
- Calc-mica schist and calc-phyllite
- Dark schist and dark phyllite
- Calcie marble
- Dolomite marble
- Quartzite
- Light mica schist
- Albite gneiss and porphyroblastic albite schist of the gneisslamellae
- Microcline augen gneiss of gneiss lamellae 1-4
- Amphibolite dykes
- Orthogneiss and old roof of the Sonnblick and Ankogel-Hochalm massifs

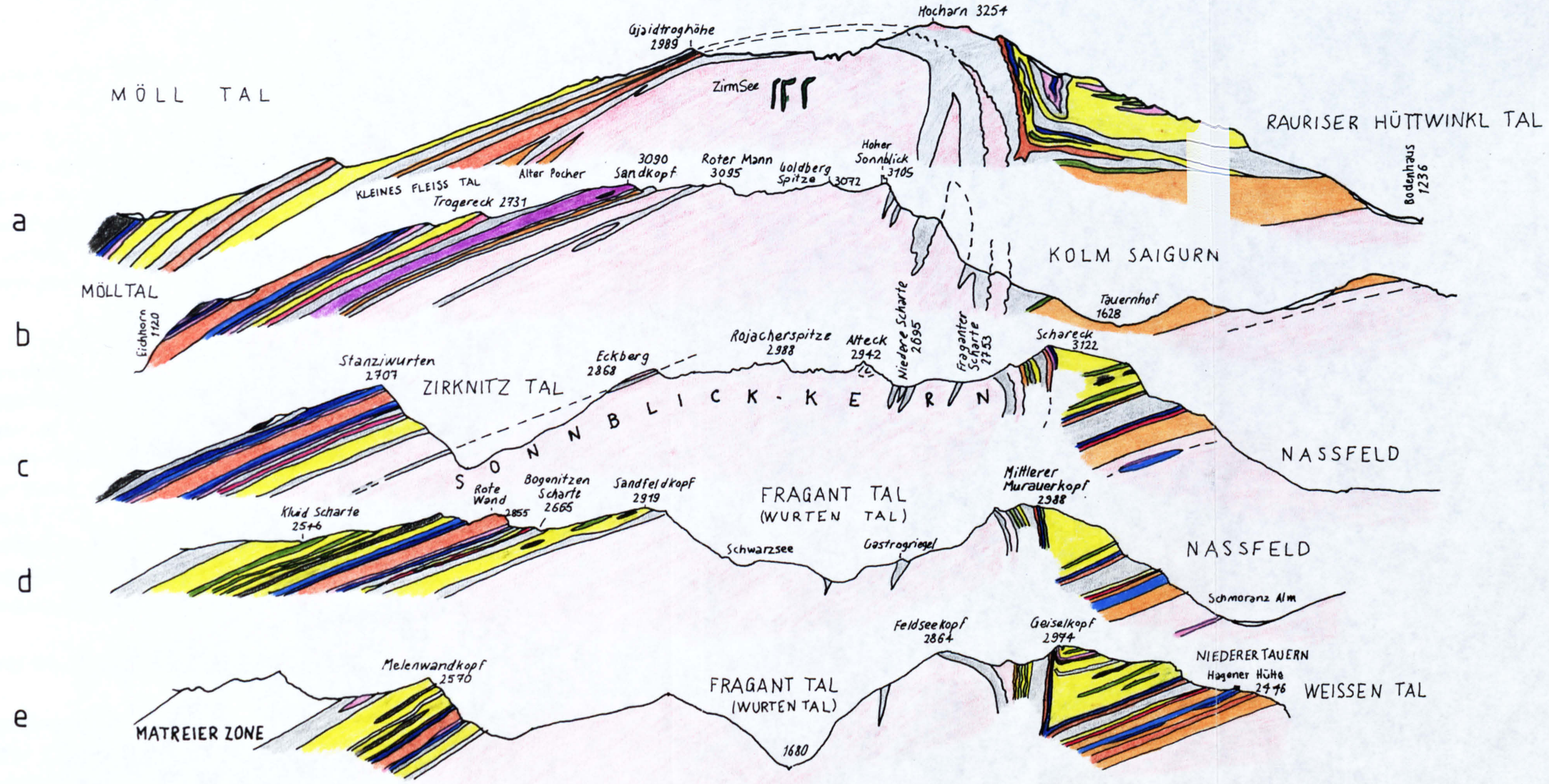

scale 1:50,000

strike and which range from the metre scale to thicknesses in the order of 200m. Several of these lamellae are augen gneisses similar to the Zentralgneis Complex. Other lamellae are fine grained or strongly mylonitized and could represent either orthogneisses or metasediments.

The continuity of the domal gneiss structure is interupted by the presence of two NW-SE strips of Schieferhülle material towards the northern end of the northeastern margin of the Dome. Exner's tectonic sketch of the Sonnblick group (Exner 1964, plate 1) implies that the Sonnblick Dome is comprised of three different tectonic gneiss units; the main gneiss body, the "Wurten Wedge" of the Sonnblick Dome and the "Knappenhaus Cylinder" which forms a continuation of the Sonnblick Gneiss Lamella. These units are bounded by faults which may be traced into the metasedimentary units at the northeastern margin of the Dome.

The late faults which cut across the area are parallel to the Möll-Drau fault line which is a fault zone extending fom the Periadriatic Line in the southeast, which appears to 'run out' within the Mallnitzer Mulde to the North of the Dome. Satellite imagery (Tollman 1976) suggest that the fault zone extends as far as the Grossglockner within the Tauern Window. The fault zone is covered by Quaternary deposits but is considered to be an approximately 60m wide mylonite zone based on refraction seismic studies at Lurnfeld, near Möllbrücke (Heinz and Wallach 1979). Mineral ages of approximately 20Ma in the Pennine units to the North of the Mölltal Line compared to 80 My ages to the south suggest that the Mölltal mylonite zone probably accommodates normal shear displacements and was associated with uplift of the Tauern Window in the Tertiary.

4:3 General Strain Distribution within the Sonnblick Dome

The distribution of strain within the Sonnblick Dome is heterogeneous on a variety of scales. Two different domains can be identified from field evidence based on the intensity of the foliation and its geometry relative to the Zentralgneis-Schieferhülle contact. At the top of the Dome a strong, mylonitic foliation parallels the contact of Zentralgneis with the overlying Schieferhülle. The importance of this foliation appears to decrease downwards through the Dome and at lower structural levels well-foliated augen gneisses pass into gneisses which only show a weak foliation and locally retain primary granitic textures (Plate 1 and 2). The foliation at these lower levels is geometrically less easily related to the overlying contact.

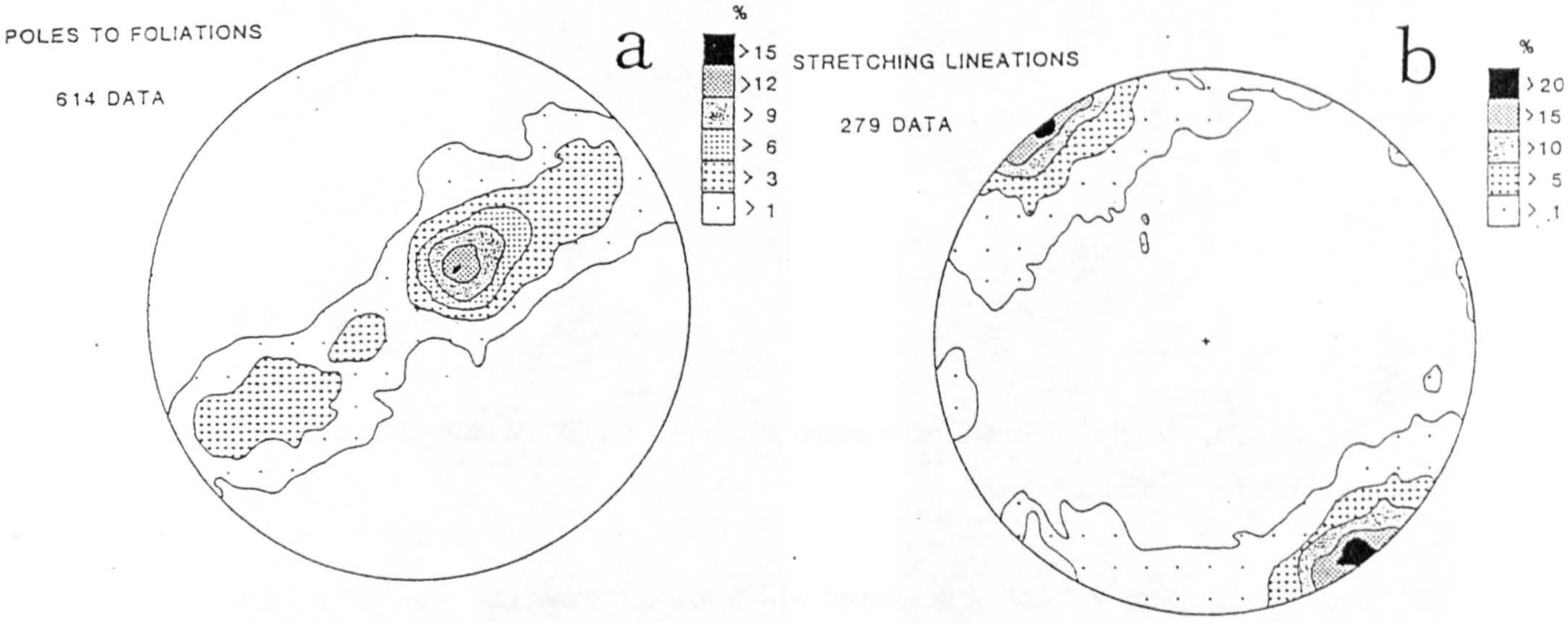

Figure 4.2. Equal area lower hemisphere projection of **a)** poles to foliations and **b)** stretching lineation data measured on the foliation planes. Stereonets are contoured using the Statis program developed by N.Woodcock (Cambridge), modified by C.Davis for use on Amdahl V7.

The contacts between the different strain zones are rarely discrete and partitioning of strain is commonly gradational over a range of several metres. Within the 'Low Strain Gneiss', areas of 'Intermediate Strain Gneiss' having a well developed foliation, are preserved (Plate 1). These zones appear to be discontinuous although this may partly represent the inability to follow contacts across mountainous topography. Similarly, small areas of 'Low Strain Gneiss' are seen within moderately well foliated gneiss. The distribution of these units represent the increasingly heterogeneous nature of deformation at lower structural levels relative to the more pervasive large strain deformation observed at the top of the dome.

Progressing eastwards towards the Sonnblick Lamella, the decrease in width of the Dome is not associated with a significant increase in strain within the gneissic basement. The formation of the lamella and the overall shape of the Dome appears therefore, to be related to the internal strain within the basement.

Fabrics are usually planar, S-tectonites which contain an identifiable mineral stretching lineation defined by mica and occasionally quartz ribbons. Occasionally, no mineral stretching lineation is developed. Foliations within the dome generally strike NW-SE and have poles which fall on a single, sub-vertical great circle (Figure 4.2a). This reflects the fact that all phases of folding which affect the foliation have sub-

Figure 4.3a. Weakly deformed coarse augen gneiss with a foliation defined by a slight quartz elongation and alignment of micas.

Figure 4.3b. Strong foliation developed within mafic enclave (S_e) which is oblique to a weak foliation within the surrounding gneiss (S_g).

Figure 4.3c. Elongate quartz domains surrounded by anastamosing mica-rich domains defining a moderate foliation within the coarse augen gneiss. Feldspar shows evidence for brittle deformation in the form of fractures which are filled by quartz fibres.

Figure 4.3d. S-C fabric in coarse augen gneiss showing a dextral shear sense. C-plane is parallel to the pencil.

Figure 4.3e. Strong, closely-spaced, mylonitic foliation within high strain augen gneiss at a higher structural level in the Dome. Asymmetric augen provide useful shear criteria in the field.

Figure 4.3f. Banded amphibolite unit in which two scales of banding can be seen. Coarser banding is associated with intrusion of aplite dykes, while finer scale banding is associated with differentiation during deformation and production of a strong foliation. In this example the banding has been disrupted by later extensional deformation.

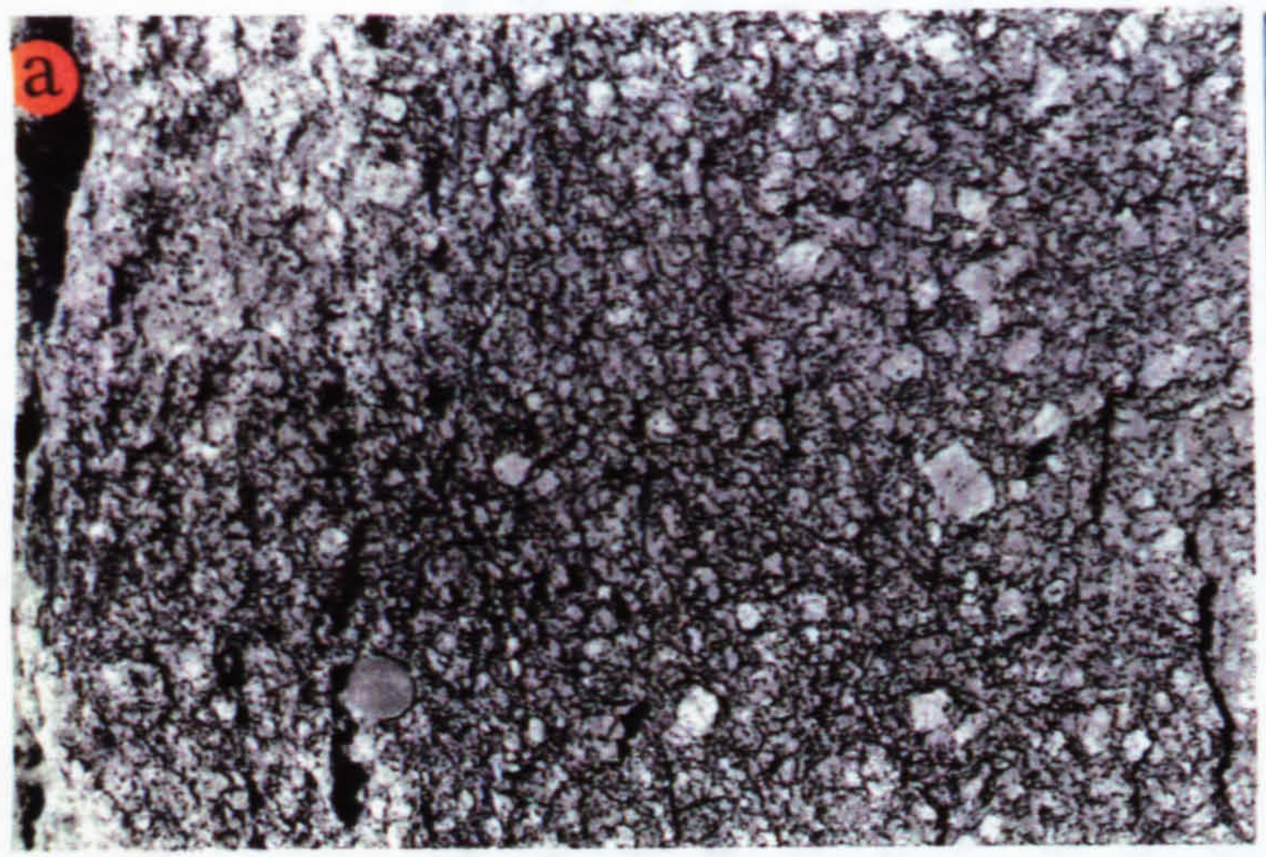
a

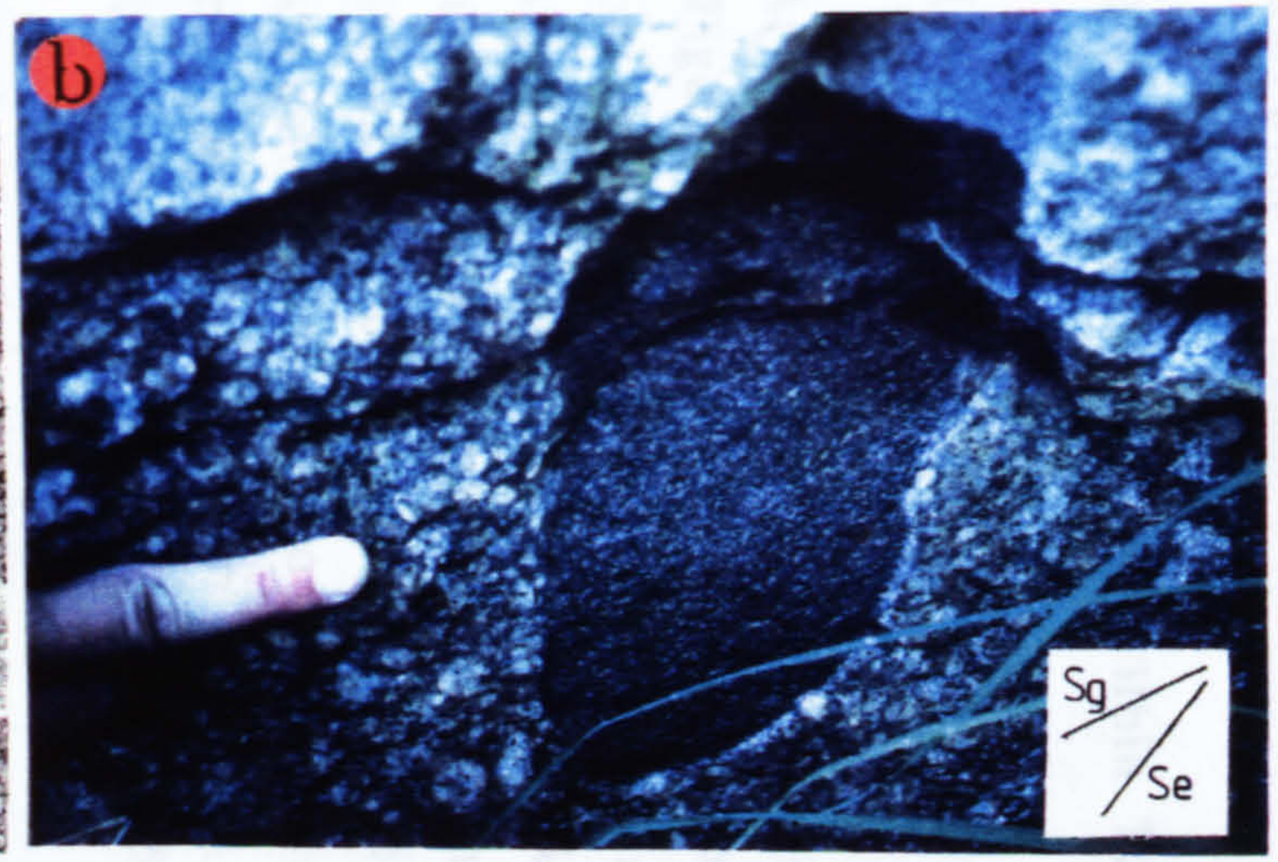
b
Sg
Se

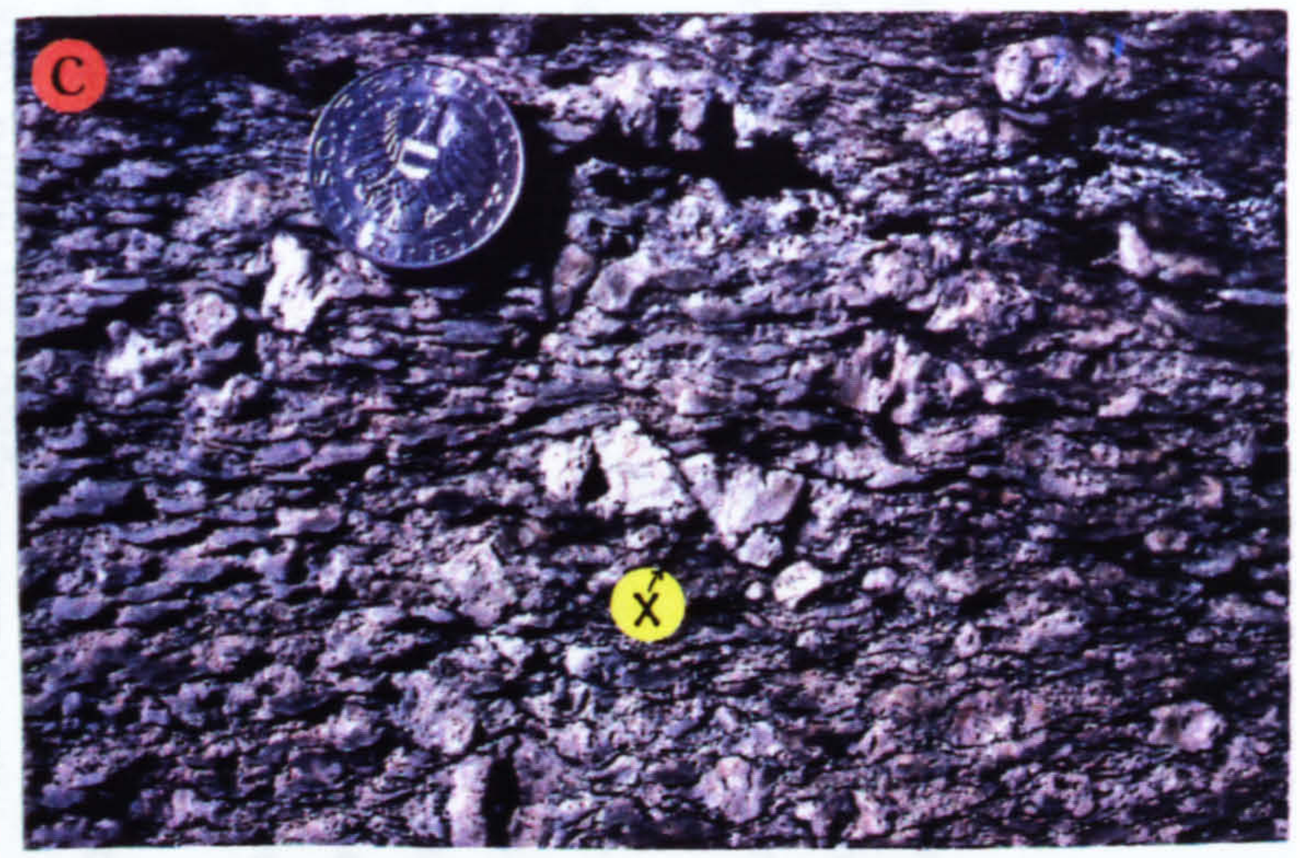
c
x

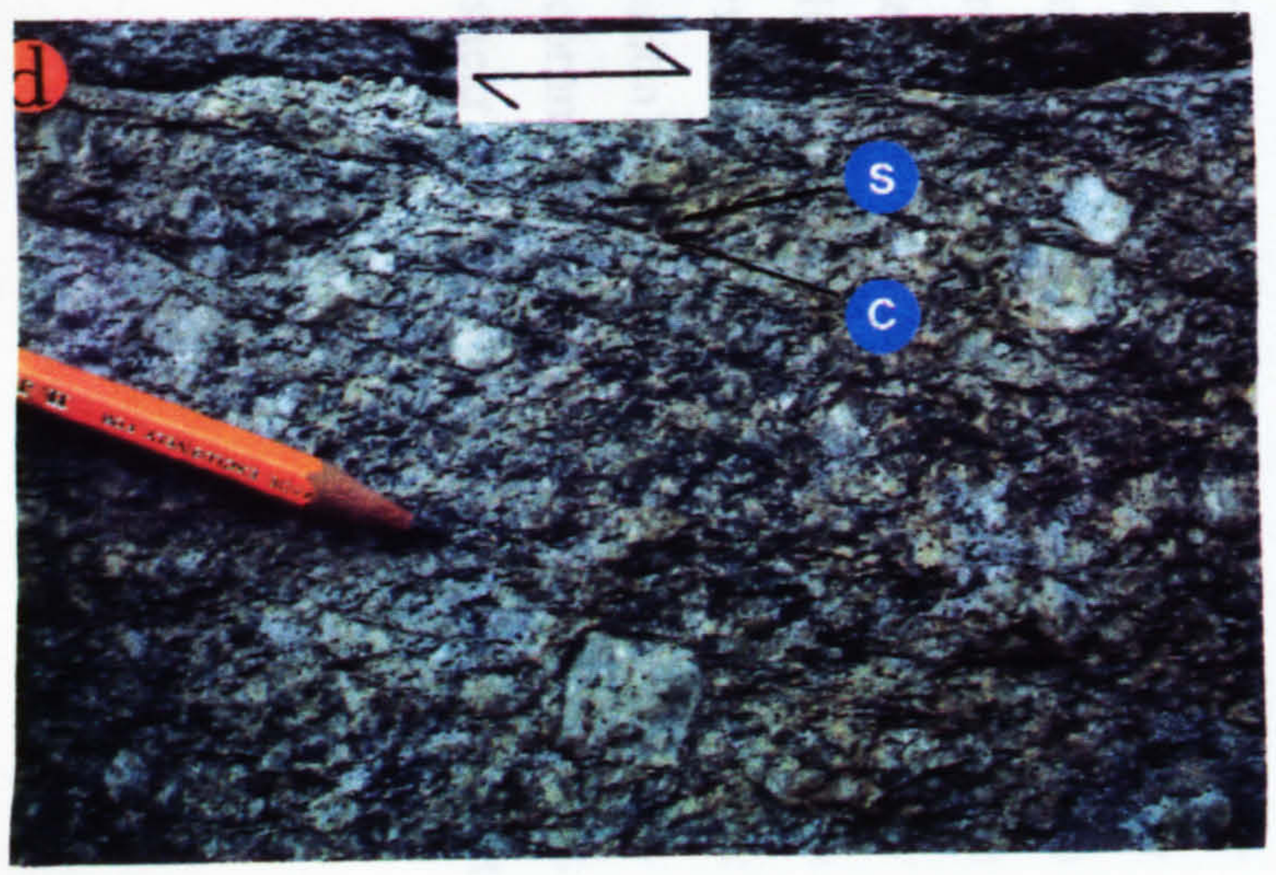
d
s
c

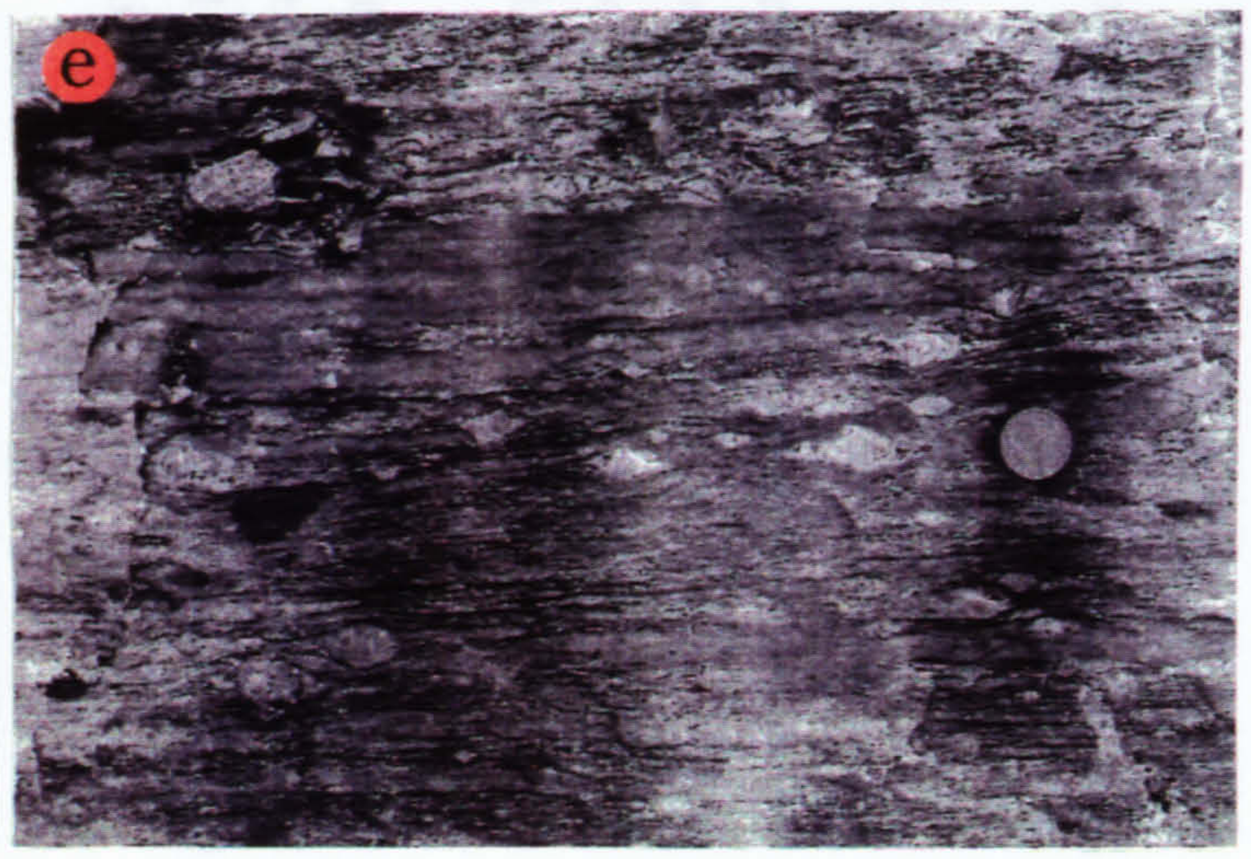
e

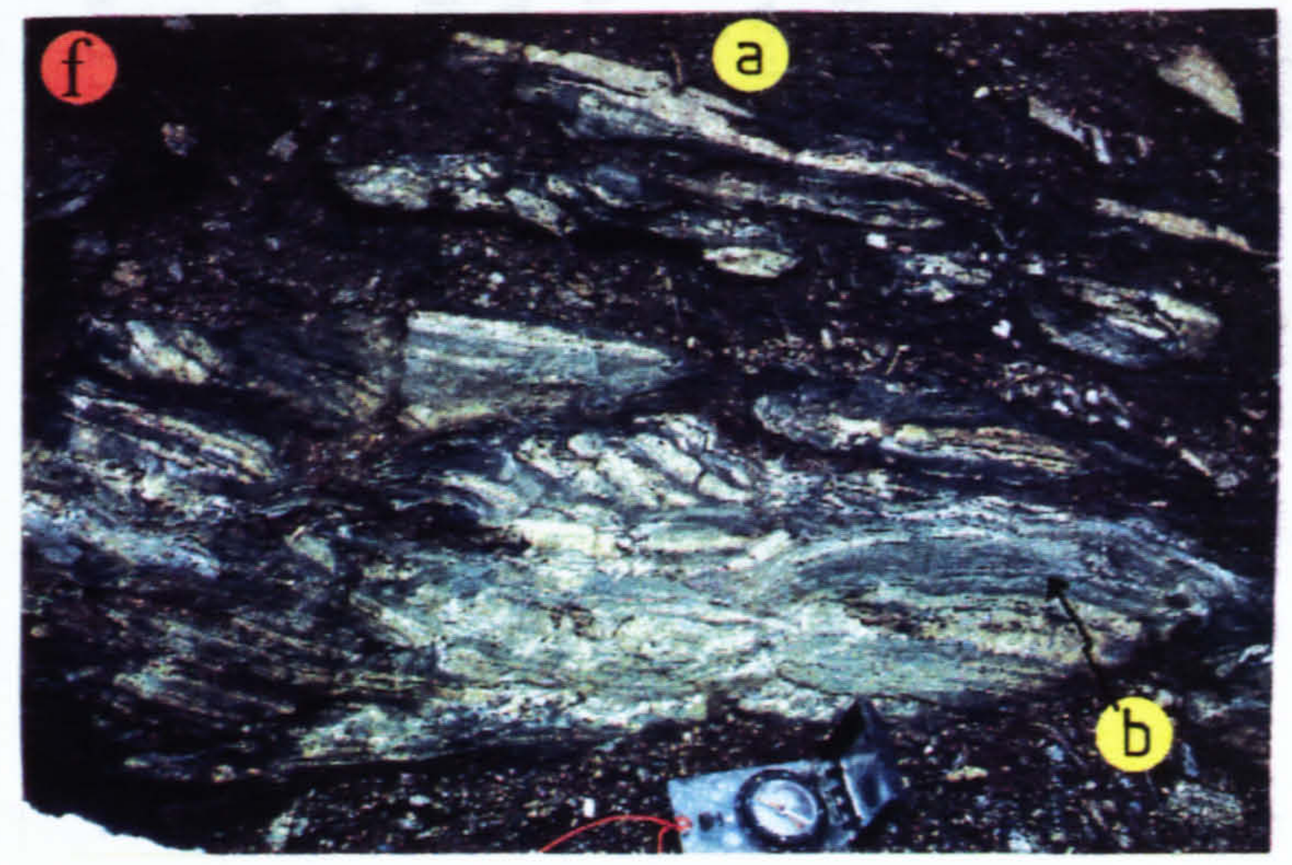
f
a
b

horizontal hinges which have a NW-SE azimuth (see 4:6). Locally, strong L-tectonites are developed and these are oriented sub-parallel to the dominantly NW-SE oriented mineral stretching lineations seen everywhere else within the Dome (Figure 4.2b).

Several folding episodes complicate the orientation of the gneissic foliation at most levels of the Sonnblick Dome, while overprinting relationships illustrate the formation of several foliations. In any particular domain within the lower structural levels of the Dome it is difficult to establish exactly when the foliation developed within the overall deformation history of the gneiss. However, the characteristics of equally well-developed foliations are similar at both at a mesoscopic and microscopic scale. Characteristics of these foliations are now discussed in terms of their relative structural positions within the Dome.

4:4 Foliation Development Within The Sonnblick Gneisses

4:4.1 Foliations Within Lower Structural Levels of the Zentralgneis

At low structural levels, the Zentralgneis varies from relatively undeformed granites (eg. Figures 3.1 and 4.3a) to moderately strained gneisses, in which mylonitic quartz ribbons and a mica foliation anastomose around K-feldspar augen (Figure 3.1b). In weakly deformed gneisses, the foliation is defined by uneven mica domains which anastomose around quartz and feldspar augen. These mica domains retain a cluster distribution derived from the original granite. Mafic enclaves (xenoliths?) within these weakly deformed gneisses commonly have a penetrative planar fabric oblique to the external gneiss foliation (Figure 4.3b). This could represent deformation associated with granite emplacement, or later Hercynian deformation.

With increasing strain, quartz elongation develops and mica domains become more planar and laterally more continuous (Figure 4.3c). White mica often becomes modally more important with increasing strain, which probably reflects partial alteration due to the infiltration of fluid during deformation. There is little shear displacement along the foliations developed within the lower structural levels of the dome. This is illustrated by aplite veins overprinted by a strong gneissic foliation which show little displacement along the foliation. K-Feldspar augen at these levels show signs of both brittle deformation (fractures at high angles to the foliation) and plastic deformation (slightly recrystallized feldspar tails). These features and commonly developed pressure shadows act as useful shear criteria. However, senses of shear inferred from these augen are not

generally consistent at low structural levels. Progressing towards the top of the Dome, an increasing majority of augen record a top-to-NW displacement. Locally developed S-C type fabrics within the gneiss (Figure 4.3d) (eg. Berthé *et al* 1979; Lister and Snoke 1984) also show this sense of shear.

4:4.2 Foliation Development at the Highest Structural Levels of the Sonnblick Dome

At the highest structural levels of the Sonnblick Dome, a strong, pervasive, fine-grained mylonitic foliation is developed in which feldspars form strongly deformed augen or elongate lenses parallel to the quartz-mica domainal fabric (Figure 4.3e and see Figure 3.1c). It is not possible to show unequivocally that all the mylonites at the top of the dome originated from coarse granitic gneisses and that no originally fine grained gneiss lithologies are incorporated within the mylonite sequence. However, the presence of strongly deformed feldspar augen (eg. Figure 4.3e) suggests that a large proportion of the mylonites are derived from a coarse grained granitic protolith.

The mylonitic foliation commonly contains a mineral lineation which is generally oriented NW-SE. Shear criteria on a handspecimen scale are not always recognisable but microstructural studies confirm a top-to-NW sense of shear associated with mylonitic fabric development.

Mineral stretching lineations (Figure 4.2b) combined with shear sense indicators show that top-to-NE displacements occurred locally within the high strain unit at the top of the gneiss dome (under the Peripheral Schieferhülle units of Rote Wand-Sandfeld Kopf in the south of the mapped region). This indicates at least local movement of the upper levels of the Dome towards the northeast. Similarly oriented stretching lineations have been observed to the northeast of the Dome in the Peripheral Schieferhülle of the Mallnizer Mülde (Wallis 1987).

The mylonitized gneiss observed in the south of the area is absent from the levels immediately beneath the Peripheral Schieferhülle of Baumbach Spitze and Weinflaschen Kopf, and the Schieferhülle stratigraphy differs between the north and south (Plates 1 and 2). These differences may be explained in terms of differential amounts of movement in the two areas since inferred transport directions lie perpendicular to the observed differences in stratigraphy. However, these observations suggest a

discontinuity in structural development between north and south and illustrate complications to the model of overall decreasing strain intensity with depth.

4:4.3 Banding and Foliation Development of the Sonnblick Amphibolites

On a mesoscopic scale, the mapped amphibolites are strongly deformed, banded units comprised of variably spaced mafic and felsic bands (Figure 4.3f). Deformation within individual amphibolite exposures is very heterogeneous and there is evidence for several phases of deformation having affected these units after the formation of the banding. Fine banding within the amphibolite (mm scale) lies sub-parallel to a foliation defined by an amphibole elongation on a microscopic scale. Both the foliation and this banding are thought to have formed during an early phase of shearing within the amphibolite. Some felsic units have characteristics similar to aplite dykes observed within the Sonnblick gneisses and some of the banding maybe interpreted to be the result of aplite injection into a mafic lithology (Figure 4.3f). Occasionally, aplite dykes are observed to cut the banding and to lie oblique to the foliation plane. Since aplites are considered to be late Hercynian in age (Cliff *et al* 1971; Cliff 1981) and the amphibolites appear to be dykes which cut through the Zentralgneis granitic precusors (see section 3:4.1), these features provide evidence for pre-Alpine deformation within the Zentralgneis.

4:4.4 Foliation and Banding within the Inner Schieferhülle

The Inner Schieferhülle represents the multiply deformed country rock into which the precursors of the Zentralgneis were intruded during the Variscan. The contact between Zentralgneis and Inner Schieferhülle is locally exposed within the Sonnblick area with the granitic gneisses indicating primary igneous intrusive relationships with the schist (for example, granitic apophyses within the Inner Schieferhülle schists.) Later leucogranite aplite units are observed to cut various structural features in the Inner Schieferhülle. These relationships provide some constraints on the identification of Alpine and Pre-alpine deformation within the Inner Schieferhülle and a chronological sequence of events can be recognised (Figure 4.4a):

i) Formation of quartz veins in the Inner Schieferhülle precursor.

ii) The development of banding (interlayered quartz and schistose quartz and mica bands) and a sub-parallel foliation.

iii) Aplite/leucogranite intrusion oblique to the observed metasedimentary banding

Figure 4.4a. Field sketch of contact between Inner Schieferhülle banded quartz-mica schist and foliated leucogranite unit showing the igneous contact cross cutting both the banding and a banding-parallel foliation. The aplite is foliated parallel to its margin and this foliation has been crenulated by later folding.

Figure 4.4b. Ductile shear zone developed in foliated coarse augen gneiss shows a well developed closely-spaced mylonitic fabric which is free of feldspar augen. Shear zone boundaries with the gneiss are discrete and strain gradients into the shear zone are discontinuous.

Figure 4.4c. Shear zone localized at the contact of gneiss material and a pegmatite unit within the Hochalm gneiss complex to the north of the Sonnblick Dome.

Figure 4.4d. Banded gneis unit composed of altered granitic material (g) and mylonitized aplites (a). Altered gneisses show augen and fold asymmetries consistent with sinistral shearing. Imbrication within individual aplite units occurs (x) and produces folds within the foliation developed in the roof of the small duplex. This also indicates a sinistral shear sense which is associated with top-to-SE shearing.

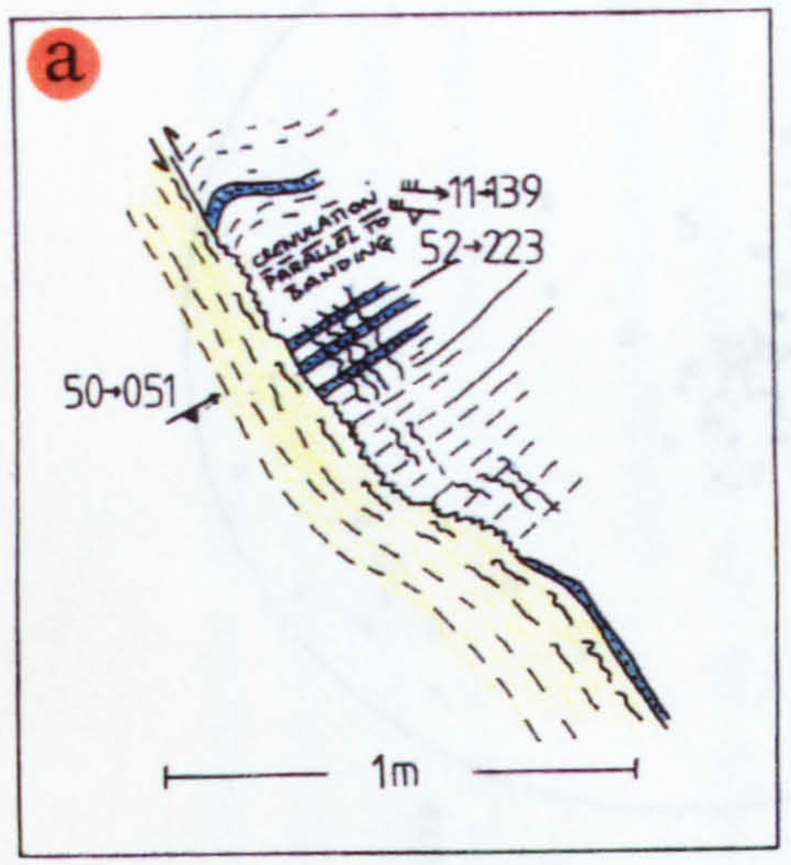

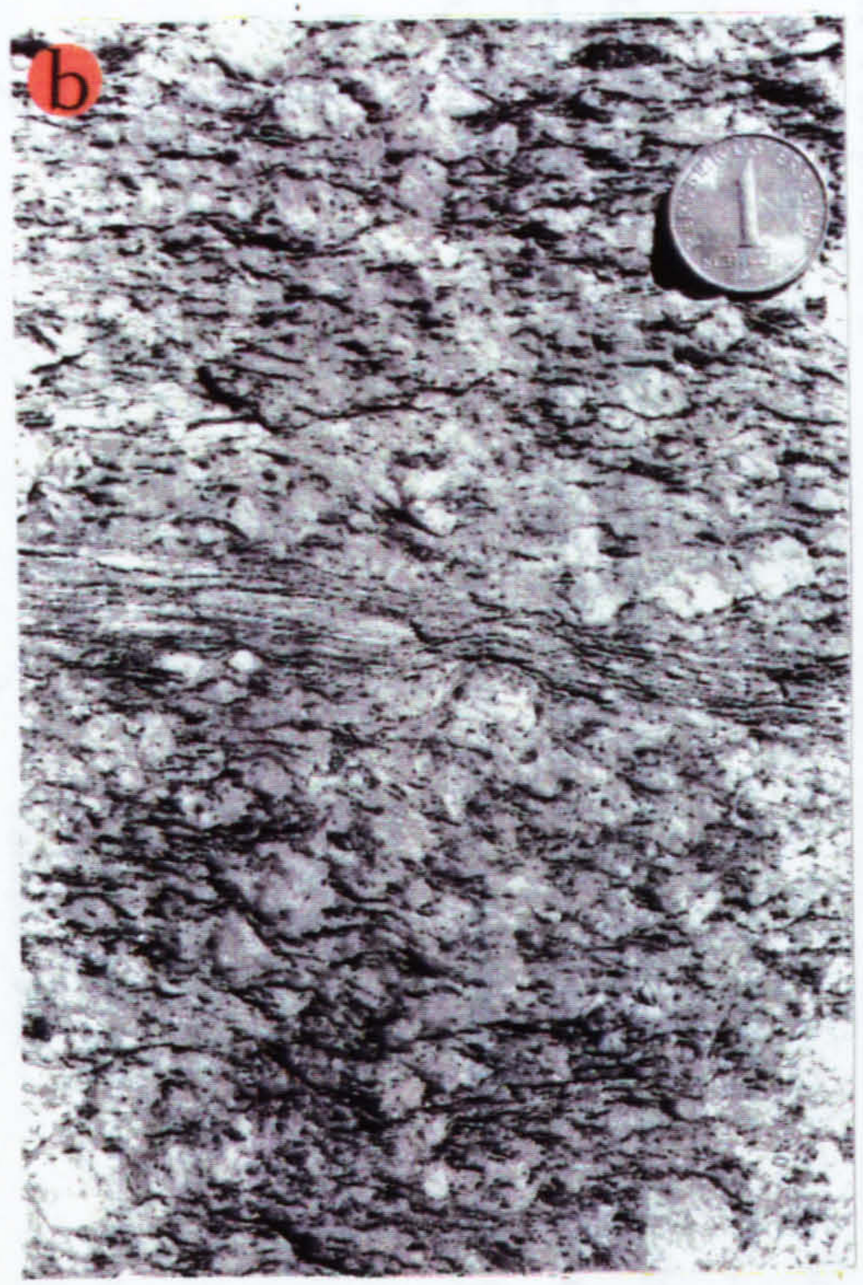

Banded Innerschieferhülle Schist
(with deformed mylonitic quartz bands).

Foliated leucogranite

Foliation (dip and azimuth)

F_3 axial plane (dip and azimuth)

F_3 hinge

Foliation trace

iv) The development of a second foliation within the aplite and Inner Schieferhülle, subparallel to the lithological contact and overprinting banding in the Inner Schieferhülle (ii above).

v) Crenulation folding of the contact and foliations, both within the aplite and Inner Schieferhülle, by F_3 folds (see 4:6.3).

Quartz veins which make up the banding often appear mylonitic. The mylonitic nature of the quartz bands and the fact that both bands and foliation are parallel suggests high strain deformation after their formation. This is supported by the presence of intrafolial folds with axial planes sub-parallel to banding, which are cut through by centimetre scale small thrust detatchments. Since these bands and associated folds are cut by aplite units, the banding and foliation are inferred to have developed prior to intrusion of the Zentralgneis precursors.

4:4.5 Foliation Development within the Peripheral Schieferhülle

The Peripheral Schieferhülle cover to the Zentralgneis Complex of the Sonnblick Dome has been studied in two ridge sections to the North and South of the mapped area. The series of schistose rocks, comprising phyllites, calc-mica schists, marbles, quartzites and gneiss lamallae, have a strongly developed foliation which lies parallel to the Zentralgneis-Schieferhülle contact and the mylonitic foliation observed in the top of the Dome (Figure 4.5). Foliations within the metasediments are generally penetrative and

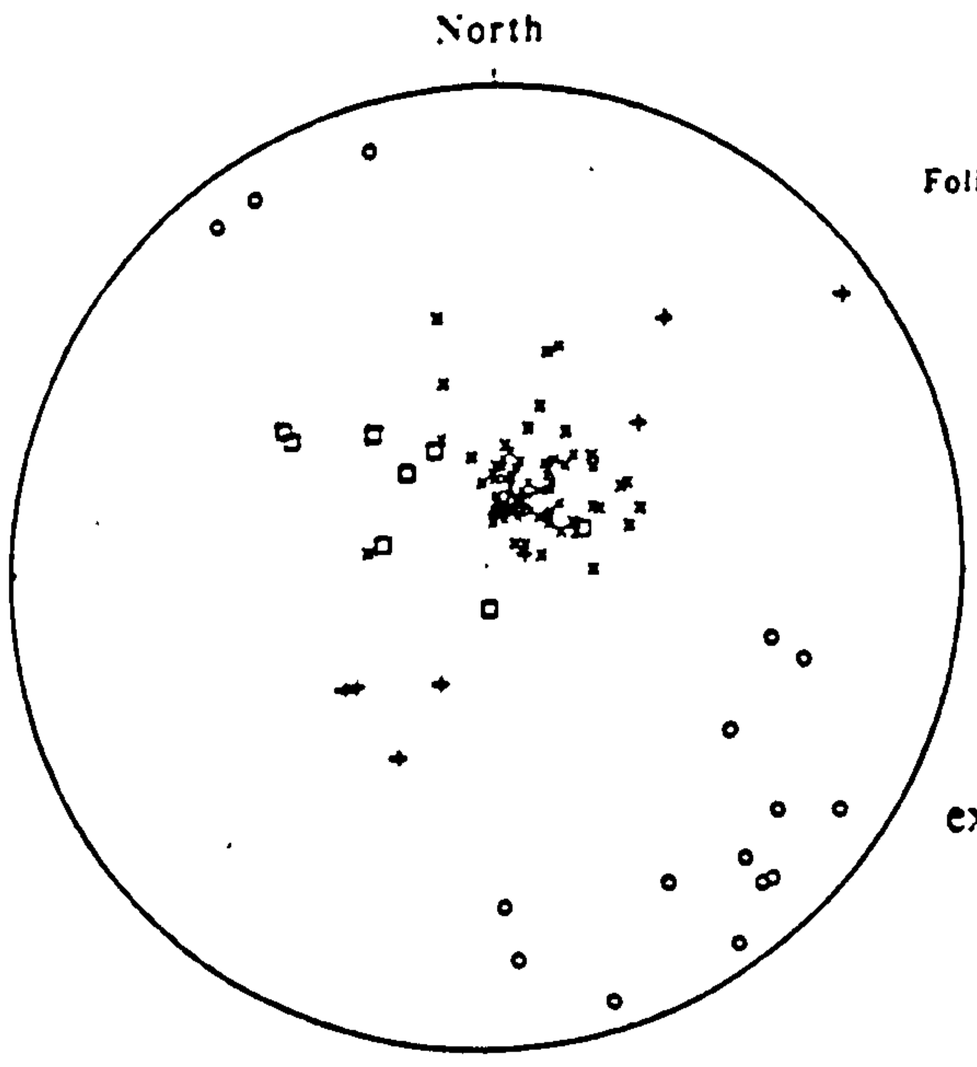

Figure 4.5. Lower hemisphere Wulff projections of foliation data from the Peripheral Schieferhülle exposed at Rote Wand-Sandfeld Kopf and Baumbach Spitze.

continuous on a handspecimen scale and show a NW-SE mineral stretching lineation (Figure 4.9a). Mesoscopic shear criteria, such as porphyroblast asymmetry and S-C fabrics, suggest a top-to-NW displacement associated with foliation development. Shear bands observed within the Peripheral Schieferhülle offset the main foliation and dip to the southeast (Figure 4.5).

4:5 Shear Zones within The Zentralgneis Complex

As well as the highly mylonitized units observed within the higher structural levels of the Dome, zones of high shear strain deformation occur at all structural levels within the Sonnblick area. These shear zones can be divided into several different types based upon lithological variation and deformation characteristics.

4:5.1 Mesoscopic Gneissic Shear Zones

Within most of the mapped area, small-scale, high-strain shear zones can be observed overprinting gneissic foliations (eg. Figure 4.4b). These zones are commonly in the order of a centimetre wide and show variable lateral extent. Mineralogically these zones appear identical to the host gneiss and contain quartz, micas, feldspar and epidote. Feldspar augen are absent suggesting feldspar breakdown and grain size reduction in these zones.

No consistent geometrical relationships are observed between these shear zones and the external gneissic foliation and they vary from sub-parallel to highly oblique. Mineral lineation in these zones tend to be oriented NW-SE although some variation is observed (Figure 4.6a and b). Commonly observed offsetting of aplite markers and the bending of external foliations into these zones suggests a shear sense associated with northwestwards overthrusting. The presence of angular intersections in excess of 45°, between the shear plane and the external foliation, within the plane containing the movement direction and the pole to the shear plane, indicates that these shear zones did not develop synchronously with the external foliation in a S-C type relationship, but overprint the external foliation.

Strain gradients on either side of these shear zones are commonly unevenly distributed and differ from an ideal, shear zone, strain profile (Ramsay and Graham 1973). Both continuous and discontinuous strain gradients (eg. Vauchez 1987) are observed. Occasionally, strain asymmetry is observed with hanging walls developing

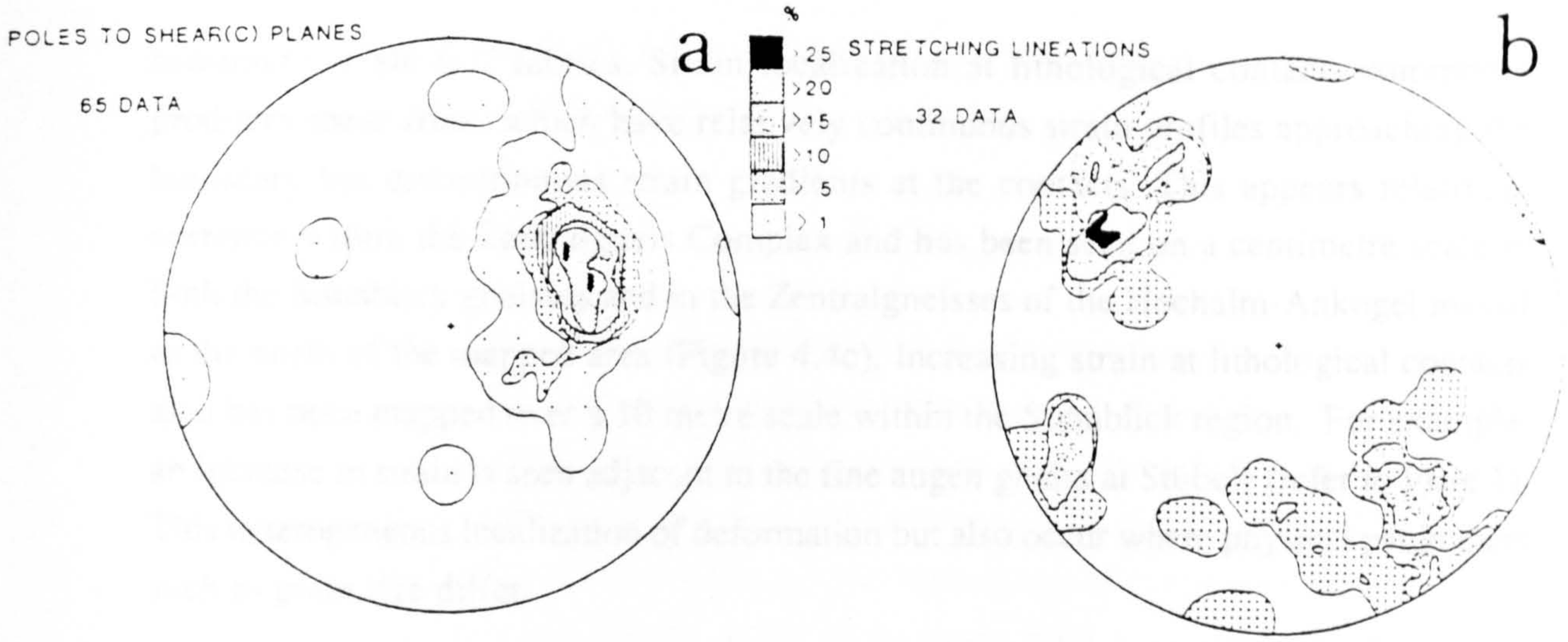

Figure 4.6. Equal area lower hemisphere projection of **a**) poles to C-planes and **b**) stretching lineations on these shear planes within mesoscopic, unaltered shear zones developed within low strain gneisses. All measurements were taken at low structural levels from exposures along the Panoramastraße road section, Fraganttal. Stereonets are contoured using the Statis program developed by N.Woodcock (Cambridge), modified by C.Davis for use on Amdahl V7.

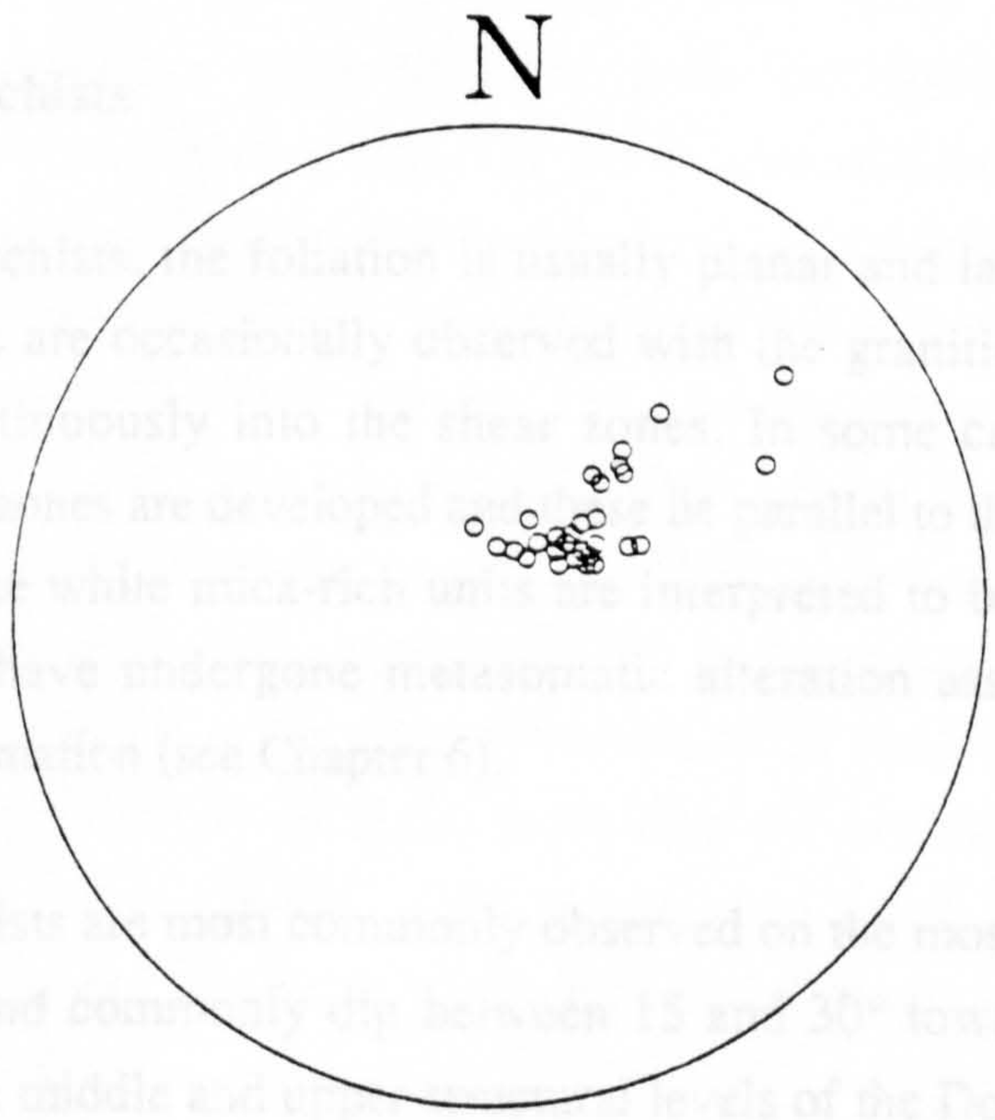

Figure 4.7. Lower hemisphere Wulff projection of poles to white-mica shear zones within the mapped area shown in plate 1.

centimetre scale S-C fabrics. Strain localization at lithological contacts commonly produces shear zones which have relatively continuous strain profiles approaching the boundary but discontinuous strain gradients at the contacts. This appears relatively common within the Zentralgneis Complex and has been seen on a centimetre scale in both the Sonnblick gneisses and in the Zentralgneisses of the Hochalm-Ankogel massif to the north of the mapped area (Figure 4.4c). Increasing strain at lithological contacts also has been mapped over a 10 metre scale within the Sonnblick region. For example, an increase in strain is seen adjacent to the fine augen gneiss at Stübele (refer to Plate 1). This heterogeneous localization of deformation but also occur where physical parameters such as grain size differ.

4:5.2 Metasomatic Ductile Shear Zones

Mica schist units reaching thicknesses in upto 2 metres are observed at all structural levels of the Dome. Two different mica schists exist, a white mica-rich lithology and a second dominated by biotite and chlorite. Both these units have a strongly developed foliation defined on a hand specimen scale by closely spaced phyllosilicate-quartz domains. No external strain markers associated with these shear zones were observed and therefore the quantification of displacements and shear strains within these zones was impossible.

a) White Mica Schists

In the white mica schists, the foliation is usually planar and laterally continuous. Gradational boundaries are occasionally observed with the granitic gneiss and strain gradients increase continuously into the shear zones. In some cases more discrete boundaries to the shear zones are developed and these lie parallel to the external foliation within the gneiss. These white mica-rich units are interpreted to be derived from the granitic gneiss which have undergone metasomatic alteration associated with fluid infiltration during deformation (see Chapter 6).

The white mica schists are most commonly observed on the most southerly limb of the Sonnblick Dome and commonly dip between 15 and 30° towards the southwest (Figure 4.7). Within the middle and upper structural levels of the Dome, these units are observed to be folded by folds of similar orientation and style as those which produce the large antiformal Sonnblick structure. At lower levels, folding is less well developed

and although no large scale folds of the white mica schists were observed, locally developed crenulation folds are preserved.

b) Biotite Schists

Biotite schists are only locally observed and are often spatially associated with amphibolite units. They are commonly less than a metre in width and are laterally discontinuous. The foliation is internally complex and shows evidence for internal folding associated with localized slip and imbrication of the foliation. The intense deformation and hydrous nature of the mineral assemblage suggests that these units may represent metasomatically altered mafic shear zones, with a possible derivation from amphibolites. Contacts with other units are commonly discrete and subparallel to the external foliation. This suggests that the strain gradient into the zone is probably discontinuous. They are also folded by small scale folds and at the outcrop scale can be seen to form a series of linked shear zones surrounding horses of augen gneiss (Figure 4.8).

4:5.3 Banded Gneiss Mylonites

A relatively low strain coarse augen gneiss containing a series of sub-parallel aplite dykes, passes into a banded lithology consisting of thin (up to 5cm wide) quartzo-feldspathic units and schistose, white mica-rich units immediately northeast of the Schwartzsee (Figure 4.4d and refer to 3:5). The white mica-rich bands of this lithology contain strongly asymmetrical feldspar augen with recrystallized feldspar tails and a well developed S-C fabric. Mineral stretching lineations combined with shear sense indicators indicate a consistent top-to-SE displacement. The quartzo-feldspathic units are fine-grained and have mineralogies similar to the aplite dykes in the area. They differ from aplites in containing a strong mylonitic foliation parallel to their margins. This banded unit is limited to a several metre wide zone which can be traced laterally for at least 500 metres, and is interpreted as a strongly sheared version of the underlying aplite-injected, gneiss lithology. The parallelism of aplite units with the strongly developed shear foliation requires high shear strains, while syndeformational fluid infiltration is suggested by the metasomatic alteration of the granitic lithology to a white mica-rich lithology (see Chapter 6).

Quartz-feldspar bands, and the mylonitic foliation they contain, are commonly asymmetrically folded. Locally the overturned limbs of these folds are sheared out so

that the bands appear imbricated (Figure 4.4d). This imbrication produces folding in the roof of the immediately overlying mica schist. Fold hinges and the frontal branch lines of these imbricated units are oriented to the southwest and are not rotated parallel to the observed NW-SE mineral stretching lineation. These relationships are relatively unusual within the Sonnblick area and suggests that folding and imbrication took place at relatively late stages of the shear deformation.

4:5.4 Quartzo-Feldspathic Mylonites

Quartzo-feldspathic units, up to 2 metres wide, are commonly observed in the basement gneiss complex (eg. Figure 3:3a) and can be traced laterally over distances in excess of 1km. These units are fine-grained and contain a sub-mm spaced, mylonitic C-fabric parallel to their margins. Mineral stretching lineations in these units dip shallowly to the northwest or southeast which, coupled with S-C relationships in micaceous areas of these units, indicate a top-to-NW shear sense.

The mylonite boundaries and the internal mylonitic foliation strike NW-SE. Variations in the dip of the mylonite units are present due to folding of the units by folds with hinge orietations parallel to the NW-SE strike (see 4:6). The mylonite units have discrete contacts with the augen gneisses and are interpreted to have originated as dykes similar to the 'Fine Gneiss'. If this was important, the smaller grain size within these original lithologies may have played an important role in the localization of deformation within these mylonites.

4:5.5 Relationship between the different Shear Zones

The shear zones described above are not observed to intersect within the mapped area and therefore, the relative timing and the three dimensional network of the shear zone system is difficult to establish on a large scale. At the outcrop scale, individual shear zone types are occasionally observed to be linked and accommodate imbrication within the Zentralgneis. The shear zones generally dip towards the southwest and are therefore oblique to the northwest displacement vector. Imbrication is therefore seen on the oblique ramps which are relatively planar structures and do not show the typical staircase geometry associated with higher level thrust faults (eg Butler 1982).

Figure 4.8. Sketch to show road section exposures showing evidence for imbricaton of the Zentralgneis. Shear zone types are shown in the figure. Shear sense is top-to-NW and shear zones are therefore oblique and lateral in nature. The metasomatic phengitic shear zone is discussed in detail in Chapter 6 and is exposed along two levels of the road section.

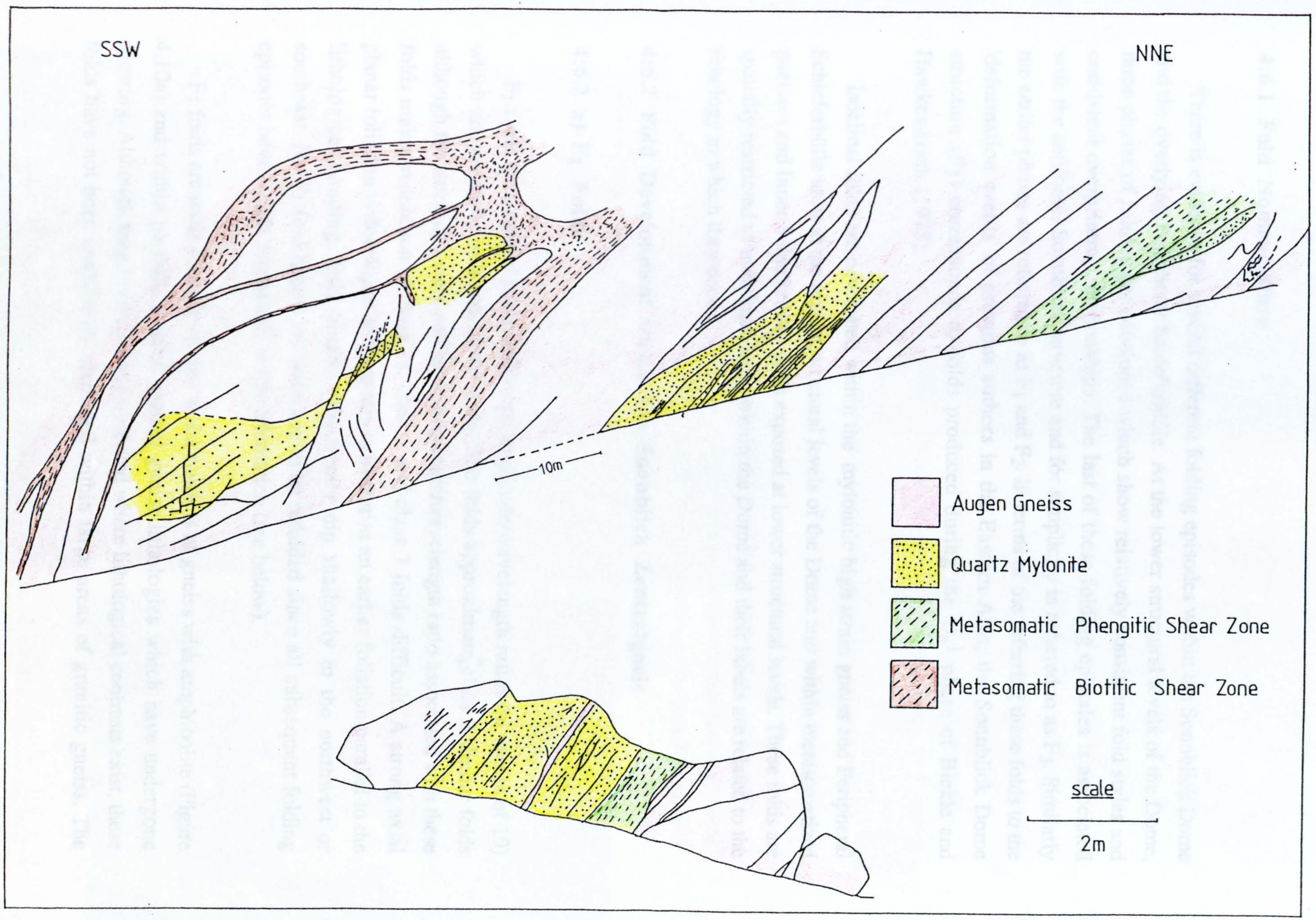
SSW
NNE
10m
Augen Gneiss
Quartz Mylonite
Metasomatic Phengitic Shear Zone
Metasomatic Biotitic Shear Zone
scale
2m

4:6 Fold Development in the Sonnblick Dome

4:6.1 Fold Nomenclature

There is evidence for several different folding episodes within the Sonnblick Dome and the overlying Peripheral Schieferhülle. At the lower structural levels of the Dome, three phases of folding are developed which show relatively consistent fold styles and consistent overprinting relationships. The last of these folding episodes is associated with the antiformal Sonnblick structure and for simplicity is referred to as F_3. Similarly the earlier phases are referred to as F_1 and F_2. In terms of the referring these folds to the 'deformation events' of previous authors in the Eastern Alps, the Sonnblick Dome structure (F_3) corresponds to folds produced during the D_a^1 phase of Bickle and Hawkesworth (1978).

Isoclinal folds are developed within the mylonitic high strain gneiss and Peripheral Schieferhülle units at the higher structural levels of the Dome and within metasomatized gneisses and Inner Schieferhülle units exposed at lower structural levels. These folds are spatially restricted to individual units within the Dome and their labels are related to the lithology in which they occur.

4:6.2 Fold Development within the Sonnblick Zentralgneis

4:6.2 a) F_1 Folds

F_1 folds are isoclinal folds with large amplitude/wavelength ratios (in excess of 10) which are generally on a sub-metre scale. The folds approximate class 2 similar folds although the isoclinal nature and large amplitude/wavelength ratio associated with these folds makes resolution of class 1c, class 2 and class 3 folds difficult. A strong axial planar foliation is developed and appears to overprint an earlier foliation parallel to the lithological banding. Fold hinges consistently dip shallowly to the northwest or southeast. No F_1 fold hinges are observed to be refolded since all subsequent folding episodes have hinges subparallel to this orientation (see below).

F_1 folds are most commonly seen at the contacts of gneiss with amphibolite (Figure 4.10a) and within partially altered banded gneiss lithologies which have undergone shearing. Although they are frequently observed where lithological contrasts exist, these folds have not been confidently identified within large areas of granitic gneiss. The

Figure 4.9a. Isoclinal F_1 folds developed within interbanded gneiss and amphibolite lithologies. An axial planar foliation associated with these folds are refolded by minor F_3 folds developed during the formation of the Dome structure.

Figure 4.9b. Large F_2 fold developed within fine augen gneiss above the cliff section of Stübele. Fold surface is an earlier developed gneissic foliation.

Figure 4.9c. Angular F_2 folds overprinted by open and rounded F_3 folds within a banded amphibolite unit. Fold interference is type 3.

Figure 4.9d. Small scale F_3 folds developed within coarse augen gneiss. An aplite marker shows limb thickness variations commonly associated with localized high shear strains on the 'overturned' limb of the crenulation folds.

Figure 4.9e. Isoclinally folded mylonitized quartz vein (fm) within high strain augen gneiss. Fold axial plane is sub-parallel to the main mylonitic foliation while hinges generally lie sub parallel to the mineral stretching lineation on this foliation.


d

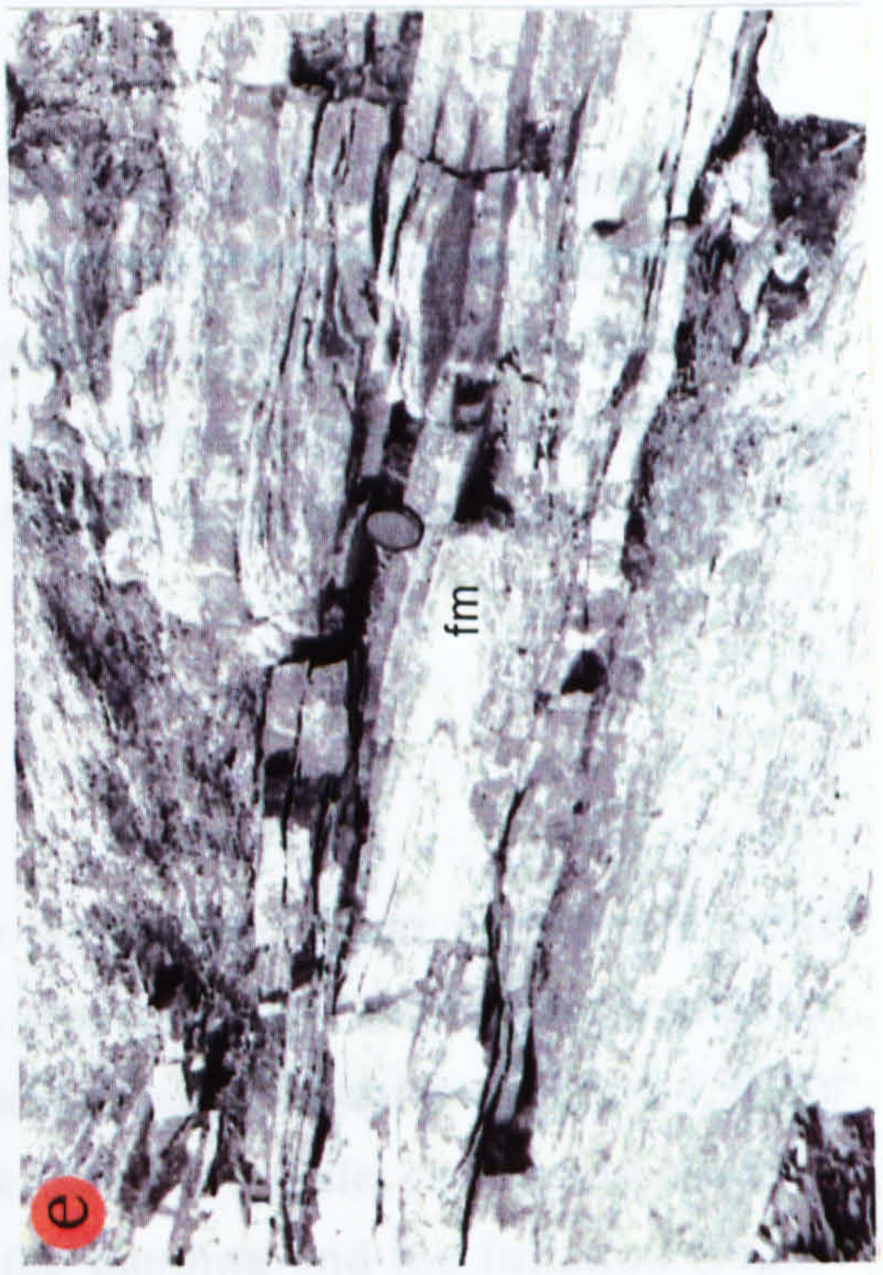
fm
e

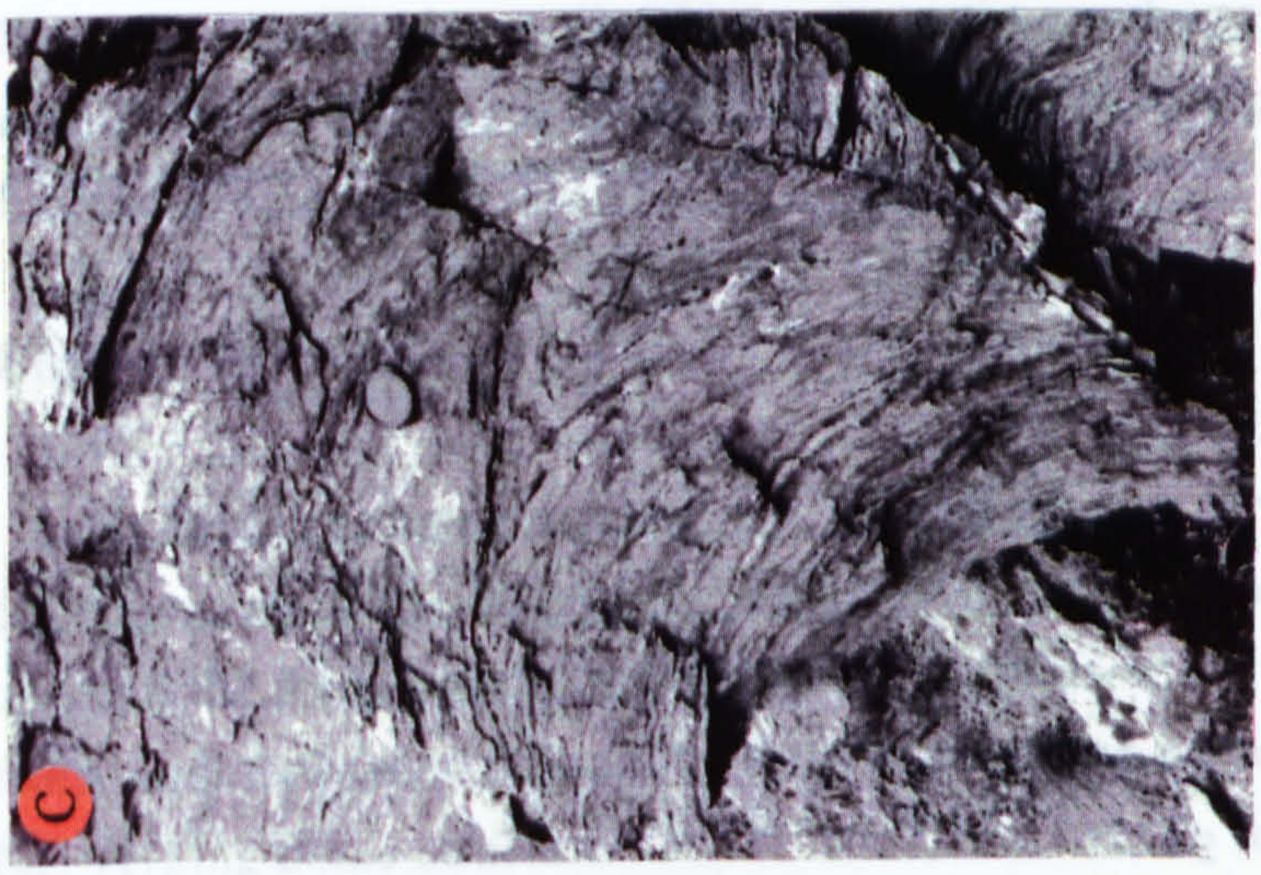
c


b

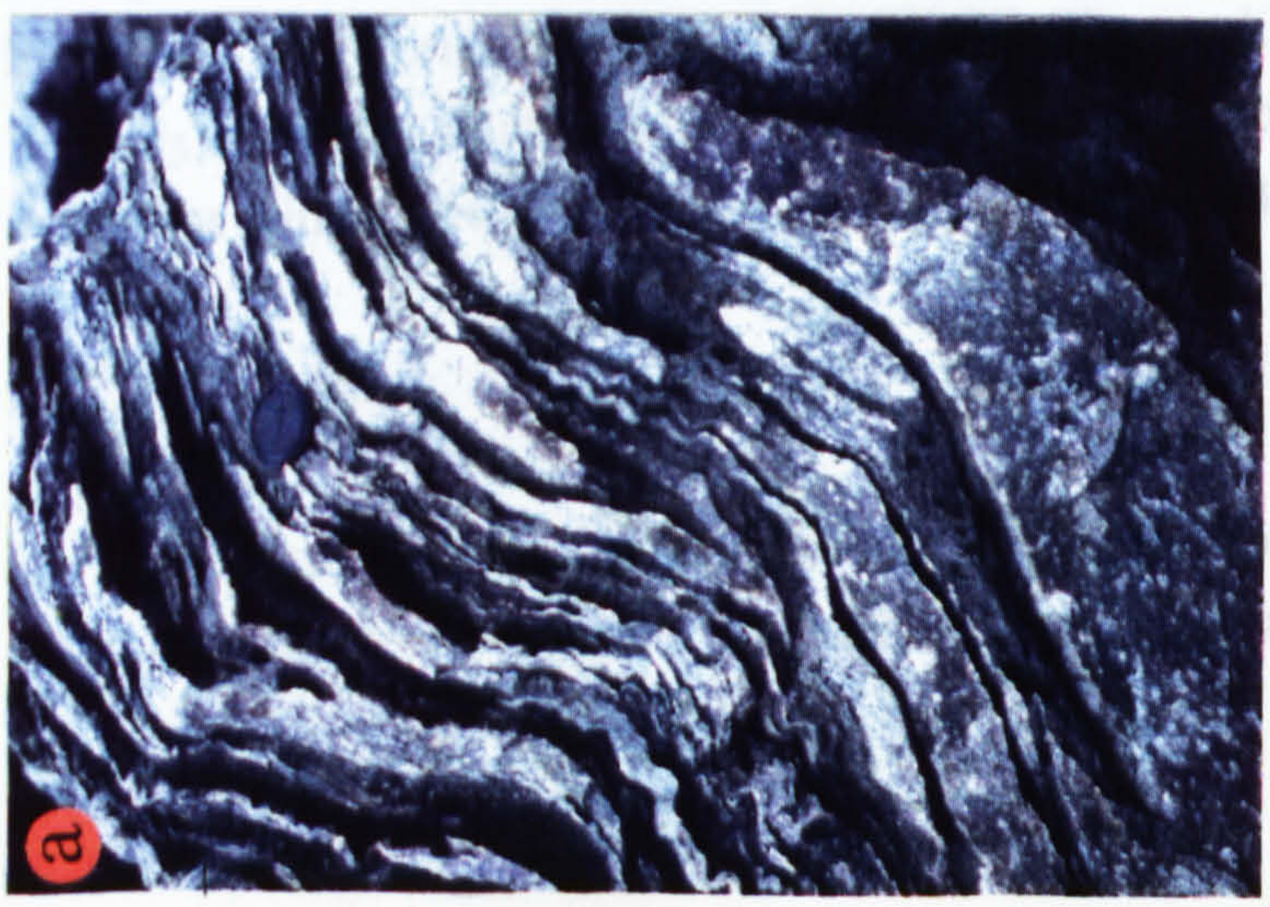
a

localization of these folds at lithological contacts has a strong similarity to theoretically and experimentally observed model 2 sheath folds described by Cobbold and Quinquis (1980) which develop during "bulk simple shear, perturbed by the presence of resistent layers grossly parallel to the shearing plane but with surface asperities". The observed folds are considered to have developed within top-to-NW, high shear strain domains and to have a sheath fold geometry.

4:6.2 b) F_2 Folds

F_2 folds are more common than F_1 folds and range from centimetre scale crenulations to tens of metres in size. F_2 folds are generally tight and relatively angular, asymmetric class 1C, 2 and 3 folds and are defined by folded foliations (Figure 4.9b) or folded lithological contacts (eg. Figure 4.10). On a sub-metre scale, commonly observed angular and tight F_2 folds in amphibolites fold the banding and the foliation (Figure 4.9c).Good examples of F_2 folds are seen throughout the Dome. However, on a large scale the best examples are seen in the cliff section above Stübele (grid ref. 136096) (Figure 4.11). F_2 hinges dip shallowly to the northwest or southeast (Figure 4.12b) while poles to F_2 axial planes define a great circle whose pole corresponds to the later F_3 fold axis (Figure 4.12a and b).

4:6.2 c) F_3 Folds

F_3 folds are open to close and vary from angular to sub-rounded in curvature depending upon the micaceous nature of the folded foliation. With increasing mica content, the folds become more angular. F_3 folds occur on a variety of scales, ranging from commonly seen crenulation folds overprinting earlier folds and foliations up to the NE-verging dome structure itself (Plate 2). As with F_2 folds, F_3 folds are comprised of class 1C, 2 and 3 layer geometries. A consistent axial plane orientation is seen throughout the Dome and this dips to the southeast at about 40° (Figure 4.13a). F_3 hinges are sub-horizontal and trend NW-SE (Figure 4.13b). Occasionally associated with F_3 folds are axial planar high strain zones which give rise to limb thickness variations which accommodate fold asymmetry (Figure 4.9d).

4:6.2 d) Folding Associated with zones of High Shear Strain

Highly strained mylonitic quartz veins parallel to the main gneiss foliation are interpreted to have undergone the same deformation as the host gneiss. These veins are

commonly isoclinally folded and have axial planes and hinges parallel to the main gneiss foliation and the NW-SE mineral stretching lineation respectively. Occasionally, hinges are observed to be curvilinear (Figure 4.9e). These folds are referred to as F_m and are inferred to have developed during the intense deformation which produced the gneissic foliation.

Within the lower levels of the Dome a complicated zone of banded, partly altered mica-rich lithology, which is interpreted to be derived from augen gneiss which is exposed in a 20 metre stream section approximately 1km northwest of Würten Speicher (grid ref. 149087). The unit cannot be traced away from the stream section and is not exposed elsewhere in the Dome.The unit contains type 1, type 2 and, most commonly, type 3 fold interference patterns (Figure 4.14a and b). The presence of all 3 fold interference types suggests that there is no constant relationship between superposed fold geometries. This in turn implies that the fold interference patterns do not form as a result of the superposition of individual, discrete folding events of constant orientation. This is supported by the consistent type 3 patterns obtained from F_1, F_2 and F_3 interaction within the rest of the Dome and the absence of type 1 and type 2 fold interference patterns.

A possible working model for formation of these interference patterns is within a high strain zone where sheath folds are developing. With progressive shearing in a high shear strain zone, fold axes may rotate into the transport direction. This leads to the progressive development of type 1 fold patterns in the nose of the sheath fold. Continued shearing may give rise to refolding of the sheath fold geometry which can result in the production of both type 2 and 3 fold interference patterns (Figure 4.15). The strong micaceous and mylonitic foliations and the observed metasomatic alteration observed within the lithology are consistent with this zone being a zone of high shear strain.

4:6.2 e) Overprinting Relationships and evidence for fold chronology in the Sonnblick Gneisses

The relative timing on which the F_1, F_2 and F_3 classification have been based has been constrained by field evidence from centimetre to 10s of metres in scale. Consistent overprinting relationships of the three sets of folds are observed. F_1 folds are overprinted by both F_2 and F_3 (Figures 4.14c and 4.9a respectively) and form type 3 interference patterns. F_1 folds therefore have hinge orientations that are sub-parallel to

Figure 4.10. Map of the area above Stübele illustrating the geometrical relationship between different lithological units folded by F_2 and F_3 folds. For exact location see Plate 1.

North

0 50 100 metres

SCALE

Cross Section Along Line A-B

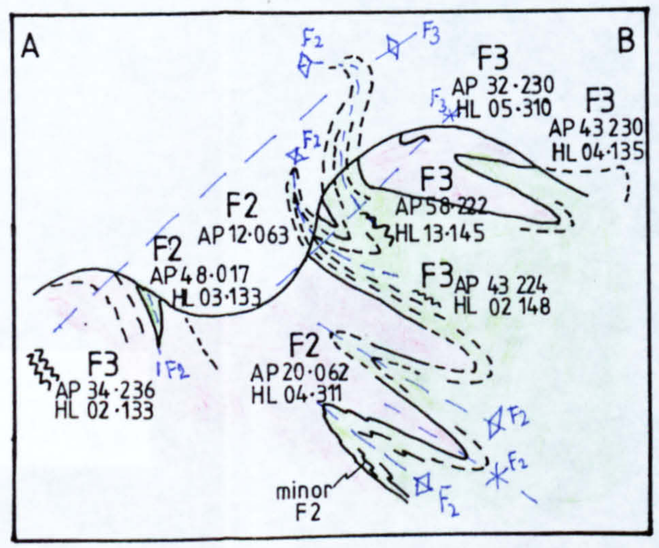

Geological Symbols

- Geological boundary (observed
- Geological boundary (inferred)
- Foliation
- Axial plane (AP) to F1 fold
- Axial plane (AP) to F2 fold
- Axial plane (AP) to F3 fold
- Mineral stretching lineation
- Hinge (HL) to F1 fold
- Hinge (HL) to F2 fold
- Hinge (HL) to F3 fold
- Antiformal axial planar trace
- Synformal axial planar trace

Zentralgneis Units

- Low strain augen gneiss
- Intermediate strain augen gneiss
- Fine grained gneiss
- Aplitic mylonite
- Micaceous shear zone
- Amphibolite

Figure 4.11. Sketch of the cliffs above Stübele illustrating large folds of F_2, F_3 and possibly F_1 generations.

NE

F3
F2
F1
F1?

Zentralgneis Units

- Intermediate strain augen gneiss
- Fine grained gneiss
- Aplitic mylonite
- Micaceous shear zone
- Amphibolite

Geological Symbols

- Geological boundary (observed)
- Geological boundary (inferred)
- Foliation
- Foliation trace
- Fault
- Axial plane (AP) to F1 fold
- Axial plane (AP) to F2 fold
- Axial plane (AP) to F3 fold
- Mineral stretching lineation
- Hinge (HL) to F1 fold
- Hinge (HL) to F2 fold
- Hinge (HL) to F3 fold
- Antiformal axial planar trace
- Synformal axial planar trace

SCALE

0 25 50 metres

(View to the North-West)

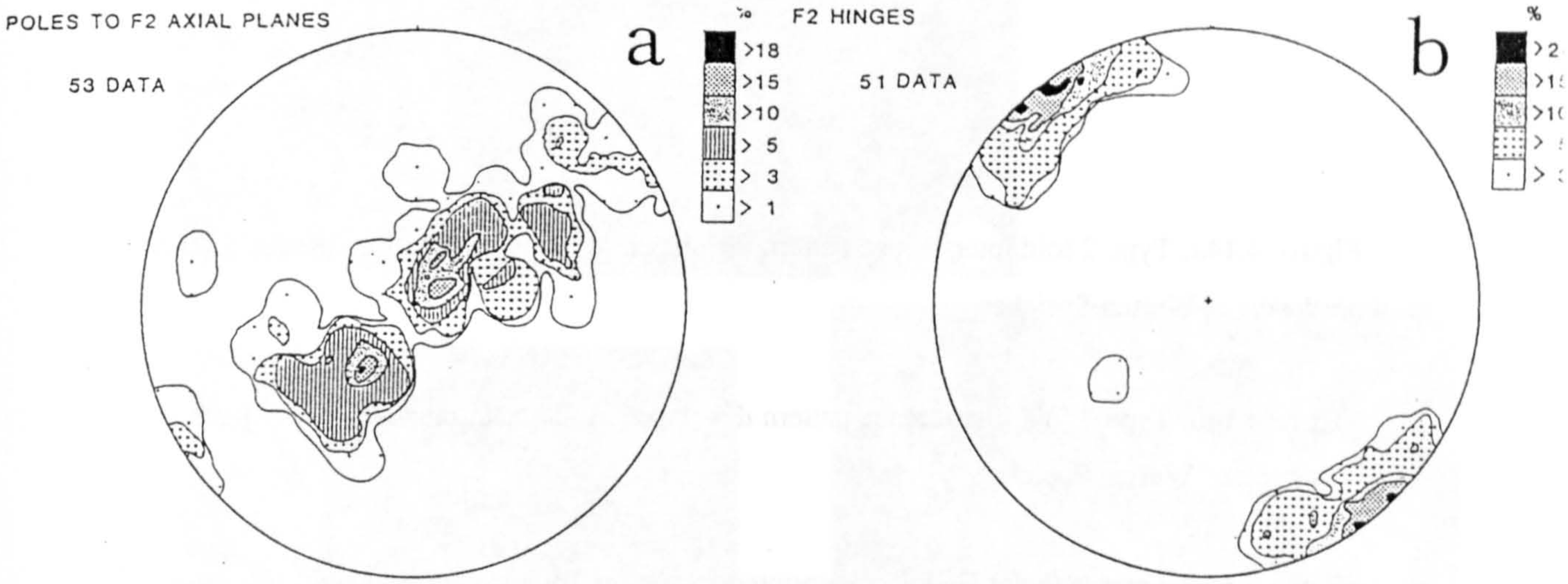

Figure 4.12. Lower hemisphere equal area projection of structural data associated with F_2 folds **a**) Poles to F_2 axial planes, **b**) F_2 hinges. Stereonets are contoured using the Statis program developed by N.Woodcock (Cambridge), modified by C.Davis for use on Amdahl V7.

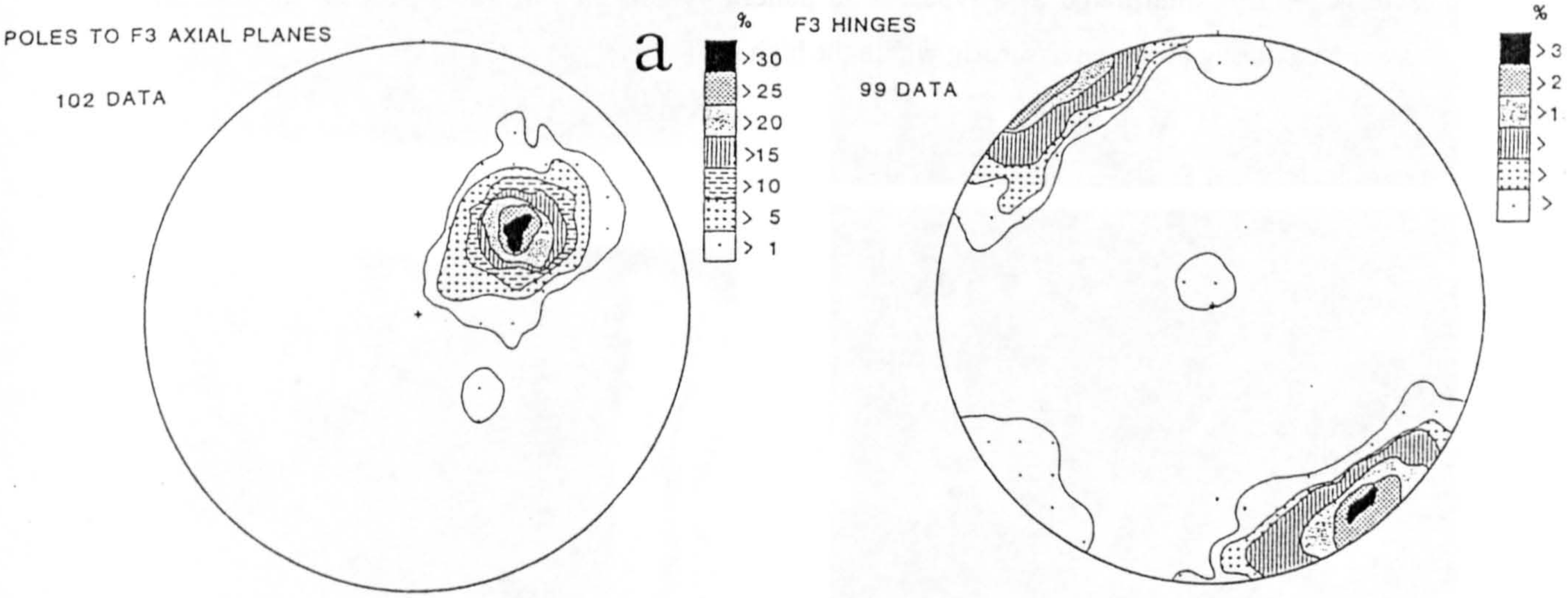

Figure 4.13. Lower hemisphere equal area projection of structural data associated with F_3 folds **a**) Poles to F_3 axial planes, **b**) F_3 hinge orientations. Stereonets are contoured using the Statis program developed by N.Woodcock (Cambridge), modified by C.Davis for use on Amdahl V7.

Figure 4.14a. Type 2 fold interference pattern developed in the metasomatised banded gneiss unit northwest of Wurten Speicher

Figure 4.14b. Type 3 fold interference pattern developed in the metasomatised banded gneiss unit northwest of Wurten Speicher.

Figure 4.14c. Tight, angular F_1 fold overprinted by a more rounded and less tight fold of F_2 generation within the banded gneiss lithology discussed in 4:33c. Fold interference is type 3.

Figure 4.14d. Isoclinally folded quartz veins within highly strained Inner Schieferhülle schists exposed on the northeastern end of Wurten Speicher. Hinges are weakly curvilinear and lie sub-parallel to the mineral stretching lineation.

Figure 4.14e. Isoclinally refolded isoclinal fold within high strain Inner Schieferhülle schists. Fold is interpreted as a type 1 fold pattern associated with the nose of a sheath fold developed during progressive shearig within the high strain zone.


c


b


e


a


d

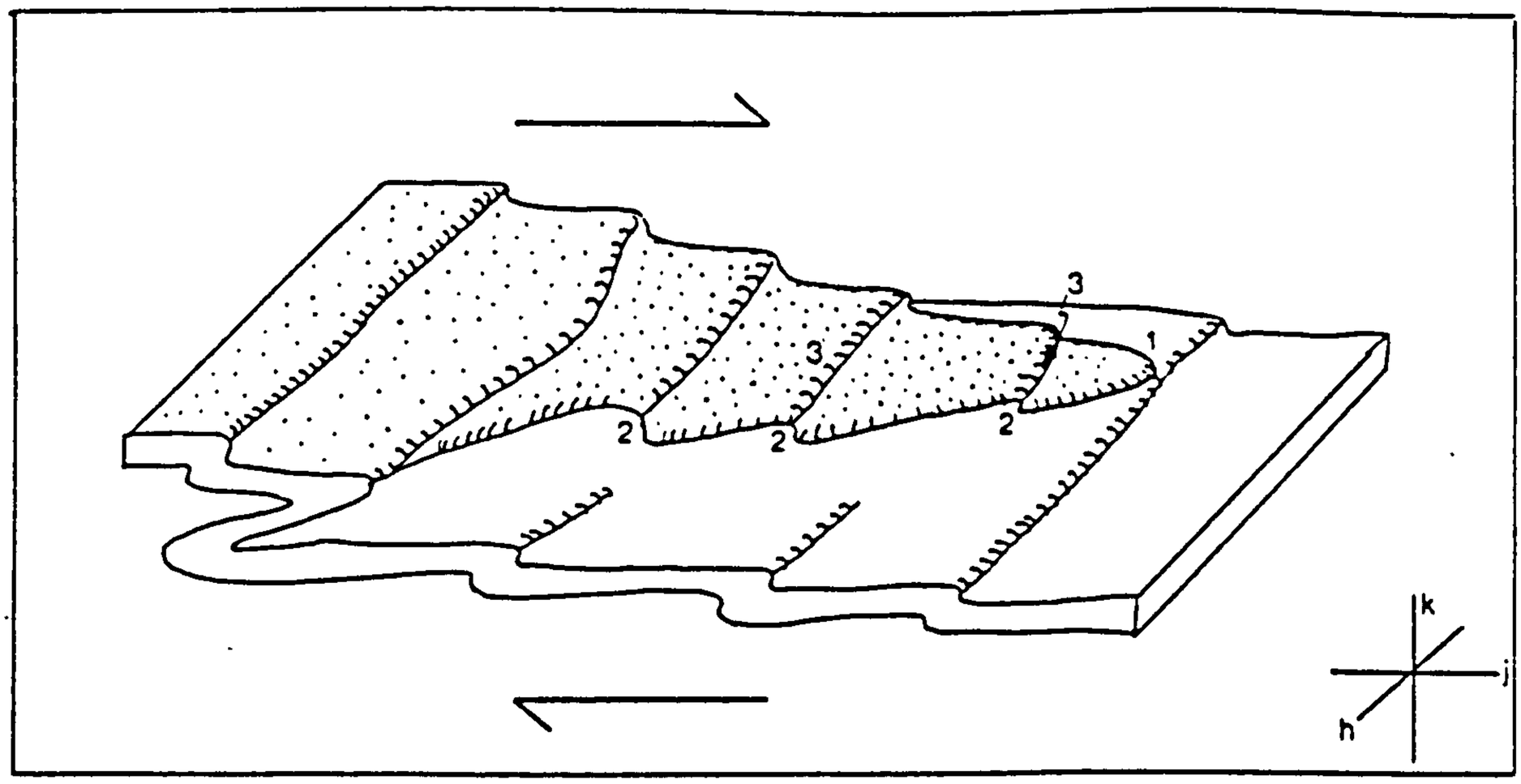

Figure 4.15. Simple model (after Knipe) illustrating the development of type 1, 2 and 3 interference patterns during a single progressive deformation within a high strain shear zone. The stippled region represents a sheath fold produced during the early stages of shear zone formation. Continued shearing may refold the sheath to produce a variety of interference patterns. Numbers represent interference types and show the location of different patterns around the fold. Type 1 patterns are developed in the nose of the sheath fold and can be observed in sections cut parallel to hk. Type two patterns may form at the edge of the sheath fold where the hinge of the sheath fold is refolded by the later folds. Type 3 patterns are observed in sections cut parallel to jk.

Figure 4.16. Lower hemisphere Wulff projections of structural data from the Inner Schieferhülle exposed in Fraganttal. a) Poles to planar features and b) Lineations.

F_2 and F_3 but have an axial planar orientation which is commonly highly oblique to the subsequent folding episodes.

Although F_2 folds are usually tighter in geometry than F_3 folds, where F_2 axial planes have an orientation similar to that of the later F_3 folds, it is often difficult to distinguish between the different generations. Northeast dipping axial planes are characteritic of F_2 folds and where these axial planes are refolded (Figure 4.9c), evidence for overprinting relationships are unequivocal. Field mapping has further illustrated the chronology of folding episodes (eg. Figure 4.10 and 4.11) and has also illustated that the pre-F3 orientation of F2 folds was approximately parallel to the Zentralgneis - Peripheral Schieferhülle contact.

No relationships relating the isoclinal folds developed within the high strain units in the higher levels of the Dome and F_1 and F_2 folds in the main body of the Dome are directly observed. However, the axial planes of these folds are folded around the Sonnblick Dome structure and these folds therefore pre-date F_3.

4:6.3 Folding Within the Inner Schieferhülle

Within the exposures on the northwestern shore of Wurten Speicher (grid ref. 158077) quartz bands are often isoclinally folded and show curvilinear hinges (Figure 4.14d). Occasionally, sheath type refolding of hinges is observed so that isoclinally folded quartz bands appear isoclinally refolded (Figure 4.14e).These folds are referred to as F_b. It is relatively easy to explain this in terms of a progressive folding episode associated with the high shear strains required to form the observed banding.

In addition to the isoclinal and sheath folds developed during production of the banding in the Inner Schieferhülle, folding of the Inner Schieferhülle by F_1, F_2 and F_3 is also seen. These folds have similar orientations to those developed in the gneisses (Figure 4.16) and commonly have axial planar foliations which show overprinting relationships. F_1 development is only observed in areas where sub-metre scale interbanding of the Inner Schieferhülle with amphibolite occurs. F_1 folding again appears to be spatially related to lithological boundaries.

Exposures on the shores of Wurten Speicher illustrate the complex nature of folding and the chronology of deformation within the Inner Schieferhülle. Schistose and quartzo-feldspathic units are isoclinally folded by folds having relatively large

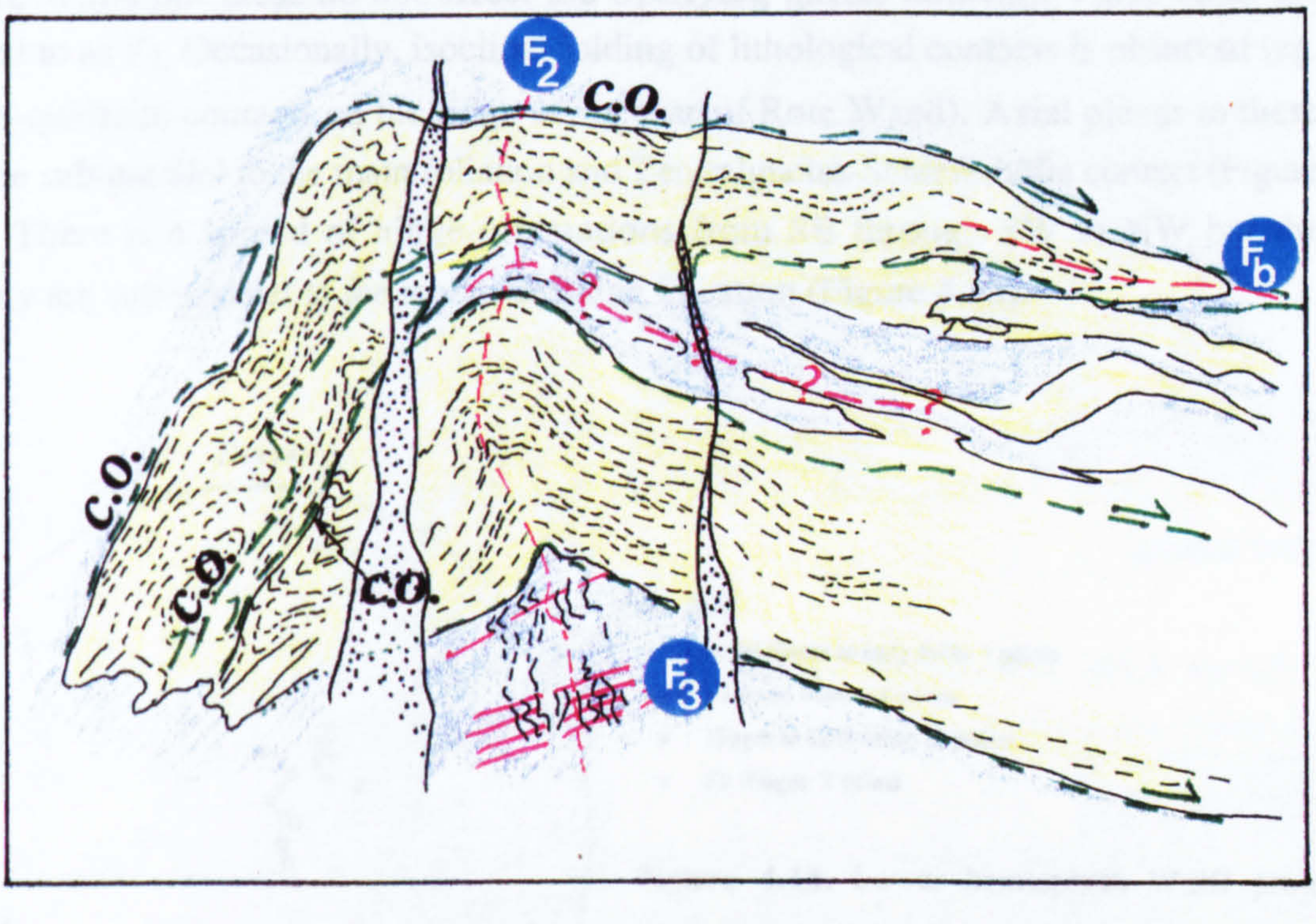

Figure 4.17. Folds and thrusts developed within quartz-mica schists of the Inner Schieferhülle. Red dashed lines refer to fold axial planes and are labelled. Fold hinges run into the plane of the figure and trend NW-SE. Green dashed lines mark thrusts faults within the schist which are marked by the cutting off of the banding (c.o)Thrustsare approximately lateral in orientation to the observed stretching lineation and arrows only show relative offset.

amplitude/wavelength ratios (Figure 4.17). The more felsic unit may represent deformed leucogranites or deformed metasedimentary arkoses. A strong foliation in this unit is internally disrupted by cut-offs which are oblique to the transport direction inferred from mineral stretching lineations. From this exposure, it is difficult to say whether these folds represent F_1 type folds or are folds associated with early shearing in the Inner Schieferhülle (F_b), although the latter is thought more likely. These detachments are in turn folded by folds similar in style to the F_2 phase observed within the surrounding gneisses. However, these have a steep axial planar foliation which in turn is folded by F_3. A foliation is also developed axial planar to these Dome-associated folds (Figure 4.17). The orientation of these structural features within the Inner Schieferhülle are similar to those observed within the gneisses, although early isoclinal hnges show a larger spread due to their curvilinear and sheath type geometries.

4:6.4 Fold Development within the Peripheral Schieferhülle

Tight to isoclinal folds affect the main foliation and are also seen developed within individual metasedimentary units (eg. extensive folding is seen in the marbles at the base of Rote Wand but these do not affect the overlying gneiss lamella). These folds are referred to as F_S. Occasionally, isoclinal folding of lithological contacts is observed (eg. marble-quartzite contacts on the ridge at the base of Rote Wand). Axial planes to these folds lie sub-parallel to the main foliation and Zentralgneiss-Schieferhülle contact (Figure 4.18). There is a spread of hinge orientations from SE through SW to NW but the majority are sub-parallel to the main stretching lineation (Figure 4.18).

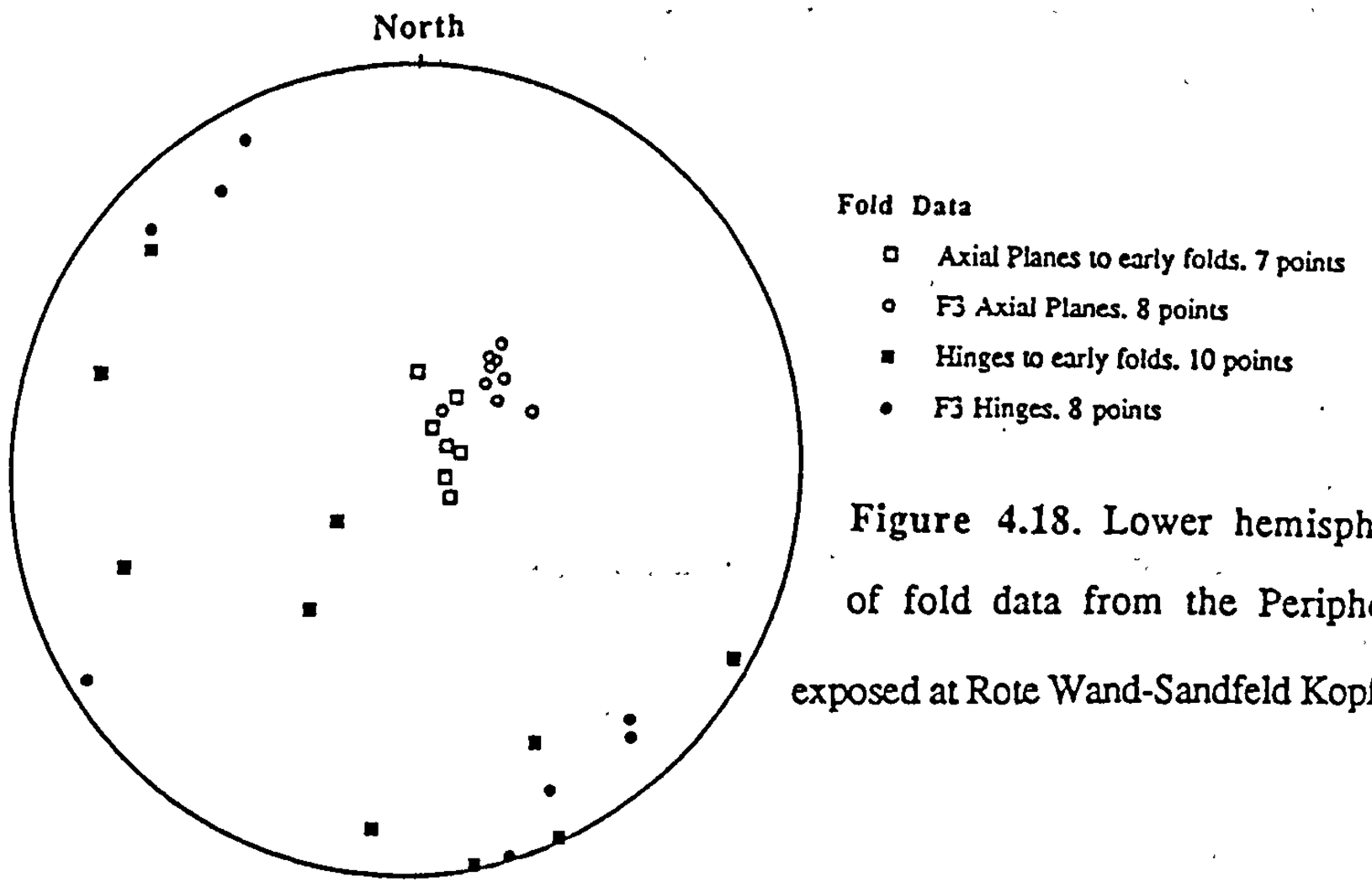

Figure 4.18. Lower hemisphere Wulff projection of fold data from the Peripheral Schieferhülle exposed at Rote Wand-Sandfeld Kopf and Baumbach Spitze.

Figure 4.19a. Normal faults exposed along the Panoramastraße road section at a height of 1480 metres. 'X' shows the location of Figure 4.19b.

Figure 4.19b. Fault zone (from 'X' in Figure 4.19a) showing a strong foliation that lies oblique to the fault zone boundaries which indicates a normal sense of shear. Lineation on the fault lies within the plane of the figure.

Figure 4.19c. Extensional shear zone developed in coarse augen gneiss. Stretching lineation in the zone is within the plane of the photo and the aplite marker (X) shows the amount of displacement along this zone. The shear zone is comprised of two zones, a discrete, 1cm wide zone showing a displacement of 1metre (shear strain ~ 100) and a 3cm wide zone accommodating 30cm of displacement (shear zone =10).

Figure 4.19d. Brittle normal fault developed in well foliated coarse augen gneiss and showing a displacement of approximately 5cm. Within the underlying more micaceous lithology, this displacement is accommodated by folding. This illustrates the heterogeneous rheological behaviour on a small scale within the gneiss complex.

Figure 4.19e. Foliation boudinage within high strain augen gneiss in the higher structural levels of the Dome. Accommodation of boudinage in the underlying gneiss is by small scale normal faulting.

Figure 4.19f. Asymmetrical boudinage within carbonate-rich units of the Peripheral Schieferhülle beneath the Rote Wand.

Figure 4.19g. Interpretation of the boudin formation of figure 4.20f. Individual boudins are interpreted to have behaved in a domino-type fashion suggesting a sinistral shear sense associated with top-to-SE extension.

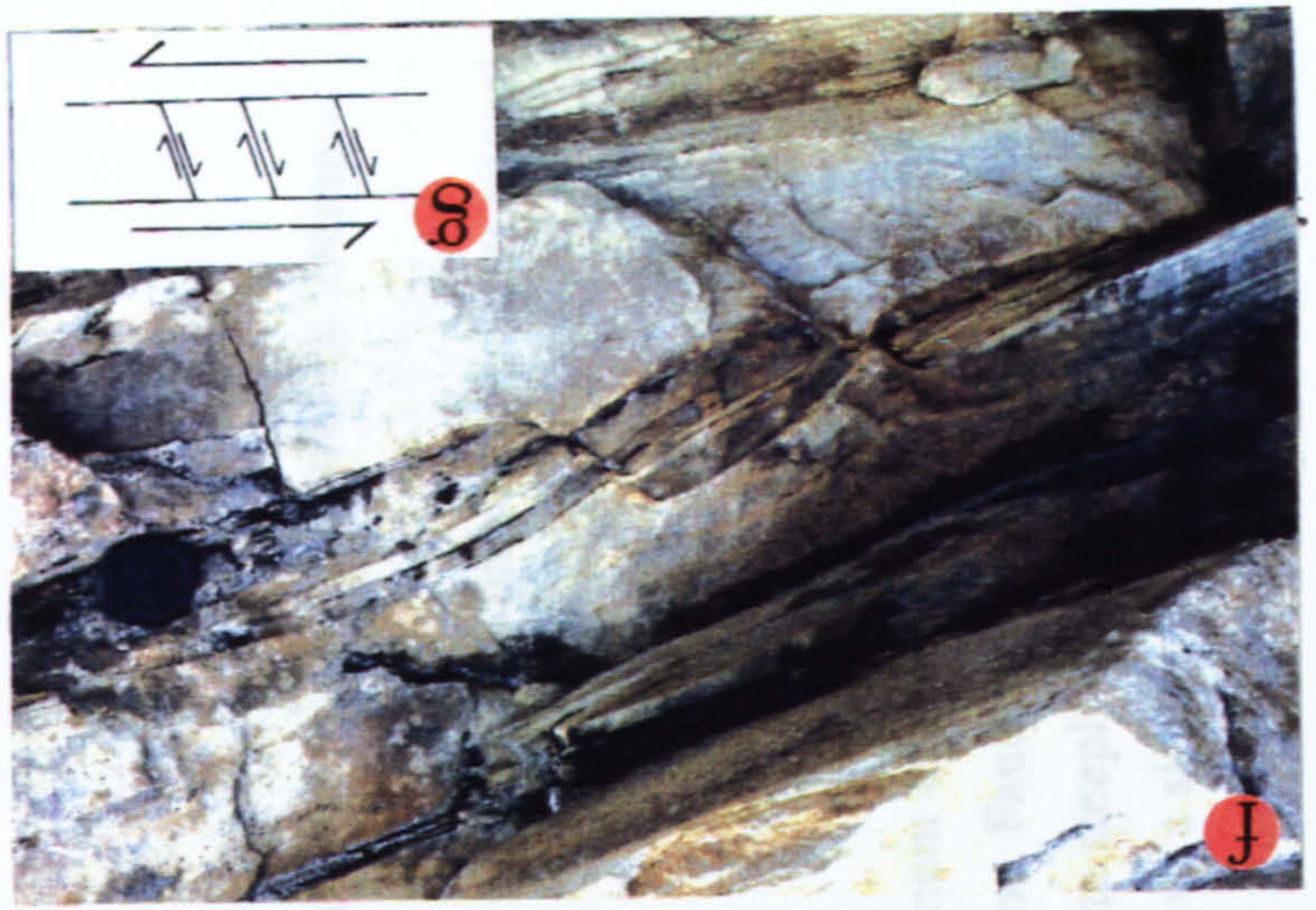
g
f

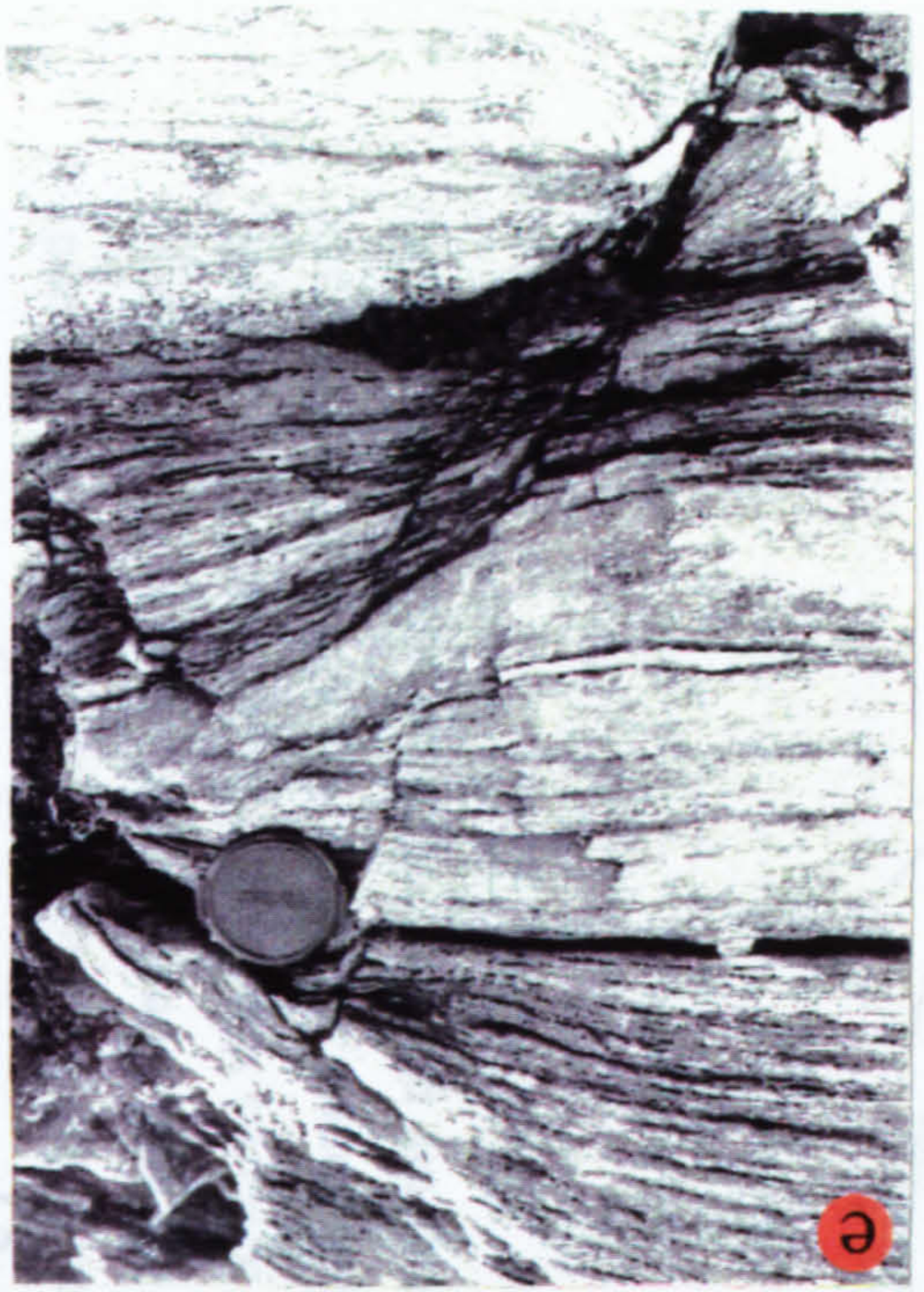
e


p
d


A
A
c

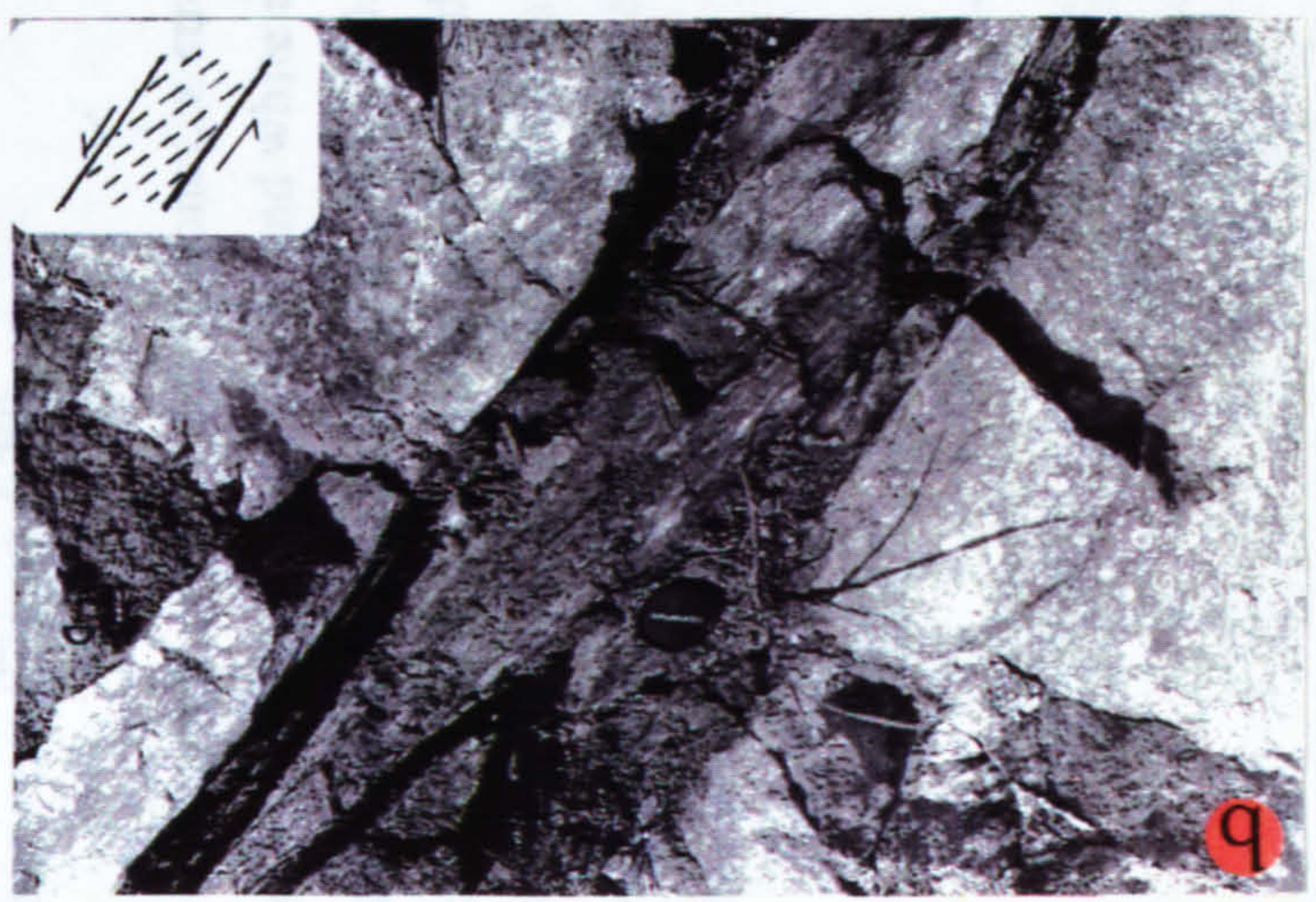
b


x
a

4:7 Evidence For Extensional Deformation within the Sonnblick Dome

There are several lines of field evidence to suggest the presence of extensional deformation within the Sonnblick area.

4:7.1 Normal Faults

Faults which have a normal dip slip component to their displacement vector are relatively common within the gneisses of the dome. Fault zones have a range of widths (1-20 cm) and orientations, but generally dip quite steeply (Figure 4.19a). Faults show almost pure dip slip components but generally have a slight sinistral component. Faults observed to be dipping towards the northeast quadrant have a stronger sinistral-component (Figure 4.20).

In the wider normal fault zones, a strong planar fabric is developed and is formed from a discrete, spaced biotite and white mica-rich foliation which anastomoses around quartz and feldspar augen (Figure 4.19b). Mineral lineations are commonly developed within the fault zone and generally trend towards the southwest or northwest (Figure 4.20). On a hand specimen scale, deformation appears to be ductile although preferential weathering due to increased mica content at the margins of the fault zones may hide zones of brittle or ductile deformation.

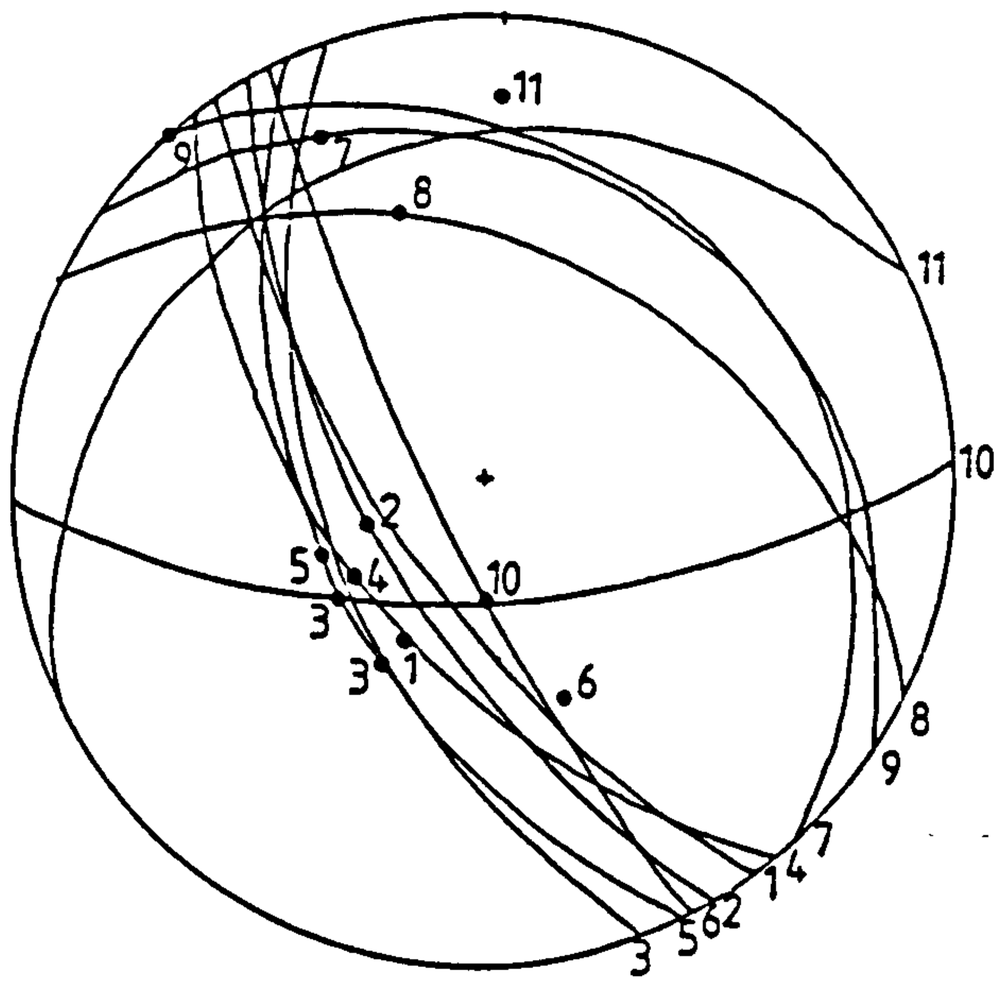

Figure 4.20. Lower hemisphere Wulff projection of faults having a component of normal dip slip recorded from the lower structural levels of the Dome. Numbers outside and inside the net refer to related fault planes and displacement directions respectively. WSW dipping faults have negligable strike slip components while the NNE dipping faults have a much lower component of dip slip.

The magnitude of displacement in many of the faults is impossible to quantify due to the absence of displaced markers. However, one fault, exposed at a height of 2030 metres on the Panoramastraße, displaces an aplite marker (Figure 4.19c) and can be used to estimate shear strains within the fault zone. Two zones of increased shear strains are associated with the zone. Most of the displacement (approximately 140 centimetres parallel to the mineral lineation on the fault) takes place along a 1cm wide zone which is now strongly weathered. In the hanging wall of the fault, the aplite is displaced by 30cm within a zone 3cm wide. Assuming that no volume loss occurs within the fault zone, shear strains in excess of 100 are calculated for the main fault zone while shear strains in the order of 10 are observed for strains in the hanging wall of the fault.

At higher structural levels, the contact between the Sonnblick gneiss and the overlying Peripheral Schieferhülle is often cut by discrete brittle faults which have a high normal dip-slip component. These faults therefore postdate the juxtaposition of Peripheral Schieferhülle and the underlying Zentralgneis Complex. At lower structural levels within the Inner Schieferhülle, normal faults often reactivate earlier foliations developed in the Inner Schieferhülle during earlier folding. These are generally the steeply dipping F_2 foliation. Evidence is also seen for a lithological control on the nature of the deformation processes taking place within normal fault zones with more micaceous lithologies undergoing ductile deformation while the same fault appears brittle, and is quartz filled, within less micaceous gneisses (Figure 4.19d).

4:7.2 Boudinage Structures

Boudinage commonly occurs in the upper levels of the Dome due to the strong planar anisotropy in the higher structural levels of the Dome, associated with increased lithological variation and the development of strong planar foliations. Within well foliated gneisses, foliation boudinage (and internal boudinage) is commonly observed on a sub-metre scale. The bending of the foliation into the necks of these zones is overprinted and partly accommodated by small scale extensional faulting (Figure 4.19e).

Within the Peripheral Schieferhülle asymmetric boudinage is commonly developed (Figure 4.19f). This may be interpreted as forming by either extension due to shear band-type structures or by a domino-type block rotation. The high angle of the fractures producing the offset in the layers argues against the first model and boudinage is interpreted to have formed from rotation of blocks in a top-to-SE shear regime (Figure 4.19g).

Figure 4.21a. En-echelon vein array developed within the northern overturned limb of the Peripheral Schieferhülle, northeast of the Feldsee Kopf. The sense of asymmetry between veins and the observed foliation suggest that the initial foliation was oblique to the fractures. The foliation has subsequently been folded to produce the tight folds observed between the veins.

Figure 4.21b. Interpretation of the structure shown in Figure 4.21a. Initial top-to-north shearing is inferred to have produced the vein array and the foliation. This was followed by dome associated folding and flattening of the overturned limb to produce the folding.

Figure 4.21c. Shear bands (c') within metasomatized gneissic shear zone indicating a dextral shear sense.

Figure 4.21d. Quartz precipitated within a metasomatized shear zone of the Inner Schieferhülle northeast of Wurten Speicher.

Figure 4.21e. Large composite mineralized vein exposed at the summit of the Schwartzsee Kopf. The vein is composed of quartz (q) with a centre of carbonate material (c). At outcrop scale the vein appears undeformed.


a
OLYMPUS

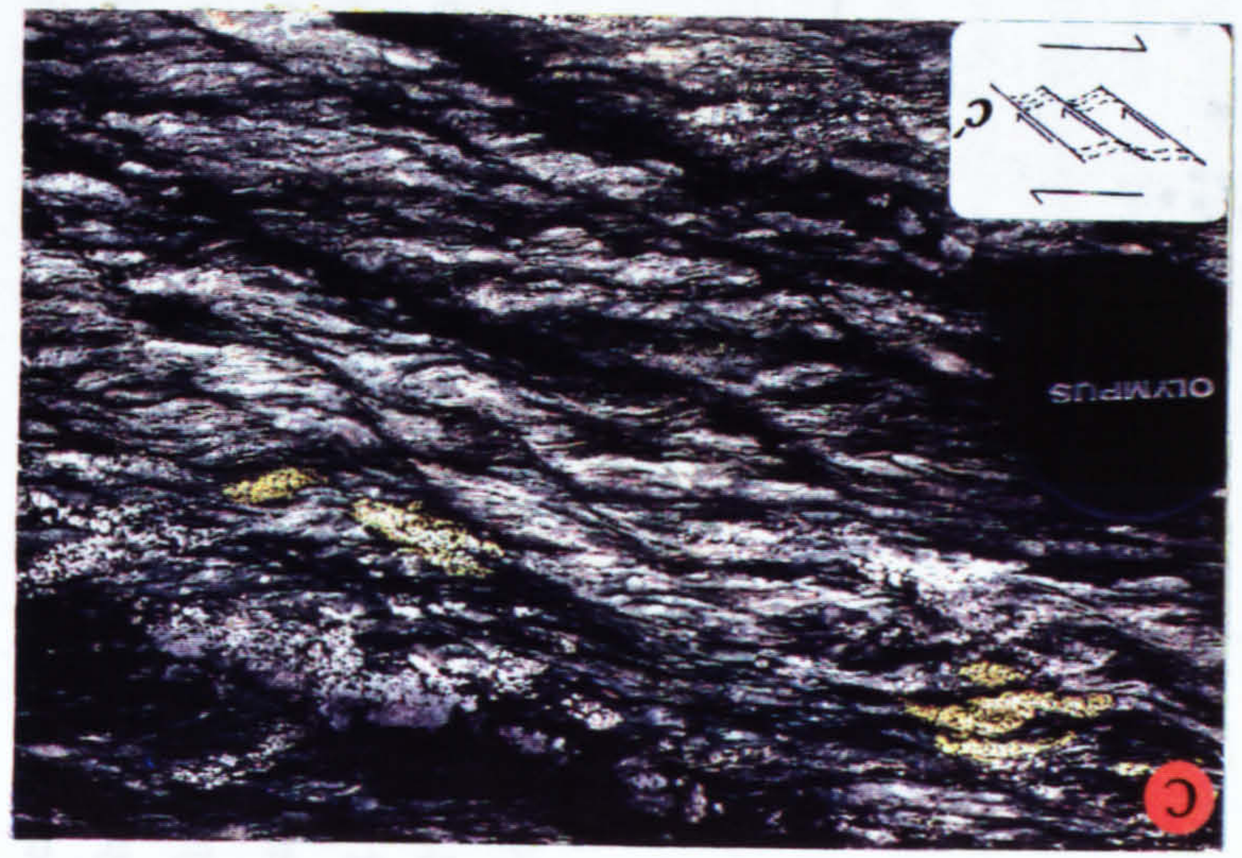
c
OLYMPUS

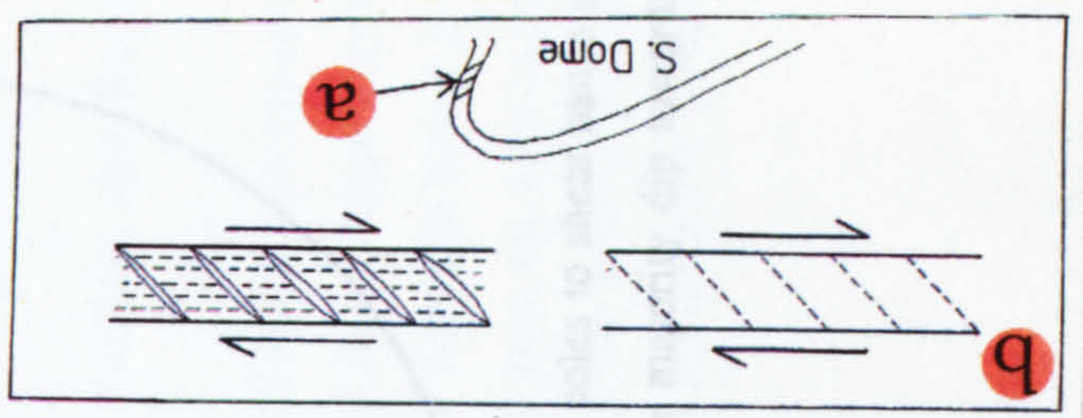
a
S. Dome
b

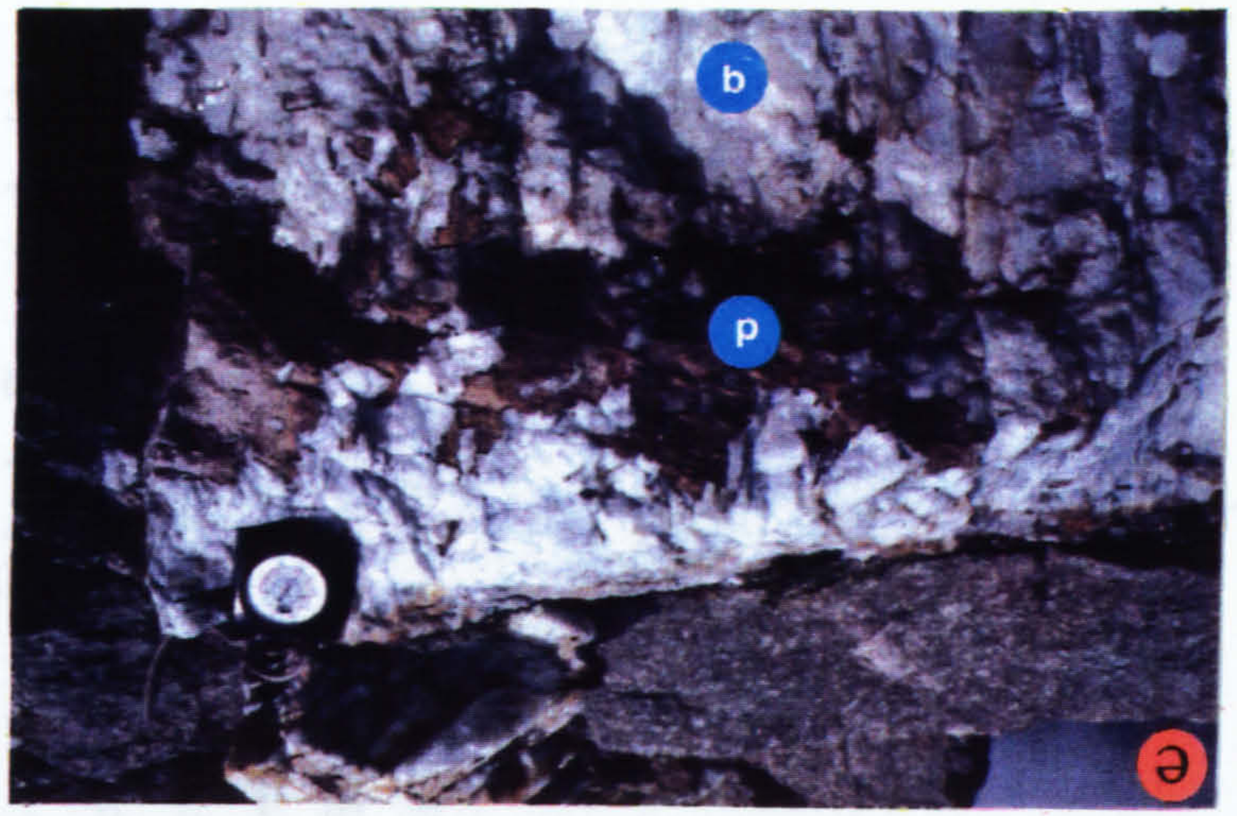
b
d
e

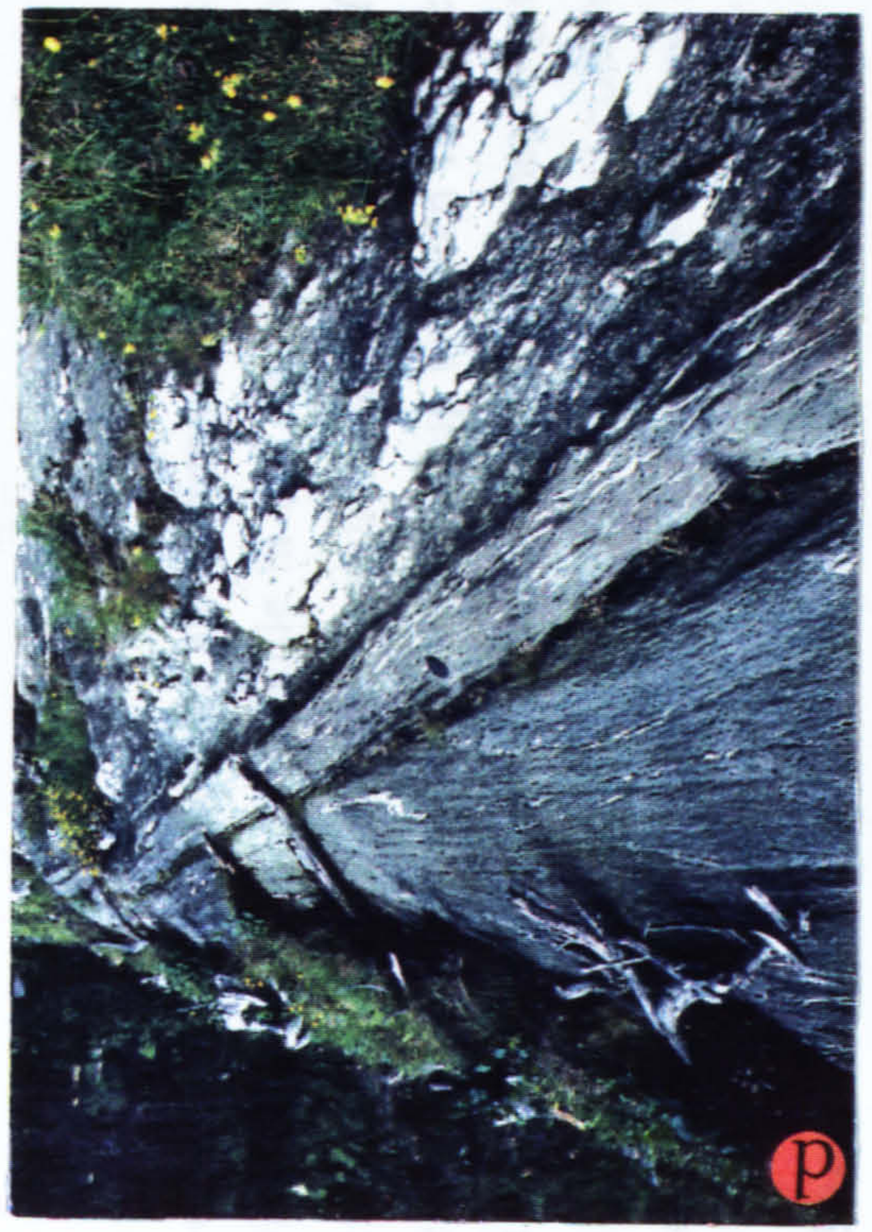
d

En-echelon tension fractures are commonly seen oblique to foliations within the overturned Peripheral Schieferhülle in the northern limb of the Sonnblick structure. Between these fractures, the foliation within the Peripheral Schieferhülle is tightly folded (Figure 4.21a). The geometrical relationship between fracture sets and the foliation suggest formation of the fractures within a top-to-NW shear regime. The later folding of the foliation between these fractures, possibly represents compression associated with formation of the dome structure and overturning of the fold limb (Figure 4.21b).

4:7.3 Shear Bands

Shear bands are locally developed within mica schists within the Dome and within the schists of the Peripheral Schieferhülle (Figure 4.21c) and are associated with extension at least on a local scale. Most bands dip to the southwest or southeast (Figure 4.22) and are associated with top-to-SE movement. Two examples of shear bands cutting F_3 crenulations have been observed in the field. However, the relative timing of these bands to other structural features can best be inferred from microstructural evidence (see section 4.11).

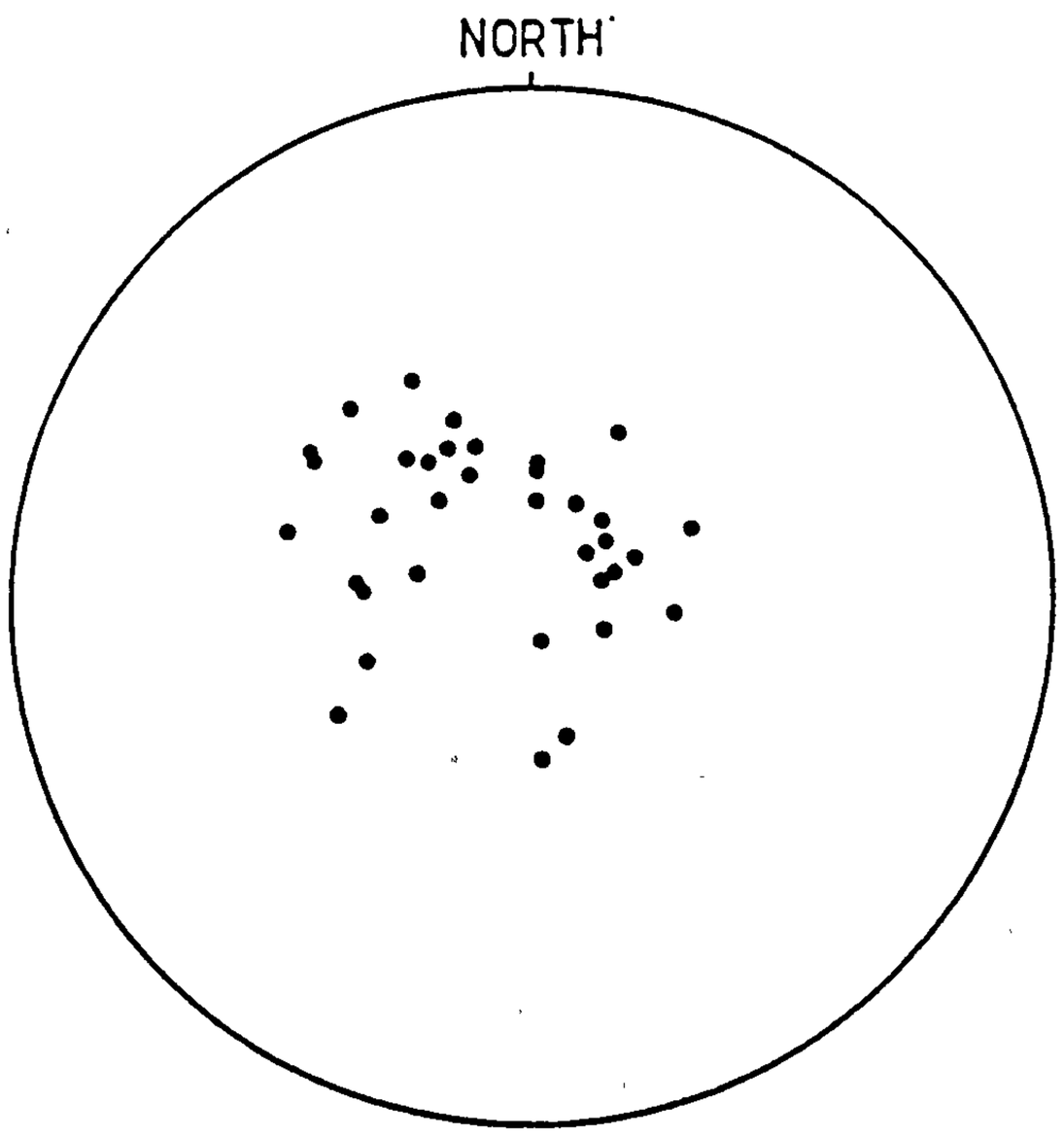

Figure 4.22. Lower hemisphere Wulff projection of poles to shear bands developed within the upper structural levels of the Sonnblick Dome. The majority dip towards the SW or SE although a few dip NE and NW.

4:8 Vein Formation

Within the Sonnblick area, several generations of vein development can be identified by cross-cutting relationships with other structural features. Several early generations of quartz vein development are seen within the Dome. Within the Inner Schieferhülle, quartz veins are found deformed by the strongly developed banded foliation as well as cross-cutting this foliation. Quartz veining is also seen developed within the ductile shear zones within the Inner Schieferhülle (eg. Figure 4.21d) and is probably associated with fluid pumping within these zones.

Of greater significance in terms of volume and economic view points, are a series of late, mineralized quartz veins. Late quartz veins commonly contain dolomitic carbonate material in which the carbonate veining appears to postdate the quartz veining (Figure 4.21e). However, the lack of carbonate veining away from the quartz vein suggests a close spatial and probably genetic relationship between the different vein types.

Large, steeply dipping quartz veins trending NNE-SSW cut all structural features observed in the dome and therefore appear to be the last deformation phase in the area. In some areas, for example the Zirknitztal, these veins can be clearly seen on air photographs. The veins show a pinch and swell geometry and have been traced for up to 8km along strike. The veins are strongly mineralized, containing gold and silver, and have a complex mineralogy comprising telluride and complex sulphur salts which are thought to have been chemically derived from the amphibolites of the Sonnblick area (Feitzinger pers. comm, 1988). Weak silicification or phyllic alteration (seriticitzation of gneiss) of the wall rocks is occasionally seen to occur, and preliminary fluid inclusion data suggest temperatures of quartz vein formation between 290-350°C (Paar and Rainer, unpublished data). These temperatures have been used to infer formation at several stages during a late Tertiary phase of Alpidic metamorphism.

4.9 Evidence for Progressive Deformation within the Sonnblick Dome

The earliest structural features associated with Alpine deformation in the Sonnblick Dome appears to be the strong foliation developed in the higher structural levels of the Dome and the development of more discrete shear zones at lower levels. Although, the structural data presented so far can be arranged into an approximate chronological sequence, there is evidence from one exposure at the base of the Astrom Spitze (at a height of 2420 metres and grid reference 186064) for different structural features being

inter-related and are derived from a single, progressive deformation in the hanging wall of a shear zone.

The shear zone is developed within coarse augen gneiss and shows a strong mineral lineation and a well developed S-C fabric associated with top-to-NNW shearing (Figure 4.23). A foliation is developed in the granitic gneiss hanging wall of the partially altered shear zone which lies sub-parallel to the margin of the shear zone, and the C-plane of the S-C fabric developed within the shear zone (Figure 4.23). The parallelism of shear zone and external foliation suggests that either the foliation developed during top-to-NNW shearing and therefore developed synchronously with the shear zone; or that the shear zone developed by reactivation of a suitably oriented earlier foliation. Mineral lineations suggest that the foliation in the gneiss developed during top-to-NNW shearing and the shear zone is therefore interpreted to have formed during the same deformation phase as the foliation.

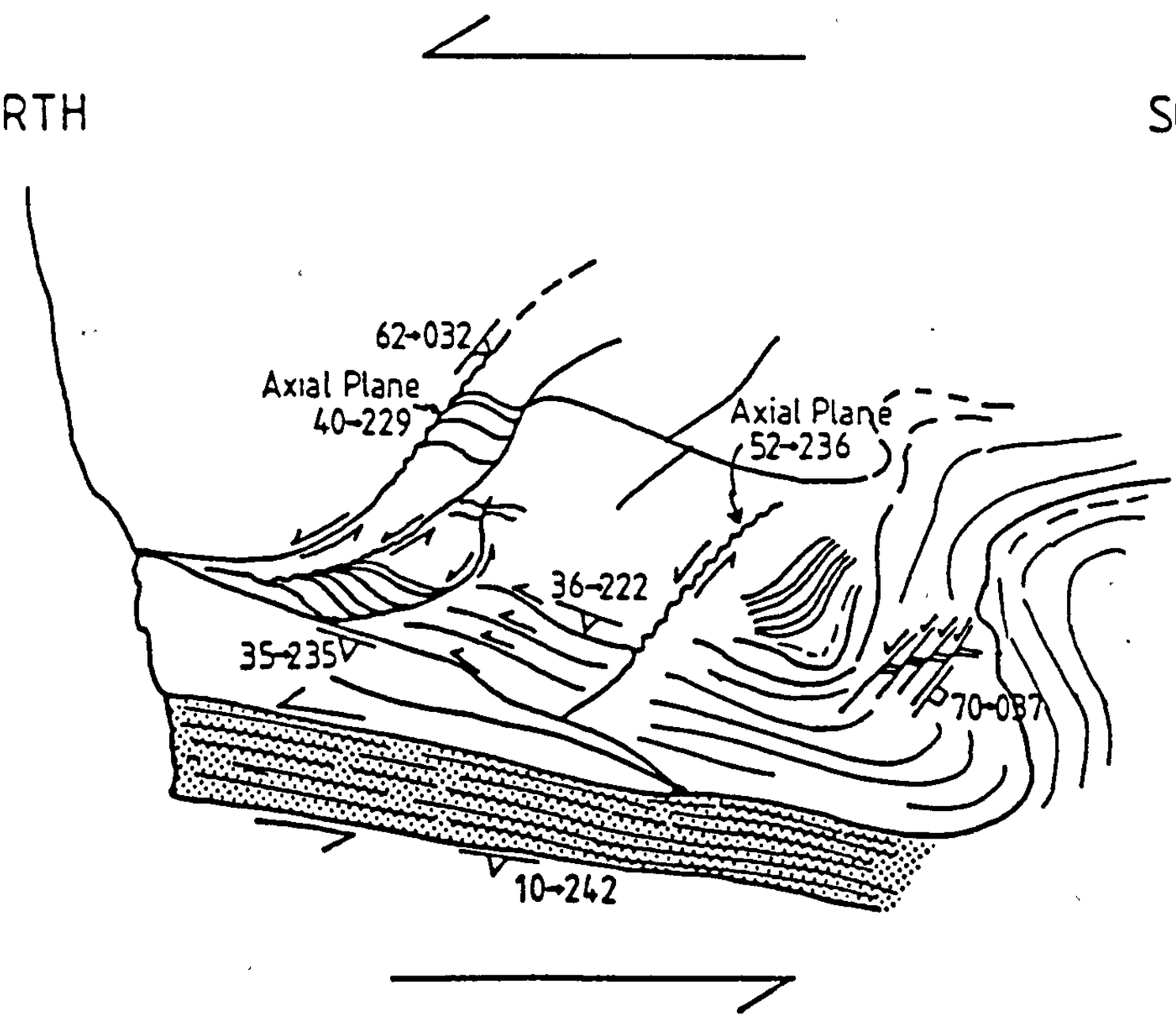

Figure 4.23. Folding, localized shearing and normal faulting developed in the hanging wall of a partly altered shear zone within the Zentralgneis (see text for discussion). Mineral lineations on the foliation of the shear zone trend NNW. Shear zone width is approximately 1 metre.

To the southern end of the exposed section, this foliation is folded in a similar orientation to F_3 folds observed elsewhere in the Dome. The underlying shear zone is not folded. In the area of the hangingwall immediately in front of the fold, the earlier foliation locally becomes reactivated and forms small discontinuous micaceous shear zones which have a similar displacement to the underlying shear zone. These reactivated surfaces are cut by shear zones which have a listric geometry and a normal sense of displacement. These features only occur immediately in front of the fold and are interpreted to be genetically related to the observed folding. Crenulation of these normal shear zones by smaller scale folds having a similar orientation to the larger scale fold above the shear zone, is locally observed.

To the northern end of the exposure, the gneiss immediately above the shear zone is unaffected by the fold, foliation reactivation or normal faulting. This area is the footwall of a small thrust which has a trailing branch line lying on the shear zone margin. A possible interpretation of these features are that shearing within the gneiss at the northern end of the exposure 'locked up' and led to strain in the trailing part of the hanging wall being accommodated by folding. Geometrically, this would require deformation to take place in the front of the fold and this is expressed by the development of thrust and listric normal shear zones.

The structures described above are therefore all associated with strain accommodation during top-to-NNW shearing. Thrusting, folding and normal fault development in this one exposure therefore appear to have developed during a single progressive deformation.

4:10 Microstructural Observations on the Sonnblick Gneisses

4:10.1. Microstructural Preservation

There are several processes by which coarsening of quartz grains and modification of microstructures may occur and several sources of energy may drive these processes. Microstructures can be modified by the conversion of elastic distortion to dislocation or twin arrays, the reorganization and reduction of dislocations by glide, climb and cross slip to lower energy configurations and by the migration of grain boundaries which will remove internal substructures in deformed grains (Knipe 1989). The rate of recrystallization by dislocation creep processes is related to both temperature, since dislocation climb is diffusion controlled, and stress (eg. Poirier 1985). Recrystallization

by grain boundary migration is dependent upon the free-energy differences between adjacent grains, (ie.that is the chemical free energy, the interfacial free energy and the internal strain energy within individual grains) (Urai *et al* 1986). The kinetics of grain boundary migration will also be dependent upon factors such as temperature.

The preservation of microstructural textures will be dependent upon the extent of recrystallization by a combination of subgrain rotation and grain boundary migration; and how quickly these processes are inhibited at the end of a deformation event. A gradual reduction in stress or strain rate at the end of a deformation phase will affect both recovery and grain boundary migration processes and will modify the steady state microstructure developed during the deformation. In such a case, the cyclic interaction of subgrain development and grain boundary migration will lead to an increase in grain and subgrain size and a reduction in dislocation density (eg. Knipe and Law 1987; Knipe 1989). However, an increase in grain size and the resetting of microstructures may also occur by recrystallization processes under static conditions provided that a high enough temperature is maintained to enable such processes to be kinetically active.

In this section, microstructural observations are presented and their significance assessed in order to further detail the kinematic evolution and structural framework of the Sonnblick Dome and relate this to Alpine metamorphism within the southeast Tauern Window.

4:10.2 Characteristics of Foliations at Low Structural Levels

a) Foliations within the Sonnblick Gneisses

Quartz in the 'Low Strain Coarse Augen Gneisses' shows evidence of having undergone deformation on a microscopic scale. Individual quartz grains are up to 1mm in size and have dentate grain boundaries and internal subgrains (Figure 4.24a). Locally observed 'left over grains' (Urai *et al* 1986)) suggest that the suturing was due to grain boundary migration. Therefore, within rocks which appear mesoscopically undeformed, quartz has undergone some recrystallization and primary igneous relationships have been modified.

Biotite in these rocks has an undulose extinction due to kinking of the crystal lattice, while feldspar shows the local development of cross-hatched twinning and undulose extinction associated with plastic deformation. Subgrains, illustrated by variations in

Figure 4.24a. Quartz texture developed within very low strain granitic gneiss. Inividual quartz grains have sutured grain boundaries indicating grain boundary migration (g), while internally, deformation bands (d) and subgrains (s) are observed. Plagioclase augen (p) show dentate grain boundaries with quartz which suggests local modification of feldspar-quartz boundaries by diffusive mass transfer during low strain deformation.

Figure 4.24b. Sutured grain boundaries (g) within K-feldspar augen and the formation of subgrains (s) indicating that in low strain gneisses, feldspar deformation occured by both recrystallization-accommodated and recovery-accommodated dislocation creep (eg. Tullis and Yund 1984).

Figure 4.24c. Grain elongation fabric developed in a quartz augen domain in intermediate strain augen gneiss. S_a marks the external foliation defined by elongate augen and mica-rich domains. S_b illustrates the weak grain fabric. An individual grain (X) can be traced from upper right to lower left. Quartz shows subgrain formation and sutured grain boundaries indicative of grain boundary migration. Micrograph taken under crossed polarized light with quartz accessory plate.

Figure 4.24d. Quartz (q)- feldspar (f)- mica (m)- epidote (e) domain within intermediate strain gneiss. T illustrates a good example of a quartz triple point with intersection angles which are close to 120°. Micrograph taken under crossed polarized light.

Figure 4.24e. Mica foliation domain in intermediate strain augen gneiss showing the preferred orientation of micas and their (001) cleavage parallel to the foliation. Note that the quartz domain above the mica domain shows no grain shape fabric associated with foliation development although subgrains and dentate grain boundaries associated with recrystallization are present. Micrograph taken under crossed polarized light.

Figure 4.24f. Quartz- and mica-rich foliation domains observed in the mesoscopic ductile shear zone shown in Figure 4.11 (see text for discussion). Micrograph taken under crossed polarized light.

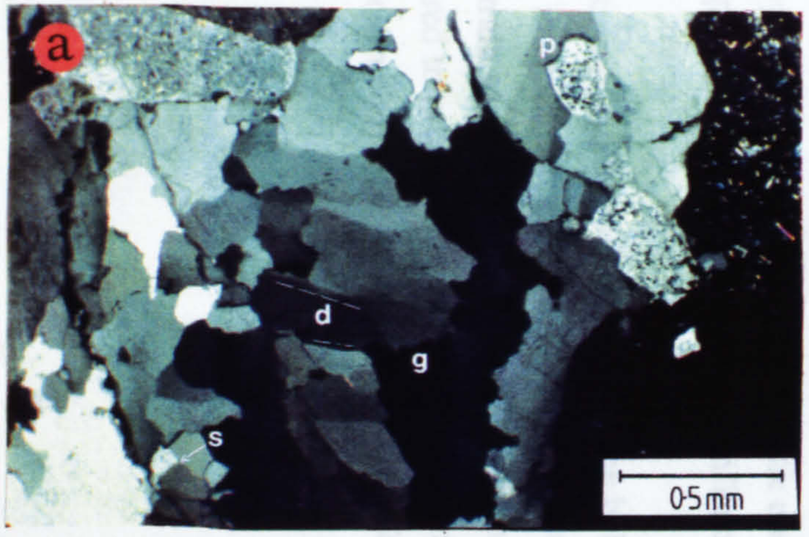
a
p
d
g
s
0·5mm

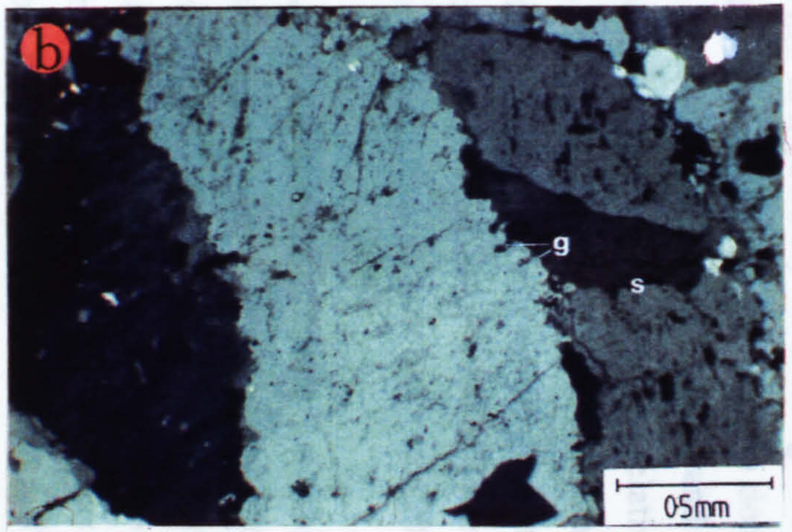
b
g
s
0·5mm

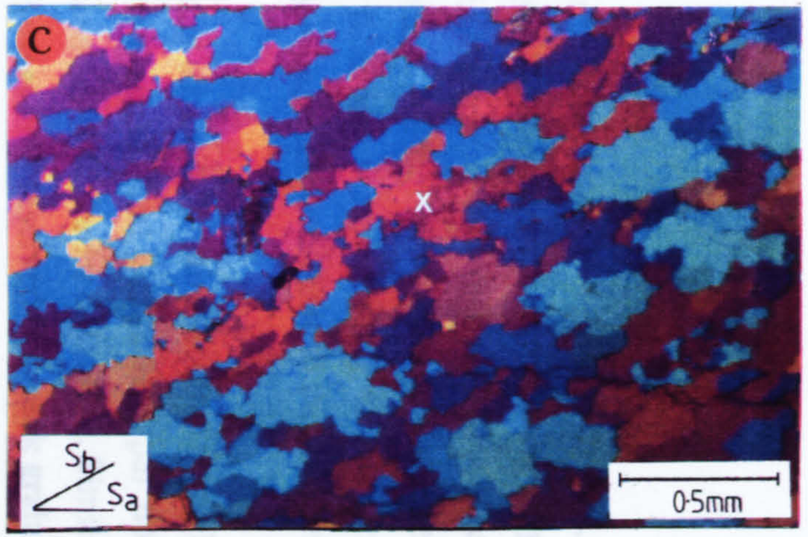
c
X
Sb
Sa
0·5mm

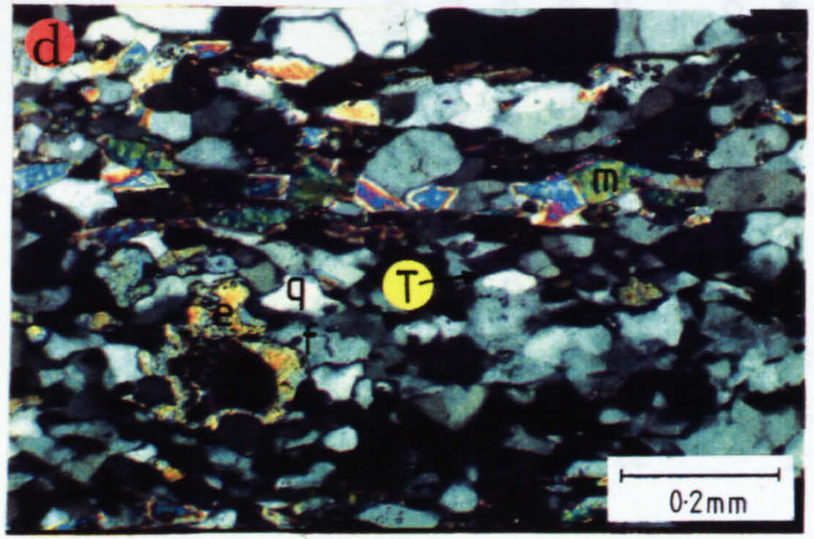
d
m
T
q
e
f
0·2mm

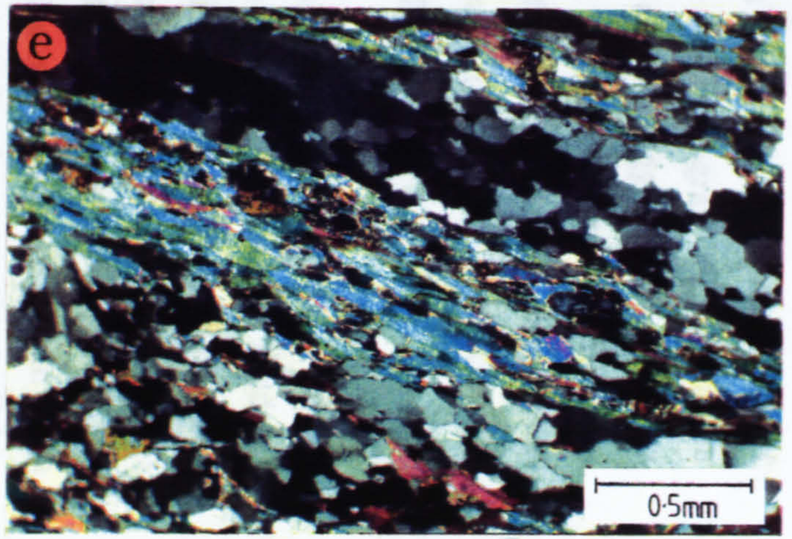
e
0·5mm

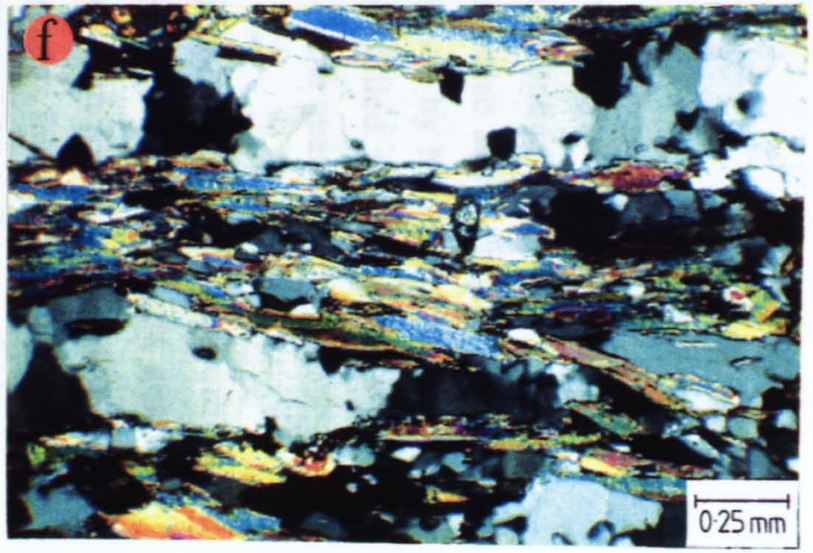
f
0·25mm

extinction through individual K-feldspar augen, commonly have sutured grain boundaries. These boundaries are indicative of grain boundary migration, while subgrain formation suggests that recovery processes were also active (Figure 4.24b) (eg. Tullis and Yund 1985). Feldspars also show deformation by brittle processes and fractures within feldspars are commonly calcite or quartz filled. Quartz within these fractures shows similar microstructures to those observed in the quartz augen.

With increasing strain, a domainal fabric is developed, composed of elongate quartz augen, mica-rich domains and quartz-feldspar domains. Individual, equant, quartz grains within augen are in the order of 0.5mm. Similar quartz microstructures to those in the low strain gneisses are preserved but weak grain elongation fabrics are occasionally observed within low to moderately deformed gneisses (Figure 4.24c). Quartz within the matrix is finer grained (~0.1mm) and occurs in domains containing feldspar, mica and epidote (Figure 4.24d). Undulose extinction and sub- and new-grain formation are observed but dentate grain boundaries are relatively absent suggesting that quartz recrystallization was dominated by subgrain rotation. This is consistent with 'slow migration' of quartz boundaries due to the presence of other phases hindering grain boundary migration (eg. Urai *et al* 1986). Where quartz triple point junctions are observed, intersection angles are in the order of 120° (Figure 4.24d).

Feldspars within the foliated matrix are a similar size to quartz and show similar microstructures to quartz indicative of recrystallization by plastic processes. Epidotes show no evidence of having undergone deformation (Figure 4.24d). Elongate epidotes have a length preferred orientation with long axis subparallel to the main foliation. This suggests either syndeformational rotation of the epidotes into parallelism with the foliation or post deformational growth along the foliation. Similarly within mica domains, mica laths and their basal (001) cleavages are generally elongate sub-parallel to the foliation (Figure 4.24e). Micas show a weak undulose extinction but generally show little evidence for them having undergone significant amounts of deformation.

The mesoscopic foliation illustrates that the bulk rock has been moderately strained. However, the internal deformation features of most of the mineral phases within the intermediate strain gneisses are not consistent with them having undergone the amounts of strain required to produce the observed foliation. This suggests that recrystallization or recovery occurred after the development of the foliation.

b) Mesoscopic Ductile Shear Zones

The shear zone shown in figure 4.11 has been studied at a microscopic scale in order to investigate the processes and mechanisms associated with the development of a small ductile shear zone. The zone contains a strong foliation defined by quartz domains, mica-rich domains and quartz-feldspar-epidote domains. Minerals within the shear zone occur in similar modal proportions to minerals in the host gneiss. This suggests that shear zone formation was close to isochemical and was probably volume conservative. Similar microstructures to those developed within the foliated gneisses are observed within the shear zone (Figure 4.24f).

Within quartz-feldspar domains, small feldspar augen have sub- and new grains developed at their tails (Figure 4.25a). The faces parallel to the foliation have sutured boundaries adjacent to quartz and mica indicating diffusive mass transfer processes operated on at least a grain scale. Finer grained quartz and feldspar making up the matrix of these domains are free of deformation fabrics when studied by optical microscopy. Diffusive mass transfer processes are also likely to have played a role in the development of the shear zone domainal fabric. No preferred grain elongation or grain boundary orientation fabrics, associated with shear zone development are observed (eg Figure 4.24f).

The boundaries between quartz and mica-rich foliation domains are often offset and have a step-like geometry due to shear band development oblique to the domain boundaries (Figure 4.25b). The orientation and sense of shear on these bands is consistent with development during formation of the shear zone. Where these shear bands cut across mica rich domains, a reduction in grain size is observed. Within quartz domains individual quartz grains are relatively coarse (≈0.2mm) and no evidence for localized shearing associated with the shear band is preserved (Figure 4.25b). This suggests that quartz microstructures associated with deformation within the shear band have undergone recovery or recrystallization. Recrystallization and coarsening of quartz after shear zone and shear band formation may also explain the absence of a grain preferred orientation within the quartz domains.

Locally preserved small K-feldspar augen (Figure 4.25c) have an undeformed core surrounded by a mantle of small, relatively strain-free, feldspar grains which occasionally dentate grain boundaries. Although the core and mantle structure suggests that feldspar deformation was by plastic processes, the turbidity of the core K-feldspar is

Figure 4.25a. Subgrains developed within small plagioclase augen of the quartz-feldspar foliation domain. Deformation in the feldspar was dominated by recovery-accommodated dislocation creep. Sutured margins between quartz and feldspar may illustrate the importance of diffusive mass transfer on a grain scale. Micrograph taken under crossed polarized light.

Figure 4.25b. Shear band (C') developed obliquely to the foliation in the shear zone of Figure 4.11. Shear band offsets the quartz-mica foliation domain boundary and bends the mica foliation. Within the quartz domain, no textures associated with localized shear along the shear band are preserved. Micrograph taken under crossed polarized light.

Figure 4.25c. Small feldspar augen in the ductile shear zone of Figure 4.11. Augen shows a core of relatively undeformed K-feldspar surrounded by a mantle of new and sub-grains. Micrograph taken under crossed polarized light.

Figure 4.25d. S-C fabric developed in leucogranite mylonite. The fabric is defined the orientation of mica laths and the S-fabric is also defined by a weak, long-axis preferred orientation of quartz and feldspar. The minerals do not show evidence for significant internal deformation although undulose extinction and subgrain development (S) is observed. Micrograph is a crossed polarized image.

Figure 4.25e. Micrograph of banded amphibolite showing a foliation (s) parallel to the banding. Banding consists of amphibole-rich domains (A) and feldspar-rich domains (F). Some amphiboles (eg. X) are highly oblique to the observed foliation and do not bend the foliation, suggesting that they grew after foliation development. Micrograph taken under crossed polarized light.

Figure 4.25f. Plagioclase porphyroblast overgrowing a foliation defined by elongate amphibole grains. Outside the porphyroblast, amphiboles are coarser and often oblique to the foliation. Small mica laths (m) are also seen oblique to the foliation and are also undeformed. Micrograph taken under crossed polarized light.

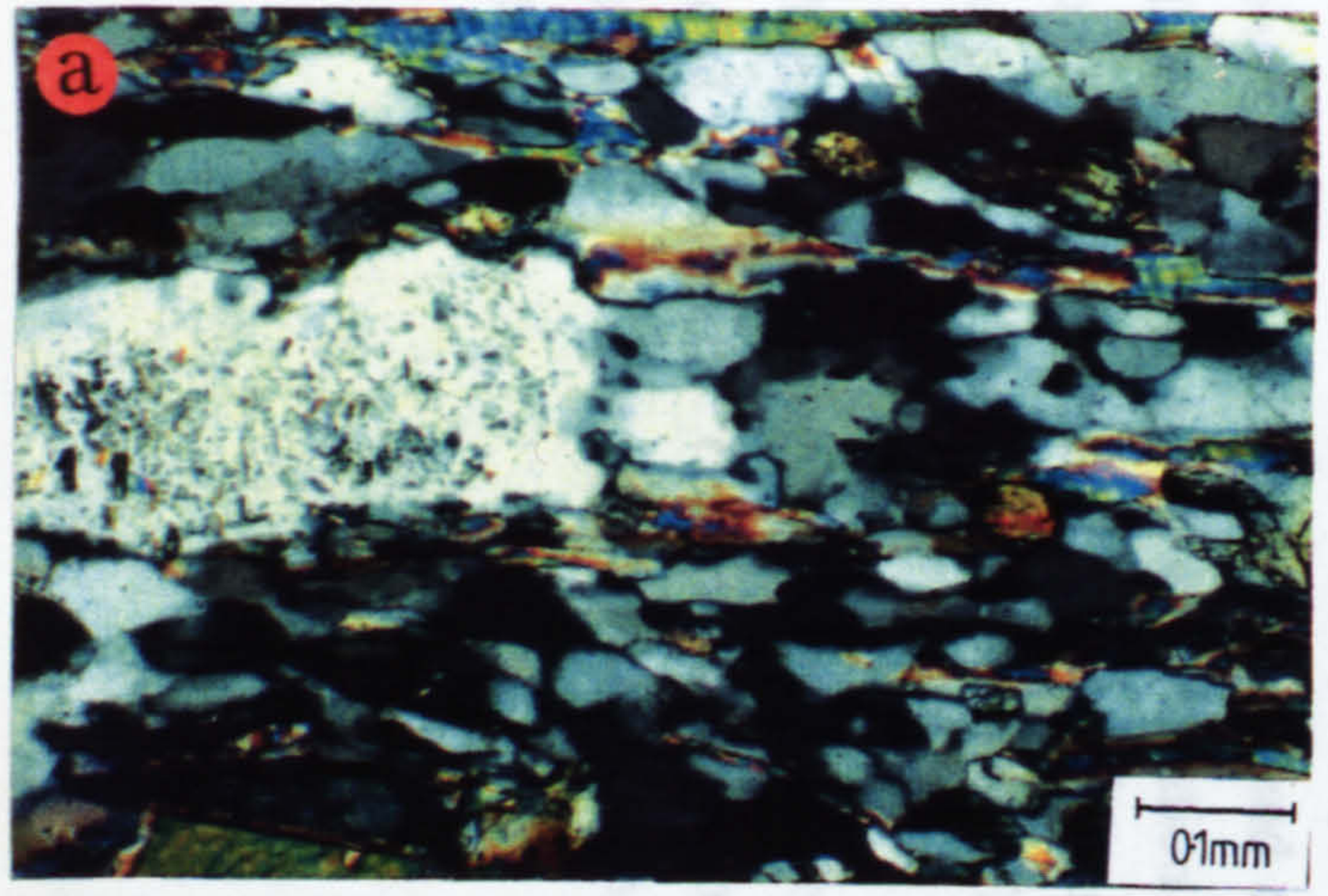
a
0·1mm

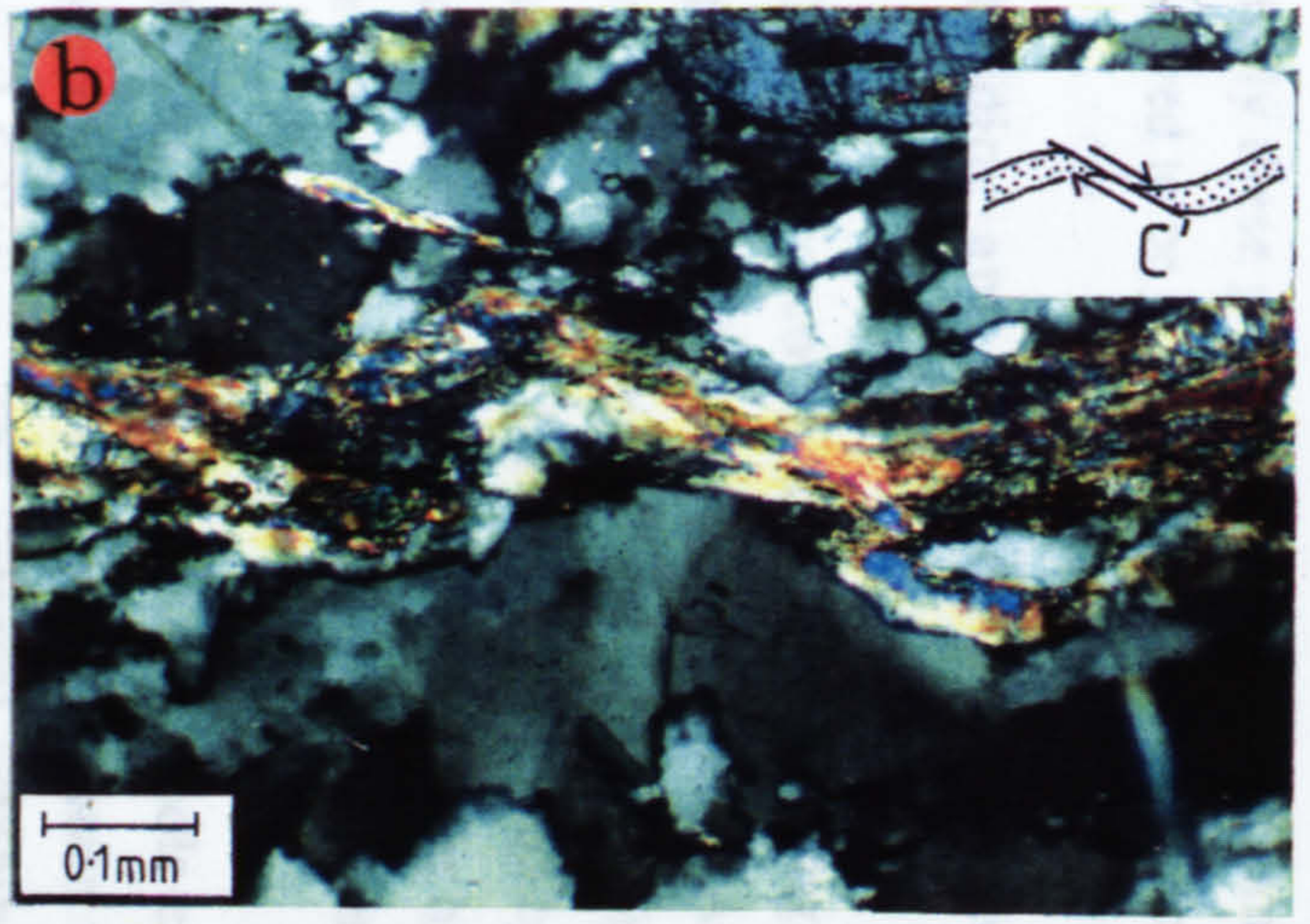
b
C'
0·1mm

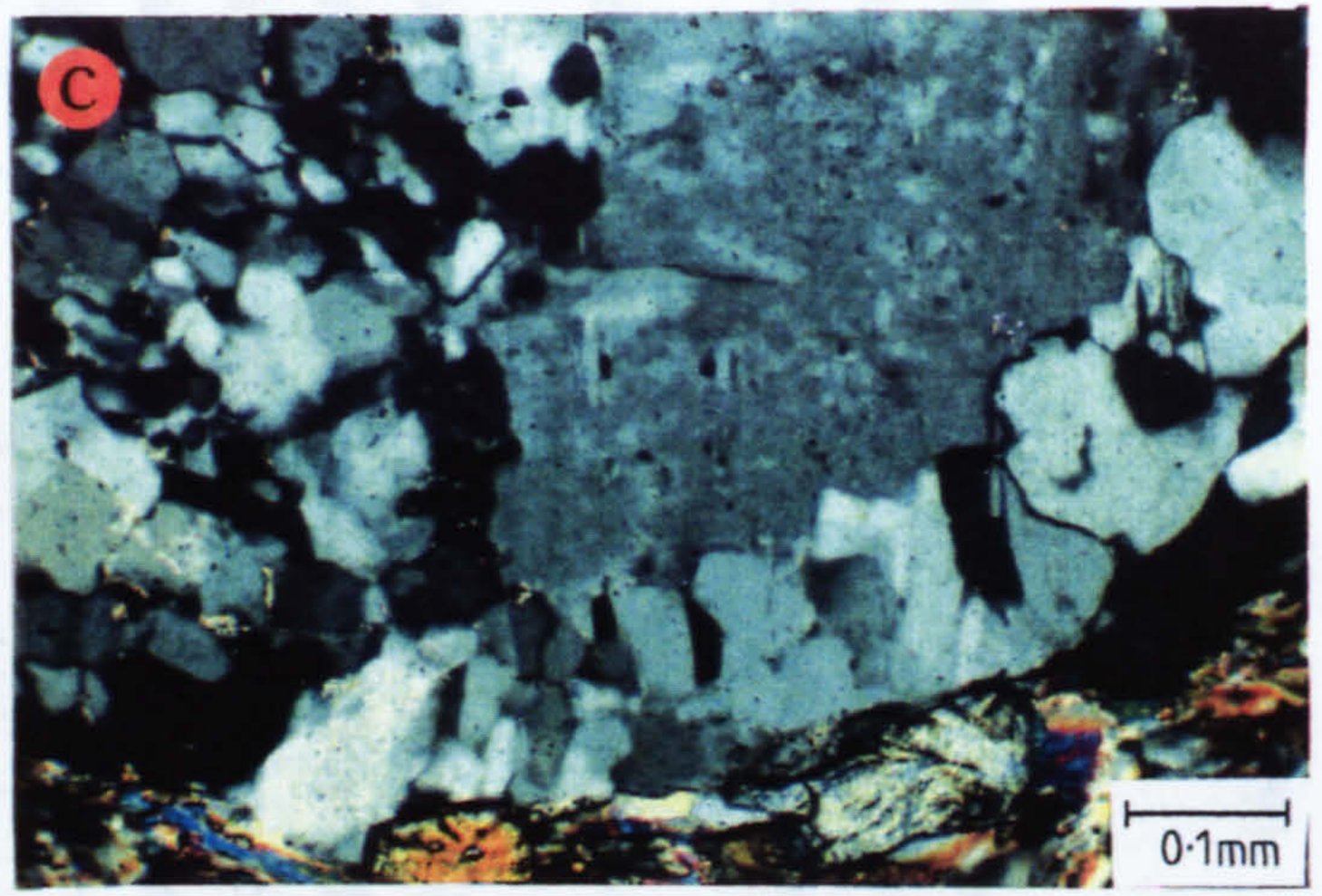
c
0·1mm

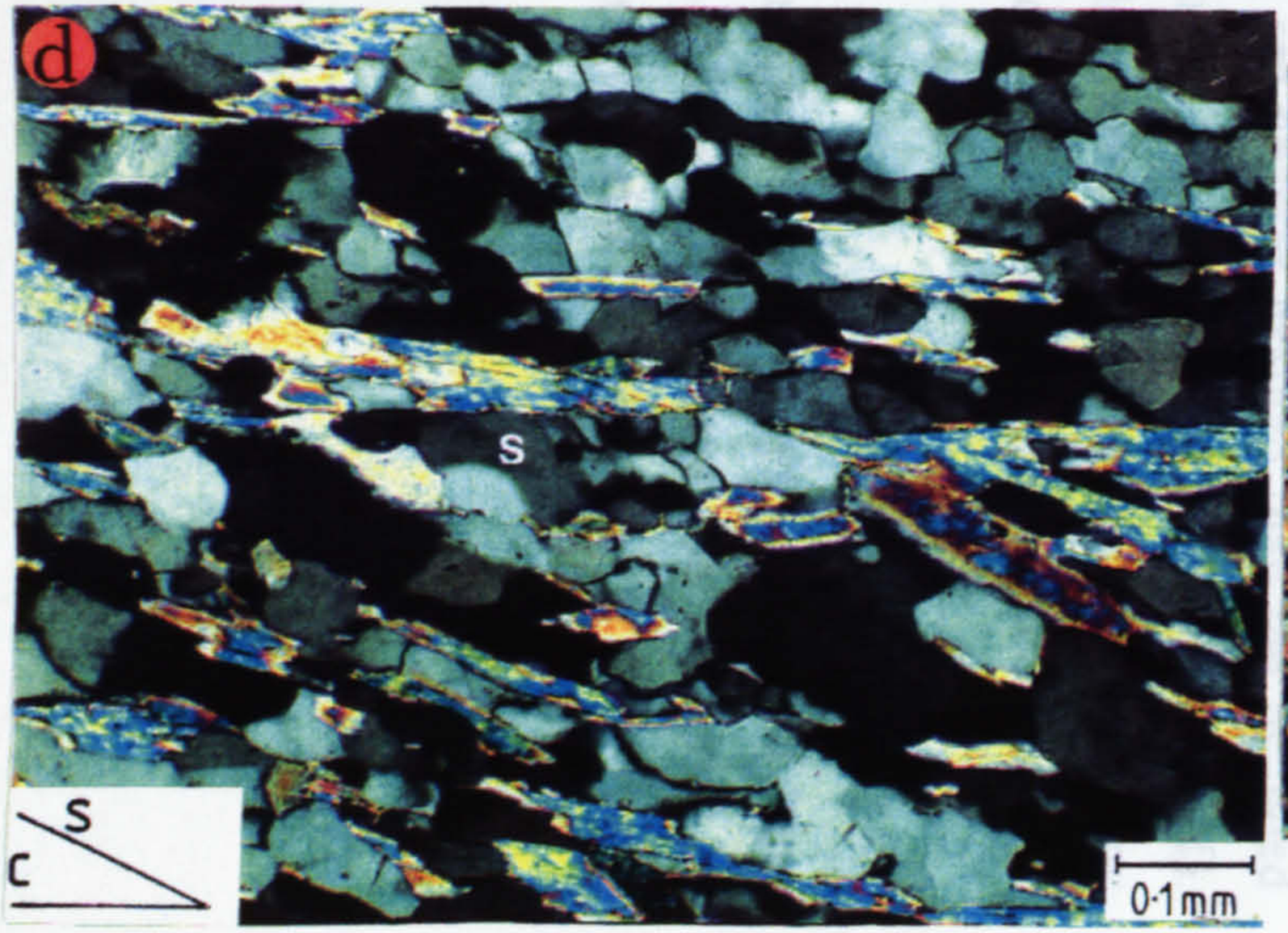
d
S
S
C
0·1mm

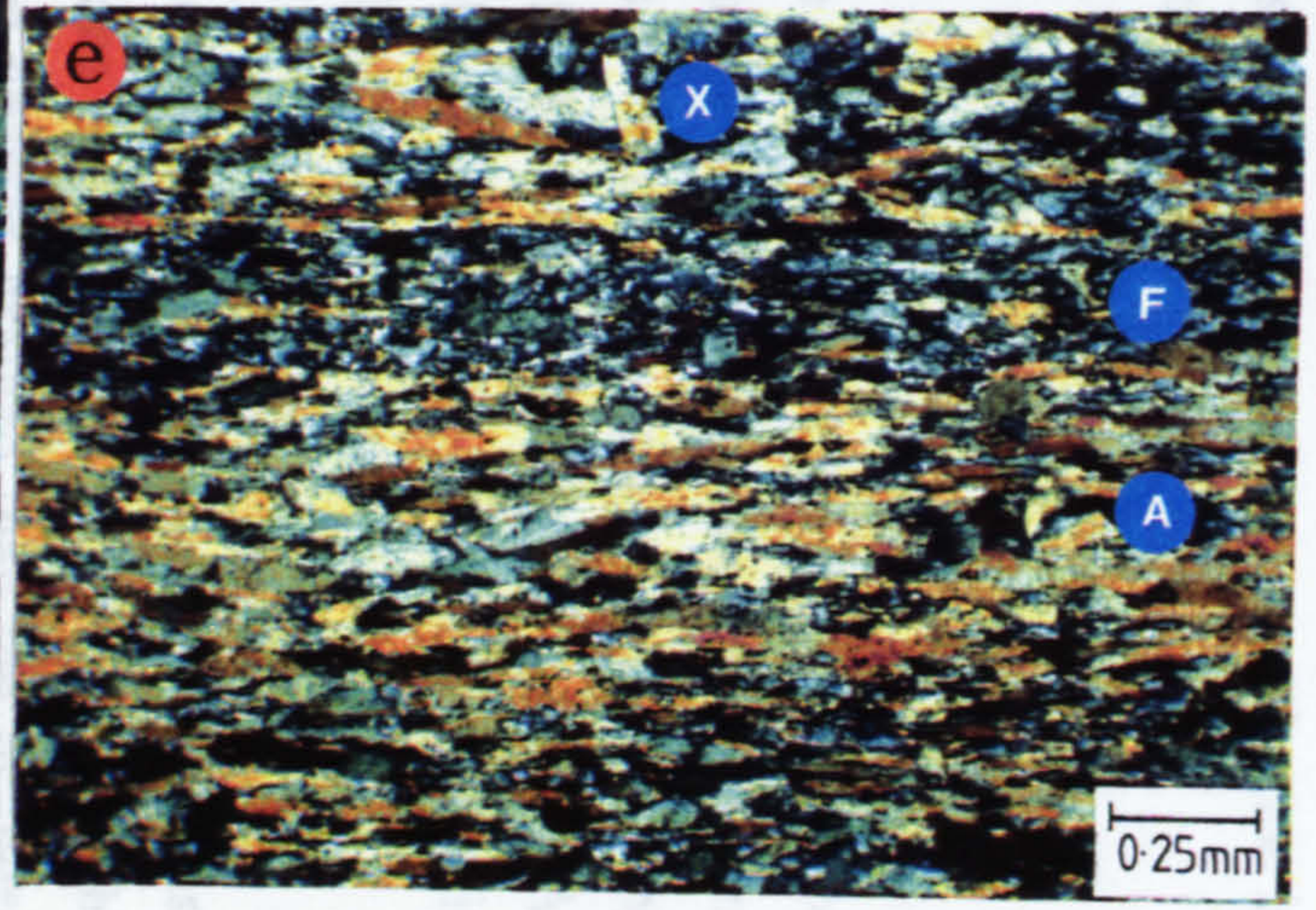
e
X
F
A
0·25mm

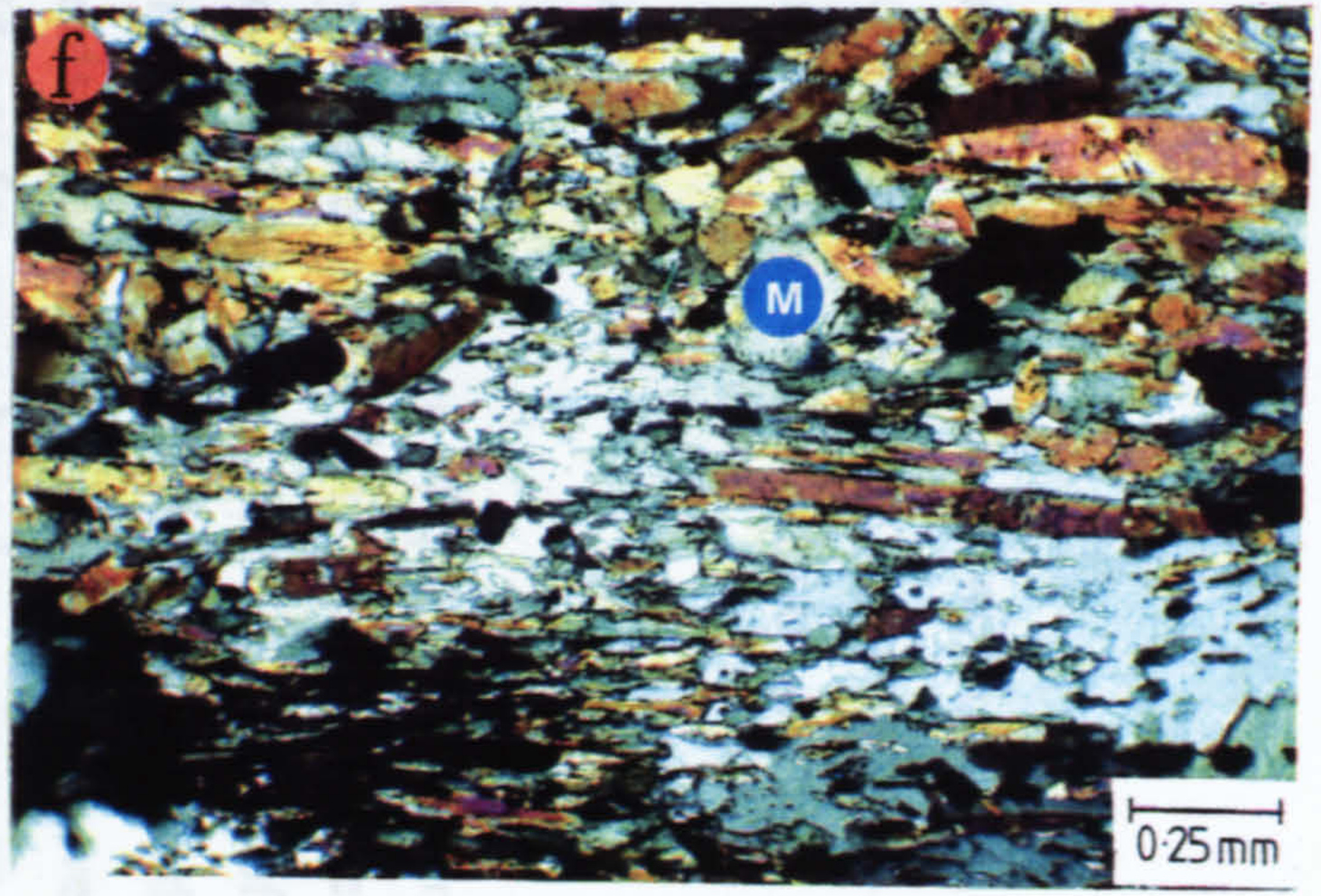
f
M
0·25mm

not reflected in the mantle grains. This implies that the mantle grains did not form as a result of subgrain rotation but that recrystallization was by grain boundary migration. This is supported by locally developed sutured grain boundaries on the mantle grains.

c) Foliation Characteristics of Mylonitic Leucogranites

On a microscopic scale, fine grained mylonitic units composed of quartz, feldspar and mica commonly show an S-C fabric, defined by the orientation of mica laths (Figure 4:25a) which is consistent with field evidence of top-to-NW shearing. The S-foliation of the fabric is also defined by a weak, preferred orientation of the long axes of quartz and feldspar (Figure 4.25d). Individual quartz and feldspar are 0.1mm in size and have relatively planar boundaries which show little evidence for grain boundary migration. Internally these grains show the development of subgrain walls and recrystallization is considered to be dominantly by subgrain rotation mechanisms.

d) Banding and Foliation Development in the Sonnblick Amphibolites

On a microscopic scale, the banding within the amphibolites can be seen to be comprised of amphibole-rich domains (A-domains) and feldspar-epidote rich domains (F-domains) in which a closely spaced foliation is developed sub-parallel to the banding (Figure 4.25e). This foliation is defined by a grain elongation of amphiboles in the A-domains, although some amphiboles lie highly oblique to the foliation. Amphiboles in these domains show little evidence for internal deformation.

The foliation defined by amphibole elongation is often overgrown by plagioclase porphyroblasts. These feldspars contain inclusions of amphiboles which parallel the external foliation. The external amphiboles are coarser grained than the included amphiboles and are commonly found oblique to the main foliation (Figure 4.25f). Feldspar must have grown after foliation development but before amphibole coarsening occured within the matrix. Mica laths are also seen oblique to the main foliation and show no signs of internal deformation (Figure 4.25f).

These features suggest that coarsening of amphiboles and recrystallization of other mineral phases after the development of the foliation. This recrystallization may be associated with the the thermal event that gave rise to the growth of feldspar porphyroblasts.

4:10.3 Foliation Development at High Structural Levels

a) Foliation Development within the Sonnblick Gneisses

Within the higher level mylonitic gneisses, microstructures within most mineral phases, except feldspar, are similar to those observed at lower levels of the Dome. Feldspar microstructures show marked differences from those seen at lower levels. Feldspars are not recognisable as discrete 'augen' but are commonly elongate grains with high aspect ratios (eg. Figure 3.1c). Microscopically, individual feldspar lenses are comprised of a number of smaller feldspar grains which show twinning, subgrain formation and sutured grain boundaries (Figure 4.26a). These provide evidence for plastic deformation and show feldspar to be deforming by dislocation creep processes during mylonite formation.

Within the gneisses and Peripheral Schieferhülle, field evidence in the form of S-C fabrics and feldspar asymmetry suggest a top-to-NW displacement associated with foliation development. Microstructural shear criteria associated with development of the main foliation, for example mica fish, partly annealed quartz grain preferred orientations, S-C fabrics and asymmetric tails around feldspar augen also indicate top-to-NW. However, shear criteria which indicate a top-to-SE sense of shear are locally developed in the higher levels of the Dome. Although this sense of shear is seen on a mesoscopic scale as discrete shear bands which overprint the top-to-NW foliation, on a microscopic scale, fine-grained, top-to-SE, shear fabrics are also developed and overprint the earlier top-to-NW fabric. The quartz fabrics produced by top-to-SE shearing are generally confined to the quartz foliation domains developed during the earlier northwestward overthrusting. It therefore appears that the later fabric is associated with reactivation of the earlier foliation. Unfortunately, because the top-to-SE fabrics are localized and can only be identified on a microscopic scale, it is impossible to assess the scale at which zones containing the pervasive top-to-SE fabric are developed and distributed within the upper levels of the Dome.

Textures developed in the later fabrics are distinct from those preserving evidence of top-to-NW shearing. Within the earlier foliations, grain sizes within quartz ribbons are generally relatively coarse (averaging≈0.5mm) and are similar to those developed within quartz domains of undeformed and lower strain gneisses.

Figure 4.26a. Feldspar textures developed in feldspar 'augen' within high strain augen gneiss. 'Augen' comprise of a number of smaller grains which show evidence for twinning (t), subgrain formation (s) and grain boundary migration (g) and illustrates feldspar deformation by recovery-accommodated and recrystallization-accommodated dislocation creep. Micrograph taken under crossed polarized light with quartz accessory plate.

Figure 4.26b. Shear band associated with top-to-SE displacement cutting through a relatively coarse, recrystallized quartz domain. Along the shear band (C'), a quartz grain shape fabric (S') is developed and shows a dextral shear sense. At the bottom centre of the figure a small shear band can be seen cutting a mica domain. Micrograph taken under crossed polarized light.

Figure 4.26c. Fine-grained shear band cutting through an individual mica grain. The mica clast shows the development of undulose extinction associated with subgrain walls which are perpendicular to the mica basal cleavage and associated with kinking of the mica lattice. Micrograph taken under crossed polarized light.

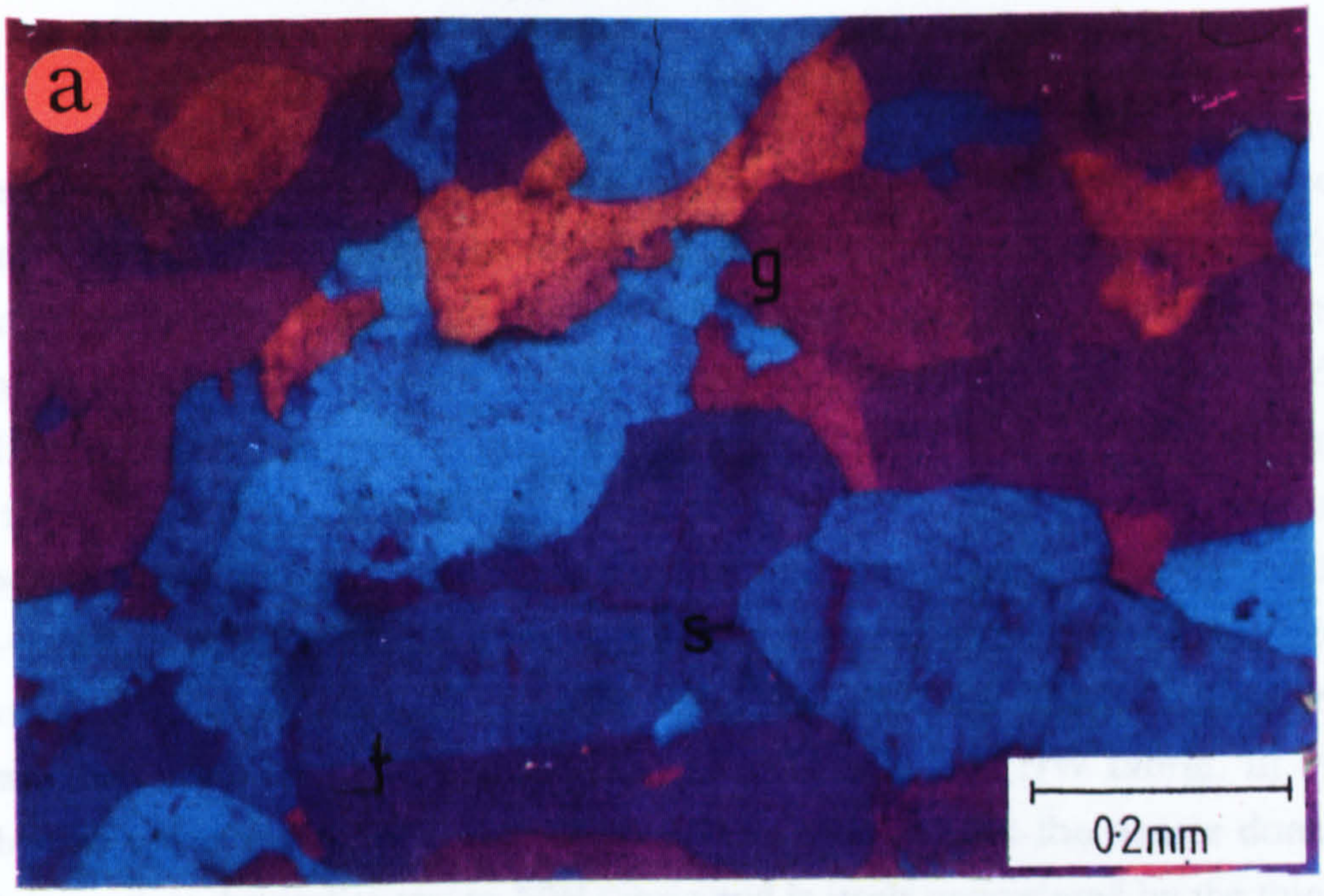
a
g
s
t
0·2mm

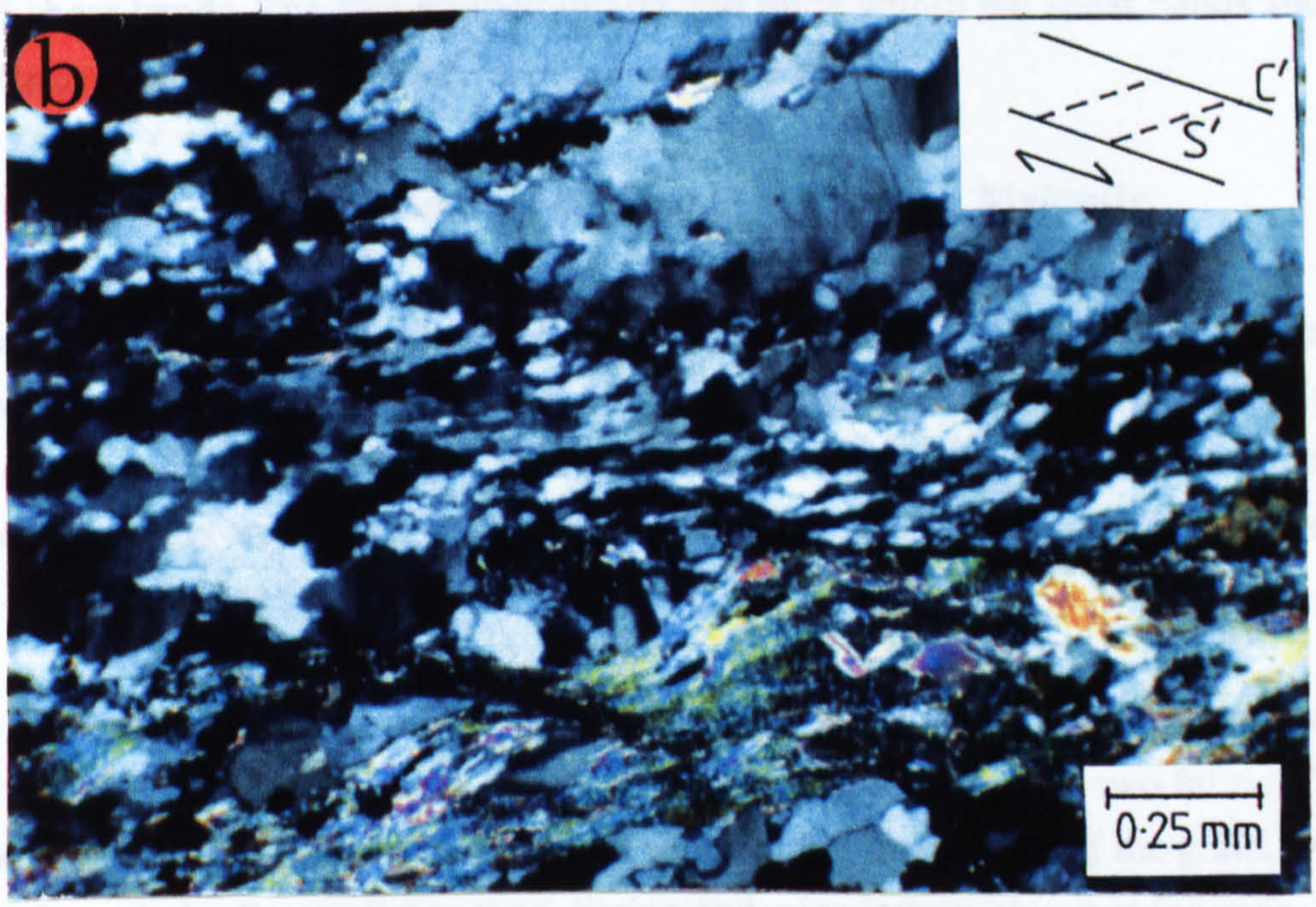
b
C'
S'
0·25 mm

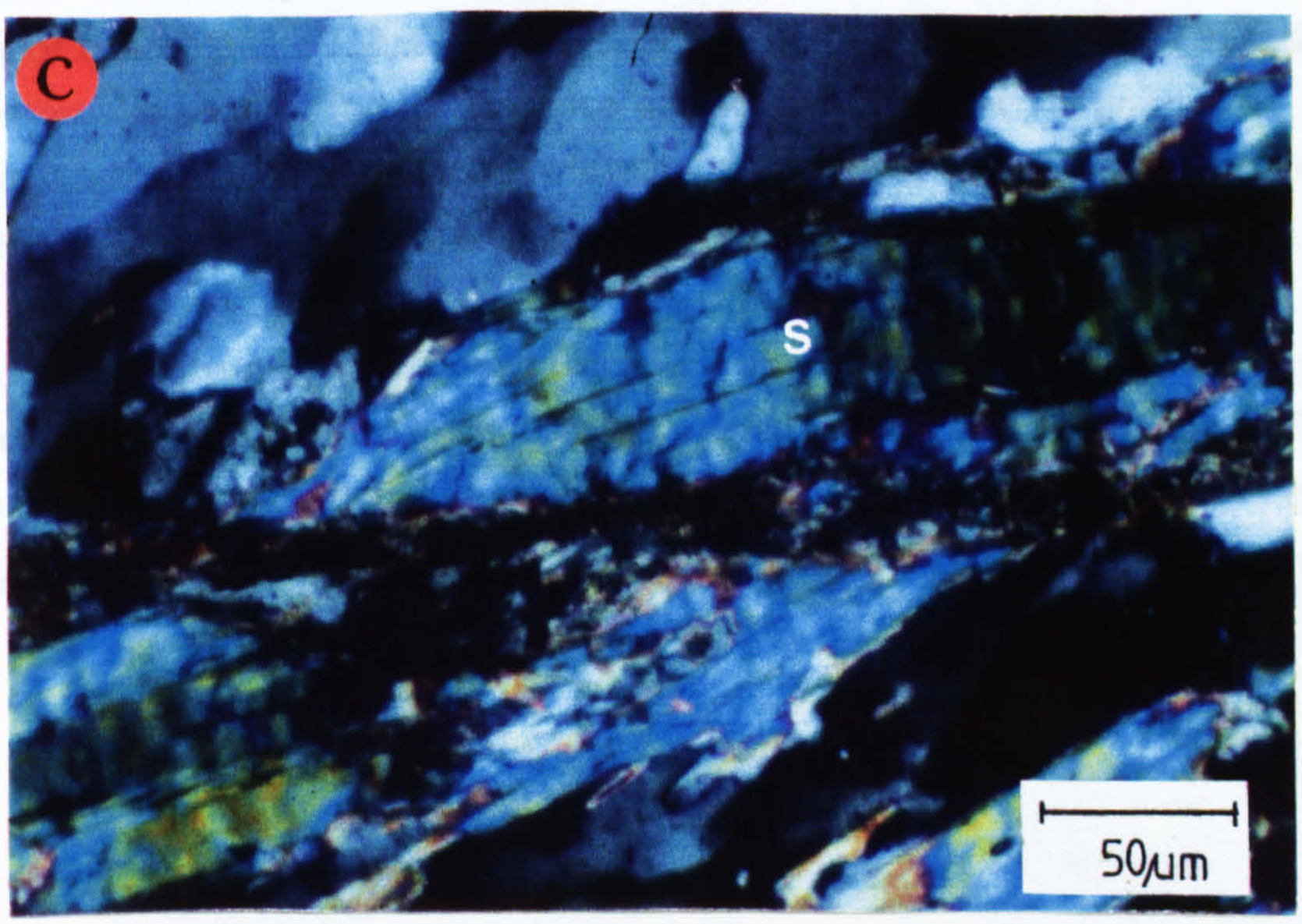
c
S
50μm

In the shear bands, quartz is strongly deformed and shows grain size reduction along millimetre wide extensional shear bands. Subgrain development and grain boundary migration appear to characterize quartz microstructures and a strong preferred grain alignment is commonly developed during shear band development (Figure 4.26b). Across these zones, ribbon type quartz grains are developed. Micas in the shear bands are very fine (Figure 4.26b), while the original mica clasts show subgrain development with subgrain walls perpendicular to (001) (Figure 4.26c). Some examples contain quartz S-C fabrics which illustrate a top-to-SE displacement sense. However, in zones in which only weak overprinting of the earlier fabric occurs, criteria such as asymmetric plagioclase augen occasionally demonstrate an original top-to-NW fabric. In these zones, the pervasive top-to-SE sense of shear preserved within the quartz domains therefore overprints the earlier top-to-NW fabric and is itself overprinted by the thinner, top-to-SE shear bands. The fine grained quartz and mica within the shear bands shows little evidence for having undergone recovery or annealing.

b) Microstructural development of a Quartz - Fluorite Mylonite

Immediately beneath the contact of high strain gneiss and the intermediate strain gneiss to the northeast of Saukopf is a fine-grained, quartzo-feldspathic gneiss with a strongly developed mylonitic fabric. Within this unit, variably mylonitized, thin fluorite and carbonate bands are observed. To the authors knowledge, mylonitic fluorite veins have never been previously described.

Quartz grains have a preferred subgrain orientation which lies at 45° to the mylonitic foliation (Figure 4.27a). Alignment of quartz grain boundaries defines two fabrics. The shorter boundaries lie parallel to the subgrain walls within the interior of the grain, while long grain boundaries lie parallel to the foliation and mica laths within that foliation. The long axes of quartz grains define an elongated grain fabric at 20-30° to the foliation. These features indicate a top-to-SE sense of shear. Feldspar asymmetry does not demonstrate a conclusive shear sense, while mica flakes show a weak fish geometry consistent with the quartz S-C fabric.

Within a strongly mylonitized quartz-rich unit it would be expected that a range of angles between S- and C-planes would be developed within different domains of the mylonite due to the cyclic nature of the interaction between subgrain formation and grain boundary migration (eg. Means 1981; Knipe and Law 1987). The consistent high-angle

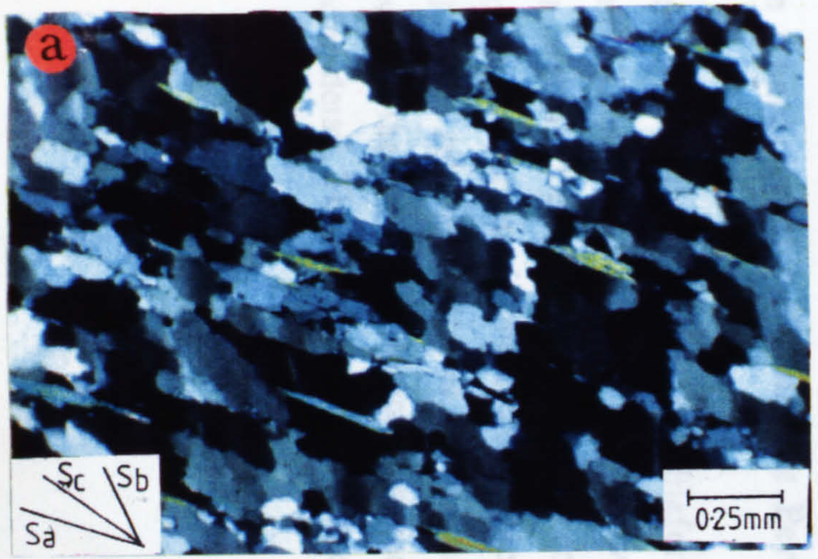
a
Sc
Sb
Sa
0·25mm

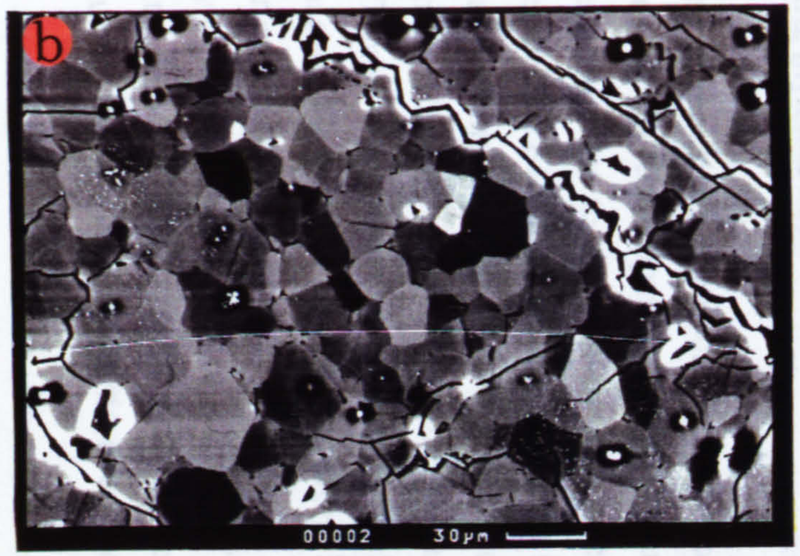
b
00002
30µm

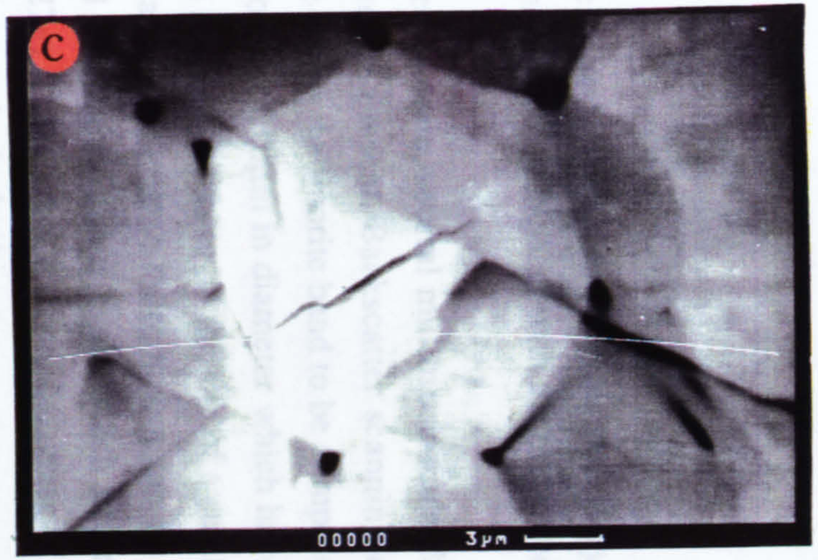
c
00000
3µm

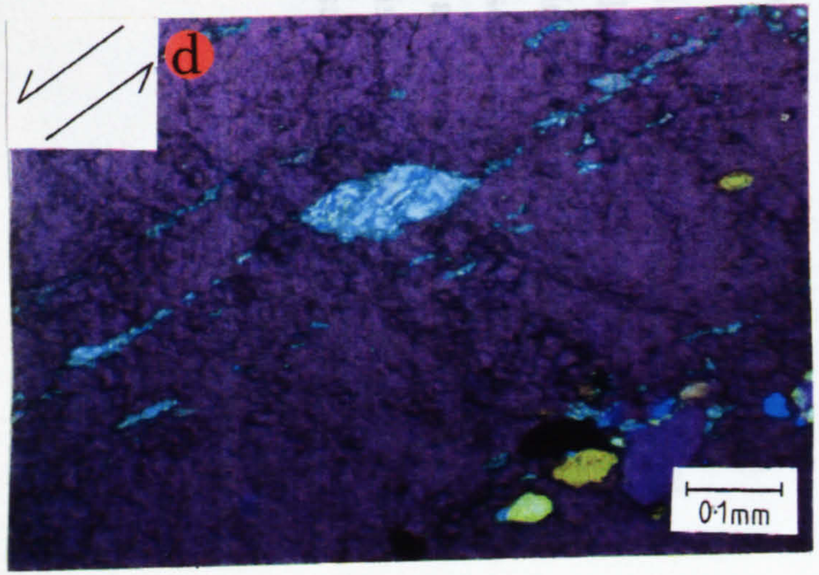
d
0·1mm

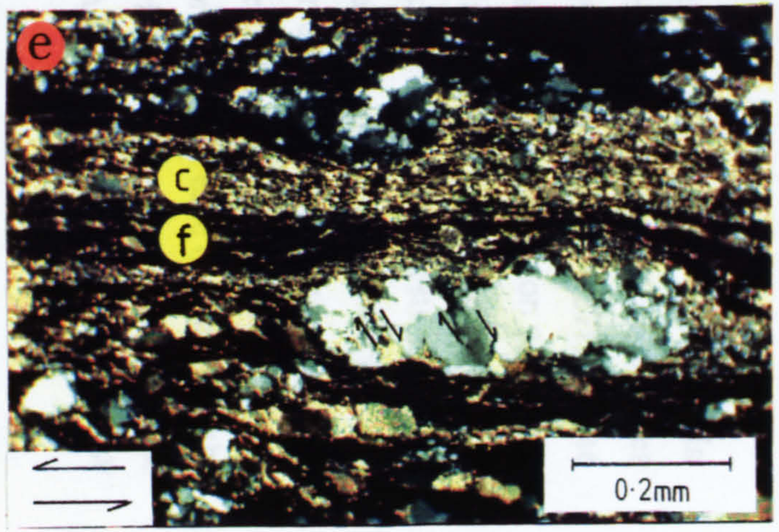
e
c
f
0·2mm

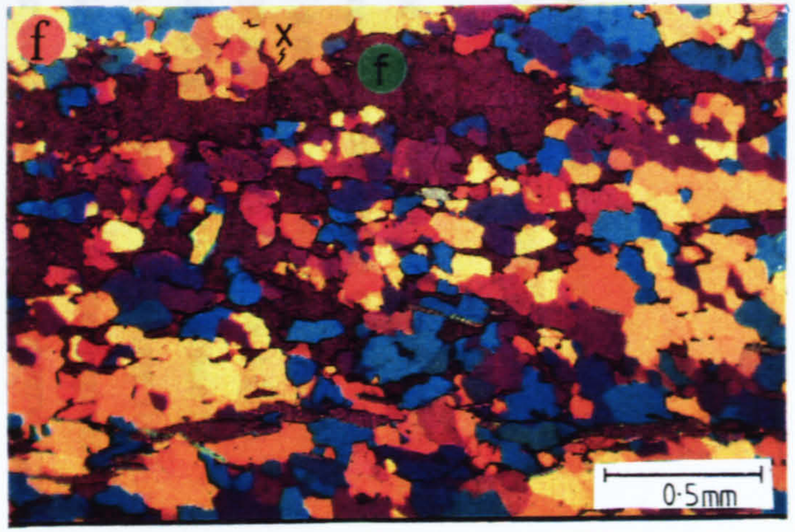
f
X
f
0·5mm

the Bogenizen Scharte (grid ref. 133066), and an albite bearing dark phyllite (Sample No. 48626) from a few metres below the Saukopf (grid ref. 133071).

i) Garnet Mica Schist (Sample 49885)

Elliptical garnets within the schist reach up to 10mm in long dimension and contain quartz inclusion trails which are polygonal, relatively equant and commonly show 120° triple junctions (Figure 4.28a). Garnet is commonly seen along the planar, quartz grain boundaries suggesting that some garnet growth occurred after annealing of the initial fabric, now defined by the quartz inclusion trails. Chloritoid is present as inclusions in the garnet and is generally subparallel to the internal foliation, though occasionally oblique. Externally, chloritoid is parallel to the external foliation which is defined by chloritoid/mica and quartz domains. The inclusion trails are relatively planar although at the grain margins are slightly folded. The internal garnet asymmetry and pressure shadows around the garnets indicate that the garnet grew syndeformationally during top-to-NW directed shearing.

Quartz domains within the schist show a variety of different fabrics and textures. Top-to-NW fabrics are illustrated by S-C fabrics where the S-foliation makes an angle of 20-30° with the external C-plane (Figure 4.28b), and mica fish which show undulose extinction toward the mica tip. Individual quartz grains show evidence for grain boundary migration and subgrain formation which appear to modify and overprint the original grain boundary orientations. Relatively large grain sizes (up to 0.5mm) are preserved within zones showing top-to-NW shear.

Some mica fish show a top-to-SE displacement, this is particularly the case immediately adjacent to extensional shear band structures. These shear bands also record a top-to-SE displacement and contain very fine grained micas (Figure 4.28c), inferred to have formed by grain size reduction during deformation. Displacement shearband-width ratios indicate these shear bands have shear strains generally below 10.

Chloritoid fish structures against southeast dipping shear bands further illustrate top-to-SE extension (Figure 4.28d). Chloritoid grains retain a weak undulose extinction and are spatially related to chlorite which also have undulose extinction and commonly bend into shear band structures. Chlorite may have formed at the expense of chloritoid during syn-extensional retrogression. In areas where the top-to-SE displacement is evident, quartz domains commonly show a well developed ribbon texture containing a subgrain

Figure 4.28a. Garnet-chloritoid-mica-quartz schist of the Peripheral Schieferhülle exposed at Bogenitzen Scharte (sample 49885). Polygonal, undeformed quartz forming inclusion trails within garnet porphyroblasts shows grain boundaries which have been overgrown by garnet (X). Within the matrix, ribbon quartz textures (R) show a preferred subgrain orientation with the same sense of shear as shear bands (C') cutting through mica porphyroclasts. Shear sense is sinistral and is associated with top-to-SE displacement. Micrograph taken with crossed polarizers.

Figure 4.28b. Quartz domain showing an internal fabric defined by quartz long axes and general grain boundary orientations. This fabric lies 20-30° to the foliation defined by mica domains. Quartz shows evidence of subgrain rotation and grain boundary migration, the latter of which appears to dominate the recrystallization process. Sense of shear is dextral and top-to-NW in the field. Micrograph taken under crossed polarized light.

Figure 4.28c. Mica cut by SE dipping shearbands associated with top-to-SE extension. Undulose extinction is preserved adjacent to the shear band at the ends of mica grains. Approximate shear strains across this band calculated from displacement/shear band width ratio, γ=6. Micrograph taken with crossed polarizers.

Figure 4.28d. Chloritoid (cd) fish structures cut by SE dipping shear band structures indicating top-to-SE extension post-dating chloritoid formation. Chlorite (chl) is observed in fish tails adjacent to shear bands. Micrograph taken in plane polarized light.

Figure 4.28e. Quartz domain showing grain elongation fabric indicating a sinistral shear sense associated with top-to-SE movement. This fabric is better developed than the elongation fabrics associated with dextral shearing (cf. Figure 4.28b). This is due to larger aspect ratios and more regular grain boundaries. This microstructure shows little evidence of annealing or coarsening by grain boundary migration. Micrograph taken under crossed polarized light.

Figure 4.28f. Zoned plagioclase porphyroblasts with albite cores and oligoclase rims. Cores contain inclusion trails of probably graphite which are folded. The asymmetry of albite and of inclusion-free oligoclase rims suggest a dextral shear sense associated with top-to-NW shearing. Micrograph taken under crossed polarized light with quartz accessory plate.

a
0·5mm
R
X
b
0·5mm
Sb
Sa
c
0·1mm
d
0·5mm
cd
ch
C'
S
e
0·1mm
Sb
Sa
f
0·25mm

preferred orientation at approximately 15-20° to the foliation. In larger quartz domains, good S-C fabrics are commonly developed (Figure 4.28e) which shows evidence top-to-SE shearing. Neither of these appears to have undergone annealing or grain coarsening.

ii) Albitic Dark Phyllite (48626)

This is a strongly foliated dark phyllitic unit containing zoned albite porphyroblasts. The strong foliation is defined by white mica-rich and quartz domains. White mica domains usually have basal cleavages parallel to the foliation. Occasionally however, thin domains elongate parallel to the foliation, have basal cleavages perpendicular to the foliation. These are interpreted as the remnant hinge zones of isoclinal folds produced during the progressive shearing in which the foliation formed.

Plagioclase porphyroblasts contain two compositional zones. Oligoclase rims of the porphyroblasts are inclusion free, while albitic cores contain very fine-grained, opaque inclusions which cannot be imaged on the SEM and are probably graphite. Feldspar core asymmetry supports the top-to-NW sense of shear. Inclusion trails within feldspar cores are often quite complex and often multiply folded, for example showing refolded isoclinal, graphite inclusion trails (Figure 4.28f). The oligoclase rims around the albite cores are asymmetric and again indicate top-to-NW shearing.

The presence of two distinct compositional zones within plagioclase porphyroblasts provides evidence for possibly two metamorphic events within the Peripheral Schieferhülle. This is supported by the absence of graphite from the matrix and from the oligoclase rims, which suggests different conditions of oxidation during oligoclase growth. Oligoclase growth in the area probably represents the peak Alpine metamorphic conditions (Chapter 5), suggesting that albite growth may have developed during the early high P, low T metamorphism observed within some units of the Peripheral Schieferhülle in the southeast Tauern Window (eg Droop 1985). These observations imply that top-to-NW shearing was taking place during both the early metamorphism and Alpine peak metamorphism.

Mica fish structures, associated with shear bands, preserve a top-to-SE movement sense. These mica fish show undulose extinction at their ends and pass into fine grained mica and quartz within the shear band. The fine grain size developed during shear band formation indicates that there has been no subsequent annealing. Shear bands are commonly seen to be developed adjacent to plagioclase porphyroblasts and are

interpreted to have formed after both stages of feldspar growth. Since oligoclase growth probably represents peak metamorphic conditions in the area, shear band formation appears to have occurred after the peak Tauern metamorphism.

4:10.4 Microstructural Evidence for the Relative Timing of Folding and Metamorphic Recrystallization within the Sonnblick Region.

a) Folding within Granitic Gneisses

Within the lower structural levels of the dome F_1, F_2 and F_3 fold phases show similar features on a microscopic scale. Within mica domains, fold hinges are form an interlocking series of relatively strain free mica laths. The long axes of these laths usually lie parallel to the fold surface and therefore lie sub-parallel to the original foliation within the pre-folded gneiss (Figure 4.29a). In one hinge of an F_3 fold an undeformed mica (marked 'M' in Figure 4.29b) is seen cutting across the axial plane of the fold. Similarly, F_3 folds within mylonite units are defined by folded foliation surfaces, comprising interlocking mineral grains which are internally undeformed (eg. Figure 4.29c).The lack of deformation within individual micas suggests that mica recrystallization occurred after the folding. This is consistent with the interlocking texture observed in the majority of micaceous hinge zones (eg. Figure 4.29a). In the same hinge, micas are kinked and show undulose extinction. This deformation is seen to intensify at the tips of the undeformed mica suggesting localized low strain deformation after recrystallization.

As well as the interlocking mica texture, fold hinges within the mica domains may occasionally contain plagioclase porphyroblasts. Feldspar in these zones cut across the fold axial plane and are undeformed. These porpyroblasts are observed in hinges of all fold generations, including F_3 (Figure 4.29d), and hinges of isoclinal folds associated with mylonite formation in the top of the Dome (Figure 4.29e). Feldspar is inferred to have grown over the mica hinge after the last phase of folding, and, this phase of feldspar growth post-dates all phases of folding within the Dome.

b) F_3 Textures within Amphibolite Units

F_3 folds observed within banded amphibolites (band thickness upto 5mm) tend to develop a cuspate-lobate geometry (Ramsay and Huber 1987) which suggests that the lighter coloured epidote-rich bands behaved more competently than the amphibole-rich

Figure 4.29a. F_3 fold developed within mica domain of a well foliated gneiss. The hinge comprises a network of interlocking micas which show no internal deformation and appear recrystallized. Micrograph is a crossed polarized image.

Figure 4.29b. F_3 fold within mica domain of well-foliated gneiss. Mica 'M' is undeformed and cuts across the axial plane of the fold which suggests recrystallization in the hinge area. The hinge zone contains micas which are kinked and have undulose extinction. This deformation is also localized at the end of 'M' and is interpreted to post-date both folding and recrystallization. Micrograph is a crossed polarized image.

Figure 4.29c. F_3 fold developed in leucogranite mylonite. S_f is the orientation of the F_3 axial plane. The folded mica domain contains an inerlocking network of mica laths which do not appear internally deformed. Subgrains developed in the hinge zone of the quartz-feldspar domain show no fabric geometrically related to the fold. Micrograph is a crossed polarized image.

Figure 4.29d. Plagioclase porphyroblast overgrowing F_3 folds within foliated gneiss. Mica shows the typical interlocked texture associated with recrystallization. Micrograph is a crossed polarized image.

Figure 4.29e. Plagioclase porphyroblast (P) overgrowing early isoclinal fold developed within high strain gneisses at the top of the Dome. Micrograph is a crossed polarized image.

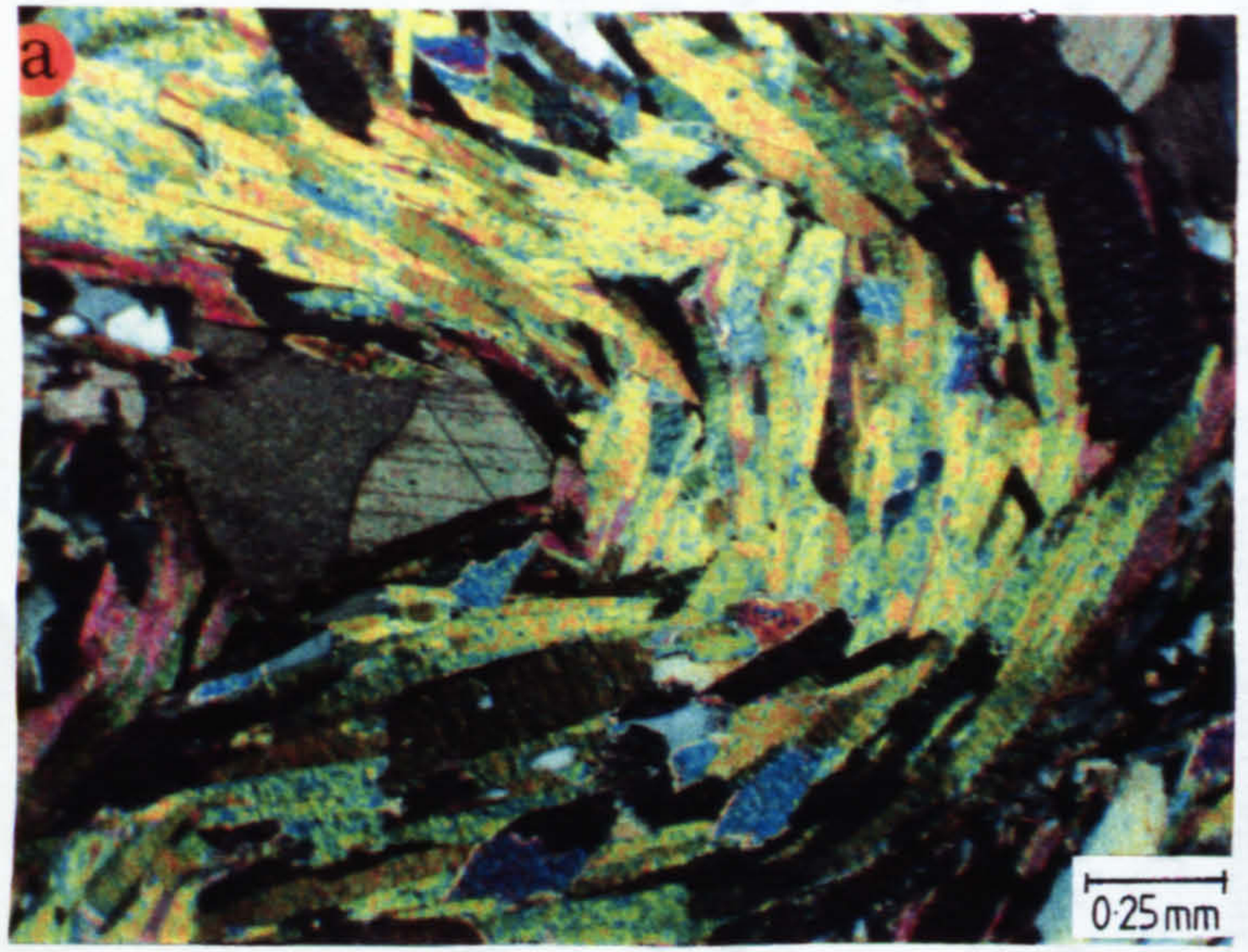
a
0·25 mm

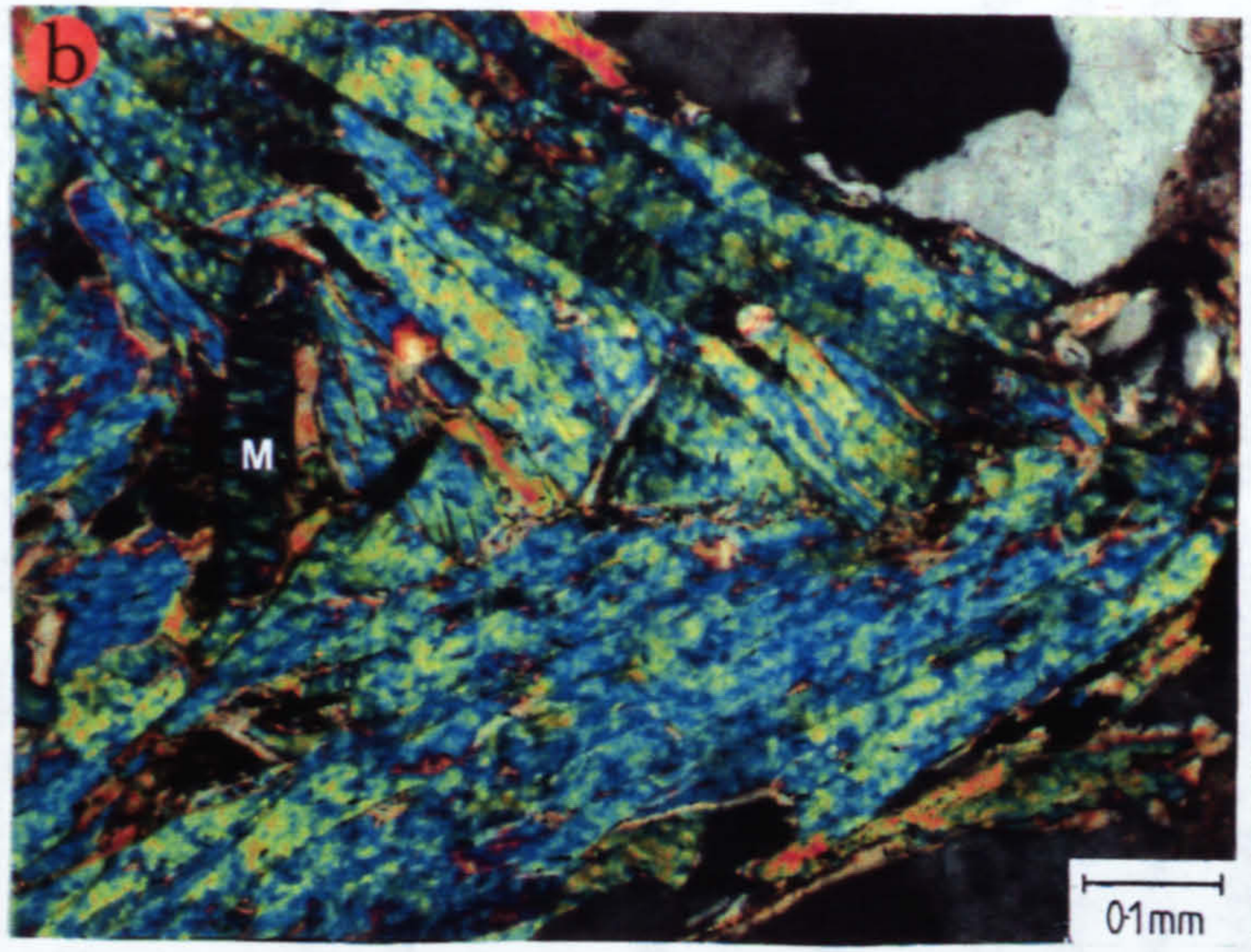
b
M
0·1 mm

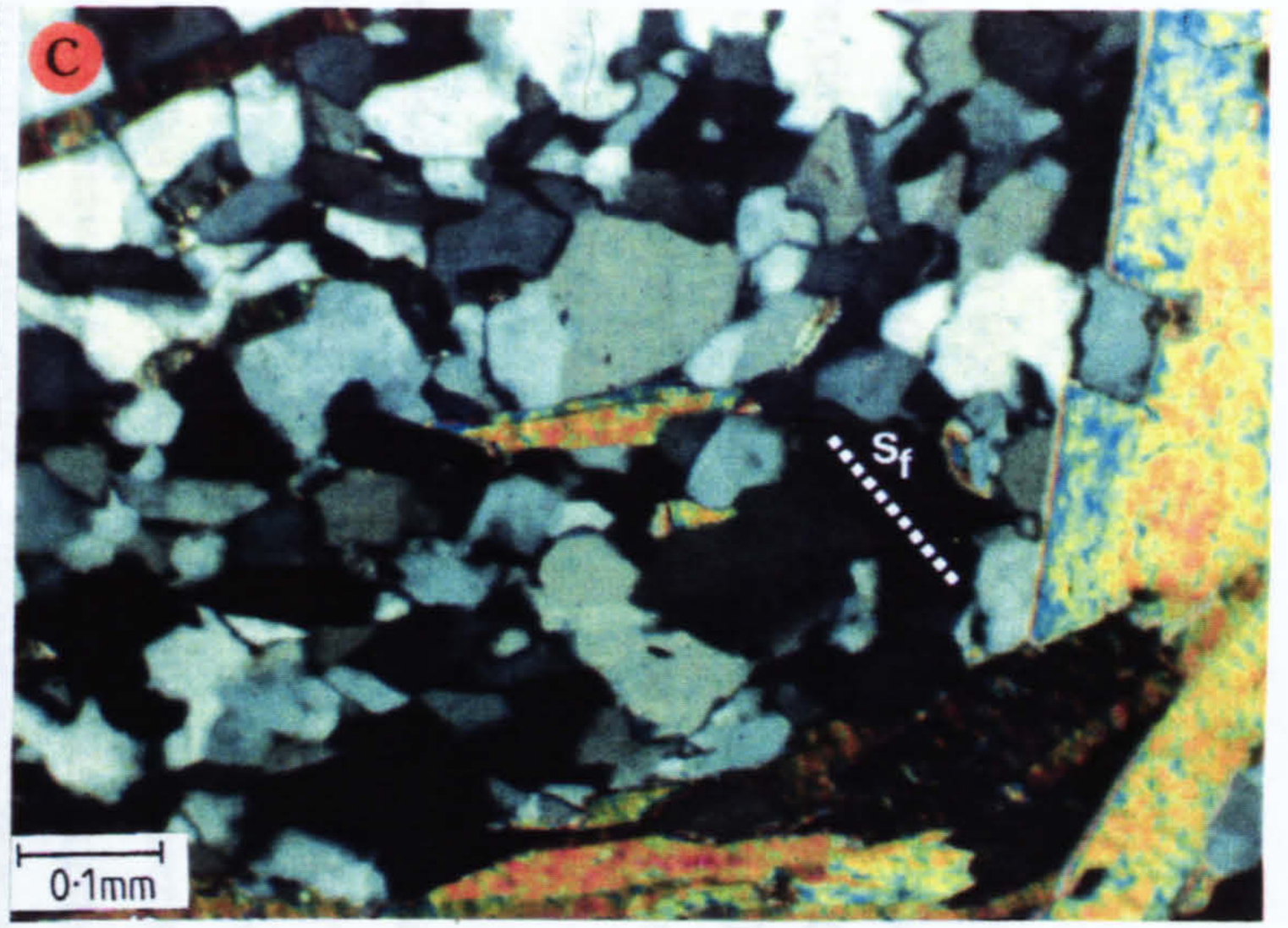
c
Sf
0·1 mm

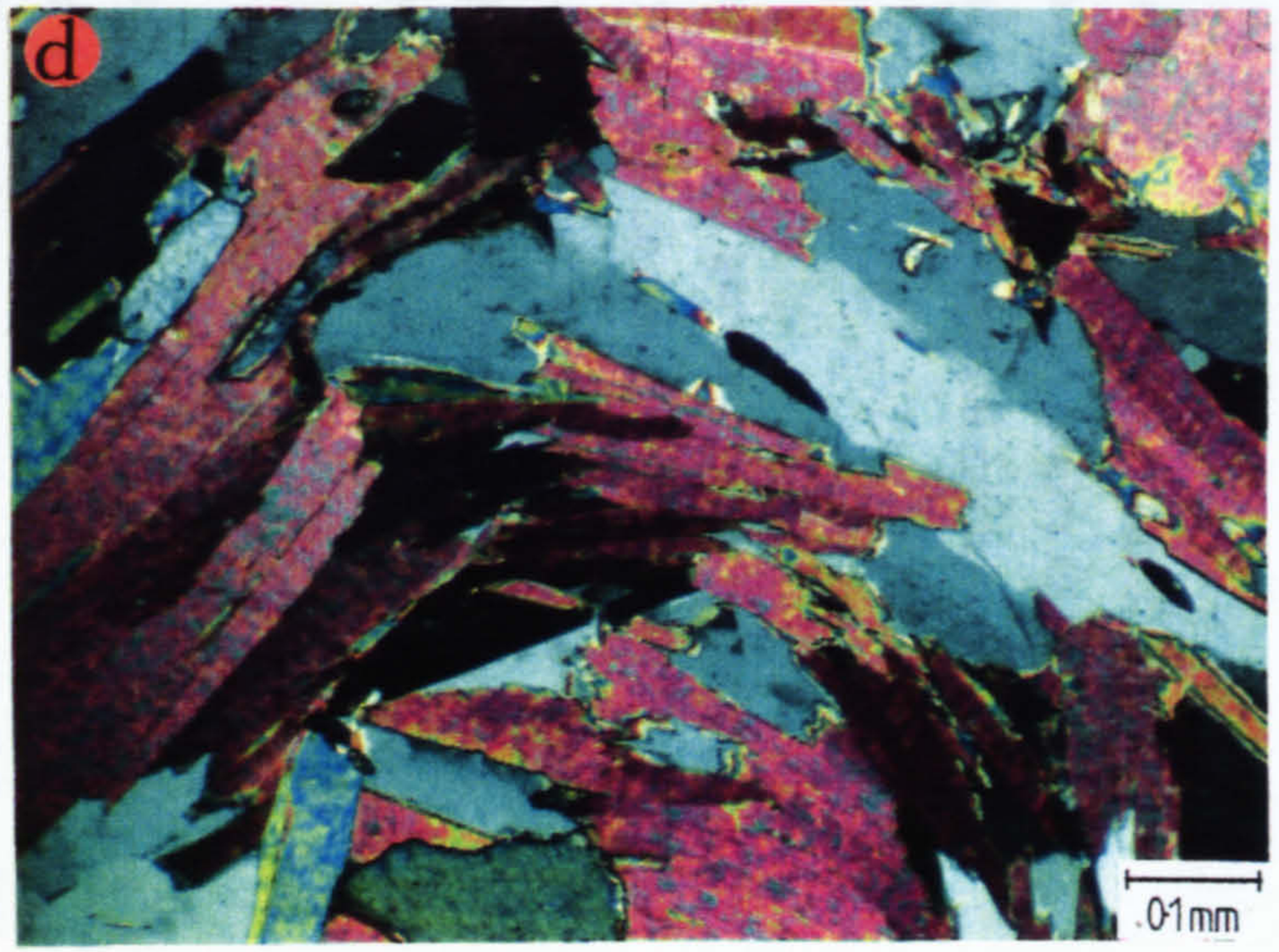
d
0·1 mm

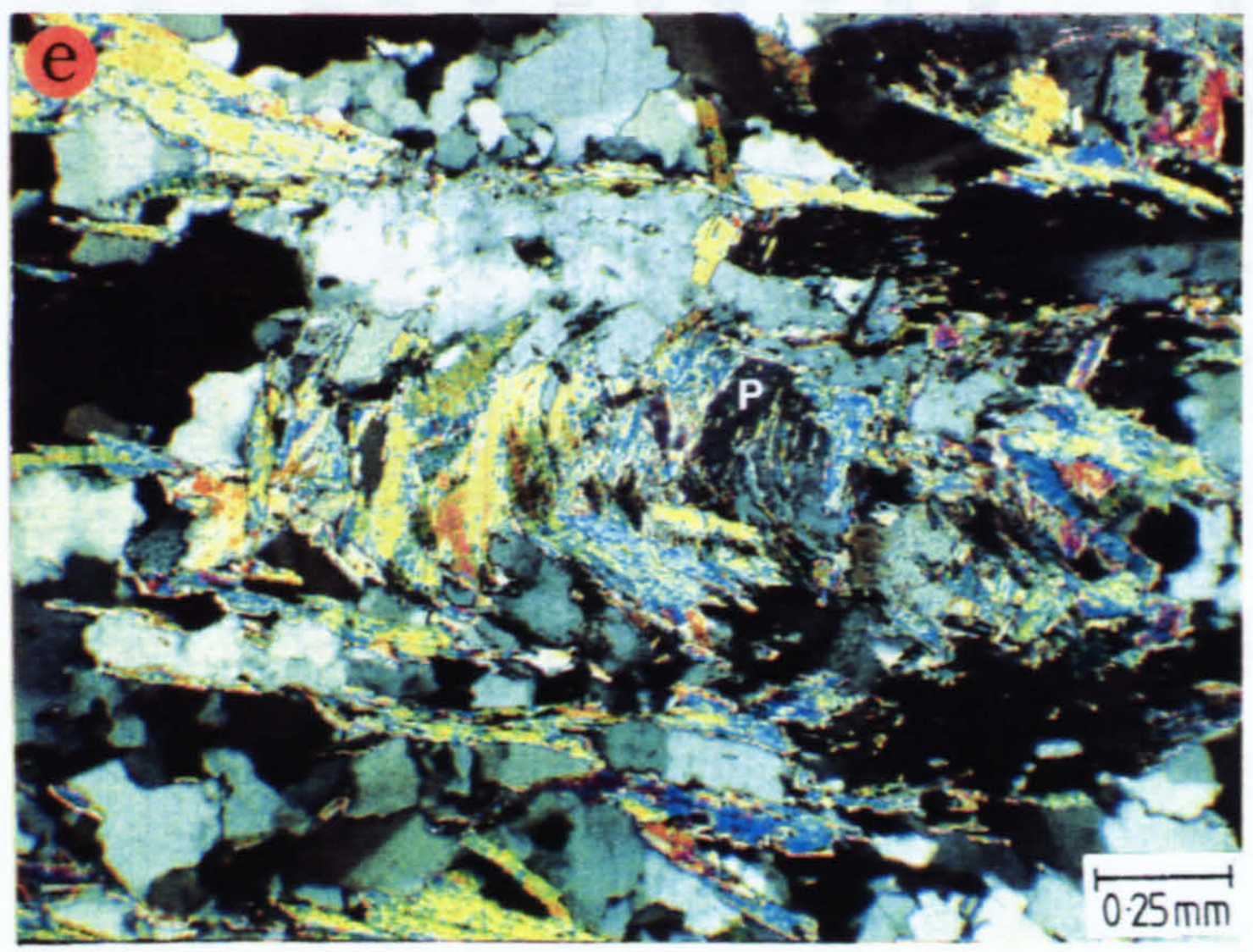
e
P
0·25 mm

bands. Epidote-rich layers form class 1 folds while the amphibole bands form class 3. Within the inner arc of these folds, amphibole-rich layers develop a strong axial planar foliation defined by the long axis of amphiboles (Figure 4.30a). Moving around the fold to the outer arc, the foliation within amphibole bands becomes sub-parallel to the banding and therefore, the fold surface and the earlier foliation that formed synchronous with banding (Figure 4.30b).

There is a lack of evidence for internal deformation within individual amphiboles. This may suggest that during F_3 folding either amphibole grains behaved passively during deformation and rotated into parallelism with the axial plane or that amphiboles must have recrystallized after or during the later stages of folding. If the latter of these is correct, this may suggest that amphibole crystallization was mimetic since the axial planar foliation is preserved. Alternatively recrystallization limited to those amphiboles deformed during the folding would preserve those amphiboles preserving the earlier foliation as well as those which recrystallized during axial planar foliation development. Sufficient evidence to distingish between these possibilities has not been observed.

4:10.5 Microstructures Associated with Normal Faulting

a) Low Structural Levels within the Dome

The normal fault zone (NFZ), exposed at a height of 1480 metres on the Panoramastraße (Figure 4.19a) has been studied in sections cut perpendicular to foliation (parallel and perpendicular to the lineation on the fault plane), by optical microscopy and compared to the undeformed granitic gneiss host.

The NFZ contains a spaced foliation, absent from the host gneiss, which is defined by white mica-, biotite- and quartz-rich domains. Both sections contain elongate quartz augen with aspect ratios in the order of 5:1 and 2:1, in sections parallel and perpendicular to the fault lineation respectively. Augen are composed of millimetre size grains which show quartz deformation by dislocation creep. No grain elongation or preferred grain boundary orientation is observed.

Both white mica and biotite domains are composed of relatively coarse (up to 5mm) mica laths which form an interlocking network and show no signs of internal deformation (Figure 4.30c). Laths are commonly oblique to the domain boundary but of an inconsistant orientation that would suggest they were associated with

Figure 4.30a. Axial planar fabric developed in Class 3, F3 folds in an amphibole-rich band of banded amphibolite. S_f shows the orientation of the F_3 axial plane. Feldspar grain elongation also defines the axial planar foliation. No internal deformation of the amphibole is observed. Micrograph is a crossed polarized image.

Figure 4.30b. Relationship of foliation in an amphibole-rich band of amphibolite to banding and F_3 fold orientation. The band boundary is illustrated in the small sketch in the top left. S_f is the axial planar foliation. S_b is the foliation parallel to banding. Micrograph is a crossed polarized image.

Figure 4.30c. Feldspar porphyroblast overgrowing mica within the normal fault zone shown in Figure 4.19b. Mica domains contain interlocking grains, some of which are oriented oblique to the foliation. No deformation within individul grains is observed and the mica is considered to have recrystallized after foliation development and normal fault movement. Micrograph is a crossed polarized image.

Figure 4.30d. Strong deformation fabric developed in a 1cm wide normal fault zone in the cliffs of the Schwartzsee. Quartz domains show a strong grain shape fabric which is locally overprinted by shear bands showing the same sense of shear. Mica fish structures also show the normal displacement. No evidence for recovery or annealing of the deformation fabric is observed. Micrograph is a crossed polarized image.

Figure 4.30e. Textures developed within a mesoscopically undeformed quartz vein. Sutured margins and amoeba structures (A) indicate extensive grain boundary migration. Undulose extinction, deformation bands and local subgrains are also developed. A small, brittle fracture (F) is overprinted by migrating grain boundaries. Micrograph is a crossed polarized image.

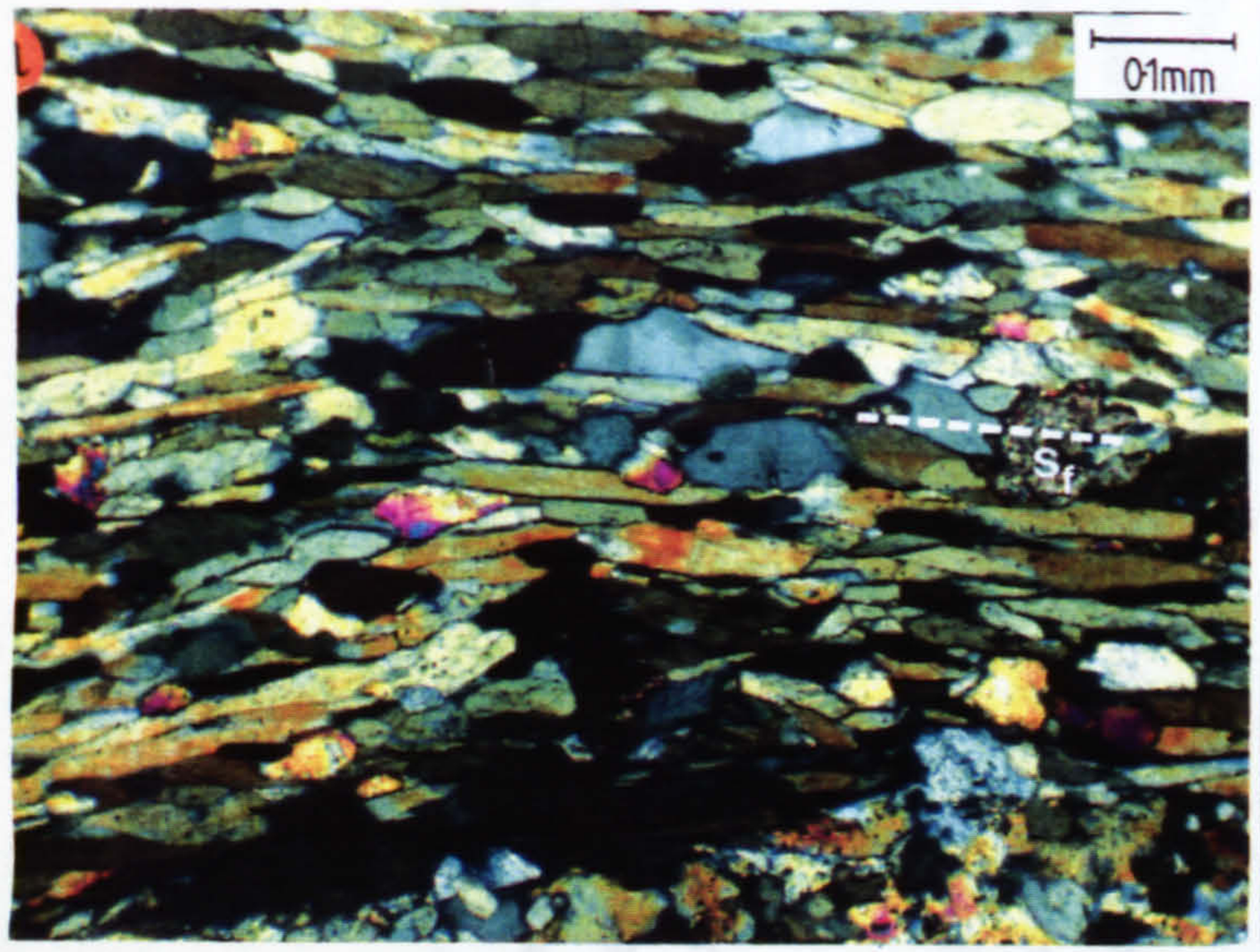
0·1mm
S_f

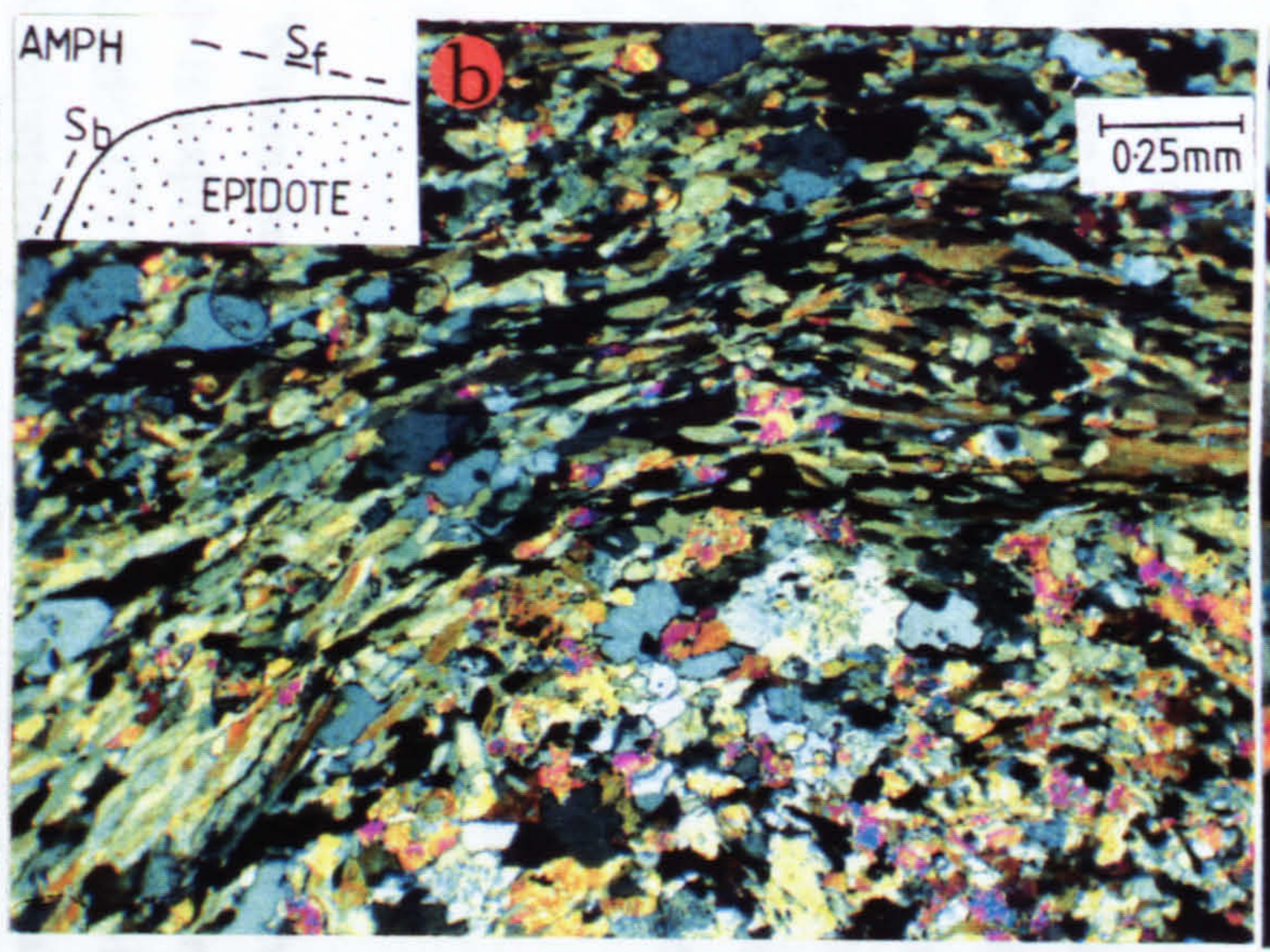
AMPH
S_f
S_b
EPIDOTE
b
0·25mm

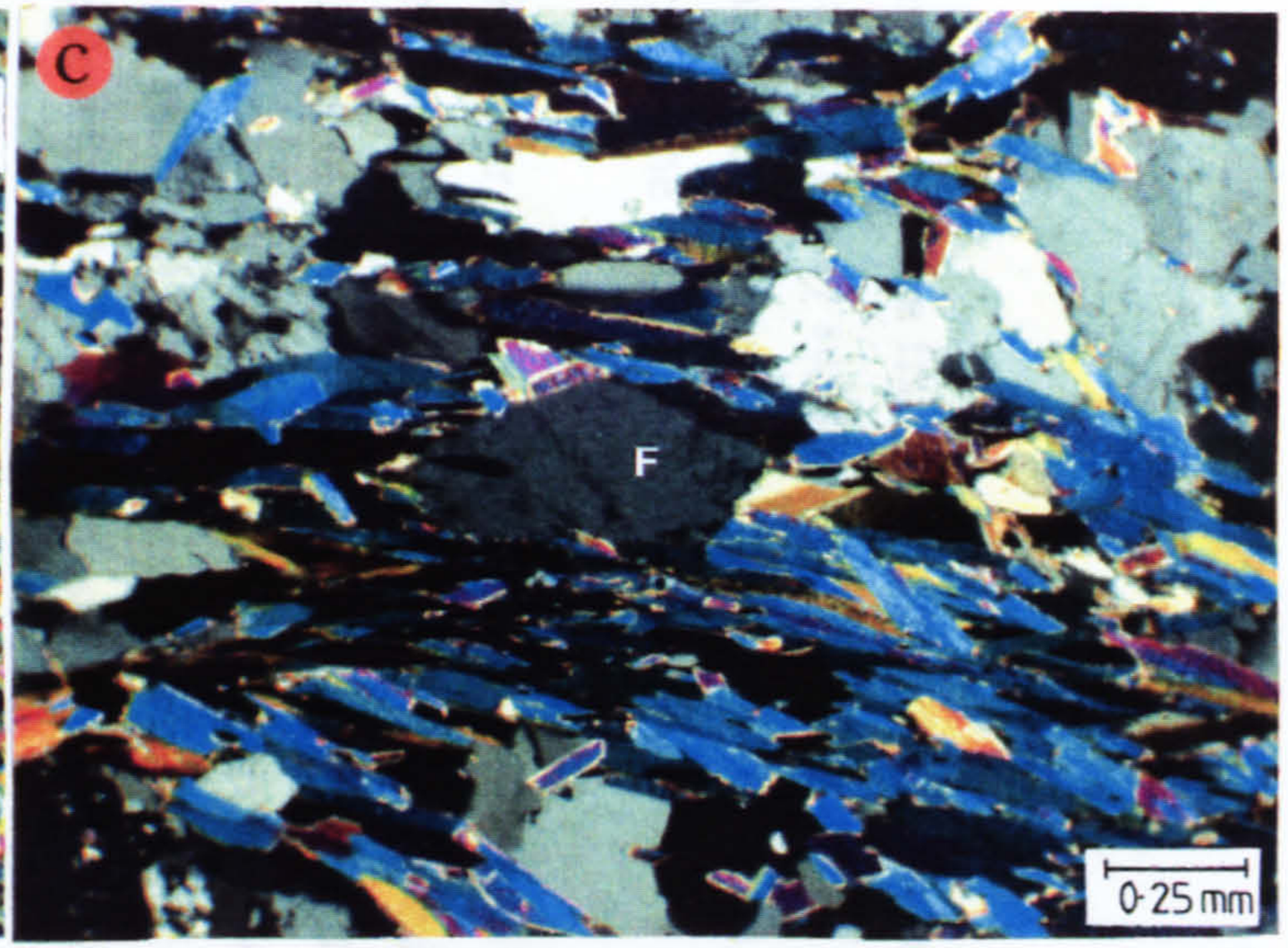
c
F
0·25 mm

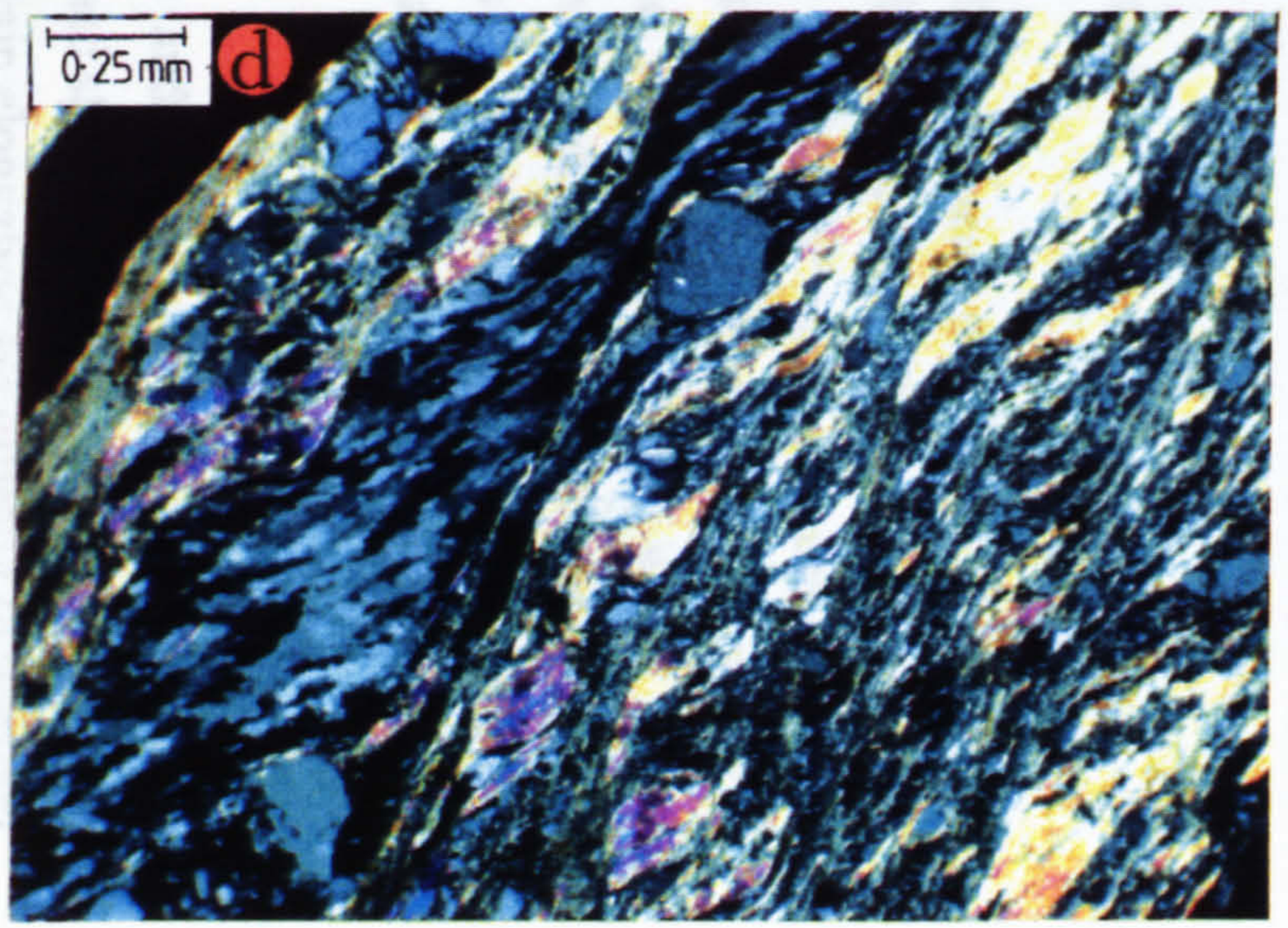
0·25 mm
d

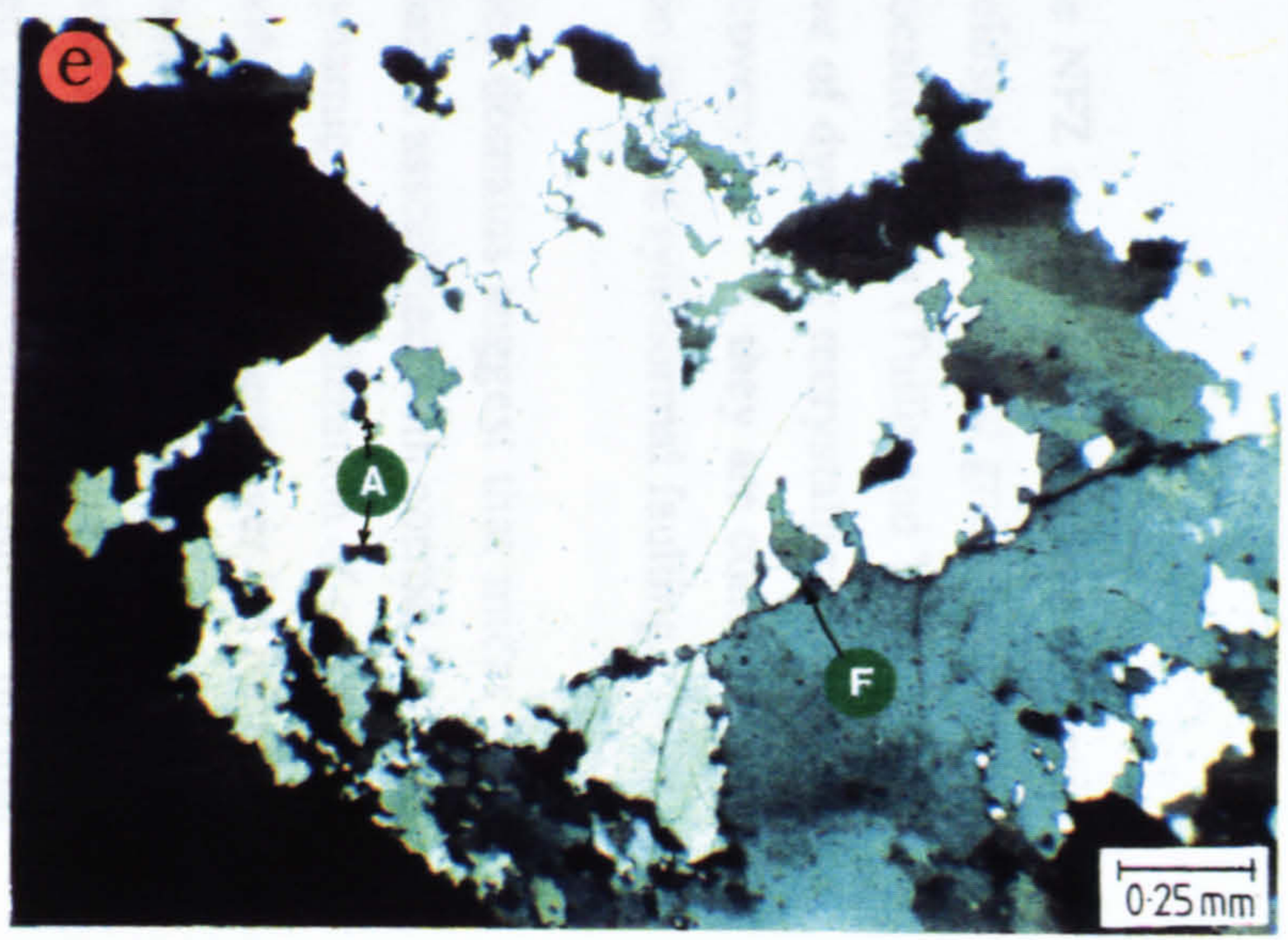
e
A
F
0·25 mm

shearing (eg. mica fish). The contacts of biotite and quartz augen are commonly very planar which may suggest some component of diffusive mass transfer of quartz during foliation development. Within the white mica domains, albite is occasionally seen to overgrow the main foliation (Figure 4.30c).

Feldspar augen are rarely discrete within the NFZ and show extensive subgrain development, suggesting recovery of deformed feldspar, and sutured grain boundaries indicative of recrystallization accommodated dislocation creep (Tullis and Yund 1985). Since these feldspar microstructures are indicative of dynamic recrystallization rather than to recrystallization associated with static recovery , they are considered to have developed during the formation of the foliation and are syn-normal faulting.

The microstructures observed within the mica domains suggest that micas have undergone recrystallization after the shear deformation associated with normal faulting. Quartz domains preserve textures indicative of dynamic recrystallization of quartz and have relatively coarse quartz grain sizes. The growth of feldspar augen over the foliation within mica domains may have occurred synchronous with recrystallization observed in quartz and mica domains. Microstructures preserved in feldspar augen are indicative of high strain plastic deformation, and are inferred to have developed during normal faulting.

b) Higher Structural Levels Within the Dome

Within the coarse augen gneisses above the Schwartzsee a centimetre wide normal fault is exposed which shows a strong grain size reduction . The zone dips at 28° towards 171° and contains a lineation with dip of 19° and azimuth of 111°. Microscopically, the zone consists of domains of quartz and white mica within a deformed matrix of quartz, white mica and carbonate material which show microstructures indicative of a top-to-SE, extensional displacement. This zone differs from the previously described top-to-SE fabrics in that like the shear bands, it is not parallel to the primary foliation within the gneiss and does not represent a reactivation of the earlier foliation.

Quartz domains are relatively continuous and contain strong grain preferred orientation which are locally bent, due to continued shearing within shear bands (figure 4.30d). The mechanisms acting to produce the grain elongation are difficult to interpret on the basis of observations on an optical scale. However, the elongation appears to have

resulted from the development of subgrain walls and the rotation of these walls to form newgrains. Very few grain boundaries indicative of grain boundary migration are observed although large areas of quartz domains near extinction simultaneously, suggesting that they may have represented large ribbon grains which have been subsequently deformed. A detailed study of the microstructures developed within these zones would require extensive electron microscopy and for the present is beyond the scope of this study. All of the quartz textures developed at a microscopic scale are indicative of dynamic recrystallization during deformation associated with normal faulting.

Coarse mica domains within the deformed zone show well developed fish structures associated with shear band formation. Micas show undulose extinction associated with fish formation and show no evidence for having undergone recrystallization. The sense of shear derived from fish structures is consistent with the normal displacement inferred from the quartz elongation fabrics (Figure 4.30d).

Carbonate material is found within the normal shear zone along shear bands and within the matrix, where it is associated with fine grained quartz and mica. Carbonate is spatially restricted to the fault zone and was not observed in the adjacent gneisses. This suggests that normal faulting was accompanied by the infiltration of a carbonate rich fluid.

4:10.6 Microstructures Associated With Mesoscopically Undeformed Veins

Late stage quartz veins which on a mesoscopic scale appear undeformed, contain quartz textures associated with deformation on a microscopic scale. A relatively coarse grain size is characterized by grain boundary migration textures (Figure 4.30e). Internally, these grains are plastically deformed. These features indicate that quartz grains within relatively undeformed veins and pods, have undergone dynamic recrystallization associated with some component of strain which must have been quite low.

The observed microstructures illustrate that the commonly observed quartz textures within the quartz domains of the well-foliated gneisses, indicate subgrain formation and grain boundary migration in the absence of a preferred grain orientation, may have formed during a late stage, low strain deformation, possibly asssociated with uplift.

Figure 4.31a. Cathodoluminescence micrograph showing growth zoning within a carbonate vug developed in the centre of a mesoscopically undeformed quartz vein.

Figure 4.31b. Late calcite vein overprinting the foliation developed within a marble unit of the Peripheral Schieferhülle. Cathodoluminescence microscopy illustates the vein and the reaction zone in the wall rock associated with the vein.

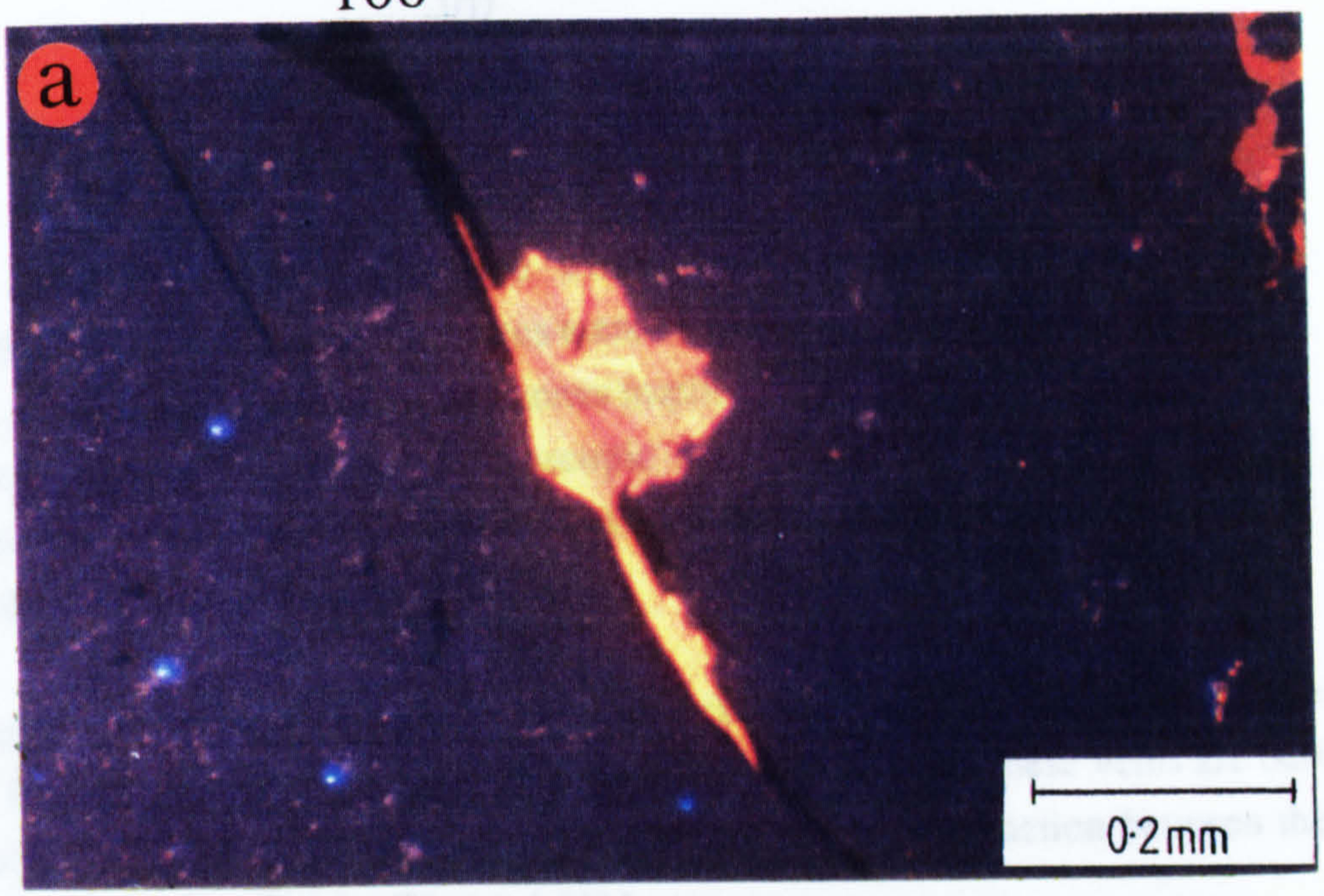
a
0·2mm

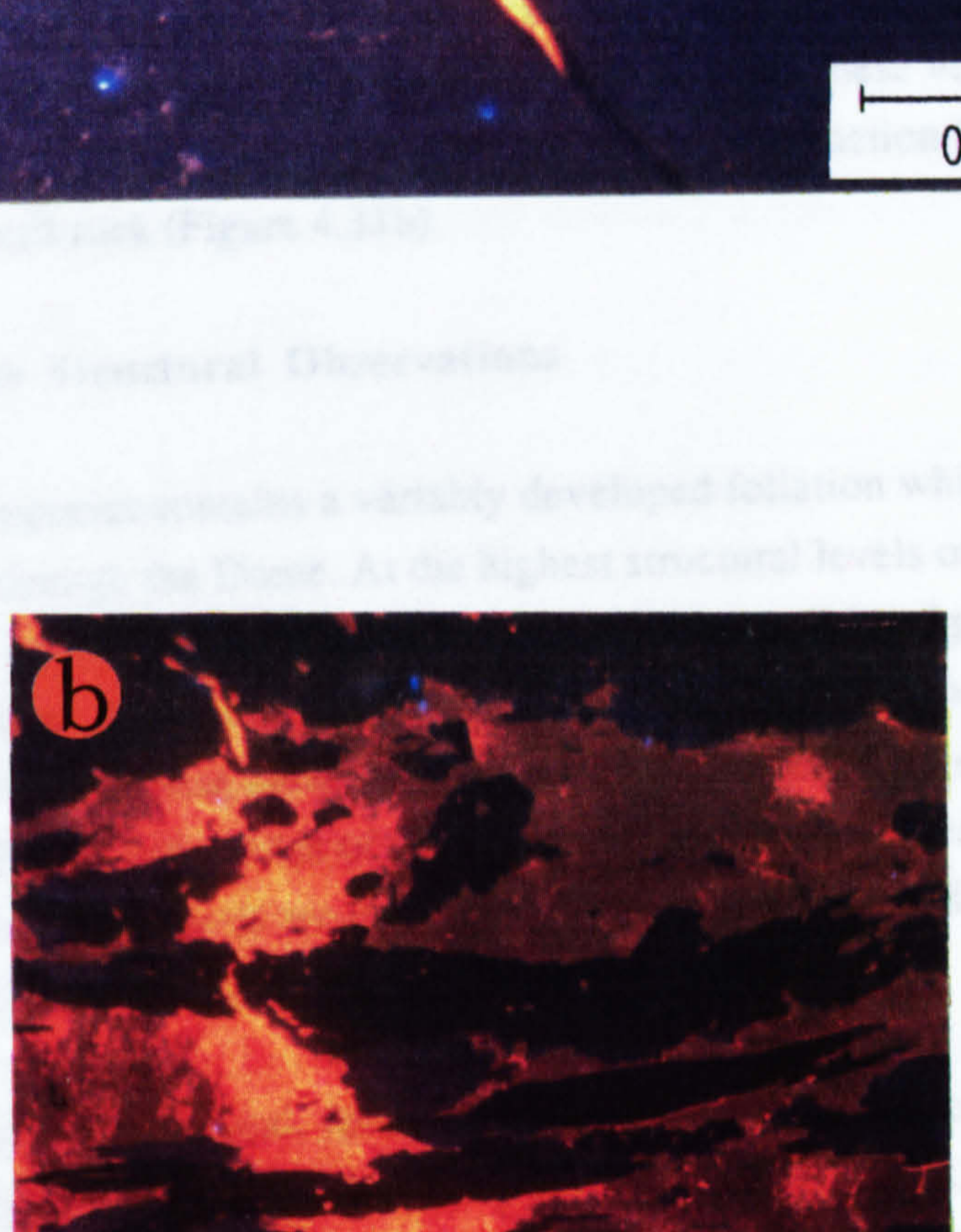
b
0·5mm

Where calcite veining is observed within quartz veins (eg Figure 4.21e), cathodoluminescence microscopy illustrates textures indicative of growth zoning (Figure 4.31a). The asymmetric nature of growth zones implies that the surrounding quartz must have undergone deformation on a microscopic scale. Such deformation could also account for the low strain deformation inferred from quartz microstructures in mesoscopically undeformed quartz veins.

Late calcite veins are also observed within the dolomitic marble units of the Peripheral Schieferhülle and cut the main foliation at high angles. These veins are best seen by cathodoluminescence microscopy which also illustrates reaction between the vein and the dolomitic wall rock (Figure 4.31b).

4:11 Summary of the Structural Observations

The Sonnblick orthogneiss contains a variably developed foliation which generally decreases downwards through the Dome. At the highest structural levels of the Dome a mylonitic foliation is developed parallel to the contact of the Zentralgneis and the Peripheral Schieferhülle. A similar foliation is developed within the Peripheral Schieferhülle. The foliation in these units contain a stretching lineation developed during top-to-NW shearing. Top-to-NE senses of shear are also locally observed. Associated with the shearing at these high levels are the development of isoclinal folds (F_m and F_p) which have hinges parallel to the northwest stretching lineation.

At lower structural levels a weak foliation is developed which is overprinted by mesoscopic ductile shear zones which have top-to-NW displacements. Where more strongly developed, foliations in the gneiss have NW-SE stretching lineations. Inner Schieferhülle rocks at these levels preserve evidence for pre-intrusive deformation in the form of a strongly developed foliation which contains folds with isoclinal and sheath morphologies (Fb). These are cut by Hercynian aplite dykes.

Microstructural observations of gneiss samples show that preserved quartz fabrics are similar, independent of the mesoscopic strain intensity, relatively coarse and only rarely record evidence for the top-to-NW sense of shear indicated at the outcrop scale.

In all but the highest structural levels of the Dome, three phases of folding can be recognized within the Zentralgneis. The first (F_1) are recognised at the boundaries of

different lithologies such as the gneiss and amphibolites and have sheath type geometries. The second (F_2) folds the well developed foliation in the middle levels of the Dome while the third (F_3) produces the large antiformal Sonnblick domal structure and folds the strong foliation developed towards the top of the Dome. All these folds have hinges which are sub-horizontal and oriented NW-SE. The axial plane of F_3 dips at about 45° to the southwest while the pre-F_3 attitude of F_2 axial planes appears to be subhorizontal.

Extensional deformation appears to overprint structures associated with emplacement of the Peripheral Schieferhülle. Normal faults and shear bands in the higher levels of the Dome contain microstructures appear free of subsequent recrystallization and preserve fine grained asymmetric fabrics which are consistent with mesoscopic shear criteria.

4:12 Discussion

4:12.1 Origin and Kinematics of Foliation Development

A recent review of criteria for the identification of magmatic and tectonic foliations within granitoids has shown that "no single criterion can consistently distinguish different types of foliations in granitoids and even the application of multiple criteria is sometimes inconclusive" (Paterson *et al* 1989). However, several features suggest that the foliations developed in the Sonnblick Dome are tectonic in origin.

Within the upper levels of the Sonnblick Dome, the strongly developed foliation is sub-parallel to both the foliation developed within the Peripheral Schieferhülle and the contact between the Peripheral Schieferhülle and the Zentralgneis Complex. The decrease in foliation intensity moving down through the Dome and the spatial correlation between this foliation and the Zentralgneiss/Peripheral Schieferhülle contact suggests that the foliation is related to the emplacement of the Peripheral Schieferhülle on to the Zentralgneis basement. Since the foliation affects the Mesozoic Peripheral Schieferhülle, it must be Alpine in age and is therefore tectonic in origin. Mineral lineations and shear criteria associated with development of this foliation suggest that emplacement took place during top-to-NW shearing and was associated with southeast to northwest overthrusting of the Pennine Mesozoic metasediments and the Austroalpine plate on to the European forland.

Moving down through the Dome, the less intense foliation of the 'intermediate strain' augen gneiss still preserves S-C fabrics and asymmetric augen which show a top-to-NW shear sense and suggest that this foliation also developed during Alpine overthrusting. Similarly displacement vectors within metasomatically altered shear zones, the leucogranite shear zones and the mesoscopic shear zones suggest that these also developed during this deformation.

At the lowest structural levels of the dome, foliations axial planar to F_2 and F_3 folds are obviously tectonic in origin and, since they fold earlier Alpine foliations, are Alpine in age. However, foliations which form the fold surface to F_2 and F_3 folds cannot be geometrically related to any macro- or meso-scopic structural feature and are therefore difficult to relate to any particular deformation phase. Foliations do not show a preferred orientation of primary phases, such as K-feldspar, and also cut aplite veins which are interpreted to mark the final stages of Hercynian magmatic activity. These foliations are therefore interpreted to be tectonic in origin and represent solid-state deformation of the original granite.

The shear zones and foliation developed at the higher structural level of the Dome are the earliest deformation features which can be confidently identified as Alpine in age. It is not possible to say whether gneissic foliations, which are overprinted by these Alpine mesoscopic shear zones, represent foliations developed during late Hercynian or early Alpine deformation. However, it is likely that component of both of these are present within the Dome.

4:12.2 Compressive and Extensional Structures and their Relationship to Alpine Metamorphism

Quartz domains inferred to have developed during top-to-NW shearing within the mylonite gneisses, the low strain gneisses or the mesoscopically undeformed gneisses are composed of relatively coarse grains which show signs of dynamic recrystallization by subgrain rotation and grain boundary migration, but rarely show signs of a preferred grain orientation. This suggests that either stress levels were sufficiently low that coarse equilibrium grain sizes could be maintained throughout foliation development, or grain coarsening took place after foliation development. Textures indicative of static recrystallization and annealing (eg. foam textures) are not observed within the Sonnblick lithologies and, if recrystallization and grain coarsening did take place after foliation

development, then a later, low strain deformation would need to be invoked in order to explain the observed quartz microstructures.

Recrystallized grain sizes within quartz domains developed during top-to-NW shearing are generally larger than 0.1mm. Stress estimates based on recrystallized quartz grain size palaeopiezometry (Twiss 1977; Mercier *et al* 1977; Christie *et al* 1980), using the above minimum grain size estimate, suggests differential stress levels of less than ≈10MPa (0.1kbar). (Figure 4.32). Applying this stress estimate to the wet quartz flow low of Koch *et al* (1980), yields strain rates of $5x10^{-15}s^{-1}$ to $2x10^{-13}s^{-1}$ for temperatures of 400°C to 500°C respectively. Since these are based on maximum grain size and minimum stress estimates, these values are maximized strain rate estimates. These estimates are significantly slower than the strain rates commonly associated with mylonite formation, which are generally in excess of $10^{-12}s^{-1}$ (Sibson 1977; Prior *et al* in press), although they are reasonable estimates of strain rates associated with low strain deformation. This suggests that the low stress levels suggested by the preserved grain size may not represent that grain size which developed during the northwesterly-directed overthrusting.

Further evidence for the modification of the original quartz microstructures can be obtained from theoretical modelling of the rate at which differential stress must be decreased, in order to preserve the microstructure associated with the highest strain of a deformation event. By assuming that quartz grain size adjustment took place by dislocation climb, the equilibrium subgrain size can be calculated for a particular stress and temperature (Knipe 1989). Since top-to-NW shearing has been shown to be continuing during Alpine peak metamorphism conditions of approximately 500°C at this structural level (see Chapter 5 and Droop 1985), the rates at which stress must be removed in order to preserve microstructures developed at these temperatures are in the order of $8x10^{-11}MPas^{-1}$ from an initial stress of 50MPa (Figure 4.33). A reduction in temperature after peak metamorphism has little effect on the rate at which stress must be reduced, because the average post-metamorphic cooling rate of approximately 25°C/Myr (Chapter 7) has little effect on the rate of stress reduction required for microstructural preservation. This is because the time scale over which stress must be reduced is significantly shorter than that over which a significant temperature reduction takes place. However, even at lower temperatures of 300°C stress must be reduced faster than $1.2x10^{-11}MPas^{-1}$ for an initial differential stress of 50Mpa. This example considers only the grain size modification by dislocation climb and neglects the effects of grain boundary migration which will tend to enhance the rate of microstructure modification

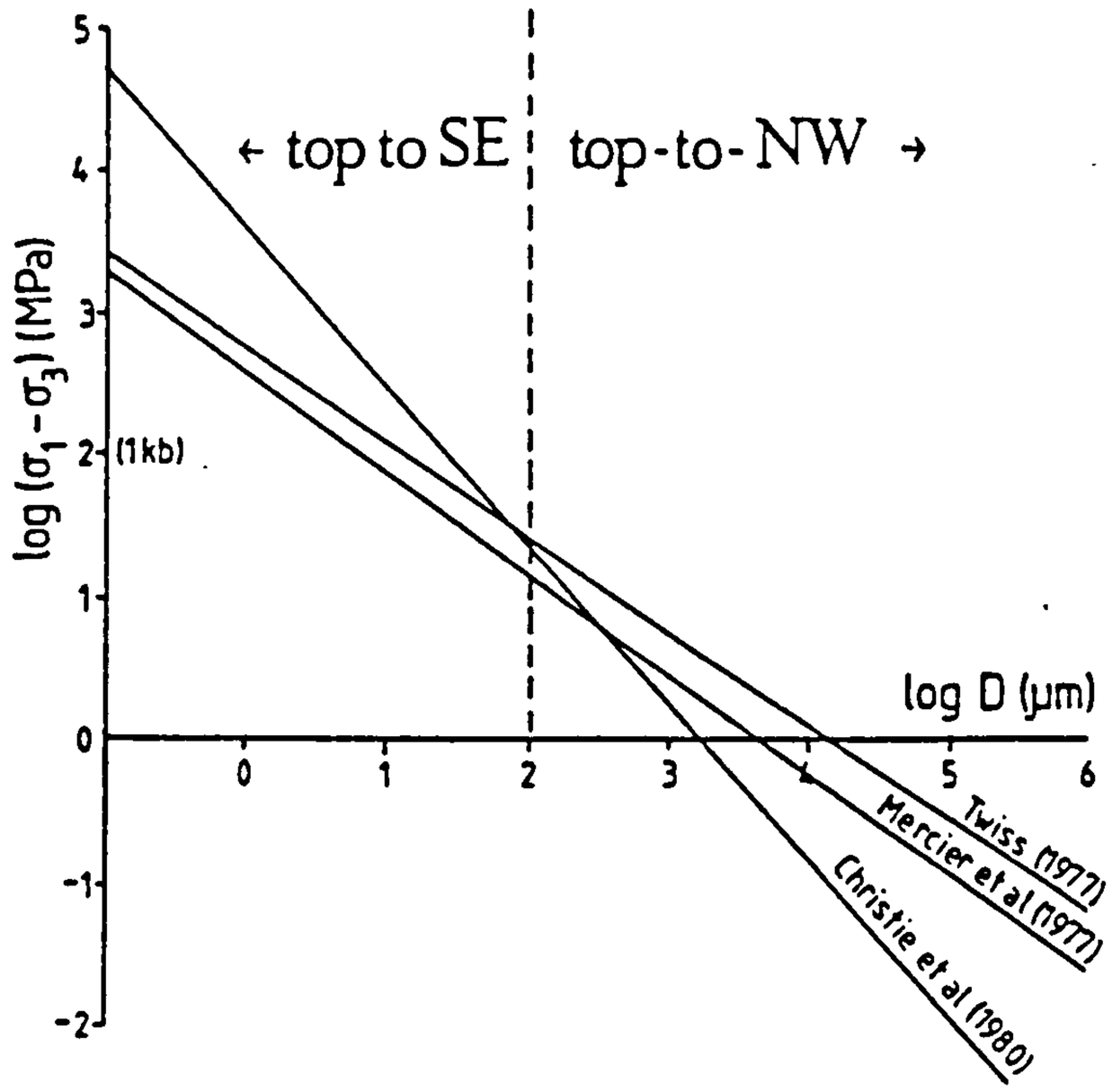

Figure 4.32. Graph of equations relating the differential flow stress ($\sigma_1 - \sigma_3$) (MPa) to the recrystallized grain size. Grain size with quartz foliation domains associated with top-to-NW shearing are generally larger than 100μm, while those associated with shear band formation are less than 100μm (Modified after Ord and Christie 1984).

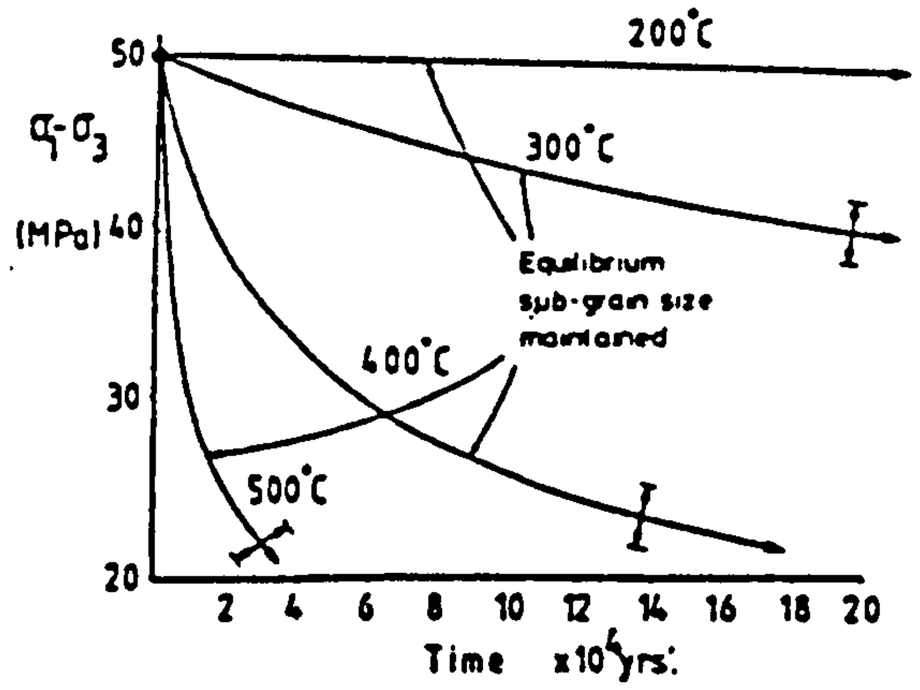

Figure 4.33. Graph to show differential stress vs time paths required to maintain an equilibrium sub-grain size assuming the rate of grain size change is controlled by the velocity of dislocation climb (after Knipe 1989). At temperatures in the order of 500°C, the differential stress reduction rate must be in excess of 1MPa per 400 years in order for microstructures associated with the deformation at the conditions of 50MPa differential stress and 500°C to be preserved.

during non-steady state deformation. Within mountain belts undergoing long, progressive deformation, stress reduction rates of the magnitude required to preserve pre- to syn- metamorphic deformation microstructures within the Sonnblick Dome are unlikely. This supports the interpretation that quartz microstructures formed during top-to-NW shearing have probably recrystallized.

Fold hinges of all generations contain domains of interlocking mica laths which are internally, relatively strain free and appear recrystallized. Recrystallization of mica in these zones does not appear to have taken place during deformation and textures are interpreted to have formed by relatively static recrystallization. The growth of albite and oligoclase porphyroblasts over all observable fold hinges including F_3 suggests that all phases of folding took place before Alpine peak metamorphism. This in turn implies that recrystallization of mica hinges was probably a static event associated with this metamorphism.

The foliations associated with top-to-NW shearing are folded on a large scale by F_3 folds and are therefore also expected to have undergone recrystallization during the Alpine metamorphism. However, although the inferred recrystallization of quartz microstructures, mentioned above, is considered to be associated with the thermal peak of metamorphism, the absence of static recrystallization textures suggests that low strain deformation must have continued after the metamorphic peak. This is supported by mesoscopically undeformed quartz veins which are considered to have developed during the later stages of the Alpine metamorphism and contain dynamically recrystallized quartz textures, indicating a low strain deformation.

Alpine garnet and oligoclase within the Peripheral Schiefehülle record an asymmetry which suggests that top-to-NW shearing was continuing during Alpine metamorphism. Furthermore, S-C fabrics associated with top-to-NW shearing within the upper levels of the gneiss and within the Peripheral Schieferhülle are still locally preserved and show that top-to-NW shearing continued, at least on a local scale, after the metamorphic peak. It is therefore possible that the low strain deformation was associated with continued northwestwards overthrusting. The general absence of asymmetric quartz grain fabrics within quartz domains of the Sonnblick gneiss is considered to reflect the fact that the continued top-to-NW shearing was of very limited extent, and quartz recrystallization is interpreted to have taken place generally after shearing had ceased.

In order to assess the kinematics of the later deformation, further work involving detailed textural analysis of the preserved quartz fabrics needs to be undertaken.

However, recent work looking in detail at quartz and calcite fabrics preserved in the Silberpfennig area of the Hochalm-Ankogel Dome to the north of the Sonnblick area has recognised a coaxial shortening with σ_1 vertical (A.Volp, University of Giessen, unpublished data), while similarly oriented coaxial fabrics have also been discovered in the western Tauern Window (J. Behrmann, pers. comm.). These fabrics appear to have developed relatively late in the deformation history of the Tauern Window and seem most likely to have developed during exhumation of the Window during gravity driven spreading of the orogenic wedge. Therefore, the relatively late-stage, low strain deformation which overprints fabrics associated with Penninic imbrication and shearing within the Sonnblick Dome may be co-axial in nature and associated with uplift of the Tauern Window.

In top-to-SE fabrics developed in the higher levels of the Sonnblick Dome, fine grained quartz fabrics are preserved. The fine grain size and presence of grain preferred orientations suggests that the preserved microstructures represent the original deformation fabrics, which have not undergone static rectrystallization associated with Alpine metamorphism. The decrease in strain rate and stress, associated with shear band formation, must have occured relatively quickly to preserve these textures and temperatures must have been sufficiently low that static recrystallization and the development of a foam texture were inhibited. However the quartz textures preseved in the extensional structures are indicative of plastic deformation in the form of dislocation creep, in conjunction with grain boundary migration. This suggests temperatures in excess of 350°C. The dependence of recrystallization processes on factors other than temperature preclude a more accurate estimate of extrinsic conditions during shear band formation. Metamorphic chloritoid which are cut by shear bands and undergo alteration to chlorite adjacent to these bands provide further evidence for shear band formation postdating metamorphism.

Extensional shear bands at high structural levels of the Dome, are therefore interpreted to have formed after the Alpine metamorphic peak. Since the affect of the shear bands would be to extend the unit in which they were developed, then shear band formation was associated with thinning of the higher levels of the Dome. Shear band formation may therefore have occured synchronous with the regional low strain coaxial flattening which is inferred to have taken place after the metamorphic peak. In this case, coaxial deformation may have resulted from the imposed regional stress field while shear band formation reflects localized deformation within this framework. This deformation

is considered to be an expression of gravitational spreading by which uplift was achieved within the collision belt.

At the lowest structural levels of the Dome, normal shear zones do not preserve microstructures which reflect the degree of deformation observed on an outcrop scale. The observed microstructures are best interpreted as reflecting recrystallization after deformation. From theoretical modelling, peak metamorphic conditions are are not expected to occur simultaneously at different structural levels of a orogenic belt and peak metamorphism is expected to occur later at lower structural levels (Thompson and England 1984). It is possible therefore that the simultaneous development of normal faults within lower structural levels and extension associated with shear band formation at higher structural levels, could lead to shear zones which predate peak metamorphism at depth and post-date the metamorphic peak at the top of the Dome. However, previous PTt paths for the southeast Tauern Window (eg Droop 1985) suggest that uplift was taking place before peak metamorphic conditions were attained. Since uplift of the Tauern Window appears to be associated with syn-convergent extension (eg Wallis 1987; Behrmann 1989; Selverstone 1989) then it is likely that normal faults were developing over a large part of Alpine history and it is not necessarily valid to constrain the extensional shearing to any period relative to peak metamorphism.

As mentioned earlier, the continuity of the domal gneiss structure is interrupted by the presence of two NW-SE trending strips of Schieferhülle material towards the northern end of the northeastern margin of the Dome. According to Exner (1964, plate 1), these divide the Sonnblick Dome into three different tectonic units (the main gneiss body, the "Wurten Wedge" of the Sonnblick Dome and the "Knappenhaus Cylinder" which forms a continuation of the Sonnblick gneiss Lamella). No difference in gneiss type or internal structures were seen between these different units. In cross-sections through the Dome (Fig. 4.1a), the metasedimentary intercalations appear as downward facing synformal closures, the axial planes of which have been folded by the antiformal structure of the Dome. However, the continuation of the strips of Schieferhülle material into two major fault structures suggest that the metasedimentary units were not folded into the dome but have been juxtaposed with gneiss material by faulting. The most southerly of these faults passes through the northeastern part of the mapped field area (plate 1) but is nowhere seen to be exposed. The kinematics associated with movement on this fault could not be assessed. However, the fact that these faults are parallel to the Mölltal Fault Line may imply that they are also associated with uplift of the Tauern Window and are normal faults.

4:12.3 A Model for the Origin of the Sonnblick Dome

Isoclinal folds, with axial planes parallel to the mylonitic foliation developed within the higher levels of the Dome, and F_1 folds developed at the contacts between lithological units have been interpreted to have developed synchronous with the foliation, during top-to-NW shearing. This shearing is interpreted to be related to emplacement of Austroalpine units onto the European foreland and thrusting of the Penninic Mesozoic sediments onto the Pennine basement.

Although hinges of F_2 and F_3 folds are subparallel to the earlier folds and the NW-SE mineral stretching lineation, they differ from the earlier folds in that they are not associated with zones of high shear strain. This is illustrated by the fact that they often occur as low strain crenulations overprinting the earlier foliation. These folds cannot therefore be interpreted as folds developed in zones of high shear strain, in which the fold hinges have progressively rotated towards the transport direction. The large scale structure of the Dome and fold development at lower structural levels therefore requires a different model for their formation which is consistent with the large scale kinematic framework established earlier.

Microstructural relationships show that both F_2 and F_3 folds developed prior to peak metamorphic conditions and therefore formed while non-coaxial shearing associated with top-to-NW overthrusting was occuring in the upper and possibly intermediate, structural levels of the Dome. Within such an environment folds associated with non-coaxial shearing may be produced when thrusts pass over a ramp-flat geometry, or by the formation of roll-over structures in the hangingwall of a thrust. Folds may also develop above the tips of blind thrusts or as culminations above a duplex as a consequence of thrusting at lower structural levels of a nappe pile.

As a thrust sheet moves over a ramp, thickening induced by a gradient in shear stress in a vertical direction may be expressed in the formation of a fold above the detatchment (Berger and Johnson 1980, 1982). Mathematical models of this behaviour (Berger and Johnson op.cit.) suggest that drag along the ramp part of the detatchment surface may give rise to localized thickening behind the ramp, which in turn produces fold asymmetry and the formation of a relatively tight fold in the thrust sheet (Figure 4.34). Although the shape of the fold is dependent upon factors such as the assumed drag parameter, the amount of thrust translation and the height of the ramp, the general form

of modelled structures show a similar resemblance to the Sonnblick Dome (compare Figures 4.34 and 4.1).

The models of Berger and Johnson (1980, 1982) consider translation to be in the plane of the cross-section so that the thrust is moving over a frontal ramp. In the case of the Sonnblick area, the movement direction is oblique to the fold structure and therefore, the models are not directly applicable. However by analogy, the Sonnblick Dome may represent asymmetric fold development above an oblique ramp dipping to the southwest. Such a model would require the presence of a deta chment beneath the Sonnblick Dome which cut up section towards the northeast.

Mapping by Exner (1964) in the Mallnitzer Mülde to the northeast of the Sonnblick Dome, has shown the presence of a white mica schist unit, considered to be part of the Inner Schieferhülle, which in cross-section, is observed to cut up through the overlying Schieferhülle cover (Figure 4.1a). Observations within the Sonnblick Dome and the immediately overlying Peripheral Schieferhülle in the Rote Wand area show that white mica schists within the Sonnblick area are commonly zones of high, localized shear strain. These features suggest that the white mica unit may represents an oblique thrust extending beneath the Dome.

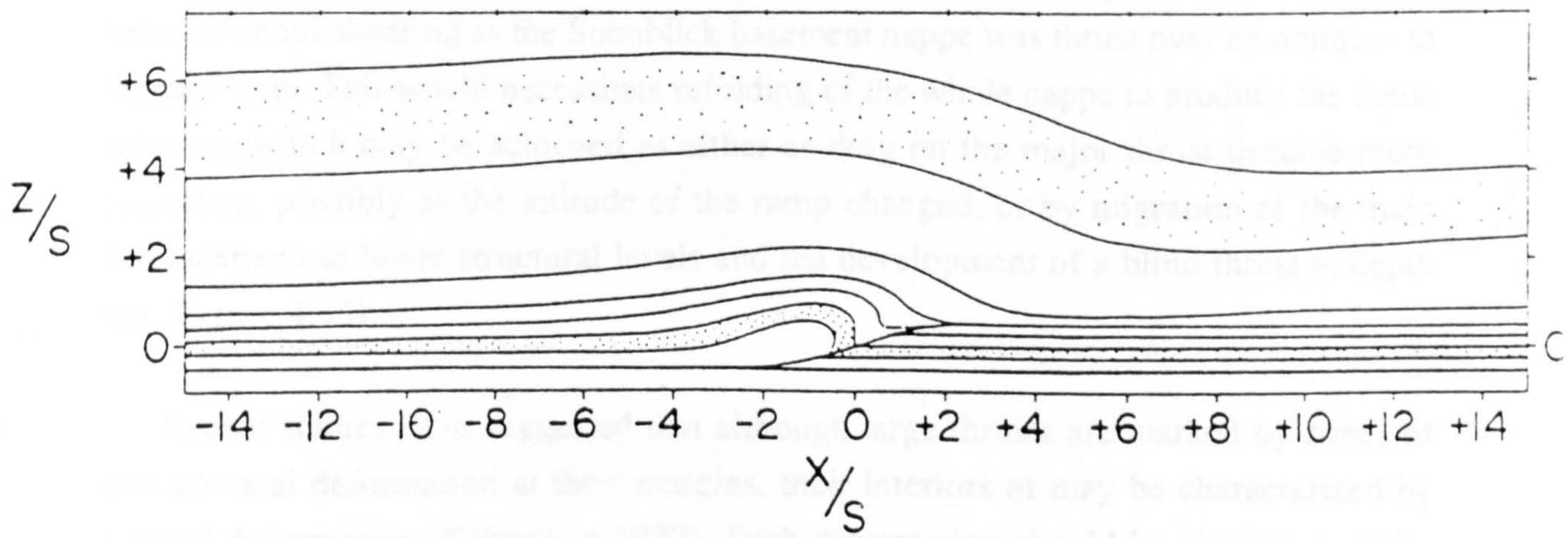

Figure 4.34. Theoretical model of deformation of a thrust sheet moving over a ramp after Berger and Johnson (1980). The thrust block has been subjected to a uniform translation ten times the height of the ramp and a high drag along the ramp. The result is nappe-like structure similar in form to that of the Sonnblick Dome (see text for discussion). S is the height of the ramp, X is the lateral distance away from the centre of the ramp and Z is the height above the centre of the ramp. Marker layers were originally horizontal.

The applicability of the fold model of Berger and Johnson (1980, 1982) to the Sonnblick Dome is further supported by observations made at the outcrop scale. The model requires that localized thickening took place above the thrust deta chment within the core of the fold. Such thickening may be accommodated by imbricate faulting or the ductile flow of material within the upper thrust plate, or by the development of thrusts which have a 'back-thrust' geometry relative to the main deta chment (Serra 1977). Within the Sonnblick Dome, imbrication along oblique thrusts, in the form of metasomatic shear zones and quartzo- feldspathic mylonites, may accommodate the thickening required by the model. Furthermore, folds with NW-SE oriented hinges, developed in the hanging wall of oblique ramps have been observed within the Dome (eg. Figure 4.23) and provide a self-similar example of what may be occuring at a larger scale.

The above model is considered a viable method of producing the domal, F_3 structure of the Sonnblick area. However, it is not immediately obvious how such a model may produce the observed F_2 folds. Several models may be applied to the formation of F_2 folds which are constrained by the fact that when the effects of F_3 are removed, the overall geometry of the axial planes to F_2 appears to be approximately sub-parallel to the contact of the Zentralgneis and overlying Schieferhülle.

One possible model for the development of F_2 folds is during the earlier stages of heterogeneous shearing as the Sonnblick basement nappe was thrust over an oblique- to lateral- ramp. This would necessitate refolding of the whole nappe to produce the dome structure which may be achieved as either as drag on the major thrust became more important, possibly as the attitude of the ramp changed, or by migration of the main displacement to lower structural levels and the development of a blind thrust at depth (eg. Figure 4.35).

Recent studies have suggested that although large thrusts are marked by zones of non co-axial deformation at their margins, their interiors of may be characterized by coaxial deformation (Behrmann 1987). Such deformation should be characterized by sub-vertical shortening and movement parallel extension of the thrust nappe. Coupled with the gravitational affects of emplacing in excess of 25km of Austroalpine crust onto the Pennine basement, it is therefore likely that a component of flattening began to affect the basement complex relatively early during continental collision. Despite the fact that the orientation of of the extension direction could not be constrained, F_2 development is

consistent with sub-vertical shortening and therefore, may result from coaxial deformation within the interior of the Sonnblick thrust sheet.

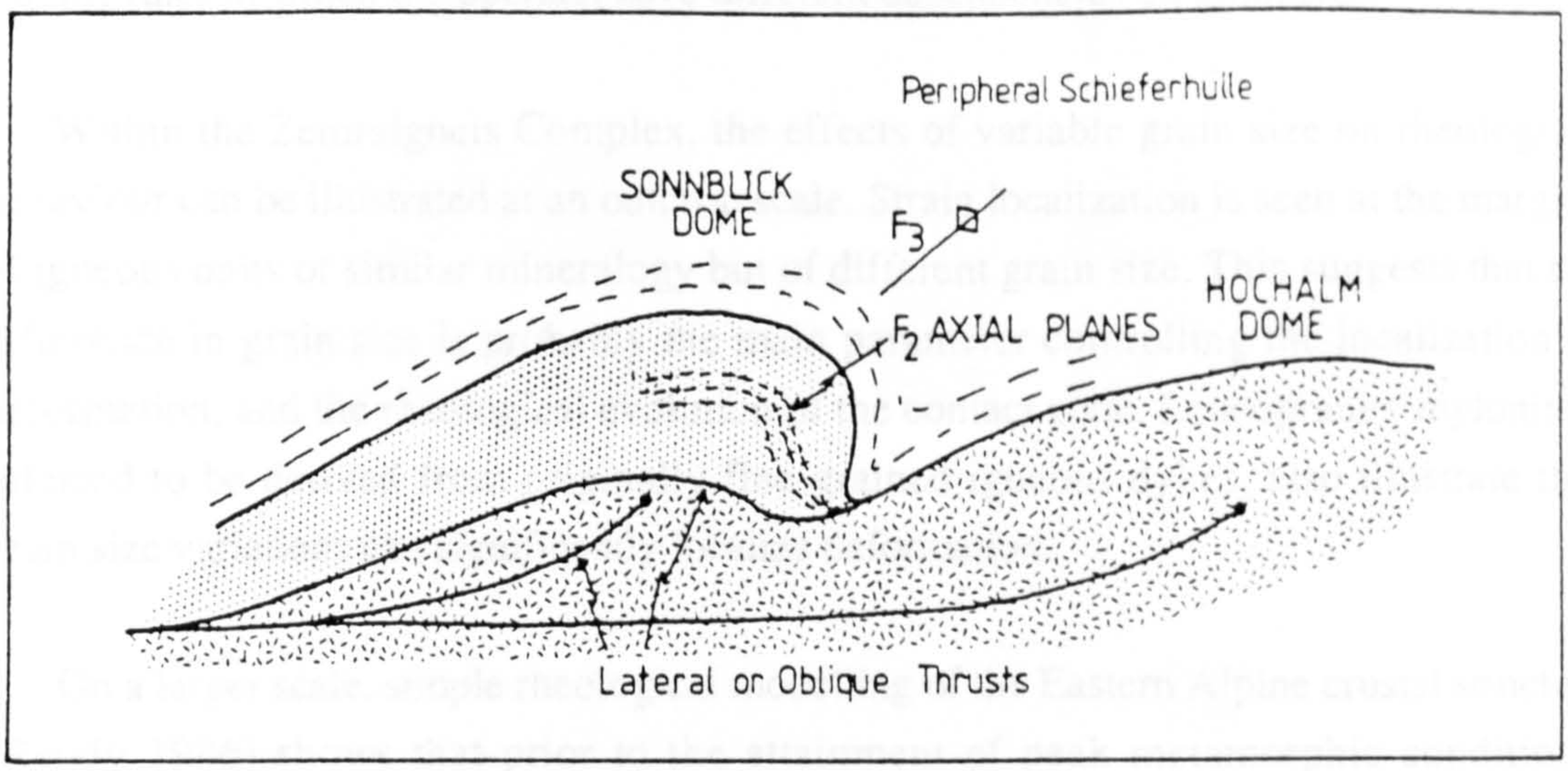

Figure 4.35. Schematic model illustrating the Sonnblick Dome structure as resulting from refolding of a Zentralgneis thrust sheet by a blind thrust at depth. An alternative model would be to form a duplex at depth which folds the overlying roof nappe.

The two models for the development of F_2 folds are difficult to test because of the recrystallization of pre-metamorphic microstructures. However the models are not mutually exclusive and it is possible that F_2 folds resulted from the interaction of thrusting over a lateral or strongly oblique ramp with coaxial deformation within the interior of the Sonnblick nappe. The formation of the domal structure and F_3 folds within the gneiss is interpreted to be the result of continued thrusting of the Sonnblick Zentralgneis over an oblique ramp dipping to the southwest which may be represented by the white mica schists within the Mallnitzer Mülde. A possible alternative is that the Dome represents a culmination above a blind thrust or duplex developed at lower structural levels. As the Dome formed, top-to-NW shearing at the highest levels appears to have continued in the southwestern flank of the Dome.

4:12.4 Partitioning of Deformation between Basement and Cover and Strain Localization Mechanisms

The rheological evolution of rocks undergoing plastic deformation will be dependent upon a number of factors; ranging from from the environmental controls of temperature, pressure, stress and strain rate to more rock-specific parameters such as mineralogy and grain size (eg Kirby 1985; Carter and Tsenn 1987; Handy 1989). The rock specific

parameters arise from the fact that different minerals may deform by different mechanisms at any particular set of conditions; while different deformation mechanisms and the rates at which the operate, have different dependencies on grain size.

Within the Zentralgneis Complex, the effects of variable grain size on rheological behaviour can be illustrated at an outcrop scale. Strain localization is seen at the margins of igneous units of similar mineralogy but of different grain size. This suggests that the difference in grain size is probably the main parameter controlling the localization of deformation, and the rheological evolution of the contact zone. Leucogranite mylonites, inferred to be derived from originally fine-grained igneous dykes, also illustrate that grain size variations can significantly localize deformation.

On a larger scale, simple rheological modelling of the Eastern Alpine crustal structure (Reddy 1986) shows that prior to the attainment of peak metamorphic conditions, deformation associated with the emplacement of the Austroalpine onto the Pennine basement will first be localized at the base of the Austroalpine unit (Figure 4.36), but will migrate downwards through the crust as the geothermal structure of the crust relaxes. Although this model idealizes the rheological structure of the crust and assumes an initial saw-tooth geotherm associated with instantaneous emplacement of the Austroalpine nappes, it predicts that the evolving thermal structure within collision zones plays an important role in the localization of deformation.

The above model ignored the lithological difference between the Zentralgneis basement and the overlying Peripheral Schieferhülle. Given that both large mineralogical and grain size differences exist between the orthogneiss of the Sonnblick Dome and the overlying metasediments, it would be expected that strain would be localized into the weaker calc-rich mica schists of the Schieferhülle, rather than the quartzo-feldspathic units of the underlying gneisses. Although the Mesozoic sediments can be inferred to be tectonically emplaced onto the gneisses, and must have undergone higher strains than the top of the underlying gneiss, field observations show that both the Schieferhülle and the upper levels of the orthogneiss are strongly deformed units across which there appears to be no significant rheological discontinuity. This observation is contrary to theoretical modelling of the lithosphere, which suggests that large zones of detatchment and shearing should develop at litho-rheological boundaries within the crust (eg. Sibson, 1983; White and Bretan 1985).

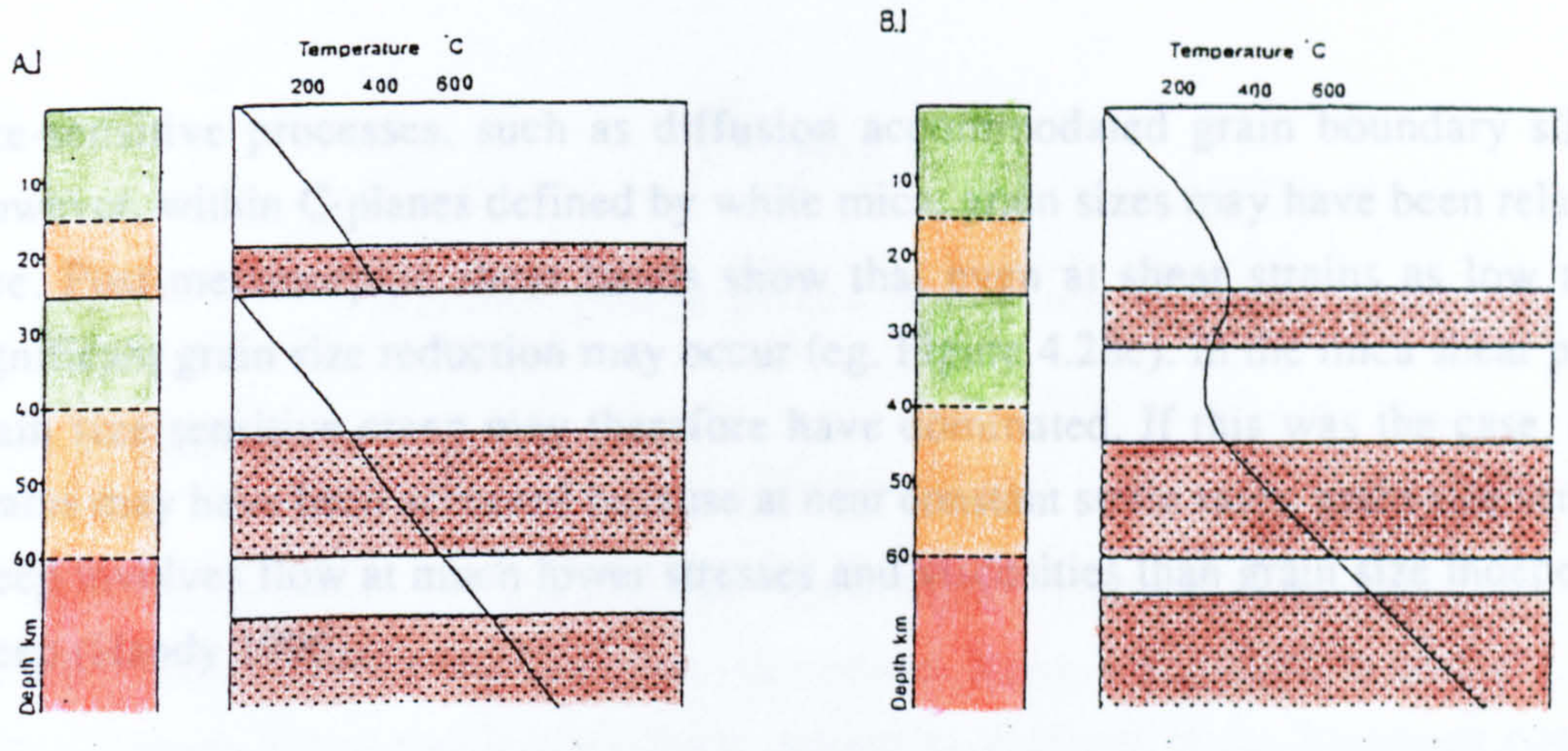

Figure 4.36.

Simple Rheological Models for the Eastern Alps:

A.I Immediatly after emplacement of a single 25km thick thrust sheet

B.I During thermal relaxation prior to uplift and erosion.

Assumed thermal structures are shown. 10^{-16} strain rate contours are calculated for a stress of 20MPa based on wet quartz, dry quartz and olivine flow laws taken from Kusznir and Park (1984).

Within the lower structural levels of the Sonnblick Dome, the white mica schist within relatively undeformed gneiss are interpreted as metasomatically-altered shear zones derived from the augen gneiss. Localization of deformation in this case is interpreted to be the result of a cyclic process of fluid infiltration, metamorphic reaction and further deformation (Chapter 6). At the higher levels of the Dome, gneiss lithologies do not appear to be metasomatically altered and it is less simple to infer fluid infiltration as a process by which strain became localized.

Within the upper levels of the gneiss, temperatures during shearing approached garnet grade conditions (see Chapter 5). At these temperatures, deformation in feldspar and quartz is considered to be dominated by the grain-size-independent plastic deformation processes, such as dislocation creep and grain boundary migration (Tullis and Yund 1985). Reduction in the grain size of feldspar and quartz, due to stress-dependent dynamic recrystallization, is unlikely to to have been sufficient to cause a change in the dominant deformation mechanism from grain-size-independent to grain-

size-sensitive processes, such as diffusion accommodated grain boundary sliding. However, within C-planes defined by white mica, grain sizes may have been relatively fine. Post-metamorphic shear bands show that even at shear strains as low as 10, significant grain size reduction may occur (eg. Figure 4.28c). In the mica shear planes, grain size sensitive creep may therefore have dominated. If this was the case, larger strains may have been achieved because at near constant strain rates, grain size sensitive creep involves flow at much lower stresses and viscosities than grain size independent creep (Handy 1990).

The absence of very large strains at depth within the Dome (except within discrete shear zones), requires that shear stresses associated with overthrusting of the Peripheral Schieferhülle be localized at the top of the Dome. This is consistent with the model of F2 fold formation and with observations in other thrust belts (Behrmann 1987), which suggest that large thrusts are characterized by coaxial deformation in their interiors but non-coaxial deformation at their margins.

The Mesozoic sediments of the Peripheral Schieferhülle consist of a series of dominantly pelitic and calcareous sediments which represent an heterogeneous mineralogical assemblage, at the grain scale and upwards. The juxtaposition of mineral phases which are out of equilibrium during deposition will favour low grade metamorphic reactions, as temperatures within the units increase. As discussed by White and Knipe (1978), White *et al* (1980) and Brodie and Rutter (1985), metamorphism may give rise to a variety of softening processes, and of particular importance in the rheological evolution will be the effect of crystallizing fine-grained products which will favour grain size-sensitive deformation mechanisms (eg. Rubie 1983; Handy 1989).

Within the studied lithologies of the Peripheral Schieferhülle, reaction products such as garnet, chloritoid and feldspar developed during the later stages of shearing, while micas and quartz are inferred to have undergone significant recrystallization. The pre-metamorphic assemblage of many of these units are dominated by mica and quartz and are therefore similar to the gneisses. In this case, deformation within the metasediments may have been controlled by similar processes to those taking place within the gneiss.

Chapter 5

Metamorphism in the Sonnblick Dome

5:1 Introduction

Previous metamorphic studies in the Tauern Window have generally concentrated on metamorphism within the para-autochthonous Inner Schieferhulle and the para-allochthonous Peripheral Schieferhulle sequences exposed in the basement complex. Such studies have illustrated the complex metamorphic history of the Pennine basement by showing the presence of Alpine blueschists, greenschists, amphibolite and eclogite metamorphic facies overprinting pre-Alpine amphibolite and eclogite assemblages in the southeast (Droop 1981,1983,1985), central (Holland 1977, 1979; Miller 1974, 1977) and western Tauern Window (Selverstone *et al* 1984).

Detailed studies in the southeast Tauern Window have constrained the retrograde pressure-temperature-time (PTt) history of the Hochalm-Ankogel area by considering mineral equilibria and thermobarometric studies in conjunction with radiogenic dating techniques (Droop 1985, Cliff *et al* 1985). Metamorphic conditions from these studies estimated pressure-temperature (PT) conditions of 7±1 kbar and 490±50°C for the northwest margin of the Sonnblick Dome. These data further showed that the heat budget required for Alpine metamorphism in this area could be totally accounted for by tectonic thickening and that the rocks followed a PTt trajectory similar to those predicted by mathematical modelling of tectonically buried rocks (England 1978, England and Thompson 1984).

There are sufficient differences in the geology of the Sonnblick and Hochalm areas that the well constrained history of the Hochalm area may differ from that of the Sonnblick. Large differences in gneiss lithology and variability are observed in the two gneiss complexes which may be indicative of different early histories and may suggest early spatial separation of the original plutons. The presence of orthogneiss thrust sheets, in the form of gneiss lamellae (Exner 1964, 1971), and of internal gneissic imbrication (eg. Figure 4.8) shows that the granitic basement did not behave passively during Alpine collision and underwent significant internal deformation and shearing. Although the amount of movement is difficult to constrain, it may be of sufficient magnitude that the early alpine metamorphic history of the two domes may be significantly different.

Deformation in the Zentralgneis basement appears to have taken place before peak metamorphism (Chapter 4). However, metamorphic isograds are folded by doming centred on the Hochalm area (Droop 1985). Although this may be explained by metamorphism taking place later at lower structural levels (eg. England and Thompson 1984), it is important to the tectonic synthesis of the area to establish the grades of metamorphism in the lower structural levels of the Sonnblick Dome.

Finally, extensional deformation, associated with uplift and unroofing of the Tauern Window (eg. Selverstone 1989, Behrmann 1989, Genser and Neubauer 1989), may have juxtaposed rocks of very different structural and metamorphic histories at a late stage in the deformation history. Evidence for this sort of emplacement has been reported from the western Tauern Window (Selverstone *et al* 1984). This may be an important consideration in the area of the Mallnitzer Mülde directly north of the Sonnblick Dome, along which the the Mölltal fault zone appears to die out.

Rocks of the Sonnblick area may have undergone a complex metamorphic history involving both Prealpine and Alpine elements. Units of the Inner Schieferhülle, now contained within the Dome show evidence for pre-granitic deformation which may have occured synchronous within metamorphism. The Inner Schieferhülle may also have undergone contact metamorphism associated with granite intrusion.

The early subduction of the Pennine basement beneath the Austroalpine units led to high pressure - low temperature metamorphism and the formation of eclogite and blueschists within some regions of the Tauern Window (eg. Frank *et al* 1987). Within the structurally lowest parts of the Peripheral Schieferhülle, pseudomorphs after lawsonite provide evidence for eoalpine high presure - low temperature metamorphism in the southeast Tauern Window (Droop 1985). This is overprinted by higher temperature Alpine regional metamorphism (Droop 1981, 1985).

The aim of this chapter is to establish the metamorphic history of the Sonnblick area. To achieve this, mineral chemistry and metamorphic assemblages are presented and the equilibrium between different phases is assessed. Equilibrium assemblages are then interpreted thermobarometrically.

5:2 Metamorphic Assemblages and Mineral Chemistry

5:2.1 Gneiss Lithologies

Orthogneisses form the majority of rock types in the Sonnblick Dome and contain quartz, potassium feldspar, plagioclase, biotite, white mica and members of the epidote group of minerals. Accessory phases include opaques, sphene, apatite, zircon and calcite. The petrography of the gneisses has been discussed earlier (Chapter 3). Compositional Data for these phases are given in Appendix 4.1.

The commonly observed inclusion filled cores and inclusion free rims of plagioclase within the gneiss are compositionally very similar. Typical albite compositions are generally greater than 97% albite (Figure 5.1), and are unlikely to represent primary igneous plagioclase compositions. Inclusions are interpreted to have formed during the breakdown of more anorthic plagioclase (eg. Ackermand and Karl 1972) and are therefore metamorphic in origin. Inclusions are not generally zoned and representative compositional analyses are given in Appedix 4.1. Modal estimates of the amounts of inclusions within the cores of plagioclases are variable and range from 0-50% by volume of the core. No consistent relationship is seen in the modal ratio of clinozoisite and white mica and both inclusion types can be found in isolation. Backscatter atomic number contrast SEM studies and electron microprobe analyses shows the white mica to be phengitic and no paragonite has been observed. Inclusion type and intensity is independent of both the deformation state of the feldspar and the proximity of the plagioclase to any other phases.

Biotites contain more Al than phlogopite or annite and have Mg/(Mg + Fe) ratios around 0.5. Muscovites contain ≈25% celadonite solid solution and between 5-10% paragonite component. Within some samples, zoned white micas are developed at the grain boundary of albite included within K-feldspar augen. Individual micas are up to ≈100μm in length and show excellent oscillatory and irregular zoning features when observed by atomic number contrast backscatter electron microscopy (Figure 5.2a,b). Microprobe analyses of these zones (Appendix 4.2) shows that dark areas of the SEM image correspond to areas of high K, Mg, Si and low Ba and Al. Lighter areas have higher Ba/K ratios and have low SiO_2 (Figure 5.2b). Si per formula unit in the phengite for dark and light areas respectfully are approximately 3.335 and 3.062.

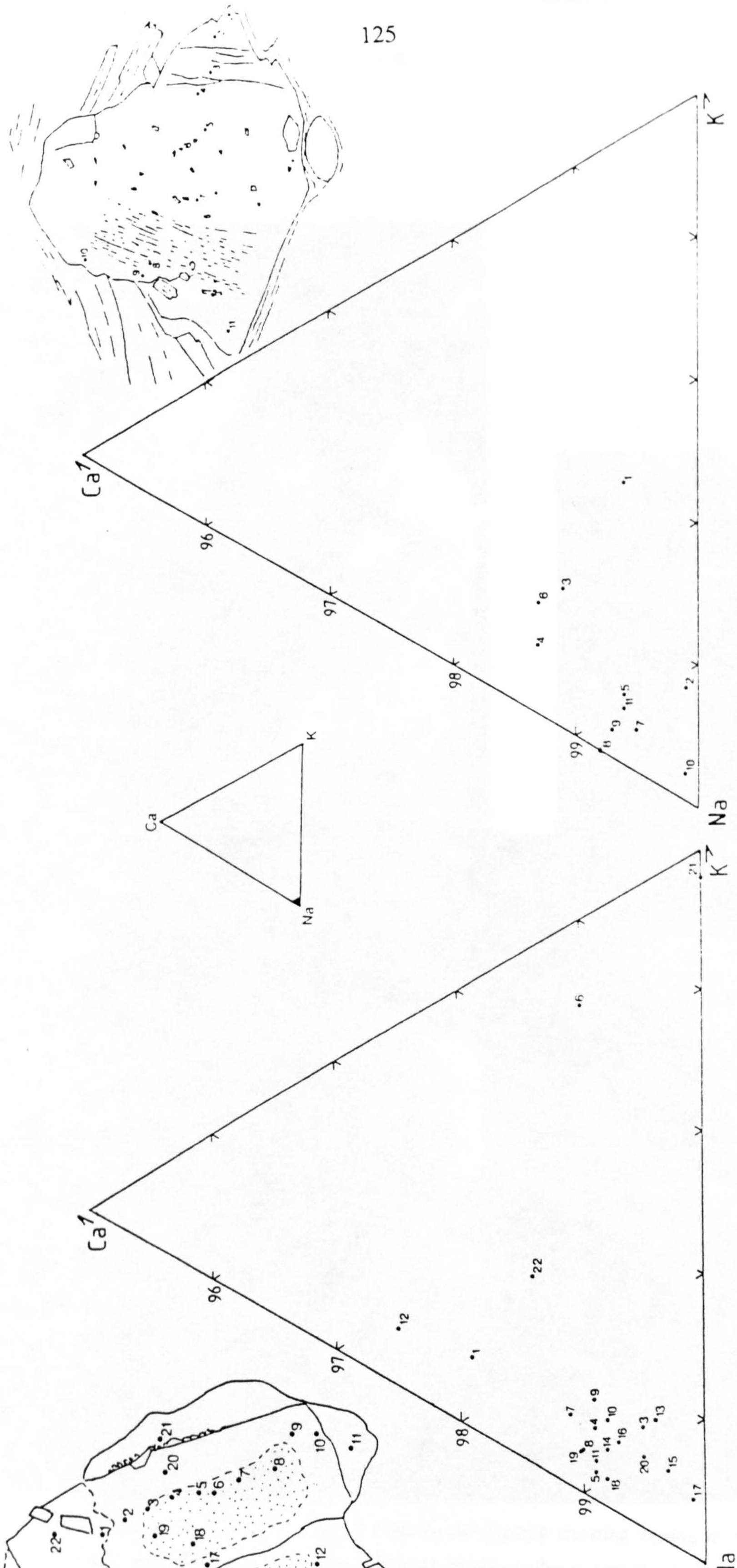

Figure 5.1. Plagioclase compositions across feldspars which contain inclusion filled cores and inclusion free rims. Both are taken from sample 48618. Numbers refer to probe analyses given in Appendix 4.1.

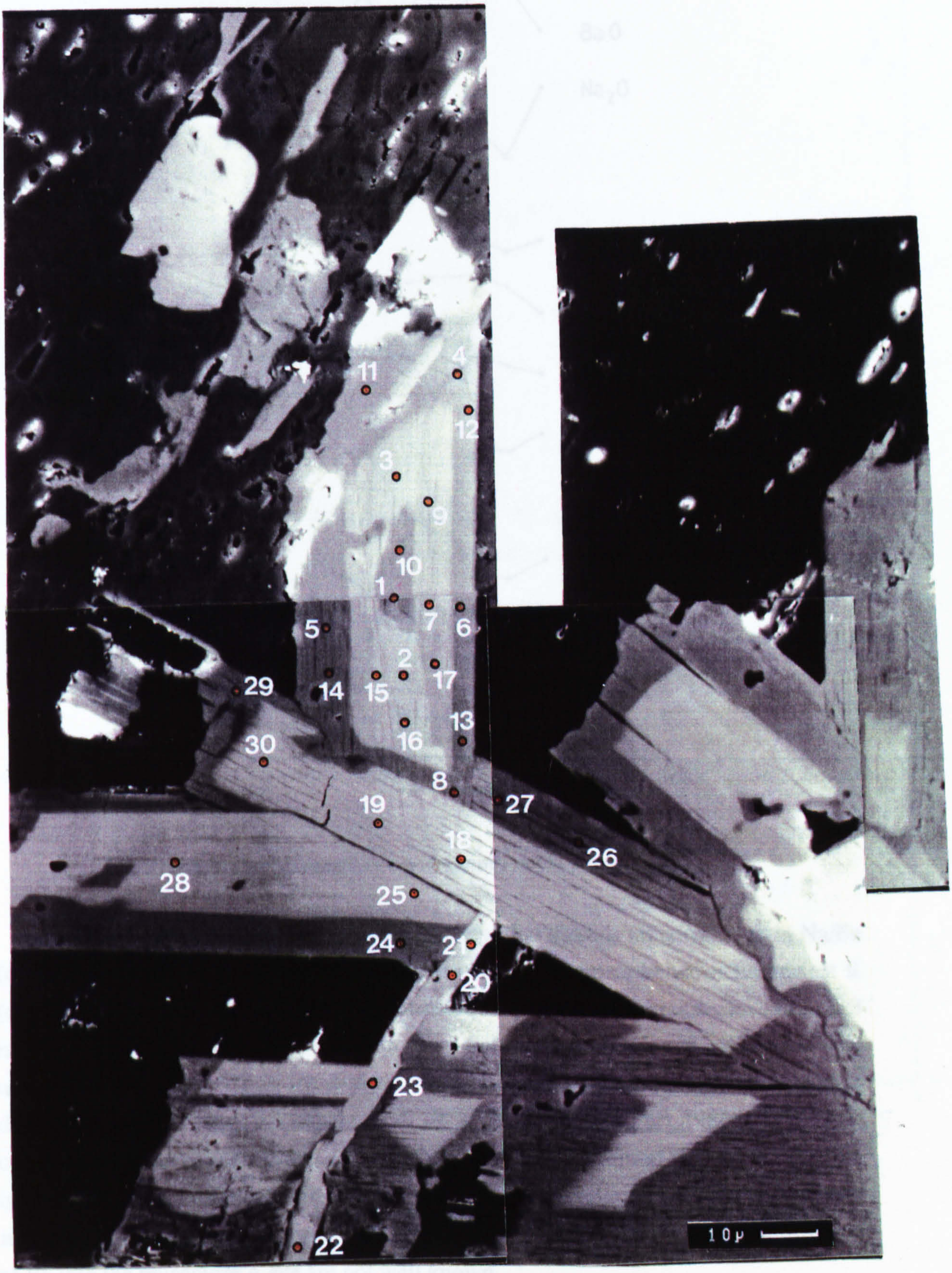

Figure 5.2 a) Atomic numder contrast electron micrograph showing zoning in white mica growing between plagioclase and K-feldspar phases. Zoning is due to variation in Ba and K. Dark areas of the mica are Ba poor, light areas are Ba rich. Points refer to probe analyses given in Appendix 4.2.

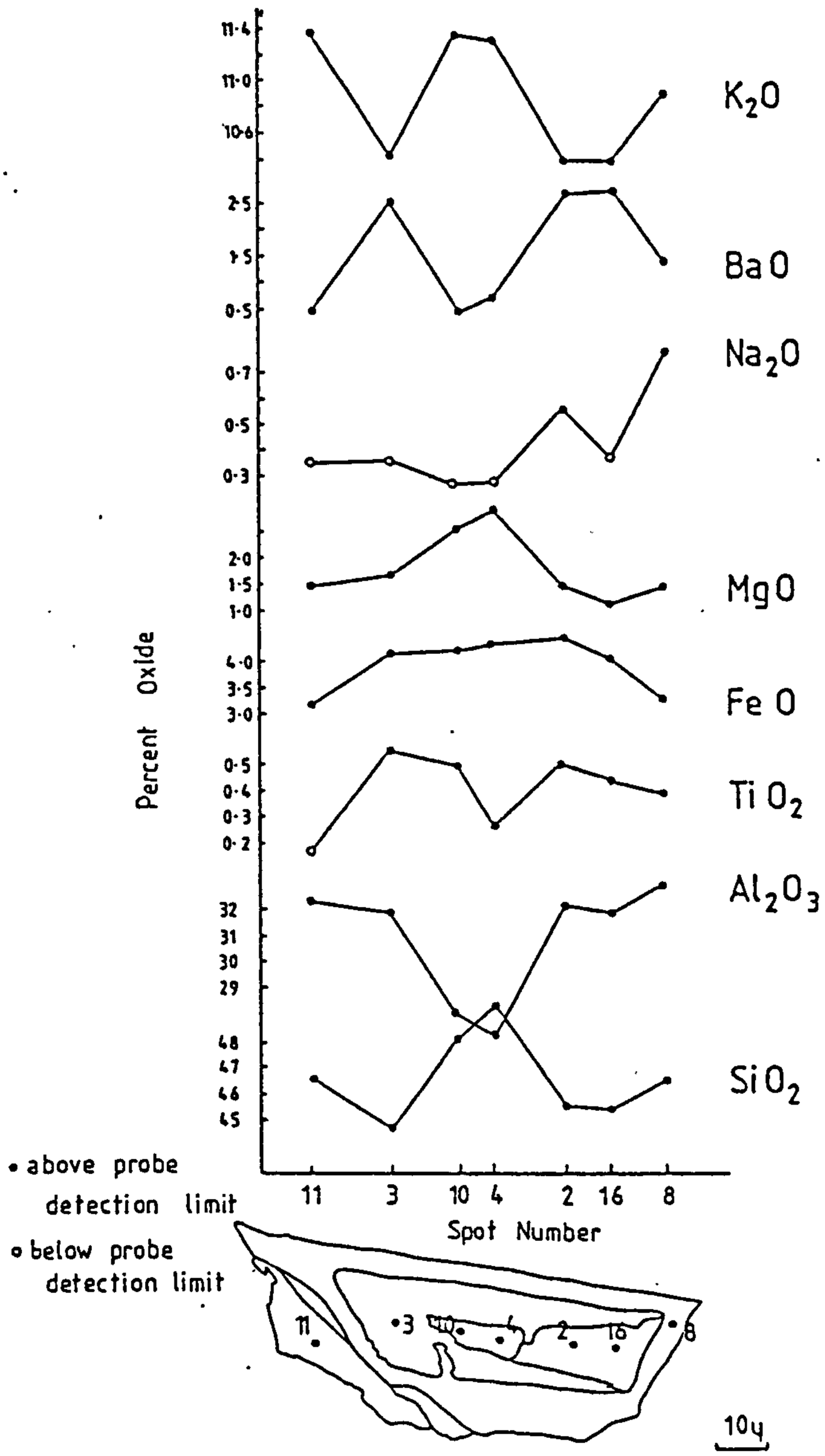

Figure 5.2 b) Profile through one of the zoned micas shown in a).

Graphical plots of mica data (Figure 5.3) show that there is no correlation in Na/Ba (correlation coefficient =0.004) while a slight correlation exists between Ba against K (correlation coefficient = 0.348). This correlation coefficient increases to 0.842, if 3 microprobe analyses taken less than 4μm away from zone margins, and interpreted to be unreliable, are omitted from the data set. Since the ratio of K and Na in white mica is dependant upon temperature (Eugster *et al* 1972; Chatterjee and Flux 1986), the absence of any correlation between Ba and Na suggests that Ba substitution into the mica A site is relatively independent of temperature. The negative correlation of Ba with K further suggests Ba is linked to the amount of K in the A site. The details regarding substitution of Ba into the muscovite A site are not well known.

Figure 5.3 Plots of A site chemistry within the zoned micas of a). O = light areas of the backscatter image, ● = dark areas of the backscatter image.

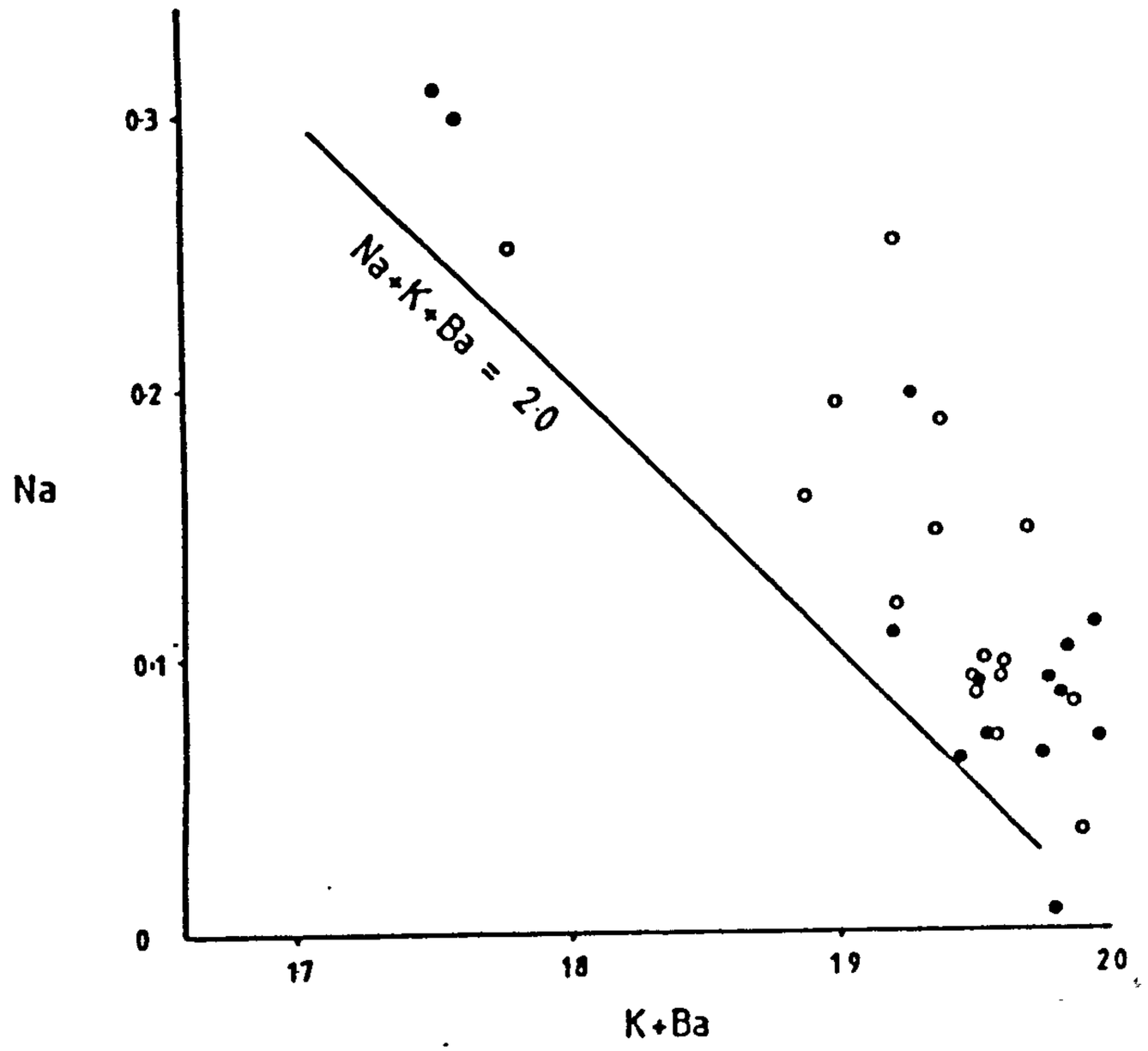
Na
0·3
0·2
0·1
0
Na+K+Ba = 2·0
17
18
19
20
K+Ba

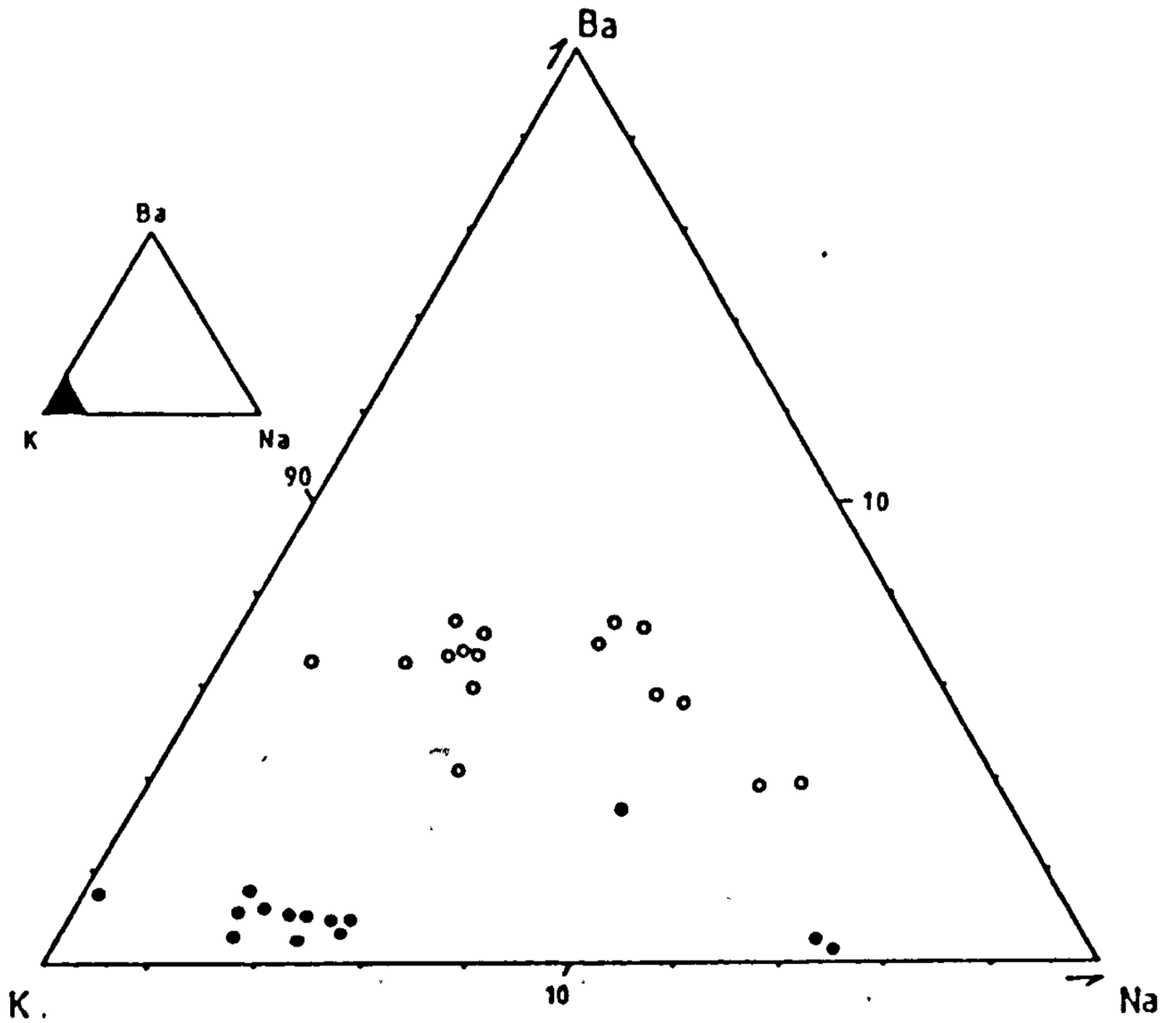
Ba
1
Ba
K
Na
90
10
10
K
Na

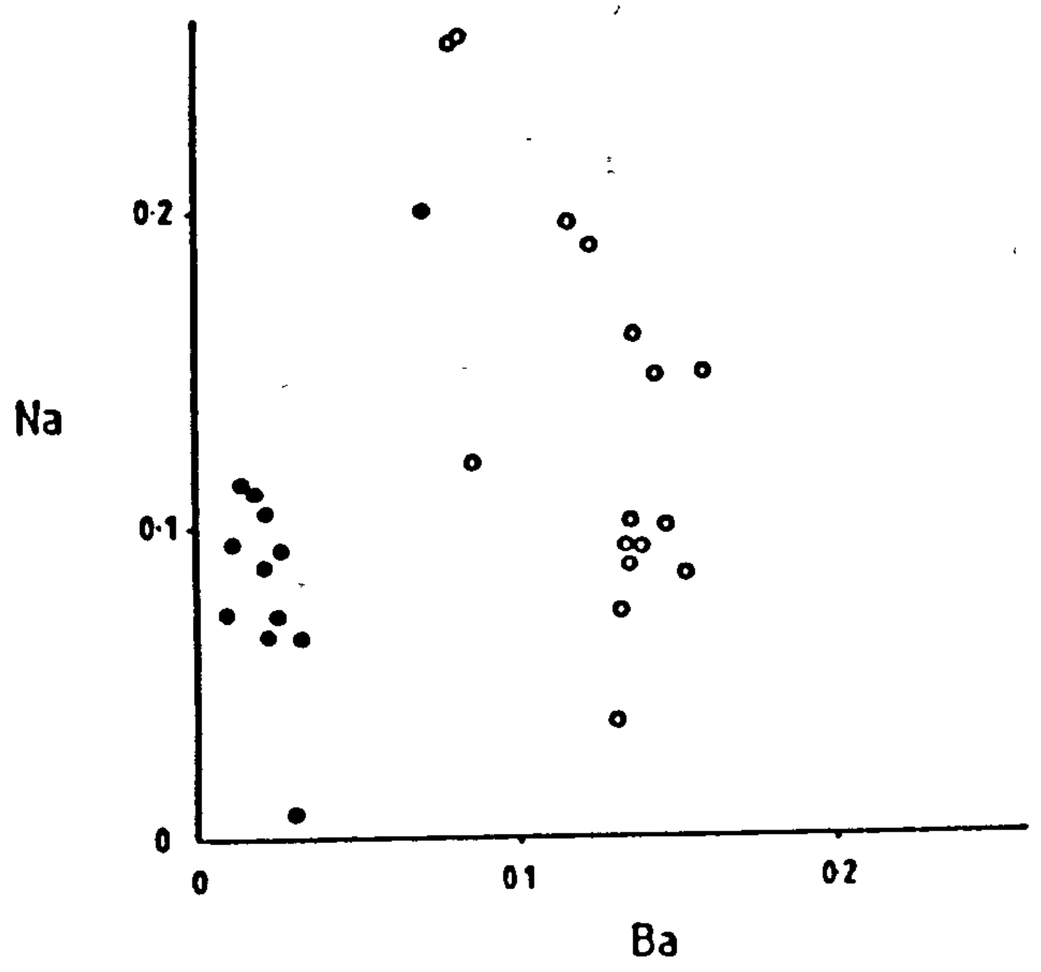
0·2
Na
0·1
0
0
01
02
Ba

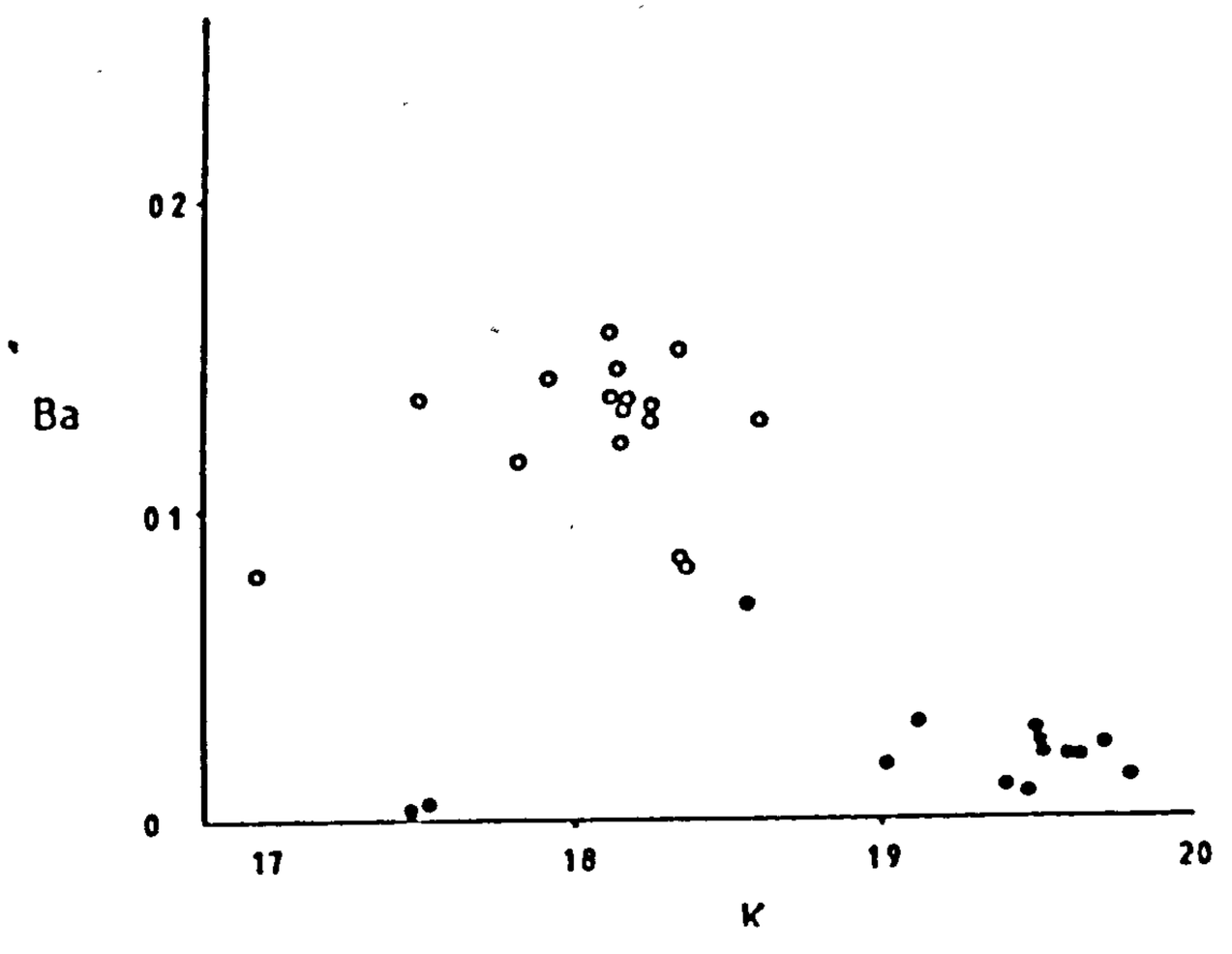
02
Ba
01
0
17
18
19
20
K

The incorporation of the Ba into the muscovite lattice may occur by two substitution reactions (Fortey and Beddoe-Stephens 1982):

$$Ba^{2+} (Mg, Fe)^{2+} = K^{+} Al^{3+} \quad (5.1)$$

and

$$Ba^{2+} Al^{3+} = K^{+} Si^{4+} \quad (5.2)$$

where reaction 5.1 is a combination of the usual phengite substitution in muscovite, $(Mg, Fe)^{2+} Si^{4+} = Al^{3+} Al^{3+}$. Inspection of composition data (Figure 5.2b) shows that in this case, reaction 5.2 is the one most likely to have taken place. Ba-K zoning may derive from original fluctuations in the Ba-K content of the K-feldspar. This is a more likely explanation than later diffusion of Ba and K which can not account for the oscillatory nature of the zoning.

Within the Sonnblick gneisses, metamorphism is not simply related to changes in PT conditions associated with the relaxation of isotherms after emplacement of the Adriatic Peninsula onto the European foreland. Shear zones have commonly undergone hydrothermal metamorphism associated with the syndefomational infiltration of a fluid phase into the zone. This often results in the development of white mica at the expense of feldspar phases. A detailed discussion of the processes and mechanisms associated with metasomatism within high strain zones is given elsewhere (Chapter 6). The fact that these zones are folded by F_3 folds suggests that this hydrothermal metamorphism is overprinted by Alpine regional metamorphism.

5:2.2 Amphibolite Units

Amphibolite units contain an assemblage of calcic amphibole, plagioclase, epidote, biotite, chlorite and quartz and opaque phases and in one sample contains garnet. A strong metamorphic banding and foliation is common and is defined by both tabular and lath-like forms of amphibole. A preferred orientation of amphibole, parallel to the external amphibolite foliation, is often recorded enclosed within plagioclase feldspar.

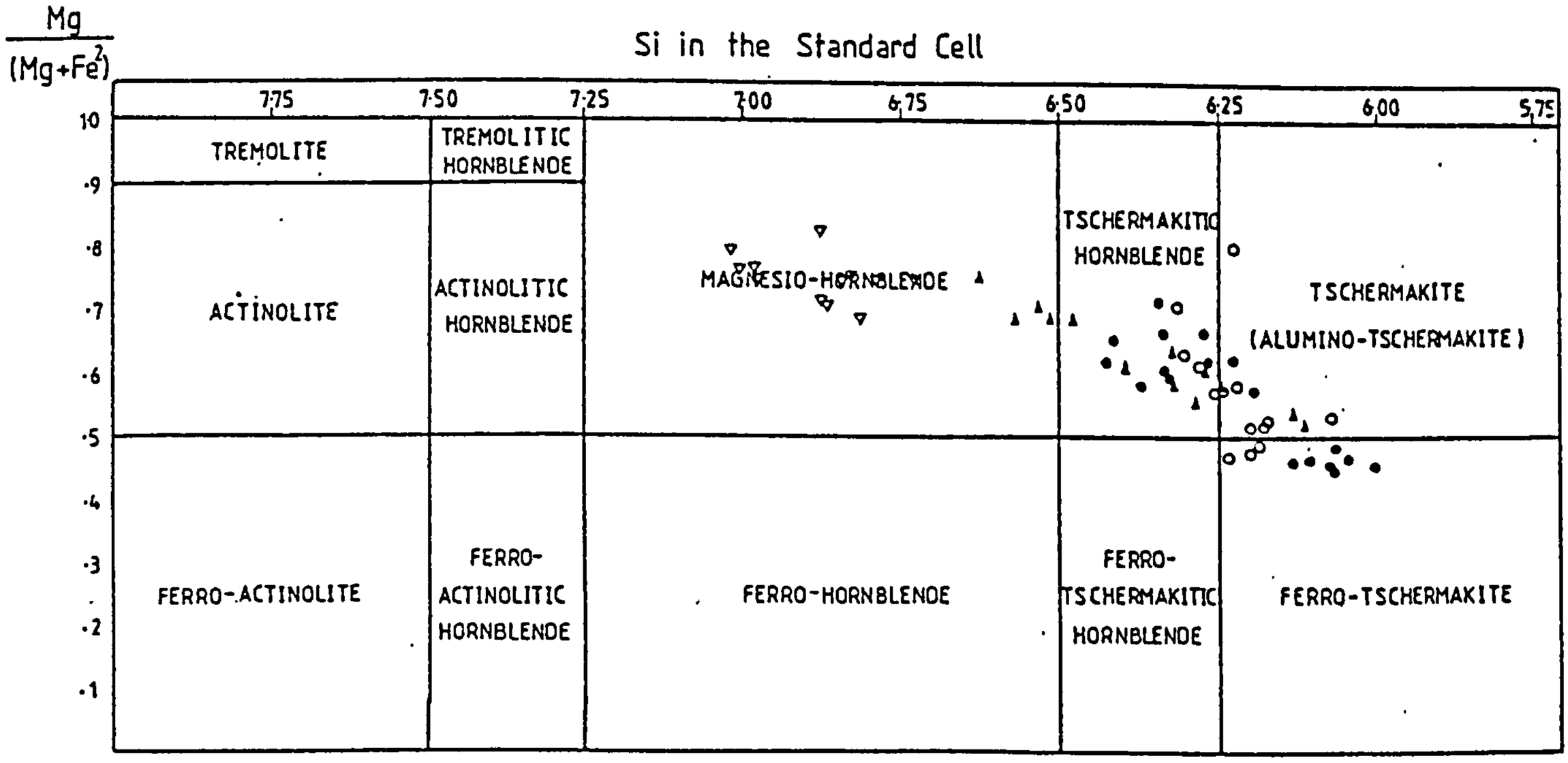

Figure 5.4. Classification diagram for calcic amphiboles after Leake (1978). (▲) = garnet amphibolite (sample 48/88), (▽) = amphibolite (sample 7694), (●) Inner Schieferhülle schist (amphibole shown in Figure 5.9a), (○) = Inner Schieferhülle schist (amphibole shown in Figure 5.9b).

Metamorphic reactions within mafic schists are commonly continuous so that at increasing grades actinolite is replaced by hornblende and plagioclase compositions change from albite to oligoclase. This enables estimates of metamorphic conditions to be made, based simply upon the composition of these mineral phases.

Following the classification of Leake (1978), amphibole compositions (Appendices 4.3 and 4.4) vary from magnesio-hornblendes through to tshermakites (Figure 5.4). These compositional data have been plotted onto formula proportion discrimination diagrams (Laird and Albee 1981) in order to constrain the conditions of amphibole growth (fig 5.5). Amphibole compositions are consistent with growth during garnet zone, lower amphibolite conditions and with formation at "medium pressures" of around 6kbars at 500-550°C (Laird and Albee 1981). This estimate is consistent with compositions of plagioclase which often show reverse zoning from albitic core compositions (An_{13}) to more calcic rims (An_{27}) (Appendix 4.3). This suggests that feldspar growth took place in conditions of increasing temperature.

Figure 5.5. Formula proportion discrimination diagram for amphibolites in mafic schists (after Laird and Albee 1981). Amphibole compositions from analysed Sonnblick Mafic amphibolites generally correspond to the medium P series and have compositions characteristic of the garnet zone.

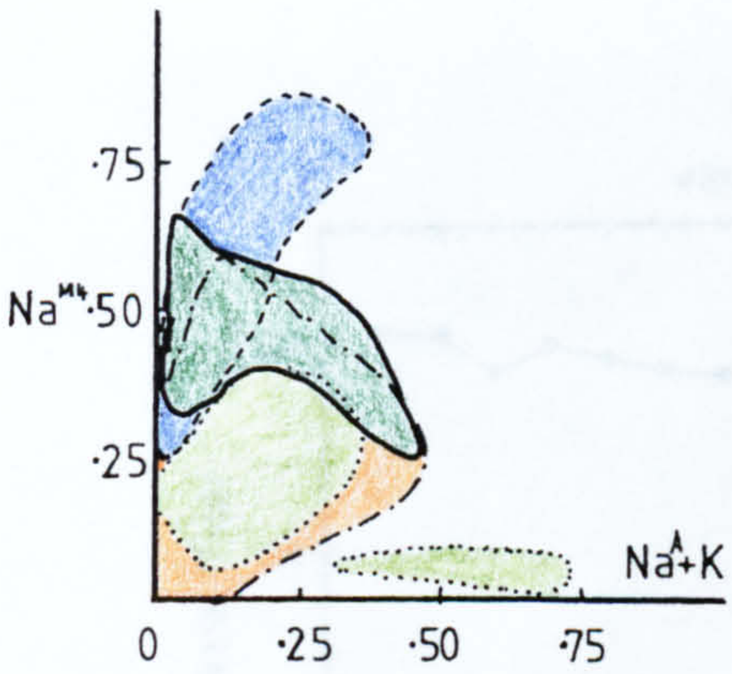
·75
Na^{M4} ·50
·25
$Na^{A}+K$
0
·25
·50
·75

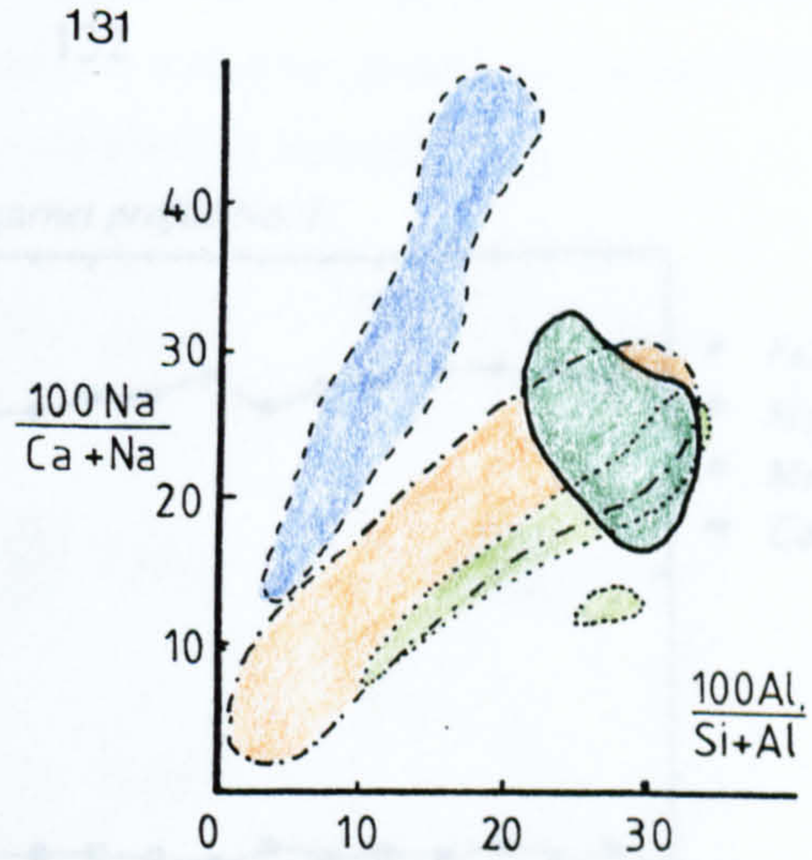
40
30
100 Na / Ca+Na
20
10
100 Al / Si+Al
0
10
20
30

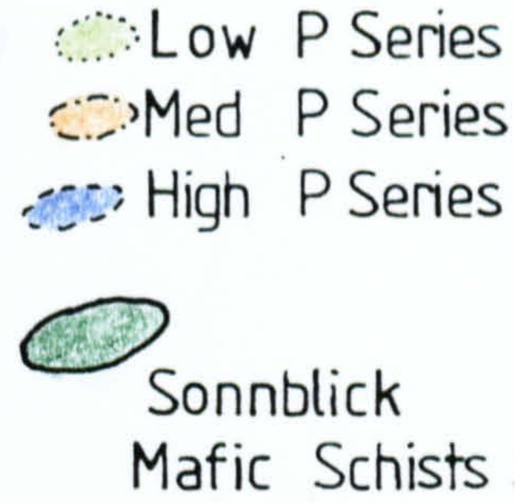
Low P Series
Med P Series
High P Series
Sonnblick
Mafic Schists

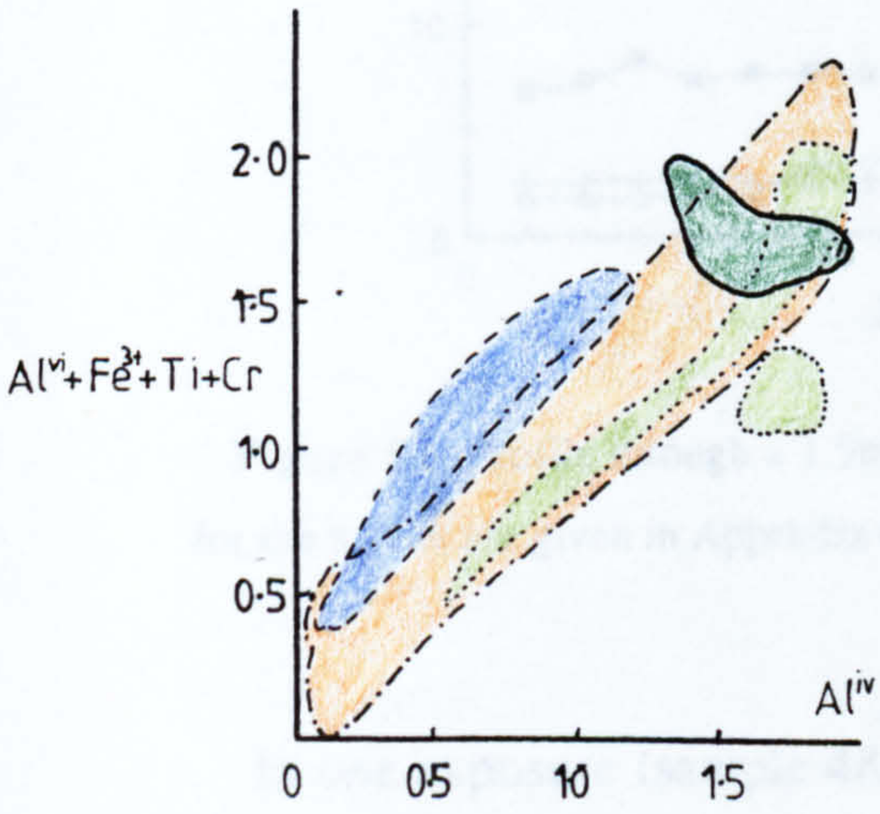
2·0
1·5
$Al^{vi}+Fe^{3+}+Ti+Cr$
1·0
0·5
Al^{iv}
0
0·5
1·0
1·5

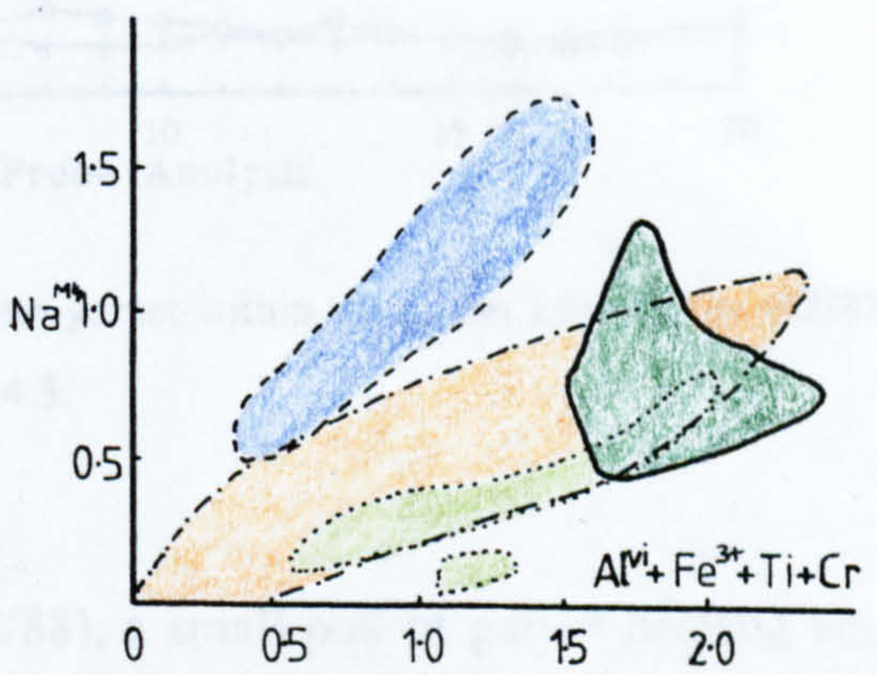
1·5
Na^{M4} 1·0
0·5
$Al^{vi}+Fe^{3+}+Ti+Cr$
0
0·5
1·0
1·5
2·0

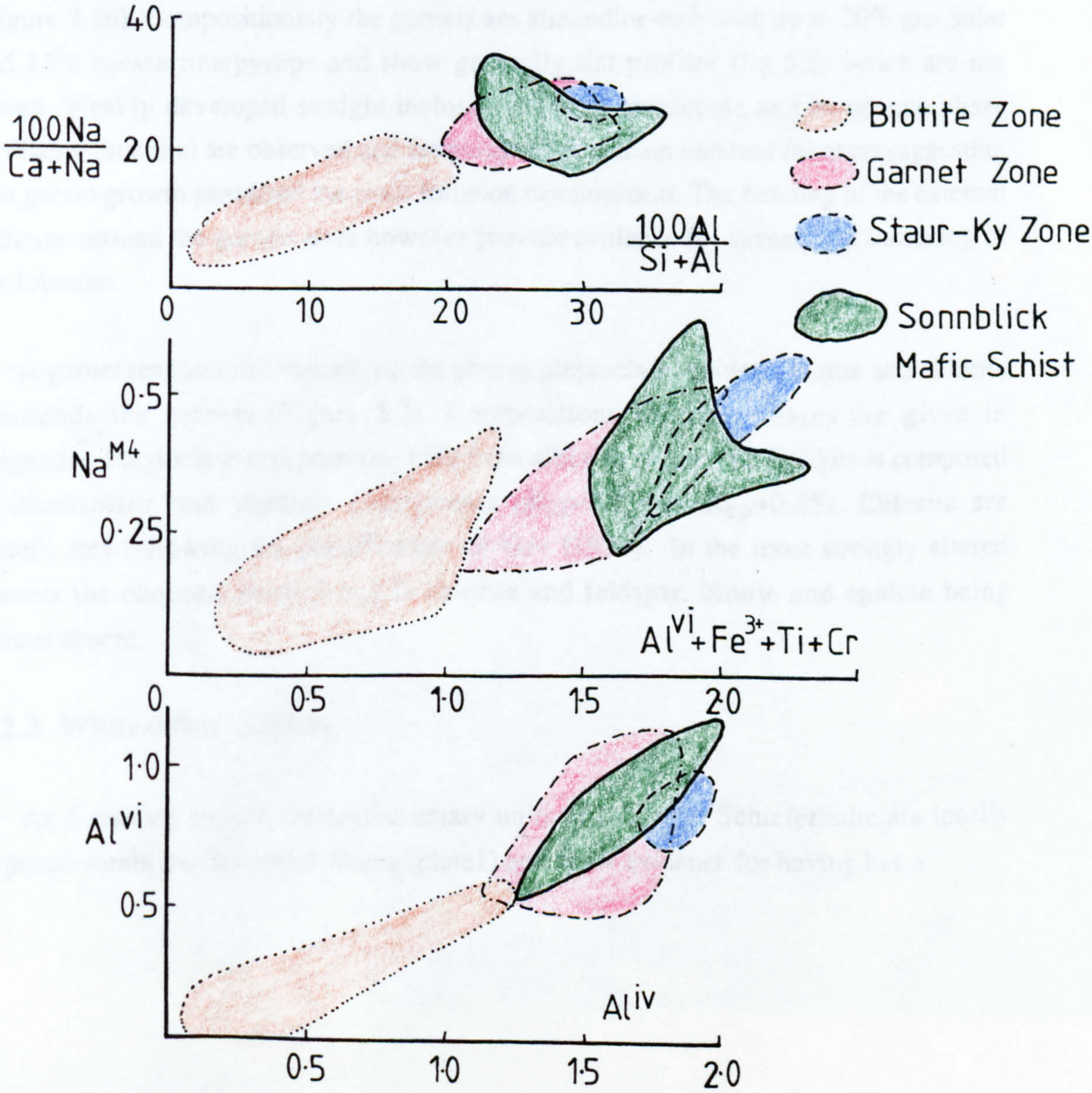
40
100Na / Ca+Na
20
100Al / Si+Al
0
10
20
30
0·5
Na^{M4}
0·25
$Al^{vi}+Fe^{3+}+Ti+Cr$
0
0·5
1·0
1·5
2·0
1·0
Al^{vi}
0·5
Al^{iv}
0·5
1·0
1·5
2·0
Biotite Zone
Garnet Zone
Staur-Ky Zone
Sonnblick
Mafic Schist

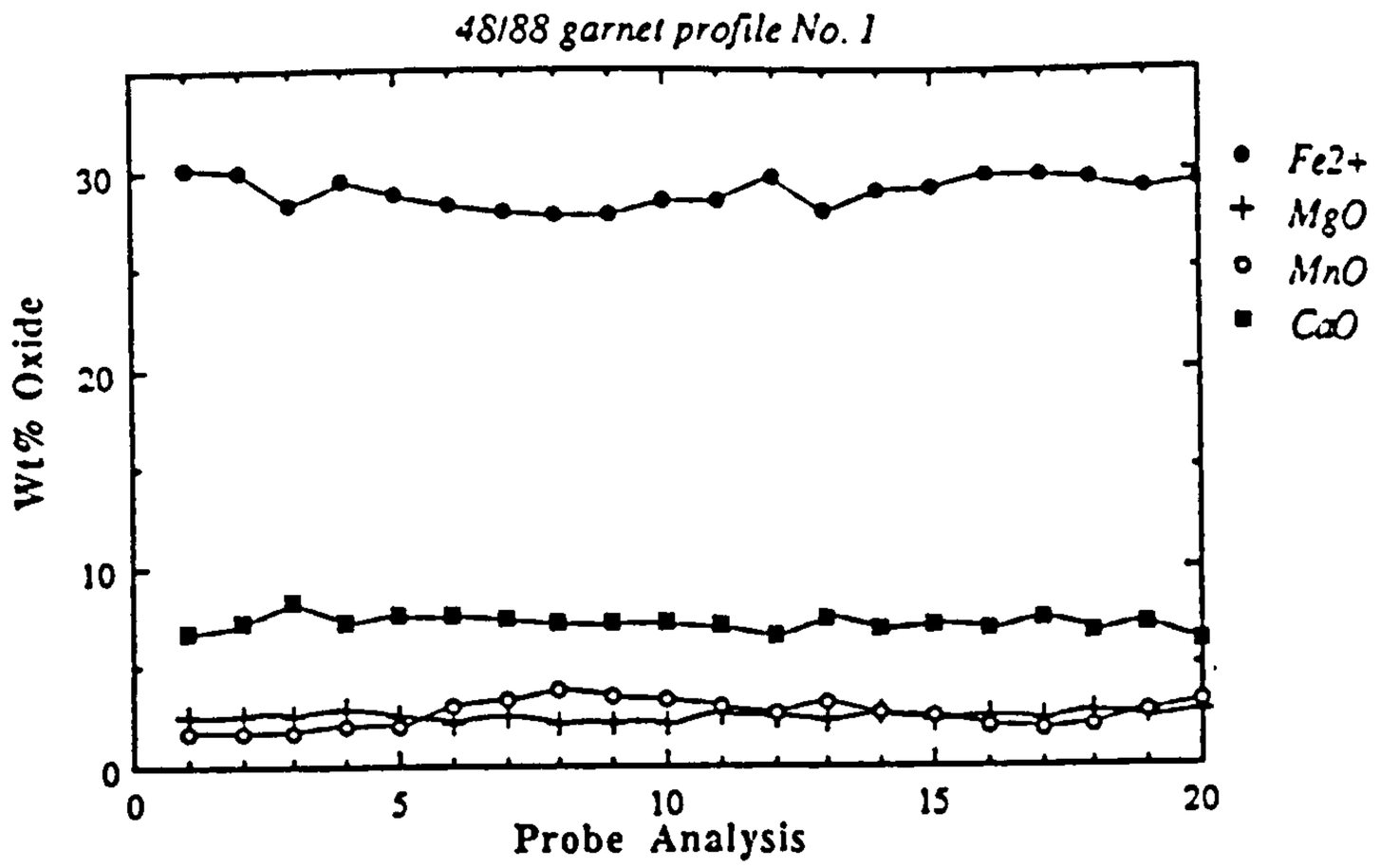

Figure 5.6. Profile through a 1.5mm garnet within the garnet amphibolite (48/88). Probe data for the profile are given in Appendix 4.3.

In one exposure (sample 48/88), a small pod of garnet bearing amphibolite, seen within a larger sheet of garnet-free amphibolite, contains garnets up to 5mm in diameter (Figure 3.3b). Compositionally the garnets are almandine-rich with up to 20% grossular and 15% spessartine/pyrope and show generally flat profiles (fig 5.6) which are not zoned. Weakly developed straight inclusion trails of amphibole and an opaque phase (probably ilmenite) are observed and are parallel to the main external foliation suggesting that garnet growth postdated the main foliation development. The bending of the external foliation around the garnets does however provide evidence for subsequent flattening of the foliation.

A garnet reaction rim containing the phases plagioclase, epidote, biotite and chlorite surrounds the garnets (Figure 5.7). Compositions of these phases are given in Appendix 4.3. Plagioclase compositions vary from albite to oligoclase. Epidote is composed of clinozoisite and pistacite components ($X_{cz} \approx 0.3$ and $X_{ep} \approx 0.65$). Chlorite are ripidol ites following the classification of Hey (1954). In the most strongly altered garnets the common mineral ogy is chlorite and feldspar, biotite and epidote being almost absent.

5:2.3 White-Mica Schists

As discussed earlier, metasedimentary units of the Inner Schieferhulle are locally exposed within the Sonnblick Dome (plate1) and show evidence for having had a

Figure 5.7. SEM atomic number contrast backscatter micrograph of garnet breakdown textures within the garnet amphibolite (48/88). Numbered spots refer to probe analyses given in Appendix 4.3.

garnet
feldspar
epidote
chlorite
biotite

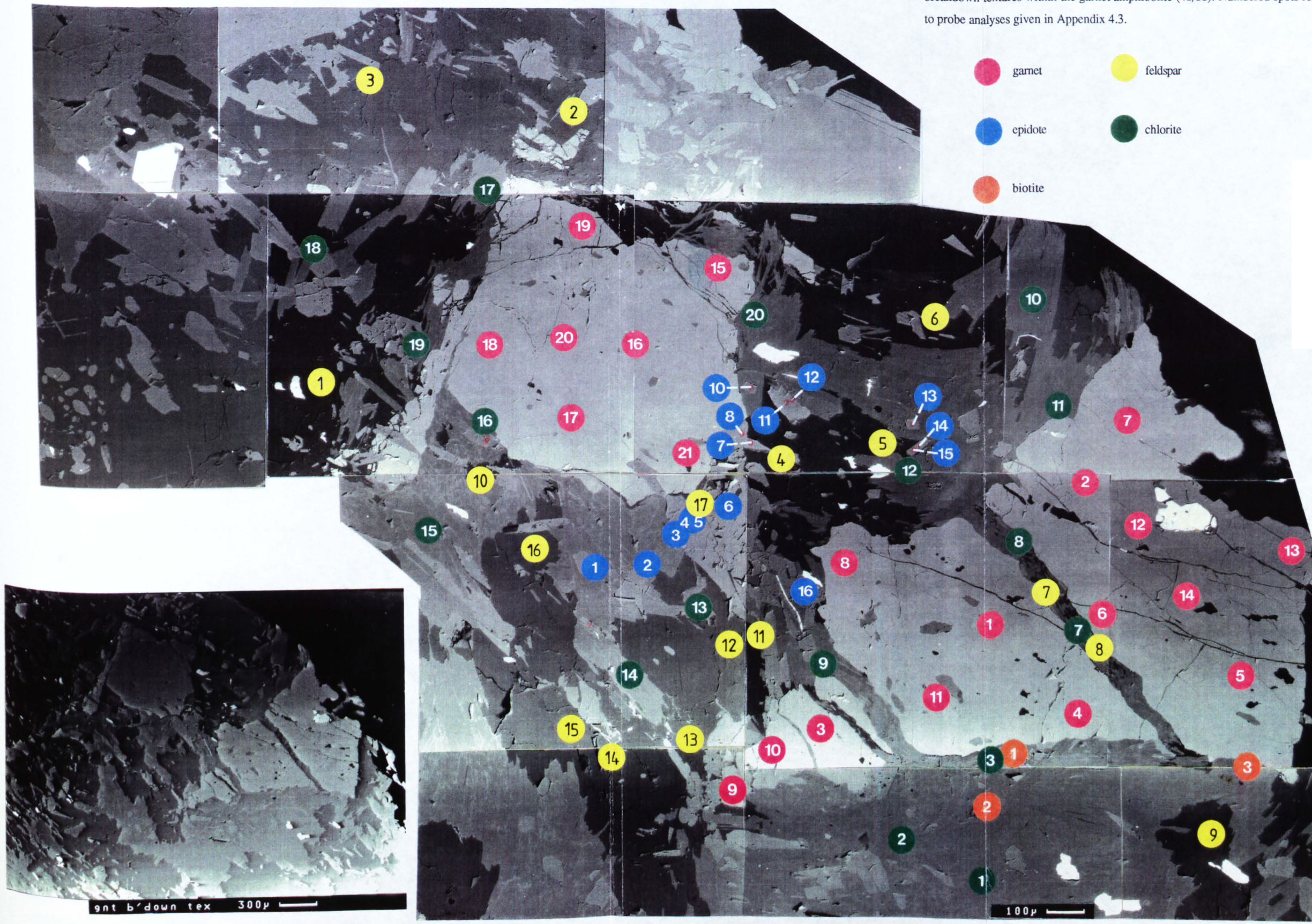

complex metamorphic and structural history. Several mineral assemblages are present within these schists and these may be used to constrain metamorphic conditions.

Observed assemblages include qtz-wm-gt-chl-ctd schists and gt-amph-bte-chl-wm-qtz schists. The first of these is found within schists of the Inner Schieferhülle at relatively low structural levels of the Dome (grid ref. 162066) and also within the Peripheral Schieferhülle, above the Dome at the Bogenitze Scharte (grid ref. 123067). Projection of these phases from quartz-muscovite and H_2O on to the AFM diagram of Thompson (1957) shows the assemblage to plot in the gnt-ctd-chl field of the diagram (Figure 5.8). This suggests garnet grade metamorphic conditions and a relatively aluminous bulk rock composition which could develop staurolite at higher grades. The presence of muscovite, chlorite and chloritoid and absence of staurolite suggests temperatures below 550°C (Hoschek 1969) assuming pressures in the order of 7kbars (Droop 1985). The chloritoid bearing assemblage is also present within units of the Peripheral Schieferhülle at Bogenitzen Scharte and suggests similar metamorphic grades at lower and higher structural levels of the Dome.

The amphibole bearing schists contains complexly zoned garnets and relict amphiboles, pseudomorphed by biotite and chlorite (fig 5.9) and do not represent an equilibrium assemblage. Chlorite is also found in stacks with biotite and textural

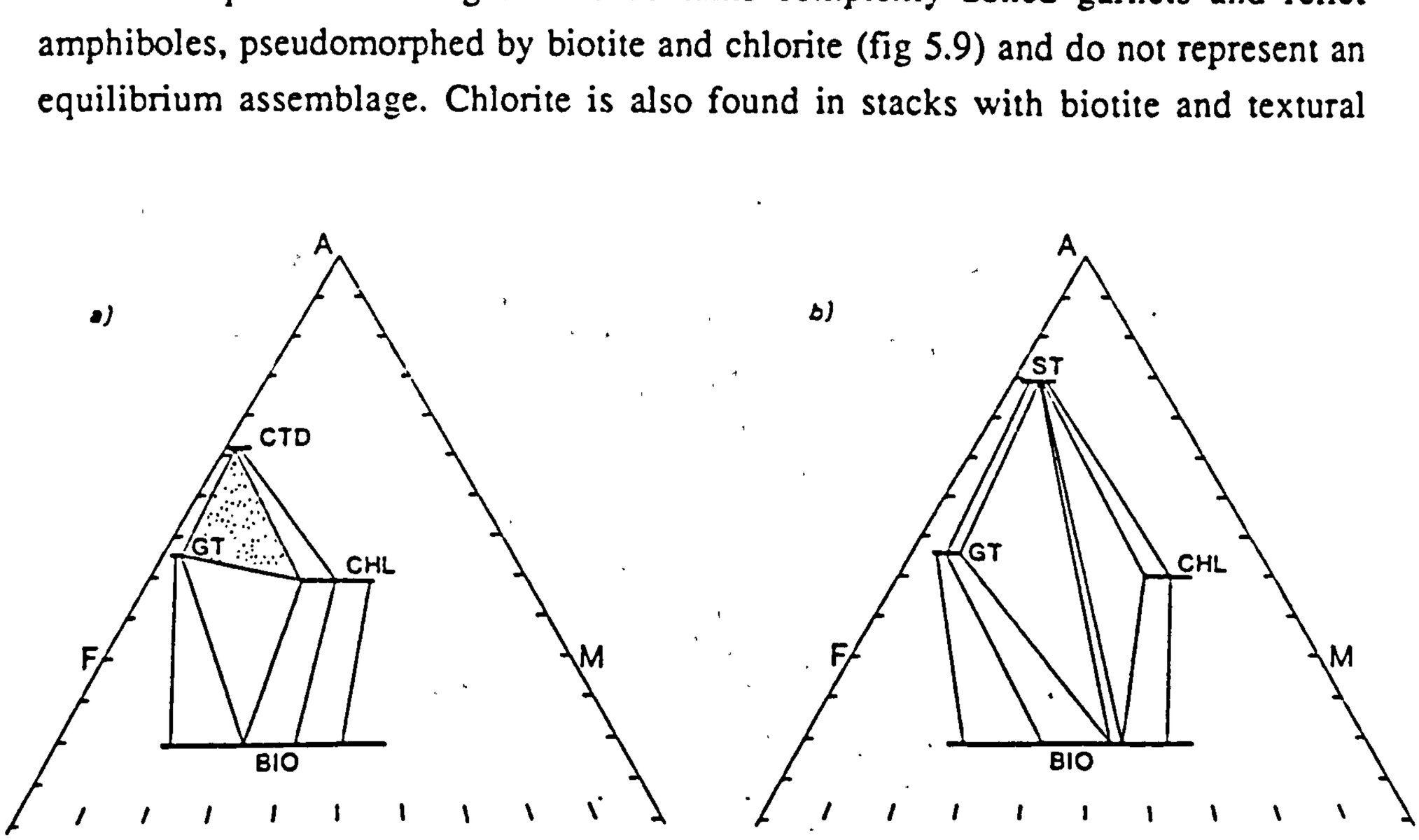

Figure 5.8. AFM assemblages projected from quartz, muscovite and H_2O. a) garnet zone, showing divarient and trivarient fields, and b) staurolite zone (after Yardley 1989). Shaded area corresponds to the observed gt-ctd-chl assemblage.

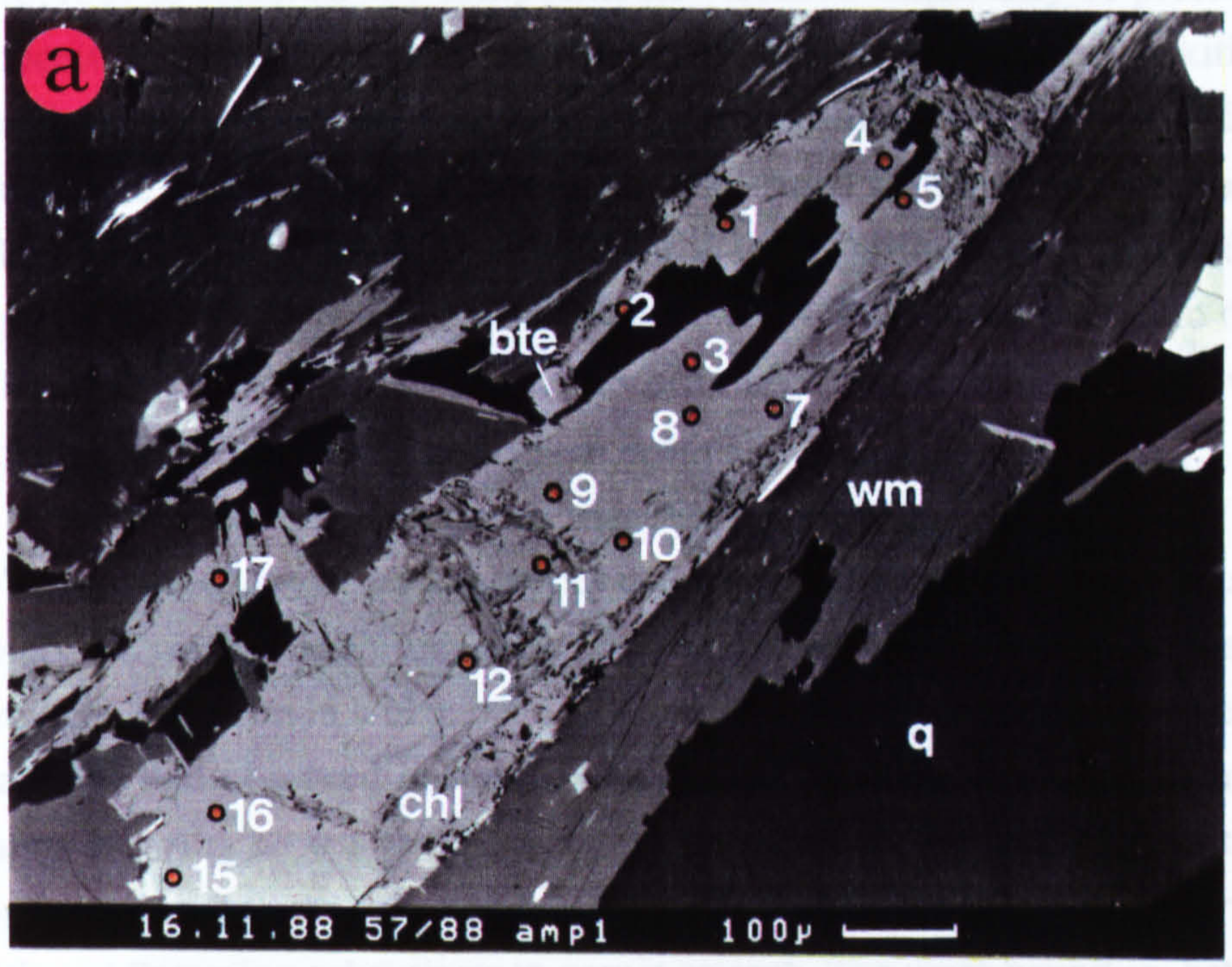

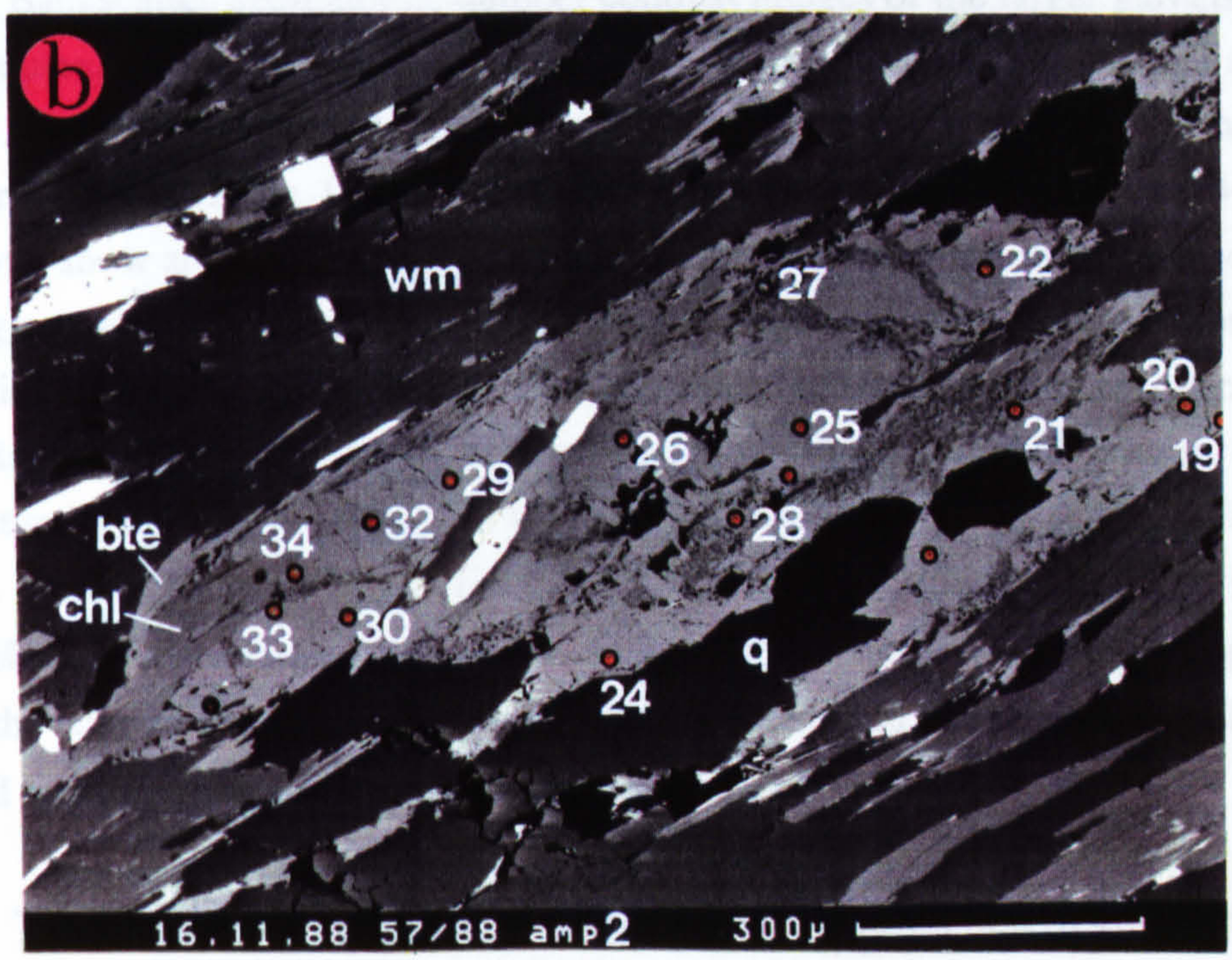

Figure 5.9. SEM Z-contrast backscatter micrographs of relict amphiboles in an Inner Schieferhülle mica schist (57/88). Numbers refer to microprobe analyses given in Appendix 4.5. Amphiboles show reaction to chlorite and biotite often along fractures perpendicular to the amphibole long axis. Quartz and white mica make up the matrix.

evidence is equivocal as to whether chlorite in the rock is in equilibrium with biotite. Two amphibole grains, showing a minimum of alteration, have been studied by microprobe to establish any compositional variation which may be present. Amphibole compositions (Appendix 4.5) are observed to vary from tschermakitic hornblende through tschermakite to ferro-tschemakite. Compositions in the two amphiboles follow a similar trend but no systematic zonation is associated with this trend. The amphibole data are plotted for comparison with amphiboles in the classification diagram of Leake (1978) (Figure 5.4). This shows that the amphibole compositions are similar to those observed in the mafic amphibolites. The compositions of biotite and chlorite, which replace amphibole in the schist, are also given in appendix 4.5.

Two distinct garnet textural types can be distinguised in these schists. Firstly large garnets (~2mm), which are optically zoned and consist of an inclusion free core surrounded by a rim in which opaque inclusions of ilmenite preserve an earlier foliation parallel to that observed in the external matrix. Secondly, small (<0.5mm), euhedral garnets growing across the main foliation which are fringed by biotite and chlorite growing parallel to the foliation and show foliation perpendicular fracturing suggesting continued flattening subsequent to garnet growth. The clear boundary between core and rim garnets suggests that they grew under different metamorphic conditions.

Backscatter SEM atomic number contrast images of the larger garnets reveal further complexities of the zoning (Figure 5.10), which along with geochemical data (Figure 5.11 and Appendix 4.5), enable three discrete zones to be distinguished (Fig 5.12). Garnet cores (Zone 1) having an average composition of 35%alm, 46%sp, 13%gr, 3%py show an irregular, often angular, morphology and appear to be made up of garnet aggregates or clusters. These form "islands" when surrounded by a second garnet zone which is in the order of 100μm wide and has a higher almandine component (Fig 5.12). This irregular morphology is inconsistent with continuous growth of garnet and texturally appears to support a two-stage growth model for the optically defined 'core' of the garnet. The optically defined 'rim' records a continuous variation from 47%alm, 31%sp, 16%gr, 3%py at its contact with zone 2 garnet, to 80%alm, 2%sp, 9%gr, 9%py at the edge of the garnet. These features are illustrated further in triangular diagrams of end member garnet components (Figure 5.11).

Three basic models can be used to explain the formation of zoning within garnets. Firstly isothermal fractionation of elements from the bulk matrix composition during garnet growth. As an example, the partitioning of manganese into garnet is in the region

Figure 5.10. SEM micrographs of zoned garnets in Inner Schieferhülle mica schist (57/88).

a) Secondary electron image showing the profile A-B. Microprobe damage is seen on the surface and can be used to accurately locate probe analyses.

b) Z-contrast backscatter image showing three distinct zones developed within the garnet. Small inclusions (probably ilmenite) in the outer garnet zone (Zone 3) are parallel to the external foliation within the schist sugesting zone 3 post-dated foliation development. A 'small' garnet is seen adjacent to the larger garnet at the bottom right of the micrograph.

c) Micrograph showing the detail of the zoning seen in b). The irregular morphology between zone 1 and zone 2 and the geochemical differences between 2 and 3 suggest three distinct phases of growth.

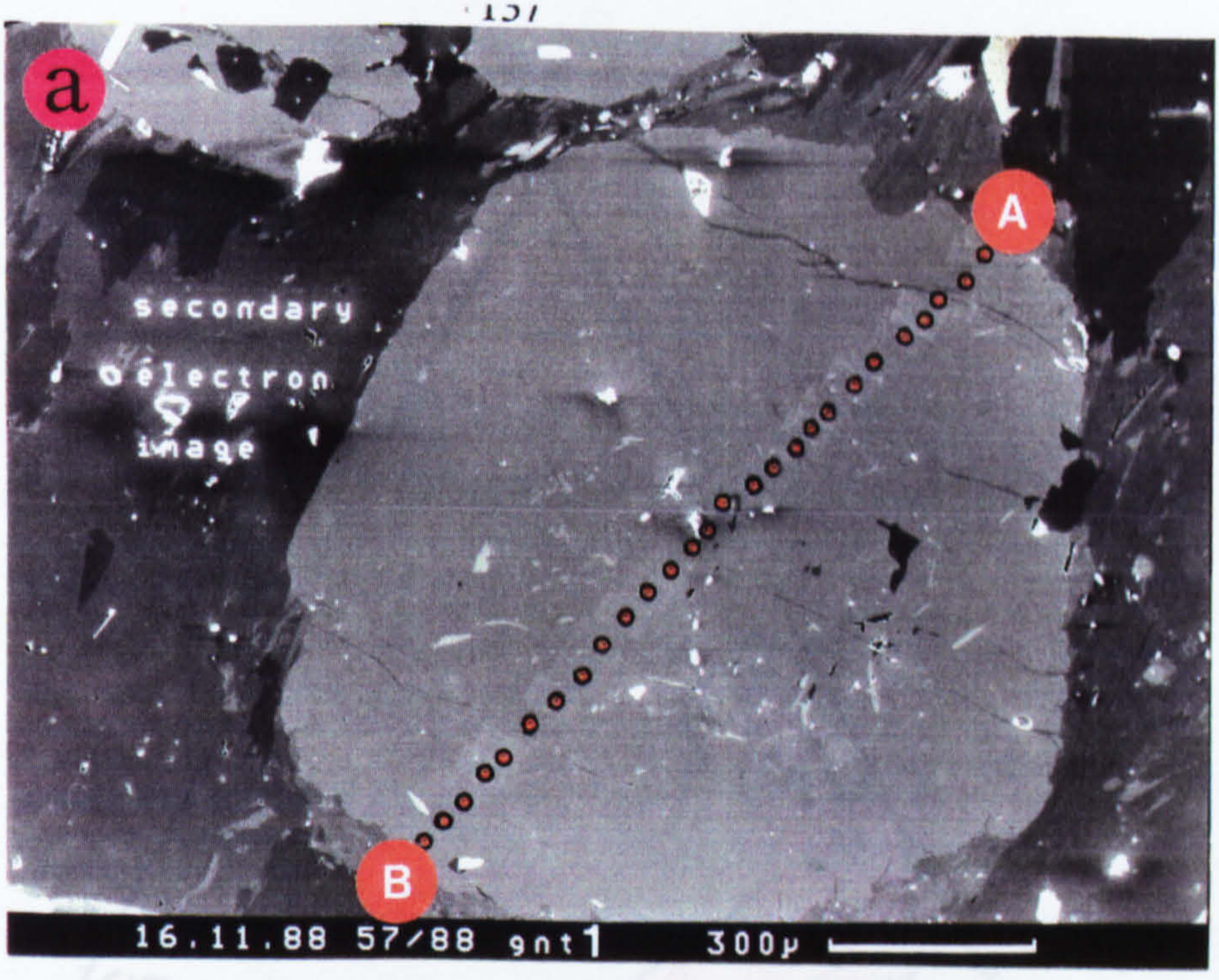
a
secondary
electron
image
A
B
16.11.88 57/88 gnt1
300µ

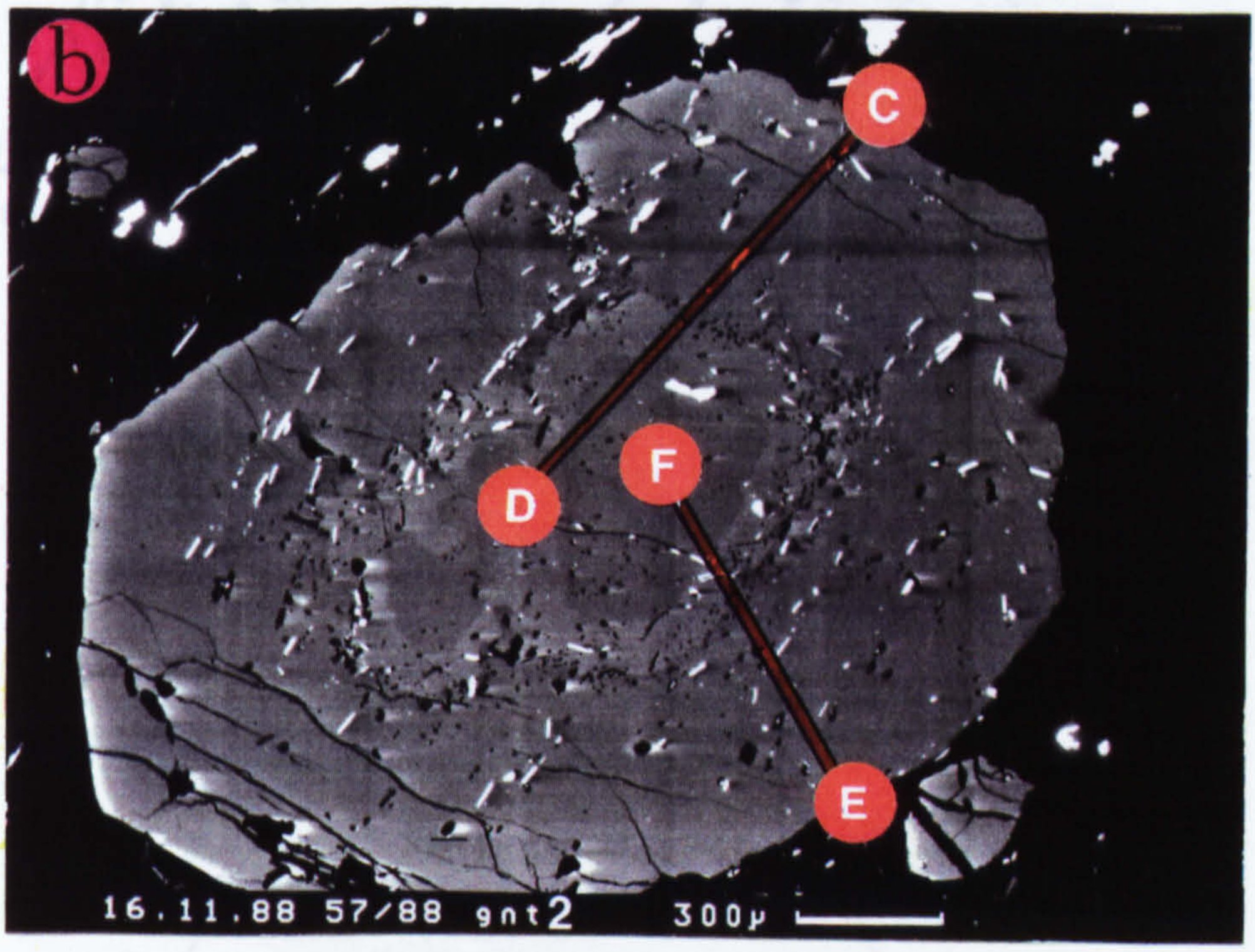
b
C
D
F
E
16.11.88 57/88 gnt2
300µ

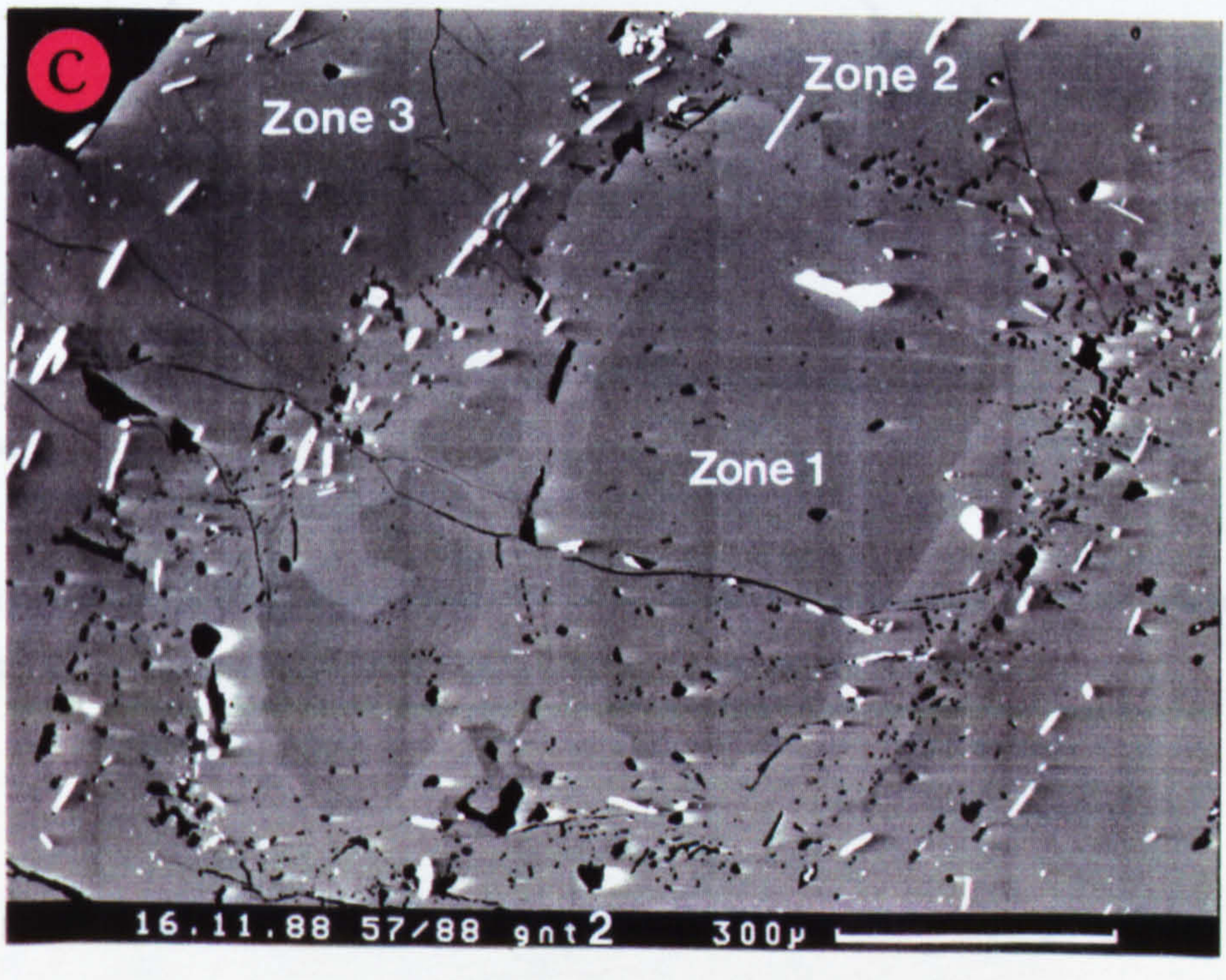
c
Zone 3
Zone 2
Zone 1
16.11.88 57/88 gnt2
300µ

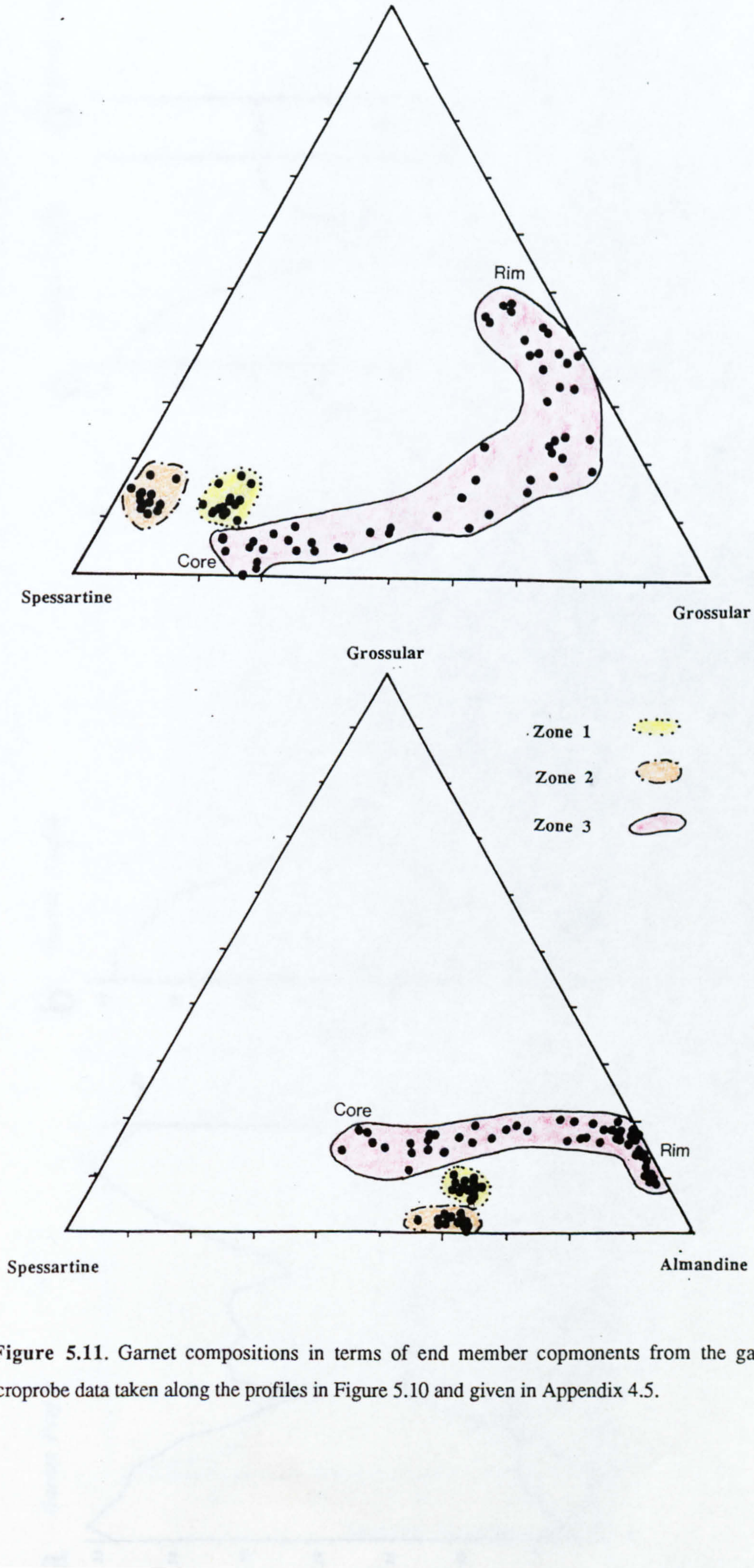

Figure 5.11. Garnet compositions in terms of end member copmonents from the garnet microprobe data taken along the profiles in Figure 5.10 and given in Appendix 4.5.

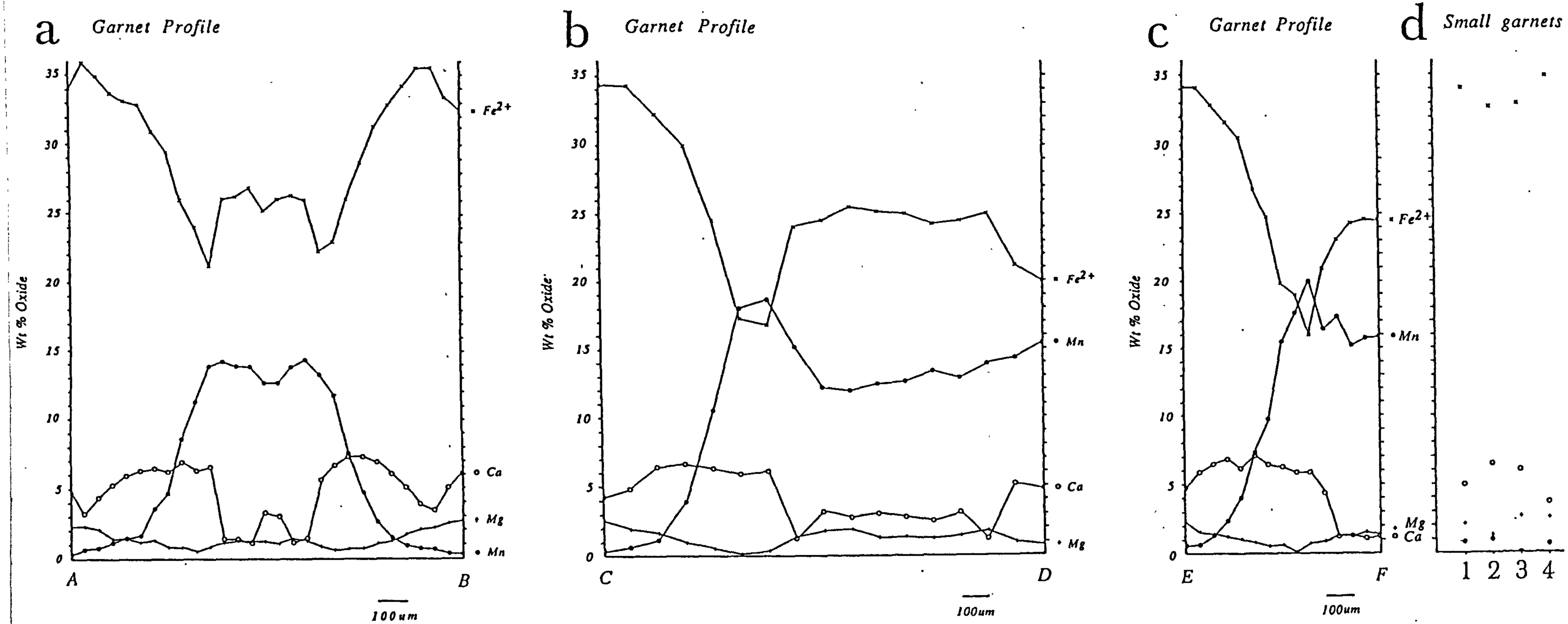

Figure 5.12. a-c) Compositional profiles A-B, C-D and E-F shown in Figure 5.10. d) shows 4 analyses taken of the small garnets. Profiles correspond to data given in Appendix 4.5 (A-B = garnet No. 1; C-D = garnet No. 2a; E-F = garnet No. 2b).

Figure 5.13. Geochemical profile along A-B of Figure 5.10a.

a) $Mg / (Mg + Fe^{2+})$

b) $Mn / (Mn + Ca)$

c) Mn / Fe^{2+}

a)

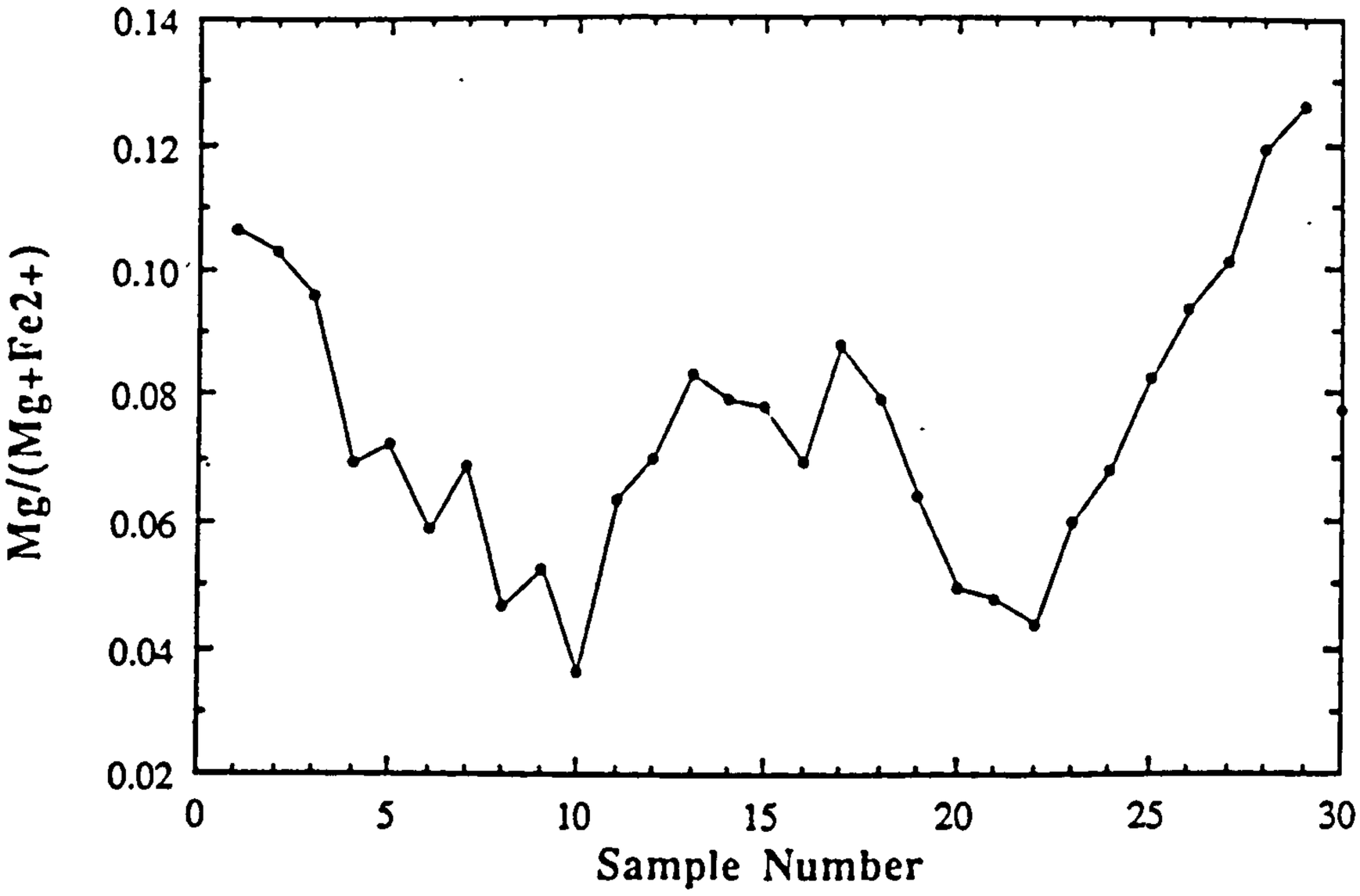
0.14
0.12
0.10
0.08
0.06
0.04
0.02
Mg/(Mg+Fe2+)
0
5
10
15
20
25
30
Sample Number

b)

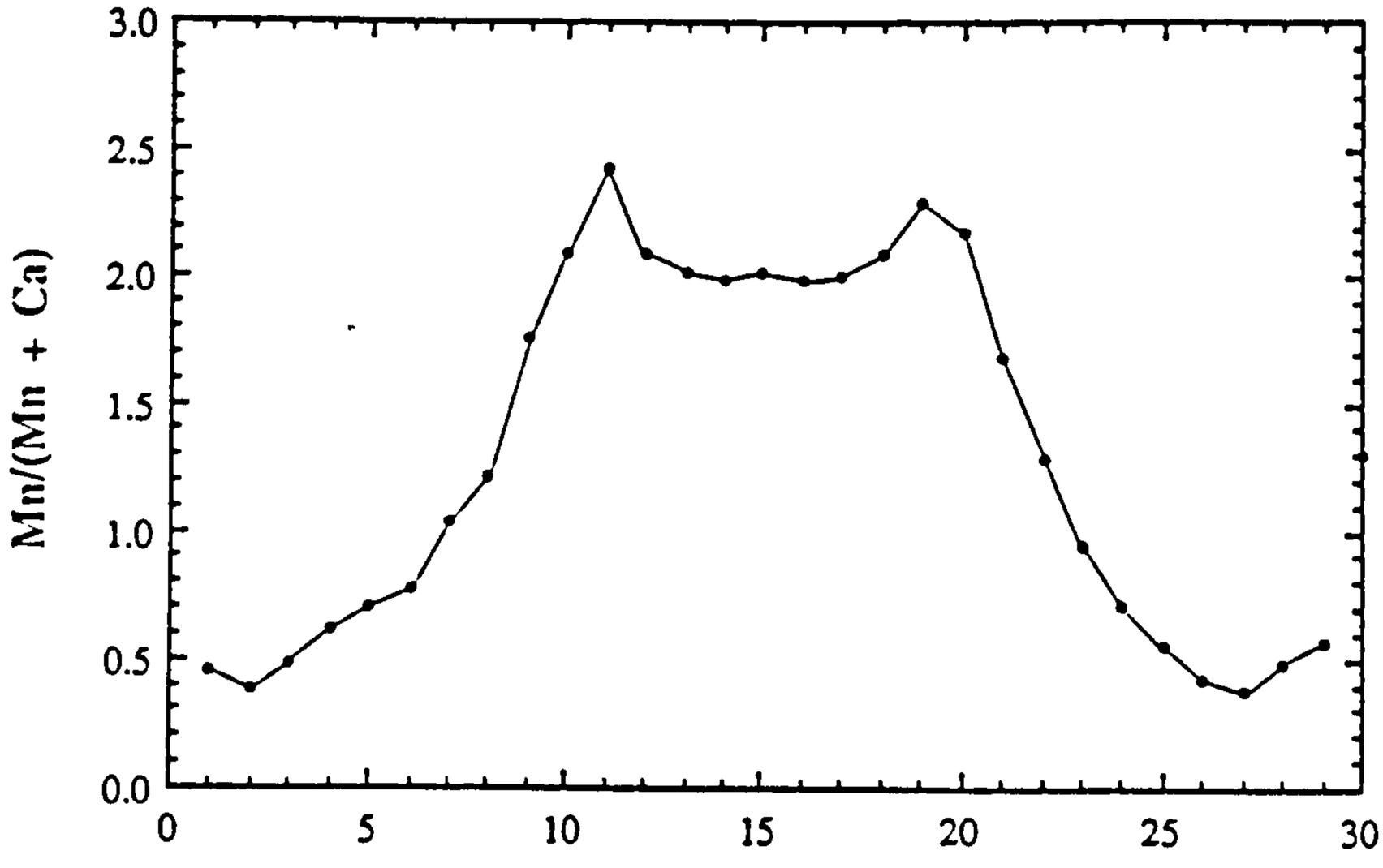
3.0
2.5
2.0
1.5
1.0
0.5
0.0
Mn/(Mn + Ca)
0
5
10
15
20
25
30
Sample Number

c)

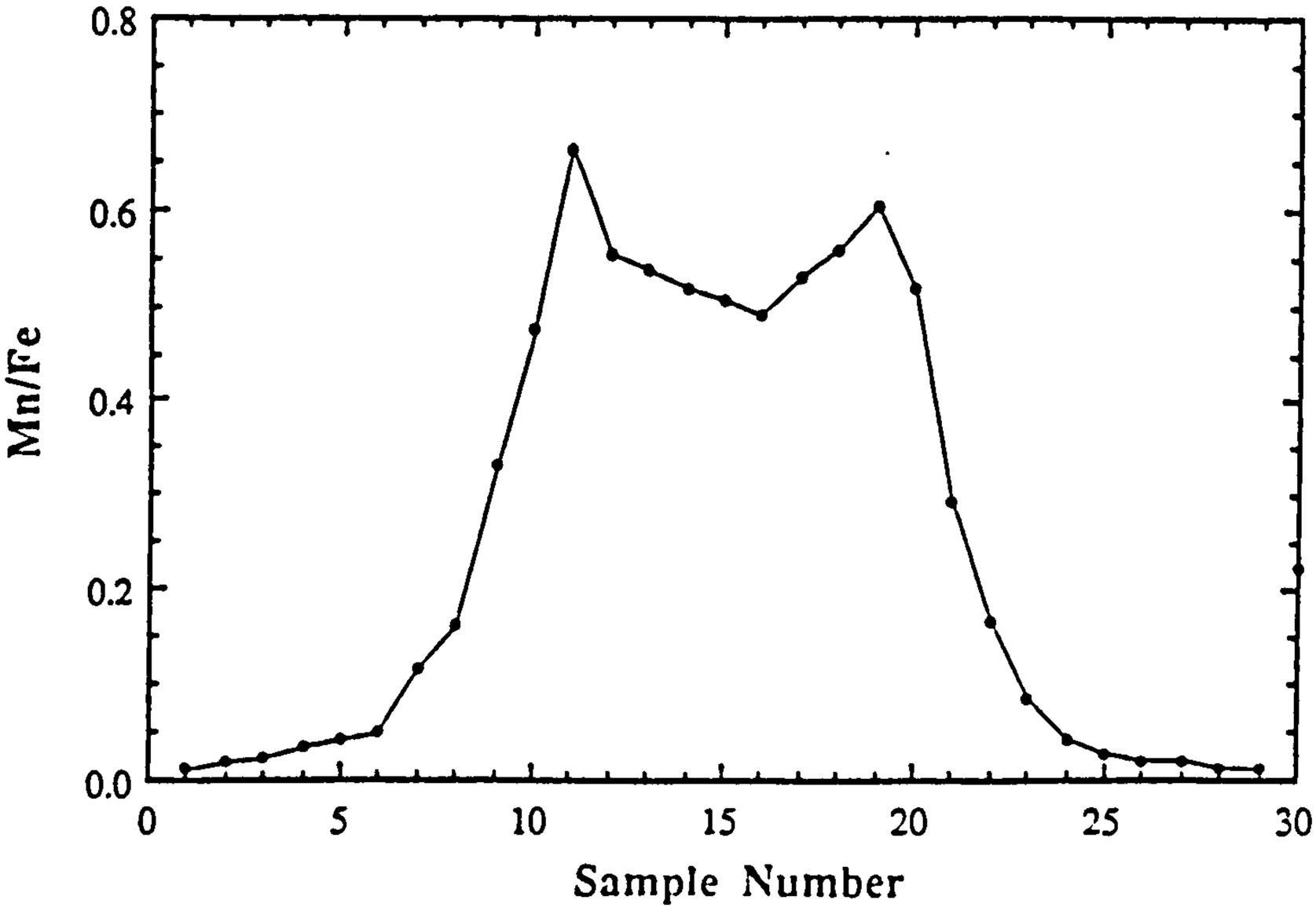
0.8
0.6
0.4
0.2
0.0
Mn/Fe
0
5
10
15
20
25
30
Sample Number

of 40 times that for other ferromagnesian minerals. Fractionation of Mn into garnet therefore occurs rapidly and leads to typical "Rayleigh"-type profiles (eg Hollister 1966). Secondly, elemental diffusion may lead to the formation of chemical zoning either during or after garnet growth (eg Loomis 1978). Finally, the growth of minerals under changing P-T and fluid conditions will alter the equilibrium distribution and partitioning of cations within the mineral and would be expected to produce zoning provided that homogenization of the earlier formed mineral species is restricted by either kinetic or physical means.

Zone boundaries observed by the SEM are clearly seen in the profiles. The garnet zoning profiles (Figure 5.11 an 5.12) show that the three zones are compositionally quite different and do not describe the common 'bell' shaped profiles associated with element partitioning and fractionation (eg. Hollister 1966). The smaller garnets record compositions similar to those observed towards the rims of zone 3 (Figure 5.12d).

Several important features can be seen in the garnet profiles. Firstly, zone 1 is depleted in manganese relative to zone 2 and the extreme fractionation of manganese into garnet, expected to produce a large concentration of Mn at the garnet core, is not observed. The increase in Mn/(Mn + Ca) and Mn/Fe from zones 1 to 2 (Figures 5.13b,c) is evidence for reverse zonation relative to the "normal" fractionating model described by Hollister (1966).

An increase in magnesium to iron ratio has been related to garnet growth under increasing temperature conditions (Thompson *et al* 1977). The increase of Mg/(Mg+Fe) from zone 1 to 2 (Figure 5.13a) may be indicative of increasing temperature during garnet growth. However, the continuous decrease in Mg/(Mg+Fe) across zone 2 sugests growth during decreasing temperature conditions. This contrasts a continuous increase in the in magnesium to iron ratio from core to rim across zone 3, which suggests prograde growth. However, the strong partitioning of manganese into garnet is generally sufficient to overcome slight changes in P-T conditions and the zoning of Ca and Mn are unlikely to be due to varying external conditions, such as T and P, but probably reflects heterogeneous behaviour of the matrix reservoir and cation availability during metamorphism.

From consideration of the grossular component in the garnet, and the significant increase in the grossular component of the garnet within zone 3 garnet, it can be inferred that zone 3 garnet probably developed during breakdown of amphibole and the

formation of biotite. This model for explaining grossular zonation within garnet does not explain the presence of zone 1 garnet or the absence of fractionated Mn profiles from zones 1 and 2.

Similar control of the grossular component in garnet on the breakdown of a calcic phase, has been illustrated by Desmons *et al* (1977), who suggested that plagioclase solid-solution may control Ca fluctuations in garnet. Droop (1981), working on Inner Schieferhülle schists from the area immediately north of the Sonnblick area, has also suggested that a discrete increase in the Ca content in the rims of garnets may have been controlled by the breakdown of Hercynian anorthite to Alpine albite.

The nucleation step of the garnet crystallization is likely to require significant degrees of overstepping and so may be described by disequilibrium growth conditions (Loomis 1983). Increased garnet overstepping has been shown to decrease the spessartine component of garnet, while Mg/Fe ratio increases due to the rise of the Fe-Mg loop on the garnet phase diagram (Loomis 1983). Such growth in terms of disequilibrium growth models (Loomis 1983) can be shown to produce reversely zoned profiles and may explain the zoning profiles observed across zones 1 and 2. The relative ease of nucleation of zone 3 garnet on the earlier garnet phases may have reduced the degree of overstepping required to initiate garnet growth during amphibole breakdown. If this were the case then near equilibrium growth may be expected. This is consistent with the zone 3 profiles which show a normal fractionation trend commonly associated with equilibrium growth models for garnet (Loomis 1983).

The fact that the small garnets only preserve the latter stages of zone 3 growth suggest that they either grew at a relatively late stage with regard to the initiation of zone 3 garnet growth. Since zone 3 garnet is interpreted to have developed during increasing temperature conditions, this would suggest that the small garnets nucleated at higher temperature than the zone 3 garnet, developed on the surface of zone 2 'cores'. Thus, the delay in nucleation of the smaller garnets may be due to the increased overstepping required to nucleate the small garnets relative to that required to continue growth around the previously developed garnet.

The outer margins of the garnets occasionally show strong zoning in Ca and Fe. This zoning cannot be explained by simple resorption of the garnet since no change in Mn is observed. It may represent later growth associated with the flattening of the foliation around the garnet. Diffusive reequilibration with the immediate matrix may have

occured. However, these rims appear to be spatially related to sites of low stresses and appear adjacent to the strain shadows around the garnets. This may suggest that they grew as a response to deformation in the rock and sites of extension provided sites suitable for small volumes of late garnet growth.

5:3 Geothermometry and Geobarometry

In this section, thermobarometric techniques are used to estimate the P-T conditions at which metamorphism within the Sonnblick area took place. Since the gneisses are by far the volumetrically most important lithology within the Sonnblick Dome, an ideal appoach would be to apply thermobarometers to the granitic gneiss lithologies so that metamorphic conditions at different structural levels may be assessed. There are several experimentally- and theoretically- derived thermobarometric formulations which may be applied to typical gneiss assemblages. In the following section these are assessed and, where considered reliable, are applied to the gneiss assemblage. The preserved small areas of semi-pelitic schists and amphibolites provide other assemblages which may be used to infer metamorphic conditions and hence test those temperatures and pressures derived from the gneisses. Unfortunately, these do not have the spatial distribution to enable metamorphism at different levels of the Dome to be assessed.

5:3.1 Feldspar Thermometry

Feldspar geothermometry has been considered a viable method of investigating recrystallization and mineral equilibration during metamorphism and is based on the partitioning of feldspar end-member components between coexisting plagioclase and alkali feldspar. The thermometer relies upon the equilibrium condition that the chemical potential of albite in each phase must be equal, that is;

$$m_{ab}^{AF} = m_{ab}^{PF} \ .$$

There are two main approaches to feldspar geothermometry, one relying upon a semi-empirical approach, (Barth 1951, 1968; Seck 1971a, b; Brown and Parsons 1981, 1985) the other being based on the thermodynamic mixing properties of the feldspars (Stormer 1975; Powell & Powell 1977; Haselton *et al* 1983; Price 1985; Green & Usdansky 1986a).

The experimental approach is limited because feldspar experiments to date have not been reversed and have not established complete equilibrium between the two feldspars Experimentalists in the past have relied on the estimation of albite compositions from orthoclase compositions (Seck 1971a,b; Johannes 1979), while the early models of Barth (1951) failed to recognize the effects of pressure, Al-Si ordering and bulk composition, as well as temperature on the equilibrium feldspar compositions. Modifications to the Seck thermometer (Brown and Parsons 1981) cannot account for the problems associated with poor compositional constraints on Seck's original experimental dataset and doubts are therefore cast on the validity of the thermometers developed in the last decade.

The early thermodynamically calibrated feldspar thermometers (eg Stormer 1975) fail to account for the affects of minor components on feldspar activity-composition relations (eg. Stormer 1977; Powell and Powell 1977) and also rely strongly on the state of order of the feldspar lattice and the assumed mixing parameters (Brown and Parsons 1981, 1985). The limited data for natural feldspar mixing parameters suggests that a theoretically derived thermometer will be difficult to apply to natural assemblages. This has been illustrated by temperatures obtained using mixing parameters derived for ordered and disordered structural states applied to the feldspar data of Stormer (1975) and Whitney and Stormer (1977) which show differences of up to 150°C (Ferry 1978). Finally, the assumption that the structural state of the feldspar during growth is represented by the present structural state of the feldspar and the problem of the peristerite gap at amphibolite facies conditions, place further constraints on the use of thermodynamically modelled feldspar thermometers.

The problems illustrated above would also be expected to affect other thermodynamically derived thermometers which have been based on either ideal site mixing parameterizing the dataset of Seck (1971a,b) or previously published or calculated ternary feldspar mixing relations (Ghioso 1984; Price 1985; Green and Usdansky 1986a).

Application of Sonnblick data to the determinitative curves of Stormer (1975, figure 3) suggests temperatures of between 400-500°C for geological reasonable pressures up to 10kbars. Given the limitations of the two-feldspar thermometer with regards to minor components, the lack of knowledge on the degree of ordering, the limited data on feldspar mixing properties and the difficulty in interpreting published mixing parameters (Bachinski and Müller 1979), the application of feldspar thermometers must

be limited to those conditions and compositions for which they were specifically calibrated. Furthermore, these factors also make the significance of calculated temperatures difficult to interpret. This casts doubt on the use of the feldspars to infer metamorphic temperatures. For these reasons, temperatures calculated for the Sonnblick gneisses by feldspar thermometry are considered to be unreliable estimates of metamorphic temperatures.

5:3.2 Mica Solid-Solution Thermometry

Chemical variations in the white micas can be considered in terms of muscovite - paragonite - margarite (mu-pa-ma) end-members and in terms of the muscovite - celadonite or phengite solid solution series. The muscovite-paragonite solvus has in the past been used to infer peak metamorphic temperatures. However this solvus is of little use because both the experimentally and theoretically derived solvi do not account for the complexities of changing solvi topologies which can be controlled by numerous other factors (see Guidotti 1982 and Chatterjee and Flux 1986). Hence, Chatterjee and Flux (1986, p.691) 'caution against applying the binary mica solvus to natural mica pairs for temperature estimation' and the thermometer is therefore not used in this study.

5:3.3 Plagioclase breakdown Reactions

Experimental work for the equilibrium reaction,

$$2 \text{ zoisite/clinozoisite} + \text{muscovite} + 2 \text{ quartz} = 4 \text{ anorthite} + \text{K-feldspar} + 2 H_2O \qquad (5.3)$$

has been investigated under reverse conditions by Ackermand and Karl (1972). The experiments consisted of equilibrium reactions for both synthetic mineral phases and for natural "gefüllte" plagioclase samples. Derived reaction lines in PT space are shown in Figure 5.14. Both lines show similar gradients ($dP/dT \approx 0.016$) although the natural samples are displaced to lower temperatures by approximately 40°C probably due to this system being impure and possibly due to different structural states of the zoisite in each case.

Equilibrium in the assemblage has been investigated using the Thermocalc program of Powell and Holland (1988) which utilizes an extended, internally-consistent data set (Holland and Powell pers.comm. 1988 and 1989). The thermodynamic mole-fractions of the end member phases have been calculated from electron microprobe data assuming

ideal mixing (Powell 1978). Activity coefficients for muscovite and paragonite are calculated from the Margules parameters and mixing expressions of Chatterjee and Froese (1975) and have values of 1.43 and 3.04. No data for non-ideality is available for mixing between celadonite and other white mica phases. The activity of anorthite in plagioclase is calculated by,

$$a_{an}=X_{an}\exp[(610.34/T)-0.3837] \qquad (5.4)$$

following the activity coefficient of Hodges and Royden (1984) and assuming a constant temperature of 500°C. The activity coefficient of albite, calculated from Newton *et al* (1980) approaches one for the observed plagioclase composition. Unit activity coefficients were also assumed for biotite and epidote.

Four independent reactions describe equilibrium in the system (Table 5.2) Applying the activity data to these reactions enables average temperature estimates to be made from a internally consistent multiple reaction technique (Powell and Holland 1988). Average temperature estimates calculated from these reactions of 467°C are low. Statistical evaluation of the data (represented by the 'f' value in Table 5.2) shows that the average temperaure calculated from these reactions does not pass the χ^2-test of significance at any reasonable pressures (table 5.2). This may suggests that either the assumption of equilibrium in this sample is not valid or that the activity-composition relationships cannot be represented by the applied simple model.

Table 5.1. Sonnblick Gneiss - Plagioclase Breakdown Equilibria For Sample 50333

Activities		Independent set of reactions (for sdT = 30°C)
mu	0.661	1) mu + 2cel = east + 2ksp + 3q + $2H_2O$
pa	0.017	2) pa + 2cz + 2q = 4an + 4 ab + H2O
cel	0.193	3) 5mu + 4 cel + 6cz = 2east + 12 an + 7ksp + 10 H_2O
phl	0.0541	4) 9mu + 4phl + 6cz = 6east + 12an + 7ksp + $10H_2O$
ann	0.0342	
east	0.0278	Calculations (@ suggested P of 6.0 kbars)

		T(P)°C	sd	dP/dT	ln K
ep	0.527				
cz	0.435	1)	568	29	0.0252	2.321
an	0.005	2)	407	25	0.0334	-6.338
ab	0.91	3)	405	17	0.0340	-25.223
ksp	0.95	4)	487	21	0.3460	-23.600
q	1.0				
		avT°C	442	104	f=5.7	

P kbars	3.0	4.0	5.0	6.0	7.0	8.0	9.0
avT(°C)	352	384	415	442	467	489	517
sd	96	99	102	104	107	109	112
f	5.4	5.5	5.6	5.7	5.8	5.9	6.0

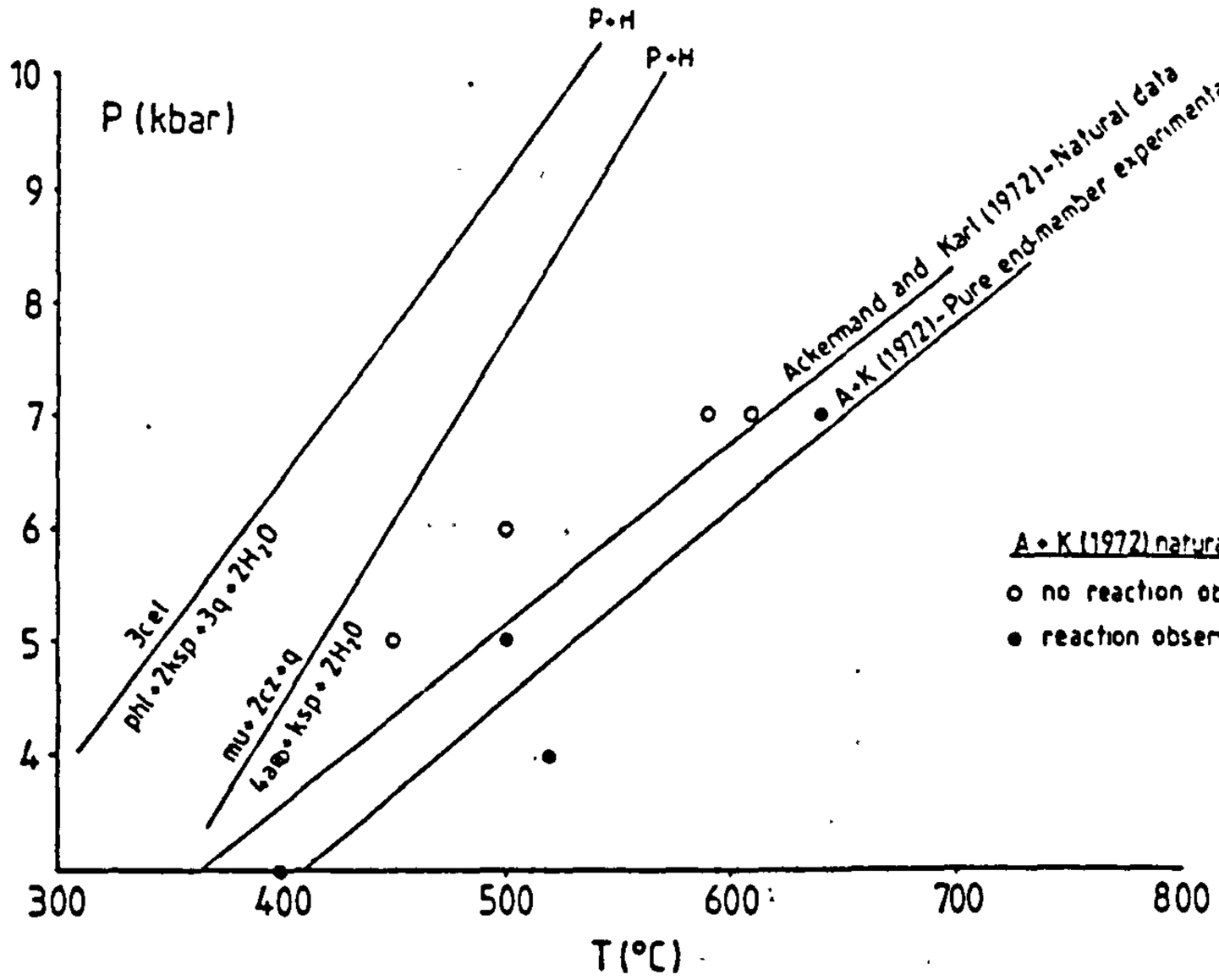

Figure 5.14. Experimental data of Ackermand and and Karl (1972) for both the reaction of pure end-member phases and for naturally occurring 'gefüllte' plagioclase compared with the same reaction calculated using the thermodynamic data set of Powell and Holland (1988). Also shown is the location of the celadonite reaction used for the Massonne and Schreyer (1987) geobarometer which was also calculated using the Powell and Holland data set. Activities of phases used to derive these lines are given in table 5.1.

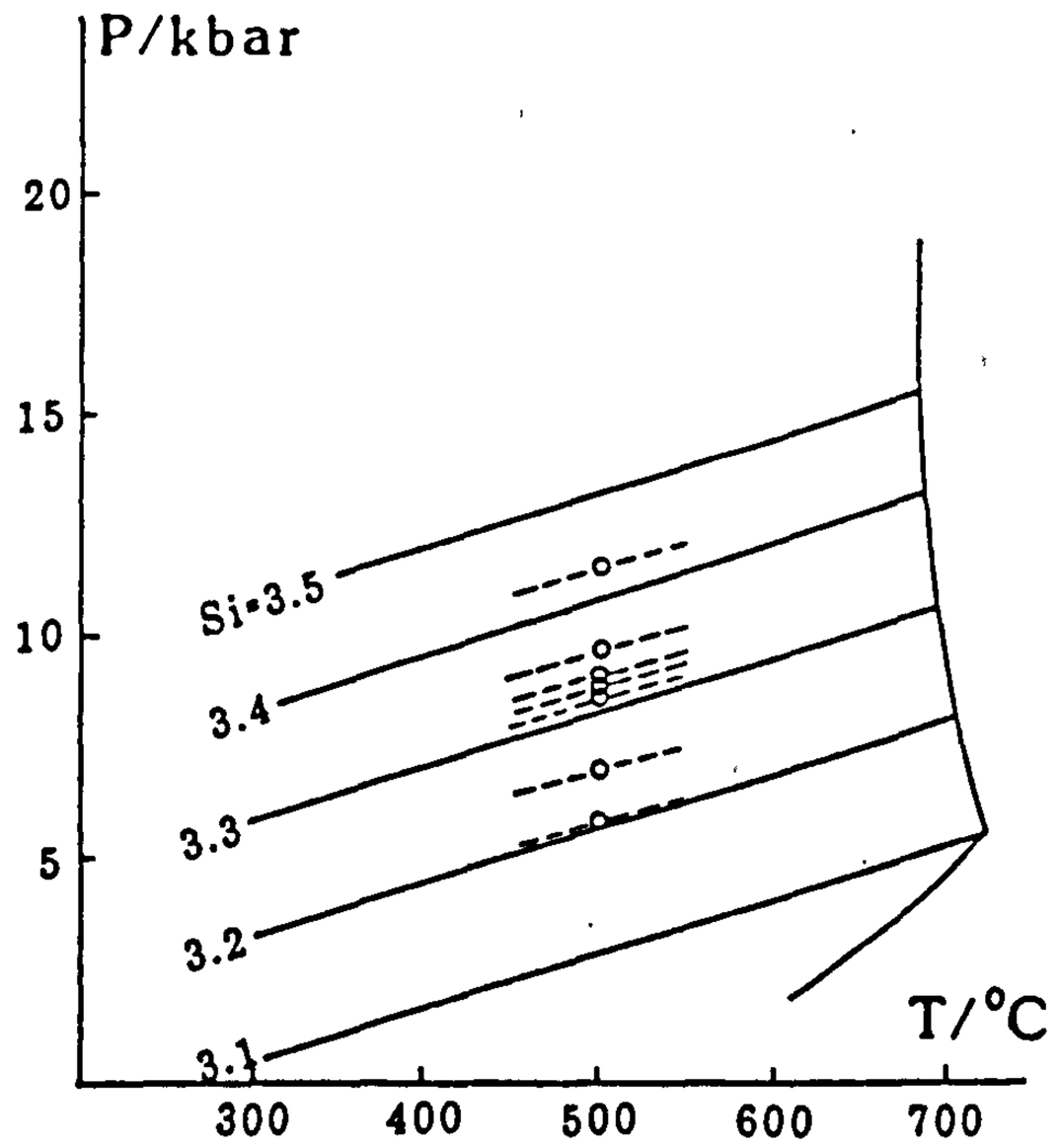

Figure 5.15. P - T - Si isopleth diagram (after Massonne and Schreyer 1987). 7 representative, phengite Si compositions, taken from gneisses with the phlogopite, K-feldspar and quartz limiting assemblage, are shown for assumed temperatures of 500°C. Dotted lines show the effect on estimated pressures of 50°C error in the assumed temperature.

Using the activity-composition relationships mentioned above, the location of reaction 5.4 in PT space can be found (Figure 5.14). It can be seen that at high pressures there is a significant deviation between the two sets of data which decreases with decreasing pressure.

5:3.4 Phengite Thermobarometry

Muscovite-celadonite solid solution is represented by an exchange reaction which takes the mica off the ideal mu-pa-ma plane and is expressed by $(MgFe)Si = Al^{iv}Al^{vi}$. Experimental work in the KMASH system (Velde 1965) established an increase in the celadonite content of phengite with increasing pressure or decreasing temperature and thus implied that the composition of phengite may form the basis of a geothermobarometer. A thermodynamic approach to phengite geobarometry for equilibria in the chlorite-muscovite-biotite-quartz system, has been drived from the experimental work of Velde (1965) by Powell & Evans (1983) and from the data set of Massonne and Schreyer (1987) by Bucher-Nüminen (1987). Within the Sonnblick gneisses, chlorite is only seen as an alteration product of biotite, suggesting that the assemblage does not represent equilibrium. Consequently, these barometers cannot be used to derive pressure estimates for the gneisses.

The early experimental work of Velde (1965,1967), utilizing data up to only 4.5 kbars, has been recently expanded by experimental data between 3-24 kbars and temperatures of 350-700°C (Massonne and Schreyer 1987). This data enabled a geobarometer to be developed based on the phengite composition within a limiting K-feldspar-phlogopite-quartz assemblage based on the reaction,

$$cel = phl + 2ksp + 3SiO_2 + 2H_2O \quad . \qquad (5.5)$$

The barometer relies upon fitting compositional data to a construction of Si isopleths in PT space. Representative analyses from six gneiss samples from several localities in the Sonnblick area have been plotted on to the P-T-Si isopleth graph for phengite following the barometer of Massonne and Scheyrer (1987) (Figure 5.15). The assumed temperature of 500°C is only an estimate based upon garnet grade assemblages within Inner Schieferhülle pelites (see 5:2.3). Errors in estimated pressure due to errors in the assumed temperature are less than 1kbar per 50°C (Massonne and Schreyer 1987). Backscatter atomic number contrast SE microscopy shows the micas are not zoned and are low in Ba.

Estimated pressures vary between 5.8 - 11.6kbars but the majority of the data plot in the pressure range 8-9kbars. The estimated pressure of 11.6kbars is obtained from the 20cm normal fault zone shown in Figures 4.19a and 4.19b. The immediate wall rock to this zone yields an estimated pressure of 8.6 - 9.6kbars. The pressure estimate of 5.8kbars is derived from a sample taken at relatively high structural levels within the dome. This spatial difference does not account for a difference of 2-3 kbars in pressure, equivalent to a 6-10 km difference in depth.

The location of the celadonite forming reaction (equation 5.4) in PT space has also been approached using the thermodynamic data set of Powell and Holland (1988) and Holland and Powell (pers.comm., July 1988). The position of the reaction curve in PT space has been calculated using the activity relationships given in Table 5.1. Assuming a temperature of 500°C, a pressure of ≈9.2 kbars is obtained.

5:3.5 Feldspar - Mica Thermometer

A thermometer depending upon the equilibrium distribution of sodium and potassium in the equation,

K-feldspar + paragonite = albite + muscovite (5.6)

has been derived by Kotov *et al* (1969), Talantsev(1971) and more recently by Green & Usdansky (1986b). As reported by Guidotti (1982), all but the latter failed to account for bulk composition within non limiting assemblages or departures from ideality.

The plagioclase-muscovite thermometer of Green and Usdansky (1986) combines models for ternary albite solutions with white mica activity models at different temperatures. The problems of assigning mixing models to low temperature feldspars as well as assigning binary, white mica activities to ternary mica formulations may give rise to substantial errors in the temperatures calculated by this method. No experimental data which reverses equilibrium relations is available to test or constrain the proposed thermodynamic model. Testing of the model involved comparison of feldspar-mica derived temperatures with temperature estimates derived independently from the same rocks. The observation that these temperatures are "similar" may not be sufficient license to validate thermometric data obtained by this method. As a result of these uncertainties this formulation is not considered further.

5:3.6 Garnet breakdown reactions

The reaction rim comprising plagioclase, epidote, biotite and chlorite (Figure 5.7) within the garnet bearing amphibolite has been investigated using the internally consistent dataset of Powell and Holland (1988). Again, activity relationships were calculated from representative microprobe analyses (Appendix 4.3) and the activities for phases involved in the reaction have been calculated by assuming ideal mixing (Powell 1978). The problems of non-ideality in chlorite, biotite, and amphibole are difficult to account for due to the large compositional variation shown by these phases in the natural environment and the lack of data pertaining to these variations. Activity coefficients of these phases are assumed to be 1.0. Anorthite activities are calculated from the equation of Hodges and Royden (1984) given earlier (Equation 5.5). Calculated activity coefficients for albite, using the formulation of Newton *et al* (1980), are greater than 0.9 for the observed plagioclase compositions and are ignored.

For the system involving the garnet breakdown products, the minerals considered to be in equilibrium are made from 13 end-members. Limiting the largest uncertainty on a calculated temperature to 20°C, a set of only 4 independent reactions can be derived. These reactions and their position in PT space are given in Table 5.2. Calculation of the average temperature from multiple reaction consideration and utilising a thermodynamically consistent data set (Powell and Holland 1988 and pers. comm. 1989), yields a temperature of 547±27°C (Table 5.2).

For statistical confidence of 95%, a value of 'f', a function used in the χ^2-test, of less than 1.61 is required. In this case a value of f=1.47 is well within the requirements of the χ^2-test. This shows that the calculated temperature is statistically valid. The calculated average temperature corresponds to an estimated pressure of ≈7kbars (Table 5.4).

It should be noted that statistically valid 'f'-values are also calculated for temperature calculations at pressures between 6 and 10 kbars. The fact that the data is statistically valid is therefore not a sufficient indication that the temperature, and associated pressure, are geologically reasonable.

Table 5.2. 48/88 Garnet Amphibolite - Garnet breakdown Equilibria

	Activities
an	0.293
ab	0.788
clin	0.022
hb	0.0168
parg	0.0081
cz	0.293
ep	0.65
ed	0.0068
phl	0.0206
ann	0.0616
east	0.0211
naph	0.0163
q	1.0
H_2O	1.0

Independent set of reactions (for sdT<20°C)

1) 4 clin + 18 cz +21 q = 26 an + 5hb + 20 H_2O
2) 21 ab + 16 clin + hb + 72 cz = 104 an + 21 parg + 80 H_2O
3) ab + clin + 6cz + 3q = 10 an + ed + 6H_2O
4) 14 ab + 11 clin + phl + 48 cz = 68 an + 14 parg + east + 54 H_2O

Calculations (@ suggested pressure of 6.5kbar)

	T(P)°C	sd	dP/dT	ln K
1)	545	19	0.0357	-14.986
2)	513	20	0.0388	-70.259
3)	529	19	0.0352	-5.845
4)	516	20	0.0352	-46.630

avT°C 547 27 f=1.47

P (kbars)	3	4	5	6	7	8	9	10
avT (°C)	436	465	492	520	547	574	601	627
sd (°C)	31	30	29	28	27	27	28	28
f	1.8	1.7	1.6	1.5	1.5	1.5	1.5	1.5

5:3.7 Amphibole Breakdown Reactions

The breakdown of amphibole to biotite and chlorite and the simultaneous growth of zone-3 garnet may be able to place tight constraints on the temperatures at which this reaction took place. Amphibole is considered to have developed synchronous with zone 2 garnet and is not considered to be part of the equilibrium assemblage now preserved in the rock. Equilibrium between chlorite and the other phases cannot be established on textural relationships. The breakdown reaction involving amphibole appears to be associated with the last phase of metamorphism within the schists and, since zone 3 garnet appears to have grown during increasing temperature conditions (see 5:2.3), is interpreted to represent the regional Tertiary Alpine metamorphism.

Considering an equilibrium assemblage of gnt-ms-chl-bte-qtz, where garnet composition is represented by the rim of zone 3, the assemblage can be represented by 13 end member phases. Mole fractions of the end-member phases are calculated by assuming ideal mixing (Powell 1978). Unit activity coefficients are assumed for garnet, biotite and chlorite phases and for the celadonite component of white mica. Muscovite and paragonite activity coefficients of 1.15 and 3.25 respectively were calculated from the data of Chatterjee and Froese (1975). Using the thermocalc program of Powell and Holland (1988), 6 independent reactions can be located in PT space (Table 5.3). In this case, the largest uncertainty on a calculated temperature for a reaction to be included in the independent reaction set was 30°C. No reactions were observed when this value was

Table 5.3. 57/88 White mica schist - amphibole breakdown reaction

Representative Analyses used in Thermocalc Calculation

	SiO_2	TiO_2	Al_2O_3	Fe_2O_3	FeO	MnO	MgO	CaO	Na_2O	K_2O
gt	37.26		21.07	0.09	35.92	0.69	2.31	3.26		
bte	34.24	1.17	17.06	3.37	17.71	0.39	9.02	0.02	0.14	9.58
ms	47.17	0.44	30.88		2.19	1.32	0.01	1.45	0.81	10.29
chl	25.02	0.13	21.59		26.81	0.42	13.47		0.26	

Mole fractions calculated by Thermocalc assuming ideal mixing (Powell 1978)

gt	$X_{alm} = 0.513$	$X_{py} = 0.00077$		
bte	$X_{phl} = 0.0388$	$X_{ann} = 0.0519$	$X_{east} = 0.0315$	$X_{naph} = 0.00563$
ms	$X_{mu} = 0.580$	$X_{cel} = 0.0752$	$X_{pa} = 0.0693$	
chl	$X_{clin} = 0.00464$	$X_{daph} = 0.00357$		

	Activities
alm	0.513
py	0.00077
phl	0.0388
ann	0.0519
east	0.0315
naph	0.00563
mu	0.667
cel	0.0752
pa	0.2252
clin	0.00464
daph	0.00357
q	1.0
H_2O	1.0

Independent set of reactions (for sdT<30°C)

1) 4mu + 6clin = 7py + phl + 3east + 24 H_2O
2) east + 4 cel + 6clin = 7py + 5phl + 24 H_2O
3) mu + 3clin + 3q = 4py + phl + 12 H_2O
4) mu + 3 daph + 3q = 4alm + ann + 12 H_2O
5) 3cel + pa + 6clin = 7py + naph+ 24H_2O
6) alm + 4mu + 6clin = 8py + ann + 3 east + 24 H_2O

Calculations (@ suggested pressure of 6.5 kbars)

	T(P)°C	sd	dP/dT	ln K
1)	603	27	0.3754	-29.371
2)	588	29	0.2950	-20.366
3)	603	29	1.2465	-15.252
4)	661	27	0.2935	11.822
5)	589	29	0.2870	-22.423
6)	595	28	0.3706	-35.579
avT°C	640	33	f=2.03	

P (kbars)	4.0	5.0	6.0	7.0	8.0	9.0
avT (°C)	630	636	640	643	644	645
sd (°C)	39	36	33	29	25	22
f	2.6	2.3	2.0	1.8	1.5	1.3

reduced to 20°C. An average temperature of 640±33°C is calculated from the 6 reactions (Table 5.3). This temperature estimate is outside the χ^2-test of statistical significance. However, temperature estimates which pass the χ^2-test are calculated at higher pressure conditions. As shown in the case of the breakdown of garnet in the garnet amphibolite, the fact that a temperature may pass the χ^2-test is not sufficient evidence to that the temperature is geologically significant.

Omitting chlorite from the equilibrium assemblage does not enable any reactions to be found within a reasonable PT window, even when the largest uncertainty on an individual reaction is increased to 40°C.

5:3.8 Cation Exchange Thermometry

The distribution of magnesium and iron between coexisting ferromagnesian mineral pairs under equilibrium conditions has been used to estimate temperatures attained during peak metamorphic conditions. The rationale behind such thermometers is that cation exchange is associated with only very small volume changes, and hence pressure dependance is small, and they are also independent of the activity of components in the metamorphic fluid.

Exchange thermometers suffer from a lack of precise calibration; inaccurate models of solid phase thermodynamics, especially at temperatures below 600°C; errors associated with mineral formulae normalization and from the unknown effects of cation order and disorder within mineral phases (Essene 1989). Exchange thermometers may also suffer from reequilibration of ferromagnesian phases by diffusive cation exchange during cooling.

"Blocking" of cation exchange will be dependant largely upon temperature although cooling rate and grain size will also be important (Dodson 1973,1976,1979). The post-peak metamorphic cooling history of the rock may therefore be an important consideration in the assessment of estimated temperatures. Given these limitations, many exchange thermometers have been proposed and a few are now considered with respect to the amphibolite and white mica schist lithology of the Inner Schieferhülle.

5:3.8 a) Garnet-Biotite Thermometry

The distribution of Mg and Fe between garnet and biotite at equilibrium can be expressed,

$$Fe_3Al_2Si_3O_{12} + KMg_3AlSi_3O_{10}(OH)_2 = Mg_3Al_2Si_3O_{12} + KFe_3AlSi_3O_{10}(OH)_2 \quad (5.7)$$

(almandine) (phlogopite) (pyrope) (annite)

for which the equilibrium constant, K, is given by,

$$K = \frac{a_{py}}{a_{alm}} \cdot \frac{a_{ann}}{a_{phl}} \quad (5.8)$$

Calibration of this reaction has been attempted by compa ring both experimental phase equilibria (Thompson 1976) and quartz-magnetite isotopic exchange data (Goldman and Albee 1977) with natural mineral assemblages. Since natural assemblages were involved, these calibrations are limited since they cannot account for the effects of minor components within garnet and biotite.

Experimental calibration of the garnet-biotite thermometer for binary Fe-Mg exchange between 550-800°C ($alm_{90}py_{10}$) and 600-700°C ($alm_{80}py_{20}$) at a pressure of 2.07kbars, lead to the thermometer

$$12454 + 4.662\,T\,(K) + 0.057\,P\,(bars) + 3\,RT\,\ln K = 0 \quad (5.9)$$

(Ferry and Spear 1978), where

$$K = (Mg/Fe)_{gnt} / (Mg/Fe)_{bte} \quad (5.10)$$

Again the effects of Ca and Mn substitution in garnet or for Al^{vi} and Ti substitution in biotite cannot be accounted for since ideal binary mixing is assumed. The Ferry and Spear (1978) thermometer is therefore limited to conditions where the substitution of other phases into garnet and biotite is low, that is (Ca+Mn) / (Ca+Mn+Mg+Fe) < 0.2 in garnet and (Al^{vi}+Ti) / (Al^{vi}+Ti+Mg+Fe) < 0.15 in biotite (Ferry and Spear 1978). For biotite, the assumption of ideal Fe-Mg mixing, may be a reasonable assumption (Müller 1972; Wones 1972; Schulein 1975 ; Ganguly 1978). However, this may not be valid for

garnet outside the experimental range investigated by Ferry and Spear (op.cit.) (eg. Ganguly and Saxena 1984).

Various modifications to the Ferry and Spear thermometer have been proposed in order to account for non-ideality of garnet mixing and the substitution of components other than iron and magnesium into the garnet and biotite lattices.There are therefore presently a variety of garnet-biotite calibrations that are available. These usually combine experimental calibration of the ideal portion of the Fe-Mg exchange between garnet and biotite and an empirical calibration of the deviation from ideality. Pigage and Greenwood (1982) have corrected for Ca and Mn in garnet using the thermodynamic mixing parameters summarized by Ganguly (1979), based largely on the data of Ganguly and Kennedy (1974). Hodges and Spear (1982) corrected for Ca and Mn assuming ideal mixing in all binaries except pyrope-grossular. Non-ideality in this binary join was corrected by the temperature dependent mixing parameter calorimetrically derived by Newton *et al* (1977).

Corrections for non-ideal Mg-Fe mixing in garnet have been suggested based on thermodynamic and statistical analysis of natural data (Ganguly and Saxena 1984). However, such non-ideality is contradicted by the mixing parameters derived by Newton and Haselton (1981) and by the low interaction parameters obtained from regression analysis of natural data from the Alpine Ötztal region (Hoinkes 1986). Comparison of the non-ideal Fe-Mg mixing model with metamorphic phase relationships in the Ötztal region has further shown that obtained temperatures are too low to be consistent with the observed staurolite grade metamorphism. This in turn suggests that there is a problem in applying the non-ideality correction model.

Indares and Martignole (1985) consider the effects of Ca and Mn substitution in garnet and couple this with Al^{vi} and Ti substitution in biotite. Unfortunately the mixing parameters for biotite non-ideality are derived from studies at approximately 800°C and so cannot be justifiably extrapolated to amphibolite grade conditions.

i) Inner Schieferhülle

For the Inner Schieferhülle schist lithology (sample 57/88) biotite forms during the breakdown of amphibole, synchronous with the development of zone 3 garnet. Biotite and the rims of garnets are therefore considered to be in equilibrium. The similar

compositions of the smaller garnets and the larger garnet rims suggests that smaller garnets also grew synchronously with biotite.

Average biotite analyses have been used with compositions taken from close to the rims of zone-3 garnets and from the smaller garnets in order to estimate temperatures of equilibration. Estimated temperatures derived from 4 different formulations of the thermometer are shown in Table 5.4. Temperatures were calculated for a pressure of 7kbars although the pressure dependancy of the thermometers is less than 4°C/kbar.

Table 5.4. Temperature calculated for Inner Schieferhülle schist (57/88) based on different calibrations. F+S = Ferry and Spear (1978), H+S = Hodges and Spear (1982), P+G = Pigage and Greenwood (1982) and I+M = Indares and Martignole (1985).

Garnet Sample	°C F+S	H+S	P+G	I+M
average zone-3 rim	539	582	614	568
rim edge (pt 2, profile1)	529	565	592	546
average small garnets	518	574	610	569

Individual thermometers show a relatively close spread of temperatures but differences are seen between the original Ferry and Spear calibration and the modified versions. The small amounts of Mn and Ca at the rims of the garnet and of Al^{vi} and Ti in biotite are within the compositional constraints of the Ferry and Spear thermometer and suggest that the modified calibrations may have overestimated the affects of minor phase substitution. The data obtained by the Ferry and Spear calibration are therefore interpreted to be the equilibration temperatures between garnet and biotite of ≈530°C. Errors given on the calibration are are quoted by Ferry and Spear (1978) to be in the order of ±50°C.

ii) Garnet amphibolite

Within the garnet bearing amphibolite, biotite is locally found within the rection rim around the garnet and equilibrium between garnet and biotite in the amphibolite may not be justified. However, biotite and garnet are locally observed in contact with each other and these contacts appear stable. Analyses from touching phases have been used to try and estimate temperatures using the previously discussed garnet - biotite thermometers assuming a pressure of 7 kbars. Activity coefficients for mixing in garnets have been

calculated following Newton and Perkins (1982). All calculate close to unity and therefore garnet solid solution is also considered ideal.

The Ferry and Spear (1978) calibration on two biotite - garnet pairs yield temperatures of 537±50°C and 572±50°C. Estimates from the other calibrations vary from 650-1000°C and are considered meaningless. The garnet-biotite temperatures fall within error of each other and of the temperature calculated for the white mica schist. The accuracy of the calculated numbers must however be treated with suspicion due to the problems of possible disequilibrium.

5:3.8 b) Garnet - Hornblende Thermometry

As previously discussed for garnet-biotite, the partitioning of ferrous iron and magnesium between two coexisting phases can often be used to infer temperatures of formation of the mineral pair. Such a thermometer has been calibrated for garnet-hornblende equilibria by Graham and Powell (1984), who applied analytical data to a semi-empirical thermodynamic formulation and calibrated this using data obtained from garnet-clinopyroxene-hornblende assemblages where garnet-clinopyroxene thermometry had previously been used to constrain temperatures (Ellis and Green 1979).

The general form of the thermometer,

$$T(K) = \frac{2880 + 3280\, X_{Ca}^{gnt}}{\ln K + 2.426} \qquad (5.11)$$

assigns all non-ideality in the system to the Ca content of the garnets and fails to account for activity-composition relationships in calcic amphiboles, for which very little thermodynamic data is available. No correction is made for Mn substitution in garnet nor for possible asymmetric almandine-pyrope mixing (Ganguly and Saxena 1984). The thermometer is therefore effectively limited to garnet compositions with a low spessartine component ($X_{Mn} < 0.1$). The magnitude of errors in thermometer calibration associated with the assumptions of no pressure dependency and of no post-metamorphic diffusive resetting cannot be quantified.

Since only ferrous iron is used in the calculation of palaeotemperatures, then the oxidation state of iron, which may be modified during the post metamorphic history of the amphibole, is of significant importance. Several recalculation schemes have been

proposed for the calculation of Fe3+ in amphiboles (see Robinson *et al* (1982) for summary). Such methods however can significantly overestimate the ferric iron content of metamorphic amphiboles, especially when garnet is present in the assemblage. In the case of calcic amphiboles, the suggested recalculation scheme (Leake 1978) involves summation of the cations (other than Na and K) to 15, is used. In the case of amphiboles in the Sonnblick area, amphibole recalculation by this method generates large Fe^{3+} totals.

i) Inner Schieferhülle

Within the garnet - amphibole bearing white mica schist of the Inner Schieferhülle (57/88), amphibole is considered to have grown synchronous with zone-2 garnet (see 5:2.3). Unfortunately the composition of this garnet is outside the $X_{Mn} < 0.1$, compositional constraint of the thermometer (Graham and Powell 1984). Estimated temperatures of 367±50°C and 299±50°C for 'all Fe as Fe^{2+}' and 'calculated Fe^{3+}' respectively, are therefore misleading and should be considered with caution.

The low estimates obtained by the thermometer probably reflects the effects of unknown non-ideality relationships in the amphibole as well as the effect of Mn substitution in garnet. An idea of the magnitude of the latter on calculated temperatures can be achieved by modifying the equilibrium constant of the above reaction (5.11) using the mixing parameters of Ganguly and Saxena (1984). The validity of such a correction requires testing, against spessartime-rich-garnet - amphibole bearing samples for which an independant estimate of temperature is known which is beyond the scope of the present study. However the modified garnet-hornblende thermometer transforms to

$$T = \frac{2880 + 3280\, X_{Ca}^{gt} + 1510.5\, X_{Mn}^{gt}}{\ln K + 2.426} \qquad (5.12)$$

which yields temperatures of 477°C and 392°C for 'all Fe as Fe^{2+}' and 'calculated Fe^{3+}' respectively. The Mn correction therefore appears to increase the calculated temperatures although again, the temperatures derived from the iron values recalculated for ferric iron are extremely low. This suggest that the Fe^{3+} recalculation significantly overestimates ferric iron values in these amphiboles.

ii) Garnet Amphibolite

The large modal volume of amphibole in this rock relative to the volume of garnet breaking down suggests that on mass balance considerations, near equilibrium relationships between the garnet and hornblende compositions may still exist between remaining garnet and amphibole. Garnet-hornblende thermometry in the amphibolite, using average mineral compositions for garnet and amphibole, estimates temperatures of 575±50°C and 459±50°C for 'all Fe as Fe^{2+}' and 'calculated Fe^{3+}'respectively. Since the composition of iron in the amphibole lies between these two extremes, then a tempeature betwee these limits would be expected. Temperatures calculated by garnet-hornblende thermometry in the amphibolite correspond, within error, with temperatures estimated from garnet-biotite thermometry in the white mica schists of the Inner Schieferhülle.

5:3.8 c) Garnet-Phengite Thermometry

A 'preliminary' geothermometer , again utilizing the distributtion of Fe and Mg between garnet and a ferromagnesian phase has been proposed by Krogh and Råheim (1979) for the equilibrium relationship

$$Fe_3Al_2Si_3O_{12} + 3\,kMgAlSi_4O_{10}(OH)_2 = Mg_3Al_2Si_3O_{12} + 3kFeAlSi_4O_{10}(OH)_2$$
$$\text{(Almandine)} + \text{(Mg-phengite)} = \text{(Pyrope)} + \text{(Fe-phengite)} \qquad (5.13)$$

Calibration of the thermometer combines experimental data derived at 1000°C and 30kbars with published compositional data for garnet-phengite occurences from P-T environments at eclogite facies conditions.

Since ΔV for exchange reactions is generally small then extrapolation of the thermometer to sub-eclogite pressures may be reasonable. However extrapolation to temperatures below 650°C is suspect since no experimental data exist to constrain the above reaction at amphibolite facies conditions. Assumption of ideal solutions for both garnet and phengite is likely to give rise to substatial errors in estimated temperatures.

Extrapolation of the thermometer to P-T conditions of 375°C and 2.5kbars (Krogh and Råheim 1979) is unconstrained but does yield "good P-T estimates". The significance of such numbers however, is questionable.

An empirical garnet-muscovite thermometer has recently been calibrated from comparisons with the garnet-biotite thermometer of Ferry and Spear (1978) (Hynes and Forest 1988). The thermometer takes the form

$$T(K) = \frac{4.79 \times 10^3}{\ln K + 4.13} \qquad (5.14)$$

where,

$$\ln K = \frac{\ln Kd + 0.8\,(W_{FeMg}) - W_{FeMg}\,(X_{Fe} - X_{Mg}) - 3000\,(X_{Mn})}{RT} - 2.978\,X_{Ca}\left(\frac{844}{T}\right)$$

$$+ 5.906\left(X_{Ca}\left(\frac{844}{T}\right)\right)^2$$

and

$$Kd = \frac{X_{Mg}^{ms}\,X_{Fe}^{grt}}{X_{Fe}^{ms}\,X_{Mg}^{grt}} \qquad W_{FeMg} = \frac{200\,X_{Mg}}{X_{Mg} + X_{Fe}} + 2500\,\frac{X_{Fe}}{X_{Mg} + X_{Fe}}$$

This thermometer is derived assuming no pressure dependance for partitioning between garnet and muscovite, no ferric iron partitioning, ideal mixing in muscovite and utilizes the non-ideal mixing model of Ganguly and Saxena(1984) modified for a non-linear calcium effect after Hoinkes (1986). Temperatures are also calibrated using the Ganguly and Saxena model without the Hoinkes' calcium correction. Temperatures estimated for equilibrium between the small garnets and the matrix of white mica within the Inner Schieferhülle, yields temperatures of 498°C, 539°C and 535°C for the Krogh and Råheim (1979), Ganguly and Saxena (1984) and the Hynes and Forest (1988) calibrations respectively. Using the same calibrations with average zone-3 rim compositions gives temperatures of 508°C, 543°C and 542°C. Errors on these temperatures are again in the order of ±50°C.

As discussed earlier, the Krogh and Råheim formulation is suspect but the temperature estimates for the other two formulations compare well with temperatures estimated by garnet-biotite thermometry in the same rock.

5:4 Discussion

5:4.1 Conditions of Alpine Metamorphism

Several different thermometers and barometers have been applied to the different lithologies found within the Sonnblick Dome. However, only a few of these enable the conditions of Alpine metamorphism to be tightly constrained. Within the schists of the Inner Schieferhülle, at intermediate structural levels of the Dome, application of garnet-biotite and garnet-phengite thermometry yields temperatures of 530-542±50°C. Within the garnet amphibolite, exposed only several metres away from the Inner Schieferhülle schists, the equilibrium between plagioclase, chlorite, biotite, epidote, hornblende and quartz within the breakdown rim of garnet, yields similar temperatures of 547±27°C which corresponds to a pressure in the order of 7kbars.

The above temperatures corresponds to the best estimates of the Tertiary Alpine metamorphism since equilibrium is easy to justify and mineral compositions are such that minor component substitution does not significantly modify calculated temperatures. These temperatures are consistent with amphibole mineral chemistry and the absence of staurolite within chloritoid bearing white mica schists. The presence of chloritoid also suggests that the +50°C error associated with cation exchange thermometry is over exaggerated since temperatures in excess of 560°C would be expected to form staurolite (Hoschek 1969). Temperatures for peak Alpine metamorphism are therefore inferred to have been 540±50°C.

Similar temperatures of 550±50°C from garnet-biotite thermometry within the garnet amphibolite may be coincidental. Although seen in contact with the garnet, biotite forms one of the phases within the garnet reaction rim which suggests that they may not be in equilibrium.

Within the amphibole bearing Inner Schieferhülle schist, the breakdown of amphibole and synchronous development of zone 3 garnet yields garnet-hornblende temperatures of 640±33°C. This temperature is considered to be meaningless because the presence of chloritoid in more aluminous schists requires temperatures below about 550°C. This interpretation is further supported by the poor statistical significance of the calculated temperature which does not pass the χ^2-test. The calculated temperature probably reflects disequilibrium within the assumed 'equilibrium assemblage' but may also represent limitations in the assumed mixing relationships for the different phases.

Feldspar thermometry and mica solid solution thermometry have already been discounted as a means of establishing metamorphic temperatures for the orthogneiss assemblages. However, the breakdown of plagioclase to albite, epidote and white mica, and the geobarometer of Massonne and Scheyrer (1987) have been applied to the gneiss assemblage. The high pressures estimated by the phengite geobarometer (9-10 kbars) are considered too high and are not reconcilable with the pressure estimates of 7±1kbar to the northeast of the Dome (Droop 1981, 1985) and suggested by the garnet rim assemblage mentioned earlier.

There is no evidence to establish the timing of anorthite breakdown reaction. However assuming temperatures in the order of 500-550°C for the Tertiary alpine metamorphism, pressure estimates from the experimental data of Ackermand and Karl (1972) (4.2-5.6 kbars) are very low relative to the pressure estimates from the garnet breakdown reaction (≈7kbars) and from Droop (1981, 1985). When the equilibrium relationship associated with plagioclase breakdown is located in PT space using the data set of Powell and Holland (1988), pressure estimates of 7.8-9.0 kbars are obtained for temperatures of 500-550°C. These calculated pressure estimates are not significantly different from those calculated by Droop (1985) from the higher structural levels of the Peripheral Schieferhülle to the northeast of the Sonnblick Dome, especially when the difference in structural level is taken into account.

The calculated pressures of 7.8-9.0 kbars are therefore interpreted to provide the best estimates of pressure during the Tertiary metamorphism from assemblages within the Sonnblick Dome. These pressures and temperatures suggests that even though the initial breakdown reaction may have taken place significantly earlier, recrystallization of mineral phases within the gneiss took place during the Tertiary metamorphism.

In summary, the Tertiary Alpine metamorphism within the middle levels of the Sonnblick Dome is considered to have taken place at conditions of 540±50°C and 8±1kbar.

5:4.2 Prealpine and Eoalpine Metamorphism

Temperatures obtained from equilibrium between phases in the reaction rim of garnet record temperatures which are interpreted as representing peak metamorphic temperatures during the Tertiary. However, the garnet within the garnet amphibolite and the amphibole and garnet zones 1 and 2 within the Inner Schieferhülle, provide evidence

for an earlier metamorphism. This metamorphism may represent either early Alpine metamorphism associated with the prograde PT path or may be due to Prealpine or Hercynian metamorphism. Evidence for the first of these from the Peripheral Schieferhülle to the northeast of the Sonnblick Dome (Droop 1985) suggests that Eoalpine metamorphism in this part of the Tauern was probably at higher pressure but lower temperature than the later Tertiary metamorphic climax.

Within the garnet amphibolite, temperatures derived from garnet-hornblede thermometry, calculated from end member Fe^{2+}:Fe^{3+} estimates suggest a temperature which lies between the limits of 459-575°C (±50°C). However, the presence of the garnet reaction rim suggests that garnet may not be in equilibrium with the matrix assemblage. On mass balance considerations, and assuming isochemical metamorphism on the scale of the thin section, the composition of the amphibole may not have changed significantly during garnet breakdown. Hence, temperatures calculated from garnet-hornblende equilibria may still represent conditions of the Pre- or Eo-Alpine metamorphism. However, this uncertainty, coupled with the uncertainty in the Fe^{2+}:Fe^{3+} ratio of the amphibole makes the calculated temperature ineffective at constraining conditions of the earlier metamorphism.

Problems also arise in attempting to assess the conditions early metamorphism associated with amphibole and garnet equilibria within the Inner Schieferhülle schists. In this case, amphibole is interpreted to have grown synchronous with zone 2 garnet and there is little difficulty in assuming the correct garnet composition in equilibrium with hornblende. However, the problems of the Fe^{2+}: Fe^{3+} ratios within the hornblende and the more significant effects of the Mn substitution during possible disequilibrium growth of garnet makes the significance of the calculated temperatures difficult to interpret. It is impossible in these cases to therefore establish whether the low temperatures (299-367 ± 50°C) represent the conditions of garnet formation or are merely a function of minor component substitution. Although the Mn-correction to the Graham and Powell (1984) thermometer is based simply on previously modelled garnet mixing parameters which have not been tested in combination with hornblende, the increase in temperature associated with this correction suggests that minor component substitution may have significantly affected calculated temperatures.

These limitations to the calculated temperatures indicate that the conditions of the earlier metamorphism, within the schists and amphibolites, could not be well constrained.

5:4.3 The Spatial Variation of Metamorphism in the southeast Tauern Window

The limited distribution of metamorphic assemblages which may be used to constrain metamorphism, means that the spatial variation of metamorphism within the Sonnblick Dome is difficult to constrain. Assemblages preserved within the Schieferhülle schists and the garnet amphibolite, at a height of 2000m and just over a kilometre below the Zentralgneis - Peripheral Schieferhülle contact, suggest peak metamorphic temperatures of 540±50°C. Pressure estimates are less easily constrained but are considered to be in the order of 8±1kbar.

Mineral asssemblages preserved within the immediately overlying Peripheral Schieferhülle, indicate a similar garnet grade metamorphism. To the northeast of the Dome, metamorphic conditions of 490°C and 7±1kbar are estimated at a structural position 2-5km above the staurolite - biotite isograd centred on the Hochalm Dome (Droop 1985). Metamorphic conditions within the Dome are consistent with the staurolite - biotite isograd being at a structural level ≈1km below the lower structural levels of the Sonnblick Dome.

Similar grades of metamorphism within the Sonnblick Dome and metasediments of the Peripheral Schieferhülle suggest that metamorphic isotherms cut through the tectonic contact between the two units. This represents the emplacement of the two units prior to metamorphism by Dome associated folding.

The Auernig amphibolite unit, which lies towards the base of the Peripheral Schieferhülle in the Hochalm area, records peak metamorphic conditions similar to the those estimated in the Sonnblick Dome (eg. Cliff *et al* 1985). The thermal history of the Auernig amphibolite, established by geochronological methods (Cliff *et al* 1985), is also very similar to the thermal history of the gneiss sample 48419, taken from the lower structural levels of the Sonnblick Dome (see Figure 7.5b). This thermal history is characterized by rapid cooling between the time of white mica and biotite closure temperatures.

The rapid cooling observed at the base of the Peripheral Schieferhülle has been shown to be associated with rapid decompression (Droop 1985). Since similar temperature - time curves are observed for the Auernig amphibolite and the lower levels

of the Sonnblick Dome, it can be inferred that the two areas are also likely to have had similar pressure histories. The PT history of the lower levels of the Sonnblick Dome are therefore considered to follow a similar PT path as that suggested by Droop (1985) for the lower levels of the Peripheral Schieferhülle in the area to the northeast of the Sonnblick Dome.

Using this PT path, the average uplift rate of 4mm/a can be constrained by the mineral isotope data between the time of metamorphism (white mica closure) and the isotopic closure of biotite (Chapter 7). From the locus of the PT path (Droop 1985), even faster rates of uplift are likely immediately after metamorphism.

5:4.4 Metamorphic Conditions during Alpine Deformation

The relationships between deformation and metamorphism have been discussed earlier (see section 4:12.2). However, the metamorphic conditions during deformation can now be constrained.

1) At the lower structural levels of the Dome, metamorphism at 540±50°C is considered to have led to recrystallization of the fabrics associated with deformation, including those developed during the formation of the Dome. The presence of microstructures indicative of quartz plasticity suggests that recrystallization either occured in a dynamic environment where low differential stresses existed, or suggests a later, low-strain deformation overprints the recrystallized rock.

2) Oligoclase and chloritoid bearing assemblages suggest garnet grade metamorphic conditions at the higher levels of the Dome. Porphyroblast asymmetry shows mineral growth occured during top-to-NW shearing.

3) Shear bands at high structural levels show deformation microstructures which have not undergone coarsening or post-tectonic recrystallization or recovery. These features combined with alteration of chloritoid to chlorite against shear bands, is argued as evidence for thinning and extension of the upper levels of the Dome along the retrograde PT path of the area. Plastic deformation of quartz in the shear bands requires minimum temperatures in the order of 350°C. Biotite isotope data constrains temperatures of this order to the period before 20Ma ago. This indicates that thinning of the upper levels of the Dome, and the overlying Schieferhülle, was associated with rapid uplift of the area. The shear bands are therefore interpreted to represent localized

extensional features which form part of the regional extensional deformation accomodating uplift.

Chapter 6

Metasomatic Shear Zone development within the Sonnblick Gneisses

6:1 Fluid-Rock Interaction in rocks undergoing Deformation and Metamorphism

Ductile shear zones and mylonites are commonly developed within crustal rocks and represent the heterogeneous partitioning of strain into approximately planar bodies. These zones show non-coaxial progressive deformation, approximating to simple shear, relative to the undeformed precursory lithology. Shear sense indicators within such zones (eg. Berthé *et al* 1979; Simpson and Schmid 1983; Bouchez *et al* 1983; Lister and Snoke 1984; Weijarmer and Rondeel 1984; Hanmer 1986), coupled with mineral elongations and stretching axes, enable the direction and sense of movement to be established. Once established the kinematic framework is extremely useful in the reconstruction of regional histories and the balancing of collision belts (for recent examples see Balé and Brun 1989; Hansen 1989; Mukhopadhyay and Haimanot 1989).

Recent studies have illustrated the complexities of foliation and fabric development within shear zones and have considered the interaction of deformation mechanisms, crystallographic preferred orientation development and strain path evolution (eg Lister and Williams 1979, 1983; Watts and Williams 1983; Law *et al* 1984; Law 1987; Culshaw 1987; Vauchez 1987; Knipe and Law 1987; Passchier 1988; Shimamoto 1989; Knipe 1990). The complexities of shear zone nucleation (Poirier 1980; Tullis and Yund 1985; Segall and Simpson 1986), propagation (Coward and Potts 1983; Simpson 1983) and fabric development (Knipe and Law 1987; Law 1987) have also been studied and have further illustrated the complex nature of natural rock deformation.

Retrogressive metamorphism has been recognised as being spatially related to the localized deformation found within shear zones for over a century (eg. Teall 1885). The commonly hydrous nature of shear zone assemblages relative to undeformed protoliths indicates that metamorphism is often associated with the infiltration of a fluid phase (Beach 1976, 1980; Brodie 1980; McCaig 1984; O'Hara 1988; Sinha *et al* 1988; Gilotti 1989; Klaper in press). Shear zones are therefore excellent natural examples for the study of the complex interactive behaviour between deformation, metamorphism and a fluid phase and the consequent effects on the rheological behaviour of rocks. It is only

recently that this behaviour has begun to be understood, albeit at a relatively simple, mechanistic level.

There are many ways that deformation and metamorphism may interact (Brodie and Rutter 1985) and recent studies, concentrating on mylonite and shear zone studies, have emphasized this (Beach 1976,1980; Brodie and Rutter 1985; Knipe and Wintsch 1985). Many more studies have been concerned with the cycle of mineral dissolution, material transfer and mineral re-precipitation associated with deformation, which is known as pressure solution (see McClay 1977, Kerrich 1978 and Rutter 1983 for reviews and Lehrer and Bataille 1985 for a detailed mathematical approach).

The modification of active deformation mechanisms and processes by metamorphism has been summarized by Brodie and Rutter (1985). Newly formed, or recrystallized, mineral phases replacing previously deformed, work-hardened grains will undergo rapid creep and will lead to reaction-softening (White and Knipe 1978; White *et al* 1980). Newly formed grains may also be weaker than the phase they are replacing. This is particularly important during fluid infiltration associated with shear zone formation, where the new mineral assemblage is commonly retrogressive in nature and contains hydrated mineral phases. Preferred growth orientations may lead to geometrical softening if the new grains are oriented in a way favourable for the accommodation of deformation.

In retrogressive metamorphic reactions, newly formed phases are commonly of a smaller size than the primary mineral phases. A reduction in grain size effectively decreases diffusive pathlengths and may lead to more rapid deformation by grain size sensitive processes. A change in grain size may also produce a change in the dominant deformation mechanism operating in the rock and may enhance strain rates and change the rheological behaviour of the rock (eg. Rubie 1983; Handy 1989).

The rates of mineral reactions or transformations and the chemistry of the fluid phase may change the point defect concentration and trace element chemistry of a mineral phase. Such a change may affect dislocation processes and may lead to either strain softening or strain hardening.

At a mechanistic level, deformation may affect metamorphic transformations via dislocation formation, grain size reduction, permeability enhancement, temperature changes (due to shear heating) and by changing the rate of diffusive mass transfer by

locally increasing chemical potentials (Brodie and Rutter 1985). These processes may all affect the kinetics of metamorphic reactions.

On a more detailed scale, deformation features such as elastic strain, dislocation tangles and the development of twinning, may all give rise to localized, high internal free energy within the lattice of mineral phases (Wintsch 1985). These features have been shown experimentally to provide sufficient energy for metastable mineral growth (Green 1972) and theoretically, to increase the solubility of a mineral phase, as well as change chemical potentials in the fluid phase (Wintsch and Dunning 1983). These changes in chemical potentials and cation activities may give rise to metamorphic reactions, as illustrated by the the formation of myrmekite at sites of K-feldspar deformation (Simpson and Wintsch 1989) and by the deformation-enhanced growth of sillimanite (Wintsch and Andrews 1988).

The large water budget of the crust (Fyfe 1985, Fyfe and Kerrich 1985) suggests that the effects of a fluid phase may have a significant importance in the study of crustal processes. Fluids transport both heat and mass and affect both chemical and mechanical processes taking place in the crust. Fluids therefore affect the large scale rheological behaviour of the crust as well as deformation and metamorphic processes on a grain scale.

The importance of a fluid phase is related to its ability to transfer both material and heat which in turn may initiate and drive mineral reactions and enhance deformation within the metamorphic rock pile. Mass transfer processes are important features of rocks undergoing metamorphism and deformation at all scales and are therefore important considerations in the understanding of orogenic processes. At mid-crustal levels these processes are intimately related to the presence of a fluid phase.

Two competing, end-member, transport processes can be considered in association with fluid-assisted, mass transfer (Korzhinskii 1970). Diffusion, in which 'material is transfered by diffusion through stationary pore solutions' (Korzhinskii 1970 p3), and advection where 'components are transferred by a stream of aqueous solutions through a porosity in the rock' (Korzhinskii 1970 p3). Modelling of these processes suggests that advection is the process by which large scale metasomatism within the crust may be established (Hofmann 1972; Fletcher and Hofmann 1974; Etheridge *et al* 1984).

The ability of a fluid to move through a rock is an important consideration during mass transfer processses which will be dependant upon the permeability of the rock and the pressure gradient driving fluid flow. Permeability is largely controlled by the porosity within the rock. However, the prevailing metamorphic and deformation environment will modify permeabilities by affecting the number, distribution and orientation of fractures as well as the fluid assisted precipitation and dissolution of minerals (Rumble *et al* 1982; Rumble and Spear 1983).

The introduction of a fluid phase into a rock may have a significant effect on the deformation mechanisms and processes taking place within that rock. Experiments on quartzite samples have demonstrated that water enhances both recovery and dislocation glide during deformation (Jaoel *et al* 1984). Absorbed water in grain boundaries may also lead to an increase in dislocation mobility at grain boundaries known as the Rebinder effect (Westwood *et al* 1967).

The presence of water promotes plastic flow and quartz recrystallization at lower stresses than those required under dry conditions. Dennis and Atkinson (unpublished data) have shown experimentally that shear stresses required for slip along fault zones in wet Westerly granite were significantly lower than those required under dry conditions, due to stress corrosion cracking (Atkinson 1984). Small amounts of water may also give rise to hydrolytic weakening within minerals (see Kirby 1984 for brief summary) and the fluid phase may be important in producing reducing conditions which will promote the incorporation of hydrogen into the mineral lattices of many oxides, including quartz (Hobbs 1984). These defects will influence rates and processes such as dislocation mobility and plastic yield strength, which are dependent on defect concentration (Kirby 1984).

Large fluid fluxes and associated mass and heat transport will promote chemical reactions and may enhance reaction kinetics within the metamorphic pile (Rubie and Thompson 1985). Chemical reaction and mineral nucleation will take place at thermodynamically favourable locations, such as high dislocation density sites, in order to "reduce the stored energy of deformation" (Hobbs 1976, p 107) and make mineral grains energetically more stable.

Metasomatic shear zones behave as natural 'rock laboratories' in which the interaction of the deformation and metamorphism during syn-deformational fluid infiltration may be investigated. The aim of this study is to look at the development of a

1.5 metre wide metasomatised shear zone, developed within the Sonnblick augen gneisses, in order to examine the processes and mechanisms taking place at mid-crustal conditions during continental collision.

6:2 Characteristics of the Shear Zone at Outcrop

A white mica-rich schist is exposed at a height of 1440 and 1470 metres on a recent road cutting along the Mölltaler Panoramastraße (grid ref. 165058). The schist forms part of a complicated series of altered shear zones, mylonites and weakly deformed augen gneisses observed in a small area of the road section (see Figure 4.8). The shear zone is at the lowest exposed levels of the Sonnblick Dome, is found close to the core of the Sonnblick antiformal structure and, although poorly exposed, can be traced for over 200 metres.

The shear zone is marked by a gradational contact from weakly foliated augen gneisses to a well foliated micaceous unit which is approximately 1.5 metres wide and dips at approximately 45° to the south west. A weak foliation (35° towards 218°) within the gneiss adjacent to the shear zone is defined by slight elongation of quartz augen and by a locally developed preferred orientation of micas. Moving towards the shear zone, a stronger foliation is developed and is defined by greater quartz elongation and the development of mica-rich domains at the expense of feldspar. The foliation becomes progressively stronger and sub-parallel to the shear zone margin towards the shear zone.

The white mica-rich shear zone is schistose and contains a well developed foliation parallel to the shear zone boundaries. The top of the shear zone forms a discrete contact with a mylonitic leucogranite (see Figure 4.8) but the lower boundary is marked by a gradual increase in white mica towards the shear zone and the development of a more intense foliation. Mineral stretching lineations are subhorizontal and trend northwest-southeast. Shear sense indicators in the form of bent foliations and microstructural observations indicate that the shear zone developed during top-to-NW shearing above an oblique ramp.

The shear zone is a relatively tabular feature. However, in one exposure the zone appears to widen and the metasomatic alteration becomes less intense (Figure 4.8). Within the wider zone, a strong foliation is developed and multiple phases of folding are observed on a centimetre scale, at the base of the altered unit. The last phase of folding within this zone has a similar orientation to that of the F_3 folds (described in Chapter

4:6.2) and may be associated with Dome formation. This phase of folding overprints two earlier fold phases which are tight, angular folds with centimetre scale amplitudes. All three fold types have similar hinge orientations which are subparallel to the stretching lineation observed in the shear zone. These localized foldsare interpreted to be associated with shear zone development and are not considered to represent the F_1 or F_2 folds observed elsewhere in the Dome.

Cutting through the gneiss in the vicinity of the shear zone are a series of chlorite/mica-rich fractures which dip at ≈50° to the southwest and contain slickenlines plunging to the south west (10° towards 233°). Associated with these fractures is the local development of S-C type fabrics and the bending of the external foliation into the fracture zone. These fractures appear to represent late extensional deformation and are consistent with those structures described in Chapter 4:7.

Within the Sonnblick Dome, an increase in the amount of white mica in the gneiss is observed to be associated with deformation and localized shearing (eg. 4:5.3). The gradational contact observed between the shear zone and the augen gneiss, especially where the shear zone appears to widen, suggests that the shear zone represents an extreme case of the breakdown of the granite gneiss lithology. The shear zone is therefore interpreted to be derived from the low strain coarse augen gneiss.

6:3 Mineralogy and Crystal Chemistry of the Shear Zone Assemblage

The shear zone mineral assemblage is dominated by phengitic white mica, quartz and K-feldspar. Backscatter electron microscopy does not reveal any zoning within these phases although variations of upto 5% in orthoclase component of the feldspar are indicated by electron microprobe analyses. No detailed microprobe investigation has yet been made, although this may be useful in constraining feldspar growth processes (eg. Wintsch and Knipe 1983; Knipe and Wintsch 1985). The composition of micas and feldspar in the shear zone are given in Appendix 4. Relict clinozoisite is occasionally observed and shows resorption features indicative of disequilibrium and reaction. No other major phases were observed by optical microscopy.

6:4 Geochemistry of the Metasomatic Shear Zone

The mineralogical alteration of granitic gneisses to phyllonitic ductile shear zones within the Sonnblick Dome is accompanied by changes in the bulk rock geochemistry, in

terms of both major and trace element abundances. Variations in major element geochemistry between deformed rocks and their undeformed protolith have been widely documented (eg Teall 1885; Beach and Tarney 1978; Beach 1980; Sinha *et al* 1986, 1988). More recently, the mobility of trace and rare earth elements during shear zone formation has also been recognised (Alderton *et al* 1980; Dorstal *et al* 1980; Winchester and Max 1984; Stähle *et al* 1987; O'Hara 1988).

A simple prediction on the mobility of a particular component can be made by considering the ionic potential, Z/r, of an ion (where Z= ionic charge and r= ionic radius in Å for the ion in its normal coordination state) (Pearce 1983). Elements with low (<3) or high (>12) ionic potentials are generally mobile while those with intermediate values are generally immobile (eg Loughnan 1969). However, the above studies have shown that elements once considered immobile, for example Ti, P, Zr, Y, Nb and REE (Winchester and Max 1984) are often mobile.

6:4.1 Major and Trace Element Geochemistry

The chemical alteration has been studied by XRF analysis on whole rock gneiss and shear zone samples and the compositions are given in Appendix 3.2. Seven thin slab whole rock samples, used in the radiogenic isotopic study of the shear zone (Chapter 7:3.3) have also been studied by XRF and show similar compositions to the larger shear zone sample. Slight variations in element concentrations between the thin slabs reflect the modal variations in syn-deformational K-feldspar porphyroblasts used to define the plane of sectioning for the thin slabs. The differences in chemical composition between the shear zone and the unaltered gneiss are illustrated in Figure 6.1.

6:4.2 Gresen's Method of Composition-Volume Relationships

A method of investigating compositional and volume changes associated with metasomatic alteration of rocks has been suggested by Gresens (1967). This method considers composition and volume changes simultaneously and takes into account both chemistry and changes in rock density.

For mass transfer between 100g of a rock A, reacting to produce a rock B, Gresens derived an equation (equation 14, Gresens 1967),

$$X_n = 100\left[f_v\left(g_B/g_A\right)C_n^B - C_n^A\right] \qquad (6.1)$$

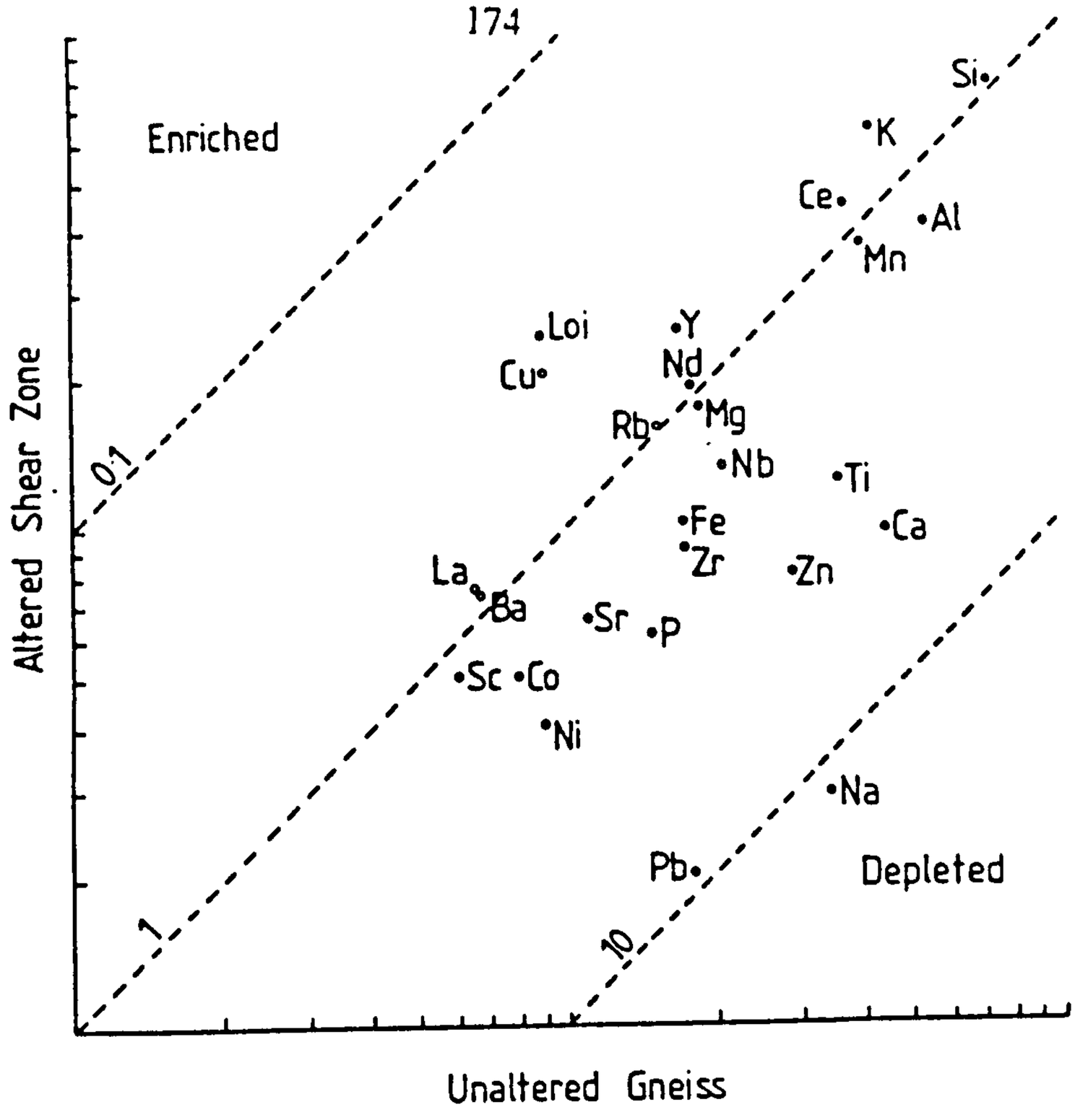

Figure 6.1. Geochemical comparison of unaltered gneiss (sample 55/87) and the shear zone lithology (sample 24/87) on a log-log correlation diagram.

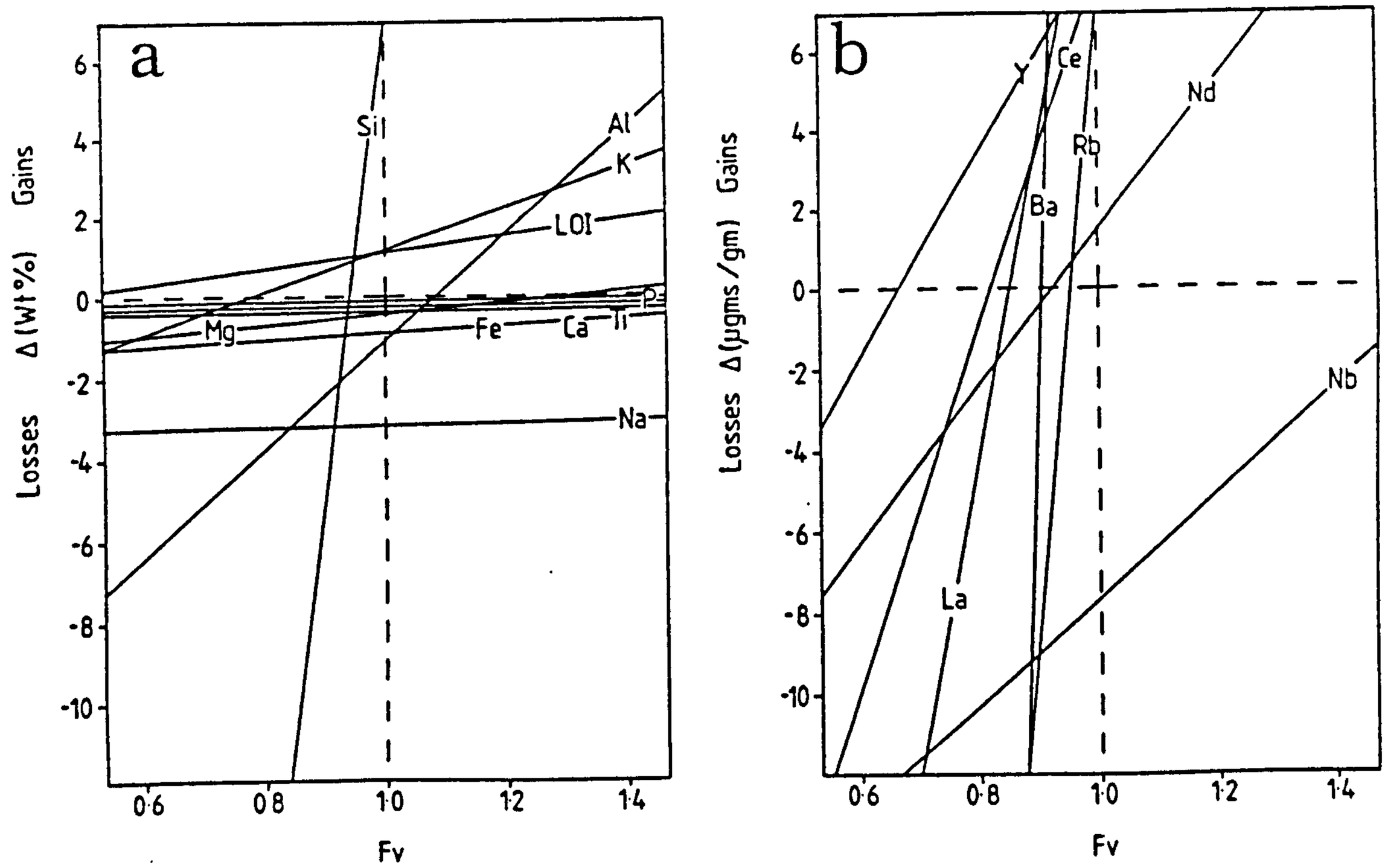

Figure 6.2. Gresens' diagrams showing the relationship between elemental variation and volume changes (F_v) for the unaltered gneiss and the shear zone lithology (see text for discussion). a) shows major element variations between the two lithologies. b) is constructed for trace element variations.

relating the mass gain or loss (X_n) of component, n, to volume changes (f_v) in the rock system. In the above equation, g is the specific gravity and C is the concentration of component, n, in the unaltered sample, A, and altered sample, B. f_v is the volume factor, which represents the ratio of the rock volume after reaction to the volume of rock before reaction. From this equation a series of linear equations relating X for each analysed component to f_v may be derived and plotted on a composition-volume (C-V) diagram.

C-V diagrams have been constructed for the alteration of gneiss (sample 55/87) to phyllonitic shear zone (sample 24/87), (Figure 6.2). A coincidence of elements cutting the "no compositional change" line at similar f_v values can be used to quantify volume changes associated with alteration (eg McCaig 1987, Vocke *et al* 1987).

The lines derived for Al, P and Ti, elements which are often considered "immobile" in metamorphic environments, are widely spaced (Figure 6.2a). This suggests that at least two of these components were mobile during the alteration process. There is a weak cluster of lines representing components Si, Al, Mg and K around $f_v = 1$, the point representing isovolumetric alteration. Sodium plots below the 'no gain or loss' line for all values of f_v. Conversely, potassium plots above the line, except when substantial volume losses in the order of 30% occur. Shear zone formation therefore appears to be associated with removal of Na_2O but the addition of K_2O.

A similar C-V diagram has been constructed for the trace elements (Figure 6.2b). Here a stronger coincidence of components is observed between $f_v = 0.8$-1.0. These components include Ce, La and Nd, commonly thought to be immobile during metamorphism and Ba and Rb which are commonly considered mobile (Pearce 1983).

Given the large spread in the intersection of element lines with the 'no loss or gain' line, it is difficult to identify an obvious volume factor which characterizes the volume change associated with shear zone formation. The spread of this data suggests that elemental variations associated with shear zone formation cannot be explained by a change in volume and that the absolute abundance of most elements must have changed by mass transfer processes. The metasomatic nature of the shear zone is therefore confirmed.

The largest cluster of intersections are around the $f_v = 0.9$ value. This is the best estimate available for the volume change associated with shear zone formation and corresponds to a volume loss of 10% during shear zone development. A volume factor of 0.9 closely corresponds to the f_v value shown by SiO_2 as it cuts the "no loss or gain" line. This suggests that within the shear zone, the absolute amount of SiO_2 has not changed. This does not preclude the possibility that silica was probably mobile, but would suggest that no net gain or loss of Si in or out of the system occured.

Using a volume factor of 0.9, the relative change in different components can be derived from the set of linear equations, one for each of the lines, such that:

$$100g \text{ gneiss} + 0.94g\ H_2O + 0.64\ K_2O = 92.14g \text{ phyllonite} + 1.02g\ SiO_2 + 0.27g\ TiO_2 + 2.41g\ Al_2O_3 + 0.98g\ Fe_2O_3 + 0.58g\ MgO + 0.38g\ CaO + 3.20g\ Na_2O + 0.10g\ P_2O_5$$

This is associated with the breakdown of plagioclase, K-feldspar, epidote, biotite and opaques and the formation of white mica and locally K-feldspar. In terms of trace element geochemistry the formation of the shear zone is associated with the enrichment of Y, and the strong depletion of Cr, Zn, Pb, Sr, Nb, Zr and V.

6:5 Microstructural Observations on the Metasomatic Ductile Shear Zone

In order to investigate the processes associated with development of the shear zone, a series of thin sections have been investigated which represent a traverse, (over a metre) from the gneissic host of the shear zone through to the shear zone centre. Although, the foliation intensity and mineralogy change gradationally over the traverse, four zones can be defined from the observed microstructures. These zones correspond to foliated coarse augen gneisses in the wall rock; more strongly deformed micaceous augen gneiss nearer to the shear zone; the approximate boundary of the shear zone and the white mica schists within the shear zone.

6:5.1 Weakly foliated coarse Augen Gneiss

Weakly foliated augen gneiss approximately 20 cm from the shear zone has a foliation which is defined by the elongation of quartz augen and locally by aligned micas and slightly elongate matrix quartz. The matrix consists of two types of domains, quartz-feldspar rich domains and mica-epidote domains. At the microscopic scale, these contain microstructures which are very similar to those developed within the low-intermediate

strain coarse augen gneisses described in Chapter 4 (section 4:10.2a.). These descriptions are not repeated here. However, some features of the microstructure have not been observed within the typical gneisses and can be seen to become progressively stronger towards the shear zone. Such features therefore appear to be spatially related to shear zone development.

K-feldspar augen upto 1cm are present and show a variety of microstructural features. Perthitic exsolution is observed in the form of planar lamellae and blebs which are discontinuous through the whole grain. Locally, en-echelon arrays of exsolved albite within the K-feldspar can be seen (Figure 6.3a). This suggests that during albite exsolution, deformation was at least occuring on a local scale within the rock. These arrays are seen to affected by later deformation expressed in the form of undulose extinction.

Microstructural features in K-feldspar such as the development of localized twinning and undulose extinction (Figure 6.3b), indicate feldspar plasticity during deformation. Feldspar porphyroclasts also show sub- and new- grain formation with recrystallized grain diameters in the order of 30μm which show no signs of grain boundary migration (Figure 6.3c). Individual new-grains also show internal deformation in the form of undulose extinction. Tullis and Yund (1985) have suggested that plastic deformation of feldspars requires temperatures of 450°C.

Within K-feldspar augen, thin bands in the order of <0.1mm which are both intra- and trans-granular in form are observed (Figure 6.3d). These bands are composed of fine grained, recrystallized albite and are subparallel to the shear zone foliation. The density and width of these bands increases in samples that are progressively closer to the shear zone, suggesting that they formed as a discrete response to deformation associated with shear zone development.

There is usually no apparent displacement of the feldspar across these bands and, coupled with the intra-granular nature of most of the bands, suggests that albite is replacing K-feldspar rather than growing within discrete fractures associated with brittle deformation. Where small displacements across these bands do take place, this may be due to the bands acting as heterogeneities which may have localized later deformation. These small heterogeneous displacements are commonly accompanied by localized plastic deformation in the feldspar lattice (Figure 6.3e).

Figure 6.3a. En echelon albite exsolution in K-feldspar augen. Deformation bands in the K-feldspar (right) do not significatly affect the albite lamellae although later deformation microstructures, whose nature is difficult to resolve optically, cut the lamellae and also the plastic deformation microstructures (f). Scale bar= 0.1mm .

Figure 6.3b. K-feldspar showing evidence of having undergone plastic deformation. Enhanced twinning is seen at the corners of the porphyroclast while undulose extinction is pervasive through the grain. At one corner, myrmekite (m) replaces the strained feldspar which may be an example of deformation-enhanced reaction (eg Simpson and Wintsch 1989). Scale bar= 0.5mm.

Figure 6.3c. Subgrain formation in albite suggesting deformation took place at temperatures in excess of 450°C. Scale bar= 0.2mm.

Figure 6.3d. Intra- and transgranular albite bands within K-feldspar augen. Scale bar= 0.5mm.

Figure 6.3e. An increase in the displacement and offset of K-feldspar (marked ID), across an albite band (Ab), is accompanied by plastic deformation in the K-feldspar lattice. This is shown by the development of undulose extinction in the feldspar. Scale bar= 0.5mm

Figure 6.3f. Clinozoisite (Cz) surrounding allanite (Al) within a K-feldspar augen. Cz extends into the albite rich band (Ab) and is distributed symmetrically along the band on either side of the allanite grain. Enhanced twinning in the K-feldspar can be seen at the upper margin of the allanite grain. Scale bar= 0.2mm.

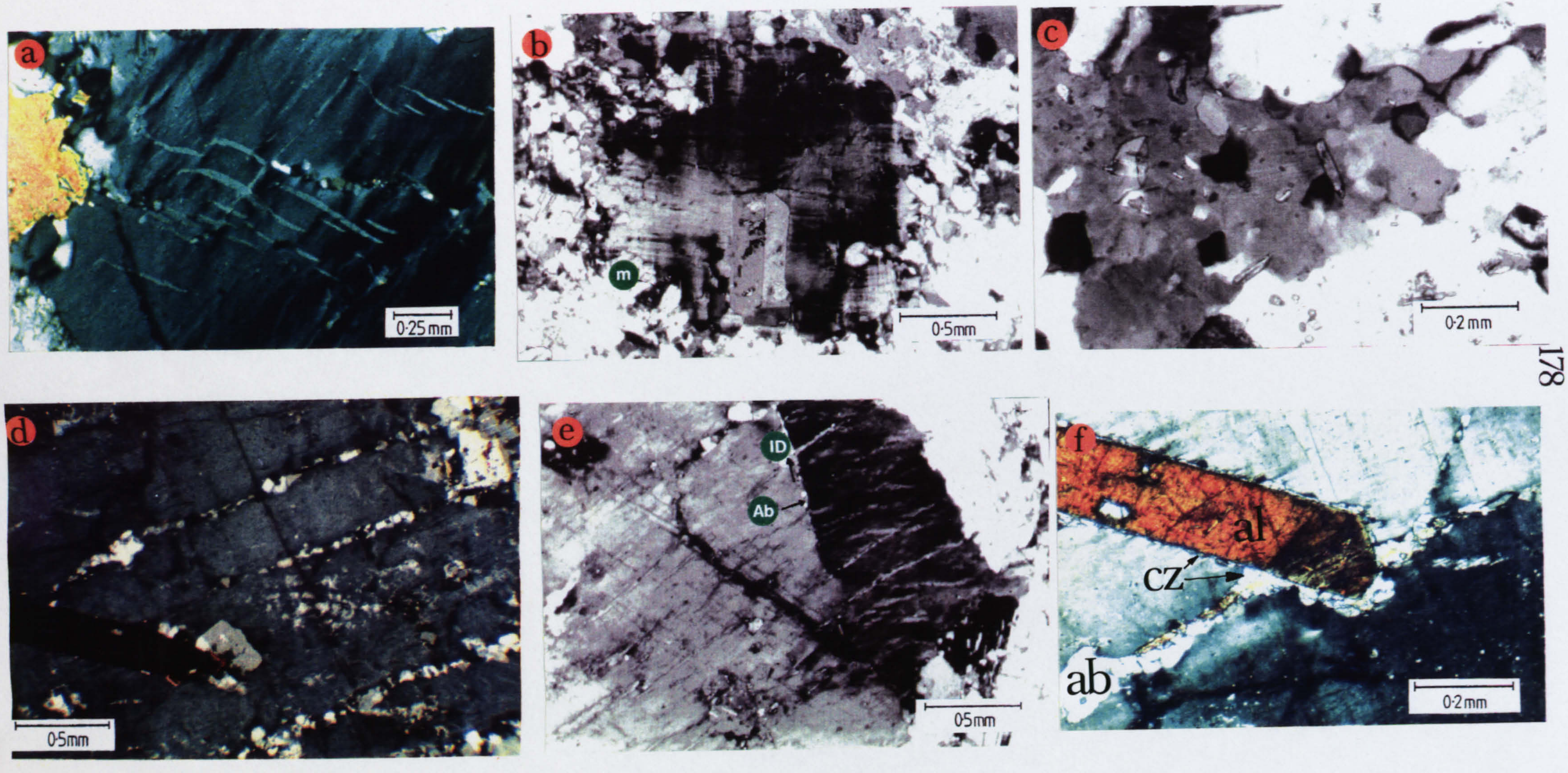
a
0·25 mm
b
m
0·5mm
c
0·2 mm
d
0·5mm
e
ID
Ab
05mm
f
al
cz
ab
0·2mm

The albite bands are occasionally seen to intersect primary inclusions of allanite within the K-feldspar (Figure 6.3f). Surrounding the euhedral allanite is a small rim of clinozoisite which extends into and along the albite-rich band with which it is in contact. A symmetrical distribution of clinozoisite on both sides of the allanite grain along the band, suggests that clinozoisite growth was diffusion-controlled, rather than due to advection of a fluid along a fracture (see McCaig and Knipe in press).

The albite trails are similar in many ways to the "segregation bands" of Hanmer (1981), who associated the formation of quartz bands within feldspars as a deformation enhanced replacement reaction. The bands are highly oblique to later fractures in the feldspars. Such fractures commonly form at high angles to glide planes in feldspars (Mitra 1978) and suggests that albite crystallization may have occurred along planes accommodating glide in the feldspar.

Replacement of K-feldspar by albite is also observed around primary igneous inclusions of plagioclase, now pseudomorphed by albite, clinozoisite and white mica (see Chapter 5), which are present within the K-feldspar augen. Albite rims around pseudomorphed plagioclase are recognised by the absence of twinning and by the lack of included phases. Albite growth is enhanced in areas of high sodium content, for example where perthitic exsolution lamellae or albite bands are in contact with the plagioclase inclusion (Figure 6.4a). Replacement of K-feldspar and the migration of the grain boundary also occur in areas where there is evidence for plastic deformation of the K-feldspar in the forms of twinning and bending of the feldspar lattice (Figure 6.4b). This reaction is therefore also seen to be enhanced by deformation.

6:5.2 Foliated Augen Gneiss

The mineral assemblage in this zone is also similar to that in the weakly foliated wall rock and consists of perthitic K-feldspar, albite, quartz, biotite, white mica, epidotes, sphene, chlorite and some accessory phases. However, microstructures and mineral textures are significantly different and there is an increase in the modal abundance of white mica at the expense of feldspar.

The more strongly developed foliation is defined by mica-rich domains upto 0.5mm wide which are variably spaced within a quartz-feldspar aggregate. White micas defining the foliation, have a preferred orientation with their basal (001) cleavage lying approximately in the plane of the foliation. The foliation wraps around feldspar augen

Figure 6.4a. Albitic replacement of K-feldspar taking place around a primary plagioclase phenocryst now pseudomorphed by albite, white mica and clinozoisite. The morphology of the albite shows enhanced albite growth along perthitic exsolution lamellae (P), albite bands (A) and discontinuites in the K-feldspar which offset exsolved albite lamellae (D). The fracture also gives rise to kinking of the replacing albite and must therefore must have been active during the later stages of albite growth.

Figure 6.4b. Albite rims (marked by the lack of inclusions) around partially pseudomorphed plagioclase replacing K-feldspar which shows evidence for plastic deformation in the form of twinning and undulose extinction. Scale bar 0.5mm.

Figure 6.4c. Albite overgrowing white mica hinge at the shear zone margin. Scale bar= 0.5mm.

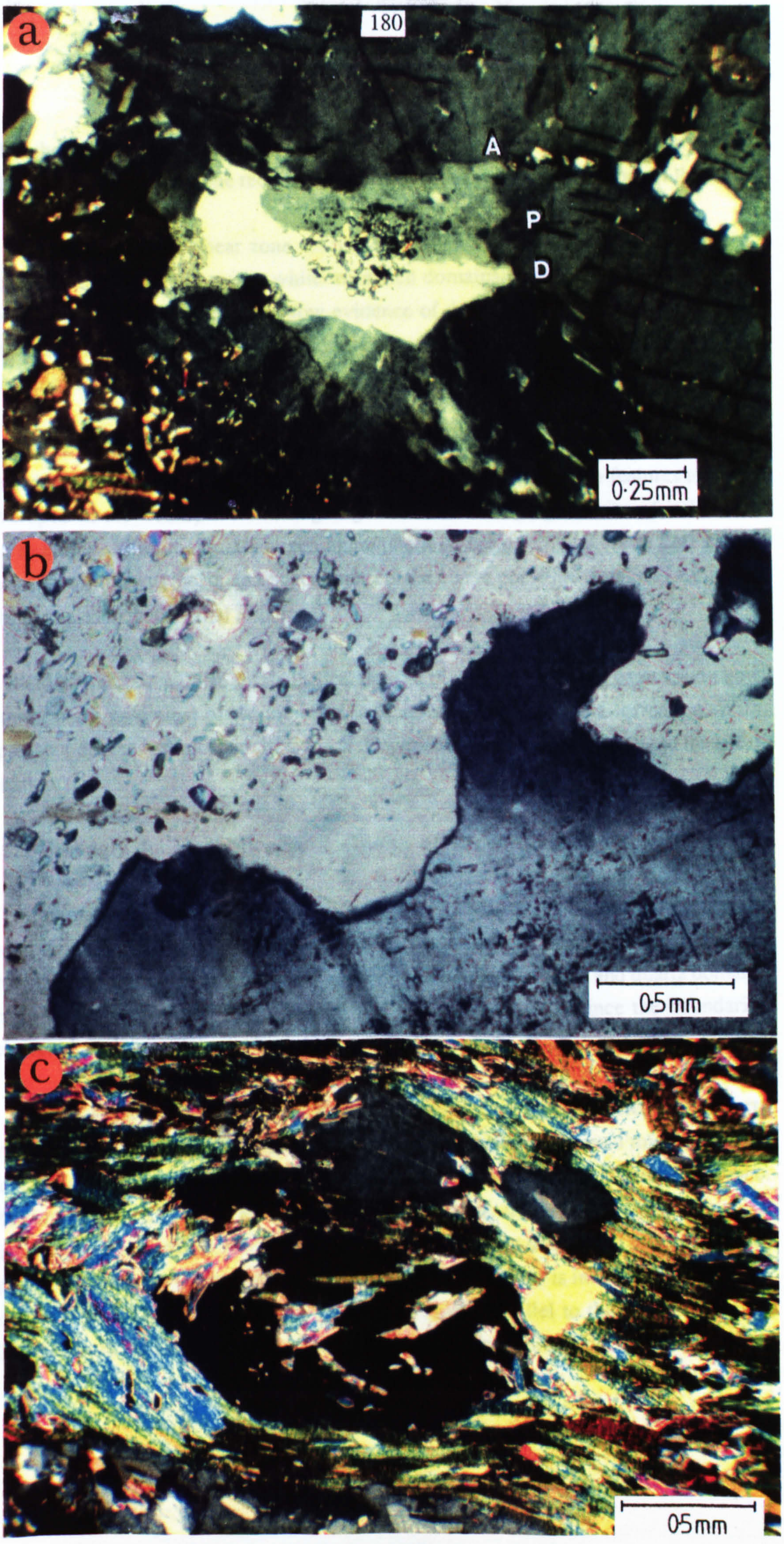
a
180
A
P
D
0·25mm
b
0·5mm
c
05mm

within the rock but micas in the foliation show little in the way of internal deformation and appear to have undergone recrystallization during the subsequent history of the rock.

Moving towards the shear zone, an progressive increase in the white mica content occurs and discrete, 1mm-wide, white mica-rich domains develop. At the margins of these domains other phases also show evidence of dissolution. Epidote minerals and sphene show ragged morphologies and often appear strongly resorbed both indicating disequilibrium.

Quartz grains are more lenticular than the previous sample and have aspect ratios in the order of 2:1. Microstructurally, quartz shows similar deformation features to those developed in the weakly foliated augen gneiss. The average grain size of individual quartz grains within the quartz augen aggregate is in the order of 0.5mm. Late brittle fractures, confined to the quartz augen, transect the above microstructures and are found at high angles to the external foliation.

Feldspar augen are also less euhedral than in the weakly foliated gneiss and show sutured margins typical of reaction and associated with white mica formation. With increasing degrees of feldspar alteration, feldspars become elongate parallel to the shear foliation.

6:5.3 Strongly foliated Micaceous Gneiss at the shear zone boundary

A dramatic reduction in feldspar content and an increase in the amount of white mica and foliation intensity occurs entering into the shear zone. A strong domainal fabric is present, again dominated by white mica and quartz rich bands. Mica and quartz domains are in the order of 1mm wide although this is slightly variable since the boundaries between domains are not usually distinct.

Quartz textures, within quartz augen, are similar to those developed in quartz domains of the poorly foliated gneiss. This suggests that the observed microstructures have not formed as a response to increasing deformation approaching the shear zone. Moving progressively towards the shear zone centre, quartz augen begin to show discrete grain boundaries where in contact with white mica domains. These boundaries are often marked by a thin layer of darker material. This layer is interpreted as the non-soluble material left after pressure solution of quartz parallel to the foliation. Quartz dissolution is also necessary to produce the quartz-free mica-rich domains and this

suggests that diffusive mass transfer was an important mechanism of strain accommodation during shear zone formation.

K-feldspar and plagioclase porphyroclasts are smaller and less common then previous samples. The feldspars are elongate parallel to the mica foliation and show irregular grain boundaries indicative of instability and reaction to white mica. The lenticular nature of the feldspar relicts shows that feldspar breakdown occured preferentially along grain boundaries which were parallel to the foliation. Internally, feldspars show signs of plastic deformation in the form of undulose extinction. This may represent deformation during the initiation of the shear zone as observed in the feldspars in the immediate wall-rock. Mica domains also contain biotite which differs from biotite in the host in that it is brown in thin section as opposed to green. Mica domains wrap around most feldspar grains as would be expected if the feldspars represent porphyroclastic relicts of the primary igneous mineralogy.

Few calcium phases are present within the rock. Very little epidote is observed and the only calcium bearing phase is apatite. Shear zone formation would seem to be associated with a depletion in Ca. This is confirmed by the geochemical data shown in the Gresens diagram of Figure 6.2a. Furthermore, no sinks for the sodium, released during albite breakdown, are present.

Locally along the margin of the shear zone, at the wider zone discussed earlier, a complicated sequence of multiphase folding is observed on a hand specimen scale within the quartz and mica-rich shear zone lithology. On a microstructural scale, the foliation in the shear zone is locally deformed by three fold phases. Microstructures in the hinges of these folds are very similar to those developed in the fold hinges seen elsewhere in the Dome (see 4:10.4).

Micaceous fold hinges of the first and second generation are commonly overgrown by albite porphyroblasts. The albite is commonly zoned having a more albite-rich core and oligoclase rims. The core is generally smaller than the surrounding rim. Albite growth is intimately linked with mica fold hinges and therefore appears to be related to mica deformation in these zones. Where mica hinges are free of albite overgrowth, the mica is generally coarse with microstructures indicative of low strain deformation. (Figure 6.4c). The growth of oligoclase is considered to be associated with peak Alpine metamorphism. This suggests that shear zone formation was pre-metamorphic in age.

6:5.4 Shear Zone Centre

The mineralogy of the shear zone is dominated by white mica, quartz and K-feldspar, with the feldspar concentrated within discrete bands parallel to the shear zone foliation. The matrix of the rock is largely composed of quartz and white mica and shows a complex foliation development. No individual quartz augen are preserved and an astomosing foliation is defined by closely spaced, 50-100μm, quartz and white mica domains which define an S-C fabric (Berthé *et al* 1979; Lister and Snoke 1984) which indicate top-to-NW shearing. Mica shows very little evidence of deformation internally although occasionally, micas contain undulose extinction and subgrains, with sub-grains boundaries perpendicular to their lengths.

Discrete bands in the shear zone contain asymmetrical feldspars that are upto 2mm in diameter, contain sigmoidal quartz inclusion trails. Commonly, the inclusion trails at the shear zone centre are straight, sub-parallel to each other and at high angles to the shear zone foliation, although they become parallel to the shear zone foliation at the grain rim (Figure 6.5a). This sort of pattern has been described for porphyroblast growth in domains of coaxial deformation within non-coaxially deforming shear zones (Bell *et al* 1985). However, some porphyroblasts contain trails which are quite oblique to other observed trails (Figure 6.5a). This suggests that the model of Bell *et al* (op. cit.) is not applicable to these porphyroblasts. The feldspars are considered to have grown during simple shear deformation and represent an example of rotating porphyroblasts. Such an interpretation is consistent with the top-to-northwest shearing obtained from preserved S-C fabrics and the bending of the external foliation into the shear zone.

Feldspar porphyroblasts locally show evidence for plastic deformation, with the development of twins and undulose extinction, adjacent to inclusions of quartz and white mica (Figure 6.5b). Inclusions therefore appear to localize deformation within the K-feldspar. This deformation may be associated with rotation of the porphyroblast or with enhanced stress due to the feldspars acting as stress risers during subsequent deformation.

White mica envelopes are developed around K-feldspar augen. These have an asymmetrical distribution and are found on the sides of the feldspar which face the shortening direction of the resolved shear stress (Figure 6.5a). Quartz inclusions within the feldspar porphyroblasts are up to 200μm in size and are a similar size to matrix quartz. Quartz grains in the quartz domains of the matrix have undergone recovery and

Figure 6.5a. Syn-deformational K-feldspar porphyroblasts containing quartz inclusion trails which define the earlier stages of shear foliation development. Inclusions trails indicate a dextral sense of shear which is consistent with the formation of mica rich domains (m) lying in the flattening field of the incremental strain ellipse. This data confirms that the shear zone accommodates NW verging thrust imbrication within the Sonnblick gneisses.

Figure 6.5b. Localization of late plastic deformation within K-feldspar porphyroblasts at the edges of mica and quartz inclusions. Plastic deformation is indicated by the localized development of undulatory extinction (u) in the feldspar. The localization of these microstructures at inclusion boundaries suggests that this deformation may be due to differential thermal contraction during uplift and cooling. Scale bar= 0.1mm.

Figure 6.5c. Shear band development within the shear zone is marked by the offset of the shear associated foliation and a reduction in grain size is in the deformed zone. No identifiable recrystallization is recognised. Scale bar= 0.1mm.

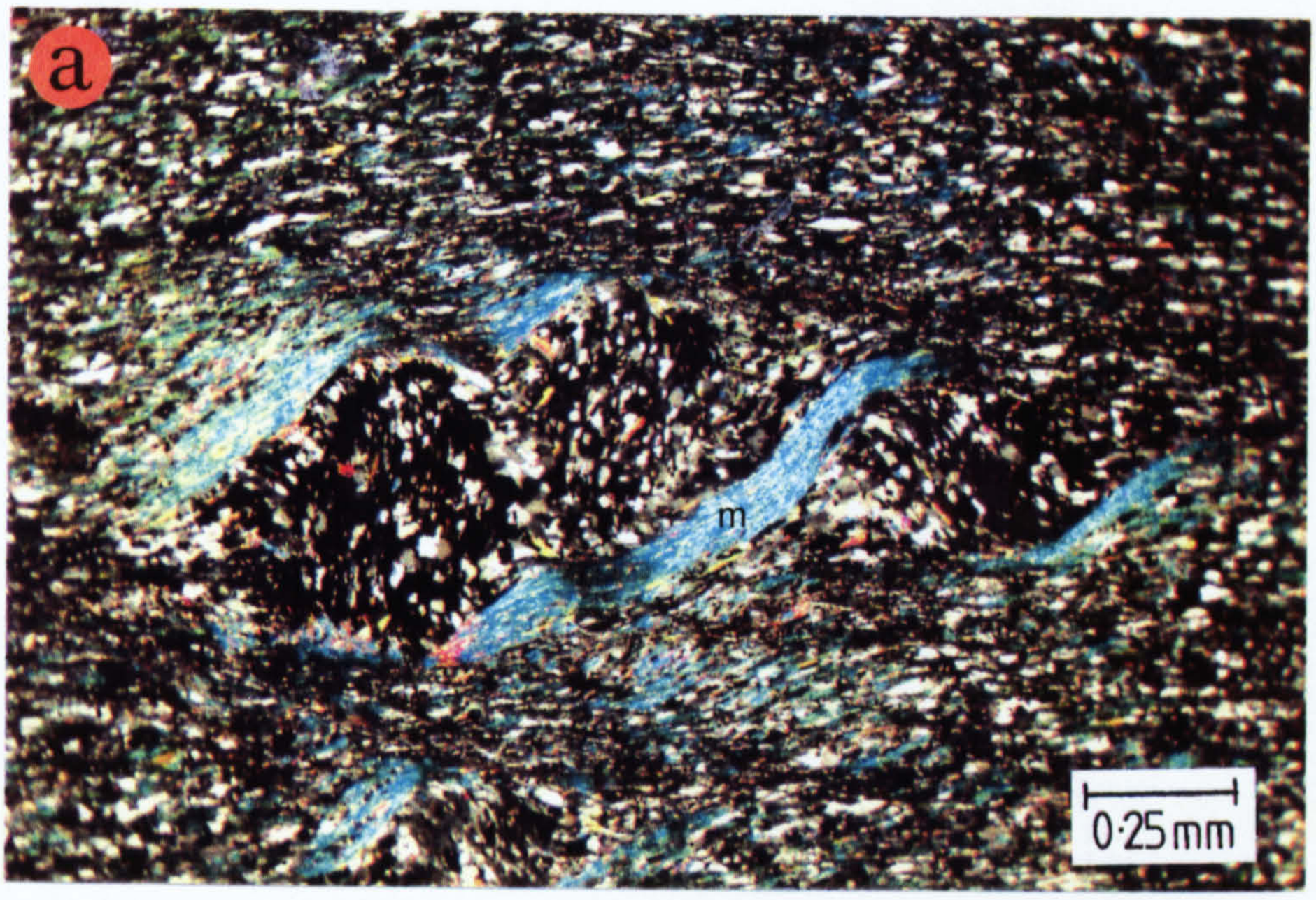
a
m
0·25 mm

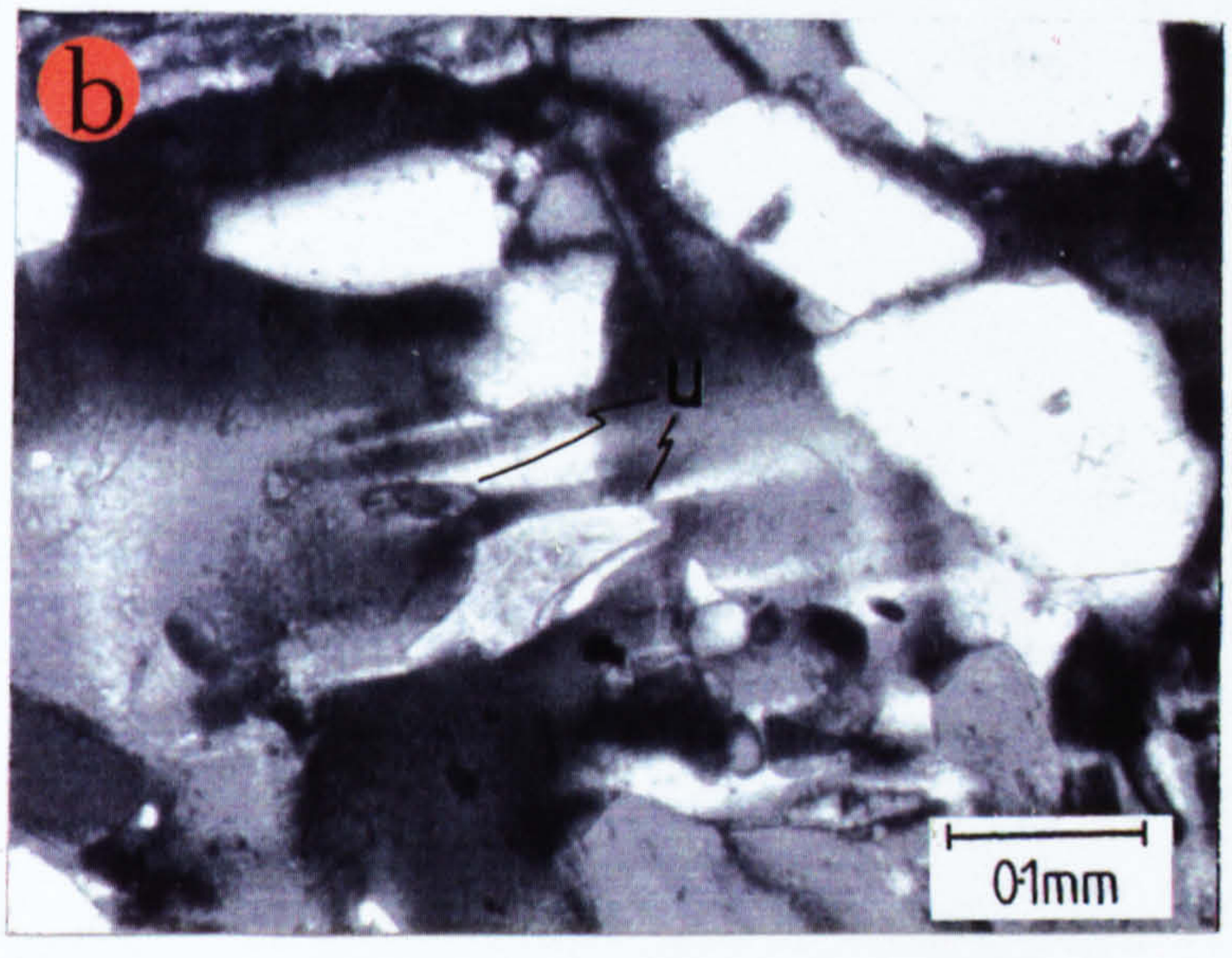
b
u
0·1mm


c
0·1mm

recrystallization, but show an elongation parallel to the S-fabric developed between the micaceous C-planes.

Shear bands develop between closely spaced feldspar porphyroblasts due to strain localization between them. These zones are mica-rich which may be a result of quartz dissolution by deformation-enhanced dissolution processes. The sense of shear on these zones is consistent with the bulk sense of shear associated with the shear zone. These zones are interpreted to have formed syn-deformationally during shear zone formation.

A second set of shear bands or extensional crenulational cleavage (ecc) cuts the S-C fabric. In this case, shear band formation is associated with a grain size reduction and shear strains of about 5. A fine grain size is preserved in the shear bands and micas which bend into these zones have undergone plastic deformation and show evidence of bending of the phyllosilicate lattice (Figure 6.5c). These show similar microstructures to shear bands developed towards the top of the Dome and are similarly interpreted to be post-metamorphic features associated with localized extension.

6:6 Discussion

6:6.1 The Relative Timing of Shear Zone Formation

The top-to-NW shear sense associated with formation of the shear zone is consistent with other overthrust senses in the Sonnblick Dome and suggeststhat the shear zone developed during emplacement of the Austroalpine nappe complex onto the the Pennine basement during Alpine continental collision. Small folds in the partly metasomatised footwall of the shear zone have similar orientations and may be of F_3 origin. Similar white mica-rich shear zones at higher structural levels of the Dome are observed to be folded by F_3. Since F_3 is considered to have developed prior to peak Alpine metamorphism (see Chapter 4), the shear zones may also be interpreted to have developed prior to peak metamorphism. This is supported by the development of albite porphyroblasts over mica folds within the shear zone. These porphyroblasts are interpreted to have grown during Alpine metamorphism (see 4:10.4a).

The shear zone is at a similar structural levels to the garnet amphibolite and Inner Schieferhülle schist studied in Chapter 5. Alpine metamorphic temperatures affecting the shear zone are therefore considered to be similar and in the order of $540 \pm 50°C$. As the shear zone is interpreted to have developed prior to metamorphism, temperatures of

shear zone formation were probably below this value. However, evidence of plastic deformation in feldspars suggests temperatures in excess of 450°C (Tullis and Yund 1985) for shear zone development. However, this deformation may represent the later stages of shear zone formation and it is possible that deformation initiated below these temperatures.

6.6.2 Constraints on the Metasomatic Fluid Phase

In order to understand the processes occuring in the shear zone, it is useful to consider the interaction of fluid and mineral phases. This can be done by considering the equilibrium rock and fluid compositions in cation activity space. With increasing strain, a greater modal percentage of white mica is observed along with a decrease in the amount of K-feldspar and plagioclase. The shear zone and gneiss assemblage can therefore be considered in terms of the Na-Ca-K-Al-Si-H_2O system and the observed alteration may then be considered in terms of the cation activities of Na^+, K^+, Ca^{2+} and H^+. Cation activity ratios have been calculated from the thermodynamic data set of Helgeson *et al* (1978) using their SUPCRIT program and have been used to construct diagrams in log activity-ratio space. The theory behind their construction and the calculation of equilibrium boundaries has recently been summarized by Bowers *et al* (1984) and is not discussed here.

The gneiss assemblage of albite, K-feldspar and muscovite has an equilibrium fluid composition given by point X in figure 6.6. The observed alteration in the shear zone could be explained by the infiltration of large amounts of a fluid lying within the muscovite stability field of the diagram (for example, point Y of figure 6.6). If a high fluid/rock ratio existed, the infiltration of such a fluid will result in buffering of the mineral assemblage and the incongruent breakdown of feldspar to white mica and quartz. This is the general reaction observed in the shear zone. A fluid within the muscovite field may have been derived from an equilibrium albite, K-feldspar, muscovite assemblage at higher temperature or lower pressure (Figure 6.7). Alternatively, fluids in equilibrium with pelitic schists (point P of Figure 6.6) may also have given rise to muscovitization of the original gneiss.

The main driving force for large scale fluid movement is variations in pressure within the crust (Etheridge *et al* 1983,1984). On a crustal scale, fluid flow will tend to be towards the surface, although fluids may move downwards during seismic activity by seismic pumping (Sibson 1977; McCaig 1988). At the conditions of shear zone

Figure 6.6. Activity diagram showing fluid compositions in equilibrium with a granitic orthogneiss (plag-ksp-wm) assemblage (X) and with pelites (P) at T=500°C and P=7kb. Point X has been calculated assuming unit activities apart from in K-feldspar (a=0.91), albite (a=0.95) and muscovite (a=0.56) where activities have been calculated by mixing on sites. In the case of muscovite, modelling activity in terms of a Redlich-Kister activity model makes no significant difference to the calculated activity. Position Y shows the approximate composition of a fluid in equilibrium with a gneiss assemblage at higher temperature (see figure 6.7). The infiltration of such a fluid into gneisses in equilibrium with X, will result in feldspar breakdown and the formation of white mica.

Figure 6.7. Activity diagram illustrating the effects of external conditions on the equilibrium fluid composition (marked by small circles) assuming all mineral phases have unit activity. It can be seen increasing T and decreasing P moves the fluid composition nearer to origin and into the muscovite field. The point E, represents the equilibrium fluid composition at 500°C and 7kb but with non-unit activities for K-feldspar (a=0.91), albite (a=0.95) and muscovite (a=0.56). mineral composition, in particular the effects of differing mineral activities, on fluid compositions in equilibrium with a gneiss (plag-ksp-wm) assemblage.

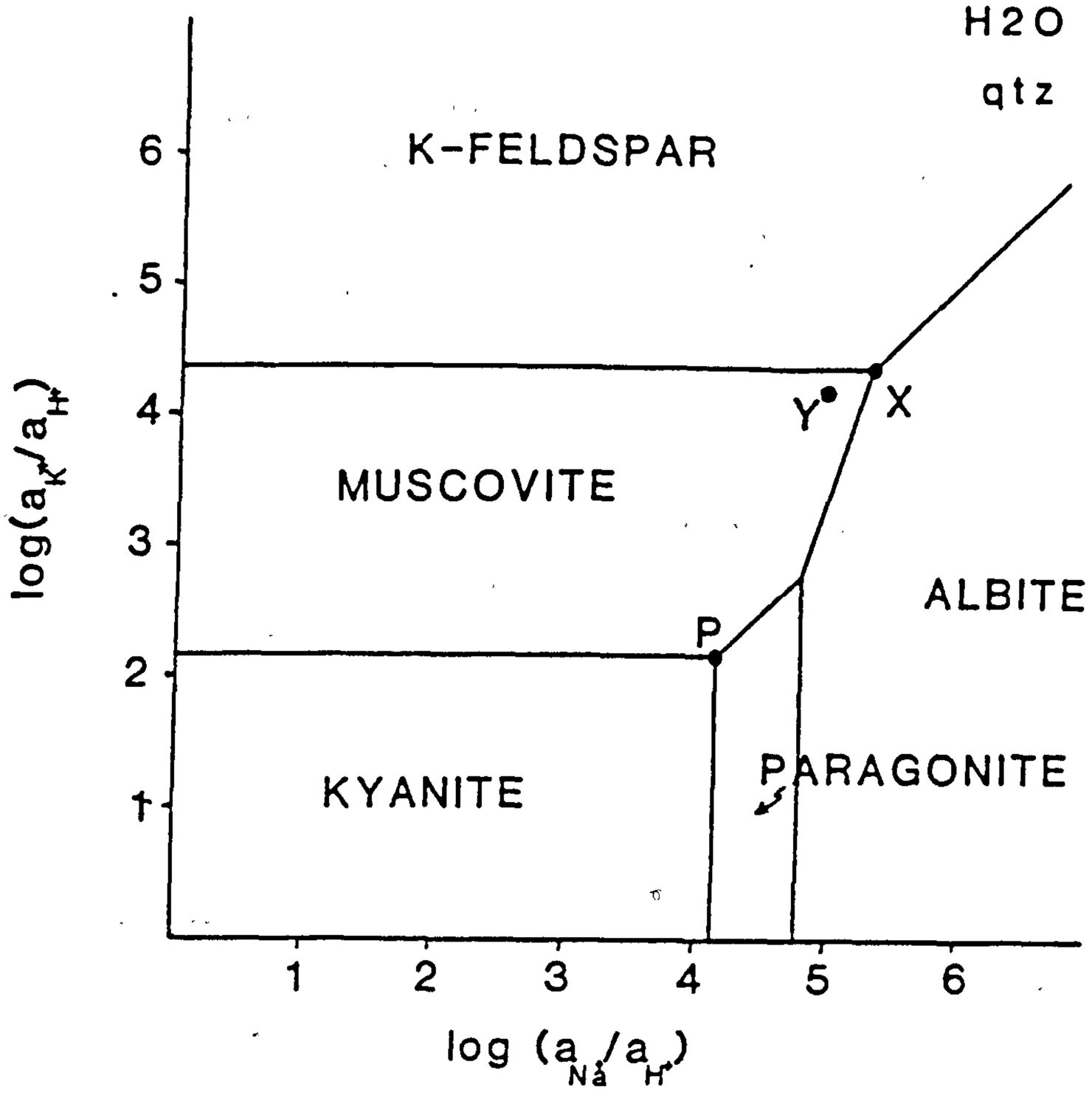
H2O
qtz
K-FELDSPAR
MUSCOVITE
ALBITE
KYANITE
PARAGONITE
X
Y
P
6
5
4
3
2
1
1
2
3
4
5
6
log (a_K+/a_H+)
log (a_Na+/a_H+)

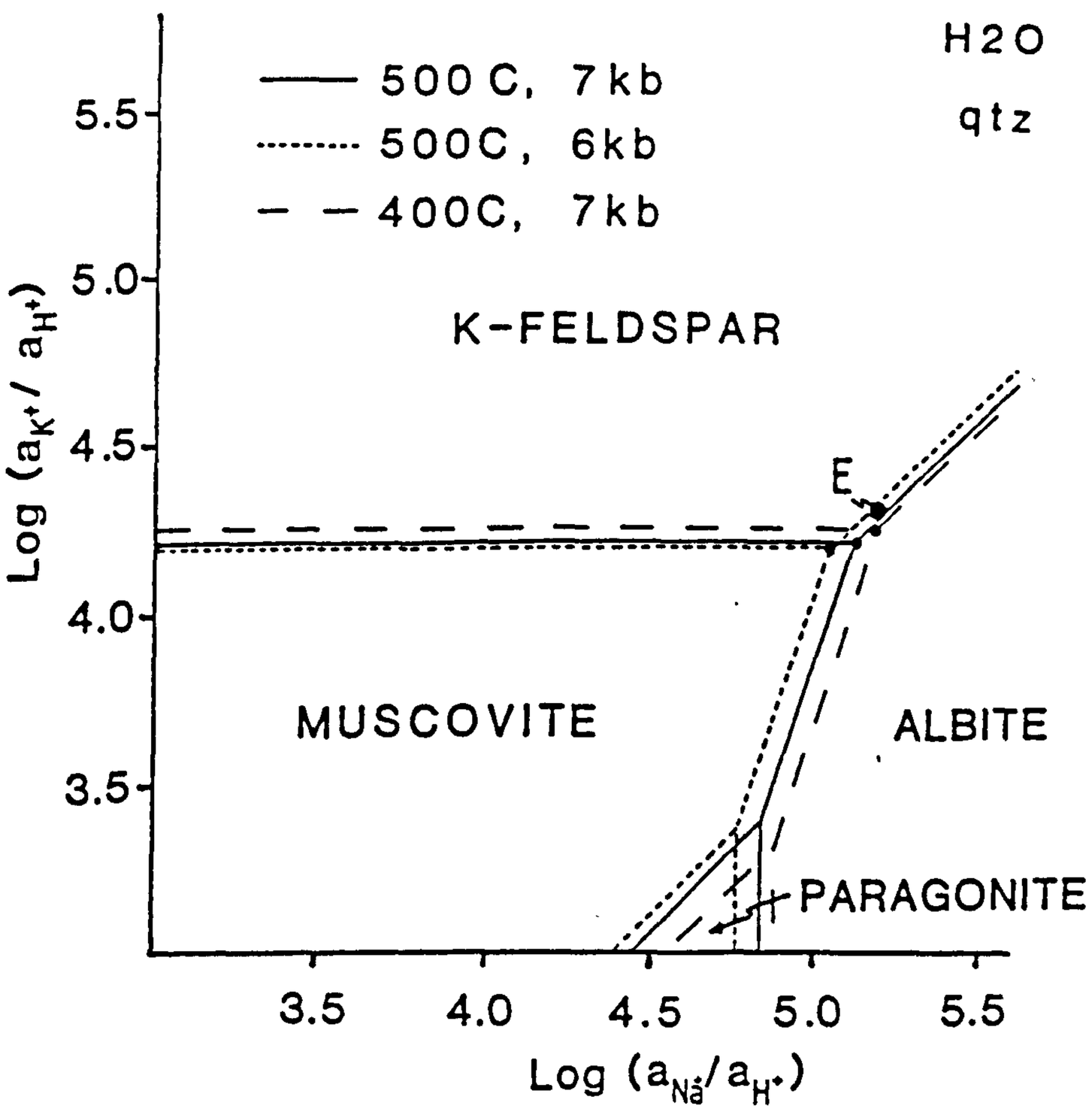
H2O
qtz
500 C, 7kb
500C, 6kb
400C, 7kb
K-FELDSPAR
MUSCOVITE
ALBITE
PARAGONITE
E
5.5
5.0
4.5
4.0
3.5
3.5
4.0
4.5
5.0
5.5
Log (a_K+ / a_H+)
Log (a_Na+/a_H+)

formation considered here, fluid flow will tend to be upwards due to the high lithostatic pressures within the crust (Wood and Walther 1984). Fluid flow will therefore be from higher to lower pressure. A gneiss assemblage at lower pressure is therefore unlikely to be the fluid source. It is worth noting however that large, local pressure variations during deformation may be possible.

Higher temperature fluids in equilibrium with two feldspars generally possess a larger K/Na ratio than those at lower temperatures and will therefore leach sodium and deposit potassium, when moving to lower temperatures. This is illustrated by the higher a_{Na+}/a_{H+} ratio, relative to a_{K+}/a_{H+}, for gneiss assemblages at two different temperatures (Figure 6.7). The down-temperature movement of metamorphic fluids will therefore be accompanied by the precipitation of potassium-bearing phases while sodium-bearing phases are dissolved.

At higher temperatures, the plagioclase within a gneiss assemblage is likely to have a reduced albite activity due to an increased anorthite component in the plagioclase. Similarly, the activity of muscovite may change depending upon P-T and fluid compositions. Therefore, although it can be inferred that the fluid, which caused metasomatic alteration within the shear zone, plots in the muscovite field in the log activity-ratio space, the values of the activity ratios cannot be inferred for this shear zone.

Muscovitization of feldspar bearing lithologies may also occur if fluids in equilibrium with pelitic schists (point P in Figure 6.6) pass through them. Pelitic schists are exposed within the Schieferhülle overlying the Sonnblick gneiss (Droop 1985). However, since the Sonnblick Dome is considered to be situated above a thrust (Chapter 4) it is possible that Schieferhülle material may also be present beneath the Sonnblick Dome in the footwall of the thrust.

Using the above data, it is not possible to distinguish between a granitic or pelitic schist fluid source. However, geochemical data in the form of fluid inclusion, crush-leach, or stable isotope analyses may constrain fluid compositions, fluid-rock ratios and fluid sources (eg. McCaig *et al*, in press). Unfortunately, post-deformational metamorphic recrystallization within these shear zones may have modified fluid inclusion or stable isotope compositions and it is difficult to assess whether such data would reflect fluid compositions associated with shear zone formation or later fluid compositions associated with metamorphism.

The approach illustrated above considers only an interpretation based on the general metasomatic product of fluid infiltration and the evolutionary path by which this result is obtained has not been considered. However, microstructural observations presented earlier suggest that the simple breakdown of feldspar to white mica may not be the case. This complicates the simple model presented above.

6:6.3 The effect of deformation on the Mineral Reactions

The observations on the samples, taken from a traverse through the gneiss host to the shear zone, show that feldspar breakdown to white mica is not the only reaction taking place during shear zone development. A number of reactions occured which do not appear compatible with the infiltration of an external fluid phase but are closely related to deformation associated with shear zone development (Reddy 1989). These are now considered.

6:6.3a A model for the Feldspar Exchange Reaction

The replacement of K-feldspar by albite towards the shear zone takes place along planar bands which are interpreted as planes of localized deformation, accommodating small amounts of slip associated with shear deformation. Primary plagioclase inclusions also show rims of albite replacing K-feldspar at sites where the internal strain energy of the of the K-feldspar has been enhanced by deformation. The exchange of K-feldspar by albite is therefore interesting because the reaction appears to have been enhanced by deformation.

The change in feldspar composition can be considered to occur by non-conservative grain boundary migration. This may be considered in terms of the individual replacement of K^+ for Na^+ within the K-feldspar lattice and the migration of the albite/K-feldspar grain boundary through the K-feldspar lattice. The driving force for grain boundary migration may take several forms; intragranular lattice defect energy, grain boundary energy, chemical free energy and external load-supporting elastic strain energy (Urai *et al* 1986). The replacement of K-feldspar occurs where the feldspar lattice is deformed (Figure 6.17), which suggests that intragranular defect energy provides the dominant driving force. However, the exchange of K-feldspar by albite involves the addition on Na^+ and the removal of K^+ from the reaction site and diffusive mass transfer of material was therefore important, at least on a local scale.

As previously discussed, the metasomatic alteration within the shear zone may be interpreted to be due to the infiltration of a fluid which plots in the muscovite field of the activity diagram (Figure 6.6). In this case, no reaction between feldspars would be expected. Since the replacement reaction is inferred to take place at the site of deformation in K-feldspar, deformation may provide the energy to drive the reaction.

For diffusive exchange to take place, chemical potential gradients are required and the processes by which these potential differences were established need to be considered, if the reaction is to be fully understood. An increase in the internal strain energy of feldspar due to twin production or localized slip and lattice kinking associated with deformation, may be sufficient to drive chemical reactions (Brodie and Rutter 1985; Wintsch and Dunning 1983).

Localized strain will affect feldspar stability and as a result, a reduction in K-feldspar stability in activity space relative to albite and muscovite may occur (Figure 6.8). The magnitude of this instability will be dependant upon a number of factors including dislocation density, grain size and fluid composition (Wintsch 1985, figure 2). However, the metastability may be in the order of several hundred calories per mole, which is sufficient to drive chemical reactions (Wintsch 1985).

Fluid in equilibrium with the two feldspar assemblage would not be in equilibrium with the strained K-feldspar and may react with strained K-feldspar to produce albite (Figure 6.8). A similar example of the replacement of K-feldspar by a myrmekitic intergrowth of albite and quartz has recently been shown to be deformation-enhanced, associated with increasing strain energy in the K-feldspar (Simpson and Wintsch 1989).

The above discussion assumes that the metasomatising fluid was in equilibrium with a granitic source rock. An alternative explanation is that the growth of albite occurs in response to infiltration of fluid derived from pelites. Since the alteration of feldspar to muscovite involves the consumption of H^+, and the concentration of H^+ is significantly less than Na^+ or K^+, the compostion of a fluid derived from a pelitic assemblage may move into the albite field in the activity diagram (McCaig *et al* in press). In order to reach equilibrium, this fluid must then change compostion by the replacement of K-feldspar by albite. In this case, strain in the K-feldspar lattice could help to localise nucleation and growth of albite by reducing the energy barriers to these processes (cf. Putnis and McConnell 1982).

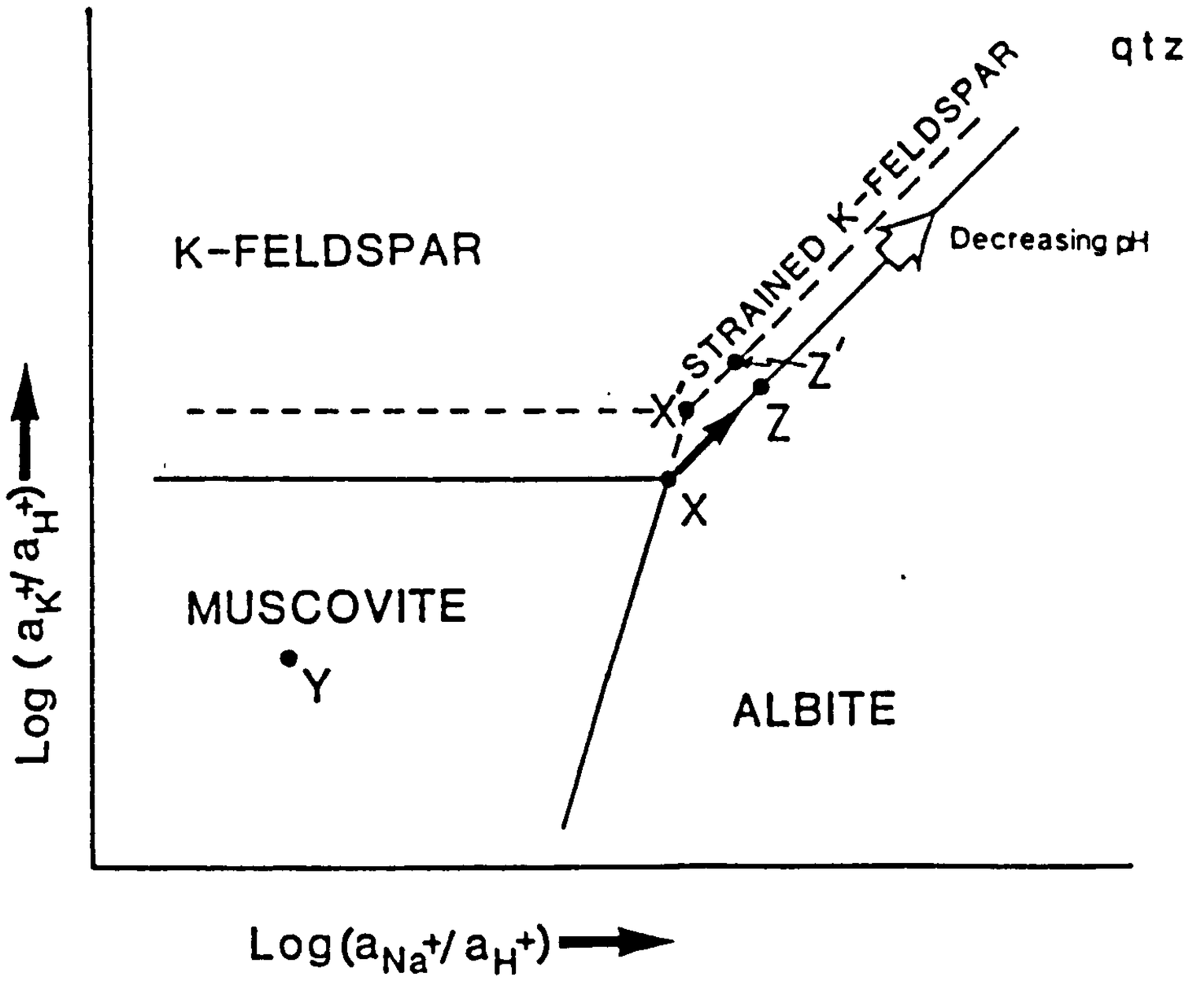

Figure 6.8. Schematic activity diagram illustrating how local fluid chemistry may be affected by deformation. A fluid in equilibrium with albite, muscovite and K-feldspar (X) will be unstable with respect to the strained K-feldspar assemblage (X') and the breakdown of deformed K-feldspar may occur. If the local fluid composition is buffered by the two feldspars (Z), (eg Simpson and Wintsch 1989), then the fluid will give rise to replacement of strained K-feldspar, in equilibrium with Z', for albite.

It is unlikely that such a fluid would have left K-feldspar stable in the main part of the shear zone while completely removing albite. However, the K-feldspar is not primary but forms porphyroblastswhich may have devloped during the later stages of shearing (see 6:6.3c). The original fluids did give rise to extensive K-feldspar breakdown. This model may therefore support a pelitic lithology for the source of the metasomatising fluid.

6:6.3b The formation of white mica

Approaching the shear zone, the feldspars are observed to be replaced by muscovite which is a direct response to the infiltration of acidic fluids (section 6:2). Where these reactions are first observed at the shear zone margin, they have not gone to completion. The reaction is often observed to be spatially related to microstructural features of the

shear zone, such as fractures cutting across K-feldspars which are parallel to the external foliation in the shear zone. These zones represent localized deformation and metamorphic reaction constrained to small shear zones within the feldspar.

At the margins of the shear zone, feldspar replacement by white mica is limited and feldspar commonly shows evidence for brittle deformation. Fractures developed within feldspar and are filled by either white mica or quartz depending on whether the fractures are formed parallel or perpendicular to the external foliation. Instantaneous fracturing and the opening of dilatent sites within feldspar augen will lead to rapid fluid infiltration into the fracture zone. The associated drop in fluid pressure within this zone will lead to rapid precipitation of quartz on the walls of the fracture due to the reduction in quartz solubility with decreasing pressure (eg. Fyfe *et al* 1978).

The rapid nucleation and precipitation of quartz as a response to a rapid decrease in fluid pressure, would effectively seal the feldspar surface so that reaction with the more acidic fluid was prevented. Mass transfer in this case was by advective processes and the cyclic development of microcracks.

Where the fracture is subparallel to the shear foliation and fractures filled with white mica are developed, evidence for rapid fluid pressure variations are not observed. Mica growth therefore appears to be a response to progressive deformation in which externally derived fluids may give rise to mica production.

Where fluid volumes were relatively low, and fluid compositions were to a large extent buffered by the mineral assemblage (for example at the shear zone margin) transiently low permeabilities may be produced which would enhance fluid pressure and favour brittle deformation. Fracturing of feldspar would increase the surface area of the feldspar which in turn would be expected to increase reaction rates, enhance permeabilities and lead to rapid dissolution of feldspar, due to the reaction between an externally derived fluid and the feldspar. As the feldspar reaction had not gone to completion, this suggests that the integrated fluid-rock ratios and the rate of fluid fluxing at the shear zone margin must have been low.

The anisotropic nature of feldspar reaction, which produces elongate feldspar grains, could be related to the ability of the fluid to access foliation-parallel feldspar surfaces due to enhanced fluid flow along the foliation planes rather than across them. The feldspar

margin parallel to the foliation would therefore be expected to "see" a larger volume of reactive fluid than the ends of the feldspar where fluid access may be limited.

Simple shear deformation within the shear zone may also give rise to significant increases in the internal strain energy of the feldspar.This increase in internal energy has been shown to be sufficient to drive mineral reactions in a system closed to externally derived fluids (Simpson and Wintsch 1989). In this case where externally derived fluids play a large role in the metasomatic alteration and mineral reaction, the increase in internal strain energy may be sufficient to locally increase reaction rates. Compressive stresses acting at 45° to the shear foliation would enhance dissolution and reaction by incongruent pressure solution (Beach 1976) leading to the observed elongated feldspar morphology.

6:6.3c Models for the development of Syn-Deformational K-Feldspar Porphyroblasts

An explanation for the development of K-feldspar porphyroblasts along shear parallel bands within a shear zone, in which igneous K-feldspar has undergone dissolution, is problematical. The initial alteration associated with the breakdown of feldspar and the production of white mica, required the infiltration of more acidic fluids, lying within the muscovite stability field of the activity diagram (Figure 6.6). As discussed earlier, geometrical softening associated with feldspar breakdown may have localized later strain and enhanced permeability which led to localization of fluid flow. Early brittle deformation of feldspars may have increased feldspar reaction rates, but no evidence for this process remains. Quartz inclusion trails show that syn-deformational K-feldspar growth occured after the development of a micaceous foliation at the expense of white mica.

The reaction of muscovite to K-feldspar can be represented by the equation;

$$KAl_3Si_3O_{10}(OH)_2 + 6SiO_2 + 2K^+ = 3KAlSi_3O_8 + 2H^+$$

so that the equilibrium constant, K, is given by;

$$\log K = 3\log a_{Ksp} + 2\log a_{H+} - \log a_{ms} - 6\log a_{SiO_2} - 2\log a_{K+}$$

The forward reaction will therefore be favoured by an increase in the activities of muscovite, quartz or K^+, or by a decrease in K-feldspar or hydrogen ion activities. Changes in PT conditions will also affect the equilibrium.

As temperature increases and/or pressure decreases, the fluid composition in equilibrium with granite will migrate towards the origin of the activity diagram (eg. Figure 6.7). If the original composition of the fluid causing metasomatism (eg. point Y in Figure 6.6) was in a position such that as the temperature increased, the K-feldspar - muscovite equilibrium line passed through it, then a further increase in temperature and/or decrease in pressure will result in the formation of K-feldspar at the expense of muscovite.

Such a model is consistent with the previously presented argu ments that shear zone development took place during prograde conditions (increasing T and decreasing P) (see 6:6.1). It is also consistent with the development of the foliation prior to the development of K-feldspar, as indicated by preserved inclusion trails. The fact that K-feldspar growth is not pervasive through the whole zone, but occurs within discrete bands, may be due to continued, localized fluid infiltration from higher temperature gneisses at depth. K-feldspar growth may have hardened the K-feldspar domains to deformation and localized strain and fluid infiltration to micaceous zones.

An alternative model for K-feldspar growth may be considered, based upon the possible effects of localized deformation. The exchange of H^+ for cation species such as K^+ on feldspar and mica surfaces occurs rapidly under experimental conditions (Garrels and Howard 1959). Such exchange reactions have been shown to increase the pH of the solution by a significant amount depending upon the PT conditions and fluid-rock ratio (Tamm 1930, Gruner 1944).

Hydrolysis reactions at the surfaces of white micas may give rise to ion exchange between solution and mineral and will increase potassium activity in solution while reducing H^+ activity (Wintsch 1985). This will stabilize feldspar relative to white mica, due to increasing log activity ratios and a decrease in the local pH of the solution (Figure 6.8). Localized shearing of micas along basal (001) cleavages by the "box car" model of White (1977) may provide "new" surfaces where reaction may take place. This will lead to changes in fluid composition which will favour the formation of K-feldspar. It has been suggested that this shearing may inhibit feldspar growth by increasing dislocation

densities in newly grown feldspars which would favour rapid dissolution (Bell *et al* 1985).

In zones of low permeability, external buffering of the mineral assemblage may be overtaken by hydrolysis reactions at mica surfaces, or by the destabilization of mica due to enhanced internal strain energies. Deformation partitioning may give rise to zones of progressive shortening within a rock undergoing bulk simple shear (Bell 1983). These factors may be sufficient to crystallize feldspar at the expense of white mica.

In summary, the effect of changing temperature and pressure during shear zone development may explain the growth of K-feldspar. Again however, the effects of deformation provide an alternative explanation for the observations. In this case, the two models do not conflict but may take place simultaneously but it is impossible to assess the relative contribution of each.

6:6.4 Strain Localization Processes

The replacement of relatively strong feldspar by the weaker white mica due to the infiltration of an externally-derived fluid into the shear zone, may lead to softening which may enhance strain rates in the shear zone and lead to the localization of deformation by reaction-enhanced ductility (White and Knipe 1978; Rubie 1983; Handy 1989). Post-deformational recrystallization within the shear zone has destroyed the detailed microstructures related to the development of this zone. However, the reduced grain size associated with the formation of white mica at the expense of feldspar will increase diffusive pathways. This in turn may enhance diffusion-controlled processes such as diffusion-enhanced grain boundary sliding and pressure solution processes. Locally preserved mica hinges indicate that mica recrystallization was associated with grain coarsening which still preserved the precrystallization mica orientation. Mica growth within the shear zone therefore appears to have been oriented with (001) lying parallel to the foliation. Since (001) is an easy plane of slip within micas, geometrical softening is likely to have played a role in strain localization.

Feldspar deformation at the shear zone margin is dominated by brittle processes although moving progressively towards the shear zone, there is less evidence for brittle deformation and strain accommodation by feldspar breakdown and reaction enhanced ductility dominates. Metamorphic reactions may lead to enhanced permeability (Rumble *et al* 1982; Rumble and Spear 1983). Therefore, continuous metamorphic reaction

associated with fluid infiltration into the shear zone may have kept permeabilities relatively high and enabled fluid flow to be further concentrated into zones already undergoing reaction. Reaction-enhanced permeabilities would then further localize fluid flow and fluid-enhanced deformation and metamorphism (Brodie and Rutter 1985), which would ultimately lead to rapid feldspar dissolution (eg Mitra 1978; Tullis and Yund 1985).

Dynamic deformation processes within the shear zone would be expected to produce zones undergoing varying strain rates and varying intensities of deformation (Knipe 1989). Such variations, caused by localized work hardening and softening processes could give rise to varying permeabilities within the shear zone and may produce both zones of increased or reduced permeabilities within a zone of already enhanced fluid flow.

6:7. Conclusions

The growth of mica at the expense of feldspars occured in response to the infiltration of an external fluid which removed Na and added K to the rock. This fluid may have been derived from a pelitic asssemblage or from gneisses at lower pressure or higher temperature. The last of these is more consistent with models for reaction taking place in the shear zone and is the the preferred fluid source.

Localization of strain within the Sonnblick gneiss is seen to be associated with intense metasomatic alteration of the granitic lithology to a white mica schist. Softening, associated with the mechanical and chemical breakdown of feldspars to white mica, is likely to have localized fluid infiltration into the shear zone. The continued interaction of fluid infiltration, chemical reaction and softening within the shear zone gave rise to the large strains inferred for the zone.

The growth of K-feldspar porphyroblasts within the shear zone can be explained by an increase in temperature and a reduction in pressure along a PTt path caused by overthrusting of the Austroalpine sheet (see Chapters 4 and 5). However, the sites of K-feldspar and albite growth in the shear zone and gneiss may be strongly controlled by deformation and a direct influence of deformation on the direction of reaction is a possibility.

Chapter 7

Geochronology of the Sonnblick Dome

7:1 Geochronology of the Eastern Alps

Previous geochronological studies have illustrated both the Prealpine and Alpine development of the Eastern Alps. Within the Tauern Window, U-Pb and Rb-Sr dating techniques (Cliff, 1971,1977, 1981; Cliff and Cohen 1980; Hawkesworth 1976) have confirmed the Pre-Alpine age of the Zentralgneis Complex which was previously based on field relationships (Exner 1964; Cliff *et al* 1971). These data indicate that the intrusion of the granite precursors occured *c*.320 Ma ago (Cliff 1981), although plutonism may have extended into the Late Permian in the case of more evolved granites (Cliff 1971, 1981).

Of more interest in terms of Alpine tectonics are mineral age data collected over the last 25 years. The available mineral data for the Alps upto 1986 has recently been compiled for the whole of the Eastern Alps (Frank *et al* 1987). Towards the Eastern Tauern Window, mineral data for biotite and white mica using both Rb/Sr and K/Ar techniques indicates an abrupt age break across the Pennine-Austroalpine contact. Ages within the Pennine basement are commonly in the range of 20-30 Ma, while 70-90 Ma ages have been reported from the Austroalpine (Oxburgh *et al* 1966; Lambert 1970; Cliff *et al* 1971; Hawkesworth 1976; Waters 1976). These ages have been interpreted as cooling ages and record the time at which the particular isotope system within a mineral phase, became closed to reequilibration within the host rock. The dates recorded in the Austroalpine units are thought to indicate uplift and erosion of the Austroalpine plate, associated with overthrusting of the Austroalpine units towards the northwest. Although this may be the case, juxtaposition of the two units is considered to represent the superposition of out-of-sequence thrusting and later, synconvergent extension (Wallis 1987).

The mineral data has been used to infer a 35-40 Ma age for the peak of metamorphism within the Peripheral Schieferhülle of the southeast Tauern Window (Lambert 1970; Hawkesworth 1976). More recently, mineral isotope data has been combined with detailed petrological studies in order to define the details of PTt paths and to access the timing of peak metamorphism as well as the subsequent uplift and cooling

histories (eg. Blackenburg *et al* (1989) for the western Tauern Window and Cliff *et al* (1985) for the southeastern Tauern Window).

In the Zentralgneis unit of the Hochalm-Ankogel massif, Cliff *et al* (1985) illustrated changing rates of uplift over the last 25 Ma and differential uplift of at least 4km associated with dome development. In conjunction with P-T trajectories of rocks from different structural levels, geochronological data enabled a comprehensive picture of the thermal history of the Hochalm Zentralgneis Dome to be developed.

7:2 "Closure Temperature" and the Effects of Deformation

The above studies have relied largely upon the concept of the isotopic closure temperature, which is defined as the 'temperature of the mineral at its apparent age' (Dodson 1973), and represents the temperature at which the diffusion of a particular isotope within a particular mineral effectively ceases. The kinetics of the closure process are generally considered to have a strong dependence on temperature, although grain size and cooling rate are also important (Dodson 1973, 1979; Cliff 1985). Published closure temperatures (Tc) for mineral phases have been determined by field observations or hydrothermal diffusion experiments. In this study, the empirical closure temperatures determined from the Central Alps for Rb/Sr in biotite ($T_{CRb/Sr}$ = 300±50°C; Jäger *et al* 1967) and muscovite ($T_{CRb/Sr}$ = 500±50°C; Purdy and Jäger 1976) are used because these accommodate an Alpine cooling rate of 30°C/Ma. These 'closure temperatures' are also similar to experimentally derived values (Dodson 1973, 1979).

The 'closure temperature' concept assumes resetting of the isotopic system by volume diffusion processes. However, recrystallization of mineral phases below the closure temperature can also enable isotopic readjustment and homogenization. Since recrystallization processes are also dependent upon pressure, strain, strain rate and the presence of a fluid phase and not necessarily temperature, the deformation history of the analysed suite of samples may be of great importance to the interpretation of isotopic results.

7:3 Geochronological Studies Within the Sonnblick Dome

This chapter presents Rb-Sr geochronological data in order to constrain both the timing of different events within the Sonnblick area and to investigate the post-metamorphic thermal history of the Sonnblick Dome. This work is not presented as an

exhaustive study since the data set is far from complete and is still being collected. However, the results obtained so far provide useful controls on the absolute timing of events and the thermal history of the Dome. This study has involved whole-rock Rb-Sr analyses of 2-5kg samples in order to date the intrusive age of the Sonnblick gneiss precursory granites and provide an 'isochron' from which later modification of Rb-Sr systematics may be compared. Whole-rock thin slab dating has been used in an attempt to date shear zone formation, while mineral data collected from the Sonnblick region has been used to constrain the uplift and thermal history of the area after peak metamorphism. Sample preparation and analytical techniques for this work are presented in Appendix A1:1 and A2:4.

7:3.1 The Age of the Sonnblick Gneiss Precursors

Rb-Sr analyses on whole rock samples taken from around the Sonnblick Dome have been used in order to date both the early granite and provide a reference isochron which may be compared with the mineral and thin slab data. All samples were taken from weakly foliated coarse augen gneisses and were studied by optical microscopy to assess the contribution of late contamination from calcite veins and pressure shadows.

Regression of nine whole-rock analyses (Table 7.1) yields an age of 303±83 Ma (Figure 7.1). The larger error in the age reflects the scatter of data about the regression line which is indicated by the large MSWD value of 79.4. This scatter may have resulted from several sources. An obvious source of scatter is a primary heterogeneous distribution of Sr within the granite due to incomplete mixing or small true time differences in the timing of the granite crystallization. Slight secondary disturbance of the isotope system may have occured during subsequent deformation and metamorphism during Late Variscan or Alpine tectonism. The homogeneity within the Sonnblick granite gneisses is illustrated by the very small spread in $^{87}Rb/^{86}Sr$ values (0.756 - 1.195). This small spread contributes to the large error associated with the calculated age.

The data shows the gneiss precursor to be Pre-Alpine in age and is consistent with previous work which has yielded the more precise intrusion ages for the Zentralgneis Complex ranging from late Carboniferous (Cliff 1981) to Lower Permian for more evolved granites (Cliff 1971). The calculated initial Sr ratio (0.7059) is consistent with geochemical evidence for the Zentralgneis precursors being I-type in origin (Finger and Steyrer 1988 and Chapter 3:3).

Table 7.1. Whole-rock Rb-Sr data for granite gneisses in the Sonnblick Dome.

Sample	Sa wt.	Sp wt.	N-87/S-87	Rb ppm	Sr ppm	Rb/Sr	84Sr/88Sr	87Sr/86Sr	2s	87Rb/86Sr
48415	0.1958	0.3698	0.56149 (36)	136.11	542.06	0.251	0.011550 (6)	0.709179	(16)	0.727
48416	0.0494	0.0926	0.71036 (26)	170.93	467.58	0.366	0.012274 (4)	0.710062	(16)	1.058
48419	0.0724	0.1066	0.83301 (44)	157.37	521.18	0.302	0.010641 (2)	0.709767	(12)	0.874
48605	0.0589	0.1001	0.69500 (10)	151.64	580.50	0.261	0.010783 (2)	0.709127	(16)	0.756
48607	0.0441	0.1070	0.58452 (6)	182.07	440.98	0.413	0.014335 (8)	0.711358	(26)	1.195
49114	0.0567	0.1164	0.70725(128)	186.73	458.99	0.407	0.012995 (2)	0.710932	(10)	1.177
29/86	0.0686	0.1053	0.86252 (96)	169.97	589.47	0.288	0.010336 (10)	0.709577	(20)	0.834
32/87	0.0646	0.1015	0.82693 (8)	166.80	465.74	0.358	0.011398 (1)	0.710329	(10)	1.037
184/87	0.0446	0.0926	0.62627 (62)	166.74	499.95	0.334	0.012473 (2)	0.709665	(16)	0.965

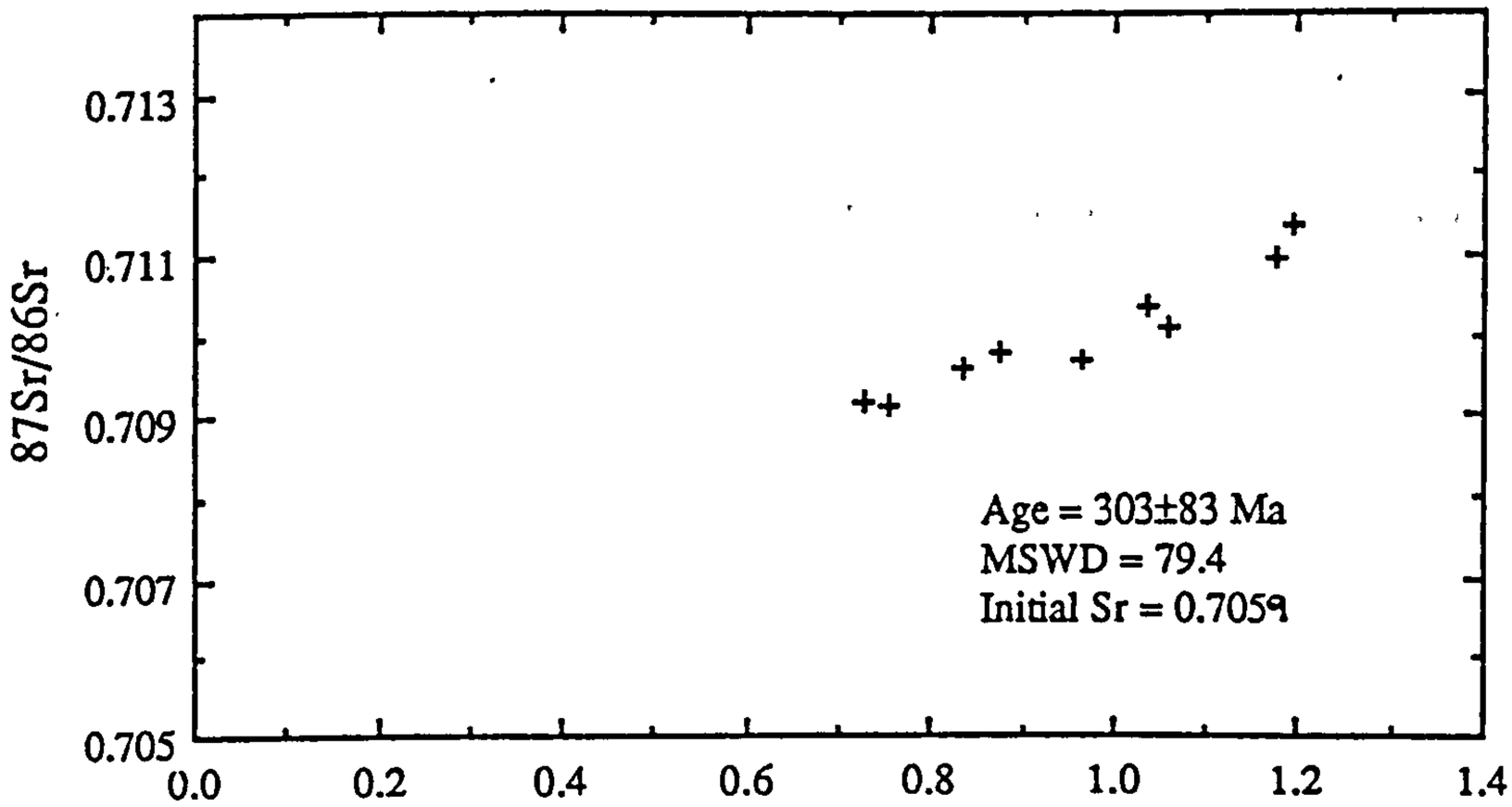

Figure 7.1. Rb-Sr diagram for low strain granitic gneisses from the Sonnblick Dome. Calculated age is based on a model 1 York fit.

7:3.2 Mineral Data Within The Sonnblick Dome

Minerals separated from whole rock samples may be used to date the passage of the rock through the minerals closure temperature provided that the radiogenic ^{87}Sr present within the mineral at the time of isotopic closure can be estimated. The initial $^{87}Sr/^{86}Sr$ ratio may be estimated from other mineral phases with low Rb/Sr ratios (commonly plagioclase) which were in isotopic exchange equilibrium with the mica at the time of closure. Evidence to suggest that plagioclase analyses provide an adequate estimate of the initial ratio has been provided by Cliff *et al* (1985) from studies on the Hochalm Zentralgneis.

Figure 7.2. Map showing the distribution of mineral age data and local cooling rates for the Sonnblick Dome.

MAP SHOWING MINERAL AGE DATA

FOR THE SONNBLICK REGION

North

Sonnblick

Schareck

Sand Kopf

Eckberg

Stossl Spitze

Rote Wand

Kamm spitze

0 1 2 3 4 5 km

SCALE

× 13·3

Eckberg ×11·5

21 22·9 ● 22·4
×13·2 23

23·5 +27

×11·4
17 ●22·9

27 ● 23·2 ×9·3
×15·8

Stossl Spitze 25·8 ● 20·8
20/40 ○23·5 ×10·4

×11·6

21 ● 20·6
×8·8

27·7 ○ 19·2
19/24 ×8·6

● Rb-Sr BIOTITE AGES

○ Rb-Sr WHITE MICA AGES

× FISSION TRACK AGES (Staufenberg 1.985, 1987)

+ K-Ar WHITE MICA AGES (Lambert 1967)

21/40 AVERAGE COOLING RATES (°C/Ma) 100-300°C / 300-500°C

The location of the calculated mineral pair ages (Table 7.2) are illustrated in Figure 7.2, as are the earlier K-Ar analyses of Lambert (1970) and the apatite fission track results of Staufenberg (1985,1987). Biotite ages vary from 19.2 to 23.5 Ma while limited white mica ages of 23.5 to 27.7 Ma are recorded. The consistency of biotite age results from the Sonnblick area further support the assumption that plagioclase provides a reasonable estimate of the initial ratio. The decrease in age from white mica through biotite to the fission track ages reflects the decreasing 'closure temperature' of the respective mineral phases. The variations in biotite and fission track age data show a parallel trend with younger ages in the southeastern part of the Dome.

Table 7.2. Mineral Rb-Sr data for the gneiss samples within the Sonnblick Dome.

Sample	Height*(m)	Rb ppm	Sr ppm	Rb/Sr	87Sr/86Sr	2s	87Rb/86Sr	Age	(error)
48415 Bio	2260	804 83	52.28	15.395	0.722175	(23)	44.604	22 9	(0 3)
48415 Pl		76.93	53.52	1.437	0.709024	(50)	4.159		
48416 Bio	2200	968 40	49.79	19.448	0.727727	(48)	56.379	22 4	(0.3)
48416 Pl		110.10	313.66	0.351	0.710105	(20)	1.016		
48419 Bio	1560	881 10	17.64	49.943	0.752388	(56)	145.132	20 8	(0.3)
48419 Pl		76 80	574.65	0.134	0.709589	(44)	0.388		
48419 wm		512 53	64.05	8.002	0.717937	(50)	23.175	25 8	(C 3)
48605 Bio	1530	898 40	9.46	95.008	0 800163	(60)	277.374	23.2	(0.3)
48605 Pl		79.50	440.35	0.181	0.708894	(10)	0.524		
48607 Bio	2100	1033.58	46 19	22.378	0.731966	(14)	64.900	22 9	(0.3)
* repeat			46.22		0.731985	(64)			
48607 Pl		88.85	373.77	0.238	0.711087	(12)	0 689		
* repeat			373.99		0.711087	(12)			
48610 Bio	1360	986 30	18.46	53.429	0.756574	(48)	155 326	20.6	(0.2)
48610 Pl		101.60	274 94	0.370	0 711459	(12)	1.071		
48612 Bio	790	931 76	86 20	10 810	0.718737	( )	31.310	19.2	(0 3)
48612 Pl		142.70	402 46	0 355	0.710480	(10)	1.027		
48612 wm		655.41	71.36	9.184	0.720334	(76)	26.050	27.7	(C 4)
223/85 Bio	1760	1056.44	48 53	21.769	0.730632	(42)	63.125	23.5	(C 5)
223/86 Pl		150.98	426.93	0.354	0.709888	(12)	1.023		

7:3.3 Dating by the Thin Slab Technique

In this part of the study, an attempt has been made to date the formation of shear zones within the Sonnblick area. Discrete layers containing syndeformational K-feldspar porphyroblasts are interbanded with K-feldspar-poor layers within the metasomatic shear zone discussed in Chapter 6. Banding lies parallel to the shear zone margin and to the well developed shear zone c-foliation, which is interpreted to have developed during top-to-NW shearing. Data has been presented to suggest that preserved microstructures represent those developed by recrystallization of the shear zone matrix after shearing. Recrystallization is probably associated with peak metamorphic conditions.

In order to study the isotope systematics of these shear zones a thin slab whole rock Rb-Sr technique has been used (see Appendix 1). The thin slab method has been a contentious procedure for dating of geological events due to the difficulty in interpretation of the results and therefore its reliability (eg Hofmann 1979; Peucat and Martin 1985). However, the method may provide valuable information with regard to re-equilibration of Sr isotopes when used in conjunction with mineral isotopic data and detailed petrological and microstructural observations (eg. Thoni 1986,1988). It may therefore a be reliable geochronological method for dating geological events in areas showing a complex deformation and metamorphic history.

A representative sub-volume of the shear zone (30mm x 60mm x 30mm) containing discrete bands of K-feldspar and mica layering was taken from the unweathered interior of a 3kg sample (sample 24/87). This block was divided into 14 smaller blocks, weighing between 7-18 gm, based on mineralogical layering. These blocks, which are illustrated in Figure 7.3a, were analysed for Rb and Sr following the technique described in Appendix 2:4. Regression of all the thin slab data (Table 7.3 and Figure 7.3b) yields a regression age of 22.3 ± 2.1 Ma although there is large scatter reflected in the MSWD of 33.9.

Data from the thin slabs falls into two domains; those containing a high K-feldspar content (points c,d,e,f,j,k and l) and those which are K-feldspar poor (a,b,g,h,i and n), which can be individually considered during regression analysis. Sample 'm' has an intermediate mineralogy and has not been assigned to either of the domains. Regression of this domainal data yields an isochron with an age of 17.1±1.0 Ma (MSWD=0.81) for the K-feldspar rich samples, while the mica rich bands define an errorchron of age 29.0± 5.7 Ma (MSWD=10.5). These data have low MSWD values relative to the regression line calculated using all of the data.

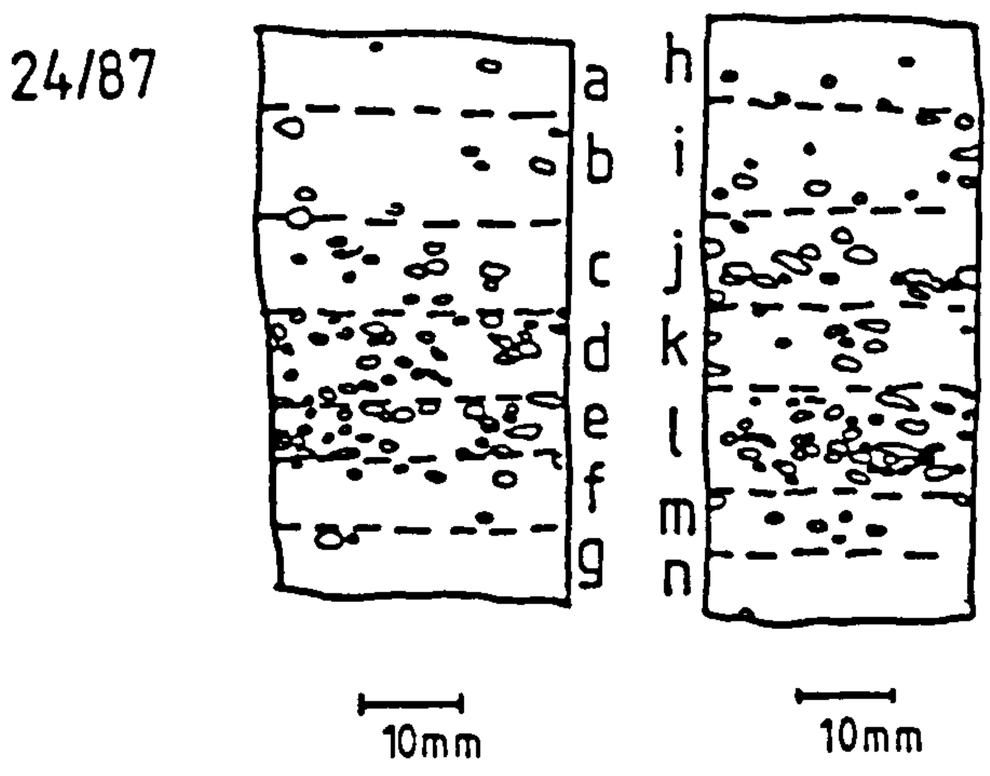

Figure 7.3a. Sketch of thin slabs usedfor dating showing the distribution K-feldspar throughout the slabs.

Table 7.3. Geochronological Data for the metasomatic shear zone discussed in Chapter 6.

Sample		Sa wt	Sp wt	N 87 S 87	Rb ppm	Sr ppm	Rb/Sr	84Sr/88Sr	87Sr/86Sr	2s	87Rb/86Sr
24 87	(a)	0 0516	0 1560	0 41565 (32)	161 35	39 51	4 084	0 112368 (26)	0 719260	42	11 829
	(b)	0 0462	0 1547	0 34587 (26)	148 73	46 64	3 189	0 105847 (52)	0 718187	48	9 205
	(c)	0 0489	0 1448	0 41100 (24)	156 24	59 12	2 260	0 065874 (8)	0 717432	26	6 546
	(d)	0 0509	0 1471	0 43989 (16)	163 23	78 61	2 076	0 057485 (10)	0 717277	54	5 013
	(e)	0 0512	0 1497	0 44748 (14)	167 97	128 34	1 309	0 038187 (12)	0 715760	48	3 790
	(f)	0 0543	0 1963	0 33899 (2)	157 33	70 76	2 223	0 077251 (78)	0 717366	50	6 439
	(g)	0 0534	0 1467	0 48806 (20)	172 13	45 85	3 755	0 090224 (32)	0 718981	54	10 875
	(h)	0 0539	0 1546	0 44965 (16)	165 58	39 77	4 163	0 106306 (28)	0 719507	60	12 060
	(i)	0 0512	0 1537	0 42527 (6)	163 89	54 80	2 991	0 082345 (34)	0 718072	60	8 562
	(j)	0 0564	0 1510	0 45225 (8)	155 45	86 33	1 801	0 049559 (88)	0 717123	22	5 215
	(k)	0 0460	0 1453	0 40335 (4)	163 57	86 47	1 892	0 057160 (70)	0 717150	12	5 478
	(l)	0 0605	0 1532	0 49717 (14)	161 62	122 51	1 319	0 035289 (8)	0 716753	20	3 820
	(m)	0 0649	0 1643	0 47345 (18)	153 92	67 01	2 297	0 058891 (14)	0 717645	38	6 652
	(n)	0 0448	0 1410	0 41540 (18)	160 59	42 25	3 801	0 105112 (298)	0 718871	92	11 009
24/87 WR		0 0417	0 1250	0 41886 (18)	161 22	98 78	1 816	0 054416 (16)	0 716304	70	5 380
24/87 wmica		0 0614	0 1596	0 97385 (10)	324 97	87 29	3 723	0 048231 (24)	0 719273	42	10 784
24/87 ksp		0 0534	0 1357	0 50356 (10)	164 28	444 84	0 369	0 014673 (2)	0 715747	12	1 059
24/87 ksp		0 0141	0 0685	0 29876 (8)	186 34	450 13	0 414	0 021639 (2)	0 715817	12	1 195

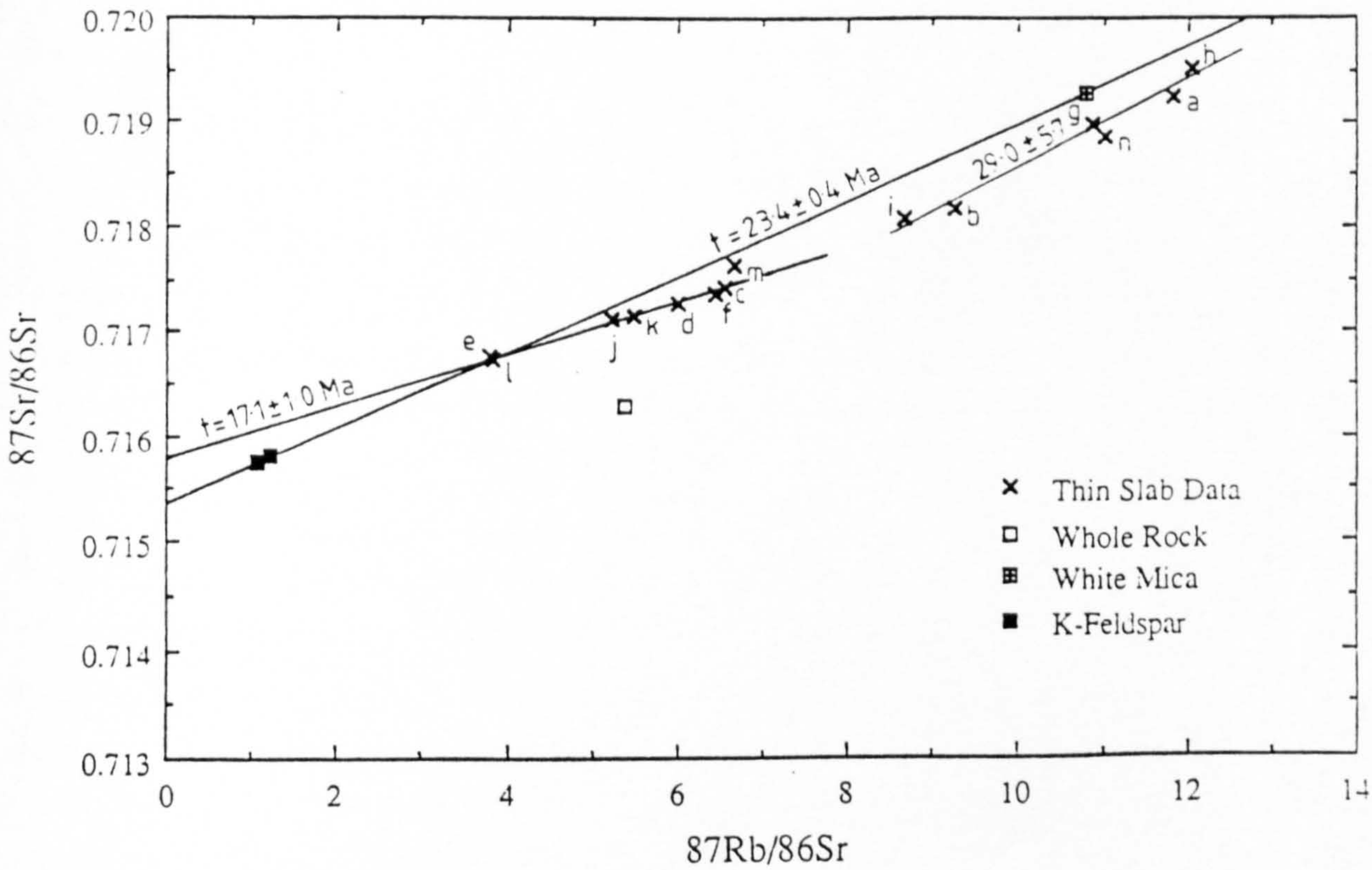

Figure 7.3b. Rb-Sr diagram for thin slabs and mineral data from the metasomatic shear zone discussed in chapter 6. All ages are calculated using a model 1 Yorkfit. Letters indicate slabs shown in Figure 7.3a.

White mica, K-feldspar and whole-rock analyses from a sample taken from approximately 30cm from the thin slab sample, do not fall on the same regression line. Repeat analyses of feldspar data and the similarity of the white mica mineral data with the white mica-rich thin slab data (Figure 7.3b) suggests that the mineral data are reliable. The whole-rock datum differs significantly from the mineral pair regression line suggesting that the whole-rock analysis is probably erroneous. Unfortunately a repeat analysis of the whole-rock sample has yet been made to verify this conclusion.

The calculated regression age of 23.4 ± 0.4 Ma for the mineral data are within error of the thin slab age. A similar initial $^{87}Sr/^{86}Sr$ ratio for this mineral age and the thin slab initial ratio of 0.7154±1, appears to provide further evidence for the homogenization of isotopic ratios approximately 23 Ma ago.

7:3.4. $^{40}Ar/^{39}Ar$ Analysis from a Sonnblick Amphibolite Unit

Hornblende separated from a 3kg sample of Sonnblick amphibolite has been analysed by $^{40}Ar/^{39}Ar$. The temperature at which argon diffusion in hornblende effectively ceases is considered to be 500±50°C (Harrison 1981). Since peak metamorphic temperatures within the area are considered to be in this range, $^{40}Ar/^{39}Ar$ ages should theoretically give an indication of the timing of the peak Alpine metamorphism. Since the closure temperature for Rb-Sr in white mica is also considered to be 500±50°C, amphibole and white mica data should provide an independent estimate of the metamorphic / cooling age.

The results of the analysis (Table 7.4, Figure 7.4) yield an integrated age of 88.5 ± 4.0 Ma. The spectrum however does not form a plateau and has a form commonly associated with the presence of excess argon (eg. Lanphere and Dalrymple 1976). The integrated age is therefore considered to be geologically meaningless and the spectrum can only be used to indicate that the maximum age of metamorphism, marked by the lowest age step of the profile, was at 60Ma. The obtained amphibole age does not correlate well with white mica ages of 23-28 Ma and is interpreted to represent the incorporation of excess argon within the hornblende.

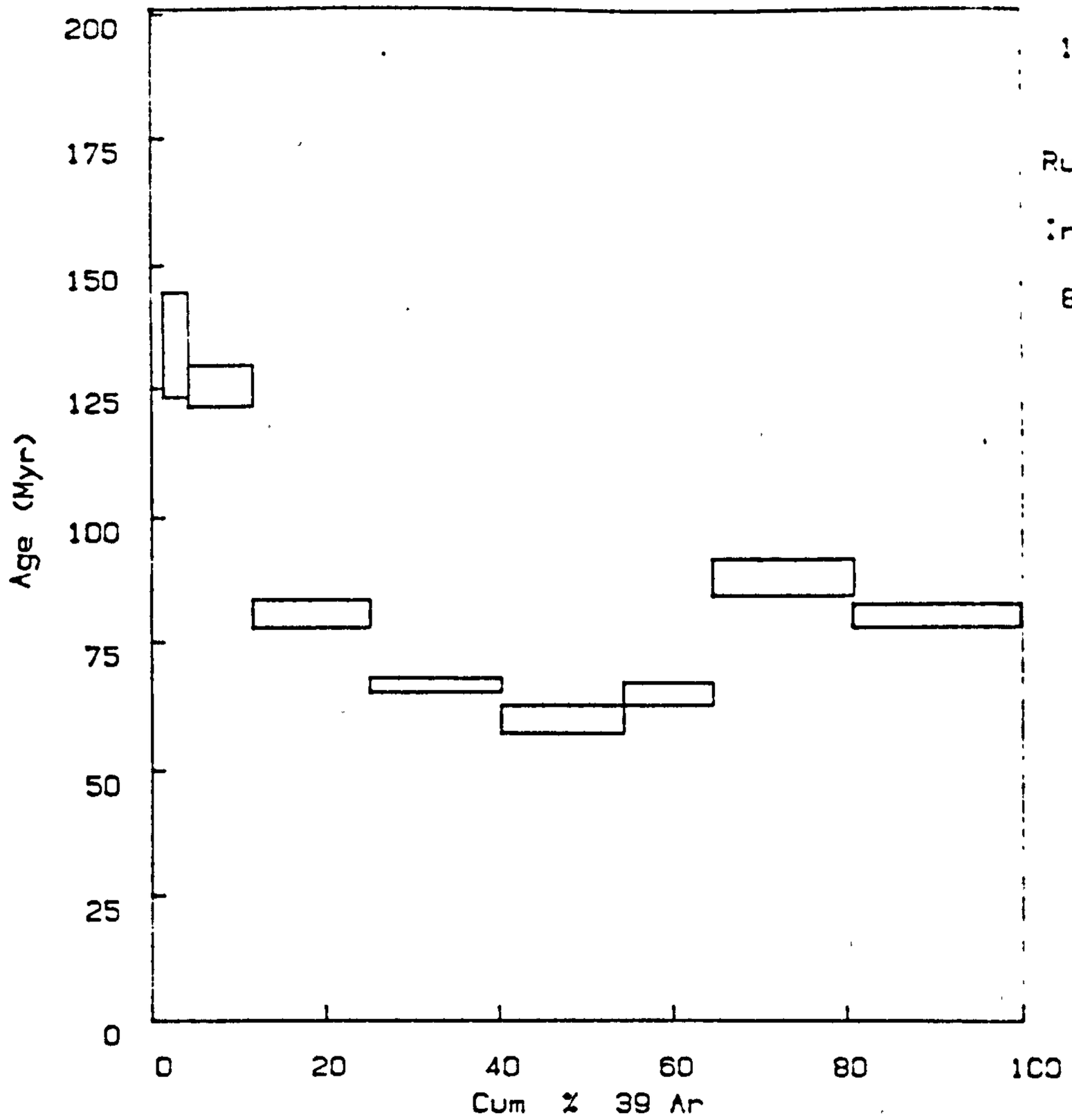

Figure 7.4. Argon release spectrum for hornblende separated from sample 185/87. The integrated age of 88.5 ± 4.0 Ma is interpreted to be insignificant due to excess argon.

Table 7.4.

185/87 Hnb., run 979, weight =0.07975 gms. J value =0.004407 +/- 3.0 %

Temp	39K	37Ca	38Cl	Ca/K	*40/39K	%Atm 40	Age	Err	%39
	(	Vol. *10-9 cc	)						
750	0.106	0.833	0.006	15.661	78.699	91.6	537.17	175.30	1.7
860	0.164	1.660	0.002	20.173	17.414	59.9	133.40	10.64	2.6
945	0.467	8.123	0.003	34.618	16.325	37.3	125.34	4.01	7.5
970	0.833	12.928	0.006	30.893	10.340	32.9	80.39	2.37	13.4
1000	0.931	14.405	0.004	30.807	8.505	24.0	66.39	1.39	15.0
1030	0.866	13.405	0.003	30.805	7.615	24.1	59.55	2.68	14.0
1080	0.645	10.681	0.003	32.929	8.251	25.0	64.44	2.39	10.4
1125	0.998	16.103	0.002	32.117	11.269	20.7	87.44	3.69	16.1
1340	1.183	18.827	0.006	31.669	10.272	32.9	79.88	2.49	19.1

Integrated values, analytic & J errors(2 sigma)

Age (My)	88.50	3.99	6.54
*40/39K	11.409	4.62 %	

Wt %K = 0.251 ,*40 = 8.86 x 10-7 cc/gm

7:4 The Interpretation of the Geochronological Results

7:4.1 The Age of Metamorphism and Implications for the Rate of Uplift and Cooling Based on Mineral Isotope Data

Metamorphic temperature estimates in the order of 540±50°C within the Sonnblick Dome (Chapter 5) suggest that the calculated mica ages are cooling ages, representing the time at which volume diffusion of radiogenic strontium in white mica and biotite ceased (500±50°C and 300±50°C respectively). Since the white mica closure temperature is of the same order as metamorphic temperatures, the calculated white mica ages are inferred to be good estimates of the time of metamorphic recrystallization. This suggests that peak metamorphic conditions were attained ≈25-28 Ma ago. The ^{40}Ar-^{39}Ar amphibole age has no significance due to excess argon. However, a similar analysis from the Auernig amphibolite (Cliff *et al* 1985), gave an integrated, interpreted metamorphic age of 24Ma. A more reasonable interpretation of this data would be an age of 21.9Ma, associated with the youngest step of the step-heating spectrum (Rex pers.comm.1990; Blanckenburg and Villa 1988). Peak metamorphic ages in the order of 35 Ma have been presented for the Schieferhülle at the southwestern margin of the Sonnblick Dome (Lambert 1970).

The data presented here suggests that the Sonnblick Dome was at a structural level between that of the Hochalm massif to the northeast and the Peripheral Schieferhülle to the southwest. However, at present there is insufficient data to establish the details of the spatial and temporal distribution of metamorphism within the Sonnblick Dome and more white mica samples are currently been analysed to extend the data set.

In the Sonnblick area, geochronological samples have been taken over a range of elevations in the order of 2.0 km. In the southeast Tauern Window, average uplift rates in the order of 1mm/a are required to expose the Pennine basement after peak metamorphism in the Tertiary. At these rates, the effect of sampling over a range of topographic heights would lead to significant variations in calculated ages, which would need to be accounted for if spatial variations in age data were to be interpreted. However, between the time of white mica and biotite closure, cooling rates in the order of 20-40°C/Ma are calculated (Figure 7.2). Although details of the retrograde pressure - time path for the Sonnblick Dome is difficult to constrain, Cliff et al (1985) suggest that the uplift rate in the southeast Tauern Window was in the order of 5mm/Ma immediately after peak metamorphism. At this rate of uplift, the effects of sampling over a 2km

vertical height can give rise to mineral age variations in the order of 0.4Ma which are within error of the calculated mineral ages. Topographic corrections commonly required for fission track dating, where uplift rates are much slower (eg Staufenberg 1985, 1987), have therefore been ignored. Spatial variations in closure ages of white mica and biotite throughout the Dome are therefore interpreted to be real.

The systematic increase in biotite and fission track ages towards the northwest of the Dome, indicates earlier cooling in the northwest below 300°C and 100°C respectively. The younger white mica age, obtained from the southeastern limit of the Dome, suggests that conditions of Alpine metamorphism were maintained for longer at the deeper structural levels inside the Dome than at the higher levels, close to the Zentralgneis and Peripheral Schieferhülle contact. This may represent a difference in structural level between the two white mica samples during metamorphism, the older age being expected at higher structural levels (England and Thompson 1984). However, the orientation of isotherms during metamorphism and subsequent uplift relative to the to the structural level is not yet known and may complicate this simple picture.

In the Sonnblick area, the method of accounting for topography has been used for apatite fission track data (Staufenberg 1985,1987). Regression of Sonnblick fission track data on a sample elevation - age graph gave an uplift rate of 0.24 mm/a. However this line only fits the data in the northwest of the Dome. To the southeast an uplift rate of 0.20 mm/a appears more valid. It should be noted however that there is a significant amount of scatter about these regressed lines in excess of the quoted analytical error (Figure 7.5a). This may be due to local variations in uplift rate, local deviations from the assumed 100°C blocking temperature for apatite fission tracks or counting errors associated with the 'population' method of fission track dating.

The mineral age data presented in this thesis, can be combined with the fission track data to derive average cooling rates for areas in the Dome (Figure 7.2). The effects of topography in considering mica-fission track data, has been overcome by utilising the uplift rates of 0.24 mm/a and 0.20mm/a so that fission track data can be recalculated for the same height as the biotite samples. Once elevation has been taken into account, the time to cool from the 300°C biotite blocking temperature to the 100°C fission track blocking temperature can be calculated. Where both white mica and biotite ages have been obtained from the same sample, cooling rates have also been calculated. Here possible errors associated with the topographic correction are ignored. Local average

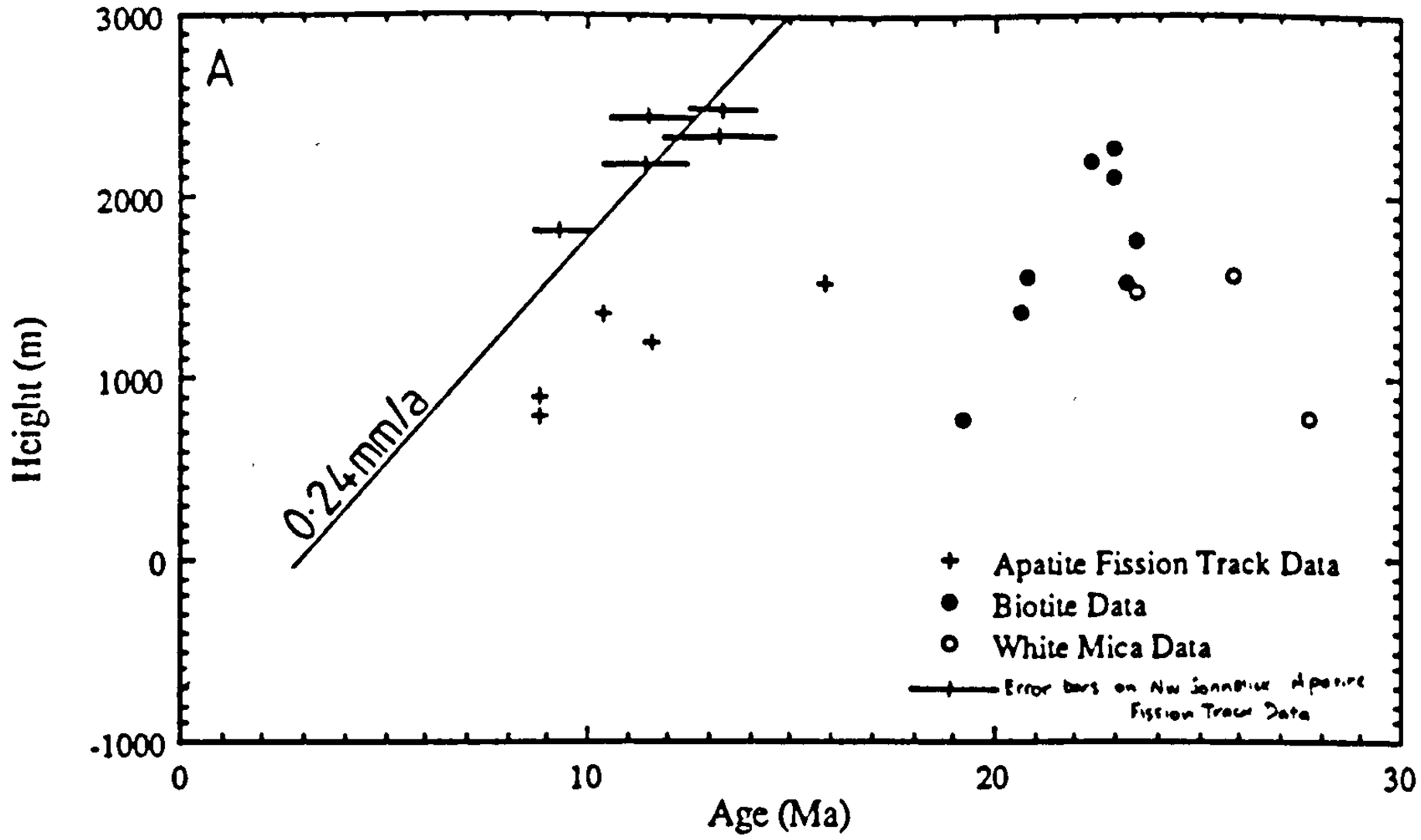

Figure 7.5a. Diagram illustrating the relationship between heights above sea level and of the sample and its age. The distribution of mineral data suggests variable rates of cooling and uplift within the Sonnblick Dome. 5 apatite fission track ages (shown with error bars) are interpreted to indicate a 0.24mm/a uplift rate for the northwestern part of the Dome (Staufenberg 1987). To the southeast a slower uplift rate of 0.2mm/a seems more probable.

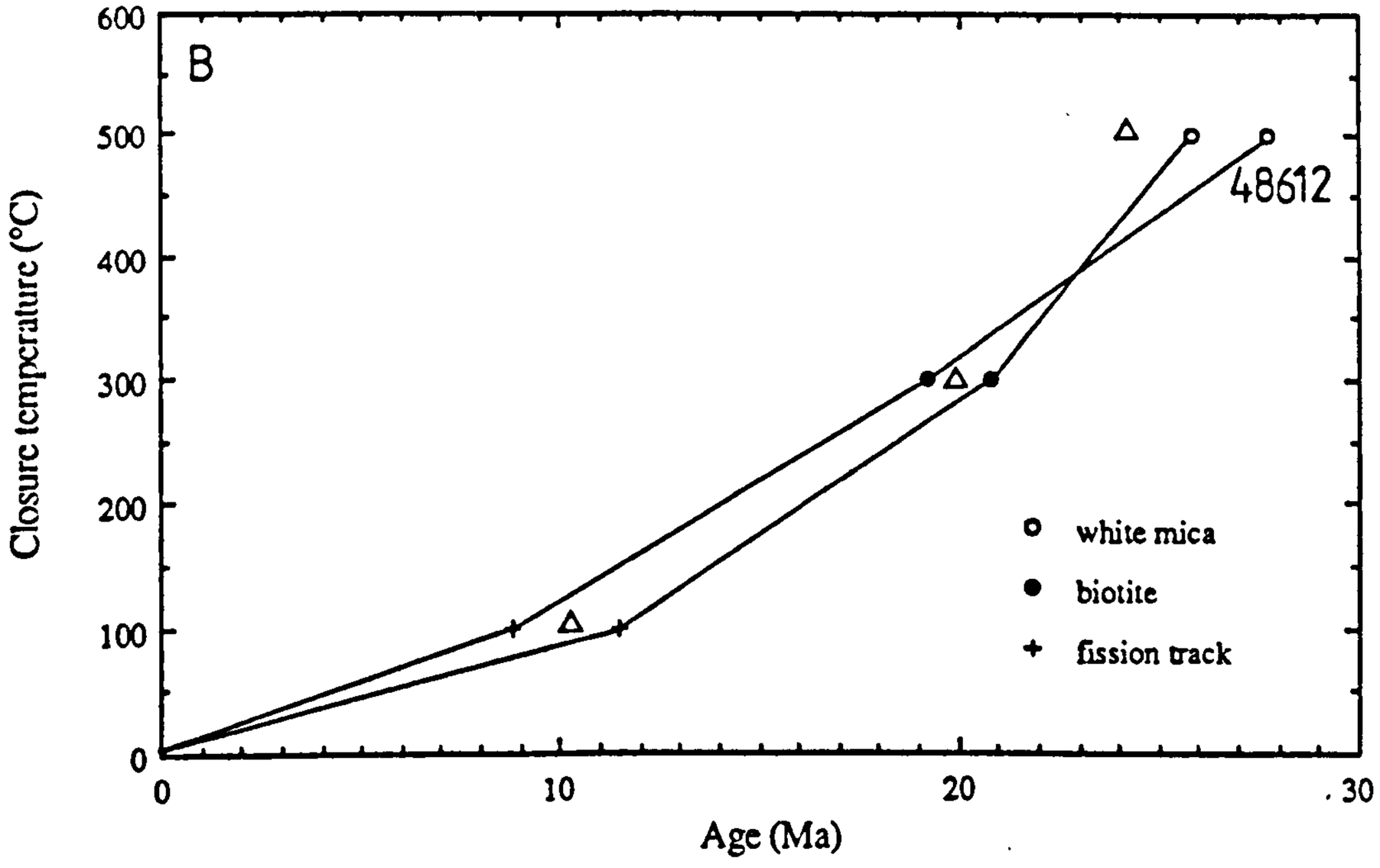

Figure 7.5b. Cooling rates for two samples from which both white mica and biotite ages have been obtained. Fission track ages are approximated by converting nearby fission track dates to the same topographic height as the mica samples. Triangles show points on the temperature - time path for the Auernig amphibolite to the northeast of the Sonnblick Dome (Cliff et al 1985). (see text for discussion).

cooling rates from 500-300°C and 300-100°C have been calculated and their distribution is shown in Figure 7.2.

Biotite analyses from the same samples as the white micas indicates that the centre of the Dome appeared to cool to 300°C before the sample to the southeast of the Dome. Average cooling rates for the 2 samples (Figure 7.5b) show a more rapid cooling rate from 500-300°C in the centre of the Dome, but similar cooling rates over the 300-100°C range from 17°C/Ma to 27°C/Ma and are relatively similar through the Dome. If horizontal isotherms, which are stationary relative in a vertical sense, are assumed, then this suggests that cooling from 500°C to 300°C was associated with significant amounts of uplift within the central and northwestern parts of the Dome. By the time temperatures had cooled below 300°C, cooling rates suggest that uplift rates across the area were probably relatively similar.

Cooling rates within the Hochalm Dome, varying from 10°C/Ma in the flank to 50°C/Ma in the core, are interpreted to be linked with Dome formation (Cliff et al 1985). These data for the Sonnblick area do not enable a link to any major structural feature to be inferred. A variation in cooling rate associated with the formation of the Sonnblick Dome structure is not observed and would not be expected since the Dome is interpreted as to be pre-metamorphic in origin and mica ages are interpreted as cooling ages after metamorphism. At this stage however, it appears that the data presented here agrees with the earlier data of Lambert (1970) and Staufenberg (1987) that the northwestern end of the Sonnblick Dome was uplifted more rapidly than the southeastern end of the Sonnblick Dome.

In Chapter 4, it was suggested that the Sonnblick Dome moved up an oblique ramp during top-to-NW shearing. This sense of thrusting on an oblique ramp would produce uplift of the northwestern end of the Dome. Although F_3 fold development was considered to have taken place before the peak of metamorphism, while the mineral ages refer to post-metamorphic cooling, continued top-to-NW thrusting within discrete thrust zones beneath the Sonnblick Dome would be consistent with the calculated mineral ages.

7:4.2 The Dating of Deformation and Recrystallization by the Thin Slab Isochron Method

In the absence of later isotopic redistribution, thin slabs with the same initial $^{87}Sr/^{86}Sr$ ratio but different $^{87}Rb/^{86}Sr$ ratios, associated with modal variations in mineralogy, would be expected to form an isochron that gave the true age of formation of shear zone formation. Similarly, mineral separates of phases which crystallized during shearing at temperatures below their closure temperature, would also be expected to yield the age of the shear zone. However, post-deformational temperatures in the order of the white mica closure temperature suggest that the white mica age represents both the time at which the shear zone temperature dropped below 500°C and the approximate time of peak metamorphism.

Since the shear zone mineralogy is composed of varying amounts by white mica, K-feldspar and quartz, it would be expected that the thin slabs would fall onto a line connecting the mineral end-member data. However, the presence of specific domains, which yield ages of 17.1 Ma and 29.0 Ma for K-feldspar-rich and K-feldspar-poor thin slabs respectively, is unexpected and must be interpreted.

The younger age implies that the system may not have remained a closed system after the 'closure' of the white mica to isotope diffusion. Alternatively, the initial distribution of radiogenic ^{87}Sr within the shear zone was not homogenous but decreased with increasing Rb/Sr, so that at 'closure' a line joining various thin slab points had a negative gradient, which then evolved with time to produce the 17Ma isochron now observed.

The majority of the thin slab data plot below the K-feldspar - white mica isochron. Addition of radiogenic Sr would lead to thin slabs plotting above the mineral isochron while removal of radiogenic Sr from K-feldspar would lead to an increase in the calculated age.

The feldspar-poor slabs record an age with large scatter that is within error of the mineral age and the inferred metamorphic age and is therefore difficult to interpret. This difference in ages between K-feldspar -rich and K-feldspar poor domains, may represent heterogeneous requilibration on a small scale, with extensive equilibration taking place in the feldspar rich bands, may reflect increased strains and fluid infiltration in the matrix due to stress localization around the porphyroblasts.

Within strongly foliated rocks, it is likely that the dominant permeability pathway will be parallel to the developed foliation and fluid flow will tend to be parallel to the foliation rather than across it. This is supported by the localized development of K-feldspar porphyroblasts within bands parallel to the foliation. Although localized fluid flow may be expected to give rise to localized isotopic equilibration parallel to the foliation, this is not indicated by the isotopic evidence (for example compare points f and g with m and n in Figure 7.3b)

The older age of the white-mica rich samples may be a function of the cessation of recrystallization and closing of the white mica below 500°C after peak metamorphic conditions, while continued exchange of rad^{87}Sr with an external source may have continued down to temperatures in the order of 300°C in K-feldspar (eg. Thoni 1986). A possible source of rad^{87}Sr is white mica, which has also been shown to be open to rad^{87}Sr loss form its rims at temperatures as low as 300°C (Thoni 1986). It is possible therefore that continued exchange between K-feldspar and the rims of white mica grains took place down to temperatures in the order of 300°C within a system closed to isotopic exchange above the scale of a few centimetres. The partial isotopic equilibration, associated with radiogenic cores and less radiogenic rims, within micas may explain the excess scatter of the data in the mica-rich bands.

It is interpreted therefore, that after isotopic equilibration during the initial formation of the shear zone, redistribution of radiogenic Sr occured by recrystallization of micas during the peak Alpine metamorphism and by volume diffusion in syn-deformational K-feldspars. After recrystallization partial equilibration of K-feldspar with the rims of white mica occured down to temperatures in the order of 300°C. This resulted in the differential rotation of the isochron depending upon the relative amounts of K-feldspar. Where K-feldspar was absent less equilibration took place and therefore isochron rotation was less significant. If this scenario is correct, the age of 29.0±5.7 can be used to infer that the minimum age of metamorphic recrystallization was 23.3 Ma. The isochron yielding an age of 17.1 ±1.0 Ma for K-feldspar rich samples may in turn probably represents a cooling age.

Chapter 8

Summary

1) Detailed structural mapping, in conjunction with microscopic observations, has enabled the structural history of the Zentralgneis unit of the Sonnblick Dome to be established. Within gneiss terrains, the ability to constrain a particular structural observation to a particular orogenic event is often difficult. Comparison of structures developed in the Zentralgneis and the overlying Peripheral Schieferhülle has allowed the Alpine deformation history of the Zentralgneis to be established. This history is dominated by non-coaxial deformation associated with overthrusting of the Austroalpine units onto the Pennine basement. Field and microstructural observations show that this thrusting was northwest-directed and was not, as thought by earlier workers (eg. Bickle and Hawkesworth 1978) associated with N-NE overthrusting.

2) Early folds, localized within high strain zones and the contacts of amphibolite and granite gneisses, are interpreted as sheath type folds that have hinges which have rotated towards the displacement vector. Overprinting these, low strain folds associated with formation of the Dome are modelled has having developed as the result of thrusting of the Sonnblick Zentralgneis unit over an oblique ramp, dipping to the southwest beneath the Dome. Previously published mathematical models of fold formation in the hanging wall of a thrust, across which a large amount of drag is present, are very similar in geometry to that observed in the Sonnblick area.

A necessary requirement for this model to be valid is the presence of a detachment dipping to the southwest beneath the Sonnblick Dome. A white mica schist, considered to be part of the Inner Schieferhülle (Exner 1964) and exposed within the Mallnitzer Mulde, appears to cut up section through the overlying Schieferhülle and may represent the detachment as exposed at the present day erosion surface. Establishing the structural relationships of development of this white mica schist to its surrounding units, and establishing the the along strike variations of these relationships, may provide an interesting follow up study which may be used to test the structural model for Dome formation.

3) Examination of microstructures from a wide range of lithologies and variously deformed units within these lithologies has illustrated that on a grain scale, textures preserved within the matrix of the gneiss appear to be independent of the mesoscopic strain state of the rock, as defined by the foliation intensity. Fabrics developed during

top-to-NW shearing have undergone coarsening by dynamic recrystallization at all but the highest levels of the Dome. What is not clear is whether the preserved quartz microstructures formed during a continuous reduction in stress, or whether microstructures were first annealed during the Alpine metamorphism and subsequently affected by a low differential stress.

At the base of the overlying Schieferhülle, garnet and feldspar textures indicate that top-to-NW shearing continued during the metamorphic peak. Locally developed top-to-SE fabrics and shear bands, are interpreted as localized extensional features developed during rapid uplift at approximately 4mm/yr associated with post-metamorphic regional extension.

The data shows that a model involving relatively rapid emplacement onto the Pennine basement, followed by isostatic uplift and the relaxation of isotherms is not valid for the southeast Tauern Window. Estimated metamorphic ages suggest that top-to-NW shearing was continuing until at least 25Ma ago and therefore a more progressive model of Eastern Alpine evolution must be developed.

4) Conditions of peak Alpine metamorphism have been established for the lower structural levels of the Sonnblick Dome using standard thermobarometry techniques on gneisses, amphibolites and Inner Schieferhülle schists. Temperatures have been estimated at 540±50°C with pressures of approximately 8±1kbar.

The retrograde PT path has been investigated using Rb-Sr mineral dating on white mica and biotite. Since the peak of metamorphism is similar to the closure temperature of white-mica, the absolute time of metamorphism can be inferred as ≈25Ma ago.

In combination with biotite cooling ages and previously published fission-track ages, the average cooling rate of the Sonnblick gneiss can be determined, for the periods between 500-300°C and 300-100°C, at 20-40°C/Ma and 27-17°C/Ma respectively. The nature of the PT path shows the initial cooling rates to be associated with rapid uplift which is considered to be associated with regional uplift.

At present, the extent of differential uplift within the Dome has not been established by mineral age dating. Since the formation of gneiss domes within the southeast Tauern Window takes place both before and after metamorphism, the post-metamorphic thermal history of the southeast Tauern Window will be an important consideration for in

constraining the tectonic evolution of the area. With this in mind, more data is currently being collected with a view to establishing the uplift and cooling paths within the Sonnblick Dome and assessing these data with respect to other data from around the southeast Tauern Window.

5) During overthrusting of the Austroalpine units to the northwest, ductile shear zones developed within the gneiss. These have been examined in terms of their geochemical and structural development in order to interpret some of the processes which may control strain localization within the crust. The localization of strain within these shear zones is commonly associated with the infiltration of a fluid phase and formation of white mica at the expense of feldspar. The sources of fluid which may drive such a reaction include gneiss assemblages and pelitic schists which are undergoing dehydration reactions. The presence of such shear zones and evidence for imbrication within the Zentralgneis, in conjunction with the development of gneiss lamellae around the Dome, suggests that the Zentralgneis cannot be considered as an autochthonous unit when considering it terms of Alpine deformation.

6) Strain localization within the metasomatic shear zones occurs as a result of reaction softening, geometrical softening and possibly the development of a fine grained reaction product which facilitates grain size sensitive creep. However, complications to the feldspar breakdown reaction are observed and feldspar growth occurs locally within the shear zone, usually at sites of deformation. Although the site of reaction is commonly a zone of localized deformation, it is not possible to assess whether deformation drives the reaction or if it merely contributes to the total energy required for reaction.

References

Abbate, E., Bortolotti, V. and Principi, G. 1980. Apennine ophiolites: a peculiar oceanic crust. *Ofioliti*, **5**, 59-96.

Ackermand, D. and Karl, F. 1972. Experimental studies on the formation of inclusions in plagioclases from metatonalites, Hohe Tauern, Austria. (Lower temperature stability limit of anorthite plus potash feldspar). *Contributions to Mineralogy and Petrology*, **35**, 11-21.

Ackermand, D., Morteani, G. and Raase, P. 1978. Metamorphism of the Penninic Series in the Western Tauern Window (Austria/Italy). In: *Alps, Apennines, Hellenides* (edited by Closs, H. *et al*). Inter-Union Commision of Geodynamics, Scientific Report 38. Stuttgart. pp121-125.

Alderton, D.H.M., Pearce, J.A. and Potts, P.J. 1980. Rare earth element mobility during granite alteration: Evidence from southwest England. *Earth and Planetary Science Letters*, **49**, 149-165.

Atkinson, B.K. 1984. Subcritical crack growth in geological materials. *Journal of Geophysical Research*, **89**, 4298-4312.

Authaud, F. and Matte, P.H. 1977. Late Palaeozoic strike slip faulting in southern Europe and Northern Africa. *Bulletin of the Geological Society of America*, **88**, 1305-1320.

Bachinski, S.W. and Muller, G. 1971. Experimental determination of the microcline-low albite solvus. *Journal of Petrology*, **12**, 329-356.

Balé, P. and Brun, J.-P. 1989. Late Precambrian thrust and wrench zones, northern Brittany (France). *Journal of Structural Geology*, **11**, 391-406.

Bally, A.W., Bernoulli, D., Davis, G.A. and Montadent, L. 1981. Listric normal faults. *Oceanol. Acta (Paris), 26e Congr. Géol. Int., Colloq. Géol. des Marges Continentales*. 87-101.

Barth, T.F.W. 1951. The feldspar geological thermometers. *Neues Jahrbuch für Mineralogie*, **82**, 143-154

Barth, T.F.W. 1968. Additional data for the two feldspar geothermometer. *Lithos*, **1**, 305-306.

Bayer, R., Cazes, M., Dal piaz, G.V., Damotte, B., Elter, G., Gosso, G., Hirn, A., Lanza, R., Lombardo, B., Mugnier, J.-L., Nicholas, A., Nicolich, R., Polino, R., Rore, F., Sacchi, R., Scarasia, S., Tabacco, I., Tapponier, P., Tardy, M., Taylor, M., Thouvenot, F., Torreilles, G. and Villien, A. 1987. Premiers résultants de la traversée des Alpes occidentales par seismique reflexion verticale (Programme ECORS-CROP). *Comptes- Rendus de l'Académie des Sciences de Paris*, **305**, 1461-1470.

Beach, A. 1976. The interrelations of fluid transport, deformation, geochemistry and heat flow in early proterozoic shear zonesin the Lewisian complex. *Philosophical Transactions of the Royal Society of London*, **A280**, 569-604.

Beach, A. 1980. Retrogressive metamorphic processes in shear zones with special reference to the Lewisian Complex. *Journal of Structural Geology*, **2**, 257-263.

Beach, A. and Tarney, J. 1978. Major and trace element patterns established during retrogressive metamorphism of granulite facies gneisses, NW Scotland. *Precambrian Research*, **7**, 325-348.

Behrmann, J.H. 1987. Flow partitioning and fabric evolution. *The Geological Society of London*, **144**, 676.

Behrmann, J.H. 1988. Crustal scale extension in a convergent orogen: The Sterzing-Steinach mylonite zone in the Eastern Alps. *Geodynamica Acta*, **2**, 63-73.

Behrmann, J.H. and Ratsbacher, L. 1989a. A structural test of eclogite emplacement models in the Austrian Alps. *Terra Abstracts*, **1**, 261.

Behrmann, J.H. and Ratsbacher, L. 1989b. Archemides revisited: a structural test of eclogite emplacement models in the Austrian Alps. *Terra Nova*, **1**, 242-252.

Behrmann, J.H. and Wallis, S.R. 1987. Hangenverschuppung des Tauernfenster- Südrandes bei Kals (Osttirol) als Zeuge von eo-alpinem Underplating. *Jahrbuch der Geologischen Bundesanstalt, Wien*, **130**, 133-138.

Bell, T.H. 1985. Deformation partitioning andporphyroblast rotation in metamorphic rocks: A radical reinterpretation. *Journal of Metamorphic Geology*, **3**, 109-118.

Bell, T.H., Rubenach, M.J. and Fleming, P.D. 1986. Porphyroblast nucleation, growth and dissolution in regional metamorphic rocks as a function of deformation partitioning during foliation development. *Journal of Metamorphic Geology*, **4**, 37-67.

Berger, P. and Johnson, A.M. 1980. First-order analysis of deformation of a thrust sheet moving over a ramp. *Tectonophysics*, **70**, T9-T24.

Berger, P. and Johnson, A.M. 1982. Folding of passive layers and forms of minor structures near terminations of blind thrust faults - Application to the central Appalachian blind thrust. *Journal of Structural Geology*, **4**, 343-353.

Bernoulli, D. 1986. Geologic-tectonic history of the Alpine-Mediterranean system. In: *Third EGT Workshop- The Central Segment* (edited by Freeman, R., Mueller, St. and Giese, P.). European Science Foundation, Strasbourg, France. 21-24.

Berthé, D., Choukroune, P. and Jegouzo, P. 1979. Orthogneiss, mylonite and non coaxial deformation of granites: the example of the South Armorcian Shear Zone. *Journal of Structural Geology*, **1**, 31-41.

Bickle, M.J. and Hawkesworth, C.J. 1978. Deformation phases and the tectonic history of the Eastern Alps. *Bulletin of the Geological Society of America*, **89**, 293-306.

Bickle, M.J. and Pearce, J.A. 1975. Oceanic rocks in the Eastern Alps. *Contributions to Mineralogy and Petrology*, **49**, 177-189.

Bickle, M.J., Hawkesworth, C.J., England, P.C. and Athey, D.R. 1975. A preliminary thermal model for regional metamorphism in the eastern Alps. *Earth and Planetary Science Letters*, **26**, 13-28.

Blanckenburg, F.V., Villa, I.M., Baur, H., Morteani, G. and Steiger, R.H. 1989. Time calibraton of a P-T path from the western Tauern Window, Eastern

Alps: The problems of closure temperatures. *Contributions to Mineralogy and Petrology*, **101**, 1-11.

Bouchez, J.-L., Lister, G.S. and Nicholas, A. 1983. Fabric asymmetry and shear sense in movement zones. *Geologische Rundschau*, **72**, 401-420.

Bowers, T.H., Jackson, K.J. and Helgeson, H.C. 1984. *Equilibrium Activity Diagrams for Coexisting Minerals and Aqueous Solutions at Pressures and Temperatures to 5Kb and 600°C*. Springer-Verlag. Berlin. pp 397.

Brace, W.F., Walsh, J.B. and Frangos, W.T. 1968. Permeability of granite under high pressure. *Journal of Geophysical Research*, **73**, 2225-2236.

Brodie, K.H. 1980. Retrogressive metamorphic processes in shear zones with special reference to the Lewisian Complex. *Journal of Structural Geology*, **2**, 257-263.

Brodie, K.H. and Rutter, E.H. 1985. On the relationship between deformation and metamorphism, with special reference to the behaviour of basic rocks. In: *Metamorphic Reactions: Kinetics, Texures and Deformation* (edited by Thompson, A. and Rubie, D.C.). Advances in Physical Geochemistry, **4**. Springer-Verlag, New York. pp 138-179.

Brooks, C., Hart, S.R. and Wendt, I. 1972. Realistic use of two error regression treatment as applied to rubidium-strontium data. *Reviews in Geophysics and Space Physics*, **10**, 551-577.

Brown, W.L. and Parsons, I. 1981. Towards a more practical two-feldspar geothermometer. *Contributions to Mineralogy and Petrology*, **76**, 369-377.

Brown, W.L. and Parsons, I. 1985. Calorimetric and phase-diagram approaches to two-feldspar geothermometry : a critique. *American Mineralogist*, **70**, 356-361.

Bucher-Nurminen, K. 1987. A recalibration of the chlorite-biotite-muscovite geobarometer. *Contributions to Mineralogy and Petrology*, **96**, 519-522.

Carter, N.L. and Tsenn, M.C. 1987. Flow properties of continental lithosphere. *Tectonophysics*, **136**, 27-63.

Chappel, B.W. and White, A.J.R. 1974. Two contrasting granite types. *Pacific Geology*, **8**, 172-174.

Chatterjee, N.D. and Flux, S.J 1986. Thermodynamic mixing properties of muscovite - paragonite crystalline solutions at high temperatures and pressures and their geological applications. *Journal of Petrology*, **27**, 677-693.

Chatterjee, N.D. and Froese, E. 1975. A thermodynamic study of the pseudobinary join muscovite-paragonite in the system: $KAlSi_3O_8$-$NaAlSi_3O_8$-Al_2O_3-SiO_2-H_2O. *American Mineralogist*, **60**, 985-993.

Chopin, C. 1987.Very high pressure metamorphism in the western Alps: Implications for subduction of continental crust. *Philosophical Transactions of the Royal Society of London*, A **321**, 183-197.

Chopin, C. and Maluski, H. 1980. ^{40}Ar-^{39}Ar dating of high pressure metamorphic micas from the Gran Paradiso (Western Alps): Evidence against the blocking temperature concept. *Contributions to Mineralogy and Petrology*, **74**, 109-122.

Christie, J.M., Ord, A. and Koch, P.S. 1980. Relationship between recrystallized grain-size and flow stress in experimentally deformed quartzite. *Transactions of the American Geophysical Union*, **61**, 377.

Clar, E. 1973. Review of the structure of the Eastern Alps. In: *Gravity and Tectonics* (edited by De Jong and Scholten). Wiley, pp253-270.

Cliff, R.A. 1971. Strontium isotope distribution in a regionally metamorphosed granite from the Zentralgneis, south-east Tauernfenster, Austria. *Contributions to Mineralogy and Petrology*, **32**, 274-288.

Cliff, R.A. 1977. Rb-Sr isotopic measurements on granite-gneissses from the Granatspitzkern, Hohe Tauern, Austria. *Vehreinigung Geologische Bundesansialt Wein*, **1977/2**, 101-104.

Cliff, R.A. 1981. Pre-Alpine history of the Pennine Zone in the Tauern Window, Austria: U-Pb and Rb-Sr geochronology. *Contributions to Mineralogy and Petrology*, **77**, 262-266.

Cliff, R.A. 1985. Isotopic Dating in Metamorphic Belts. *The Journal of the Geological Society of London*, **142**, 97-110.

Cliff, R.A. and Cohen, A. 1980. Uranium-lead systematics in a regionally metamorphosed tonalite from the Eastern Alps. *Earth and Planetary Science Letters*, **50**, 211-218.

Cliff, R.A., Droop, G.T.R. and Rex, D.C. 1985. Alpine metamorphism in the south-east Tauern Window, Austria: II. Heating, cooling and uplift rates. *Journal of Metamorphic Geology*, **3**, 403-415.

Cliff, R.A., Norris, R.J., Oxburgh, E.R. and Wright, R.C. 1971. Structural, metamorphic and geochronological studies in the Reisseck and southern Ankogel Groups, the Eastern Alps. *Jahrbuch der Geologischen Bundesanstalt, Wien*, **114**, 121-272.

Cobbold, P.R. and Quinquis, H. 1980. Development of sheath folds in shear regimes. *Journal of Structural Geology*, **2**, 119-126.

Coward, M.P. and Dietrich, D. 1989. Alpine tectonics- An overview. In: *Alpine Tectonics* (edited by Coward, M.P., Dietrich, D. and Park, R.G.). The Geological Society of London Special Publication No.**45**, 1-29.

Coward, M.P. and Potts, G.J. 1983. Complex strain patterns developed at the frontal and lateral tips to shear zones and thrust zones. *Journal of Structural Geology*, **5**, 383-399.

Coward, M.P., Dietrich, D. and Park, R.G. 1989. *Alpine Tectonics*. The Geological Society of London Special Publication No.**45**. pp450.

Culshaw, N. 1987. Microstructure, c-axis pattern, microstrain and kinematics of some S-C mylonites in Grenville Gneiss. *Journal of Structural Geology*, **9**, 299-311.

De Graciansky, P.C., Poagh. C.W., Cunningham, R., Loubere, P., Masson, D.G., Mazzullo, J.M., Montadert, L., Muller, C., Otsuka, K., Reynolds, L.A., Sigal, J., Snyder, S.W., Townsend, H.A., Vaus, S.P. and Waples, D. 1985. The Goban Spur transect: Geologic evolution of a sediment-starved passive continental margin. *The Bulletin of the Geological Society of America*, **96**, 58-76.

Decker, K., Faupl, P. and Müller, A. 1987. Synorogenic sedimentation on the Northern Calcareous Alps during the Early Cretaceous. In: Geodynamics of the Eastern Alps (edited by Flügel, H.W. and Faupl, P.). Deuticke, Wien. pp 126-141.

Dercourt, J., Zonenshain, L.P., Ricou, L.E., Kazmin, V.G., Le Pichon, X., Knipper, A.L., Grandjacquet, C., Sbortshikov, I.M., Geyssant, J., Lepuvier, C., Pechersky, D.H., Boulin, J., Sibuet, J.C., Savostin, L.A., Sorokhtin, O., Westphal, M., Bazhenov, M.L., Lauer, J.P. and Biju-Duval, B. 1986. Geological evolution of the Tethys belt from the Atlantic to the Pamirs since the Lias. *Tectonophysics*, **123**, 241-315.

Dewey, J.F., Pitmann, W.C.III, Ryan, W.B.F. and Bonnin, J. 1973. Plate tectonics and evolution of the Alpine systems. *Bulletin of the Geological Society of America* , **84**, 137-180.

Dietrich, V. 1980. The distribution of ophiolites in the Alps. *Ofioliti*, **5**, 7-53.

Dodson, M.H. 1973. Closure temperatures in cooling geochronological and petrological systems. *Contributions to Mineralogy and Petrology*, **40**, 259-274.

Dodson, M.H. 1976. Kinetic Processes and thermal history of slowly cooling rocks. *Nature*, **259**, 551-553.

Dodson, M.H. 1979. Theory of cooling ages. In: *Lectures in Isotope Geology* (edited by Jäger, E. and Hunziker, J.C.). Springer-Verlag, Berlin. pp 207-214.

Dorstal, J., Strong, D.F. and Jamieson, R.A. 1980. Trace element mobility in the mylonite zone within the ophiolite aureole, St.Anthony Complex, Newfoundland. *Earth and Planetary Science Letters*, **49**, 188-192.

Dölzlmüller, H., Finger, F. and Schermaier, A. In Press. Die Ausbildung der Zirkone im Granitgneis des Hohen Sonnblicks (Penninikum, Ostalpen) und ihre Aussage zur Gesteinsgenese.

Droop, G.T.R. 1981. Alpine metamorphism of pelitic schists in the south-east Tauern Window, Austria. *Schweizerische Mineralogische und Petrographische Mitteilungen*, **61**, 237-273.

Droop, G.T.R. 1983. Pre-Alpine eclogites in the Pennine Basement Complex of the Eastern Alps. *Journal of Metamorphic Geology*, **1**, 3-12.

Droop, G.T.R. 1985. Alpine metamorphism in the south-east Tauern Window, Austria: 1. P-T variations in space and time. *Journal of Metamorphic Geology*, **3**, 371-402.

Eberli, G.P. and Froitzheim, N. 1989. Deta chment-controlled extension of the Tethyan southern continental margin (Eastern Alps, Switzerland). *Terra Abstracts*, **1**, 57.

ECORS-CROP Deep Seismic Sounding Group. 1989. A new picture of the Moho under the western Alps. *Nature*, **337**, 249-251.

Ellis, D.J. and Green, D.H. 1979. An experimental study of the effect of Ca upon garnet-clinopyroxene Fe-Mg exchange equilibria. *Contributions to Mineralogy and Petrology*, **71**, 13-22.

England, P.C. 1978. Some thermal considerations of the Alpine metamorphism-Past, present and future. *Tectonophysics*, **46**, 21-40.

England, P.C. and Thompson, A.B. 1984. Pressure-temperature-time paths of regional metamorphism: I. Heat transfer during the evolution of regions of thickened continental crust. *Journal of Petrology*, **25**, 894-928.

Essene , E.J. 1989. The current status of thermobarometry in metamorphic rocks. In: *The Evolution of Metamorphic Belts* (edited by J.S. Daly, R.A. Cliff and B.W.D. Yardley). Geological Society of London Special Publication, No.43, 1-44.

Etheridge, M.A. and Cooper, J.A. 1981. Rb/Sr isotopic and geochemical evolution of a recrystallized shear (mylonite) zone at Broken Hill. *Contributions to Mineralogy and Petrology*, 78,74-84.

Etheridge, M.A., Wall, V.C. and Vernon, R.H. 1983, The role of the fluid phase during regional metamorphism and deformation. *Journal of Metamorphic Geology*, 1, 203-226.

Etheridge, M.A., Wall, V.J., Cox, S.F. and Vernon, R.H. 1984. High fluid pressures during regional metamorphism and deformation: impications for mass transport and deformation mechanisms. *Journal of Geophysical Research*, 89, 4344-4358.

Eugster, H.P., Albee, A.L., Bence, A.E., Thompson, J.B. and Waldbaum, D.R. 1972. The two-phase region and excess mixing properties of paragonite-muscovite crystalline solutions. *Journal of Petrology*, 13, 147-179.

Exner, Ch. 1964. *Erläuterungen zur Geologischen Karte der Sonnblickgruppe.* Geologische Bundesanstalt, Wien. 130pp.

Faupl, P., Pober, E. and Wagreich, M. 1987. Facies development of the Gosau Group of the eastern parts of the Northern Calcareous Alps during the Cretaceous and Palaeogene. In: Geodynamics of the Eastern Alps (edited by Flügel, H.W. and Faupl, P.). Deuticke, Wien. pp 142-155.

Faure, G. 1986. *Principles of Isotope Geology*. J.Wiley, New York. 589pp.

Ferry, J.M. and Spear, F.S. 1978. Experimental calibration of the partition of Fe and Mg between garnet and biotite. *Contributions to Mineralogy and Petrology*, 66, 113-117.

Finckh, P. Frei, W., Freeman, R., Heitzmann, P., Lehner, P., Mueller, St., Pfiffner, A. and Valasek, P. 1987. Nationales Forschungsprogramm 20 'Geologische Tiefenstruktur der Schweiz' - Problemstellung und erste Resulte. *Bulletin der vereinigung Schweizerischer Petroleum - Geologen und - Ingenieure*, 54, 59-74.

Finger, F. and Steyrer, H.P. 1988. Granite- types in the Hohe Tauern (Eastern Alps, Austria)- Some aspects on their correlation to Variscan plate tectonic processes. *Geodynamica Acta*, **2**, 75-87.

Fletcher, R.C. and Hofmann, A.W. 1974. Simple models of diffusion and combined diffusion-infiltration metasomatism. In: *Geochemical Transport and Kinetics* (edited by Hofmann, A.W., Giletti, B.J., Yoder, H.S.Jr. and Yund, R.A.). Publication **634**, Carnegie Institute of Washington. Washington D.C. pp 242-262.

Flügel, H.W. and Faupl, P. 1987. *Geodynamics of the Eastern Alps*. Deuticke, Wien.

Fortey, N.J. and Beddoe-Stephens, B. 1982. Barium silicates in stratabound Ba-Zn mineralization in the Scottish Dalradian. *Mineralogical Magazine*, **46**, 63-72.

Frank, W. 1987. Evolution of the Austroalpine Elements in the Cretaceous. In: *Geodynamics of the Eastern Alps* (edited by Flügel, H.W. and Faupl, P.). Deuticke, Wien. pp 379-406.

Frank, W., Höck, V. and Miller, C. 1987. Metamorphic and tectonic history of the central Tauern Window. In: *Geodynamics of the Eastern Alps* (edited by Flügel, H.W. and Faupl, P.). Deuticke, Wien. pp 34-54.

Frank, W., Kralik, M., Scharbert, S. and Thöni, M. 1987. Geochronological data from the Eastern Alps. In: *Geodynamics of the Eastern Alps* (edited by Flügel, H.W. and Faupl, P.). Deuticke, Wien. pp 272-281.

Franz, G. and Ackermand, D. 1980. Phase relations and metamorphic history of a clinohumite-chlorite-serpentine-marble from the western Tauern Window (Austria). *Contributions to Mineralogy and Petrology*, **75**, 97-110.

Frasl, G. 1954. Anzeichen schmelzflüssigen und hochtemperierten Wachstums an der großen Kalifeldspäten einiger Porphyrgranite, Porphyrgranitgneise und Augengneise in Österreich. *Jahrbuch der Geologischen Bundesanstalt, Wien*, **97**, 71-132.

Frasl, G. 1957. Der heutige Stand der Zentralgneisforschung in den Ostalpen. *Mineralogisches Mitteilungsblatt, Joanneum, Graz*, **2/1957**, 41-63.

Frasl, G. 1958. Zur Seriengleiderung der Schieferhülle in den Mittleren Hohen Tauern. *Jahrbuch der Geologischen Bundesanstalt, Wien*, **101**, 323-472.

Frasl, G. and Frank, W. 1966. Ein führung in die Geologie und Petrographie des Penninikums im Tauernfenster. In: *Zur Mineralogie und Geologie des Landes Salzburg und der Hohen Tauern, "Der Aufschluß"*, **15**. Heidelburg. pp 30-58.

Frey, M., Hunziker, J.C., Frank, W., Bocquet, J., Dal Piaz, G.V., Jäger, E. and Niggli, E. 1974. Alpine metamorphism in the Alps- A review. *Schweizerische Mineralogische und Petrographische Mitteilungen*, **54**, 247-290.

Frisch, W. 1979. Tectonic progradation and plate tectonic evolution of the Alps. *Tectonophysics*, **60**, 121-139.

Frisch, W. 1981. Plate motions in the Alpine region and their correlation to the opening of the Atlantic Ocean. *Geologische Rundschau*, **70**, 402-411.

Frisch, W. 1984. Sedimentological response to late Mesozoic subduction in the Penninic Windows of the Eastern Alps. *Geologische Rundschau*, **73**, 33-45.

Frisch, W., Gommeringer, K., Kelm, U. and Popp, F. 1987. The upper Bündner Schiefer of the Tauern Window- A key to understanding Eoalpine orogenic processes in the Eastern Alps. In: *Geodynamics of the Eastern Alps* (edited by Flügel, H.W. and Faupl, P.). Deuticke, Wien. pp 55-69.

Fry, N. 1989a. Southwestward thrusting and tectonics of the western Alps. In: *Alpine Tectonics* (edited by Coward, M.P., Dietrich, D. and Park, R.G.). The Geological Society of London Special Publication No.**45**, 83-109.

Fry, N. 1989b. Kinematics of the Alpine arc. *Journal of the Geological Society of London*, **146**, 891-892.

Fyfe, W.S. 1976. Chemical aspects of rock deformation. *Philosophical Transactions of the Royal Society of London* , **A283**, 221-228.

Fyfe, W.S. 1976. Chemical aspects of rock deformation. *Philosophical Transactions of the Royal Society of London* , **A283**, 221-228.

Fyfe, W.S. 1985. Fluids, thrusting and crustal deformation. *Tectonophysics*, **119**, 29-36.

Fyfe, W.S. and Kerrich, R. 1985. Fluids and thrusting. *Chemical Geology*, **49**, 353-362.

Fyfe, W.S., Price, N.J. and Thompson, A.B. 1978. *Fluids in the Earth's Crust*. Elsevier, Amsterdam.

Fynn, G.W. and Powell, W.J.A. 1979. *The Cutting and Polishing of Electro-Optic Materials*. Adams-Hilger. London. 216pp.

Ganguly, J. 1979. Garnet and clinopyroxene solid solutions and geothermometry based on Fe-Mg distribution coeficient. *Geochimica et Cosmochimica Acta*, **43**, 1021-1029.

Ganguly, J. and Kennedy, G.C. 1974. The energetics of natural garnet solid solutions. *Contributions to Mineralogy and Petrology*, **48.**, 137-148.

Ganguly, J. and Saxena, S.K. 1984. Mixing properties of alumino-silicate garnets: constraints from natural and experimental data, and applications to geothermo-barometry. *American Mineralogist*, **69**, 88-97.

Garrels, R.M. and Howard, P. 1959. Reactions of feldspar and mica at low temperature and pressure. In:*Clays and Clay Minerals*. (edited by A. Swineford). Pergamon Press, New York. pp 68-88.

Genser, J. and Neubauer, F. 1989. The uplift of pull-apart metamorphic domes by tectonic unroofing as a consequence of orogen-parallel crustal wrenching. *Terra Abstracts*, **1**, 256.

Ghiorso, M.S. 1984. Activity/composition relations in the ternary feldspars. *Contributions to Mineralogy and Petrology*, **87**, 282-296.

Gilotti, J.A. 1989. Reaction progress during mylonitization of basaltic dikes along the Särv thrust, Swedish Caledonides. *Contributions to Mineralogy and Petrology*, **101**, 30-45.

Goffé, B. and Chopin, C. 1986. High pressure metamorphism in the western Alps: Zoneography of metapelites, chronology and consequences. *Schweizerische Mineralogische und Petrographische Mitteilungen*, **66**, 41-52.

Goldman, D.S. and Albee, A.L. 1977. Correlation of Mg/Fe partitioning between garnet and biotite with $^{18}O/^{16}O$ partitioning between quartz and magnetite. *American Journal of Science*, **277**, 750-767.

Graham, C.M. and Powell, R. 1984. A garnet-hornblende geothermometer: calibration, testing and application to the Pelona Schist, southern California. *Journal of Metamorphic Geology*, **2**, 13-22.

Green, H.W. II. 1972. Metastable growth of coesite in highly strained quartz. *Journal of Geophysical Research*, **77**, 2478-2482.

Green, N.L. and Usdansky, S.I. 1986a. Ternary-feldspar mixing relations and thermobarometry. *American Mineralogist*, **71**, 1100-1108.

Green, N.L. and Usdansky, S.I. 1986b. Toward a practical plagioclase - muscovite thermometer. *American Mineralogist*, **71**, 1109-1117.

Gresens, R.L. 1967. Composition-volume relationships of metasomatism. *Chemical Geology*, **2**, 47-65.

Gruner, J.W. 1944. The hydrothermal alteration of feldspars in acid solutions between 300°C and 400°C. *Economic Geologist*, **39**, 578-589.

Guidotti, C.V. 1982. Micas in metamorphic rocks. In: Micas (edited by S.W. Bailey). Mineralogical Society of America Reviews in Mineralogy, No. **13**, 357-468.

Günzler-Seiffert, H. 1941. Persistente Brüche im Jura der Wildhorn-Decke des Berner Oberlandes. *Eclogae Geologicae Helvetiae*, **34**, 164-172.

Handy, M.R. 1989. Deformation regimes and the rheological evolution of fault zones in the lithosphere: The effects of pressure, temperature, grainsize and time. *Tectonophysics*, **163**, 119-152.

Hanmer, S. 1981. Segregation bands in plagioclase: non-dilational quartz veins formed by strain enhanced diffusion. *Tectonophysics*, **79**, T53-T61.

Hanmer, S. 1986. Asymmetrical pull-aparts and foliation fish as kinematic indicators. *Journal of Structural Geology*, **8**, 111-122.

Hansen, V.L. 1989. Structural and kinematic evolution of the Teslin suture zone, Yukon: A record of an ancient transpressional margin. *Journal of Structural Geology*, **11**, 717-733.

Haselton, H.T.Jr., Hovis, G.L., Hemmingway B.S. and Robie, R.A. 1983. Calorimetric investigation of the excess entropy of mixing in analbite-sanidine solid solutions: lack of evidence for Na,K short-range order and implications for two feldspar thermometry. *American Mineralogist*, **68**, 398-413.

Hawkesworth, C.J. 1976. Rb-Sr geochronology in the Eastern Alps. *Contributions to Mineralogy and Petrology*, **54**, 225-244.

Häusler, H. 1987. The northern Austroalpine margin during the Jurassic: Breccias from the Rädstadter Tauern and Tarntaler Berge. In: *Geodynamics of the Eastern Alps* (edited by Flügel, H.W. and Faupl, P.). Deuticke, Wien. pp 103-111.

Heinz, H. and Wallach, G. 1979. Ergebnisse refraktionsseismischer Messungen im Gebiet des Lurnfeldes (Drautal, Oberkärnten). *Vehreinigung der Geologisches Bundesanstalt Wein*, **179,2**, 77-83.

Helgeson, H.C., Delaney, J.M., Nesbitt, H.W. and Bird, D.K. 1978. Summary and critique of the thermodynamic properties of rock forming minerals. *American Journal of Science*, **278A**, 1-229.

Hickman, M.H. and Glassley, W.E. 1984. The role of metamorphic fluid transport in the Rb-Sr isotopic resetting of shear zones: Evidence from Norde Strømfjord, West Greenland. *Contributions to Mineralogy and Petrology*, **87**, 265-281.

Hobbs, B.E. 1984. Point defect chemistry of minerals under a hydrothermal environment. *Journal of Geophysical Research*, **89**,4026-4038.

Hodges, K.V. and Royden, L. 1984. Geologic thermobarometry of retrograded metamorphic rocks: an indication of the uplift trajectory of a portion of the Northern Scandinavian Caledonides. *Journal of Geophysical Research*, **89**, 7077-7090.

Hodges, K.V. and Spear, F.S. 1982. Geothermometry, geobarometry and the Al_2SiO_5 triple point at Mt. Moosilauke, New Hampshire. *American Mineralogist*, **67**, 1118-1134.

Hofmann, A.W. 1972. Chromatographic theory of infiltration metasomatism and its application to feldspars. *American Journal of Science*, **272**, 69-90.

Hofmann A.W. 1979. Rb-Sr dating of thin slabs: An imperfect method to determine the age of metamorphism. In: *Lectures in Isotope Geology* (edited by Jäger, E. and Hunziker, J.C.). Springer-Verlag, Berlin. pp 27-29.

Hoinkes, G. 1986. Effects of grossular-content in garnet on the partitioning of Fe and Mg between garnet and biotite. *Contributions to Mineralogy and Petrology*, **92**, 393-399.

Holland, T.J.B. 1977. Structural and metamorphic studies of eclogites and associated rocks in the Central Tauern region of the Eastern Alps. *Unpublished D.Phil. thesis, Oxford Univ.ersity.*

Holland, T.J.B. 1979. High water activities in the generation of high pressure kyanite eclogites of the Tauern Window, Austria. *Journal of Geology*, **87**, 1-27.

Hollister, L.S. 1966. Garnet zoning: An interpretation based on the Rayleigh fractionation model. *Science*, **154**, 1647-1651.

Homewood, P. and Latelin, O. 1988. Classic Swiss clastics (flysch and molasse). The Alpine connection. *Geodynamica Acta*, **2**, 1-11.

Hoschek, G. 1969. The stability of staurolite and chloritoid and their significance in the metamorphism of pelitic rocks. *Contributions to Mineralogy and Petrology*, **22**, 208-232.

Höck, V. and Miller, C. 1987. Mesozoic ophiolitic sequences and non-ophiolitic metabasites in the Hohe Tauern In: *Geodynamics of the Eastern Alps* (edited by Flügel, H.W. and Faupl, P.). Deuticke, Wien. pp 16-33.

Hsü, K.J. 1989. Time and place in Alpine orogenesis- The Fermor Lecture. In: *Alpine Tectonics* (edited by Coward, M.P., Dietrich, D. and Park, R.G.). The Geological Society of London Special Publication No.45, 421-443.

Hunziker, J.C., Desmons, J. and Martinotti, G. 1989. Alpine thermal evolution in the central and western Alps. In: *Alpine Tectonics* (edited by Coward, M.P., Dietrich, D. and Park, R.G.). The Geological Society of London Special Publication No.45, 353-367.

Hynes, A. and Forest, R.C. 1988. Empirical garnet - muscovite geothermometry in low grade metapelites, Selwyn Range (Canadian Rockies). *Journal of Metamorphic Geology*, 6, 297-310.

Indares, A. and Martignole, J. 1985. Biotite- garnet geothermometry in the granulite facies: the influence of Ti and Al in biotite. *American Mineralogist*, 70, 272-278.

Irving, E. 1977. Drift of major continental blocks since the Devonian. *Nature*, 270, 304-309.

Janoschek. W.R. and Matura, A. 1980. Outline of the Geology of Austria. *Abhandlungen der Geologischen Bundesanstalt Wien*, 34, 7-98.

Jaoul, O., Tullis, J. and Kronenberg, A.K. 1984. The effect of varying water contents on the creep behaviour of Heavitree quartzite. *Journal of Geophysical Research*, 89, 4298-4312.

Jäger, E., Niggli, E. and Wenk, E. 1967. Rb-Sr Altersbestimmungen an Glimmeren der Zentralalpen. *Beitr. geol. Karte Schweiz.* NF 1344, Bern, 1-67.

Joannes, W. 1979 Ternary feldspars: Kinetics and possible equilibria at 800°C. *Contributions to Mineralogy and Petrology*, 68, 221-230.

Karl, F. 1959. Vergleichende Petrographische Studien an der Tonalitgraniten der hohen Tauern und der Tonalitgraniten einiger periadritischen Intrusivmassif. *Jahrbuch der Geologischen Bundesanstalt, Wien*, **102**, 1-192.

Kázmér, M. and Józsa, S. 1989. The missing volcanic arc of the Palaeogene Alpine subduction. *Terra Abstracts*, **1**, 58.

Kerrich, R. 1978. A historical review and synthesis of research on pressure solution. *Zentralblatt für Geologie und Paläontologie, Teil 1*, **H 5-6**, 512-550.

Kieslinger, A. 1936. Ganggesteine im Zentralgneis am Zirmsee, Kärnten. *Jahrbuch der Geologischen Bundesanstalt, Wien*, **86**.

Kirby, S.H. 1984. Introduction and digest to the special issue on chemical effects of water on the deformation and strengths of rocks. *Journal of Geophysical Research*, **89**, 3991-3995.

Kirby, S.H. 1985. Rock mechanics observations pertinent to the rheology of continental lithosphere and localization of strain along shear zones. *Tectonophysics*, **136**, 1-26.

Klaper, E.M. (in press). Reaction-enhanced formation of eclogite facies shear zones in granulite facies anorthosites.

Knipe, R.J. 1989. Deformation mechanisms- recognition from natual tectonites. *Journal of Structural Geology*, **11**, 127-146.

Knipe, R.J. 1990. Microstructural analysis and tectonic evolution in thrust systems: Examples from the Assynt region of the Moine Thrust Zone, N.W. Scotland. In: *Deformation of Minerals, Ceramics and Rocks* (edited by D.J. Barber and P.G. Meredith). The mineralogical Society Series, **1**, 228-258.

Knipe, R.J. and Law, R.D. 1987. The influence of crystallographic orientation and grain boundary migration on microstructural and textural evolution in an S-C mylonite. *Tectonophysics*, **135**, 155-169.

Knipe, R.J. and Wintsch, R.P., 1985. Heterogeneous deformation, foliation development, and metamorphic processes in a polyphase mylonite. In: *Metamorphic*

Reactions: Kinetics, Texures and Deformation (edited by Thompson, A. and Rubie, D.C.). Advances in Physical Geochemistry, **4**. Springer-Verlag, New York. pp 180-210.

Knipper, A., Rico, L.E. and Dercourt, J. 1986. Ophiolites as indicators of the dynamic evolution of the Tethyan Ocean. *Tectonophysics*, **123**, 213-240.

Koch, P.S., Christie, J.M. and George, R.P. 1980. Flow law of 'wet' quartzite in the quartz field. *EOS, Transactions of the American Geophysical Union*, **61**, 376.

Korzhinskii, D.S. 1970. *Theory of Metasomatic Zoning*. Oxford University Press. London. pp 162.

Kotov, N.V., Mil'kevich, R.I. and Turchenko, S.I. 1969. Palaeothermometry of muscovite-bearing metamorphic rocks based on X-ray and chemical analysis of muscovite. *Doklady Akademii Nauk SSSR*, **184**, 1180-1182.

Krogh, E.J. and Råheim, A. 1978. Temperature and pressure dependence of Fe-Mg partitioning between garnet and phengite, with particular reference to eclogites. *Contributions to Mineralogy and Petrology*, **66**, 75-80.

Laird, J. and Albee, A.L. 1981. High pressure metamorphism in mafic schists from Northern Vermont. *America Journal of Science*, **281**, 97-126.

Lambert, R.St.J. 1970. A potassium-argon study of the margin of the Tauernfenster at Döllach, Austria. *Eclogae Geologica Helvetica*, **63**, 197-205.

Lanphere, M.A. and Dalyrymple, G.B. 1976. Identification of excess ^{40}Ar by the $^{40}Ar/^{39}Ar$ age spectrum technique. *Earth and Planetary Science Letters*, **32**, 141-148.

Laubscher, H.P. 1970. Bewegung und Wärme in der alpinen Orogenese. *Schweizerische Mineralogische und Petrographische Mitteilungen*, **50**, 565-596.

Laubscher, H.P. 1986. The tectonics of the western and southern Alps: Correlation between surface observations and deep structure. In: *Third EGT Workshop-*

The Central Segment (edited by Freeman, R., Mueller, St. and Giese, P.). European Science Foundation, Strasbourg, France. 93-101.

Laubscher, H.P. 1988. Material balance in Alpine orogeny. *Bulletin of the Geological Societry of America* , **100**, 1313-1328.

Laubscher, H.P. and Bernoulli, D. 1982. History and deformation in the Alps. In: *Mountain Building Processes* (edited by Hsü, K.). Academic Press, London.pp 85-102.

Law, R.D. 1987. Heterogeneous deformation and quartz crystallographic fabric transitions: natural examples from the Moine Thrust Zone at the Stack of Glencoul, northern Assynt. *Journal of Structural Geology*, **9**, 819-833.

Law, R.D., Knipe, R.J. and Dayan, H. 1984. Strain partitioning in thrust sheets. *Journal of Structural Geology*, **6**, 477-498.

Leake, B. 1978. Nomenclature of amphiboles. *Mineralogical Magazine*, **42**, 533-563.

Lehrer, F.K. and Bataille, J. 1985. Nonequilibrium thermodynamics of pressure solution. *Pure and Applied Geophysics*, **122**, 53-85.

Lein, R. 1987. Evolution of the Northern Calcareous Alpes during Triassic times. In: *Geodynamics of the Eastern Alps* (edited by Flügel, H.W. and Faupl, P.). Deuticke, Wien. pp 85-102.

Lemoine, M. and Trümpy, R. 1987. Pre-oceanic rifting in the Alps. *Tectonophysics*, **133**, 305-320.

Lemoine, M., Bas, T., Arnaud, H., Dumont, T., Gidon, M., Bourbon, M., De Graciansky, P.C., Rudkiewicz, J.L. and Tricart, P. 1986. The continental margin of Mesozoic Tethys in the western Alps. *Marine and Petroleum Geology*, **3**, 178-199.

Lemoine, M., Gidon, M. and Barfety, J.C. 1981. Les massifs cristallins externes des Alpes occidentales: d'anciens blocs basculés nés au Lias lors du rifting téthysien. *Comptes-Rendus de l'Académie des Science de Paris*, **292**, 917-920.

Lister, G.S. and Snoke, A.W. 1984. S-C mylonites. *Journal of Structural Geology*, **6**, 617-638.

Lister, G.S. and Williams, P.F. 1979. Fabric development in shear zones: Theoretical controls and observed phenomena. *Journal of Structural Geology*, **1**, 283-297.

Lister, G.S. and Williams, P.F. 1983. The partitioning of deformation in flowing rock masses. *Tectonophysics*, **92**, 1-34.

Lloyd, G.E. 1987. Atomic number and crystallographic contrast image with the SEM: a review of backscatter techniques. *Mineralogical Magazine*, **51**, 3-19.

Loomis, T.P. 1975. Reaction zoning of garnet. *Contributions to Mineralogy and Petrology*, **52**, 285-305.

Loomis, T.P. 1983. Compositional Zoning in crystals: a record of growth and reaction history. In: *Kinetics and Equilibrium in Mineral Reactions* (edited by S.K. Saxena). Advances in Physical Geochemistry, Volume 3. Springer Verlag, New York. pp 1-61.

Loughnan, F.C. 1969. *Chemical Weathering of the Silicate Minerals*. Elsevier, New York.

Lowrie, W. 1986. Palaeomagnetism and the Adriatic Promontory. In: *Third EGT Workshop- The Central Segment* (edited by Freeman, R., Mueller, St. and Giese, P.). European Science Foundation, Strasbourg, France. 25-28.

Ludwig, K.1986. Isoplot. A plotting and regression program for radiogenic isotope datafor IBM-PC compatible computers. *United States Geological Survey, Open File Report*, **88:557**.

Makris, J. 1971. Aufbau der Kruste in den Ostalpen aus Schweremessungen und die Eigebnisse der Refraktionsseismik. *Hamburger Geophysikalische Einzelschriften*, **15**, Walter de Gruyter and Co., Hamburg. 65pp.

Massonne, H.-J. and Schreyer, W. 1987. Phengite geobarometry based on the limiting assemblage with K-feldspar, phlogopite and quartz. *Contributions to Mineralogy and Petrology*, **96**, 212-224.

McCaig, A.M. 1984. Fluid-rock interaction in some shear zones from the Pyrenees. *Journal of Metamorphic Geology*, **2**, 129-141.

McCaig, A.M. 1987. Deformation and fluid-rock interaction in metasomatic dilatent shear bands. *Tectonophysics*, **135**, 121-132.

McCaig, A.M. 1988. Deep fluid circulation in fault zones. *Geology*, **16**, 867-870.

McClay, K.R. 1977. Pressure solution and Coble creepin rocks and minerals: A review. *Journal of the Geological Society of London*, **134**, 57-70.

Means, W.D. 1981 The concept of a steady state foliation. *Tectonophysics*, **78**, 179-199.

Mercier, J.C.C., Anderson, D.A. and Carter, N.L. 1977. Stress in the lithosphere. Inferences from steady state flow of rocks.*Pure and Applied Geophysics*, **115**, 199-226.

Miller, C. 1974. On the metamorphism of eclogites and high-grade blueschists from the Penninic terrain of the Tauern Window, Austria. *Schweiz. miner. petrogr. Mitt.*, **54**, 371-384.

Miller, C. 1977. Chemismus und phasenpetrologische Untersuchungen der Gesteine aus der Eklogitzone des Tauernfensters, Österreich. *Tschermaks miner. petrogr. Mitt.*, **24**, 221-277.

Miller, H., Mueller, St. and Perrier, G. 1982. Structure and dynamics of the Alps- A geophysical inventory. In: *Alpine-Mediterranean Geodynamics* (edited by Berckhemer, H. and Hsü, K.J.). Geodynamics Series of the American Geophysical Union, Washington, **7**, 175-203.

Milnes, A.G. 1978. Structural zones and continental collision, central Alps. *Tectonophysics*, **47**, 369-392.

Mitra, G. 1978. Ductile deformation zones and mylonites: the mechanical processes involved in the deformation of crystalline basement rocks. *American Journal of Science*, **278**, 1057-1084.

Mueller, St. 1989. Deep reaching geodynamic processes in the Alps. In: *Alpine Tectonics* (edited by Coward, M.P., Dietrich, D. and Park, R.G.). The Geological Society of London Special Publication No.**45**, 303-328.

Mukhopadhyay, D.K. and Haimanot, B.W. 1989. Geometric analysis and significance of mesoscopic shear zones in the Precambrian gneisses around the Kolar Schist Belt, south India. *Journal of Structural Geology*, **11**, 569-581.

Müller, R.F. 1972. Stability of biotite: A discussion. *American Mineralogist*, **57**, 300-316.

Newton, R.C. and Haselton, H.T. 1981. Thermodynamics of the garnet - plagioclase - Al_2SiO_5 - quartz geobarometer. In: *Thermodynamics of Minerals and Melts* (edited by Newton, R.C. *et al*). Springer-Verlag, New York. pp 131-147.

Newton, R.C., Charlu, T.V. and Kleppa, O.J. 1977. Thermochemistry of high pressure garnets and clinopyroxenes in the system CaO-MgO-Al_2O_3-SiO_2. *Geochimica et Cosmochimica Acta*, **41**, 369-377.

Newton, R.C., Charlu, T.V. and Kleppa, O.J. 1980. Thermochemistry of the high structural state plagioclases. *Geochimica etCosmochimica Acta*, **44**, 933-941.

O'Hara, K. 1988. Fluid flow and volume loss during mylonitization : An origin for phyllonite in an overthrust setting, North Carolina, U.S.A. *Tectonophysics*, **156**, 21-36.

Oberhänsli, R., Hunziker, J.C., Martinotti, G. and Stern, W.B. 1985. Geochemistry, geochronology and petrology of Monte Mucrone: An example of Eo-alpine eclogitization of Permian granitoids in the Sesia-Lanzo Zone, western Alps, Italy. *Chemical Geology*, **52**, 165-184.

Ohnenstetter, M., Ohnenstetter, D., Vidal, P., Cornichet, J., Hermitte, D. and Mace, J. 1981. Crystallization and age of zircons from Corsican

ophiolitic albitites: Consequences for oceanic expansion in Jurassic times. *Earth and Planetary Science Letters*, **54**, 397-408.

Ord, A. and Christie, J.M. 1984. Flow stresses from microstructures in mylonitic quartzites from the Moine Thrust Zone, Assynt area, Scotland. *Journal of Structural Geology*, **6**, 639-654.

Oxburgh, E.R. 1968. An outline of the geology of the Central Eastern Alps. *Proceedings of the Geologists' Association*, **79**, 1-46.

Oxburgh, E.R. 1972. Flake tectonics and continental collision. *Nature*, **239**, 202-204.

Oxburgh, E.R. and Turcotte, D.L. 1974. Thermal gradients and regional meta-morphism in overthrust terrains with special reference to the eastern Alps. *Schweizerische Mineralogische und Petrographische Mitteilungen* , **54**, 641-662.

Oxburgh, E.R., Lambert, R.St.J., Baadsgaard, H. and Simons, J.G. 1966. Potassium-argon age studies across the southeast margin of the Tauern Window, the Eastern Alps. *Sonderabdruck aus den Verhandlungen der Geologischen Bundesanstalt*, **1966**, 17-33.

Passchier, C.W. 1988. Analysis of deformation paths in shear zones. *Geologische Rundschau*, **77**, 309-318.

Pavoni, N. 1980. Crustal stresses inferred from fault-plane solutions of earthquakes and neotectonic deformation in Switzerland. *Rock Mechanics*, **Supplement 9**, 63-68.

Pearce, J.A. 1983. Role of the sub-continental lithosphere in magma genesis at active continental margins. In: *Continental Basalts and Mantle Xenoliths* (edited by Hawkesworth, C.J. and Norry, M.J.). Shiva Publishing.

Pearce, J.A., Harris, N.B.W. and Tindle, A.G. 1984. Trace element discrimination diagrams for the tectonic interpretation of granitic rocks. *Journal of Petrology*, **25**, 956-983.

Pearson, D.G. 1988. *The Petrogenesis of Pyroxenites Containing Octahedral Graphite and Associated Mafic an Ultramafic Rocks of the Beni Bousera Peridotite Massif, N.Morocco.* Unpublished Ph.D. Thesis, University of Leeds.

Pecerrillo, A. and Taylor, S.R. 1976. Geochemistry of Eocene calc-alkaline volcanic rocks from the Kastamonu area, northern Turkey. *Contributions to Mineralogy and Petrology*, **58**, 63-81.

Peucat, J.-J. and Martin, H. 1985. Are Rb-Sr thin slabs meaningful? *Neues Jahrbuch Mineral Abh*, **152**, 1-21.

Pigage, L.C. and Greenwood, H.J. 1982. Internally consistent estimates of pressure and temperature: the staurolite problem. *American Journal of Science*, **282**, 943-969.

Pitcher, W. 1982. Granite type and tectonic environment. In: *Mountain Building Processes* (edited by K.Hsü). Academic Press, London. pp263.

Platt, J.P. 1986. Dynamics of orogenic wedges and the uplift of high-pressure metamorphic rocks. *The Bulletin of the Geological Society of America*, **97**, 1037-1053.

Platt, J.P. 1987 The uplift of high-pressure - low-temperature metamorphic rocks. *Philosophical Transactions of the Royal Society of London, A* **321**, 87-103.

Platt, J.P., Behrmann, J.H., Cunningham, P.C., Dewey, J.F., Helman, M., Parish, M., Sheply, M.G., Wallis, S. and Weston, P.J. 1989. Kinematics of the Alpine arc and the motion history of Adria. *Nature*, **337**, 158-161.

Poirier, J.P. 1980. Shear localization and shear instability in materials in the ductile field. *Journal of Structural Geology*, **2**, 135-142.

Poirier, J.P. 1985. *Creep of Crystals*, Cambridge University Press.

Powell, R. 1978. *Equilibrium Thermodynamics in Petrology*. Harper Row, London.

Powell, R. and Evans, J.A. 1983. A new geobarometer for the assemblage biotite-muscovite-chlorite-quartz. *Journal of Metamorphic Geology*, **1**, 331-336.

Powell, R. and Holland, T.J.B. 1988. An initially consistent data set with uncertainties and correlations: 3. Application to geobarometry, worked examples and a computer program. *Journal of Metamorphic Geology*, **6**, 173-204.

Powell, R. and Powell, M. 1977. Plagioclase-alkali feldspar geothermometry revisited. *Mineralogical Magazine*, **41**, 253-256.

Price, J.G. 1985. Ideal site mixing in solid solutions, with applications to two-feldspar geothermometry. *American Mineralogist*, **70**, 696-701

Prior, D.J. 1988. *Deformation Processes in the Alpine Fault Mylonites, South Island, New Zealand.* Unpublished Ph.D. Thesis, University of Leeds.

Prior, D.J., Knipe, R.J.K. and Handy, M.R. *In Press.* Estimates of the rates of microstructural changes in mylonites. In: *Deformation Mechanisms, Rheology and Tectonics* (edited by R.J.K. Knipe and E.H. Rutter). Geological Society of London Special Publication.

Pupin, J.P. 1980. Zircon and granite petrology. *Contributions to Mineralogy and Petrology*, **73**, 207-220.

Purdy, J.W. and Jäger, E. 1976. K-Ar ages on rock forming minerals from the Central Alps. *Memorie Dia Scienze Geologiche Padova*, **30**, 1-31.

Raith, M., Hermann, P.K. and Abraham, K. 1977. Petrology and metamorphic evolution of the Penninic ophiolites in the western Tauern Window. *Schweizerische Mineralogische und Petrographische Mitteilungen*, **57**, 187-232.

Ramsay, J.G. and Huber, M.I. 1987. *The techniques of Modern Structural Geology. Volume 2: Folds and fractures.* Academic Press, London.

Ramsey, J.G. and Graham, R.H. 1970. Strain variations in shear belts. *Canadian Journal of Earth Sciences*, **1**, 786-813.

Ratsbacher, L. 1986. Kinematics of Austro-alpine cover nappes: Changing translation path due to transpression. *Tectonophysics*, **125**, 335-356.

Ratsbacher, L. 1987. Strain, rotation and translation of Austroalpine nappes. In: *Geodynamics of the Eastern Alps* (edited by Flügel, H.W. and Faupl, P.). Deuticke, Wien. pp 237-243.

Ratsbacher, L. and Neubauer, F. 1989. West-directed décollement of Austro-Alpine cover nappes in the eastern Alps: geometrical and rheological considerations. In: *Alpine Tectonics* (edited by Coward, M.P., Dietrich, D. and Park, R.G.). The Geological Society of London Special Publication No.**45**, 243-262.

Ratsbacher, L. and Oertel, G. 1987. Superposed deformation in the Eastern Alps: Strain analysis and microfabrics. *Journal of Structural Geology*, **9**, 263-276.

Ratsbacher, L., Frisch, W. and Ring, U. 1987. Stacking, dispersion and extension as a consequence of Alpine transpression in the Eastern Alps. *Terra Cognita*, **7**, 118.

Ratsbacher, L., Frisch, W., Neubauer, F., Schmid, S.M. and Neugebauer, J. 1989. Extension in compressional orogenic belts: The case of the Eastern Alps. *Terra Abstracts*, **1**, 256.

Reddy, S.M. 1986. Prediction of changing deformation mechanisms and rheological evolution in the Eastern Alps from thermal-tectonic modelling. *Tectonic Studies Group Conference Program*, p84.

Reddy, S.M. 1989.The interaction of deformation and metamorphic processes within ductile shear zones in the Zentralgneis Complex, Austria. Terra Abstracts, **1**, 380.

Robertson, A.H.F. and Dixon, J.E. 1989. Tethyan tectonostratigraphic terranes: Fact or fiction. *Terra Abstracts*, **1**, 54.

Rubie, D.C. 1983. Reaction-enhanced ductility: The role of solid-solid univariant reactions in deformation of the crust and mantle. *Tectonophysics*, **96**, 331-352.

Rubie, D.C. 1984. A thermal tectonic model for high pressure metamorphism and deformation in the Sesia Zone, Western Alps. *Journal of Geology*, **92**, 21-36.

Rubie, D.C. and Thompson, A.B. 1985. Kinetics of metamorphic reactions at elevated temperatures and pressures: An appraisal of available experimental data. In: *Metamorphic Reactions: Kinetics, Texures and Deformation* (edited by Thompson, A. and Rubie, D.C.). Advances in Physical Geochemistry, **4**. Springer-Verlag, New York. pp 27-79.

Rubie, D.C. and Thompson, A.B. 1985. Kinetics of metamorphic reactions at elevated temperatures and pressures: An appraisal of available experimental data. In: *Metamorphic Reactions: Kinetics, Texures and Deformation* (edited by Thompson, A. and Rubie, D.C.). Advances in Physical Geochemistry, **4**. Springer-Verlag, New York. pp 27-79.

Rumble, D. III., Ferry, J.M., Hoerring, T.C. and Boucot, A.J. 1982. Fluid flow during metamorphism at the Beaver Brook Fossil Locality, New Hampshire. *American Journal of Science*, **282**, 886-919.

Rumble, D.III. and Spear, F.S. 1983. Oxygen-isotope equilibrium and permeability enhancement during regional metamorphism. *Journal of the Geological Society of London*, **140**, 619-628.

Rutter, E.H. 1983. Pressure solution in nature, theory and experiment. *Journal of the Geological Society of London* , **140**, 725-740.

Sander, B. 1911. Geologische Studien am Westende der Hohen Tauern. I. , **83**, 257-319.

Savostin, L.A., Sibuet, J.C., Zonenshain, L.P., Le Pichon, X. and Roulet, M.J. 1986. Kinematic evolution of Tethys belt from the Atlantic Ocean to the Pamirs since the Triassic. *Tectonophysics*, **123**, 1-35.

Schulien, S. 1975. Determination of the equilibrium constant and the enthalpy of reaction for the Mg^{2+}-Fe^{2+} exchange between bitotite and a salt solution. *Fortschr. Mineral.*, **52**, 133-139.

Seck, H.A. 1971a Koexistierende Alkalifeldspate und Plagioklase im System $NaAlSi_3O_8$-$KAlSi_3O_8$-$CaAl_2Si_2O_8$-H_2O bei Temperaturen von 650°C bis 900°C. *Neues Jahrbuch fur Mineralogie Abhandlungen*, **15**, 315-345.

Seck, H.A. 1971b. Der Einfluß der Drucks auf die Zusammensetzung koexietierender Alkalifeldspate und Plagioklase im system $NaAlSi_3O_8$-$KAlSi_3O_8$-$CaAl_2Si_2O_8$-H_2O. *Contributions to Mineralogy and Petrology*, **31**, 67-86.

Segall, P. and Simpson, C. 1986. Nucleation of ductile shear zones on dilatent fractures. *Geology*, **14**, 56-59.

Selverstone, J. 1985. Petrologic constraints on imbrication, metamorphism and uplift in the SW Tauern Window, Eastern Alps. *Tectonics*, **4**, 687-704.

Selverstone, J. 1988. Evidence for east-west crustal extension in the eastern Alps: Implications for the unroofing of the Tauern Window. *Tectonics*, **7**, 87-105.

Selverstone, J. and Spear, F. 1985. Metamorphic P-T paths from pelitic schists and greenstones in the southwest Tauern Window, Eastern Alps. *Journal of Metamorphic Geology*, 3,439-466.

Selverstone, J., Spear, F., Franz, G. and Morteani, G. 1984. High pressure metamorphism in the SW Tauern Window: P-T paths from hornblende-kyanite-staurolite schist. *Journal of Petrology*, **25**, 501-531.

Serra, S. 1977. Styles of deformation in ramp regions of overthrust faults. In: *Rocky Mountain Thrust Belt, Geology and Resources*. Wyoming Geological Association Guidebook, Casper. pp487-498.

Shimamoto, T. 1989. The origin of S-C mylonites and a new fault model. *Journal of Structural Geology*, **11**, 51-64.

Sibson, R.H. 1977. Fault rocks and fault mechanisms. *Journal of the Geological Society of London*, **153**,191-213.

Simpson, C. 1983. Strain and shape variations associated with ductile shear zones. *Journal of Structural Geology*, **5**, 61-72.

Simpson, C. and Schmidt, S.M. 1983. An evaluation of criteria to deduce the sense of movement in sheared rocks. *Bulliten of the Geological Society of America*, **94**, 1281-1288.

Simpson, C. and Wintsch, R.P. 1989, Evidence for deformation-induced K-feldspar replacement by myrmekite. *Journal of Metamorphic Geology*, **7**, 261-275.

Sinha, A.K., Hewitt, D.A. and Rimstidt, J.D. 1986. Fluid interaction and element mobility in the development of ultramylonites. *Geology*, **14**, 883-886.

Sinha, A.K., Hewitt, D.A. and Rimstidt, J.D. 1988. Metamorphic petrology and strontium isotope geochemistry associated with the development of mylonites: An example from the Brevard Fault Zone, North Carolina. *American Journal of Science*, **288A**, 115-147.

Slapansky, P. and Frank, W. 1987. Structural evolution and geochronology of the northern margin of the Austroalpine in the northwestern Schladming Crystalline (NE Radstätter Tauern). In: *Geodynamics of the Eastern Alps* (edited by Flügel, H.W. and Faupl, P.). Deuticke, Vienna. 244-262.

Spakman, W. 1986a. The upper mantle structure in the central European-Mediterranean region. In: *Third EGT Workshop- The Central Segment* (edited by Freeman, R., Mueller, St. and Giese, P.). European Science Foundation, Strasbourg, France. 215-219.

Spakman, W. 1986b. Subduction beneath Eurasia in connection with the Mesozoic Tethys. *Geologie en Mijnbouw*, **65**, 145-153.

Staufenberg, H. 1985. *Hebungs- und Abkühlungsgeschichte des Östlichen Tauernfensters und seiner ostalpinen Umrahmung, abgeleitet aus Apatit-Spaltsspürenaltern.* Unpublished Doktors der Naturwissenschaften genehmigten Dissertation, Technische Universität München. pp78.

Staufenberg, H. 1987. Apatite fission track evidence for postmetamorphic uplift and cooling history of the Eastern Tauern Window and the surrounding Austroalpine

(Central Eastern Alps, Austria). *Jahrbuch der Geologischen Bundesanstalt Wein*, **130**, 571-586.

Stähle, H.J., Raith, M., Hoernes, S. and Delfs, A. 1987. Element mobility during incipient granulite formation of Kabbaldurga, southern India. *Journal of Petrology*, **28**, 803-834.

Stormer, J.C.,Jr. 1975. A practical two-feldspar geothermometer. *American Mineralogist*, **60**, 667-674.

Streckeisen, A. 1976. To each plutonic rock its proper name. *Earth Science Reviews*, **12**, 1-33.

Talatsev, A.S. 1971. The plagioclase - muscovite geothermometer. *Doklady Akademii Nauk SSSR*, **196**, 1193-1195

Tamm, O. 1930. Experimentelle Studien uber die Verwitterung und Tonbildung von Feldspäten. *Chemie de Erde*, 4, 420-430.

Teall, J.J.H. 1885. The metamorphism of dolerite into hornblende schists. *Quarterly Journal of the Geological Society of London*, **41**, 133-145.

Thompson, A.B. 1976. Mineral reactions in pelitic rocks: II. Calculation of some P-T-$X_{(Fe,Mg)}$ phase relations. *American Journal of Science*, **276**, 425-454.

Thompson, A.B. and England. P.C. 1984. Pressure - temperature -time paths of regional metamorphism: II. Their inference and interpretation using mineral assemblages in metamorphic rocks. *Journal of Petrology*, **25**, 929-955.

Thompson, A.B., Lyttle, P.T. and Thompson, J.B. 1977. Mineral reactions and A-Na-K and A-F-M facies types in the Gassetts Schist, Vermont. *American Journal of Science*, **277**, 1124-1151.

Thompson, A.B., Tracy, R.J., Lyttle, P. and Thompson, J.B.Jr. 1977. Prograde reaction histories deduced from compositional zonation and mineral inclusions in garnet from the Gassetts schist, Vermont. *American Journal of Science*, **277**, 1152-1167.

Thompson, J.B. and Waldbaum, D.R. 1969. Mixing properties of sanidine crystalline solutions: III. Calculations based on two-phase data. *American Mineralogist*, **54**, 811-838.

Thöni, M. 1986. The Rb-Sr thin slab isochron method: An unreliable geochronologic method for dating geologic events in polymetamorphic terranes? Evidence from the Austroalpine basement nappe, the Eastern Alps. *Memorie Dia Scienze Geologiche Padova*, **38**, 283-352.

Thöni, M. 1988. Rb-Sr isotopic resetting in mylonites and Pseudotachylites: Implication for the deta chment and thrusting of the Austroalpine basement nappes in the Eastern Alps.

Titterington, D.M. and Halliday, A.N. 1979. On the fitting of parallel isochrons and the method of maximum likelihood. *Chemical Geology*, **26**, 183-195.

Tollman, A. 1976. Tektonische Auswertung der Satellitenbilder der Ostalpen. In: *Österreich im Satellitenbild* (edited by H. Beckel). Otto Müller Verlag, Salzburg. pp107.

Tollman, A. 1977. *Geologie von Österreich, Band 1: Die Zentralalpen*. Deuticke, Wien. 766pp.

Tollman, A. 1987a. The Alpidic evolution of the Eastern Alps. In: *Geodynamics of the Eastern Alps* (edited by Flügel, H.W. and Faupl, P.). Deuticke, Wien. pp 361-378.

Tollman, A. 1987b. Late Jurassic/Neocomian gravitational tectonics in the Northern Calcareous Alps in Austria. In: *Geodynamics of the Eastern Alps* (edited by Flügel, H.W. and Faupl, P.). Deuticke, Wien. pp 112-125.

Trümpy, R. 1980. *Geology of Switzerland, a guide book. Part A. An outline of the geology of Switzerland*. Wepf and Co., Basel. 104pp.

Tullis, J. and Yund, R.A. 1985. Dynamic recrystallization of feldspar: a mechanism for ductile shear zone formation. *Geology*, **13**, 238-241.

Twiss, R.J. 1977. Theory and applicability of a recrystallized grainsize palaeopiezometer. *Pure and Applied Geophysics*, **115**, 227-244.

Udias, A. 1982. Seismicity and seismotectonic stress field in the Alpine-Mediterranean. In: *Alpine-Mediterranean Geodynamics* (edited by Berckhemer, H. and Hsü, K.J.). Geodynamics Series of the American Geophysical Union, Washington, **7**, 75-82.

Urai, J.L., Means,W.D. and Lister, G.S. 1986. Dynamic recrystallization of minerals. In: *Mineral and Rock Deformation Laboratory Studies- The Paterson Volume* (edited by Hobbs, B.E. and Heard, H.C.). American Geophysics Union Geophysical Monograph, **36**, 161-199.

Vauchez, A. 1987. The development of discrete shear-zones in a granite: stress, strain and changes in deformation mechanisms. *Tectonophysics*, **133**, 137-156.

Velde, B. 1965. Phengite micas:Synthesis, stability and natural occurence. *American Journal of Science*, **263**, 886-913.

Velde, B. 1967. Si^{4+} content of natural phengites. *Contributions to Mineralogy and Petrology*, **14**, 250-258.

Vocke, R.D.Jr., Hanson, G.N. and Grünenfelder, M. 1987. Rare earth element mobility in the Roffna Gneiss, Switzerland. *Contributions to Mineralogy and Petrology*, **95**, 145-154.

Wallis, S.R. 1987. *The structural and kinematic development of the Austroalpine-Pennine boundary in the SE Tauern.* Unpublished PhD. Thesis, University of Oxford.

Waniek, L., Van Gils, J.M. and Ritsema, A.R. 1982. *European Seismological Commission- Activity Report 1980-1982.* K.N.M.I. de Bilt (The Netherlands). 90pp.

Waters, D.J. 1976. *Structural, metamorphic and geochronological studies in the south east Tauern Window.* Unpublished Ph.D. Thesis, Univerity of Oxford.

Watts, M.J. and Williams, G.D. 1983. Strain geometry, microstructures and mineral chemistry in metagabbro shear zones: a study of softening mechanisms during progressive mylonitization. *Journal of Structural Geology*, **5**, 507-517.

Weijarmer, R. and Rondeel, H.E. 1984. Shear band foliation as an indicator of sense of shear: field observations in central Spain. *Geology*, **12**, 603-606.

Westphal, M., Bazhenov, M.L., Lauer, J.P., Pechersky, D.M. and Sibuet, J.-C. 1986. Palaeomagnetic implications on the evolution of the Tethys belt from the Atlantic Ocean to the Pamirs since the Triassic. *Tectonophysics*, **123**, 37-82.

Westwood, A.R.C., Goldheim, D.L. and Lye, R.G. 1967. Rebinder effect in MgO. *Philosophical Magazine*, **16**, 505-519.

Wheeler, J. 1989. Extensional shearing on the western boundary of the Dora Maira massif, Italian western Alps. *Terra Abstracts*, **1**, 256.

White, A.J.R. and Chappel, B.W. 1983. Granitoid types and their distribution in the Lachlan Foldbelt, southeastern Australia. In: *Cicum-Pcific Plutonic Terranes* (edited by J.A. Roddick). *Geological Society of America Memoir*, **159**, 21-34.

White, S.H. and Bretan, P.G. 1985. Rheological controls on the geometry of deep faults and the tectonic delamination of the continental crust. *Tectonics*, **4**, 303-309.

White, S.H. and Knipe, R.J. 1978. Transformation- and reaction- enhanced ductility in rocks. *Journal of the Geological Society of London* , **135**, 513-516.

White, S.H., Burrows, S.E., Carreras, J., Shaw, N.D. and Humphreys, F.J. 1980. On mylonites in ductile shear zones. *Journal of Structural Geology*, **2**, 175-187.

Whitney, J.A. and Stormer, J.C., Jr. 1977. The distribution of $NaAlSi_3O_8$ between co-existing microcline and plagioclase and its effect on geothermic calculations. *American Mineralogist*, **62**, 687-691.

Williams, P.F. and Compagnoni, R. 1983. Deformation and metamorphism in the Bord area of the Sesia-Lanzo zone, western Alps, during subduction and uplift. *Journal of Metamorphic Geology*, **1**, 117-140.

Winchester, J.A. and Max, M.D. 1984. Element mobility asociated with syn-metamorphic shear zones near Scotchport, NW Mayo, Ireland. *Journal of Metamorphic Geology*, **2**, 1-11.

Wintsch, R.P. 1985. The possible effects of deformation on chemical processes in metamorphic fault zones. In: *Metamorphic Reactions: Kinetics, Texures and Deformation* (edited by Thompson, A. and Rubie, D.C.). Advances in Physical Geochemistry, **4**. Springer-Verlag, New York. pp 251-268.

Wintsch, R.P. and Andrews, M.S. 1988, Deformation induced growth of sillimanite: stress minerals revisited. *Journal of Geology*, **96**, 143-161.

Wintsch, R.P. and Dunning, J. 1985. The effect of dislocation density on the aqueous solubility of quartz and some geologic implications: A theoretical approach. *Journal of Geophysical Research*, **90**, 3649-3657.

Wintsch, R.P. and Knipe, R.J. 1983. Growth of a zoned plagioclase porphyroblast in a mylonite. *Geology*, **11**, 360-363.

Wones, D.R. 1972. Stability of biotite: A reply. *American Mineralogist*, **57**, 316-317.

York, D. 1969. Least squares fitting of a straight line with correlated errors. *Earth and Planetary Science Letters*, **5**, 320-324.

Appendix 1

Sample Preparation

A1:1 Whole Rock Powders and Mineral Seperates

Geochemical samples were taken from relatively 'fresh' exposures and had any weathered surfaces removed prior to any further preparation. All samples weighed between 1 and 5kg, the majority being in the order of 2.5-3kg. The samples were rinsed with warm and then distilled water to clean their surfaces. Once dry, the samples were reduced to approximately 100cm^3 'blocks' using a hydraulic splitter. The splitter was thoroughly cleaned between samples. The 'blocks' were then crushed in an adjustable jaw crusher, coned and quartered and a 200g fraction was removed for whole-rock analyses. The remainder was used for mineral separation.

The fraction removed for whole-rock analyses was crushed to <2mm diameter chips, was coned and quartered and approximately 90g of the fraction was crushed in an agate swing mill to <250 mesh. The tema barrel used for this was specifically reserved for granitic rocks and was rigorously cleaned after each sample. Contamination from the tema has been tested by making qualitative spectrographic analyses on the results of two-minute, quartz grinding tests. These show that the barrel may give trace amounts of contamination for Fe, Al, Ca , Mg, Ti and Cu. Very approximate relative values are quoted at Co <10ppm; Cr<10ppm; Cu≈7ppm and Ni<10ppm.

The rock chips retained for mineral separation were crushed further in the jaw crusher and periodically sieved to obtain the 60-90# and 90-120# (mm) size fractions. These size fractions were then 'deslimed' by adding a little detergent and distilled water to the fraction and placing this in an ultrasonic bath for 15 minutes. The fractions were then rinsed repeatedly in distilled water, given a final wash in acetone and then dried. Mineral separates were obtained by passing the size fraction through Franz-type magnetic separators at a variety of settings and, in the case of feldspar, by using heavy liquid (Methylene iodide and Tetra bromoethane) separation techniques.

In the case of micas, relatively pure separates were ground under alcohol, 'deslimed' and again washed to remove small inclusions of quartz and feldspar. Separates were finally hand-picked clean and slide mounts were made in order to assess the purity of each sample. Purity was assessed by counting approximately 400 grains. In the case of

biotite, all analysed samples were greater than 97% pure, the only observed impurity being chlorite. White mica and amphibole separates were thoroughly hand-picked to ensure absolute purity.

A1:2 Whole rock Thin Slabs

A large sample of the shear zone sample, 24/87, was dissected so that a cube of unweathered material could be obtained. This cube was further cut into 4 approximately equal, orthorhombic blocks. Two adjacent blocks were chosen for thin slab work. Each of the two blocks were sawn into 7 thin slabs. The location of thin slab boundaries was based on modal differences, specifically the amount of K-feldspar. These boundaries are illustrated in Figure 7.3a, while the weight and dimensions of each slab is shown in Table A1. The thin slabs were then crushed in a stainless steel pestle and mortar, specifically reserved for granitic lithologies, which was rigorously cleaned after each sample.

Sample	Block Dimension (mm)	Band Thickness (mm)	Weight (gms)
a	30x15	8	10.057
b	30x15	11	13.343
c	30x15	7	8.358
d	30x15	9	11.053
e	30x15	5	6.318
f	30x15	7	8.165
g	30x15	8	9.536
h	30x22	8	15.241
i	30x22	9	17.857
j	30x22	9	15.916
k	30x22	8	14.241
l	30x22	8	14.201
m	30x22	4	7.402
n	30x22	6	12.065

Table A1.1 Size and weight of individual thin slabs from shear zone sample 24/87

A1:3 Sample Preparation for Microscopy and Electron Microprobe

A1:3.1 Thin Section Preparation

Both covered and uncovered-polished thin sections were used for optical examinations and were prepared in the Departmenrt of Earth Sciences thin section labs at the University of Leeds. Lead contamination from the lead laps used for polishing in Leeds, make electron microscopy and electron microprobe analysis difficult and so this contamination was removed by further polishing sections for 3-5 minutes on a silk lap

with 1/4 micron diamond paste. During the later stages of this project, samples used for electron microscopy were Syton polished. The Cambridge Instruments Syton™ is a silica colloid polisher designed specifically for the removal of surface damage for specimens to be studied by electron channeling (Lloyd 1987).

The silica colloid is suspended in an NaOH solution and polishing is achieved by a combination of dissolution and mechanical abrasion (Fynn and Powell 1975; Lloyd 1987). The extent of each of these depends on the hardness and chemistry of the individual sample as well as the applied pressure and the angular velocity of the rotating lap. The thin section to be polished was placed in a specially designed thin section holder and was held under pressure against a foam lap which rotates as the specimen oscillates from the centre to the rim of the lap. The specimen was left to polish for between 4 and 12 hours.

A1:3.2 Polished Block Preparation

For orientation contrast and electron channeling backscatter electron microscopy polished blocks were used since these polish better and therefore provide better images than Syton polished thin sections. To make a polished block a small flat chip, with sample label and orientation on its reverse side, was placed face downwards in a polythene mould. Metaset™ mounting material was mixed with hardener in the ratio $10cm^3$: 5 drops, thoroughly stirred and poured into the mould to a depth of approximately 15mm. The specimen was centred in the mould using a wooden spatula to aid later polishing. The sample was then left overnight to enable complete setting of the resin.

When set, the meniscus on the back of the block must be removed and the back surface must be made parallel to the front of the block. This was achieved using a rotating coarse diamond plate and was a critical step in sample preparation since electrons are lost in the microscope if the sample surface is not perpendicular to the electron beam. A hole of 2mm depth was drilled into the back of the block with a 1/10th inch drill bit. This was used to hold the thin metal bar which applies the pressure to the sample during Syton polishing.

Before polishing on the Syton, the resin on the front of the sample was removed by grinding the surface with 200 grade carborundum. This was followed by repeated grinding (at 600 grade) and washing until all damage caused by the 200 grade abrasive,

was removed. Further polishing on a cloth covered steel lap, using diamond paste abrasive, cuts down the time required for Syton polishing. Therefore, sequential polishing using 9, 3, 1 and 1/4 micron pastes was carried out to enhance the pre-Syton surface polish. The cloth lap was thoroughly cleaned between different samples and a new cloth lap was used for the different abrasives. Polishing at each grade was for approximately 8-10 minutes per sample. After washing each block was further polished using the Syton polisher.

Before using on the SEM or electron microprobe, polished sections and blocks were mounted on conductive, metal stubs with Bostick™. Contact beween stub and the the surface of the block or section was made using carbon paint and the surface of the sample was coated with a thin layer of graphite.

Appendix 2

Analytical Techniques

A2:1 X-Ray Fluorescence Analysis (XRF)

Major elements compositions were determined using fusion beads. 0.400g of dried whole rock sample was weighed into a Pt/Au alloy crucible, 4.000g of lithium tetraborate flux was added and the two powders were thoroughly mixed together. The Pt/Au crucible was covered, placed in a furnace @ 1100°C for one hour and then allowed to cool. Any reduction in weight, due to water loss from the hygroscopic flux, was made up by the addition of more flux. The mixture was remelted and cast into a 46mm diameter copper ring. Quantification of the amount of volatiles and non-structurally bonded water was made by 'loss on ignition' on 1g of the whole rock sample heated at 1000°C for 1 hour.

Trace element analyses were determined using powder briquettes comprising ≈15g of the whole rock powder and ≈4ml of Moviol P.V.A. Powder and Molviol were mixed thoroughly in clean, throw-away containers and the resulting mixture was compressed under a pressure of 10 tons in a polished steel hydraulic press. The press surfaces were cleaned after each sample. The resulting briquettes were dried for 1 hour at 110°C and were placed in a vacuum desiccator prior to analysis.

XRF analyses were performed on a Phillips PW1400 XRF at Leeds. Machine drift was corrected by reference to internal laboratory standards which were always included in a run. Operating conditions for the machine vary with the analysed element and are shown in Table A2.1. For element oxides in excess of 5%, the reproducibility is generally better than 1% although with decreasing amounts of element oxide reproducibility generally decreases and at around 1% oxide reproducibility falls within 5% (Pearson 1989). For trace elements, values below 10ppm are generally outside the detection limits of the machine.

A2:2 Electron Microprobe Analyses

Mineral analyses were carried out in the Dept. of Earth Sciences, Leeds using a Jeol JXA-50A electron microprobe which uses an energy dispersive Link 860 series 2 analysing system operating at a beam current of 1nA and an accelerating voltage of 20kV. Count times for analyses were for 100 seconds except in the case of carbonates

Table A 2.1 Operating conditions for the PW 1400 XRF Spectrometer.

Measuring program 1. Rhodium target with power set at 40 kV by 60 mA

Element	line	Collimator	Detector	Crystal	2-theta	offsets +	offsets -	time (secs)
Na	Ka	Coarse	Flow	PX 1	23.65	1.6	1.6	160
Mg	Ka	Coarse	Flow	PX 1	23.60	1.2	1.2	80
Al	Ka	Coarse	Flow	PET	144.90	---	---	30
Si	Ka	Coarse	Flow	InSb	144.56	---	---	20
P	Ka	Coarse	Flow	Ge	141.03	---	---	20
K	Ka	Fine	Flow	LiF 200	136.69	---	---	8
Ca	Ka	Fine	Flow	LiF 200	113.09	---	---	8
Ti	Ka	Fine	Flow	LiF 200	86.14	---	---	8
Mn	ka	Fine	Flow	LiF 200	62.97	---	---	8
Fe	Ka	Fine	Flow	LiF 200	57.52	---	---	4

Measuring program 2. Rhodium target with power set at 80 kV by 30 mA

Element	line	Collimator	Detector	Crystal	2-theta	offsets +	offsets -	time (secs)
Cr	ka	Fine	Flow	LiF 200	69.38	1.0	1.0	80
Co	Ka	Fine	Flow	Lif 220	77.39	0.5	---	80
Ni	Ka	Fine	Flow	LiF 200	48.67	1.0	---	80
Cu	Ka	Fine	Flow	LiF 200	45.03	0.6	1.0	80
Zn	Ka	Fine	Scint	LiF 200	41.76	1.0	---	80
Rb	Ka	Fine	Scint	LiF 200	26.62	0.5	0.8	80
Sr	Ka	Fine	Scint	LiF 200	25.15	0.6	0.6	80
Y	Ka	Fine	Scint	LiF 200	23.80	0.8	0.8	80
Zr	ka	Fine	Scint	LiF 200	22.55	0.4	0.8	80
Nb	Ka	Fine	Scint	LiF 220	30.39	0.6	0.6	80
Ba	Ka	Fine	Scint	LiF 220	15.54	0.5	0.3	80
Pb	Lb	Fine	Scint	LiF 200	28.26	0.5	1.0	80

Measuring program 3. Rhodium target with power set at 80 kV by 30 mA

Element	line	Collimator	Detector	Crystal	2-theta	offsets +	offsets -	time (secs)
Th	La	Fine	Scint	LiF 220	39.19	0.9	0.5	400
U	La	Fine	Scint	LiF 200	26.11	1.0	0.4	400

Measuring program 4. Rhodium target with power set at 50 kV by 50 mA

Element	line	Collimator	Detector	Crystal	2-theta	offsets +	offsets -	time (secs)
Sc	Ka	Fine	Flow	LiF 200	97.73	0.6	0.6	400
V	Ka	Fine	Flow	Lif 220	123.12	---	1.1	160

PAGES MISSING IN ORIGINAL

where prolonged count times led to sample damage. A count time of 60 seconds was used for carbonates. Beam current was set by using a Faraday cage between specimen exchanges and the stability of the beam current was periodically monitored by blanking the beam and comparing the detected current with the blanked reading taken after each resetting of the Faraday cage. Co was used as a calibration standard.

ZAF corrections were done 'on-line' and programs written by E. Condliffe were used for the recalculation of garnet, feldspar and phyllosilicate end-members.

A2:3 Scanning Electron Microscopy (SEM)

Details of the theory behind backscatter SEM techniques and the operating instructions for different modes of imagery are given by Lloyd (1987) and Prior (1988) respectively. Most of the electron microscopy was carried out on a Camscan Series 2 SEM at 25kV accelerating voltage and a working distance of between 16-24mm. For orientation contrast micrographs, a Camscan Series 4 SEM was used. This enabled shorter working distances (down to 6mm), and hence enhanced resolution, to be employed at accelerating voltages of 20-30kV.

A2:4 The Rb-Sr Isotopic Technique

A2:4.1 Extraction

During the following description of chemical extraction proceedures, quartz-distilled (QD) and sub-boiled (SB) Analar reagents were used routinely and care was taken to avoid contamination.

30 ml teflon beakers were cleaned in 15M HNO_3 for 24 hours, transferred to distilled water and left for a further 24 hours. Beakers were then boiled twice in SB H_2O and placed in ovens to dry. Between 50 and 200mg of sample was added to the sample followed by an amount of Leeds Green spike (compositon 0.4148$\mu M^{87}Rb$, 0.01312$\mu M^{84}Sr$ and isotopic ratios of $^{85}Rb/^{87}Rb=0.00791$, $^{88}Sr/^{86}Sr=1.234$, $^{87}Sr/^{86}Sr=0.1959$ and $^{84}Sr/^{86}Sr=1592$). To avoid either underspiking or overspiking, the amount of spike required was approximately calculated from a graph of (sample weight)/(spike weight) against ppm element (Figure A2.1). The exact weights of sample and spike added to the beaker were calculated by 'measuring by difference'.

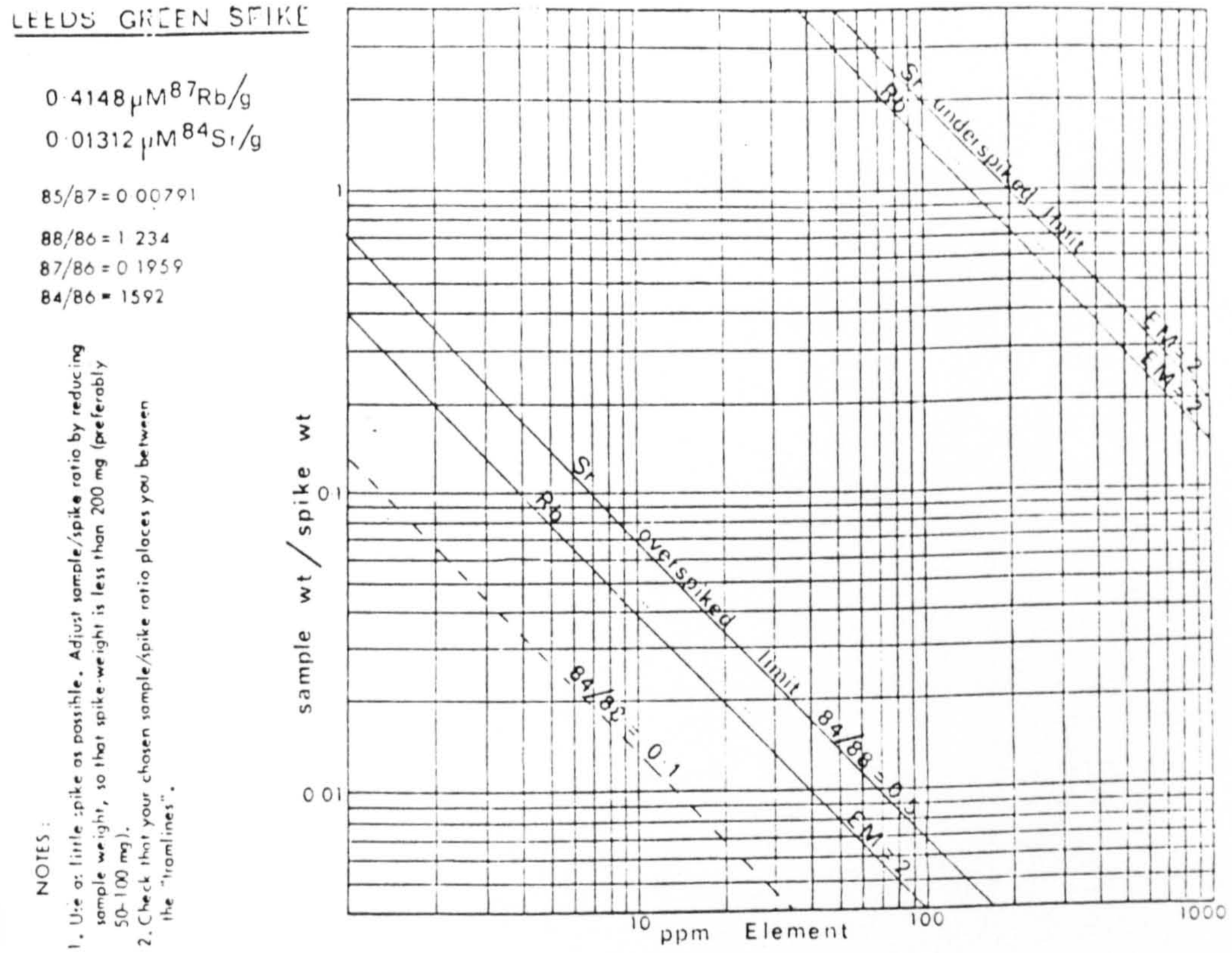

1ml of 15M HNO_3 was added to the sample and was followed by the addition of 8ml of 40% HF. The beaker was covered with Parafilm® and left overnight for the sample to dissolve. Following dissolution, the solution was evaporated to dryness beneath air flow hoods heated by electric lamps. When dry, another 1ml of 15M HNO_3 was added and again evaporated to dryness. This was followed by the addition of 10ml of 6M HCl and the resulting solution was again evaporated. The residue was dissolved in 2ml of 2.5M HCl and the solution was transferred to clean centrifuge tubes and centrifuged to remove any remaining solids.

1ml of the solution was added to previously cleaned cation exchange columns calibrated for the collection of Rb and Sr. Acid washes were added to the columns and the Rb and Sr elutions were collected separately in clean teflon beakers. Both Rb and Sr bearing solutions were evaporated to dryness and the exchange columns were cleaned with 6M HCl, SBQD H_2O and 2.5M HCl, ready for a second Sr extraction which is required to remove any remaining Rb. The dry Sr residue was dissolved in 1ml of 2.5M HCl and was added to the exchange columns. Acid washes were again added, the Sr elution was collected and evaporated to dryness. After use, columns were again cleaned.

A2:4.2 Sample Loading

Single and triple Ta-filament beads were prepared for Sr and Rb respectively. Beads were boiled twice in SB water and were placed in an oven to dry. Once dry, the beads were outgassed at 4.5A under a vacuum better than 10^{-5} Torr for 5 minutes.

For Rb, the dried sample was taken into solution with a little SBQD water, loaded onto the two side filaments and evaporated to dryness at 2 Amps. Prior to loading Sr onto the single Ta filament, one drop of phosphoric acid was added to the filament to promote stable isotope emission.

A2:4.3 Mass Spectrometry

Sr isotopic analyses and Sr abundance determinations were made in the same run on the automated VG 54E double collector mass spectrometer operating at 8kV accelerating voltage and magnet setting of 2kG. Masses 88,87 and 86 were reassessed automatically along with Rb interference at mass 85. The ^{86}Sr tail was monitored at mass 87.3 and the background was 84.5. $^{87}Sr/^{86}Sr$ was corrected for mass fractionation assuming the fractionation was linearly correlated with mass and was normalized to $^{86}Sr/^{88}Sr$. Over the period of this study, 52 routine analyses of the NBS987 international standard ($^{87}Sr/^{86}Sr$= 0.1194), gave 0.710275±41. Measured $^{87}Sr/^{86}Sr$ ratios were therefore 'corrected' by subtracting 0.000045.

Rb was analysed on a manuel VG Micromass 30 mass spectrometer again at an accelerating voltage of 8kV and a magnet setting of 2kG. Rb was measured over 9-12 sets.

A2:4.4 Age Calculations

The increase of ^{87}Sr at the expense of ^{87}Rb can be expressed by the relationship

$$^{87}Sr/^{86}Sr = {}^{87}Sr/^{86}Sr_i + {}^{87}Rb/^{86}Sr\ (e^{\lambda t} - 1) \quad \text{(Faure 1986)}$$

where $(^{87}Sr/^{86}Sr)_i$ was the initial ratio of the system, λ is the decay constant, taken to be 1.42×10^{-11} (Steiger and Jäger 1977), and t is the age. This forms a straight line relationship on a graph of $^{87}Sr/^{86}Sr$ against $^{87}Rb/^{86}Sr$ where the gradient of the line equals ($e^{\lambda t}$ -1) and the intercept on the $^{87}Sr/^{86}Sr$ axis is equal to the initial $^{87}Sr/^{86}Sr$ ratio.

Rearranging the equation gives

$$t = (1/\lambda) \ln \{1+ (({}^{87}Sr/{}^{86}Sr - {}^{87}Sr/{}^{86}Sr_i) / {}^{87}Rb/{}^{86}Sr) \}$$

Statistical analysis of isotopic data has been carried out using the Isoplot program of Ludwig (1990), and age calculations are based on a Model 1 Yorkfit linear regression (York 1969). This model assumes that the *only* cause for scatter from a straight line are the assigned errors. The points are therefore weighted proportionally to the inverse-square of these errors. All errors are quoted at the 2 sigma, 95% confidence limit. Errors for $^{87}Rb/^{86}Sr$ and $^{87}Sr/^{86}Sr$ are taken as 1% and 0.05% respectively and an error correlation of zero have been assumed in all age calculations.

The relationship between observed and predicted scatter is given by the Mean Square of Weighted Deviates (MSWD) which is essentially the ratio of the observed scatter of the points from the best-fit line to the scatter predicted by the assigned errors of the points. If the assigned errors are the only source of scatter, then the MSWD will be close to 1. Brooks *et al* (1972) recommend that 2.5 be used as the cut-off level to distinguish between isochrons (MSWD < 2.5) and errorchrons (MSWD >2.5). Model 1 errors are calculated using the maximum-likelihood algorithm of Titterington and Halliday (1979).

Appendix 3:1.Sonnblick Gneisses XRF Data

Key

LCAG - Low Strain Coarse Augen Gneiss

ICAG - Intermediate Strain Coarse Augen Gneiss

FAG - Fine Augen Gneiss

FG - Fine Gneiss

ML - Micaceous Leucogranite (Aplite)

WMS- White Mica Schist

BS- Biotite Schist

AMPH- Amphibolite

ALI = mol (Al_2O_3 / $CaO + Na_2O + K_2O$)

Q, A and P refer to quartz, alkali feldspar and plagioclase totals recalculated to 100%.

Sample No.	48415	48416	48419	48605	48607	48610	49114	29/86	45/86	32/87	55/87	57/87	184/87	28/88	32/88	57/88
Rock Type	ICAG	ICAG	LCAG	ICAG	ICAG	ICAG	LCAG	ICAG	LCAG	LCAG	ICAG	LCAG	LCAG	LCAG	FAG	LCAG
SiO2	70.88	70.18	70.47	69 42	71.10	70 54	70 89	69.47	71.36	70.83	72.00	71.72	70 21	69 31	68 57	69 85
TiO2	0.92	0.35	0.34	0 34	0 31	0.31	0 33	0.35	0.32	0.31	0.36	0.29	0.35	0.37	0 38	0 35
Al2O3	14.62	14 71	14.69	15.29	14.73	14.71	14.59	14.98	14.61	14.95	14.43	14 28	14.60	14 86	15.54	14 86
Fe2O3	1.99	2.30	2.25	2.49	2.00	1.90	2.15	2.44	2.15	2.09	1.75	1.86	2.44	2 65	2 47	2 49
MnO	0.06	0.08	0 07	0.07	0 06	0 06	0.07	0.07	0.07	0.07	0.04	0.06	0 07	0 07	0 06	0 07
MgO	0.64	0.73	0.85	0.91	0.58	0 63	0.75	0.80	0.76	0.70	1.89	0.69	0 80	1 05	0.75	0 84
CaO	1.96	2.02	2.09	2.29	1.73	1.71	1.96	2.21	1.91	1.92	0.45	1.91	2.11	2 23	2.33	2 21
Na2O	3.81	3.84	3 85	5 00	4.64	3.98	3.82	3.95	3.92	3.95	3.42	3 67	3 79	4.11	4.12	4 04
K2O	4 06	3.82	3.98	4 04	4.16	4.32	3 96	3.92	4.05	4.21	4.15	4 23	3 94	3.77	3 98	3 93
P2O5	0.16	0.17	0.18	0 19	0.15	0.15	0.17	0.18	0.17	0.16	0.15	0.16	0.17	0.17	0 15	0 16
L.O.I.	1.25	0.79	0.86	0.57	0.51	1.02	0.86	1.04	0.90	0.63	0.91	0.99	0 63	0.99	1 11	0 93
Total	99.72	98.99	99.63	100.62	99.98	99.34	99.55	99.41	100.23	99.82	99.55	99 86	99.12	99 58	99 47	99 71
ALI	1.03	1.04	1.02	0.91	0 97	1.03	1.06	1.01	1.02	1.03	1.31	1.01	1 02	1 00	1 01	0 99
Cr	1	4	12	4	5	4	8	1	12	9	17	12	5	18	5	5
Co	7	11	9	10	7	10	7	6	8	7	8	9	5	9	8	7
Ni	6	6	8	6	7	4	8	7	10	8	9	9	6	12	7	7
Cu	2	1	4	0	4	2	0	4	2	2	9	1	4	4	8	5
Zn	42	50	44	52	46	41	47	52	51	50	29	46	54	61	60	50
Pb	135	171	144	151	188	160	174	164	178	171	155	145	167	157	159	155
Sr	533	454	469	578	442	437	421	577	449	477	110	537	504	662	673	582
Y	12	13	15	15	17	16	17	17	13	16	17	15	15	17	13	14
Zr	114	150	144	135	181	179	152	149	146	142	174	137	146	200	207	143
Nb	13	20	19	16	26	23	22	16	19	21	21	20	18	17	20	15
Pb	43	31	36	35	39	23	35	51	40	40	18	39	42	36	34	40
Ba	981	888	860	1116	831	989	672	922	714	832	673	841	881	79	1132	894
U	3	8	8	4	9	7	9	4	5	2		9	7	8	7	5
Th	25	29	23	25	29	29	27	26	23	23		32	30	35	26	23
Nd	27	27	27	30	28	31	24	29	26	26	18	28	30			
Ce	23	20	23	28	32	32	26	33	36	20	37	28	29			
La	34	31	26	34	31	32	25	33	27	24	65	30	34			
V	26	23	24	30	14	16	20	23	22	20	24	16	23	3	17	33
Sc	7	7	7	8	5	5	7	7	8	7	6	5	9	7	8	7
CIPW Norms																
Qtz	29.33	29.27	28 56	18.38	23 22	27.58	29.56	27.07	29.02	27.74	34.92	30 31	28 81			
Or	23.91	22 49	23 27	23 92	24.76	25.50	23.21	23.00	23 59	24.58	24.00	24 81	23 10			
Pl Ab	32.12	32.37	32 23	42.38	39.54	33 64	32.06	33.19	32.69	33.02	28.32	30 82	31 81			
An	8 65	8 88	9 09	7.36	7.13	7.49	8.54	9.72	8.24	8 38	1.23	8 37	9 28			
C	0.77	0.99	0 67			0.74	0 86	0 65	0.70	0.78	3.77	0 57	0 66			
Wo				1.16												
Di En				0.49												
Fs				0 67												
Hy En	1.59	1.81	2 09	1.78	1.37	1.57	1.85	1.98	1.87	1.72	4.61	1 71	1 98			
Fs	2.42	2.79	2 70	2.40	2.28	2.27	2.58	2.96	2.58	2.52	1.90	2 23	2 95			
Mt	0.29	0.33	0.32	0.36	0.29	0 28	0.31	0.35	0.31	0.30	0.25	0 27	0 35			
Ilm	0 55	0 66	0 64	0 65	0 59	0 59	0.62	0.66	0.60	0.58	0.67	0 55	0 66			
Ap	0.38	0.40	0 42	0.45	0.35	0.35	0.40	0.42	0.40	0.37	0.35	0.37	0 40			
Q	31.3	31.5	30.7	20.0	24 5	29.3	31.7	29.1	31.0	29 6	39.5	32.1	31.0			
A	25.5	24.2	25 0	26 0	26 2	27.1	24.9	24.7	25.2	26 2	27.1	26.3	24 8			
P	43 2	44.3	44 3	54.0	49.3	43 6	43.4	46.2	43.8	44 2	33.4	41.6	44 2			

Sample No.	76/88	77/88	78/88	79/88	80/88	81/88	82/88	83/88	84/88	85/88	87/88	103/88	24/87	143/87	310/87	343/87	185/87	7708
Rock Type	ICAG	LCAG	ICAG	RG	LCAG	BS	ML	LCAG	ICAG	BS	FAG	RG	WMS	WMS	WMS	WMS	AMPH	BS
SiO2	68.93	68.80	69.00	67.85	70.29	51.55	75.57	70 20	70.78	51.28	72 67	76.14	77.04	67 89	66 57	67.50	45.03	37.97
TiO2	0.35	0.33	0.30	0.67	0.35	0 93	0.08	0 32	0.35	0 88	0.28	0 12	0.10	0 36	0.02	0.16	0.77	1.05
Al2O3	14.84	15.33	14.57	16.02	14.70	17.11	14.32	15.38	14.67	16 22	13 39	12 63	13.05	15 90	18.39	18.27	15.97	17.07
Fe2O3	2.38	2.38	2.05	3.11	2.24	7.98	0.85	2 04	2.41	8.34	1 88	1.44	0.84	1.97	1.64	1.37	10.13	16.94
MnO	0.08	0.07	0.07	0.06	0.06	0.15	0.04	0 06	0.08	0.17	0 05	0 04	0 03	0 03	0.03	0.04	0.18	0.20
MgO	0.84	0.81	0.72	0.96	0.70	6 63	0.13	0 72	0.89	7.28	0 48	0.07	1.42	4 94	4.33	3.23	6.60	13.77
CaO	1.88	2.21	1.83	2.44	1.93	7.09	0.80	2.30	1.76	7.57	1.36	0 44	0.08	0.19	0.01	0.35	15.68	0.17
Na2O	4.22	4.28	4.45	4.23	4.15	1.92	4.21	4.53	4.01	3.90	3.91	3 70	0.24	0.18	0.42	0.74	1.71	0 20
K2O	4.10	4.06	4.42	3.11	3.96	3.92	2.43	3.32	3.93	1.91	4 24	5 34	5.20	5.15	4.76	4.90	0.16	9.82
P2O5	0.14	0.15	0.12	0.25	0.13	0.18	0.08	0.13	0.15	0.17	0.09	0 02	0.05	0.13	0.04	0.04	0.07	0.12
L.O.I.	1.49	0.69	1.06	0.80	0.73	1.40	1.29	0.80	0.90	1.47	1 09	0.52	2 01	2 95	3.81	3.45	3.12	1.30
Total	99.27	99.10	98.59	99.50	99.25	98.87	99.82	99 80	99.92	99.19	99.44	100.47	100.05	99.70	100.02	100.04	99.44	98 61
ALI	1.00	0.99	0.94	1.08	1.00		1.30	1.00	1.04		0 99	1.00						
Cr	9	10	8	3	11	323	3	7	7	339	8	48	0	19	0	0	334	24
Co	11	5	9	8	6	35	3	9	8	34	6	6	5	8	11	5	43	48
Ni	6	6	6	4	8	111	3	5	5	75	5	4	4	10	6	4	112	27
Cu	5	3	4	6	3	6	3	4	4	27	4	7	20	5	30	35	56	14
Zn	50	55	38	68	45	113	13	47	48	101	41	25	8	27	20	8	80	474
Rb	166	167	188	120	171	211	115	137	156	74	171	199	159	218	216	210	4	661
Sr	373	636	425	567	443	565	238	614	412	374	283	31	65	60	16	52	161	10
Y	15	13	15	12	13	18	15	10	14	18	13	49	25	9	192	75	14	17
Zr	145	136	131	195	184	90	129	152	149	102	108	144	90	166	98	220	27	159
Nb	16	15	16	14	20	8	12	16	17	6	17	16	13	19	54	17	0	51
Pb	23	34	47	27	32	29	32	48	33	19	39	22	2	5	11	0		0
Ba	927	1117	912	1386	912	503	253	981	871	329	653	98	726	387	285	194	11	436
U	6	2	7	4	6	2	4	17	5	2	12	6						
Th	22	21	22	28	25	2	11	6	28	5	31	39						
Nd													19	5	0	76	2	30
Ce													44	10	0	158	0	76
La													75	16	0	216	0	99
V	25	24	20	40	17	159	4	17	27	233	16		0	26	6	7	309	49
Sc	9	7	7	7	7	21	7	6	7	35	7		5	8	6	5	51	6
CIPW Norms																		
Qtz													55.39	44.87	44.41	42.91		
Or													30.55	29.00	27.16	28.37		
Pl Ab													2.01	1.45	3.43	6.13		
An													0.07	0 09		1.44		
C													6.96	9 52	12.19	10 98		
Wo																		
Di En																		
Fs																		
Hy En													3.52	11.72	10.41	7.88		
Fs													1.06	2.12	2.25	1.70		
Mt													0.12	0 27	0.23	0.19		
Ilm													0.19	0 65	3.67	0.30		
Ap													0.12	0.29	0.09	0 09		
Q													62.9	59.5	59.2	54.4		
A													34.7	38.5	36.2	36.0		
P													2.4	2.0	4.6	9.6		

Appendix 3:2. Shear Zone sample 24/87 and Thin Slab XRF data.

Sample	24-87 WR	24-87a	24-87b	24-87c	24.87d	24-87e	24 87 f	24.87g	55-87
SiO2	77.04	75.76	77.36	76.79	76.22	75.54	76.60	76.68	72.00
TiO2	0.10	0.09	0.09	0.09	0.12	0.12	0.11	0.09	0.36
Al2O3	13.05	12.84	13.01	13.08	13.14	13.58	13.46	13.21	14.43
Fe2O3	0.84	0.85	0.96	0.99	1.07	1.03	0.97	0.97	1.75
MnO	0.03	0.02	0.03	0 02	0.03	0.03	0.02	0.03	0.04
MgO	1.42	1.63	1.47	1.34	1.27	1.20	1.35	1.66	1.89
CaO	0.08	0.07	0.06	0.06	0.08	0.09	0.08	0.07	0.45
Na2O	0.24	0.18	0.13	0.30	0.20	0.24	0.19	0.16	3.42
K2O	5.20	4.97	5.04	5.19	5.24	5.83	5.31	5.04	4.15
P2O5	0.05	0.04	0.03	0.03	0.05	0.06	0.04	0.04	0.15
L.O.I	2.01	2.22	2.17	2.10	1.93	1.74	1.61	2.13	0.91
Total	100.50	98.68	100.36	100.00	99.35	99.46	99.75	100.09	99.55
Cr	0	3	3	0	0	1	1	0	17
Co	5	4	3	1	4	3	4	1	8
Ni	4	3	3	3	4	3	3	3	9
Cu	20	7	3	4	7	6	6	3	9
Zn	8	11	8	8	9	9	11	11	29
Rb	159	164	162	157	160	160	160	164	155
Sr	65	36	46	69	75	124	72	41	110
Y	25	22	26	23	23	28	28	28	17
Zr	90	84	84	82	96	94	94	90	174
Nb	13	13	13	14	14	14	13	13	21
Pb	2	3	4	3	2	3	4	6	18
Ba	671	554	583	672	689	872	665	557	613
Nd	19	16	18	18	18	18	22	23	18
Ce	44	34	46	34	42	49	52	54	37
La	75	55	57	71	44	68	81	75	65

MICROPROBE ANALYSES

White Mica Data

Sample	SiO2	TiO2	Al2O3	FeO	MnO	MgO	CaO	Na2O	K2O	BaO	Total	Si	Ti	Al	Fe	Mn	Mg	Ca	Na	K	Ba	Total	Alvi	Aliv	Fe+Mg+Mn+Ti	K+Na+Ca+Ba
48616 No1a	48.344	0.354	28.699	1.867	0.006	2.205		0.329	10.728		92.589	6 646	0 037	4.650	0.215	0.001	0.452		0.088	1.881		13.975	3 296	1 354	0 705	1 969
1b	48.609	0.465	30.630	1.537	0.020	1.825		0.136	11.353		94.576	6.542	0.047	4 859	0.173	0.002	0.366		0.035	1.949		13 974	3 401	1.458	0 588	1 984
1c	47.001	0.502	29.747	1.775	0.081	1.612		0.531	10.000		91.248	6 536	0 052	4 876	0 206	0 010	0.334		0.143	1.774		13 932	3 412	1.464	0 602	1 917
1d	48.222	0.297	28.815	1.723		2.226		0.366	10.670		92.396	6.638	0.031	4 675	0.198		0.457		0.098	1.874		13.979	3 313	1.362	0 686	1 972
2	46.455	0.424	30.118	1.848		1.278		0.486	10.539		91.629	6.463	0 044	4 939	0.215		0.348		0.131	1.871		14.020	3 402	1.537	0 607	2 002
3	46.084	0.468	30.741	1.663		1.041		0.630	10.533		91.150	6.438	0.048	5 062	0.194		0.217		0.171	1.877		14.102	3 500	1.562	0 459	2 048
4	48.056	0.554	31.998	1.737		1.938		1.647	9.787		95.784	6.377	0.055	5 005	0.193		0 383		0.424	1.657		14.102	3 382	1 623	0 631	2 081
5	46.007	0.514	31.186	1.810		1.429		0.423	10.659		92.033	6.374	0 054	5.093	0.210		0 295		0.114	1.884		14.024	3 467	1 626	0.559	1 998
6	46.293	0.517	31.151	1.787	0.030	1.327		0.676	10.367		92.279	6.393	0.054	5.070	0.206	0.003	0.273		0.181	1.826		14 022	3 463	1 607	0 536	2 007
late mica	47.486	0.338	29.006	1.647		2.175		0.599	11.139		92.467	6.565	0 035	4.727	0.190		0.448		0.161	1.965		14.099	3 292	1 435	0 673	2 126
48618 Inc a	44.498	1.579	30.383	4.206		0.920	0.020	0.330	10.397		92.445	6.234	0.166	5.017	0 493		0.192	0.003	0.090	1.858		14 065	3.251	1.766	0.851	1.951
b	45.358	0.386	31.506	3.113	0.056	0.943	0.021	0.175	11.334		92.894	6.296	0 040	5.155	0 361	0.007	0.195	0.003	0.047	2.007		14.113	3 451	1.704	0 603	2 057
c	50.524	0.472	27.149	3.290	0.082	2.200		1.133	10.572		95.423	6.790	0.048	4.301	0.370	0.009	0.441		0.295	1.813		14 066	3 091	1.210	0 868	2.108
d	48.723	0.232	28.381	3.897		2.239	0.069	0.856	11.233		95.676	6.588	0.024	4.524	0.441		0.451	0.010	0.224	1.938		14.205	3.112	1.412	0 916	2.172
e	46.469	0.109	31.189	4.494		0.861	1.882	0.432	11.401		96.871	6.271	0.011	4.961	0.507		0.173	0 272	0.113	1.963		14.274	3.232	1.729	0 691	2 348
f	44.103	1.579	31.141	4.373	0.090	1.052		0.603	10.544		93.538	6.129	0.165	5.101	0.508	0.011	0.218		0.163	1.870		14.171	3 230	1.871	0 902	2 033
g	44.489	1.226	31.260	4.166	0.009	1.014		0.553	10.471		93.343	6.178	0.128	5.116	0.484	0 009	0.210		0.149	1.855		14.138	3 294	1 822	0 831	2 004
h	44.153	1.454	30.173	4.144	0.012	1.202		0.385	10.332		91.943	6.221	0.154	5.011	0.488	0.012	0.252		0.105	1 857		14.101	3 232	1.779	0 906	1 962
i	43.716	1.630	31.150	4.039	0.049	0.710	0.005	0.508	10.389		92.195	6.143	0.172	5.152	0.475	0.006	0.149	0.001	0.138	1.862		14.105	3.295	1.857	0 802	2.001
j	51.661	0.504	25.901	3.415	0.004	3.042	0.065		11.172		95.869	6.906	0.051	4.081	0 382		0.606	0.009		1.905		13.953	2 987	1.094	1 039	1.914
48623 Inc 1	50.634	0.196	27.956	2.533	0.058	2.916		0.232	11.449	0.166	96.270	6.742	0.020	4.388	0.282	0.007	0.579		0.060	1.945	0.009	14.045	3.130	1.258	0.888	2 014
2	46.867	0.049	30.620	2.902	0.008	1.683			11.570	0.307	94.006	6.429	0 005	4.951	0.333	0.001	0.344			2.025	0.016	14.103	3.380	1 571	0.683	2 041
3	47.945		28.343	2.606	0.029	2.202			11.591	0.180	93 001	6.629	0.011	4.619	0.301	0.003	0.454			2.045	0.010	14.073	3.248	1 371	0 769	2 055
4	50.195	0.104	30.507	2.752	0.029	1.827		0.804	11.163	0.533	97.859	6.591		4 722	0.302	0.003	0 358		0.205	1.870	0.027	14.084	3 313	1.409	0 663	2 102
5	50.495	0.205	27.729	2.527		2.745	0.052		11.162	0.048	94.964	6.785	0.021	4.392	0.298		0.550	0.008		1.914	0.003	13.955	3.177	1 215	0 869	1 925
6	49.474	0.140	30.290	2.855	0.058	2.133		0.032	11.408	0.431	96.874	6.562	0.014	4.735	0.317	0.006	0.422		0.008	1.930	0.022	14 023	3 297	1 438	0 759	1 960
50333 No. 1	50.825	0.532	25.542	2.853	0.027	3.849	0.083	0.166	11.384		95.364	6.844	0.054	4.054	0 321	0 003	0.773	0.012	0.043	1.956		14.071	2.898	1.156	1 151	2 011
2	51.600	0.575	24.947	2.811	0.012	4.309		0.194	10.949		95.482	6.912	0.058	3.939	0 315	0.001	0 861		0.050	1.871		14.017	2.851	1 088	1 235	1 921
3	52.124	0.281	25.062	2.372	0.073	4.333	0.048	0.356	11.182		95.996	6 944	0.028	3 935	0 264	0 008	0.860	0 007	0 092	1.900		14 057	2 879	1 056	1 160	1 999
4	51.939	0.505	24.593	2.812	0.012	3.961	0.123	0.139	11.082		95.217	6.977	0.051	3 894	0 316	0 001	0.793	0 018	0 036	1.899		13.992	2 871	1.023	1.161	1 953
5	49.067	0.440	29.241	2.437	0.013	3.005	0.021	0.310	11.268		95 849	6.559	0.044	4.607	0 272	0 002	0.599	0.003	0.080	1.922		14.092	3 166	1.441	0 917	2 005
6	51.166	0.533	25.817	2.671	0.081	3.796	0.108		11.467		95.703	6.854	0 054	4.077	0 299	0 009	0.758	0.016		1.960		14 033	2 931	1 146	1 120	1 976
7	52.414	0.989	25.192	2.447	0.013	3.723			11.214		96.088	6.959	0.099	3 942	0 272	0 001	0.737			1.900		13.920	2 901	1 041	1 109	1 900
50334 No1	50.165	0.303	25.906	3.492	0.124	2.994	0.022		10.917	0.282	94.576	6 829	0 031	4.157	0 398	0.014	0 608	0.003		1.896	0.015	13 992	2 986	1 171	1 051	1 914
2	51.600	0.303	25.785	3.633	0.052	2.830			10.910	0.374	94.676	6 865	0 031	4 133	0.413	0.006	0 574			1.893	0.020	13 969	2 998	1.135	1.024	1 913
3	49.556	0.337	27.027	3.804	0.012	3.066	0.013	0.088	11.132	0.176	95.538	6 698	0.034	4.306	0.430	0.001	0.618	0.002	0.023	1.920	0 009	14 079	3 004	1 302	1.083	1.954
4	47.236	0.439	29.276	4.294		2.265	0.067	0.269	11.241	0.138	95.505	6.425	0 045	4 694	0 488		0.459		0 071	1.951	0 007	14.179	3 119	1.575	0 992	2.029
5	48.223	0.450	29.173	3.263	0.001	2.387	0.012	0.482	11.037		95.187	6 521	0 047	4 650	0.369		0 481	0 010	0.126	1.904		14.119	3 171	1.479	0 897	2 040
6	49.185	0.433	28.217	3.387	0.088	2.405		0.003	11.308		95.333	6 640	0 044	4.490	0 382	0 010	0.484	0 002	0 001	1.948		14 033	3 130	1 360	0.920	1.951

Appendix A4:1

Gneiss Data

Feldspar Data

SAMPLE	SiO2	TiO2	Al2O3	FeO	MnO	CaO	Na2O	K2O	BaO	Total	An	Ab	Or
48616 PLG a	61.150		23.666	0.064		5.488	8.733	0.141		99 390	25.6	73.6	0.8
b	61.122	0.070	23 653	0.017		5.527	8.582	0.182		99.165	26.0	73.0	1.0
c	61.835	0.083	23.512		0.011	5.033	8.528	0.151		99.220	24.4	74 7	0 9
d	62.387	0.036	22.418		0.117	4.222	8.814	0.163		98 157	21.1	78 0	1.0
e	62 758		22.015			3.913	8.930	0.095		97 781	19 4	80.1	0.6
f	64 425	0.084	20.936	0.010	0.005	2.617	10.039	0.101		98 227	12.5	86 9	0 6
g	64.505	0.072	21.437			2.753	9.764	0.160		98 816	13.4	85.7	0.9
h	64 640		21.145	0 009		2.372	10.250	0.199		98 668	11.2	87.7	1.1
i	63 691	0.015	21.150	0.088		2.619	9.694	0.115		97.418	12.9	86 4	0.7
j	64 630		20.846			2.472	9.656	0.129		97.823	12 3	86.9	0.8
k	64.905	0.029	21.003	0.023		2.272	10.443	0.114		98 853	10.7	88.7	0.6
l	64.993	0.008	21.417	0.008	0.085	2.627	9.973	0.109		99 272	12.9	86.5	0.6
m	64.078	0.056	21.054	0.018	0.026	2.650	10.189	0.066		98.250	12.6	87.0	0.4
n	63.124		21.371	0.241	0.013	1.879	7.749	2.755		97.252	9.8	73.1	17.1
48618 PLG 1a	68.408		19.924	0.048	0.024	0.383	11.232	0.081		100.126	1.9	97.6	0.5
b	67.578	0.049	20.486			1.015	11.193	0.130		100.464	4.7	94.5	0.7
c	68.927	0.002	19.537		0.053	0.059	11.953	0.135		100.679	0.5	98.8	0.7
d	68.646	0.016	19.512	0.116	0.005	0.187	11.501	0.095		100.195	0.9	98.6	0.5
e	67.092	0.025	19.382	0.004		0.191	11.087	0.044		97.829	0.9	98.9	0.2
f	67.737	0.008	19.808	0.095		0.207	10.912	0.585		99 387	1.0	95.6	3.4
g	67.917	0.027	19.537	0.029		0.227	11.162	0.085		99.002	1.1	98.4	0.5
h	68.177	0.056	19.619	0.045	0.060	0.157	11.636	0.056		99 806	1.0	98.7	0.3
i	68.571		19.639	0.053	0.080	0.137	11.672	0.115		100.280	0.9	98.4	0.6
j	67.479		19.228	0.019	0.015	0.173	11.622	0.110		98.648	0.8	98.6	0.6
k	67.439		19.248	0.086		0.199	11.579	0.046		98.597	0.9	98.8	0.3
48618 PLG 2 a	67.698	0.011	20.379	0.108		0.112	10.785	0.339		99 445	0.6	97.4	2.0
b	69.121	0.006	19.774	0.054		0.027	11.441	0.130		100 754	0.1	99.1	0.7
c	67.619	0.039	19.253	0.041		0.221	10.982	0.164		98.433	1.1	97.9	1.0
d	70.765		20.532	0.007	0.051	0.253	11.989	0.083		103 668	1.3	98.2	0.4
e	70.070	0.036	20.253	0.098		0.143	12.028	0.101		102.784	0.6	98.8	0.5
f	66.403	0.067	19.276		0.003	0.261	11.171	0.147		97.328	1.3	97.9	0.8
g	69.266	0.020	20.233			0.116	12.314	0.061		102.087	0.5	99.2	0.3
h	69.828		19.973		0.020	0.151	11.878			101.862	0.8	99.2	
i	68.667	0.072	19.690			0.136	11.402	0.036		100.092	0.7	99.1	0.2
j	69.207	0.052	19.736	0.062		0.016	11.944	0.048		101.090	0.1	99.7	0.3
k	67.607	0.023	19.121	0.035	0.043	0.090	11.493	0.078		98.505	0.6	99.0	0.4
48623 ksp 1a	64.303	0.062	17.947		0.014	0.015	0.287	16.776	0.144	99.548	0.1	2.5	97.4
1b	65.028		18.339	0.033			1.270	15.512	0.614	100 830	0.0	11.0	89.0
1c	64 953	0.176	18.022				0.557	15.697	0.304	99.762	0.0	5.1	94.9
48623 plag 1a	68.542	0.117	19.983	0.049		0.546	11.639	0.167		101.158	2.5	96.6	0.9
1b	69.260	0.043	19.899	0.053		0.416	12.423	0.055		102.150	1.8	97.9	0.3
1c	67.983		19.645			0.197	12.365	0.168		100.402	0 8	98.4	0.8
1d	68.583		19.543	0.074		0.119	11.994	0.139		100 452	0.6	98.6	0.8
48623 KSP 2 a	65 437	0.027	18.515	0.028		0.012	0.538	16.811	0.503	101.961	0.1	4.7	95.2
48623 PLG 2 a	67.484		19.502		0.023	0.203	10.248	0.409	0.001	97.891	1.1	96.4	2.5
2 b	68.423		19 425	0.026	0.044	0.230	11.620	0.105		99 967	1.1	98.3	0 6
2c	69.993		19.706	0.009		0.156	11.986	0.052		101.981	0.7	99 0	0.3
2d	68 849	0.047	19.671			0.261	11.985	0.070	0.069	100.997	1.2	98.4	0.4
2e	68.431	0.010	18.930	0.100	0.016	0.209	12.007	0.046	0.001	99.762	1.0	98.7	0.3
2f	69.162	0.023	19.519	0.188		0.269	12.530	0.099		101.883	1.1	98.4	0.5
2g	69.758		19.591	0.047		0.184	11.965	0.099		101.679	0.9	98.7	0.5
2h	67.894	0.139	18.929	0.043		0.277	11.417	0.087		98.814	1.3	98.2	0.5
2i	69.423		19.935		0.048	0.301	11.423	0.646		101.777	1.4	95.1	3.5
48623 PLG 3 a	67.953		19.138	0.045		0.219	11.225	0.115		98.695	1.0	98.4	0.6
3 b	69.950		19.937		0.052	0.053	11.051	0.090	0.233	101.368	0.2	99.2	0.5
3 c	68.483	0.098	19.235	0.020	0.025	0.153	11.312	0.144		99.451	0.7	98.5	0.8
3 d	68.009	0.051	19.390			0.301	11.600	0.390		99.856	1.4	96.5	2.1
3 e	69.095	0.015	19.926		0.034	0.245	12.622	0.106		102.044	1.0	98.4	0.6
3 f	68.314	0.107	19.263		0.079	0.269	11.026	0.109		99.168	1.4	98.0	0.6
3 g	68.368	0.105	19.293		0.076	0.269	11.197	0.109		99.465	1.4	98.0	0.6
3 h	68.434	0.105	19.331		0.076	0.269	11.478	0.109		99.851	1.3	98.1	0.6
3 i	68.736		19.599		0.037	0.330	11.694	0.061		100.495	1.5	98.2	0.3
50333 Kspar	63.940	0.150	18.790	0.030		0.030	0.900	15.760		99.750	1.1	7.9	91.0
	66.980	0.120	17.950		0.040		0.870	15.330		101.530	1.8	7.8	90.4
50333 Plag	63.380		22.680	0.050		3.920	9.380	0.200		99.700	19.0	79.9	1.1
	68.880		19.380	0.080		0.050	11.660	0.170		100.220	0.2	98.8	0.9
	68.430	0.020	19.940	0.130		0.080	11.510	0.170		100.320	0.8	98.3	0.9
	68.560	0.010	19.510	0.120	0.010	0.150	11.370	0.090		99.820	0.8	98.7	0.5
	67.670	0.070	20.080	0.030		0.540	11.380			99.770	2.6	97.4	
	68.340	0.030	19.450			0.090	11.700	0.180		99.790	0.4	98.6	1.0
	67.810	0.060	20.130	0.070		0.460	11.480	0.040		100.040	2.1	97.6	0.2
	68.260		19.530			0.010	11.640	0.130		99.570	0.1	99.2	0.7
Plag average	67.670	0.020	20.090	0.060		0.660	11.260	0.120		99.900	3.2	96.1	0.7
50334 Kspar	64.210	0.130	18.600	0.060		0.030	0.800	15.650		99.480	0.1	7.2	92.6
	63.810	0.130	18.190			0.090	1.050	15.780		99.050	0.4	9.2	90.4
	64.480	0.140	18.580	0.070		0.110	1.300	15.270		100.030	1.1	11.4	87.6
	64.100	0.110	18.740	0.010			0.950	15.740		99.680	0.2	8.4	91.4
	64.780	0.150	18.490		0.090	0.010	0.740	15.410		99 670	0.4	6.8	92.8
	64.510	0.180	18.650			0.030	0.940	15.390		99.690	0.1	8.5	91.4
50334 Plag	68.120	0.040	19.320	0.040	0.040		11.410	0.130		99.110	0.2	99.1	0.7
	67.850	0.040	19.600	0.020	0.020	0.160	11.840	0.110		99.630	0.8	98.6	0.6
	67.810	0.010	19.560	0.040	0.100	0.040	11.660	0.140		99.360	0.6	98.7	0.8
	67.760		19.740	0.100		0.210	11.680	0.100		99.590	1.0	98.4	0.6
	67.990	0.090	19.790	0.040	0.050	0.220	11.100	0.130		99.420	1.3	98.0	0.8
	67.930		19.610	0.050		0.310	11.450	0.130		99.480	1.5	97.8	0.7
	67.910	0.030	19 600	0.050	0 030	0.160	11.520	0.120		99.430	0.9	98.4	0.7

Biotite Data

Sample	SiO2	TiO2	Al2O3	FeO	Mn	MgO	CaO	Na2O	K2O	Total	Si	Ti	Al	Fe	Mn	Mg	Ca	Na	K	Total
50333 Bte No1	39.98	1.33	15.65	13.41	0.20	15.23	0 07		9.78	95.67	5 861	0.147	2.704	1.644	0.025	3.329	0.012		1 825	15 550
2	40.45	1.41	15.91	13.00	0 24	15 20		0.24	9.74	96.23	5 879	0.154	2.725	1.581	0.030	3.294		0.067	1.806	15 541
3	38.47	1.20	16.43	12.93	0.19	14.66		0.23	10.04	94.31	5.741	0.135	2 891	1.614	0.024	3.262		0 065	1 913	15 664
4	38.74	1.50	17.03	13.00	0.37	14.35	0.09	0.41	9.94	95.44	5 710	0.167	2.959	1.602	0.046	3.153	0 015	0.119	1 869	15 638
5	39.46	1.33	16.73	13 07	0.22	14.99	0.05	0.15	10.04	96.11	5.763	0.146	2 880	1.596	0.028	3 263	0.009	0 043	1 871	15 605
6	40.30	1.33	16.55	12.88	0.29	15.25	0.01		9.92	96.53	5.835	0.145	2.824	1.560	0 035	3.291	0.002		1.832	15 524
"av.comp"	39.57	1.35	16.38	13 05	0.25	14.95	0.04	0.17	9 91	95.67	5.798	0.149	2.831	1.600	0.031	3.265	0.006	0.049	1.853	15 582
50334 Bte No1	37.76	1.82	16.37	18.80	0.48	10.70	0.12	0.27	9.87	96.27	5.689	0 206	2.907	2.368	0.061	2.403	0.019	0.080	1 897	15 640
2	37.93	1.79	15.98	18.74	0.50	10.57	0.04	0.10	9.58	95.62	5.749	0.204	2.854	2.375	0.065	2.389	0.007	0.030	1 852	15 573
3	37.40	1.75	16.44	18.91	0.68	10.68	25.00		9.85	95 88	5.663	0.200	2.935	2.395	0.088	2.410	0 004		1 904	15 617
4	37.95	1.95	16.53	18.93	0.47	10.43	0.03	0.33	9.71	96.60	5 690	0.220	2.921	2.374	0.060	2.341	0.004	0.096	1 858	15 593
5	36.92	1.75	16.76	19.09	0.56	10.12	0.01	0.76	9.83	96.24	5.599	0.199	2 995	2.420	0.072	2.287	0.001	0.222	1.901	15 751
"av.comp"	37.59	1.81	16.42	18.89	0.54	10.50	0.09	0.29	9.77	95.90	5.678	0 206	2.992	2.386	0.069	2.336	0 007	0 086	1 882	15 672

Epidote Data

Sample		SiO2	TiO2	Al2O3	Cr2O3	Fe2O3	MnO	MgO	CaO	Total	Si	Ti	Al	Cr	Fe3+	Mn	Mg	Ca	Total
50333	E1	39.040	0.110	27.050	0.160	8.180	0.120		24.170	98 830	6.044	0.012	4.936	0.019	0.953	0.016		4.009	15.990
	E2	38.880	0.240	28.010	0.140	7.840	0.180	0.170	23.770	99.230	5.980	0.028	5.079	0.017	0.907	0.024	0.010	3 917	15.991
	E3	38.330	0.320	27.380	0.300	7.450	0.170		23 760	97.710	5.992	0 037	5 045	0 037	0.876	0.022		3 981	15 991
	E4	38.709	0.234	27.031	0.249	8.308	0.079	0.296	23.643	98 549	6.008	0.027	4.945	0 031	0.970	0.010	0 068	3 932	15 992
	E5	38.170	0.148	26.295	0.183	8.981	0.105	0 043	23 472	97.396	6.012	0.018	4 882	0.023	1.065	0.014	0.010	3 962	15 985
Average		38.626	0.210	27.153	0.206	8.152	0.131	0 102	23 763	98.343	6.001	0.024	4 977	0.025	0.954	0 017	0 018	3.960	15 982

Zoned White Mica Data

Sample		SiO2	TiO2	Al2O3	FeO	MnO	MgO	CaO	Na2O	K2O	BaO	Total
48618 zoned	1	49.958	0.235	27.648	4 121	0.088	2.995		0.244	11.226	0 608	97.123
	2	45 507	0.495	32.083	4 403	0.017	1.483		0.556	10.378	2 723	97 646
	3	44 676	0.552	31.823	4.122	0.084	1.695		0 346	10 428	2 513	96 240
	4	46 851	0 339	32 855	2.796	0.000	1.416		0.331	11 494	0 392	96 474
	5	47.092	0.335	32.499	3.070	0.021	1.244	0.007	0.274	11 389	0 172	96 103
	6	50.232	0.303	31.532	2.666	0.028	1.365	0.017	1.224	10.515	0 063	97 945
	7	46.115	0.318	31.887	4.071		1.498		0.970	10 665	1 566	97 090
	8	46.524	0.383	32.869	3.212		1.477		0.765	10 892	1.356	97 478
	9	45.119	0.323	32.613	3.885		0.961	0.061	0.705	10 426	2 298	96 346
	10	48.133	0.492	28.018	4.172	0.039	2.525	0.108	0.264	11 348	0.463	95 562
	11	46.644	0.177	32.311	3.162		1.494	0.056	0.347	11.356	0 485	96 031
	12	50.136	0.289	31.984	2.616	0.002	1.377		1.188	10.581	0 091	98 264
	13	47.565	0.334	32.100	2.891	0.040	1.241		0.359	11.359	0.213	96 102
	14	46.825	0.190	32.300	3.073	0.043	1.556		0.429	11.557	0.260	96.232
	15	44.734	0.278	31.571	4.289	0.023	1.351	0.005	0.551	10.291	2.941	96.033
	16	45.402	0.431	31.833	3.988	0.006	1.084		0.370	10.385	2.733	96 233
	17	46.120	0.206	33.270	3.428	0.079	0.907	0.052	0.457	10.689	1.634	96.842
	18	44.463	0.584	31.009	5.249	0.002	1.862		0.326	10.327	2.508	96.330
	19	44.824	0.632	30.728	4.756		1.606		0.263	10.327	2.440	95.576
	20	45.928	0.566	31.430	4.754	0.003	1.781	0.051	0.740	10 350	2 211	97.814
	21	48.871	0.494	30.474	4.419	0.047	1.539		0.981	10.058	1.542	98.425
	22	45.090	0.002	32.227	4.022	0.036	1.464	0.009	0.597	10.016	2.551	96.015
	23	45.281	0.463	32.138	4.120	0.070	0.821		0.135	10.643	2.431	96.103
	24	47.076	0.379	32.934	2.970		1.611	0.036	0.424	11.215	0.348	96.993
	25	45.305	0.192	31.953	4.176		1.492		0.348	10.392	2.574	96.432
	26	47.301	0.190	33.225	2.816	0.032	1.399		0.402	11.615	0.408	97.387
	27	46.771	0.072	32.854	3.031		1.223		0.248	11.390	0.426	96 014
	28	45.121	0.462	31.108	4.640		1.682		0.313	10 475	2.850	96.651
	29	46.942	0.424	32.096	3.191	0.021	1.418		0.027	11.358	0.563	96.039
	30	45.371	0.292	31.355	4.182		1.383	0.093	0.377	10.374	2.526	95.953

Sample		Si	Ti	Al	Fe	Mn	Mg	Ca	Na	K	Ba	Total
48618 zoned	1	6.670	0.024	4 351	0.460	0.010	0.596		0.063	1.912	0.032	14.118
	2	6 157	0.050	5.116	0.498	0.002	0.299		0.146	1.791	0.144	14.204
	3	6.125	0.057	5.143	0.473	0.010	0.346		0.092	1.824	0.135	14.205
	4	6.264	0.034	5.177	0.313		0.282		0.086	1.960	0.021	14.137
	5	6 310	0.034	5.133	0.344	0.002	0.249	0.001	0.071	1.947	0.009	14.099
	6	6.543	0.030	4.841	0.290	0.003	0.265	0.002	0.309	1.747	0.003	14.035
	7	6.221	0.032	5.070	0.459		0.301		0.254	1.836	0.083	14.256
	8	6.209	0.038	5.170	0.359		0.294		0.198	1.855	0.071	14.194
	9	6.153	0.033	5.242	0.443		0.195	0.002	0.187	1.814	0.123	14.193
	10	6.552	0.050	4.495	0.475	0.005	0.512	0.016	0.070	1.971	0.025	14.170
	11	6.281	0.018	5.128	0.356		0.300	0.008	0.091	1.951	0.026	14.158
	12	6.510	0.028	4.895	0.284		0.267		0.299	1.753	0.005	14.040
	13	6.366	0.034	5.064	0.324	0.005	0.248		0.093	1.940	0.011	14 084
	14	6.287	0.019	5.112	0.345	0 005	0.311		0.112	1.980	0.014	14.184
	15	6.167	0.029	5.130	0.494	0.003	0.278	0.001	0.147	1.810	0.159	14.218
	16	6.214	0.044	5.135	0.456	0.001	0.221		0.098	1.813	0.147	14.130
	17	6.201	0.021	5.273	0.386	0.009	0.182	0.007	0.119	1.834	0.086	14.118
	18	6.126	0.060	5.036	0.605		0.382		0.087	1.815	0.135	14.247
	19	6.198	0.066	5.008	0.550		0.331		0 071	1.822	0.132	14.178
	20	6.193	0.057	4.996	0.536		0.358	0.007	0.194	1.781	0.117	14.239
	21	6.463	0.059	4.750	0.489	0.005	0.303		0.252	1.697	0.080	14.087
	22	6.172		5.200	0.460	0.004	0.299	0.001	0.159	1.749	0.137	14.182
	23	6.200	0.048	5.186	0.472		0.168		0.036	1.859	0.130	14.107
	24	6.255	0.038	5.158	0.330		0.319	0.005	0.109	1.901	0.018	14.133
	25	6.187	0.020	5.144	0.477		0.304		0.092	1.811	0.138	14.172
	26	6.267	0.019	5.188	0.312	0.004	0.276		0.103	1.963	0.021	14.154
	27	6.283	0.007	5.202	0.340		0.245		0.064	1.952	0.022	14.117
	28	6.188	0.048	5.028	0.532		0.344		0.083	1.833	0.153	14.209
	29	6.314	0.043	5.089	0.359	0.002	0.284		0.007	1.949	0.030	14.077
	30	6.229	0.030	5.074	0.480		0.283	0.014	0.100	1.817	0.136	14.163

Appendix A4:3 Garnet Amphibolite 48/88

Garnet Data

Grt Sample		SiO2	TiO2	Al2O3	Cr2O3	Fe3+	Fe2+	MnO	MgO	CaO	Total	Si	Ti	Al	Cr	Fe3+	Fe2+	Mn	Mg	Ca	Sum	Uv	An	Py	Sp	Gr	Al	Sh	cation alloc
48/88 No1	1	37.83	0.18	21.05			30.03	1.82	2.54	6.73	99.98	3.014	0.011	1.977			2.001	0.109	0.302	0.575	7.988			10.2	3.7	19.4	66.8		99.0
	2	37.71	0.25	21.24	0.09		29.91	1.83	2.52	7.18	100.55	2.991	0.015	1.986	0.005		1.984	0.110	0.298	0.611	8.000	0.3		10.0	3.7	20.2	65.9		99.5
	3	37.33	0.18	20.84		0.70	28.16	1.76	2.58	8.21	99.87	2.978	0.011	1.949		0.042	1.878	0.119	0.306	0.702	8.007		1.7	10.3	4.0	21.4	62.2	0.4	99.5
	4	37.77	0.24	21.83		0.16	29.50	1.99	2.94	7.22	101.64	2.960	0.014	2.017		0.009	1.913	0.132	0.314	0.606	8.014			11.6	4.4	19.9	63.6	0.5	99.0
	5	37.41	0.80	20.90			28.82	2.08	2.61	7.53	100.16	2.977	0.048	1.981			1.918	0.140	0.310	0.642	7.996			10.5	4.8	21.8	62.9		99.1
	6	37.64	0.14	21.00	0.05	0.36	28.21	3.06	2.19	7.68	100.34	2.996	0.009	1.971	0.003	0.021	1.878	0.207	0.259	0.655	7.999	0.2	1.1	8.7	6.9	20.6	62.5		99.7
	7	37.39	0.23	21.24		0.40	27.96	3.38	2.46	7.41	100.46	2.972	0.014	1.990		0.024	1.858	0.228	0.291	0.631	8.008		0.7	9.7	7.6	19.9	61.5	0.5	99.4
	8	37.18	0.24	20.82		0.77	27.71	3.88	2.27	7.22	100.10	2.975	0.014	1.964		0.046	1.854	0.263	0.271	0.819	8.007		1.6	9.1	8.8	18.4	61.4	0.5	99.6
	9	37.14	0.30	20.60		0.65	27.75	3.53	2.21	7.26	99.42	2.986	0.018	1.955		0.039	1.867	0.240	0.265	0.626	7.998		1.9	8.9	8.0	19.0	62.2		99.7
	10	37.51	0.28	21.17	0.02	0.25	28.44	3.33	2.27	7.24	100.51	2.983	0.017	1.985	0.001	0.015	1.891	0.224	0.269	0.617	8.002	0.1	0.2	8.0	7.5	19.8	63.0	0.6	100.0
	11	37.75	0.21	20.97	0.05	0.52	28.33	3.06	2.64	7.10	100.62	2.993	0.013	1.960	0.003	0.031	1.878	0.205	0.312	0.603	7.998	0.2	1.5	10.4	6.9	18.5	62.5		99.7
	12	38.08	0.12	21.24	0.07		29.52	2.76	2.58	6.81	100.98	3.008	0.007	1.978	0.004		1.950	0.185	0.303	0.560	7.995	0.2		10.2	6.2	18.6	64.8		99.1
	13	37.45	0.13	20.70	0.01	0.60	27.89	3.18	2.30	7.45	99.72	3.000	0.008	1.955		0.036	1.868	0.215	0.275	0.639	7.998		1.8	9.2	7.2	19.6	62.2		99.6
	14	37.50	0.14	21.06	0.01	0.69	28.67	2.76	2.67	6.97	100.69	2.976	0.008	1.974	0.001	0.041	1.916	0.185	0.315	0.593	8.009		1.6	10.6	6.2	17.8	63.4	0.3	99.4
	15	37.34	0.09	21.04	0.01	0.41	29.02	2.51	2.39	7.12	99.84	2.986	0.005	1.983	0.001	0.025	1.941	0.170	0.285	0.610	8.006		1.1	9.5	5.7	19.1	64.4	0.2	99.6
	16	37.26	0.10	21.22	0.13	0.36	29.74	2.01	2.53	6.96	100.32	2.970	0.006	1.994	0.008	0.022	1.982	0.136	0.301	0.585	8.013	0.4	0.8	10.1	4.6	18.5	65.4	0.2	99.1
	17	37.82	0.05	21.31		0.15	29.75	1.80	2.36	7.43	100.68	2.997	0.003	1.991		0.009	1.971	0.121	0.279	0.631	8.002		0.4	9.3	4.0	20.6	65.6		99.9
	18	37.52	0.31	21.02	0.13	0.16	29.60	2.09	2.63	6.71	100.17	2.989	0.018	1.975	0.008	0.010	1.972	0.141	0.312	0.573	7.998	0.4	0.5	10.4	4.7	18.3	65.7		99.6
	19	37.58	0.16	21.45		0.25	29.12	2.77	2.57	7.03	100.93	2.973	0.009	2.002		0.015	1.926	0.186	0.302	0.596	8.010		0.5	10.1	6.2	19.2	63.6	0.3	99.3
	20	37.48	0.02	21.15		0.80	29.46	3.29	2.64	6.20	101.04	2.973	0.001	1.978		0.048	1.954	0.221	0.312	0.527	8.014		2.4	10.5	7.4	15.3	64.4		99.0
"average comp"		37.54	0.21	21.10	0.03	0.36	28.89	2.62	2.49	7.16	100.41	2.985	0.012	1.978	0.002	0.022	1.921	0.177	0.296	0.610	8.003	0.1	0.7	9.9	5.9	19.2	63.9	0.4	99.9
48/88 No.2	1	36.51	0.28	20.52		0.80	27.62	2.60	2.34	7.68	98.34	2.968	0.017	1.967		0.049	1.878	0.179	0.283	0.668	8.009		1.9	9.5	6.0	19.9	62.1	0.6	99.4
	2	36.73	0.18	20.66	0.04	0.48	28.31	2.26	2.07	7.82	98.54	2.980	0.011	1.977	0.002	0.030	1.921	0.155	0.250	0.680	8.008	0.1	1.1	8.4	5.2	21.1	63.7	0.4	99.8
	3	37.21	0.14	20.87	0.01	0.44	28.73	3.00	2.08	7.24	99.72	2.988	0.009	1.976	0.001	0.027	1.929	0.204	0.248	0.623	8.003		1.1	8.3	6.8	19.4	64.1	0.3	99.8
	4	37.39	0.12	20.99		0.53	28.87	2.47	2.47	7.14	100.08	2.985	0.007	1.976		0.032	1.934	0.167	0.294	0.611	8.005		1.3	9.8	5.8	18.8	64.2	0.2	99.7
	5	37.40	0.21	20.84	0.02	0.67	28.69	1.51	2.75	7.51	99.40	2.986	0.013	1.950	0.001	0.040	1.922	0.102	0.328	0.645	7.997	0.1	2.0	11.0	3.4	19.5	64.0		99.6
	6	37.29	0.08	20.76	0.07	0.85	28.22	2.32	2.48	7.79	99.86	2.993	0.005	1.957	0.004	0.051	1.887	0.157	0.296	0.667	8.008	0.2	2.4	9.6	5.3	18.6	62.5	0.2	99.5
	7	37.04	0.16	20.63	0.11	0.58	29.07	2.19	2.54	6.82	99.13	2.987	0.009	1.961	0.007	0.035	1.940	0.150	0.305	0.589	8.003	0.3	1.4	10.2	5.0	17.6	65.2	0.3	99.8
	8	37.40	0.06	21.01		0.46	28.99	3.07	2.29	6.86	100.14	2.988	0.004	1.980		0.028	1.937	0.208	0.272	0.588	8.005		1.3	9.1	7.0	18.2	64.3	0.1	99.7
	9	37.00	0.10	20.86		0.82	28.42	2.60	2.44	7.41	99.66	2.970	0.006	1.974		0.050	1.908	0.177	0.291	0.638	8.013		2.3	9.8	5.9	18.9	62.8	0.2	99.1
	10	37.20	0.19	20.82		0.99	28.06	2.80	2.46	7.66	100.14	2.970	0.012	1.960		0.058	1.874	0.189	0.293	0.655	8.011		2.5	9.8	6.3	19.1	61.9	0.4	99.3
	11	37.34	0.23	21.02		0.69	28.36	2.95	2.49	7.35	100.44	2.972	0.014	1.973		0.041	1.888	0.199	0.296	0.626	8.009		1.6	9.9	6.7	18.9	62.4	0.5	99.4
	12	37.05	0.10	20.74		0.62	28.54	2.22	2.46	7.35	99.08	2.986	0.008	1.971		0.037	1.934	0.151	0.295	0.635	8.005		1.7	9.9	5.1	19.3	63.9	0.2	99.7
	13	37.11	0.09	20.62	0.02	0.83	29.11	1.29	2.79	7.23	99.09	2.987	0.008	1.957	0.001	0.050	1.959	0.088	0.335	0.624	8.005	0.1	2.3	11.2	2.9	18.3	65.0	0.2	99.7
	14	37.35	0.11	21.00		0.53	29.95	1.74	2.70	6.82	100.00	2.983	0.007	1.978		0.032	2.000	0.118	0.322	0.586	8.006		1.4	10.8	3.9	17.3	66.4	0.2	99.6
	15	37.13	0.22	21.08		0.58	28.64	2.25	2.36	7.77	100.03	2.966	0.014	1.985		0.035	1.913	0.152	0.281	0.665	8.012		1.3	9.4	5.1	20.5	63.1	0.5	99.2
	16	37.29	0.14	20.67	0.08	0.71	28.98	2.49	2.45	6.93	99.74	2.991	0.008	1.954	0.005	0.043	1.943	0.169	0.293	0.586	8.002	0.2	1.9	9.8	5.6	17.5	64.7	0.3	100.0
	17	37.13	0.22	21.08		0.58	28.64	2.25	2.36	7.77	100.03	2.966	0.014	1.985		0.035	1.913	0.152	0.281	0.665	8.012		1.3	9.4	5.1	20.5	63.1	0.5	99.2
	18	37.42	0.06	20.91	0.03	0.68	29.19	2.65	2.42	6.92	100.27	2.988	0.004	1.967	0.002	0.041	1.948	0.179	0.288	0.591	8.006	0.1	1.9	9.6	6.0	17.6	64.6	0.1	99.6
	19	37.44	0.11	21.11		0.70	29.31	2.27	2.92	6.64	100.50	2.974	0.007	1.977		0.042	1.947	0.152	0.346	0.565	8.011		1.9	11.6	5.1	16.9	64.3	0.2	99.2
	20	37.39	0.11	21.38		0.16	29.96	2.13	2.63	6.57	100.33	2.977	0.007	2.007		0.010	1.994	0.143	0.312	0.560	8.010		0.3	10.4	4.8	18.3	66.0	0.2	99.3
	21	37.16	0.07	21.00		0.56	28.94	2.34	2.38	7.35	99.77	2.978	0.004	1.984		0.034	1.938	0.159	0.281	0.631	8.010		1.8	9.4	5.3	18.5	64.1	0.1	99.3

Amphibole Data

Sample		SiO2	TiO2	Al2O3	Cr2O3	FeO	MnO	MgO	CaO	Na2O	K2O	Total	Si	Ti	Al	Cr	Total Fe	Fe2+*	Fe3+*	Mn	Mg	Ca	Na	K	Total	Si+Al	Aliv	Alvi	Na(M4)	Na(A)	Na+K(A)
48/88 gntschist	1.1	43.38	0.33	14.57	0.01	17.13	0.16	9.41	9.72	2.69	0.36	98.64	6.315	0.037	2.500	0.002	2.129	1.148	0.937	0.019	2.042	1.518	0.760	0.068	15.343	8.815	1.685	0.815	0.484	0.276	0.344
	2	41.27	0.36	16.05	0.04	16.18	0.29	7.95	11.14	2.04	0.50	98.48	6.109	0.040	2.800	0.005	2.285	1.565	0.686	0.037	1.755	1.766	0.587	0.094	15.447	8.909	1.891	0.908	0.234	0.353	0.447
	3	45.38	0.39	13.24		16.46	0.33	9.74	9.29	1.80	0.41	98.09	6.582	0.043	2.257		2.039	0.916	1.073	0.040	2.100	1.439	0.504	0.076	15.010	8.819	1.438	0.819	0.504	0.000	0.076
	4	41.55	0.43	16.16	0.17	18.09	0.19	7.94	10.76	1.99	0.44	98.42	6.126	0.047	2.808	0.020	2.269	1.455	0.775	0.024	1.744	1.699	0.588	0.084	15.351	8.934	1.874	0.934	0.300	0.268	0.352
	5	42.55	0.32	13.96	0.08	17.82	0.15	8.86	10.55	1.86	0.42	97.42	6.315	0.035	2.442	0.009	2.254	1.334	0.877	0.018	1.961	1.678	0.534	0.080	15.292	8.757	1.685	0.757	0.322	0.212	0.292
	6	42.17	0.34	15.47	0.05	17.57	0.27	7.84	10.54	1.24	0.45	96.73	6.277	0.038	2.714	0.005	2.229	1.342	0.846	0.034	1.739	1.681	0.357	0.086	15.124	8.991	1.723	0.991	0.319	0.038	0.124
	7	42.94	0.41	15.22	0.04	17.57	0.28	8.74	10.25	1.91	0.41	98.59	6.282	0.045	2.618	0.005	2.185	1.187	0.953	0.034	1.900	1.598	0.541	0.075	15.215	8.878	1.738	0.878	0.401	0.140	0.215
	8	44.34	0.40	13.56	0.02	16.57	0.42	9.50	9.41	1.87	0.32	97.50	6.471	0.043	2.332	0.002	2.072	0.916	1.106	0.052	2.068	1.472	0.528	0.060	15.060	8.803	1.529	0.803	0.528	0.000	0.060
	9	44.73	0.30	13.56	0.02	16.73	0.34	9.46	9.26	1.74	0.36	97.57	6.507	0.033	2.328	0.002	2.087	0.890	1.145	0.042	2.052	1.443	0.491	0.067	15.001	8.835	1.493	0.835	0.491	0.000	0.067
	10	44.21	0.44	14.67		16.39	0.31	9.45	10.23	2.39	0.31	98.18	6.388	0.048	2.498		2.013	1.248	0.735	0.037	2.036	1.584	0.669	0.057	15.311	8.886	1.612	0.886	0.416	0.253	0.310
	11	46.76	0.29	12.71		16.04	0.26	10.86	9.02	2.36	0.18	99.59	6.821	0.031	2.121		2.355	0.742	1.157	0.031	2.296	1.368	0.649	0.033	15.049	8.742	1.379	0.742	0.833	0.016	0.049
	12	45.36	0.33	13.46	0.04	16.59	0.31	9.87	9.24	1.92	0.29	98.49	6.529	0.035	2.283	0.005	2.048	0.850	1.148	0.037	2.116	1.423	0.536	0.053	15.014	8.812	1.471	0.812	0.536	0.000	0.053
	13	42.46	0.48	15.61	0.01	17.22	0.29	8.43	10.33	1.87	0.44	97.96	6.238	0.053	2.703	0.002	2.156	1.273	0.843	0.035	1.847	1.626	0.533	0.083	15.243	8.941	1.782	0.941	0.373	0.180	0.243
	21	46.31	0.25	11.93	0.04	18.11	0.41	10.28	8.82	1.25	0.24	98.21	6.587	0.026	1.999	0.005	2.236	0.483	1.691	0.049	2.179	1.344	0.345	0.043	14.733	8.586	1.413	0.586	0.345	0.000	0.043
	28	39.85	0.43	17.36	0.03	18.55	0.35	8.44	10.73	1.97	0.55	98.80	6.020	0.048	3.090	0.004	2.376	1.730	0.813	0.044	1.450	1.736	0.578	0.106	15.420	9.110	1.980	1.110	0.264	0.314	0.420
	32	41.26	0.36	15.97		18.16	0.41	7.53	10.43	2.16	0.47	97.40	6.158	0.040	2.808		2.304	1.523	0.744	0.051	1.675	1.667	0.626	0.089	15.383	8.966	1.842	0.966	0.333	0.293	0.382
	33	46.39	0.31	10.90		17.53	0.36	10.65	8.73	1.82	0.22	98.27	6.678	0.033	1.850		2.181	0.627	1.484	0.043	2.285	1.347	0.508	0.040	14.895	8.528	1.322	0.528	0.508	0.000	0.040
	av. comp.	43.59	0.36	14.38	0.03	17.34	0.30	9.00	9.91	1.93	0.38	98.14	6.383	0.040	2.479	0.004	2.189	1.130	0.989	0.037	1.956	1.552	0.548	0.070	15.171						
	Matrix	43.78	0.35	14.24		16.24	0.15	9.40	9.96	1.72	0.34	97.13	6.421	0.039	2.462		2.045	1.088	0.935	0.019	2.058	1.565	0.488	0.064	15.117	8.883	1.579	0.883	0.435	0.053	0.117
	2	42.93	0.45	14.37	0.06	17.83	0.27	8.31	9.92	2.05	0.45	97.41	6.357	0.051	2.509	0.007	2.248	1.383	0.845	0.033	1.835	1.574	0.589	0.086	15.249	8.866	1.643	0.866	0.428	0.183	0.249
	3	43.07	0.43	14.81	0.02	16.37	0.10	9.40	10.23	2.06	0.41	97.76	6.308	0.048	2.573	0.003	2.042	1.167	0.878	0.012	2.052	1.606	0.585	0.077	15.288	8.881	1.682	0.881	0.393	0.192	0.269
	4	41.98	0.55	15.92	0.02	17.21	0.16	8.30	10.60	2.23	0.50	98.04	6.185	0.061	2.798	0.002	2.153	1.493	0.630	0.020	1.824	1.677	0.637	0.094	15.408	8.993	1.805	0.993	0.322	0.315	0.409
	5	44.02	0.31	13.71	0.03	16.02	0.17	9.60	10.52	1.93	0.40	97.50	6.472	0.035	2.376	0.004	1.998	1.304	0.665	0.021	2.104	1.657	0.551	0.076	15.284	8.848	1.528	0.848	0.343	0.208	0.284
	6	44.32	0.36	13.86		16.29	0.36	9.55	9.88	1.88	0.36	97.57	6.467	0.042	2.383		2.031	1.025	0.983	0.044	2.078	1.545	0.479	0.067	15.091	8.850	1.533	0.850	0.455	0.024	0.091
	7	44.55	0.36	13.62		15.67	0.29	9.80	10.06	1.85	0.37	97.13	6.520	0.040	2.348		1.953	1.079	0.839	0.036	2.138	1.578	0.487	0.069	15.114	8.868	1.480	0.868	0.422	0.045	0.114
	8	45.00	0.40	13.17	0.01	15.95	0.22	10.43	9.30	2.35	0.25	98.13	6.503	0.043	2.242	0.001	1.974	0.843	1.084	0.027	2.246	1.440	0.658	0.042	15.140	8.745	1.497	0.745	0.560	0.098	0.140

Biotite Data

Sample		SiO2	TiO2	Al2O3	FeO	Mn	MgO	CaO	Na2O	K2O	Total	Si	Ti	Al	Fe	Mn	Mg	Ca	Na	K	Total
48/88 Bte	No1	35.00	2.11	17.77	23.47	0.09	7.77	0.01	0 07	9 05	95 38	5 432	0.246	3 251	3.046	0.011	1.797	0.001	0 022	1.792	15 605
	2	34.83	2.75	17.79	23.14	0.17	6.25	0.02	0.20	9.53	94.84	5 456	0.324	3 284	3 031	0.023	1.460	0.003	0.061	1.905	15.573
	3	35.30	1.73	16.42	24.77	0.16	7.01	0.19	0.13	10 05	95.86	5.534	0.204	3.035	3.248	0.021	1.638	0.032	0.040	2 009	15.780

Epidote Data

Sample		SiO2	TiO2	Al2O3	Cr2O3	Fe2O3	MnO	MgO	CaO	Total	Si	Ti	Al	Cr	Fe3+	Mn	Mg	Ca	Total
48/88	E1	38.400	0.110	26.000		10.780	0.230	0.100	22.770	98.400	6.005	0.013	4.793		1.268	0.030	0.023	3.815	15 951
	E2	37.650	0.110	24.860	0.040	11.470	0.190	0.190	22.890	97.410	5 980	0 014	4 655	0.005	1.371	0.026	0 044	3.896	15 991
	E3	38.378	0.234	26.015		10.124	0.082	0.221	22.882	97.936	6.017	0.028	4 808		1.194	0.011	0.052	3.844	15 954
	E4	38.171	0.107	25.909	0.045	10.216	0.067	0.098	22.864	97.477	6 017	0.013	4.814	0 006	1.212	0.009	0 023	3 862	15 955
	E5	38.252	0.131	25.728	0.049	9.952	0.241		22 806	97.160	6.048	0 016	4.795	0.006	1.184	0 032		3.864	15 944
	E6	38.127	0.092	25.888	0.003	10.484	0.104	0 247	22.880	97.824	5.996	0.011	4.799		1.241	0 014	0.058	3.855	15 973
	E7	37.334		24.213	0.042	11.985	0.300	0.127	22.917	96.989	5.979		4.570	0 005	1.444	0.041	0.030	3 932	16 011
	E8	38.288	0.185	25.345	0.011	10.890	0.280	0.112	22.582	97.692	6.036	0.022	4.710	0.001	1.292	0 037	0.026	3 815	15 940
	E9	37.729	0.156	25.581		10.731	0.277	0.160	22 677	97.390	5.975	0.019	4.775		1.279	0.037	0.038	3.848	15.980
	E10	37.236	0.066	24.028		12.097	0.274	0.006	22.270	95.975	6.013	0.008	4 574		1.470	0.037	0.001	3 853	15.957
	E11	37.401	0.155	25.914	0.158	9.823	0.104	0.194	22.936	96.686	5.952	0.019	4 861	0 020	1.177	0.014	0.046	3.911	16 000
	E12	37.916	0.248	25.316	0.007	10.788	0.193		23.080	97.549	5.998	0.030	4.720	0.001	1.284	0.026		3.912	15 970
	Average	37.907	0.133	25.400	0.029	10.778	0.195	0.121	22.796	97.359	6 001	0.016	4.739	0.004	1.285	0.026	0.023	3.867	15.961

Plagioclase Data

SAMPLE		SiO2	TiO2	Al2O3	FeO	MnO	CaO	Na2O	K2O	BaO	Total	An	Ab	Or
48/88 GB plag	1	64.050	0.040	21.590	0.090	0.130	2.730	10 070	0.160	0.040	98.900	13.3	85.7	0 9
	2	63.330	0.040	22.010	0.100	0.020	3.030	9 930	0 070		98.530	14.4	85 2	0 4
	3	60.780		23.860	0.020	0.040	5.140	8.250	0.100	0.160	98.380	25 6	73 5	0 9
	4	61.440	0.040	23.330	0.150		4.900	8 560	0.130		98.540	23.9	75 4	0 7
	5	62.610		23.320	0.230		4.330	8.810	0.070	0.060	99 390	21.3	78 5	0 2
	6	61.570	0.010	24.080	0.580	0.030	5.020	8.870	0 010		100.180	23 9	76 0	0 1
	7	58.370	0.060	23.630	3.850	0.040	4.610	8.270	0 230		99 700	26.7	72 0	1 3
	8	62.020	0.030	23.910	0.150		5.180	8 690	0.060	0.030	100.080	24.7	74 9	0 4
	9	61.610		23.620	0.280	0.050	4.800	8 860	0.110	0 040	99 370	23 0	76 3	0 7
	10	60.900		23.830	0.190		5.230	8 200	0.050	0 030	98 470	26 2	73 5	0 4
	11	61.850	0.080	23.800	0.530		4.770	8 880	0.050		99 960	22 8	76 9	0 3
	12	65.200	0.020	22.180	0.070	0.080	2.660	9.980	0 040		100.270	13 4	86 4	0 2
	13	64.690		21.800	0.110	0.120	2.620	10 030	0.110	0 250	99 730	12.9	86 1	1 0
	14	65.610		21.440	0.040		2.550	10 270	0 050	0.110	99.950	12 0	87.5	0 4
	15	61.780	0.040	23.980	0.180	0.030	5.190	8 890	0 010	0 030	100.120	24.4	75.4	0 1
	16	62.750	0.040	23.600	0.290		4.570	9.350	0 030		100 630	21 2	78 6	0 2
	17	60.590		24.530	0.400		5.650	8 360	0 050	0 070	99 770	27.7	71.9	0 4
	av. comp.	62.110	0.040	23.140	0.560	0.030	4.240	9.010	0.130	0 040	99 430	21.2	77 9	0 8
48/88 Matrix	1	65.670		21.760	0.220	0.080	2.510	10.140	0 070	0.250	100.690	12.2	87.0	0 8
	2	64 600		21.990	0.160		2.920	9.730	0.100	0.120	99.620	14 1	85.1	0 8
	3	64.170	0.010	22.280	0.180	0.010	3.280	10.140	0 010		100.080	15 2	84 8	
	4	63.240		22.740	0.210	0.030	3 900	9.690	0 090		99.880	18.2	81.3	0 5
	5	63.450	0.040	23.050	0.310		3.670	9.920	0 060	0 060	100.680	17.5	82.1	0.4
	6	63.370	0.100	22.720	0.190		3.900	9 200	0 030		99 530	19 0	80 9	0.2
	7	64.080	0.030	22.420	0.210	0 020	3.360	9.800	0.060	0 070	100 080	16 0	83 5	0 5

Chlorite Data Appendix A4:3

Sample		SiO2	TiO2	Al2O3	Cr2O3	FeO	MnO	MgO	CaO	Na2O	K2O	Ba	Total	Si	Ti	Al	Fe	Mn	Mg	Ca	Na	K	Ba	Total
48/88 Chlorites	P1	25.92		21.80	0.05	22.41	0.29	17.01	0 04		0.01	0.17	87 70	5.379		5.332	3.890	0.051	5.264	0.010		0 003	0 014	19 952
	P2	25.78	0.07	21.76		22.36	0.24	17.43	0 02	0.25		0.05	87 95	5 335	0.010	5.308	3 871	0.043	5.376	0.004	0.102		0 004	20 052
	P3	26.20	0.18	21.99		22.74	0.25	17.39		0.22	0 06		89 08	5 357	0 028	5.299	3 888	0.043	5.299		0.089	0 016		20 038
	P7	25.25	0.12	20.77	0.04	25.32	0.25	14.33	0.05	0.05	0.44	0.06	86 77	5 412	0.019	5.252	4.538	0 046	4.578	0.012	0 019	0.121	0.005	20 027
	P8	25.45	0.09	20.25	0.04	26.03	0.22	14.62	0.11	0.26	0 07		87.37	5.431	0.016	5 094	4.645	0.039	4.650	0 024	.0 108	0 020		20 077
	P9	25.68	0.14	21.51		22.70	0.19	16.84	0.07	0.30	0.26	0.05	87.88	5.347	0.021	5.280	3.955	0.034	5.227	0.016	0.121	0 069	0.004	20 112
	P10	26.33	0.05	22.34	0.04	21.91	0.10	17.55		0.33	0.02	0.28	88 96	5.371	0.007	5.370	3.737	0.017	5.335		0.129	0 006	0 022	20 008
	P11	25.48	0.10	21.43	0.02	22.45	0.21	16.50	0.05	0 03	0 04		86.30	5.378	0 016	5.331	3.962	0.037	5.190	0 011	0 011	0 011		19 950
	P12	25.49	0.28	21.81	0.10	22.27	0.14	16.73		0.35	0.05		87.31	5.320	0.045	5.366	3.887	0.024	5.203		0 144	0 014		20 043
	P13	25.77		21.91		22.66	0.30	16.62		0.11	0.03	0 03	87.41	5.360		5.384	3.951	0.053	5.165		0 044	0 009	0 002	19 976
	P14	25.47	0.03	22.17		22.53	0.15	16.92	0.02		0.06	0.20	87.59	5.301	0.005	5.440	3.921	0.027	5.249	0 005		0 015	0 016	19 989
	P15	25.58	0.14	21.70	0.05	22.59	0.18	17.41		0.11	0.01		87.92	5.306	0 022	5.306	3.919	0.032	5.382		0 044	0 002		20 053
	P16	25.96	0.09	22.54		24.08	0.22	16.56	0.04		0.01		89 52	5.307	0.015	5.430	4.117	0.037	5.047	0.009		0 002		19 967
	P17	26.08	0.21	21.71		24.46	0.18	16.92	0.03	0.46	0.32	0 03	88 42	5.381	0.033	5.279	3.875	0.032	5.203	0.007	0 184	0 084	0 003	20 083
	P18	26.18	0.05	22.25		22.37	0.24	17.31	0 05		0.02	0.04	88.58	5.364	0 008	5.375	3.835	0.042	5.288	0.011		0 005	0 003	19 943
	P19	26.25		22.32	0.06	22.78	0.24	17.08	0.06			0.11	89 08	5 367		5.379	3.894	0.041	5.206	0 013			0 009	19 962
	P20	26.00	0.04	22.32	0.03	23.21	0.15	16.87	0.07		0.04		88.78	5.339	0.006	5.401	3.986	0.026	5.162	0 015		0.010		19 960

Amphibole Data **Appendix A4: 4**

Sample	SiO2	TiO2	Al2O3	Cr2O3	FeO	MnO	MgO	CaO	Na2O	K2O	Total	Si	Ti	Al	Cr	Total Fe	Fe2+	Fe3+	Mn	Mg	Ca	Na	K	Total	Si+Al	AlIV	AlVI	Na(M4)	Na(A)	Na+K(A)
57/88 gnt amp 1	42.79	0.42	13.95	0.06	18.81	0.23	7.92	9.19	2.07	0.41	96.85	6.370	0.047	2.446	0.007	2.399	1.235	1.106	0.028	1.757	1.465	0.597	0.078	15.140	8.816	1.630	0.816	0.535	0.062	0.140
2	43.48	0.33	13.56	0.03	18.66	0.22	9.08	8.76	2.11	0.37	97.95	6.346	0.036	2.334	0.003	2.356	0.783	1.496	0.028	1.972	1.370	0.597	0.069	15.035	8.680	1.654	0.680	0.597	0.000	0.069
3	43.45	0.38	14.73	0.05	18.27	0.19	8.98	9.12	2.59	0.41	99.42	6.274	0.041	2.506	0.006	2.267	0.974	1.232	0.023	1.933	1.411	0.726	0.076	15.214	8.780	1.726	0.780	0.588	0.138	0.214
4	42.60	0.35	14.50		18.74	0.39	7.64	9.33	1.42	0.42	96.56	6.338	0.039	2.543		2.396	1.093	1.239	0.050	1.694	1.487	0.410	0.080	14.978	8.881	1.662	0.881	0.410	0.000	0.080
5	43.20	0.45	14.12		18.06	0.23	8.80	9.11	2.12	0.38	97.62	6.339	0.050	2.441		2.278	0.974	1.242	0.029	1.924	1.432	0.604	0.071	15.107	8.780	1.661	0.780	0.568	0.036	0.107
6	42.79	0.44	14.96	0.03	18.53	0.19	8.23	9.29	2.12	0.49	96.17	6.269	0.048	2.582	0.004	2.330	1.100	1.171	0.024	1.798	1.458	0.601	0.091	15.151	8.851	1.731	0.851	0.541	0.060	0.151
7	42.63	0.41	14.21		18.05	0.21	8.44	9.63	2.24	0.43	97.18	6.328	0.046	2.487		2.289	1.265	0.976	0.026	1.868	1.532	0.646	0.082	15.259	8.815	1.672	0.815	0.468	0.178	0.260
8	43.38	0.27	13.75		17.91	0.12	8.74	9.41	1.50	0.42	96.63	6.415	0.030	2.397		2.275	0.995	1.220	0.015	1.926	1.490	0.430	0.080	15.001	8.812	1.585	0.812	0.430	0.000	0.080
9	43.45	0.27	13.69	0.06	17.90	0.08	8.71	9.24	2.26	0.44	97.09	6.426	0.030	2.385	0.007	2.265	1.178	1.038	0.009	1.920	1.464	0.647	0.083	15.194	8.811	1.574	0.811	0.536	0.111	0.194
10	42.57	0.44	15.03		18.27	0.20	8.57	9.48	2.51	0.37	98.45	6.229	0.048	2.592		2.291	1.135	1.100	0.025	1.869	1.486	0.713	0.070	15.268	8.821	1.771	0.821	0.515	0.196	0.268
11	42.16	0.38	15.44		18.78	0.23	8.02	10.05	2.07	0.45	98.50	6.194	0.043	2.673		2.359	1.288	1.018	0.028	1.756	1.582	0.589	0.085	15.255	8.867	1.806	0.867	0.418	0.171	0.256
12	40.55	0.33	16.59		19.15	0.20	6.52	10.67	1.77	0.55	97.03	6.107	0.038	2.944		2.449	1.710	0.702	0.026	1.465	1.721	0.518	0.105	15.344	9.051	1.893	1.051	0.279	0.239	0.344
13	40.09	0.27	17.56	0.08	19.14	0.19	6.41	11.06	1.59	0.50	97.51	6.006	0.031	3.100	0.009	2.435	1.686	0.712	0.024	1.432	1.775	0.461	0.095	15.331	9.106	1.994	1.106	0.225	0.236	0.331
14	40.30	0.32	17.18	0.11	19.21	0.16	6.14	10.77	1.30	0.56	96.71	6.075	0.036	3.053	0.013	2.462	1.675	0.748	0.021	1.380	1.739	0.381	0.107	15.226	9.128	1.925	1.128	0.262	0.119	0.226
15a	40.78	0.10	16.67		19.06	0.11	6.62	10.95	1.67	0.49	96.55	6.218	0.011	2.996		2.431	1.741	0.655	0.014	1.508	1.790	0.493	0.096	15.567	9.214	1.782	1.214	0.235	0.258	0.354
15b	40.85	0.29	17.51	0.08	19.18	0.25	6.55	11.01	1.68	0.49	98.86	6.043	0.032	3.053	0.009	2.411	1.650	0.723	0.032	1.444	1.745	0.483	0.092	15.320	9.096	1.957	1.096	0.255	0.228	0.320
16	40.53	0.36	17.17		19.02	0.26	6.48	10.84	1.60	0.62	97.47	6.070	0.040	3.029		2.418	1.689	0.693	0.033	1.446	1.739	0.463	0.118	15.319	9.099	1.930	1.099	0.262	0.201	0.319
17	40.30	0.34	17.00	0.11	19.00	0.16	6.50	10.73	1.20	0.63	96.70	6.066	0.038	3.015	0.013	2.436	1.560	0.831	0.020	1.457	1.730	0.350	0.121	15.202	9.081	1.934	1.081	0.269	0.081	0.202
19	42.40	0.37	15.32	0.06	18.99	0.17	7.83	9.64	1.88	0.46	97.88	6.251	0.041	2.662		2.398	1.262	1.079	0.021	1.677	1.522	0.537	0.087	15.147	8.913	1.749	0.813	0.478	0.059	0.146
20	42.23	0.55	14.22	0.07	19.06	0.29	7.86	8.85	2.44	0.46	97.01	6.281	0.061	2.492	0.007	2.438	1.102	1.269	0.036	1.743	1.379	0.703	0.087	15.168	8.773	1.719	0.773	0.622	0.081	0.168
21	41.71	0.43	15.85		18.95	0.18	7.42	10.25	1.97	0.43	98.00	6.177	0.048	2.767	0.008	2.393	1.463	0.885	0.023	1.637	1.626	0.565	0.082	15.272	8.944	1.823	0.944	0.374	0.191	0.273
22	42.77	0.37	14.57	0.02	18.20	0.06	8.50	9.41	2.06	0.41	97.49	6.301	0.041	2.530		2.299	1.095	1.147	0.008	1.868	1.485	0.589	0.078	15.151	8.831	1.699	0.831	0.515	0.074	0.152
23	41.61	0.31	15.66	0.06	19.29	0.35	8.67	10.21	2.03	0.45	97.29	6.238	0.035	2.767	0.002	2.457	1.696	0.723	0.044	1.491	1.640	0.591	0.087	15.318	9.005	1.762	1.005	0.360	0.231	0.318
24	42.23	0.31	14.99	0.01	18.68	0.23	7.96	9.85	1.97	0.42	97.70	6.249	0.034	2.615	0.007	2.363	1.291	1.020	0.028	1.757	1.577	0.564	0.079	15.220	8.864	1.751	0.864	0.423	0.141	0.220
25	43.24	0.54	14.81	0.02	19.51	0.08	8.56	8.20	1.50	0.46	98.72	6.224	0.058	2.513	0.001	2.449	0.463	1.885	0.010	1.837	1.265	0.420	0.084	14.769	8.737	1.776	0.737	0.420	0.000	0.084
26	41.66	0.62	15.21		18.64	0.20	7.56	9.55	1.52	0.71	96.67	6.220	0.070	2.675	0.002	2.385	1.214	1.114	0.025	1.682	1.528	0.440	0.135	15.103	8.895	1.780	0.895	0.440	0.000	0.135
28	43.64	0.60	13.92	0.09	19.66	0.34	8.41	8.47	1.89	0.43	98.93	6.316	0.065	2.375	0.010	2.467	0.762	1.618	0.041	1.814	1.313	0.530	0.079	14.922	8.691	1.684	0.691	0.530	0.000	0.079
29	41.34	0.44	15.61	0.09	18.66	0.05	7.31	9.98	2.11	0.55	96.86	6.200	0.049	2.759	0.011	2.382	1.536	0.804	0.006	1.635	1.604	0.614	0.105	15.323	8.959	1.800	0.959	0.396	0.218	0.323
30	41.42	0.43	15.78		18.95	0.21	7.02	10.44	2.09	0.54	97.49	6.200	0.049	2.784		2.406	1.714	0.658	0.027	1.566	1.675	0.606	0.103	15.385	8.984	1.800	0.984	0.325	0.281	0.384
32	41.49	0.39	15.79		18.99	0.06	7.28	10.46	2.35	0.43	97.84	6.187	0.043	2.774		2.402	1.702	0.666	0.008	1.618	1.671	0.678	0.082	15.430	8.961	1.813	0.961	0.330	0.348	0.430
33	41.39	0.48	15.81	0.14	18.54	0.18	7.38	10.26	1.90	0.43	97.28	6.173	0.054	2.780	0.018	2.356	1.473	0.840	0.024	1.641	1.640	0.550	0.083	15.272	8.953	1.827	0.953	0.361	0.189	0.272
34	40.96	0.30	16.18	0.04	18.98	0.28	7.58	10.20	2.54	0.51	98.42	6.070	0.033	2.826	0.005	2.398	1.451	0.900	0.035	1.674	1.619	0.730	0.096	15.445	8.896	1.930	0.896	0.381	0.349	0.445
Average	42.00	0.38	15.35	0.04	18.78	0.20	7.67	9.82	1.94	0.47	97.58	6.225	0.043	2.684	0.004	2.379	1.311	1.016	0.025	1.693	1.561	0.557	0.090	15.214						

Biotite Data

Sample	SiO2	TiO2	Al2O3	FeO	Mn	MgO	CaO	Na2O	K2O	Total	Si	Ti	Al	Fe	Mn	Mg	Ca	Na	K	Total
57/88 No1	33.52	1.16	17.29	21.15	0.14	9.78	0.04	0.13	8.90	92.20	5.339	0.139	3.265	2.834	0.019	2.336	0.007	0.039	1.819	15.814
2	35.00	0.64	16.77	20.67	0.86	9.05		0.04	9.86	92.28	5.582	0.077	3.152	2.757	0.025	2.151		0.013	2.007	15.771
3	34.39	1.71	17.12	20.68	0.16	8.23	0.03	0.24	9.97	92.53	5.485	0.205	3.218	2.759	0.022	1.958	0.005	0.075	2.029	15.753
"av.comp"	34.24	1.17	17.06	20.83	0.39	9.02	0.02	0.14	9.58	92.45	5.475	0.140	3.212	2.783	0.022	2.148	0.004	0.039	1.952	15.775

White Mica Data

Sample	SiO2	TiO2	Al2O3	FeO	MnO	MgO	CaO	Na2O	K2O	BaO	Total	Si	Ti	Al	Fe	Mn	Mg	Ca	Na	K	Ba	Total	Si:Al	AlVI	AlIV	Fe+Mg+Mn+Ti	K+Na+Ca+Ba
57/88 No1	46.464	0.380	32.828	2.901		0.980		1.027	10.584	0.216	95.380	6.261	0.038	5.214	0.327		0.197		0.268	1.820	0.011	14.137	11.475	3.475	1.739	0.562	2.099
2	47.129	0.497	30.472	3.350		1.342		0.607	10.428	0.263	94.099	6.439	0.051	4.907	0.383		0.273		0.161	1.818	0.014	14.048	11.346	3.346	1.581	0.707	1.993
3	47.923	0.379	29.626	3.483		2.128		0.619	10.152	0.255	94.607	6.504	0.039	4.740	0.395		0.431		0.163	1.758	0.014	14.048	11.244	3.244	1.498	0.465	1.935
4	47.173	0.486	30.607	3.426	0.042	1.339		0.999	9.979	0.141	94.334	6.423	0.051	4.912	0.390	0.005	0.272		0.264	1.733	0.009	14.069	11.335	3.335	1.577	0.718	2.006
average	47.172	0.438	30.883	3.290	0.011	1.447		0.813	10.286	0.226	94.605	6.407	0.045	4.943	0.374	0.001	0.293		0.214	1.782	0.012	14.075	11.350	3.350	1.593	0.713	2.008

Appendix A4:4

Garnet Data

Grt Sample	SiO2	TiO2	Al2O3	Cr2O3	Fe3+	Fe2+	MnO	MgO	CaO	Total	Si	Ti	Al	Cr	Fe3+	Fe2+	Mn	Mg	Ca	Sum	Uv	An	Py	Sp	Gr	Al	Sh	cation alloc
57/88 No1 1	37.28	0.06	20.90	0.12		34.01	0.37	2.28	4.74	99.76	3.003	0.004	1.985	0.008		2.290	0.025	0.273	0.409	7.998	0.4		9.1	0.8	13.3	76.3		99.6
2	37.26		21.07	0.06	0.22	35.84	0.69	2.31	3.26	100.70	2.989		1.994	0.004	0.013	2.405	0.047	0.276	0.280	8.007	0.2	0.7	9.2	1.6	8.5	79.8		99.6
3	37.25	0.13	20.96		0.48	34.81	0.78	2.07	4.37	100.84	2.984	0.008	1.980		0.029	2.331	0.053	0.247	0.375	8.006	9.0	1.2	8.2	1.8	11.1	77.5	0.3	99.7
4	37.23	0.06	20.85	0.04		33.76	1.18	1.41	5.22	99.76	3.010	0.004	1.988	0.003		2.283	0.081	0.170	0.452	7.992	0.1		5.7	2.7	15.0	76.4		99.8
5	38.83	0.07	21.07	0.04	0.38	33.12	1.44	1.45	5.92	100.30	2.969	0.004	2.002	0.003	0.022	2.232	0.098	0.174	0.512	8.015	0.1	1.0	5.8	3.3	16.0	73.8	0.1	98.9
6	36.94	0.03	20.96	0.02	0.29	32.81	1.67	1.15	8.27	100.14	2.983	0.002	1.996	0.001	0.017	2.215	0.114	0.139	0.542	8.009	0.1	0.8	4.6	3.8	17.2	73.4	0.1	99.4
7	37.41	0.12	20.93		0.77	30.97	3.57	1.28	6.46	101.51	2.980	0.007	1.966		0.046	2.063	0.241	0.152	0.551	8.008		2.1	5.1	8.1	16.1	68.4	0.2	99.5
8	36.80	0.09	19.95	0.03	0.87	29.43	4.74	0.80	8.27	98.98	3.013	0.006	1.926	0.002	0.054	2.015	0.329	0.098	0.550	7.992	0.1	2.7	3.3	11.1	15.7	67.1		99.1
9	37.14	0.07	20.93		0.90	26.06	8.59	0.80	6.96	101.46	2.969	0.004	1.973		0.054	1.742	0.581	0.096	0.596	8.015		2.8	3.2	19.6	17.3	57.2	0.1	98.9
10	36.69	0.19	20.47	0.10	0.83	23.99	11.22	0.51	6.28	100.18	2.978	0.011	1.959	0.001	0.051	1.628	0.771	0.061	0.546	8.007		2.2	2.0	25.8	15.7	53.9	0.4	99.6
11	37.06	0.28	20.75		1.03	21.21	13.82	0.81	6.55	101.51	2.964	0.017	1.957		0.062	1.418	0.936	0.096	0.561	8.011		2.6	3.2	31.4	15.7	46.4	0.8	99.2
12	36.60	0.06	20.96		0.29	26.14	14.29	1.10	1.41	100.84	2.972	0.003	2.007		0.018	1.775	0.983	0.133	0.123	8.014		0.8	4.5	33.0	3.3	58.4	0.1	99.0
13	36.56	0.14	20.87	0.04	0.51	26.28	13.89	1.34	1.36	100.98	2.964	0.009	1.995	0.002	0.031	1.782	0.954	0.162	0.118	8.015	0.1	1.3	5.4	32.1	2.3	58.5	0.3	98.9
14	36.36	0.05	21.06		0.57	26.81	13.80	1.30	1.11	101.15	2.949	0.003	2.014		0.035	1.825	0.948	0.157	0.097	8.026		1.6	5.3	32.1	1.5	59.3	0.1	98.1
15	36.64	0.05	20.35		1.23	25.28	12.62	1.20	3.27	100.63	2.974	0.003	1.948		0.075	1.716	0.867	0.145	0.284	8.013		3.7	4.8	29.1	5.7	56.5	0.1	99.1
16	36.96	0.09	21.04		0.37	26.06	12.66	1.09	3.05	101.33	2.975	0.006	1.997		0.023	1.754	0.863	0.130	0.263	8.011		0.9	4.4	29.0	7.7	57.9	0.2	99.2
17	36.37		20.69	0.01	0.87	26.38	13.80	1.43	1.16	100.70	2.960		1.986	0.001	0.053	1.796	0.951	0.173	0.101	8.021		2.7	5.8	32.1	0.7	58.6		98.4
18	36.31	0.06	21.09	0.07	0.49	26.05	14.31	1.26	1.43	100.07	2.945	0.004	2.017	0.005	0.030	1.767	0.983	0.152	0.125	8.027	0.2	1.4	5.2	33.3	2.5	57.3	0.1	98.0
19	36.60	0.32	20.46	0.03	0.93	22.29	13.23	0.85	5.60	100.31	2.967	0.020	1.955	0.002	0.057	1.510	0.908	0.103	0.486	8.008	0.1	2.2	3.4	30.4	13.3	48.9	0.7	99.5
20	36.75	0.13	20.56	0.10	1.01	22.99	11.74	0.68	6.69	100.66	2.967	0.008	1.957	0.006	0.061	1.552	0.803	0.081	0.578	8.014	0.3	2.8	2.7	27.0	16.0	50.8	0.3	99.0
21	36.29	0.12	20.56	0.05	1.10	26.13	7.56	0.74	7.31	99.88	2.950	0.007	1.972	0.003	0.068	1.776	0.521	0.089	0.637	8.023	0.2	3.2	3.0	17.8	17.9	57.8	0.2	98.3
22	36.88	0.11	20.49	0.17	0.46	28.75	4.73	0.74	7.31	99.64	2.994	0.007	1.961	0.011	0.028	1.952	0.325	0.089	0.636	8.001	0.5	1.3	3.0	10.8	19.3	65.0	0.1	99.8
23	37.28		20.93		0.36	31.29	2.60	1.12	6.87	100.45	2.996		1.983		0.022	2.102	0.177	0.134	0.591	8.004		1.1	4.5	5.9	18.8	69.9		99.8
24	36.77		20.72		0.54	32.84	1.42	1.34	6.00	99.64	2.984		1.983		0.033	2.229	0.098	0.163	0.521	8.010		1.7	5.4	3.3	15.8	73.8		99.3
25	37.21	0.09	20.90	0.06	0.34	34.21	0.94	1.72	5.05	100.51	2.990	0.006	1.980	0.004	0.020	2.299	0.064	0.207	0.435	8.004	0.2	0.8	6.9	2.1	13.5	76.5	0.2	99.8
26	36.99	0.18	21.04		0.35	35.49	0.67	2.05	3.85	100.60	2.974	0.009	1.995		0.021	2.386	0.046	0.246	0.332	8.010		0.7	8.2	1.5	10.1	79.1	0.3	99.4
27	36.99	0.05	20.95	0.01	0.33	35.53	0.63	2.25	3.44	100.18	2.984	0.003	1.993		0.020	2.397	0.043	0.270	0.297	8.008		0.9	9.0	1.5	8.9	79.5	0.1	99.5
28	37.07	0.16	20.80	0.09	0.53	33.40	0.36	2.53	5.03	99.98	2.981	0.010	1.972	0.005	0.032	2.246	0.025	0.303	0.433	8.006	0.3	1.3	10.1	0.8	12.6	74.5	0.3	99.6
29	37.29	0.02	21.37	0.02	0.28	32.43	0.39	2.63	6.04	100.49	2.972	0.001	2.008	0.001	0.017	2.161	0.027	0.312	0.516	8.015	0.1	0.8	10.5	0.9	16.4	71.3		98.9
"average comp"	36.89	0.09	20.82	0.03	0.56	29.46	6.47	1.39	4.77	100.49	2.977	0.006	1.981	0.002	0.034	1.988	0.442	0.167	0.412	8.010	0.1	1.5	5.6	14.8	12.0	65.8	0.2	99.3
57/88 2a 1	37.39	0.04	20.90	0.04		34.36	0.40	2.52	4.21	99.87	3.008	0.003	1.982	0.003		2.312	0.027	0.302	0.383	7.998	0.1		10.2	0.9	12.1	76.8		99.2
2	37.62	0.10	21.28	0.04		34.23	0.61	1.92	4.80	100.61	3.005	0.006	2.005	0.003		2.287	0.041	0.229	0.411	7.987	0.1		7.7	1.4	13.7	77.1		99.1
3	37.13	0.03	20.84		0.53	32.19	1.12	1.61	6.42	99.68	2.999	0.002	1.966		0.032	2.175	0.076	0.194	0.556	8.001		1.6	6.5	2.5	16.9	72.4		99.9
4	37.20	0.03	20.54	0.04		29.88	3.88	0.89	6.62	99.07	3.027	0.002	1.971	0.003		2.033	0.267	0.108	0.577	7.987	0.1		3.6	9.0	19.4	67.8		98.8
5	37.15	0.22	20.29	0.07		24.47	10.50	0.53	6.27	99.49	3.024	0.013	1.947	0.005		1.665	0.724	0.065	0.548	7.989	0.2		2.2	24.7	18.4	54.4		97.7
6	36.86	0.15	20.25			17.21	18.00	0.18	5.86	98.51	3.031	0.009	1.963			1.183	1.254	0.022	0.516	7.979			0.7	42.8	17.5	39.1		98.4
7	36.77	0.17	20.47			18.72	18.62	0.35	5.99	99.10	3.008	0.010	1.975			1.144	1.290	0.043	0.525	7.996			1.5	43.6	17.7	37.2		98.8
8	37.05	0.13	20.65	0.05		24.00	15.18	1.28	1.27	99.62	3.023	0.008	1.987	0.003		1.637	1.049	0.158	0.111	7.975	0.2		5.3	35.5	3.6	55.4		98.8
9	36.95	0.12	21.37			24.54	12.15	1.73	3.07	99.92	2.985	0.007	2.036			1.658	0.831	0.208	0.266	7.991			7.0	28.1	9.0	56.0		98.9
10	37.44	0.08	21.29	0.10		25.50	11.96	1.83	2.77	100.97	2.997	0.005	2.010	0.006		1.707	0.811	0.218	0.238	7.992	0.3		7.3	27.3	7.7	57.4		99.2
11	36.80	0.19	20.60	0.05		25.16	12.41	1.33	2.92	99.47	3.004	0.012	1.982	0.003		1.717	0.858	0.162	0.255	7.993	0.2		5.4	28.8	8.4	57.2		99.3
12	37.22	0.25	20.96	0.05		24.97	12.58	1.38	2.73	100.14	3.009	0.015	1.998	0.003		1.688	0.861	0.168	0.236	7.977	0.2		5.6	29.2	7.8	57.2		98.7
13	36.51	0.10	20.76			24.23	13.38	1.22	2.50	98.70	3.002	0.006	2.012			1.666	0.931	0.149	0.220	7.987			5.0	31.4	7.4	56.1		99.1
14	37.49	0.18	21.09			24.49	12.84	1.43	3.07	100.58	3.013	0.011	1.999			1.646	0.874	0.172	0.264	7.978			5.8	29.6	8.9	55.7		98.8
15	36.72	0.15	20.65			25.04	13.94	1.75	1.20	99.45	3.002	0.009	1.990			1.711	0.965	0.213	0.105	7.985			7.1	32.3	3.5	57.0		99.5
16	37.32	0.13	20.86	0.14		21.18	14.36	0.97	5.12	100.07	3.012	0.008	1.985			1.429	0.982	0.117	0.443	7.985	0.4		3.9	33.0	14.5	48.1		99.2
17	37.54	0.23	20.90	0.02		20.05	15.44	0.75	4.67	99.60	3.037	0.014	1.993	0.002		1.356	1.058	0.090	0.405	7.954	0.1		3.1	36.4	13.8	46.6		97.5
57/88 No 2b 1	37.11	0.03	20.96		0.43	34.03	0.68	2.24	4.70	100.18	2.985	0.002	1.987		0.026	2.289	0.048	0.268	0.405	8.008		1.2	9.0	1.5	12.3	75.9	0.1	99.5
rim 2	37.19	0.06	21.22		0.11	34.01	0.84	1.48	5.89	100.60	2.983	0.004	2.008		0.007	2.281	0.043	0.177	0.506	8.008		0.2	5.9	1.4	16.8	75.7	0.1	99.5
3	37.20		20.77		0.85	32.79	1.30	1.32	6.43	100.46	2.992		1.969		0.039	2.205	0.089	0.158	0.554	8.006		2.0	5.3	3.0	16.5	73.2		99.7
4	36.66	0.03	20.84	0.03	0.75	31.63	2.22	1.17	6.78	100.11	2.964	0.002	1.987	0.002	0.046	2.138	0.152	0.141	0.587	8.018	0.1	2.3	4.7	5.1	17.4	70.3	0.1	98.7
5	36.53	0.09	20.62		0.57	30.45	3.98	1.05	6.10	99.38	2.977	0.005	1.982		0.035	2.075	0.275	0.128	0.533	8.010		1.6	4.3	9.2	16.1	68.6	0.2	99.3
6	36.94		20.41	0.06	0.10	26.75	7.26	0.78	7.02	100.25	2.987		1.946	0.004	0.063	1.809	0.497	0.094	0.608	8.008	0.2	3.2	3.2	16.6	17.0	59.8		99.5
7	36.60	0.11	20.16	0.09	0.75	24.77	9.77	0.54	6.41	99.25	2.996	0.007	1.946	0.006	0.046	1.695	0.677	0.068	0.562	8.000	0.3	2.3	2.2	22.6	16.2	56.4		99.8
8	37.12	0.09	20.31		1.08	19.80	15.41	0.58	6.24	100.64	2.996	0.005	1.933		0.066	1.336	1.054	0.071	0.540	8.001		3.3	2.4	35.2	14.7	44.4		99.9
9	36.64	0.06	20.96		0.66	18.88	17.57	0.10	5.84	100.44	2.976	0.004	1.981		0.040	1.282	1.209	0.012	0.508	8.012		1.9	0.4	40.6	15.0	42.0	0.1	99.2
10	36.85	0.21	20.74	0.04	1.03	15.98	19.95	0.68	5.84	101.32	2.960	0.013	1.964	0.002	0.062	1.073	1.357	0.082	0.503	8.015	0.1	2.7	2.7	45.7	13.7	34.7	0.4	98.9
11	36.76	0.21	20.84		0.56	20.99	16.37	0.84	4.30	100.86	2.969	0.013	1.985		0.034	1.418	1.119	0.101	0.372	8.011		1.3	3.4	37.5	10.8	46.6	0.4	99.3
12	36.52	0.21	20.91		0.33	23.04	17.22	1.33	1.20	100.77	2.965	0.013	2.002		0.020	1.564	1.184	0.161	0.104	8.013		0.6	5.4	39.8	2.5	51.3	0.4	99.1
13	36.23	0.13	20.26	0.08	0.45	24.22	15.20	1.31	1.24	99.12	2.988	0.008	1.971	0.005	0.028	1.670	1.062	0.162	0.110	8.003	0.3	1.1	5.4	35.4	2.0	55.5	0.3	99.8
14	36.32	0.07	21.05	0.02	0.35	24.57	15.66	1.51	1.04	100.59	2.954	0.005	2.018	0.001	0.021	1.671	1.078	0.183	0.091	8.022	0.1	0.9	6.2	36.4	1.9	54.3	0.2	98.4
core 15	36.59	0.05	20.99		0.32	24.54	15.85	1.32	1.16	100.82	2.969	0.003	2.008		0.020	1.665	1.090	0.159	0.101	8.015		0.9	5.4	36.7	2.4	54.8	0.1	98.9
small grt rim	36.80	0.08	21.08		0.49	34.04	0.76	2.08	4.91	100.24	2.984	0.005	2.002		0.029	2.292	0.052	0.250	0.424	8.017		1.3	8.4	1.7	12.8	75.6	0.2	98.8
small grt core	37.13	0.03	20.55	0.02		32.78	0.95	1.22	6.47	99.15	3.018	0.002	1.970	0.001		2.228	0.065	0.148	0.563	7.996	0.1		5.0	2.2	19.0	73.7		98.8
small grt rim	37.77	0.09	21.22	0.08	0.31	33.00	0.09	2.59	6.00	101.16	2.990	0.005	1.981	0.006	0.018	2.184	0.006	0.305	0.509	8.004	0.3	0.7	10.2	0.2	15.6	72.6	0.2	99.8
small grt core	37.03	0.07	20.91	0.05	0.29	34.96	0.60	2.46	3.59	99.94	2.987	0.004	1.988	0.003	0.017	2.358	0.041	0.224	0.310	8.006	0.2	0.7	7.9	1.4	11.1	78.3	0.2	99.6